



National
Aeronautics and
Space
Administration

NASA CR-168243
GARRETT 21-4742-2

NASA-CR-168243-VOL-2
19840004197

AEROTHERMAL MODELING PROGRAM PHASE I FINAL REPORT

by

**R. Srinivasan, R. Reynolds, I. Ball,
R. Berry, K. Johnson, and H. Mongia**

Garrett Turbine Engine Company
A Division of The Garrett Corporation

August 1983

Volume II

LIBRARY COPY

OCT 11 1989

**LANGLEY RESEARCH CENTER
LIBRARY NASA
HAMPTON, VIRGINIA**

Prepared for

**NATIONAL AERONAUTICS AND SPACE ADMINISTRATION
NASA-Lewis Research Center
Contract NAS3-23523**

TABLE OF CONTENTS
VOLUME I

	<u>Page</u>
LIST OF ILLUSTRATIONS	vii
LIST OF TABLES	xxvii
SECTION I	
1.0 SUMMARY	1
SECTION II	
2.0 INTRODUCTION	3
2.1 Aerothermal Modeling Background	4
2.2 Garrett Empirical/Analytical Combustor Design Approach	6
SECTION III	
3.0 DESCRIPTION OF ANALYTICAL MODELS	13
3.1 The Analytical Models	13
3.2 Description of Turbulence and Scalar Transport	19
3.3 Gaseous Fuel Combustion Models	39
3.4 Spray Evaporation/Combustion Models	59
3.5 Soot Formation and Oxidation	70
3.6 Radiation Modeling	79
SECTION IV	
4.0 DESCRIPTION OF THE COMPUTATIONAL SCHEME	85
4.1 Description of the Numerical Method	85
4.2 Boundary Conditions	90
4.3 Convergence Criteria	92
SECTION V	
5.0 DATA BASE FOR BENCHMARK QUALITY TEST CASES	93
5.1 Data Base from Ideal Element Tests	93
5.2 Data Base from Garrett Gas Turbine Combustors	142
SECTION VI	
6.0 SIMPLE FLOWS	153
6.1 Flow Over a Flat Plate	153
6.2 Plane Couette Flow	165
6.3 Developing Flow in a Two-Dimensional Channel	175
6.4 Developing Pipe Flow	180
6.5 Fully Developed Pipe Flow	187
6.6 Two-Stream Mixing Layer	194
6.7 Mixing of Coaxial Jets in Ambient Air	201
6.8 Free Circular Jet	209
6.9 Flow Over a Heated Flat Plate	222
6.10 Plug Flow Reactor	237

TABLE OF CONTENTS (CONTD)

	<u>Page</u>
6.11 Laminar Diffusion Flame	240
6.12 Turbulent Premixed Flame in a Rectangular Duct	254
6.13 Free Methane Turbulent Jet Flame	288
VOLUME II	
7.0 COMPLEX NONSWIRLING FLOWS	303
7.1 Flow in a Curved Channel	303
7.2 Flow Over a Backward-Facing Plane Step	329
7.3 Flow Through a Sudden Pipe Expansion	360
7.4 Flow Over a Circular Ring	363
7.5 Flow Around a Wedge-Shaped Flameholder	366
7.6 Flow Around a Confined Disk	369
7.7 Confined Coaxial Jet Expansion	371
7.8 Nonreacting and Reacting Flow Behind a Step	384
7.9 Opposed Reacting Jet Flow	407
7.10 Axisymmetric Combustor with Coaxial Fuel and Air Jets	423
8.0 SWIRLING FLOWS	439
8.1 Free Swirling Jet in a Stagnant Medium	439
8.2 Nonreacting Swirling Combustor	465
8.3 Confined Swirler Flow	469
8.4 Swirl Combustor with Cooling Air	475
8.5 Swirling Flow in a Pipe Expansion	504
8.6 Confined Swirl-Driven Flow	528
8.7 Combusting Spray in Confined Swirling Flow	539
9.0 DILUTION JET MIXING VALIDATION	549
9.1 Effects of Finite-Difference Grid Distribution	549
9.2 Single-Sided Injection: Effects of Jet Size and Spacing	579
9.3 Single-Sided Injection: Effects of Jet Momentum Ratio and Cross-Stream Temperature Profile	585
9.4 Two-Side Jet Injection	595
10.0 CONCLUSIONS AND RECOMMENDATIONS	605
10.1 Conclusions	605
10.2 Recommendations	610
REFERENCES	611

LIST OF ILLUSTRATIONS

<u>Figure</u>	<u>Title</u>	<u>Page</u>
2.2-1	Combustor Models and Region of Application	7
2.2-2	Combustor Design Methodology	9
4.1-1	Typical Grid Spacing of the Swirling Flow Problem and Control Value around a Point P	89
5.2-1	Nonreacting Swirling Combustor Flow Validation	143
5.2-2	Cold Flow Can Combustor Mapping Setup and Test Conditions	144
5.2-3	Can Combustor for Reacting Flow Mapping	145
5.2-4	Natural Gas Nozzle and Airblast Nozzle Used for the Can Combustor Mapping	146
5.2-5	Axially Staged Burning Zones of the Piloted PM/PV Combustion System	148
5.2-6	Emission Sampling Probe Stations Inside the TFE731 Combustor	149
5.2-7	Schematic of Emissions Probe and Measurement Locations for Fuel/Air Rate Profiles in the UT76 Combustor	151
6.1-1	Watts and Brundrett ⁶⁷ Setup for Turbulent Flow over a Flat Plate	158
6.1-2	Turbulent Boundary Layer Mean Velocity Profiles with the Standard k- ϵ Model	159
6.1-3	Turbulent Boundary Layer Mean Velocity Profiles with the k- ϵ Model and Chien's Low Reynolds Number Correction (Low Reynolds Number (k- ϵ Model)	160
6.1-4	Turbulent Boundary Layer Mean Velocity Profiles with the Algebraic Stress Model (ASM)	161
6.1-5	Turbulent Boundary Layer Mean Velocity Profiles with ASM Modified by Low Reynolds Number Correction	162
6.1-6	Turbulent Kinetic Energy Profiles Predicted by the Four Turbulence Models	163

LIST OF ILLUSTRATIONS (CONTD)

<u>Figure</u>	<u>Title</u>	<u>Page</u>
6.1-7	Fluctuating Components of Axial, Radial and Transverse Velocities (u' , v' and w') Predicted by ASM, and ASM with Low Reynolds Number Correction	164
6.2-1	Geometry of Plane Couette Flow	168
6.2-2	Comparison Between $k-\epsilon$ Predictions and Measured Couette Flow Axial Velocity Profile (u_+ versus y_+)	169
6.2-3	Comparison Between $k-\epsilon$ Model Predictions and Measured Shear Stress Profile (normalized by wall shear value)	169
6.2-4	Shear Stress Normalized by Turbulence Kinetic Energy (uv/K) Standard $k-\epsilon$ Model With $C_D = 0.09$	170
6.2-5	$k-\epsilon$ Model Predicted uv/k Profiles With $C_D = 0.144$	170
6.2-6	$k-\epsilon$ Model Predicted U_+ With $C_D = 0.144$	171
6.2-7	ASM Prediction and Measured u_+ Versus y_+ Profiles	171
6.2-8	ASM Prediction and Measured Normalized Shear Stress Profile	172
6.2-9	Shear Stress (uv) Normalized by Turbulence Kinetic Energy Predicted by ASM Versus Increased Data	172
6.2-10	Correlation Coefficient ($\overline{uv}/(\overline{uv}/u' \times v')$) Predicted by ASM Versus Measurements	173
6.2-11	ASM Predictions and Measured Axial Turbulence Intensity (u'/u^*)	173
6.2-12	ASM Predictions and Measured Radial Turbulence Intensity	174
6.2-13	ASM Predictions and Measured w'	174
6.3-1	Geometry of Developing Flow in a Two-Dimensional Duct	176
6.3-2	Predicted and Measured Distributions of Center-line Axial Velocity for Developing Flow in a Two-Dimensional Duct	177

LIST OF ILLUSTRATIONS (CONTD)

<u>Figure</u>	<u>Title</u>	<u>Page</u>
6.3-3	Predicted and Measured Mean Velocity Profiles at Different Axial Stations for Developing Channel Flow	178
6.3-4	Predicted and Measured Wall Shear Stress Distributions for Developing Flow in a Two-Dimensional Duct	179
6.4-1	Developing Pipe Flow Setup of Barbin and Jones ⁶⁸	182
6.4-2	Comparison Between k- ϵ Model Predictions and Profiles of Axial Velocity at Different Axial Stations in a Developing Pipe Flow (U_b = The Average Flow Velocity)	183
6.4-3	Comparison Between ASM Predictions and Measured Axial Velocity Profiles; $D = 20$ cm, $U_b = 33.17$ m/s	184
6.4-4	Comparison Between ASM Predictions and Measurements for Nondimensionalized Axial Turbulence Velocity Fluctuations	185
6.4-5	Comparison Between ASM Predictions and Measurements for Nondimensionalized Circumferential Turbulence Velocity Fluctuations	186
6.5-1	Geometry of the Pipe Flow	189
6.5-2	Low Reynolds k- ϵ Model Axial Velocity Profile	190
6.5-3	Low Reynolds k- ϵ Model Turbulence Kinetic Energy Profile	190
6.5-4	ASM With Low Reynolds Number Correction -- Axial Velocity Profile	191
6.5-5	ASM With Low Reynolds Number Correction -- Turbulence Kinetic Energy Profile	191
6.5-6	u'/u^* Profile	192
6.5-7	v'/u^* Profile	192
6.5-8	w'/u^* Profile	193
6.5-9	\overline{uv}/u_*^2 Profile	193

LIST OF ILLUSTRATIONS (CONTD)

<u>Figure</u>	<u>Title</u>	<u>Page</u>
6.6-1	Two-Stream Mixing-Layer Setup of Saiy and Peerless ⁶⁰	196
6.6-2	Mixing Layer Mean Axial Velocity and Turbulent Kinetic Energy (TKE) Profiles Predicted by the Standard k- ϵ Model	197
6.6-3	Mixing Layer Mean Axial Velocity Profiles Predicted by the Algebraic Stress Model (ASM)	198
6.6-4	Mixing Layer Fluctuating Velocity Components (u' , v' and w') Predicted by ASM	199
6.6-5	Mixing Layer Turbulent Kinetic Energy and Shear Stress Profiles Predicted by ASM	200
6.7-1	Coaxial-Jets Mixing Setup of Champagne et al ⁵⁹	203
6.7-2	Comparison Between k- ϵ Model Predictions and Measured Axial Velocity Profiles of Coaxial Jets in Ambient Air	204
6.7-3	Comparison Between ASM Predictions and Measured Axial Velocity Profiles of Coaxial Jets in Ambient Air	205
6.7-4	Predicted and Measured Profiles of RMS Axial Velocity (u') for Coaxial Jets in Ambient Air	206
6.7-5	Predicted and Measured Profiles of Fluctuating Radial Velocity Component (v')	207
6.7-6	Predicted and Measured Sheer Stress (\overline{uv}) Profiles for the Coaxial Jets in Ambient Air	208
6.8-1	Geometry of Single Free Jet Setup Studied by Wygnanski and Fiedler	212
6.8-2	Comparison Between k- ϵ Model Predictions and Measured Axial Velocity Profiles, Initial Jet Velocity = 51 m/s Initial Jet Diameter D = 26.4 mm	213
6.8-3	Modified k- ϵ Model Predictions with C_D and C_2 Constants Given by Equations (141) and (142)	214

LIST OF ILLUSTRATIONS (CONTD)

<u>Figure</u>	<u>Title</u>	<u>Page</u>
6.8-4	Modified k- ϵ Model (k- ϵ 1) Predictions with C_D as given by Equation 62	215
6.8-5	Modified k- ϵ Model (k- ϵ 2) Predictions with C_2 and C_D as Given by Equations 60 and 62	216
6.8-6	Comparison Between ASM Predictions and Measured Axial Velocity Profiles of a Free Jet	217
6.8-7	Comparison Between ASM Predictions and Measurements for Axial RMS Turbulence Velocity Fluctuations	218
6.8-8	Comparison Between ASM Predictions and Measurements for Radial RMS Turbulence Velocity Fluctuations	219
6.8-9	Comparison Between ASM Predictions and Measurements for Circumferential RMS Turbulence Velocity Fluctuations	220
6.8-10	Comparison Between ASM Predictions and Measurements for Turbulent Shear Stress	221
6.9-1	Geometry of Flow Over a Flat Plate with Step Change in Temperature	227
6.9-2	k- ϵ Model Predictions and Measured Mean Temperature Profile on a Flat Plate with Step Change in Temperature	228
6.9-3	k- ϵ Model Prediction, and Measured RMS Temperature Normalized by $(T_{wo} - T_{\infty})$	229
6.9-4	k- ϵ Model Predictions and Measured $(\overline{vT'})$ Normalized by $U (T_{wo} - T_{\infty})$	230
6.9-5	ASM Predictions of Mean Temperature Profile	231
6.9-6	ASM Predictions of RMS Temperature Profile	232
6.9-7	ASM Predictions of $(\overline{vT'})$	233
6.9-8	ASTM Predictions of Mean Temperature Profiles	234

LIST OF ILLUSTRATIONS (CONTD)

<u>Figure</u>	<u>Title</u>	<u>Page</u>
6.9-9	ASTM Predictions of the RMS Temperature Profile	235
6.9-10	ASTM Predictions of ($\overline{vT'}$) Profiles	236
6.10-1	Princeton High Temperature Plug Flow Reactor	238
6.10-2	Comparison of 2-Step and 4-Step Kinetic Scheme With Lean Propane Premixed Flame Data from High Temperature Plug Flow Reactor	239
6.11-1	Schematic of Laminar Diffusion Flame Setup Used by Mitchell	242
6.11-2	Comparison Between Two-Step Model Predictions and Measurements for Axial Velocity and Temperature Profiles of the Mitchell's Laminar Diffusion Flame at 1.2 cm Above the Burner Plate	243
6.11-3	Two-Step Predictions and Measurements for CH ₄ , CO ₂ , H ₂ O and O ₂ Profiles, X = 1.2 cm	244
6.11-4	Two-Step Predictions and Measurements for N ₂ and CO Profiles, X = 1.2 cm	244
6.11-5	Comparison Between Two-Step Predictions and Measurements of Velocity and Temperature Profiles of the Mitchell's Laminar Diffusion Flame at X = 2.4 cm	245
6.11-6	Predicted and Measured Species Profiles at X = 2.4 cm (Two-Step)	245
6.11-7	Comparison Between Predicted and Measured Axial Velocity and Temperature Profiles and Mitchell's Laminar Diffusion Flame at X = 5.0 cm (Two-Step)	246
6.11-8	Predicted and Measured Species Profiles at X = 5.0 cm (Two Step)	246
6.11-9	4-Step Scheme, Axial Velocity Profiles	247
6.11-10	4-Step Scheme, Temperature Profiles	248
6.11-11	4-Step Scheme, Methane Profiles	249

LIST OF ILLUSTRATIONS (CONTD)

<u>Figure</u>	<u>Title</u>	<u>Page</u>
6.11-12	4-Step Scheme, CO ₂ Profiles	250
6.11-13	4-Step Scheme, CO Profiles	251
6.11-14	4-Step Scheme, O ₂ Profiles	252
6.11-15	4-Step Scheme, H ₂ O Profiles	253
6.12-1	Geometry of Turbulent Premixed Flame in a Rectangular Duct	259
6.12-2	Predicted Velocity Profiles With Design Criteria Rate Constants	260
6.12-3	Predicted Unburned Fuel Profiles With Design Criteria Rate Constants	261
6.12-4	Predicted CO Profiles With Design Criteria Rate Constants	262
6.12-5	Predicted Temperature Profiles With Design Criteria Rate Constants	263
6.12-6	Predicted O ₂ Mass Fraction With Design Criteria Rate Constants	264
6.12-7	Predicted CO ₂ Profiles With Design Criteria Rate Constants	265
6.12-8	Predicted H ₂ O Profiles With Design Criteria Rate Constants	266
6.12-9	Predicted Velocity Profiles With PM/PV Rate Constants	267
6.12-10	Predicted Unburned Fuel Profiles With PM/PV Rate Constants	268
6.12-11	Predicted CO ₂ Profiles With PM/PV Rate Constants	269
6.12-12	Predicted CO Profiles With PM/PV Rate Constants	270
6.12-13	Predicted Temperature Profiles With PM/PV Rate Constants	271
6.12-14	Predicted O ₂ Profiles With PM/PV Rate Constants	272

LIST OF ILLUSTRATIONS (CONTD)

<u>Figure</u>	<u>Title</u>	<u>Page</u>
6.12-15	Predicted H ₂ O Profiles With PM/PV Rate Constants	273
6.12-16	Predicted Velocity Profiles with the 4-Step Scheme	273
6.12-17	Predicted Unburned Fuel Profiles With the 4-Step Scheme	275
6.12-18	Predicted CO Profiles With the 4-Step Scheme	276
6.12-19	Predicted Temperature Profiles With the 4-Step Scheme	277
6.12-20	Predicted O ₂ Profiles With the 4-Step Scheme	278
6.12-21	Predicted CO ₂ Profiles With the 4-Step Scheme	279
6.12-22	Predicted H ₂ O Profiles With the 4-Step Scheme	280
6.12-23	4-Step Scheme With Modified Rate Constants for Fuel and Intermediate Fuel Reaction Steps (Modified 4-Step) Axial Velocity Profile	281
6.12-24	Modified 4-Step -- Unburned Fuel Profiles	282
6.12-25	Modified 4-Step CO Profiles	283
6.12-26	Modified 4-Step -- Temperature Profiles	284
6.12-27	Modified 4-Step -- O ₂ Profiles	285
6.12-28	Modified 4-Step -- CO ₂ Profiles	286
6.12-29	Modified 4-Step -- H ₂ O Profiles	287
6.13-1	Geometry of the Free Methane Turbulent Jet Flame Test Setup	293
6.13-2	Comparison Between Bilger Model Predictions With Measured Centerline Profiles of Temperature, CO, CO ₂ and O ₂ for Hassan and Lockwood Methane Jet Flame	294
6.13-3	Radial Profiles of Total Fuel (Bilger's Model)	295
6.13-4	Radial Profiles of Unburned Fuel Mass Fraction	296

LIST OF ILLUSTRATIONS (CONTD)

<u>Figure</u>	<u>Title</u>	<u>Page</u>
6.13-5	Radial Profiles of Temperature (Bilger's Model)	297
6.13-6	Radial Profiles of CO (Bilger's Model)	298
6.13-7	Radial Profiles of H ₂ (Bilger's Model)	299
6.13-8	Radial Profiles of O ₂ (Bilger's Model)	300
6.13-9	Radial Profiles of CO ₂ (Bilger's Model)	301
7.1-1	Configuration of the Curved Channel Test Setup	308
7.1-2	Comparison Between Predictions (k- ϵ Model) and Measurement Along the Inner (Convex) Wall	309
7.1-3	k- ϵ Model Velocity Profiles Along the Outer (Concave) Wall	310
7.1-4	k- ϵ Model With Streamline Curvature Correction -- Axial Velocity Profile Along the Inner (Convex) Wall	311
7.1-5	k- ϵ Model With Streamline Curvature Correction -- Axial Velocity Profile Along the Outer (Concave) Wall	312
7.1-6	ASM Prediction and Measured Axial Velocity Profiles Along the Inner (Convex) Wall	313
7.1-7	ASM Predictions and Measured Axial Velocity Profiles Along the Outer (Concave) Wall	314
7.1-8	ASM Predictions and Measured RMS Axial Velocity Profiles Along the Inner (Convex) Wall	315
7.1-9	ASM Predictions and Measured RMS Axial Velocity Profiles Along the Outer (Concave) Wall	316
7.1-10	ASM Predictions and Measured RMS Radial Velocity Profiles Along the Inner (Convex) Wall	317
7.1-11	ASM Predictions and Measured RMS Radial Velocity Profiles Along the Outer (Concave) Wall	318

LIST OF ILLUSTRATIONS (CONTD)

<u>Figure</u>	<u>Title</u>	<u>Page</u>
7.1-12	ASM Predictions and Measured Shear Stress (uv) Profiles Along the Inner (Convex) Wall	319
7.1-13	ASM Predictions and Measured Shear Stress (uv) Profiles Along the Outer (Concave) Wall	320
7.1-14	ASM With Streamline Curvature Correction -- Axial Velocity Profiles Along the Inner (Convex) Wall	321
7.1-15	ASM With Streamline Curvature Correction -- Axial Velocity Profiles Along the Outer (Concave) Wall	322
7.1-16	ASM With Streamline Curvature Correction -- RMS Axial Velocity Profiles Along the Inner (Convex) Wall	323
7.1-17	ASM With Streamline Curvature Correction -- RMS Axial Velocity Profiles Along the Outer (Concave) Wall	324
7.1-18	ASM With Streamline Curvature Correction -- RMS Radial-Velocity Profiles Along the Inner (Convex) Wall	325
7.1-19	AMS With Streamline Correction -- RMS Radial-Velocity Profiles Along the Outer (Concave) Wall	326
7.1-20	ASM With Streamline Curvature Correction -- uv Profiles Along the Inner (Convex) Wall	327
7.1-21	ASM With Streamline Curvature Correction -- uv Profiles Along the Outer (Concave) Wall	328
7.2-1	Geometry of the Backward Facing Plane Step Test Rig	336
7.2-2	Partial Grid Network for the Flow Behind the 3.81-cm Step	337
7.2-3	Standard k- ϵ Model -- Mean Axial Velocity Profiles for 3.81-cm Step	338
7.2-4	Predicted Streamline Plot With the Standard k- ϵ Model	339

LIST OF ILLUSTRATIONS (CONTD)

<u>Figure</u>	<u>Title</u>	<u>Page</u>
7.2-5	k- ϵ Model With Richardson Number Correction Axial Velocity Profiles for the 3.81-cm Step	340
7.2-6	Predicted Streamline Plot With Richardson Number Correction	341
7.2-7	ASM With Richardson Number Correction -- Axial Velocity Profiles for the 3.81-cm Step	342
7.2-8	ASM With Richardson Number Correction -- Turbulence Kinetic Energy Profiles for the 3.81-cm Step	343
7.2-9	AMS With Richardson Number Correction -- RMS Axial Velocity Profiles ($\overline{u^2}/U_{Ref}^2$) for the 3.81-cm Step	345
7.2-10	ASM With Richardson Number Correction -- RMS Radial Velocity ($\overline{v^2}/U_{Ref}^2$) for the 3.81-cm Step	345
7.2-11	ASM With Richardson Number Correction -- Shear Stress (\overline{uv}/U_{Ref}^2) Distribution	346
7.2-12	Comparison Between Standard k- ϵ Model Pre- dictions and Measured Streamwise Velocity Components for 2.54-cm Step Height	347
7.2-13	k- ϵ Model With Richardson Number Correction - Axial Velocity Profile for the 2.54-cm Step	348
7.2-14	ASM with Richardson Number Correction - Axial Velocity Profile	349
7.2-15	ASM with Richardson Number Correction - Turbulence Kinetic Energy Profile	350
7.2-16	Axial Velocity Fluctuations ($\overline{u^2}/U_{Ref}^2$)	351
7.2-17	Normal Velocity Fluctuations ($\overline{v^2}/U_{Ref}^2$)	352
7.2-18	Shear Stress (\overline{uv}/u_{Ref}^2) Profiles for the 2.54-cm Step	353

LIST OF ILLUSTRATIONS (CONTD)

<u>Figure</u>	<u>Title</u>	<u>Page</u>
7.2-19	Comparison Between the Standard k- ϵ Model Predictions and Measured Streamwise Velocity Components for the 5.08 cm Step	354
7.2-20	k- ϵ Model with Richardson Number Correction - Axial Velocity Profile	355
7.2-21	ASM with Richardson Number Correction - Axial Velocity Profile	356
7.2-22	ASM with Richardson Number Correction - Axial Velocity Fluctuations (u^2/U_{Ref}^2)	357
7.2-23	Shear Stress (\overline{uv}/U_{Ref}^2) Distribution	358
7.2-24	Comparison Between Predicted and Measured Wall Static Pressure Distribution	359
7.3-1	Sudden Pipe-Expansion Setup of Moon and Rudinger ⁸⁹	361
7.3-2	Comparison Between the Standard k- ϵ Prediction and Measured Axial Velocity Profiles in a Tube With Sudden Expansion	362
7.4-1	Schematic of Logan's Setup for Studying Flow Over a Ring in a Pipe	364
7.4-2	Comparison Between Predicted and Measured Axial Velocity and Turbulent Kinetic Energy for Logan's H-Ring	365
7.5-1	Wedge-Shaped Flameholder Setup	367
7.5-2	Comparison Between Measured and Predicted Streamline Plots Around a Wedge-Shaped Flameholder	367
7.6-1	APL Combustion Tunnel Setup	370
7.6-2	Comparison Between Measured and Predicted Centerline Velocity Profile Behind a Confined Disk	370
7.7-1	Geometry of Confined Coaxial Jet Expansion Setup	374

LIST OF ILLUSTRATIONS (CONTD)

<u>Figure</u>	<u>Title</u>	<u>Page</u>
7.7-2	Finite Difference Grid Network for Confined Coaxial Jet Expansion	375
7.7-3	Standard k- ϵ Model - Axial Velocity Profiles	376
7.7-4	Standard k- ϵ Model - Turbulence Kinetic Energy Profiles	377
7.7-5	k- ϵ Model with Richardson Number Correction - Mean Axial Velocity Profiles	378
7.7-6	k- ϵ Model with Richardson Number Correction - Turbulence Kinetic Energy Profiles	379
7.7-7	ASM with Richardson Number Correction - Mean Axial Velocity Profiles	380
7.7-8	ASM with Richardson Number Correction - Fluctuating Axial Velocity Profiles	381
7.7-9	ASM with Richardson Number Correction - Fluctuating Radial Velocity Profiles	382
7.7-10	ASM with Richardson Number Correction - Shear Stress Profiles	383
7.8-1	Schematic of the Test Rig for Nonreacting and Reacting Flow Behind a Step	389
7.8-2	Comparison Between the k- ϵ Model Prediction and Measured Streamwise Velocity Components for Nonreacting Flow Behind a Step	390
7.8-3	ASM with Richardson Number Correction - Nonreacting Mean Axial Velocity Profile	391
7.8-4	ASM with Richardson Number Correction - Nonreacting Axial Turbulence Intensity Profiles	392
7.8-5	k- ϵ Model with 2-Step Reaction Scheme - Mean Axial Velocity Profiles	393
7.8-6	2-Step Reaction Scheme - Mean Temperature Profiles	394
7.8-7	Four-Step Reaction Scheme-Mean Axial Velocity Profiles	395

LIST OF ILLUSTRATIONS (CONTD)

<u>Figure</u>	<u>Title</u>	<u>Page</u>
7.8-8	Four-Step Reaction Scheme - Mean Temperature Profiles	396
7.8-9	Measured Wall Temperature Distribution Behind the Step	397
7.8-10	Two-Step Reaction Scheme with Measured Wall Temperature Distribution - Mean Axial Velocity Profiles	398
7.8-11	Two-Step Reaction Scheme With Measured Wall Temperature Distribution - Mean Temperature Profiles	399
7.8-12	Two-Step Reaction Scheme With Measured Wall Temperature Distribution - CO and CO ₂ Profiles	400
7.8-13	Four-Step Reaction Scheme With Measured T _w Distribution - Mean Axial Velocity Profiles	401
7.8-14	Four-Step Reaction Scheme With Measured T _w Distribution - Mean Temperature Profiles	402
7.8-15	Four-Step Reaction Scheme With Measured T _w Distribution - CO and CO ₂ Profiles	403
7.8-16	Four-Step Reaction Scheme With Modified Rate Constants - Mean Axial Velocity Profiles	404
7.8-17	Four-Step Reaction Scheme With Modified Rate Constants - Mean Temperature Profiles	405
7.8-18	Four-Step Scheme With Modified Rate Constants - CO and CO ₂ Profiles	406
7.9-1	Geometry of the Opposed Jet Combustion Setup	410
7.9-2	2-Step Kinetic Scheme - Mean Temperature Profile	411
7.9-3	2-Step Scheme - Unburned Fuel Profiles	412
7.9-4	2-Step Scheme - CO ₂ Profiles	413
7.9-5	2-Step Scheme - CO Profiles	414

LIST OF ILLUSTRATIONS (CONTD)

<u>Figure</u>	<u>Title</u>	<u>Page</u>
7.9-6	2-Step Scheme - H ₂ O Profiles	415
7.9-7	2-Step Scheme - O ₂ Profiles	416
7.9-8	4-Step Reaction Scheme with Original Rate Constants - Temperature Profiles	417
7.9-9	4-Step Scheme - Unburned Fuel Profiles	418
7.9-10	4-Step Scheme - CO ₂ Profiles	419
7.9-11	4-Step Scheme - CO Profiles	420
7.9-12	4-Step Scheme - H ₂ O Profiles	421
7.9-13	4-Step Scheme - O ₂ Profiles	422
7.10-1	Geometry of Axisymmetric Combustor With Coaxial Fuel and Air Jets	426
7.10-2	2-Step Scheme - Total Fuel Profiles	427
7.10-3	2-Step Scheme - Unburned Fuel Profiles	428
7.10-4	2-Step Scheme - CO and Temperature Profiles	429
7.10-5	4-Step Scheme - Total Fuel Profiles	430
7.10-6	4-Step Scheme - Unburned Fuel Profiles	431
7.10-7	4-Step Scheme - CO ₂ Profiles	432
7.10-8	4-Step Scheme - CO and Temperature Profiles	434
7.10-9	4-Step Scheme - O ₂ Profiles	435
7.10-10	4-Step Scheme - H ₂ O Profiles	436
7.10-11	4-Step Scheme - H ₂ Profiles	438
8.1-1	Test Setup for Swirling Air Injected Into Stagnant Air	446
8.1-2	Standard k-ε Model - Mean Axial Velocity Profiles	447
8.1-3	Standard k-ε Model - Mean Tangential Velocity Profile	448

LIST OF ILLUSTRATIONS (CONTD)

<u>Figure</u>	<u>Title</u>	<u>Page</u>
8.1-4	Standard k- ϵ Model with 0.7 Prandtl Number - Mean Axial Velocity Profiles	449
8.1-5	Standard k- ϵ Model with 0.7 Prandtl Number - Mean Tangential Velocity Profiles	450
8.1-6	k- ϵ 1 Turbulence Model - Mean Axial Velocity Profiles	451
8.1-7	k- ϵ 1 Turbulence Model - Mean Tangential Velocity Profiles	452
8.1-8	k- ϵ 1 Model with 0.7 Prandtl Number - Mean Axial Velocity Profiles	453
8.1-9	k- ϵ 1 Model with 0.7 Prandtl Number - Mean Tangential Velocity Profiles	454
8.1-10	k- ϵ 1 Model with Richardson Number Correction - Mean Axial Velocity Profiles	455
8.1-11	k- ϵ 1 Model with Richardson Number Correction - Mean Tangential Velocity Profiles	456
8.1-12	ASM - Mean Axial Velocity Profiles	457
8.1-13	ASM - Mean Tangential Velocity Profiles	458
8.1-14	ASM - u' Profiles	459
8.1-15	ASM - v' Profiles	460
8.1-16	ASM - w' Profiles	461
8.1-17	ASM - Shear Stress (uv) Profiles	462
8.1-18	ASM - (vw) Profiles	463
8.1-19	ASM - (uw) Profiles	464
8.2-1	Nonreacting Swirling Combustor Flow Validation	466
8.2-2	Comparison Between Measured Axial Velocity and k- ϵ Turbulence Model	467
8.2-3	Comparison Between Measured Angular Velocity and Predictions of k- ϵ Turbulence Model	468

LIST OF ILLUSTRATIONS (CONTD)

<u>Figure</u>	<u>Title</u>	<u>Page</u>
8.3-1	Configuration of the Swirling Flow Investigation at Garrett	472
8.3-2	Comparison Between Predicted and Measured Axial Velocity Profiles Behind a Confined Disk	473
8.3-3	Comparison Between Predicted and Measured Axial Velocity Profiles in Confined Recirculating Swirling Flows	474
8.4-1	Brum and Samuelson Setup for Swirl Combustor with Cooling Air	480
8.4-2	Comparison Between Measured and Predicted Centerline Axial Velocity	481
8.4-3	Comparison Between Measured and Calculated Axial Velocity Profiles	482
8.4-4	Comparison Between Measured and Calculated Swirl Velocity Profiles	484
8.4-5	Turbulence Kinetic Energy Profiles	486
8.4-6	Measured Streamline Plot	488
8.4-7	Calculated Streamline Plot	489
8.4-8	Second Set of Calculations - Centerline Axial Velocity Development	490
8.4-9	Second Set of Calculations - Axial Velocity Profiles	491
8.4-10	Second Set of Calculations - Swirl Velocity Profile	493
8.4-11	Second Set of Calculation - Turbulence Kinetic Energy Profiles	495
8.4-12	Third Set of Calculations - Centerline Axial Velocity Development	497
8.4-13	Third Set of Calculations - Axial Velocity Profiles	498

LIST OF ILLUSTRATIONS (CONTD)

<u>Figure</u>	<u>Title</u>	<u>Page</u>
8.4-14	Third Set of Calculations - Swirl Velocity Profiles	500
8.4-15	Third Set of Calculations - Turbulence Kinetic Energy Profiles	502
8.5-1	Test Setup of Swirling Flow in a Pipe Expansion	511
8.5-2	k- ϵ Model for Nonswirling Flow - Axial Velocity Profiles	512
8.5-3	k- ϵ Model with Richardson Number Correction - Axial Velocity Profiles in Nonswirling Flow Field	513
8.5-4	ASM - Axial Velocity Profiles (Nonswirling)	514
8.5-5	Nonswirling u' , v' and \overline{uv} Profiles	515
8.5-6	Comparison Between k- ϵ Model Prediction and Chaturvedi Data of Mean Axial Velocity	516
8.5-7	Chaturvedi Mean Axial Velocity Data and k- ϵ Model with Richardson Number Correction	517
8.5-8	ASM Prediction and Chaturvedi Data - Mean and Fluctuating Axial Velocity Profiles	518
8.5-9	ASM Predictions and Chaturvedi Data - \overline{uv} and \overline{v} Profiles	519
8.5-10	Standard k- ϵ Model - Mean Axial and Tangential Velocity Profiles	520
8.5-11	k- ϵ Model with Richardson Number Correction - Mean Axial and Tangential Velocity Profiles	521
8.5-12	ASM - Mean Axial and Tangential Velocity Profiles	522
8.5-13	ASM - u' , v' and \overline{uv} Profiles	523
8.5-14	ASM - w' , \overline{uw} and \overline{vw} Profiles	524
8.5-15	Reynolds Stress Shear Component (uv)	525
8.5-16	Reynolds Stress Shear Component (uw)	526

LIST OF ILLUSTRATIONS (CONTD)

<u>Figure</u>	<u>Title</u>	<u>Page</u>
8.5-17	Reynolds Stress Shear Component (vw)	527
8.6-1	Confined Swirl-Driven Flow Setup of Altgeld, Jones and Wilhelmi	531
8.6-2	Comparison Between k- ϵ Model Prediction and Measured Axial Velocity Profile in Configuration I	532
8.6-3	Configuration I - Tangential Velocity Profiles	534
8.6-4	Configuration II (Exit Baffle) - Axial Velocity Profiles	535
8.6-5	Configuration II (Exit Baffle) Tangential (Swirl) Velocity Profiles	537
8.7-1	Combusting Spray in Confined Swirling Flow (El Banhawy and Whitelaw Test Setup)	542
8.7-2	El Banhawy and Whitelaw Test Case Grid System (51 x 27)	543
8.7-3	Temperature Contours	544
8.7-4	Contour Maps of CO Volume Concentration (%)	545
8.7-5	Contour Maps of CO ₂ Volume Concentration (%)	546
8.7-6	Contour Maps of O ₂ Volume Concentration (%)	547
9.1-1	Multiple Jet Mixing Coordinate System and Important Nomenclature	556
9.1-2	Finite Difference Grid Network for Fine Grid (45x26x17) Computations	557
9.1-3	Comparison Between Data and Predictions for Test No. 1, Straight Duct, TM = Const	559
9.1-4	Finite Difference Grid Network for Coarse Grid (27x26x8) Computations	561
9.1-5	Comparison Between Data and Predictions for Test No. 1, Straight Duct, 4-Node Jet	563

LIST OF ILLUSTRATIONS (CONTD)

<u>Figure</u>	<u>Title</u>	<u>Page</u>
9.1-6	Predicted Centerplane Temperature Contours with the Fine and Coarse Grid Systems	565
9.1-7	Comparison Between Data and Predictions for Test No. 6, Test Section I, TMAIN = Const	567
9.1-8	Comparison Between Data and Predictions for Test No. 6, Straight Duct, 4-Node Jet	569
9.1-9	Predicted Centerplane Temperature Contours with the Fine and Coarse Grid Systems	571
9.1-10	Finite Difference Grid Network for Fine Grid (35x33x17) Computations	572
9.1-11	Comparison Between Data and Predictions for Test No. 50, Test Section I, TM = Const	573
9.1-12	Finite Difference Grid Network for the Finer Grid (32x29x21) Computations	575
9.1-13	Comparison Between Data and Predictions for Test No. 50, Test Section I, TM = Const	577
9.2-1	Comparison Between Data and Predictions for Test No. 02, Test Section I, TM = Const	581
9.2-2	Comparison Between Data and Predictions for Test No. 4, Test Section I, One Sided	583
9.3-1	Comparison Between Data and Predictions for Test No. 2, Test Section I, TM = Const	589
9.3-2	Measured Mainstream Inlet Profiles	591
9.3-3	Comparison Between Data and Predictions for Test No. 13, Test Section I, Top Cold TM	593
9.4-1	Schematic of the Test Setup and Typical Orifice Configurations for Two-Sided Jet Injection	599
9.4-2	Comparison Between Data and Predictions for Test No. 2, Test Section I, Opposed (INL)	601
9.4-3	Comparison Between Data and Predictions for Test No. 28, Test Section I, Opposed (STG)	603

LIST OF TABLES

<u>Table</u>	<u>Title</u>	<u>Page</u>
1	Computer Models and Physical Submodels (Modules)	14
2	Source Terms for Chemical Species	42
3	Simple Flows	96
4	Streamline Curvature Effects	101
5	Recirculating Flows	103
6	Swirling Flows	109
7	Scalar Transport	114
8	Laminar Premixed Flames	119
9	Laminar Diffusion Flames	120
10	Turbulent Premixed Flames	121
11	Turbulent Diffusion Flames	122
12	Spray Evaporation and Combustion	132
13	Soot Data	138
14	Two-Step Rate Constants for Garrett/AVLABS and Premixed/Prevaporizing Reaction	254
15	Rate Constants for 4-Step Kinetic Scheme	257
16	Grid Note Distribution	330
17	Ring Configurations Investigated by Logan, et al	363

SECTION VII

7.0 COMPLEX NONSWIRLING FLOWS

For the case of simple flows, the $k-\epsilon$ model with the low Reynolds number correction in the near-wall treatment accurately predicts the mean flow properties. The ASM accurately predicts the Reynolds stress components and the mean flow properties. However, in complex flows, extra strain rates are present due to streamline curvature rising out of recirculation or curved duct geometries. This extra strain rate causes the turbulence structure to be anisotropic, and it is essential to evaluate the combustor performance submodels for complex flows. The benchmark test cases for complex nonswirling flows are identified in Tables 4 and 5. Among the complex flows, the nonswirling flow will be studied first. Swirling flow computations are presented in Section 8.0.

7.1 Flow in a Curved Channel

One of the benchmark test cases studied in the complex flow category is the flow in a curved duct. Measurements for the flow in a curved duct were made by Shivaprasad, et al.,⁷⁴ in a test setup shown in Figure 7.1-1, using an X-wire probe. Measurements of mean velocity and turbulence velocity correlations were made along both inner and outer walls (see Table 4).

Computations for this flow were made using a 2-D parabolic scheme with 100 nodal points across the duct. The nodes were closely spaced near the walls and were spaced further apart near the center of the duct. The initial profiles were specified at 1.03 m downstream of the inlet station, using the measured velocity profiles. In all these cases, boundary conditions near the walls were specified using Chien's low Reynolds number correction scheme.

Computations were made with:

- o k- ϵ model
- o k- ϵ model with streamline curvature correction
- o ASM
- o ASM with streamline curvature correction.

Figure 7.1-2 presents the predicted mean velocity profiles (solid lines) using the standard k- ϵ model and the measured profiles (symbols) along the inner convex walls. The agreement between data and predictions is good. The predicted profiles are slightly fuller than the measured results. The comparison between predicted and measured axial velocity profiles along the outer concave wall is presented in Figure 7.1-3. For this wall, the predicted velocity profiles (solid line) are fuller than the data (symbols). The predictions gradually tend to approach the measured values at $x = 1.148$ m.

In curved channel flows, the streamline curvature creates an extra strain rate on the turbulence production. A measure of the extra strain rate is given by the Richardson number. For this geometry, the Richardson number is defined by

$$Ri_c = \frac{2 \left(\frac{U}{R} \right)^2 \frac{\partial}{\partial y} (UR)}{(\partial U / \partial y)^2}$$

where U is the local mean axial velocity and R is the radius of curvature of the duct. The Richardson number was used to modify the turbulence model constant C_2 in the form outlined in Section 3.0.

The predicted mean velocity profiles along the convex wall using the k- ϵ model with and without the Richardson number correction are presented in Figure 7.1-4. The predicted results are in

good agreement with the data. A slight improvement in correlation can be seen in the profiles by applying the Richardson number correction. The predicted results for the concave wall are shown in Figure 7.1-5. For the concave wall, the Richardson number correction slightly worsens the predicted results for mean velocity.

The predicted mean velocity along the convex wall profiles using the ASM are presented in Figure 7.1-6. The predicted mean velocity profiles are slightly fuller than the data. The ASM predictions are in good agreement with the standard $k-\epsilon$ model results (Figure 7.1-2). A similar conclusion may be reached for the predictions along the concave wall (Figure 7.1-7).

The ASM predictions for root mean square (RMS) axial velocity fluctuations (u') along the convex wall boundary layer are presented in Figure 7.1-8. The predicted u' values (solid line) are slightly larger than the data (symbols). The u' predictions along the concave wall are presented in Figure 7.1-9. These profiles are in good agreement with the data.

The predicted v' profiles along the convex wall are illustrated in Figure 7.1-10. The predicted v' values are slightly higher than the data. The v' profiles along the concave wall are shown in Figure 7.1-11. The predicted profiles along the concave wall are in much better agreement compared to the results along the convex wall. Note also that the ASM correctly predicts the partitioning of the turbulence kinetic energy into u' and v' components.

The predicted Reynolds stress component \overline{uv} along the convex wall is presented in Figure 7.1-12. The predicted values are higher than the data. The corresponding profiles along the outer concave wall are shown in Figure 7.1-13. The \overline{uv} values are slightly overpredicted initially and are underpredicted further

downstream. These profiles show the same trend as the kinetic energy profiles that can be obtained from the u' and v' values.

The predicted results using the ASM with Richardson number correction are presented in the next series of figures. Figure 7.1-14 illustrates the mean velocity profiles along the inner convex surface. Comparison between Figures 7.1-6 and 7.1-14 shows that the Richardson number correction improves the mean velocity profiles along the convex surface. Along the concave surface, however, the Richardson number correction makes the velocity profiles slightly worse, as seen in Figure 7.1-15. This indicates a need for more work on the ASM to correct the effect of streamline curvature.

The predicted u' profiles using the ASM with a Richardson number correction are shown in Figure 7.1-16. These profiles are in much better agreement with data than those obtained without Richardson number correction (Figure 7.1-8). The predicted u' values along the concave surface (Figure 7.1-17) are slightly higher than those predicted without the Richardson number (Figure 7.1-9).

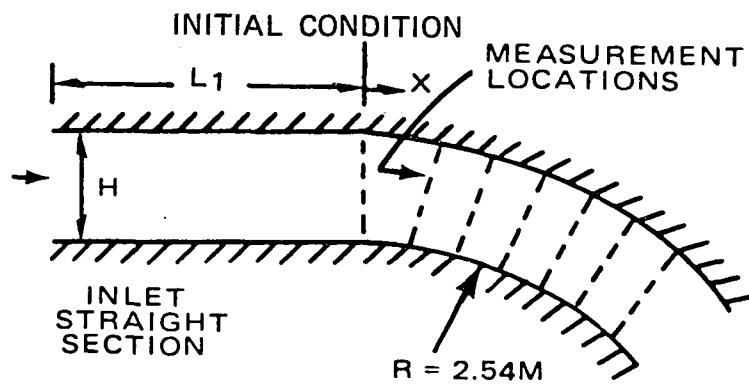
The v' predictions using the ASM with the Richardson number are presented in Figure 7.1-18. The Richardson number correction tends to reduce the v' values along the convex surface. On the concave surface, the Richardson number correction slightly increases the v' values (Figure 7.1-19).

The \overline{uv} predictions using the ASM and Richardson number are shown in Figure 7.1-20 for the boundary layer along the inner convex surface. The Richardson number correction tends to decrease the \overline{uv} values along the convex surface. Along the concave surface, the Richardson number correction tends to increase the magnitude of \overline{uv} values, as seen in Figure 7.1-21.

The flow field in a mildly curved duct is well predicted by the $k-\epsilon$ and the ASM. The anisotropic turbulence structure is correctly predicted by the ASM. The Richardson number correction improves the agreement between the data and predictions for the convex surface, but more work is needed to get good results for both convex and concave surfaces.

SHIVA-PRASAD AND RAMA-PRIYAN

FLOW IN A CURVED CHANNEL



$$L_1 = 1.03 \text{ M}$$

$$H = 0.10 \text{ M}$$

$$Re_\theta = 2400$$

$$U = 22 \text{ M/S}$$

$$\text{ASPECT RATIO} = 13.2$$

$$Y = \text{NORMAL DISTANCE FROM WALL}$$

Figure 7.1-1. Configuration of the Curved Channel Test Setup.

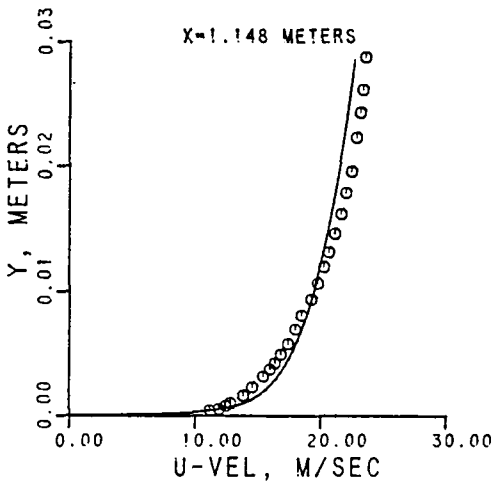
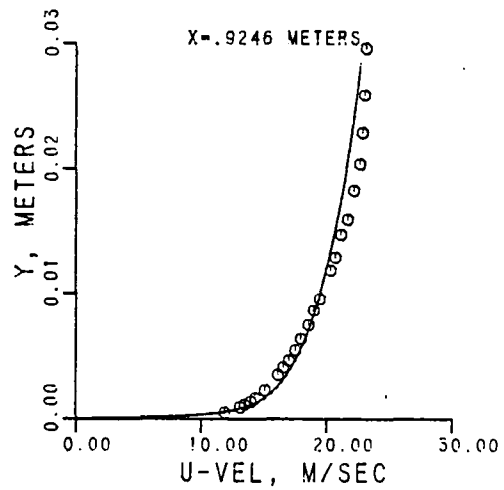
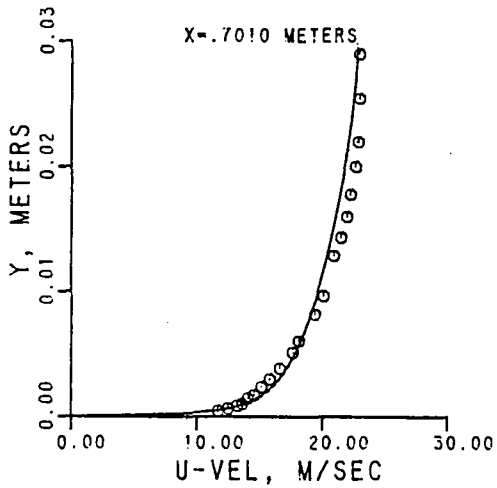
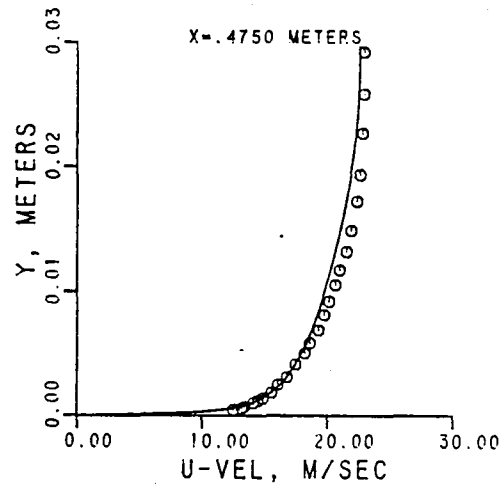
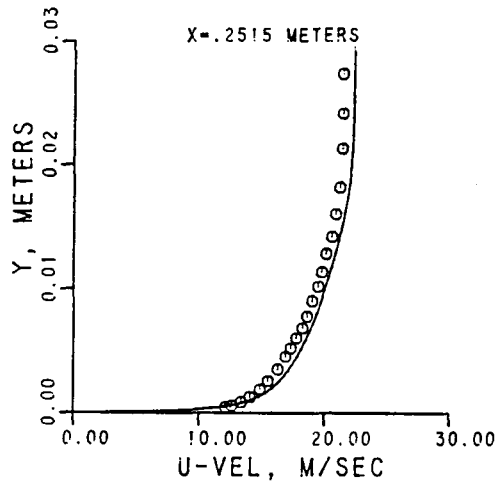


Figure 7.1-2. Comparison Between Predictions ($k-\epsilon$ Model) and Measurement Along The Inner (Convex) Wall.

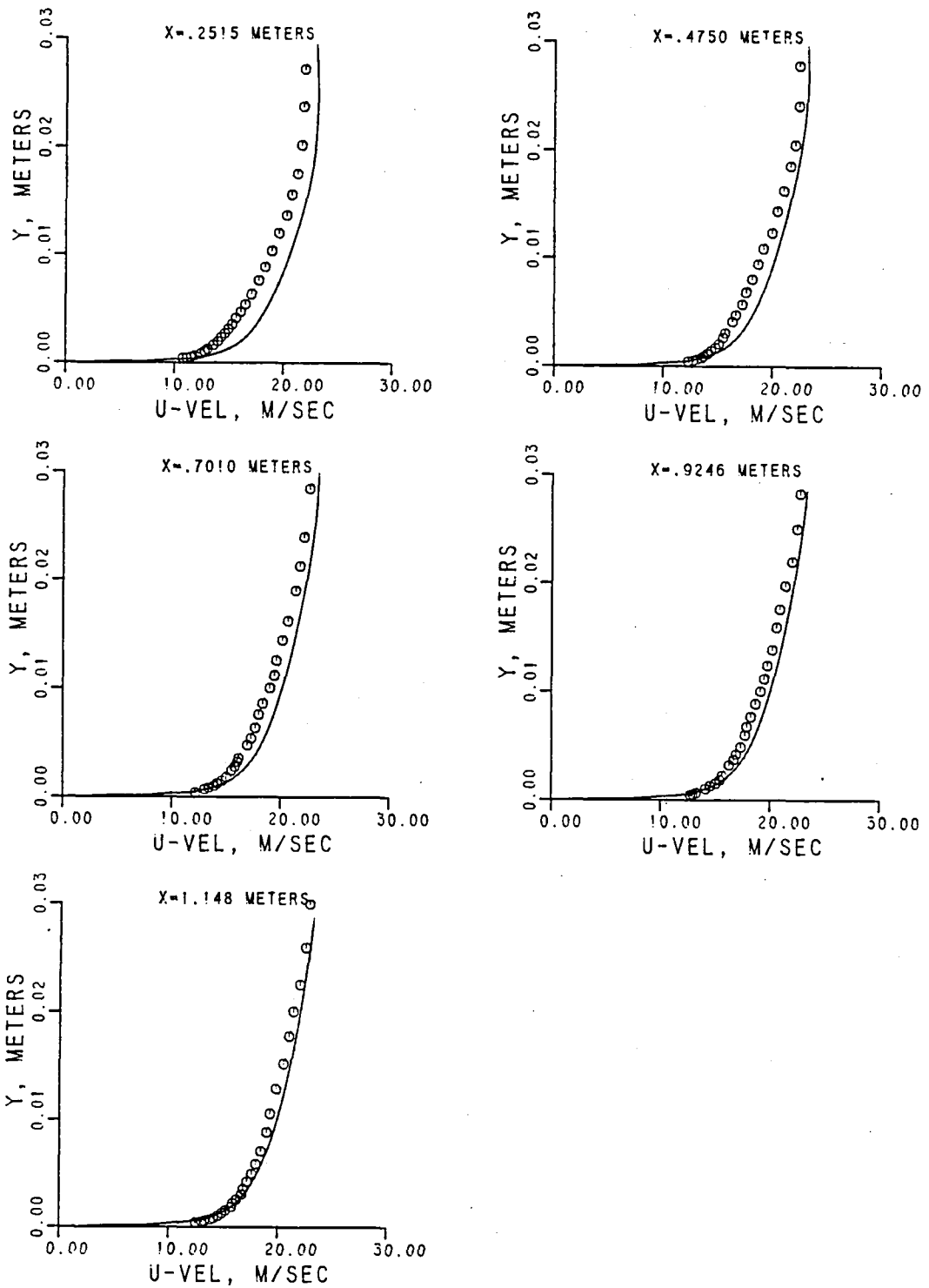


Figure 7.1-3. $k-\epsilon$ Model Velocity Profiles Along the Outer (Concave) Wall.

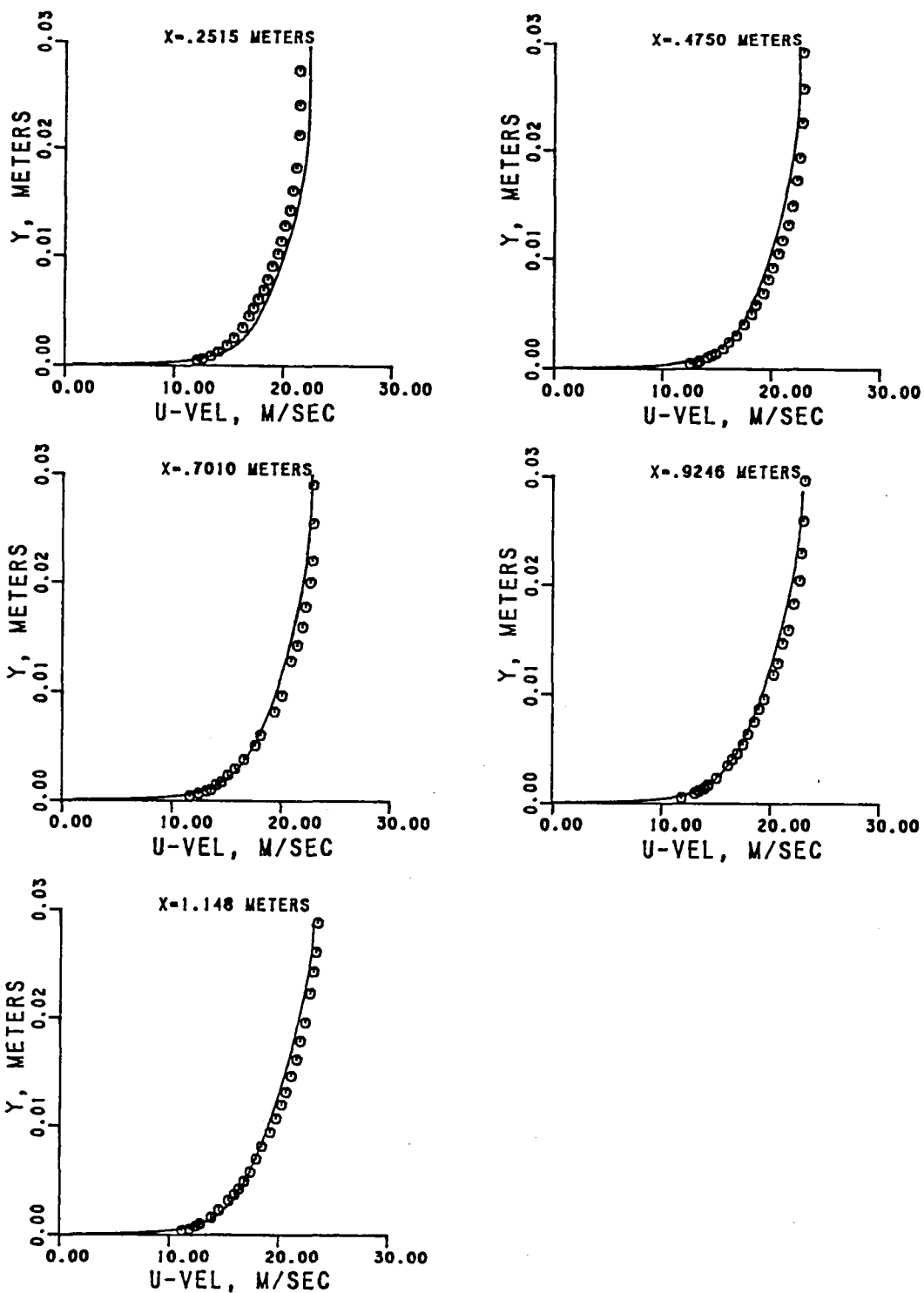


Figure 7.1-4. $k-\epsilon$ Model With Streamline Curvature Correction -- Axial Velocity Profile Along the Inner (Convex) Wall.

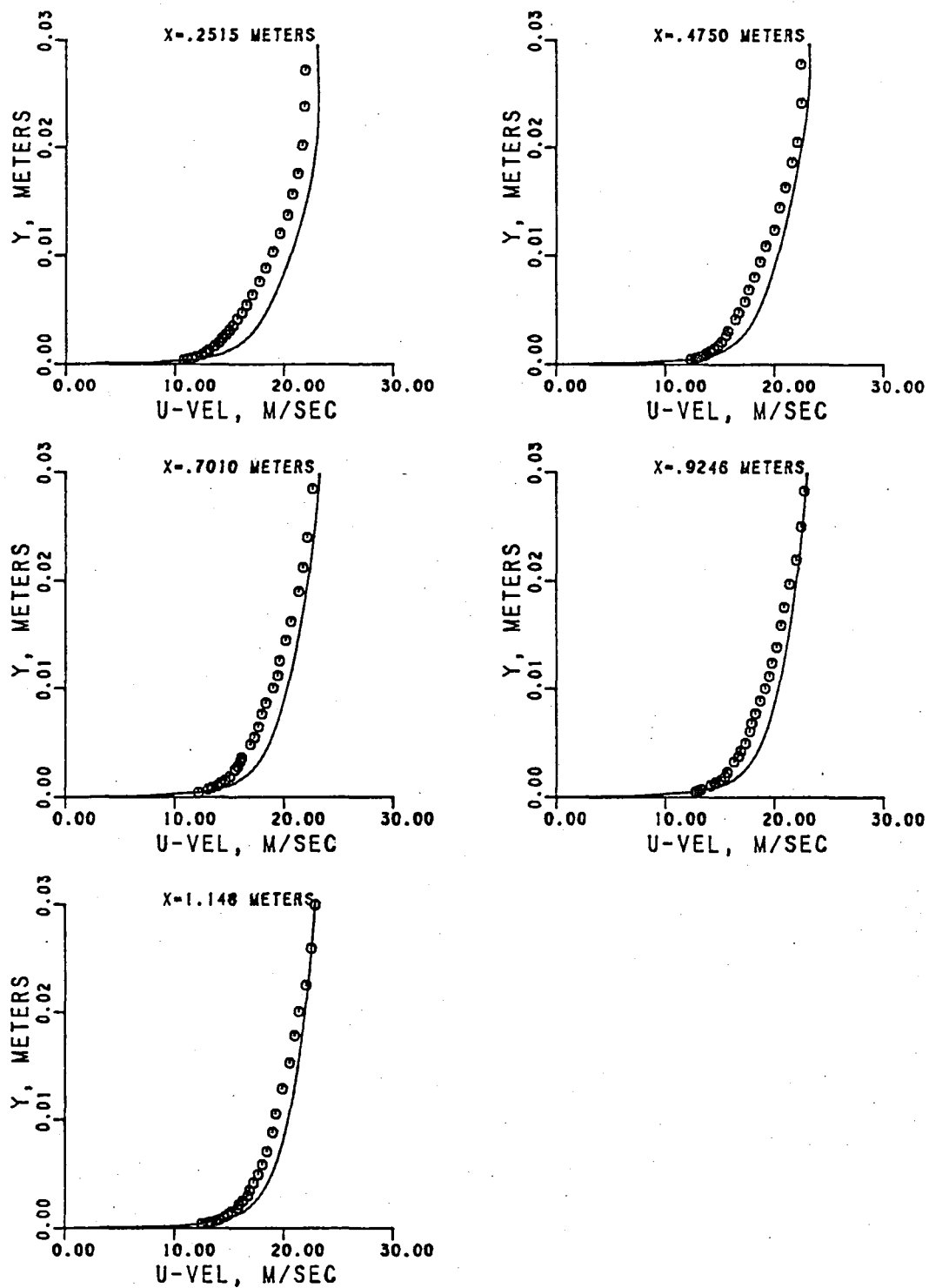


Figure 7.1-5. $k-\epsilon$ Model With Streamline Curvature Correction
 -- Axial Velocity Profile Along the Outer (Concave) Wall.

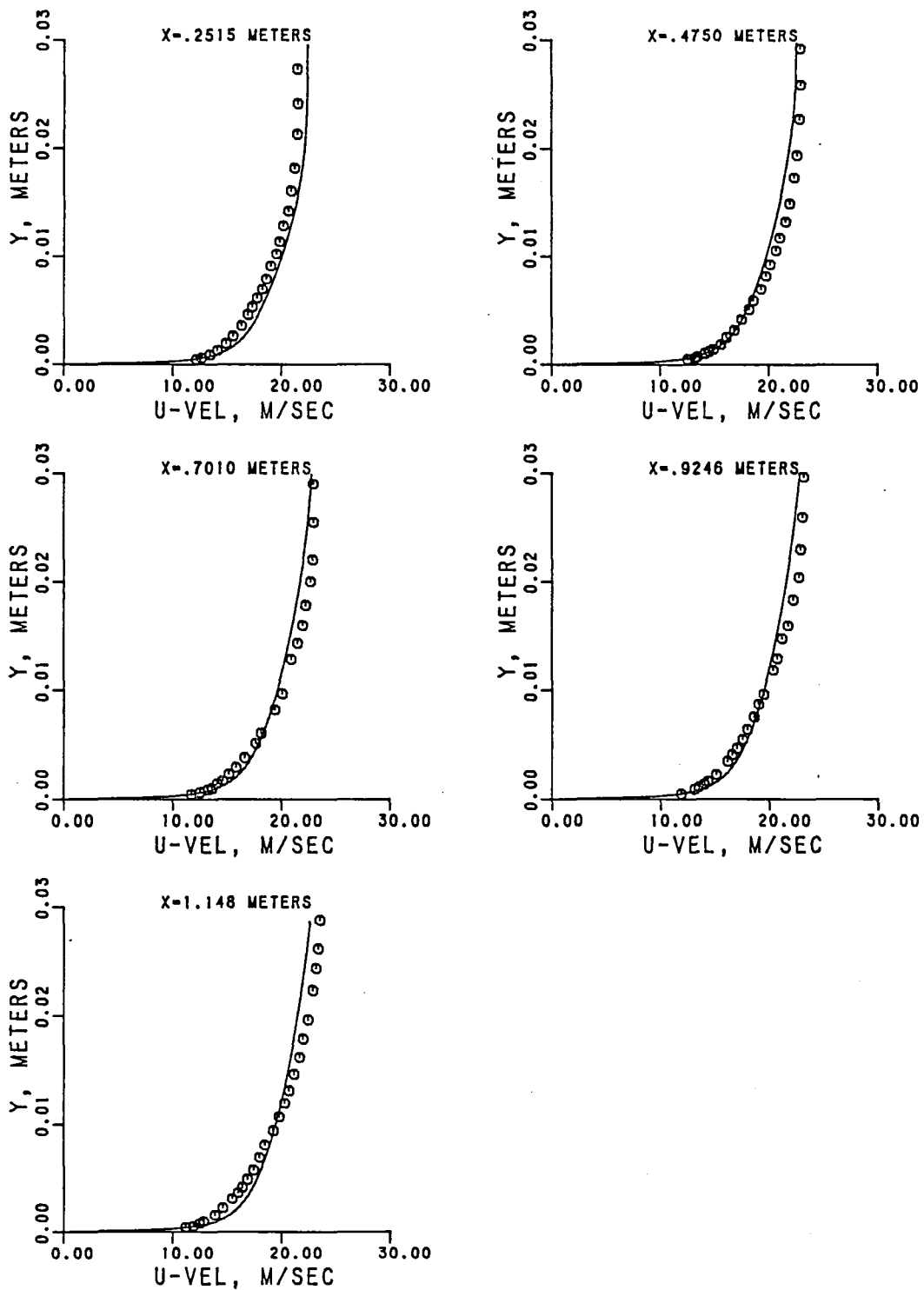


Figure 7.1-6. ASM Prediction and Measured Axial Velocity Profiles Along the Inner (Convex) Wall.

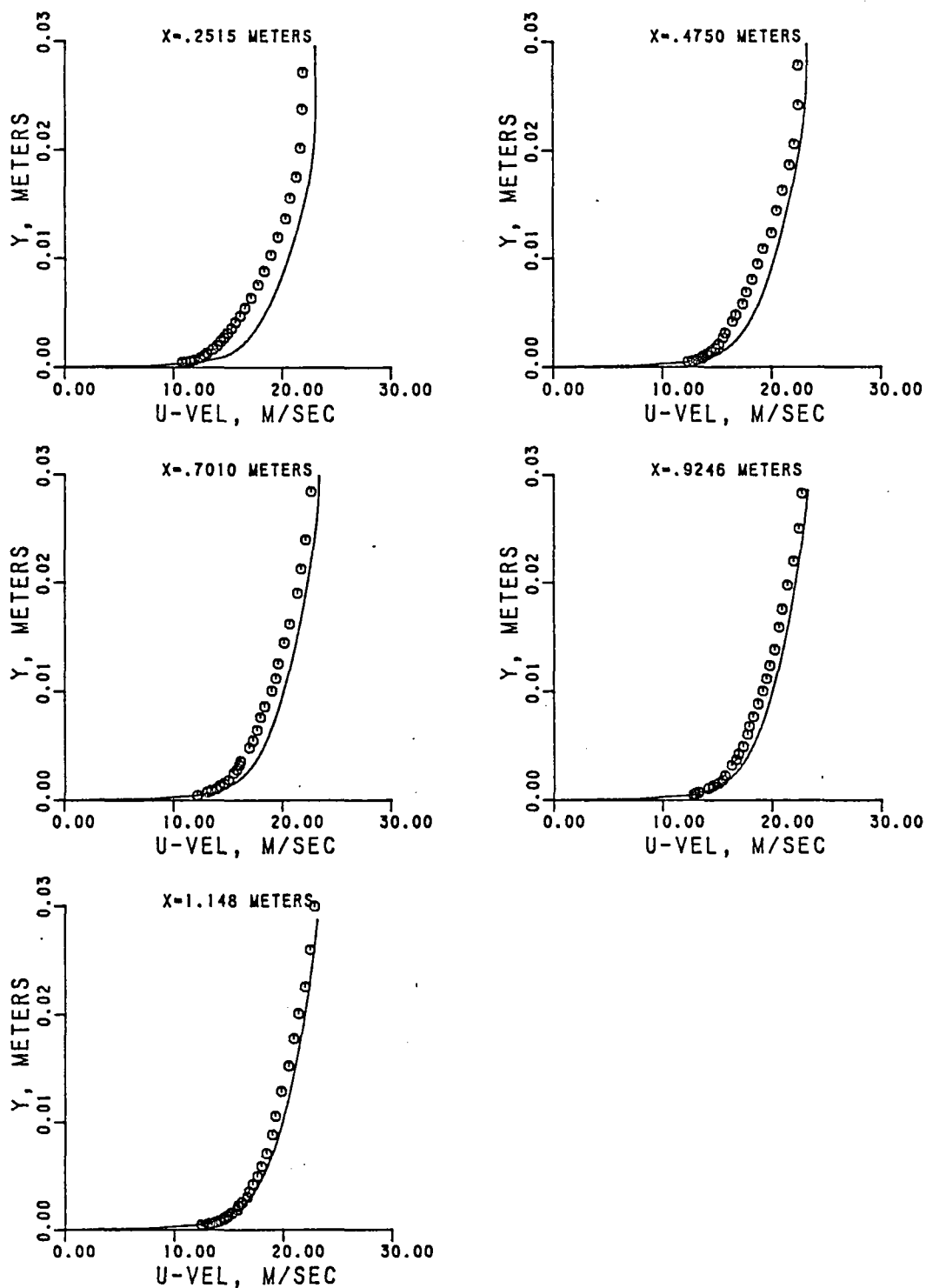


Figure 7.1-7. ASM Predictions and Measured Axial Velocity Profiles Along the Outer (Concave) Wall.

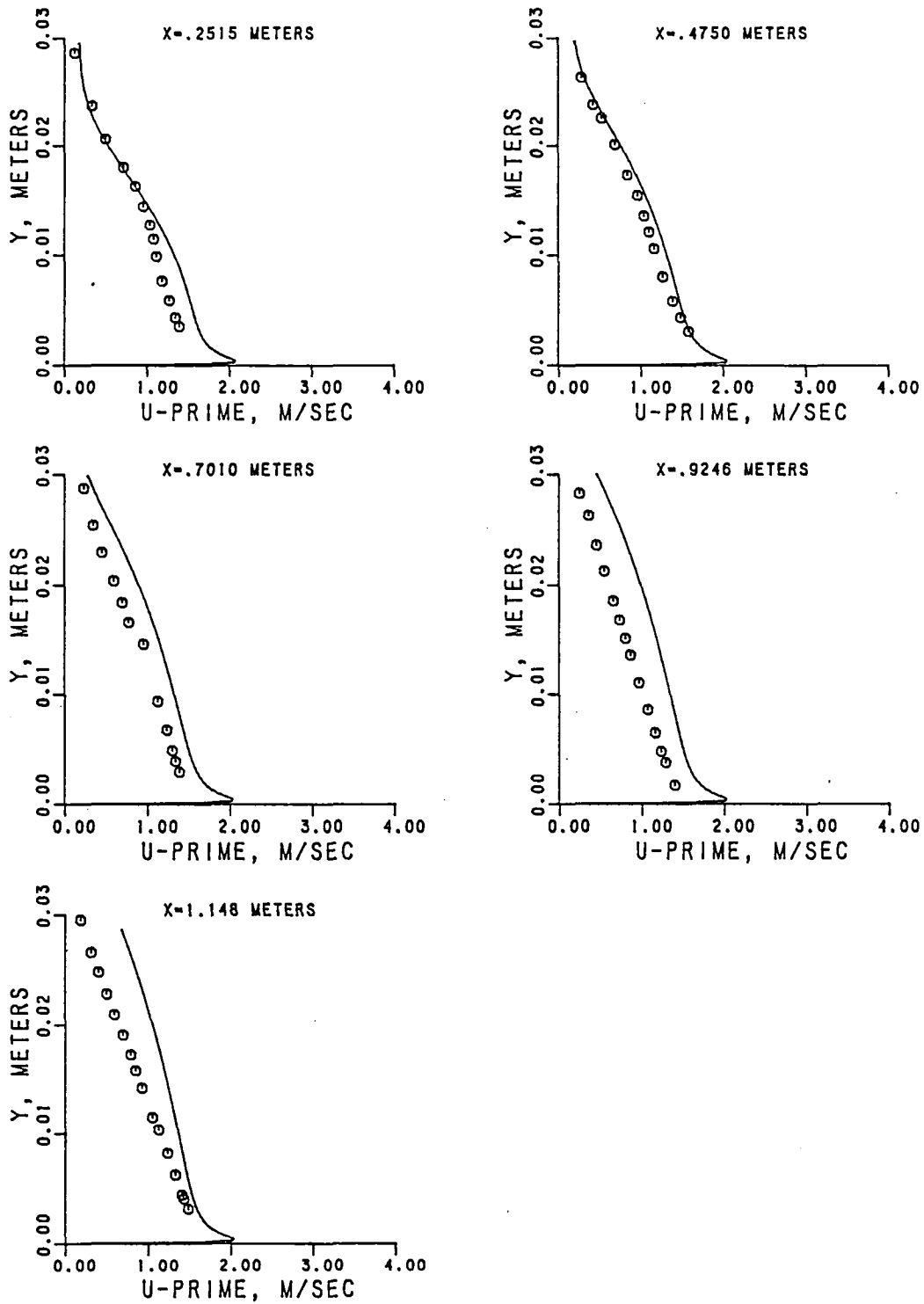


Figure 7.1-8. ASM Predictions and Measured RMS Axial Velocity Profiles Along the Inner (Convex) Wall.

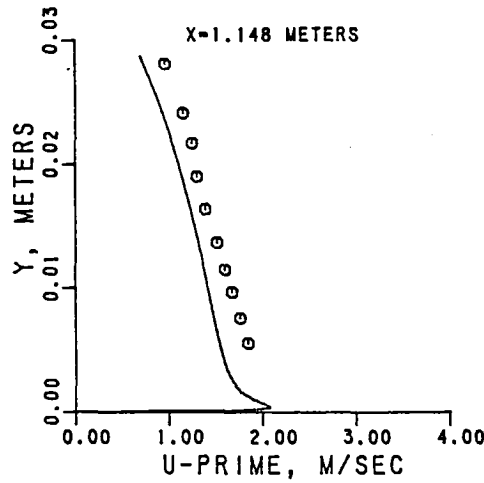
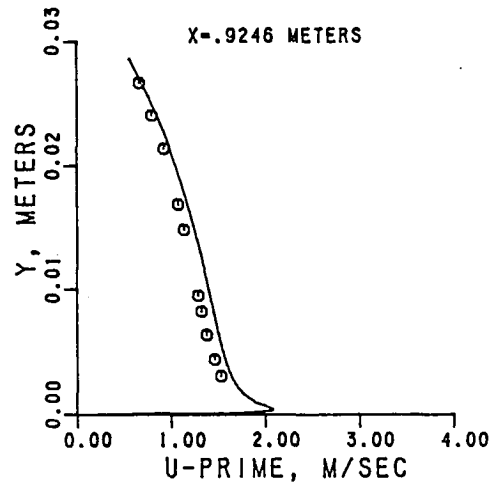
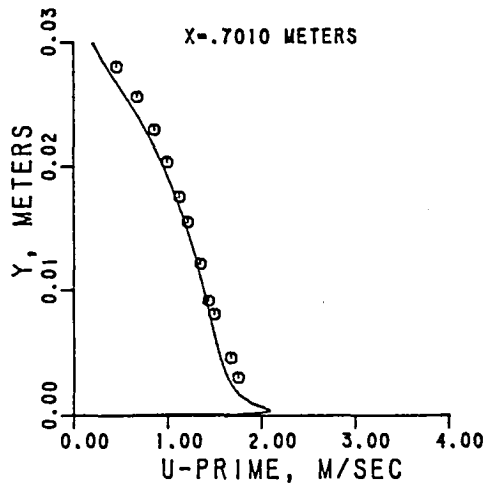
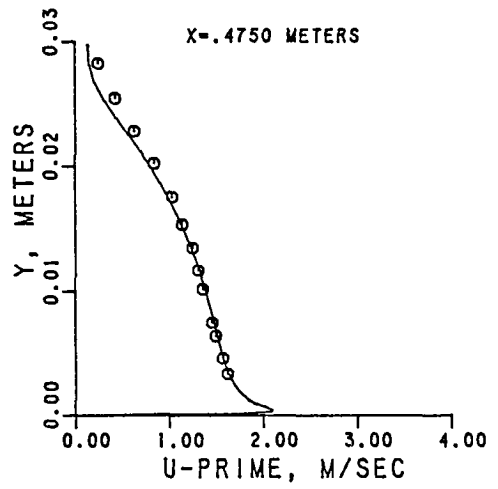
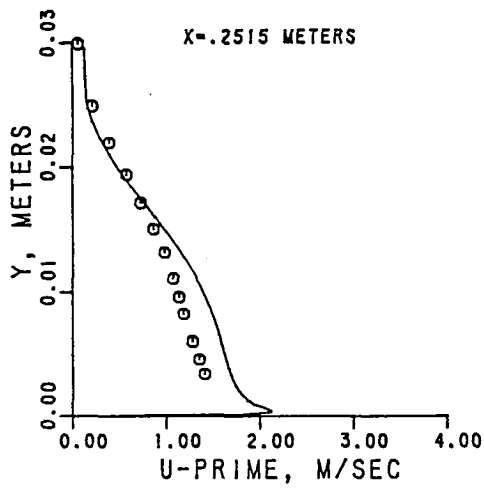


Figure 7.1-9. ASM Predictions and Measured RMS Axial Velocity Profiles Along the Outer (Concave) Wall.

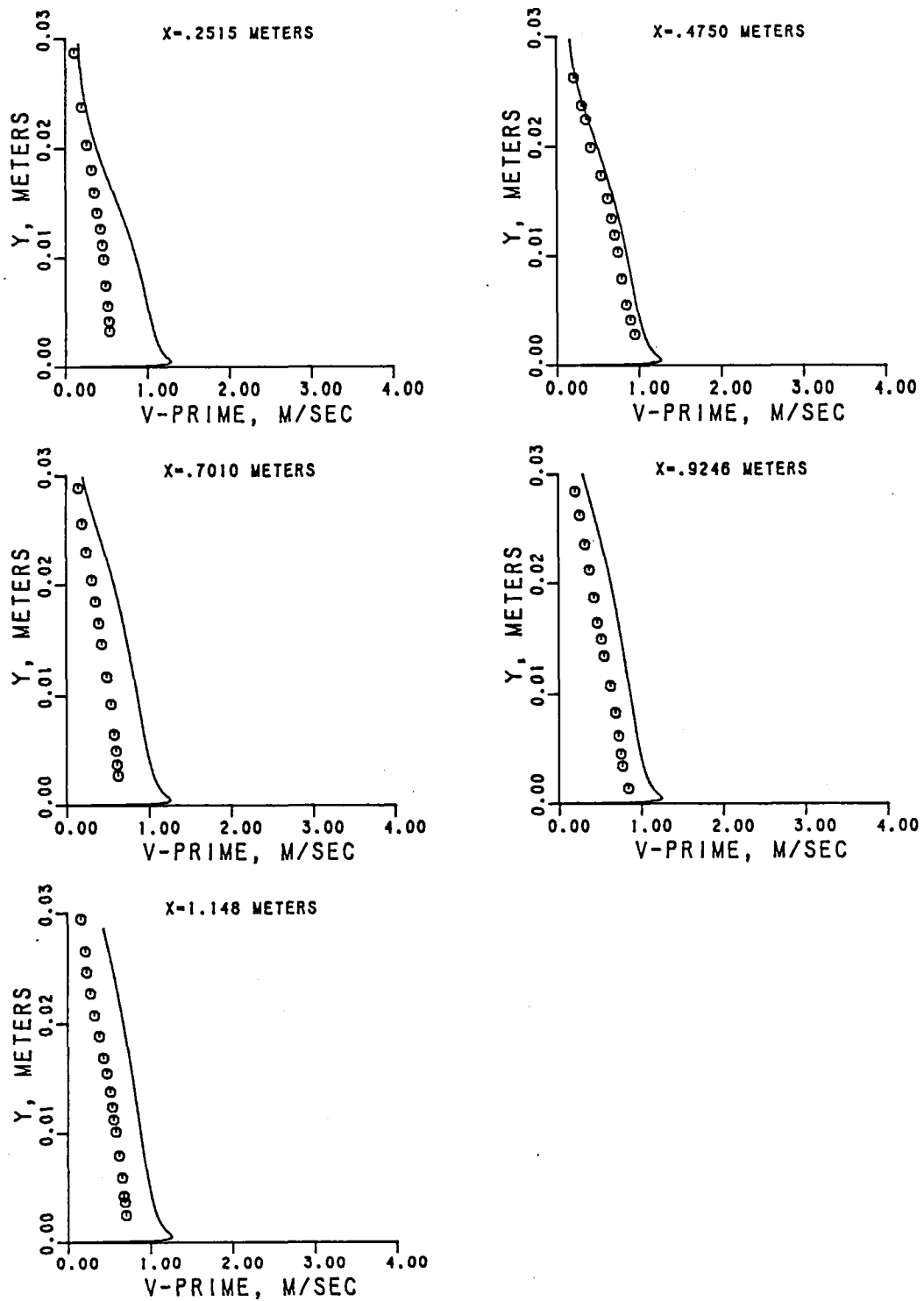


Figure 7.1-10. ASM Predictions and Measured RMS Radial Velocity Profiles Along the Inner (Convex) Wall.

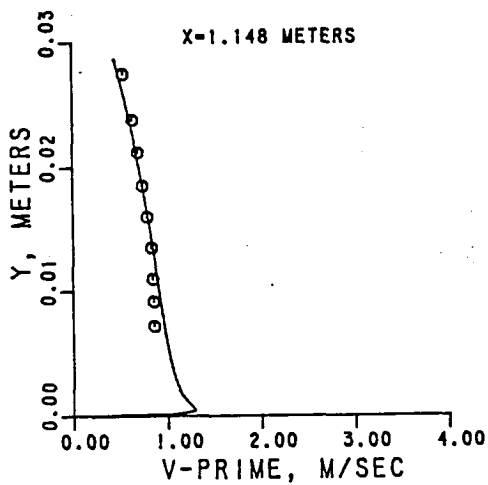
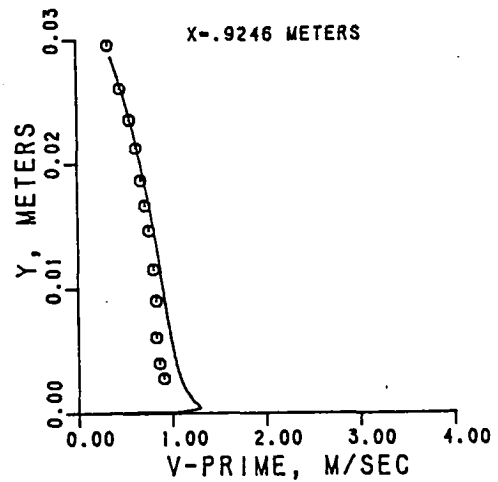
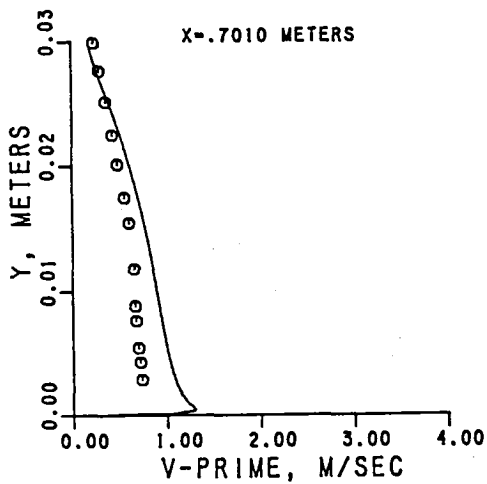
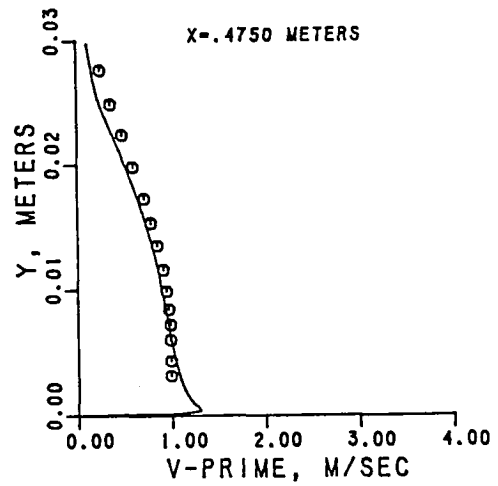
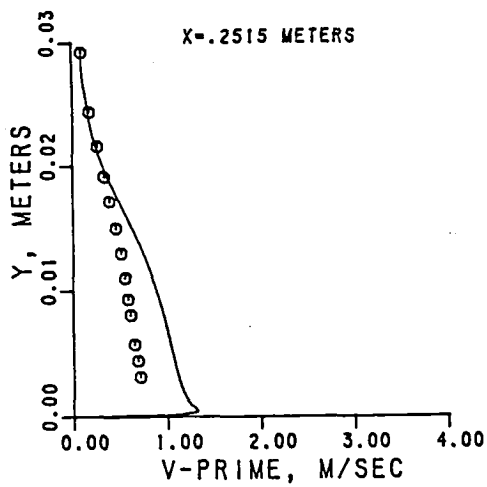


Figure 7.1-11. ASM Predictions and Measured RMS Radial Velocity Profiles Along the Outer (Concave) Wall.

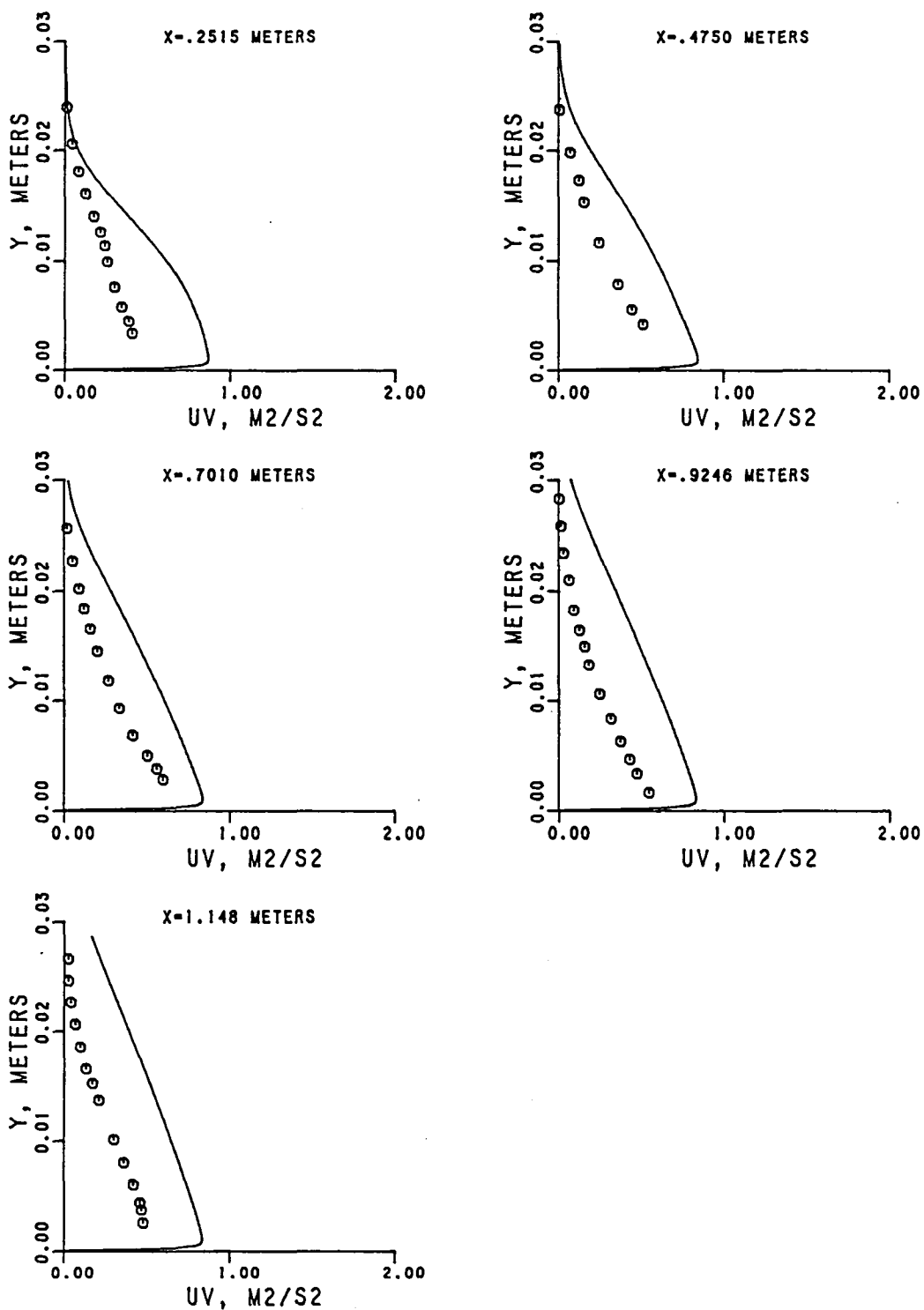


Figure 7.1-12. ASM Predictions and Measured Shear Stress (\overline{uv}) Profiles Along the Inner (Convex) Wall.

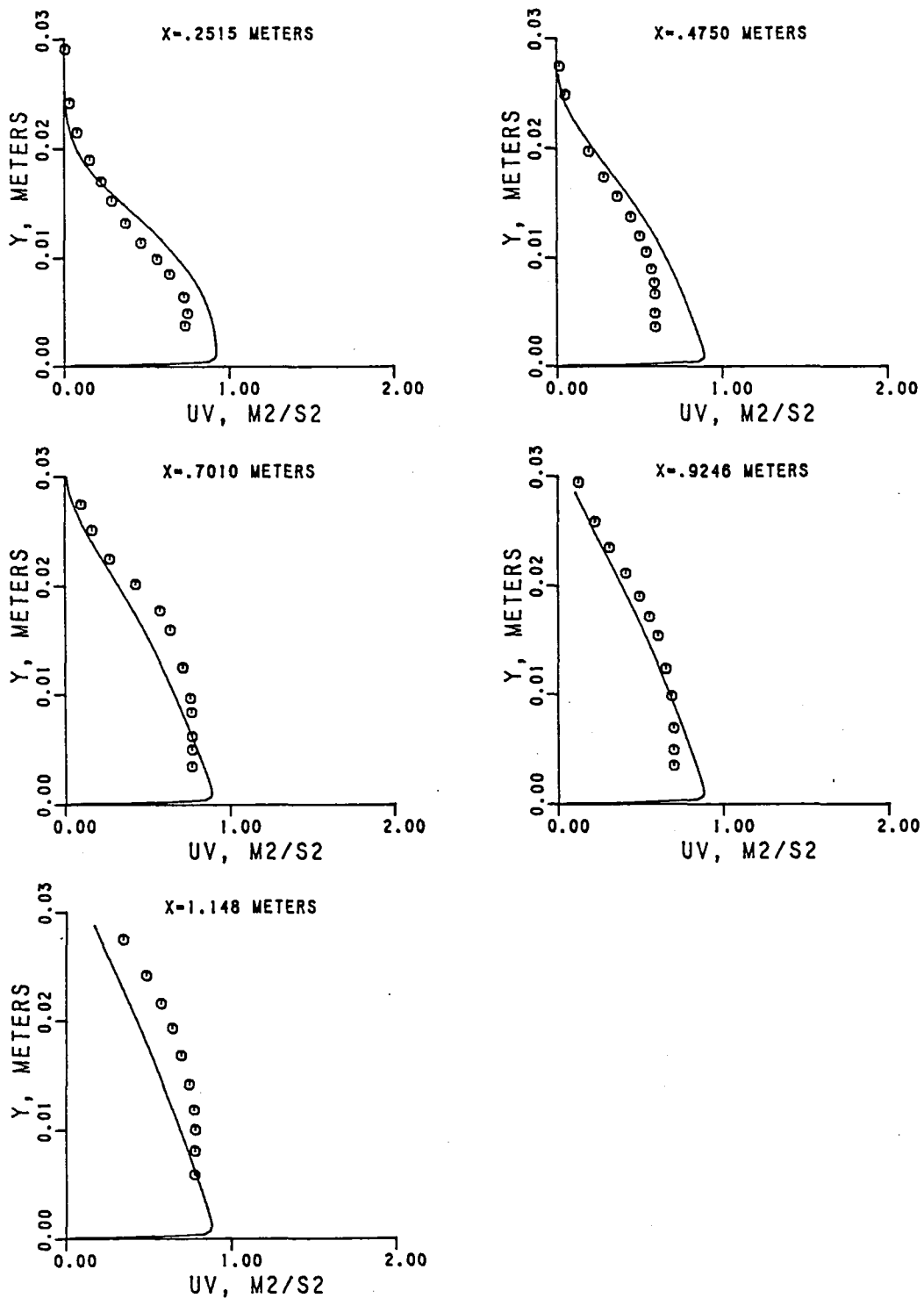


Figure 7.1-13. ASM Predictions and Measured Shear Stress (\overline{uv}) Profiles Along the Outer (Concave) Wall.

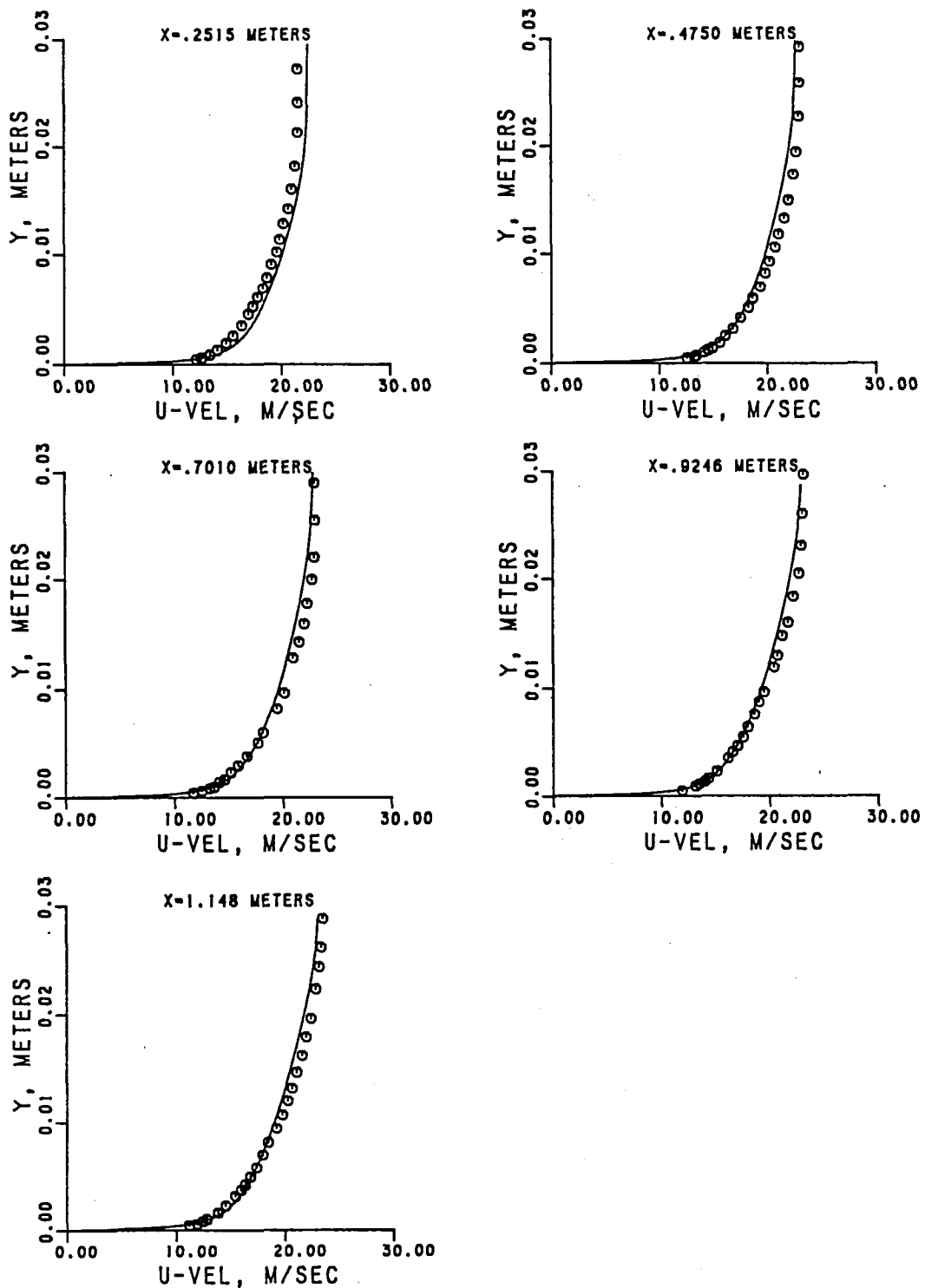


Figure 7.1-14. ASM With Streamline Curvature Correction -- Axial Velocity Profiles Along the Inner (Convex) Wall.

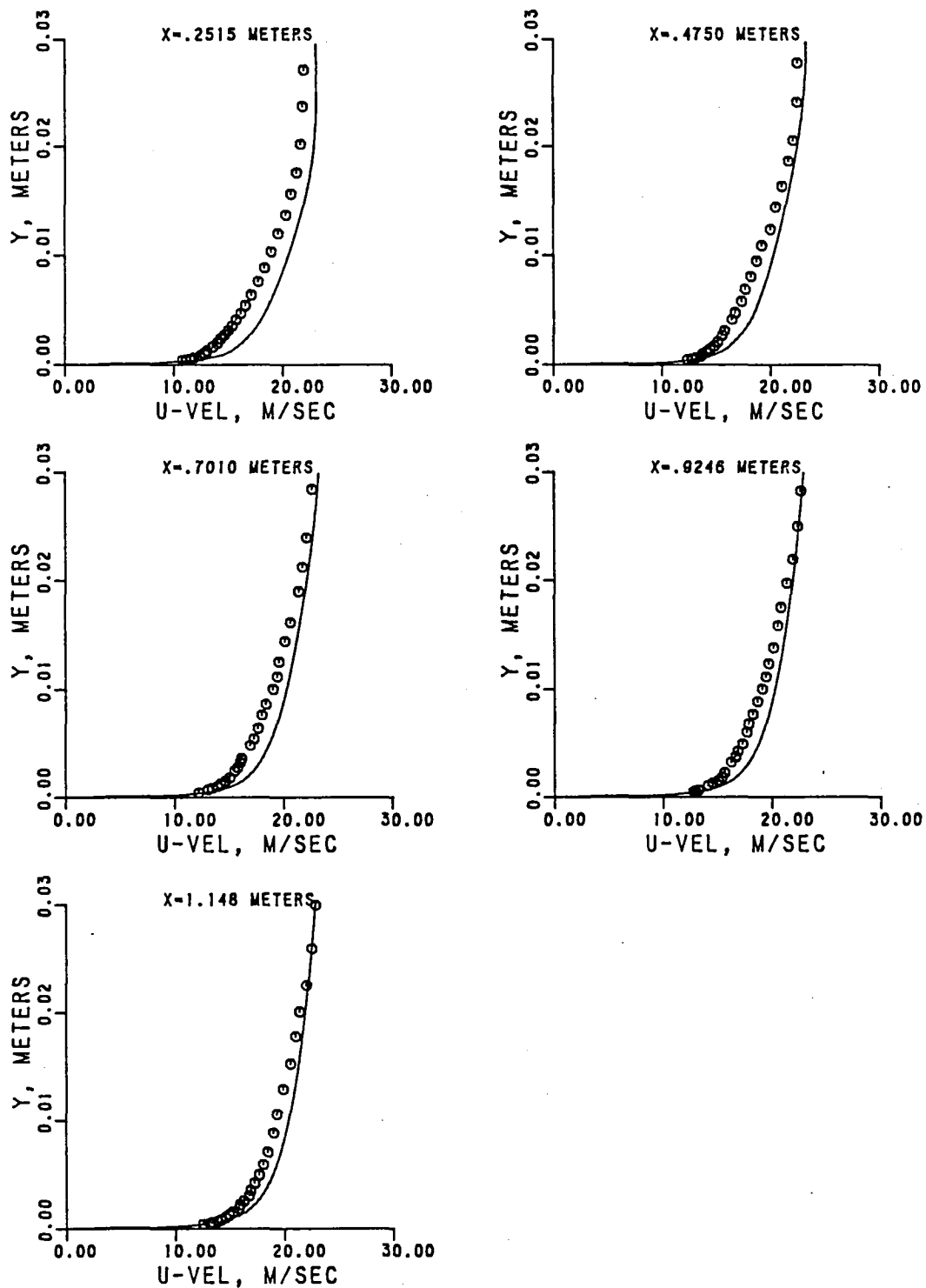


Figure 7.1-15. ASM With Streamline Curvature Correction -- Axial Velocity Profiles Along the Outer (Concave) Wall.

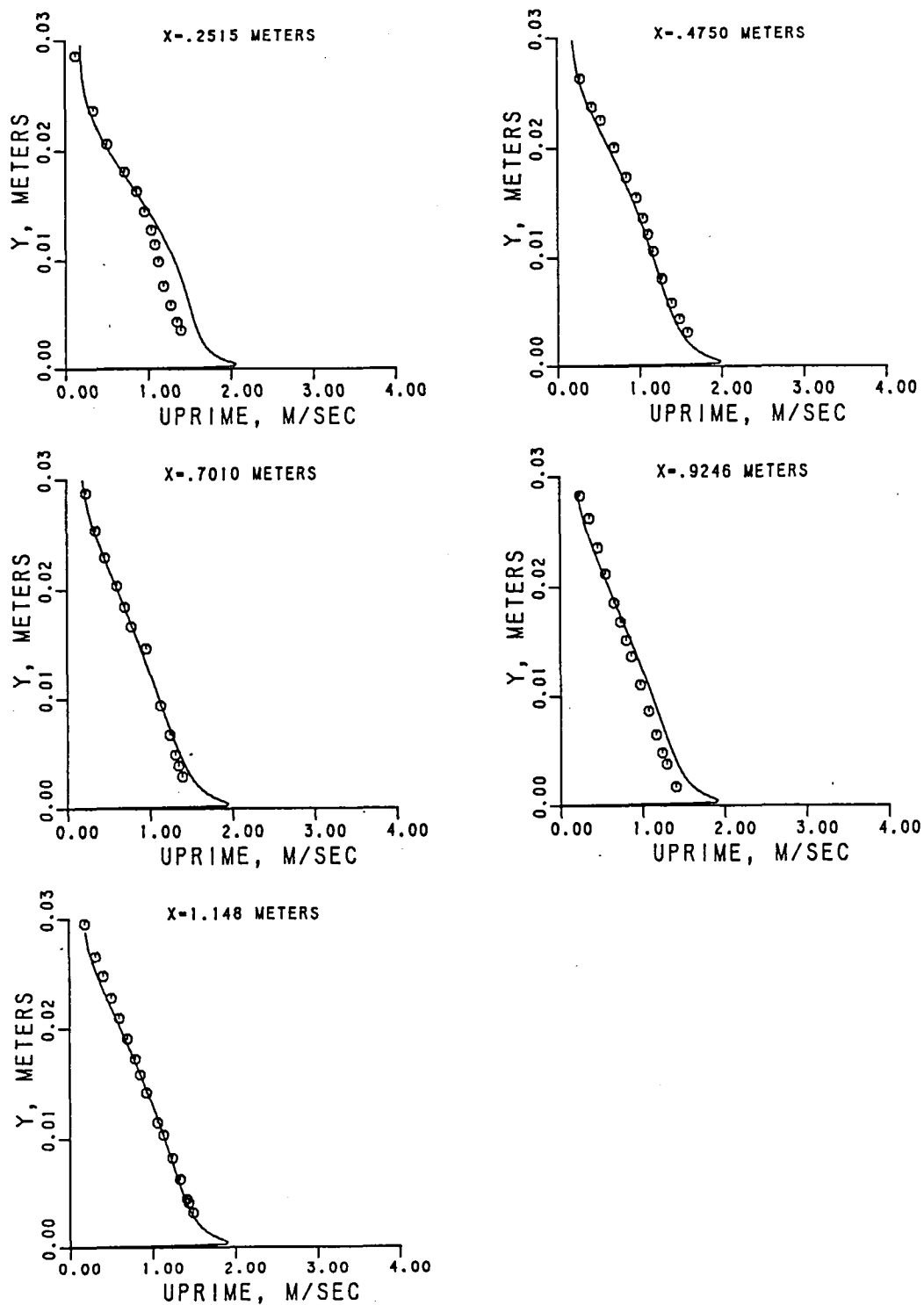


Figure 7.1-16. ASM With Streamline Curvature Correction -- RMS Axial Velocity Profiles Along the Inner (Convex) Wall.

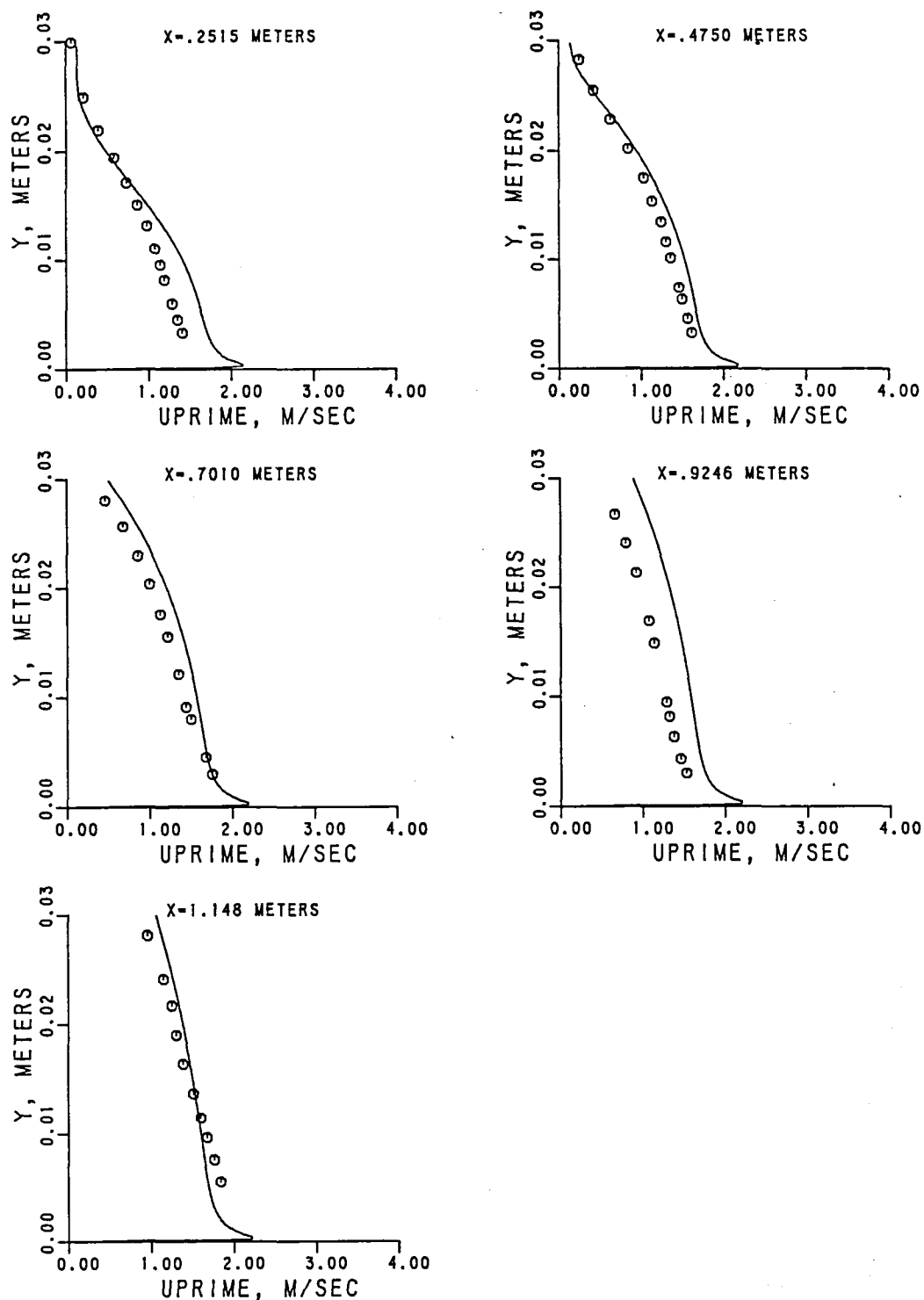


Figure 7.1-17. ASM With Streamline Curvature Correction -- RMS Axial Velocity Profiles Along the Outer (Concave) Wall.

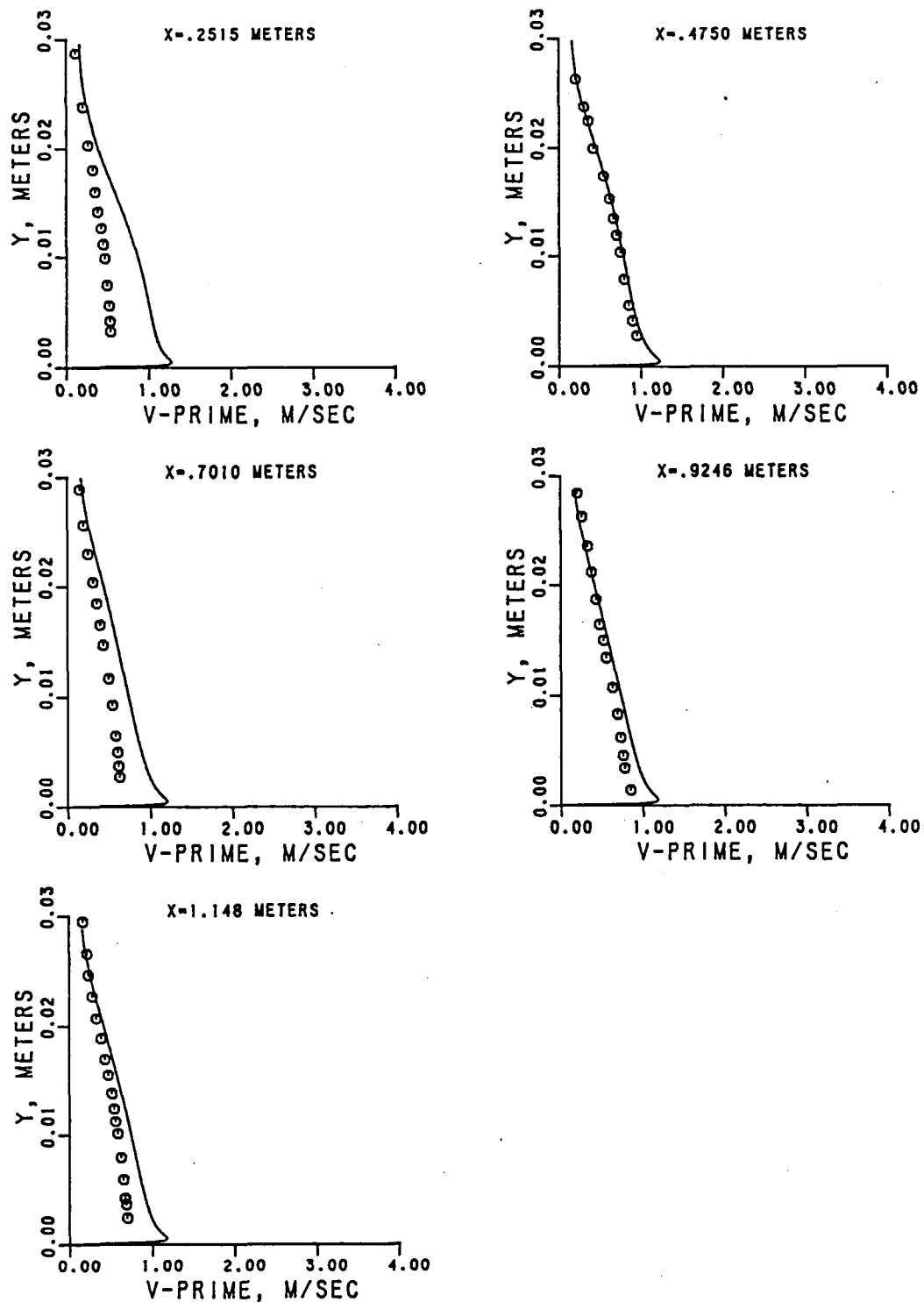


Figure 7.1-18. ASM With Streamline Curvature Correction -- RMS Radial-Velocity Profiles Along the Inner (Convex) Wall.

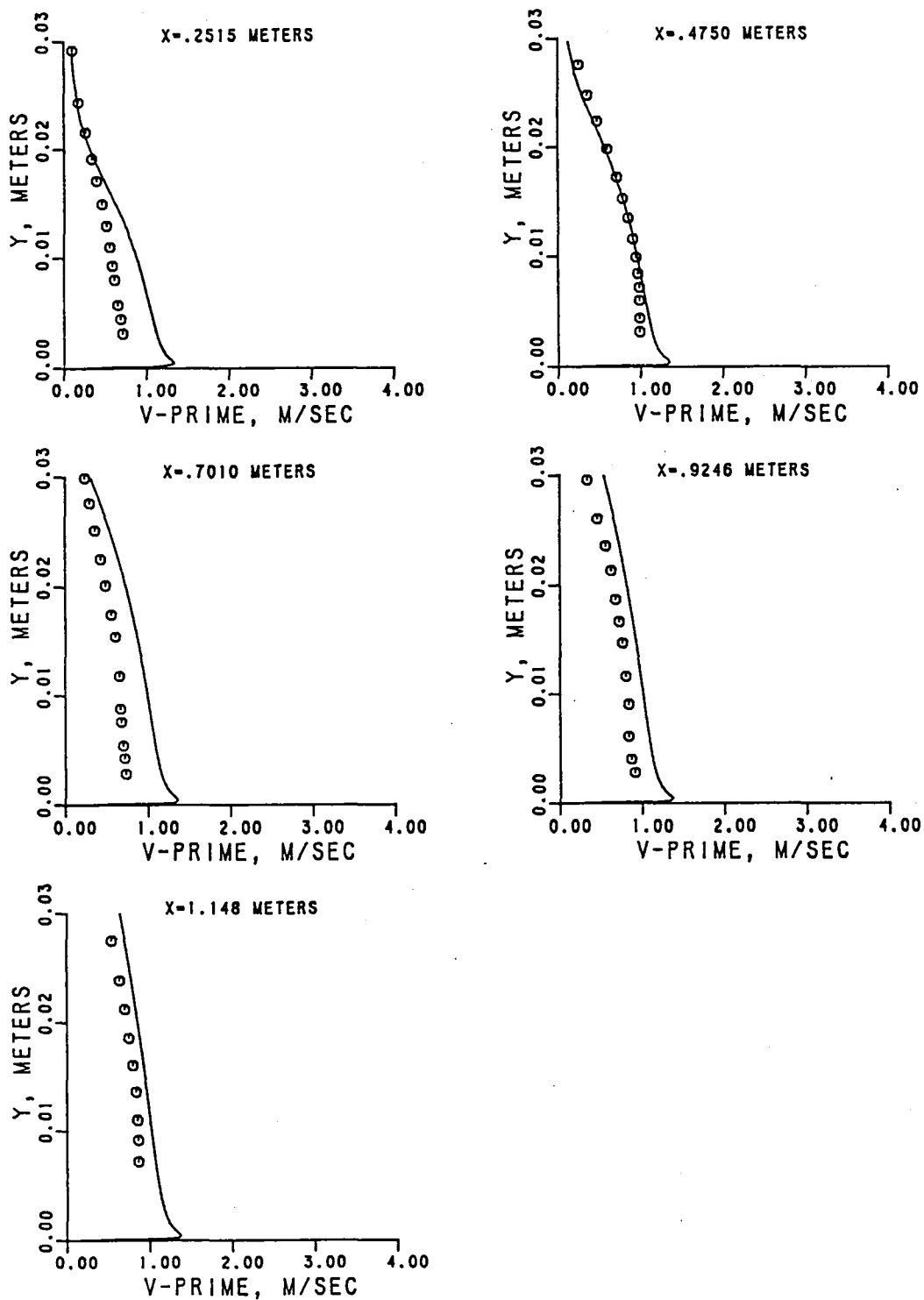


Figure 7.1-19. AMS With Streamline Correction -- RMS Radial-Velocity Profiles Along the Outer (Concave) Wall.

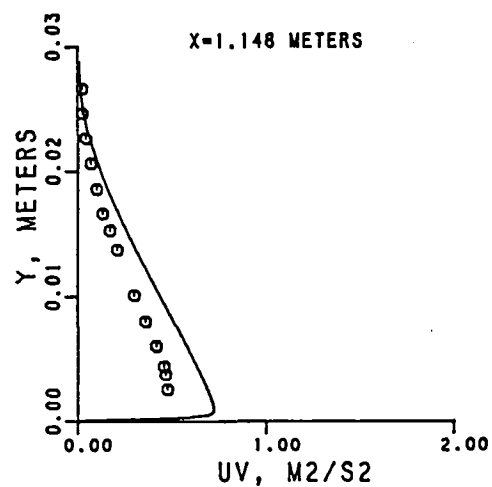
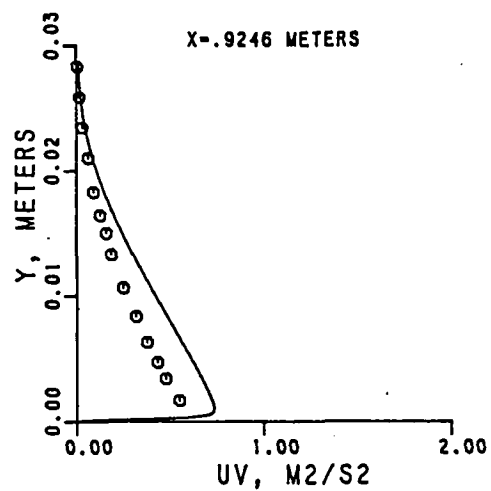
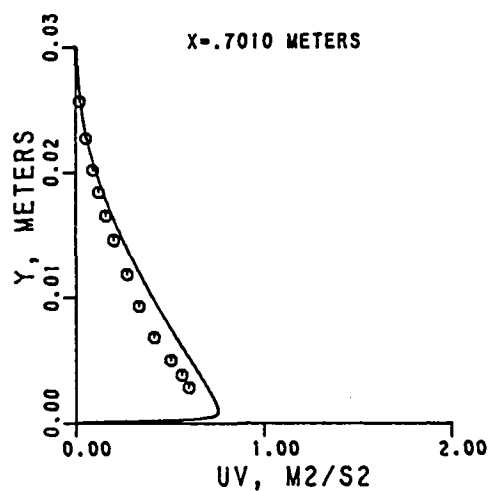
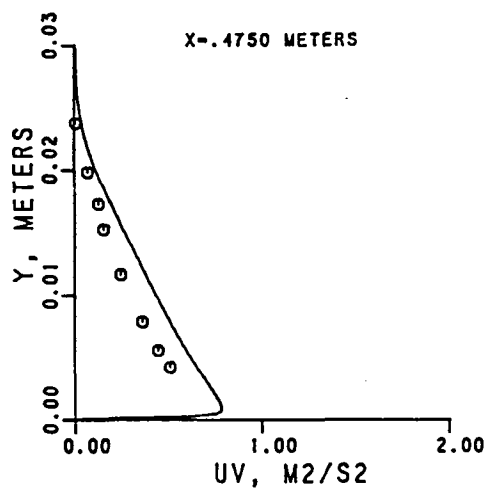
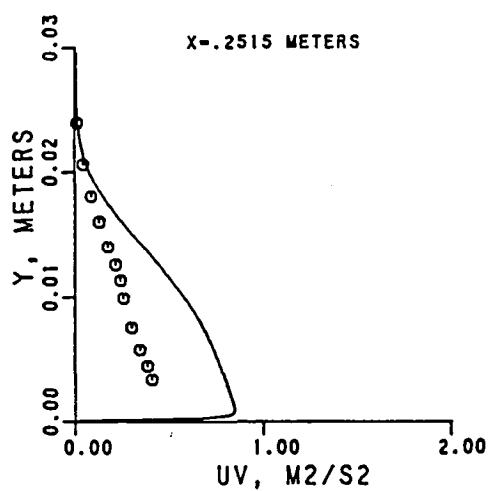


Figure 7.1-20. ASM With Streamline Curvature Correction -- \overline{uv} Profiles Along the Inner (Convex) Wall.

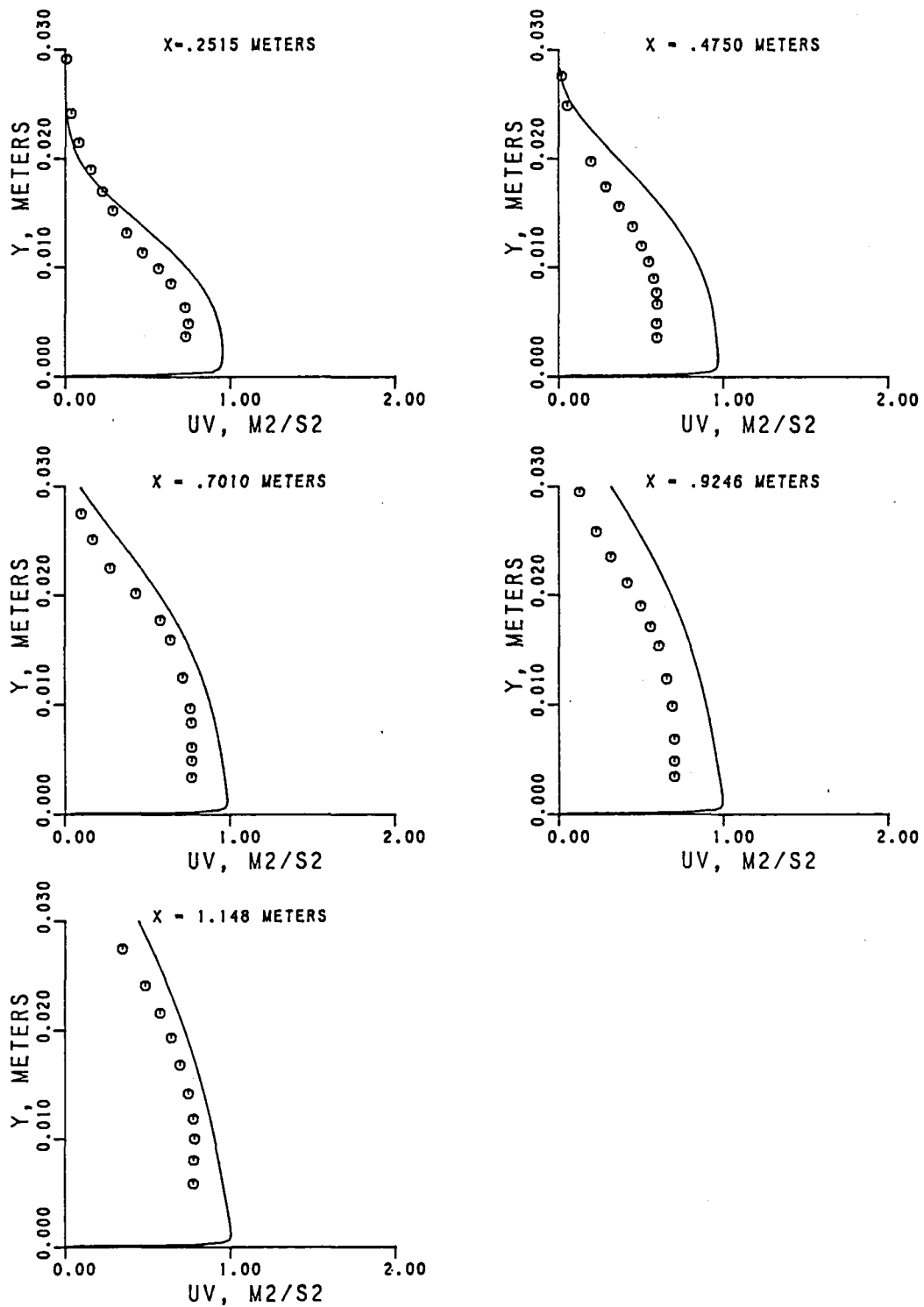


Figure 7.1-21. ASM With Streamline Curvature Correction -- \overline{uv} Profiles Along the Outer (Concave) Wall.

7.2 Flow Over a Backward-Facing Plane Step

The flow through the curved duct studied in the previous paragraph did not have any recirculation. In combustor internal flows, however, recirculation zones exist. For combustor aerothermal model evaluation, validation of the analytical models in recirculating flows is essential. One of the benchmark test cases selected among recirculating flow fields was the flow over a backward facing plane step, for which measurements were made by Johnston, et al.,^{82,83} in a rig shown schematically in Figure 7.2-1. Test data are available for step heights (HT) of 2.54, 3.81, and 5.08 cm. Computations were performed for all these cases using a 2-D elliptic code and the following turbulence models:

- o Standard $k-\epsilon$ model
- o $k-\epsilon$ model with streamline curvature correction
- o ASM with streamline curvature correction.

The numerical convergence for the nonswirling recirculating flow calculations presented in this chapter was ascertained by comparing variations in the following parameters:

- o Maximum local mass continuity residual (R_{MAX}) normalized by inlet mass flux.
- o Cumulative mass continuity residual (R_{SUM}) normalized by inlet mass flux.
- o Variations in the dependent variables from iteration to iteration ($\Delta\phi$) normalized by the inlet value.

Typically, 400 iterations were required to achieve the following levels of R_{MAX} , R_{SUM} and ΔU :

$$R_{MAX} = (10^{-5})$$

$$R_{SUM} \leq 0.001$$

$$\Delta U = (10^{-4}) \text{ from peak to minimum value over the last 10 iterations.}$$

For these computations, the inlet velocity profiles were obtained from the test data and the turbulence kinetic energy profiles were calculated by using measured $\overline{u^2}$ and assuming that $\overline{v^2}$ and $\overline{w^2}$ are equal at the inlet station. The inlet turbulence length scales were assumed to be equal to $0.02 w_1$. Along the walls, wall functions were used to specify the boundary conditions, and at the exit plane, zero axial gradient conditions were prescribed.

The model predictions were obtained for each of the three step heights by using the following set of grid nodes distributed non-uniformly over the axial distance indicated in Table 16 below:

TABLE 16. GRID NODE DISTRIBUTION.

Step Height (cm)	Number of Nodes		Axial Distance Analyzed (cm)	X-Location of Step (cm)
	Axial	Radial		
2.54	59	32	78.7	15.24
3.81	59	32	78.7	15.24
5.08	57	37	54.6	3.81

A partial layout of the grid network used with the 1.5-inch (3.81 cm) step is shown in Figure 7.2-2. A total of 32-grids were used to span 4.5 inches, out of which, 13 nodes were used for the 1.5-inch step, as shown. The first interior node was 0.1 inches ($0.07 H_T$) from the step-side wall; H_T denotes step height. The smallest axial node spacing was also 0.1 inches.

Step Height of 3.81 cm

The comparison between the standard $k-\epsilon$ model predictions and the measurements of mean axial velocity profiles at several axial stations is presented in Figure 7.2-3. The predicted results are represented by solid lines and the data correspond to symbols. The $k-\epsilon$ model predictions are in good agreement with the data up to $x = 15.2$ cm where the step is located.

For the flow region downstream from the step and upstream from the reattachment point, the following observations can be made. The correlation is good for the shear layer between the recirculation bubble and the main throughflow. For the outer portion of the recirculation bubble (ie., $U > 0$), the agreement between model and data is reasonable. However, for the reverseflow region, the model predicts qualitative trends. The measured height of the reverseflow region is greater than the model prediction. Some of this discrepancy may be due to use of wall functions. The reattachment point is predicted to lie between $x = 35.58$ and 38.94 cm, while the data indicates that the location of the reattachment point lies between $x = 38.94$ and 42.34 cm. The streamlines obtained from the standard $k-\epsilon$ model are illustrated in Figure 7.2-4. The predicted nondimensional reattachment length, L_R/HT was 6, while the measured reattachment length was 7.

Figure 7.2-5 presents predicted axial velocity profiles with the $k-\epsilon$ model modified by Richardson number correction. The streamline curvature correction improves the model predictions in the recirculation zone as well as the developing region downstream from the reattachment. The predicted streamline plot is shown in Figure 7.2-6 where recirculation zone length is predicted to be 6.5 times the step height. Without the Richardson number correction, the length was predicted to be 6.0. There is also a slight increase in the predicted amount of the recirculating flow rate over the standard $k-\epsilon$ model as evidenced from Figures 7.2-4 and 7.2-6.

The predicted mean velocity profiles using the ASM and Richardson number corrections are presented in Figure 7.2-7. The results are similar to the modified k - ϵ predictions shown previously in Figure 7.2-5.

The turbulence kinetic energy profiles predicted by the ASM with streamline curvature corrections and the data are presented in Figure 7.2-8. The data points (shown in symbols) were obtained by assuming $\overline{w^2} = \overline{v^2}$. The predicted profiles are in agreement with data up to $x = 30.99$ cm, and beyond this station the predicted levels of turbulence kinetic energy are significantly lower than the measurements.

The ASM predictions for $\overline{u^2}$ and the measured values are illustrated in Figure 7.2-9. The predicted $\overline{u^2}$ values are initially higher than the measurements, and beyond $x = 41.7$ cm, the predicted values are progressively smaller than the data. In the ASM, the Reynolds stress components are expressed as functions of k and ϵ . Hence, in regions where predicted k values are significantly smaller than the measurements, the predicted Reynolds stress components are also expected to be smaller than the data. The comparison between measured and predicted $\overline{v^2}$ profiles are shown in Figure 7.2-10. The predicted $\overline{v^2}$ values are smaller than the data, and this is attributed to the underprediction of the k values.

The ASM predictions for the Reynolds stress \overline{uv} and the data are shown in Figure 7.2-11. The model initially overpredicts the \overline{uv} values and beyond $x = 41.07$ cm, it underestimates the \overline{uv} values. This trend is very similar to the $\overline{u^2}$ profiles. Further improvements in the model predictions can be obtained if improvements are made to the predicted k values.

Step Height of 2.54 cm

The standard k - ϵ model predictions for mean axial velocity and the data for a step height of 2.54 cm (1.0 inch) are presented in

Figure 7.2-12. The predicted results are in very good agreement with the data up to $x = 20.32$ cm. Between $x = 25.4$ cm and $x = 32.18$ cm, some differences are seen between the data and the predictions. In these regions, the $k-\epsilon$ model overestimates the velocity in the recirculation or low velocity zone near the bottom wall.

When Richardson number corrections are applied to the $k-\epsilon$ model, significant improvements in the predicted mean velocity profiles were obtained, and those profiles are illustrated in Figure 7.2-13. The agreement between the data and the predictions is good in the entire flow field of interest.

The mean velocity profiles obtained from the ASM with the Richardson number correction are shown in Figure 7.2-14. The agreement between the data and the predictions is again good throughout. The measured profiles at far downstream stations are fuller than the predictions.

The ASM predictions for turbulence kinetic energy are presented in Figure 7.2-15. These profiles are similar in characteristics to those in Figure 7.2-8 for the 3.81 cm step height. The model tends to underestimate the k values beyond the reattachment point $x \approx 32$ cm. Some of this model deficiency can be improved by using an improved near-wall model.

A comparison between ASM predictions for $\overline{u^2}$ and data are illustrated in Figure 7.2-16. The model tends to overpredict the $\overline{u^2}$ values in the recirculation zone ($x < 32$ cm) and underestimate the u' values in the recovery region. This is partially attributed to the predicted lower values of wall shear stress compared to the data in the recovery region. This aspect can be seen in the mean velocity profiles; namely, the data shows a fuller profile than the predictions.

The predicted mean square velocities, $\overline{v^2}$ and the measurements are shown in Figure 7.2-17. The predicted $\overline{v^2}$ values are smaller than the data throughout the flow field of interest.

The \overline{uv} predictions for the 2.54 cm step height and the data are presented in Figure 7.2-18. The predicted \overline{uv} values are higher than the data up to the reattachment point ($x \approx 32$ cm), and beyond this point the predicted \overline{uv} magnitudes are less than the data.

The results shown for the 2.54 cm step height are very similar in character to those presented for the 3.81 cm step height.

Step Height of 5.08 cm

For the case of the 5.08 cm step height, hot-wire measurements were made by Eaton and Johnston.⁸³ Measurements of initial conditions were made at 3.81 cm upstream of the step.

The $k-\epsilon$ model predictions for mean axial velocity profiles are shown in Figure 7.2-19. The $k-\epsilon$ model predictions and the data are in good agreement up to $x = 13.97$ cm. Beyond this station, the $k-\epsilon$ model underestimates the recirculation velocities. The predicted velocity profiles when the Richardson number correction was applied are illustrated in Figure 7.2-20. With the Richardson number correction, some improvements in the predictions are obtained.

The mean velocity profiles predicted by ASM with Richardson number correction are shown in Figure 7.2-21. These profiles are similar to those shown in Figure 7.2-20 for the $k-\epsilon$ model with Richardson number correction. The ASM predictions for the axial mean square velocity fluctuations, $\overline{u^2}$, are illustrated in Figure 7.2-22. The predicted $\overline{u^2}$ values are higher than the measurements up to $x = 37.7$ cm and, beyond this station, the model underpredicts

the turbulence kinetic energy component. This trend is similar to the one observed for the 2.54 cm and 3.81 cm step heights.

The ASM predictions for \overline{uv} are shown in Figure 7.2-23. The predicted \overline{uv} values are higher than the data everywhere except the last station. This trend is also consistent with the characteristics observed for the other two steps.

The predicted pressure variations along the step side and the measurements are illustrated in Figure 7.2-24. The predicted and measured pressure coefficient profiles agree well. The $k-\epsilon$ and the ASM tend to slightly overestimate the P_s values (less than 5 percent).

For the case of flow behind a plane step, the $k-\epsilon$ model predicts the mean velocity field fairly accurately, but slightly underpredicts the size of the recirculation zone. When the streamline curvature correction is included, the $k-\epsilon$ model improves the mean velocity profiles and the length of the reattachment point. Mean velocity profiles predicted by ASM with and without streamline curvature are similar to those of the $k-\epsilon$ model. The ASM tends to overestimate the u' velocity components inside the recirculation zone and to underestimate them in the recovery region. A similar trend is observed for the \overline{uv} and k profiles. Further refinement of the ASM model is needed to improve the quantitative accuracy of the model.

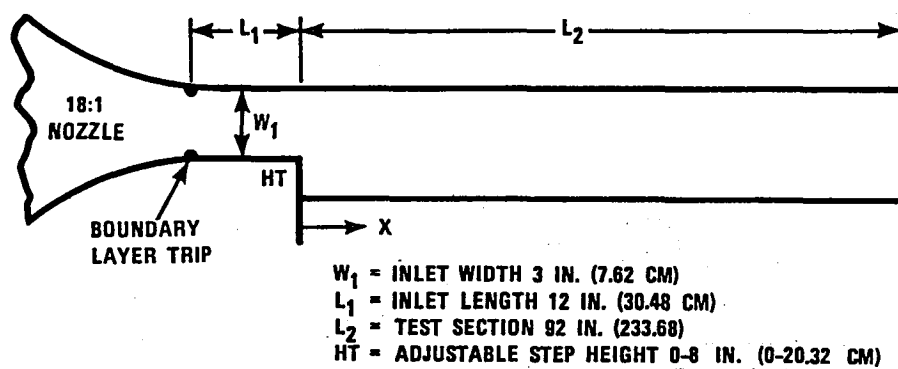


Figure 7.2-1. Geometry of the Backward Facing Plane Step Test Rig.

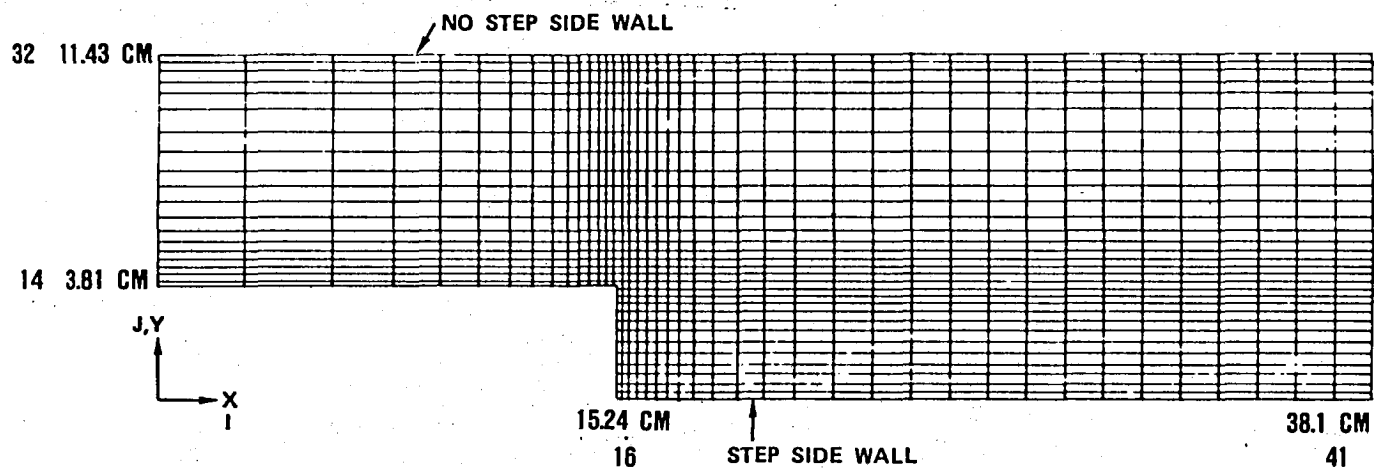


Figure 7.2-2. Partial Grid Network for the Flow Behind the 3.81 cm Step.

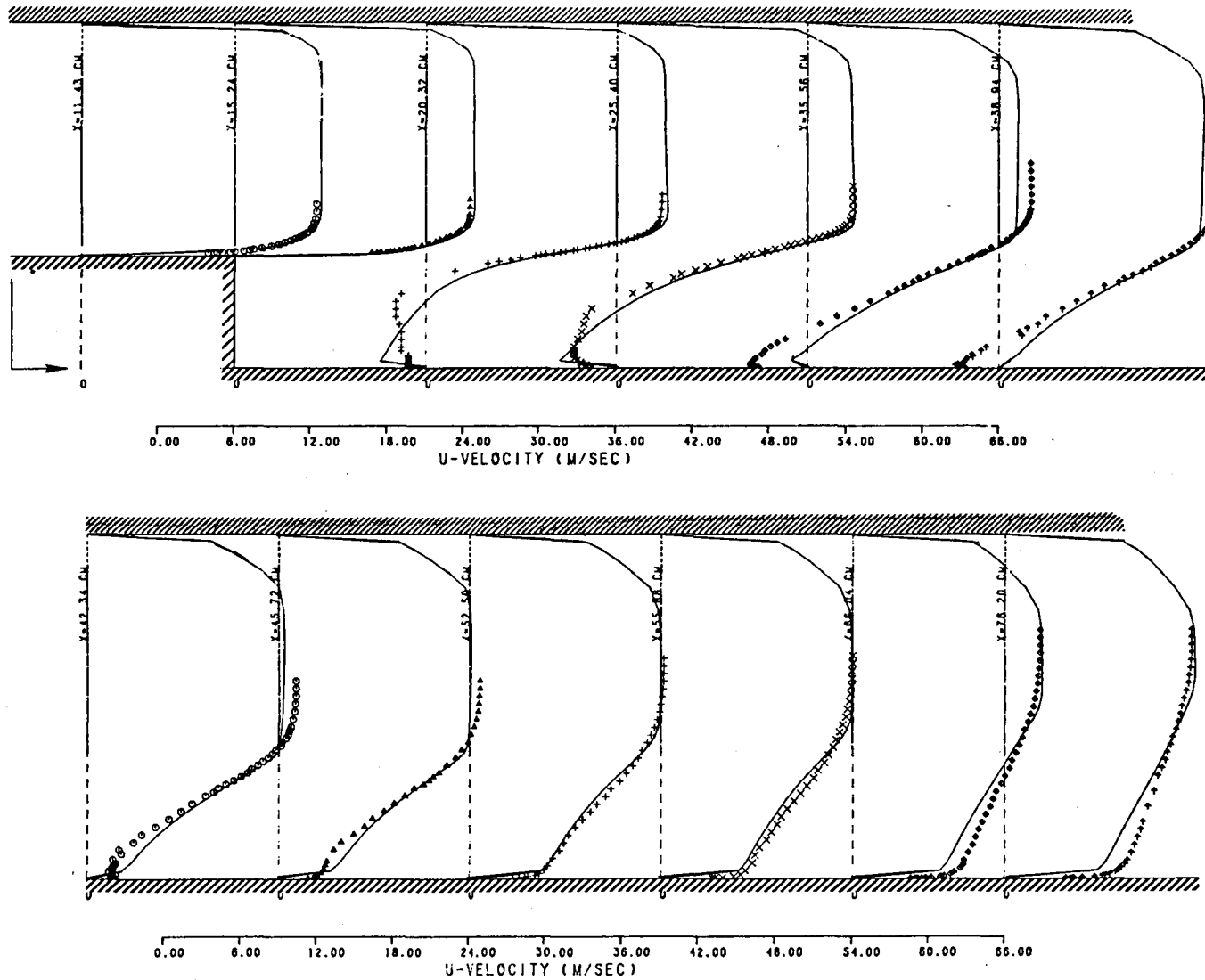


Figure 7.2-3. Standard $k-\epsilon$ Model -- Mean Axial Velocity Profiles for 3.81-cm Step.

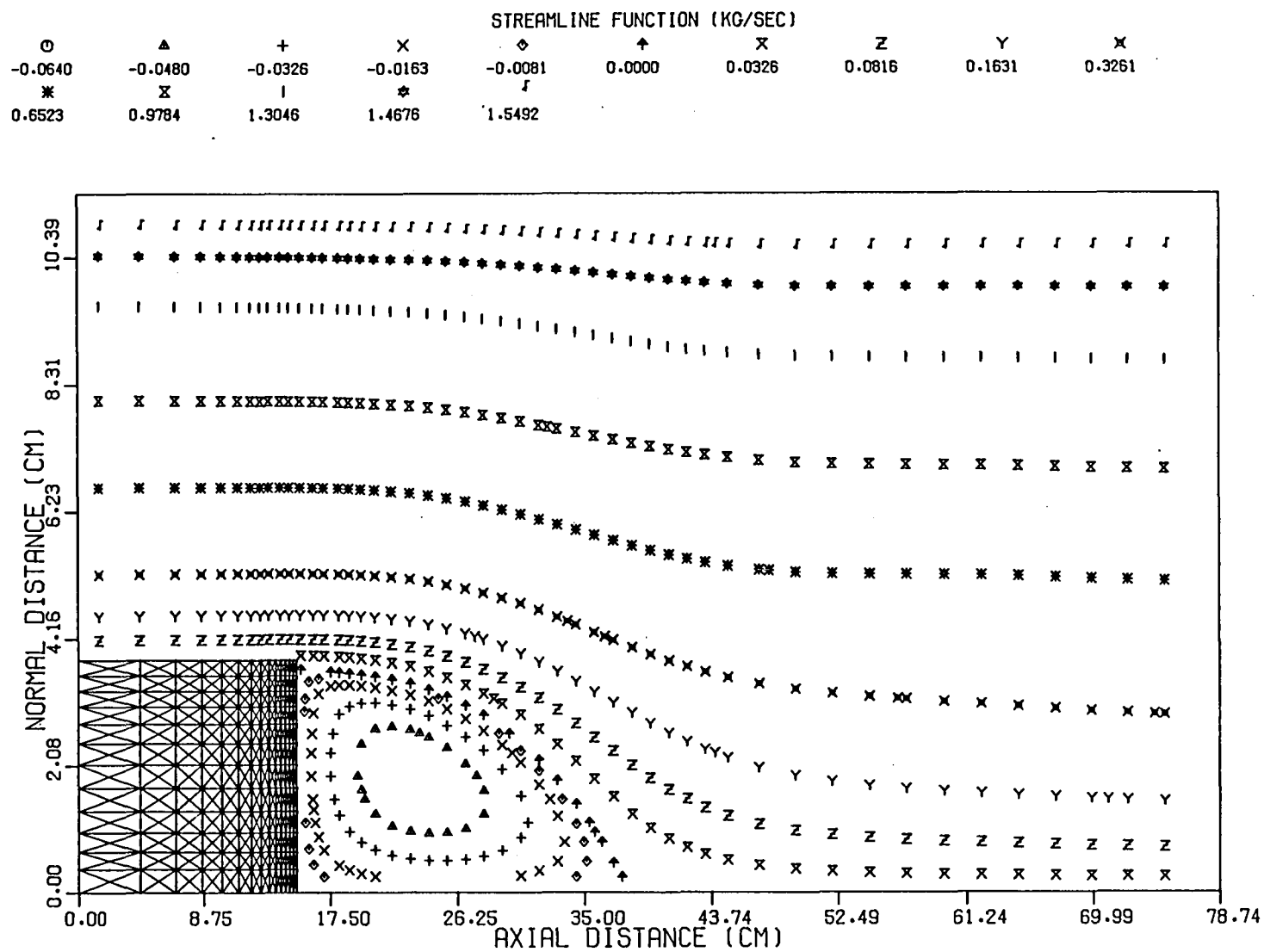


Figure 7.2-4. Predicted Streamline Plot With the Standard $k-\epsilon$ Model.

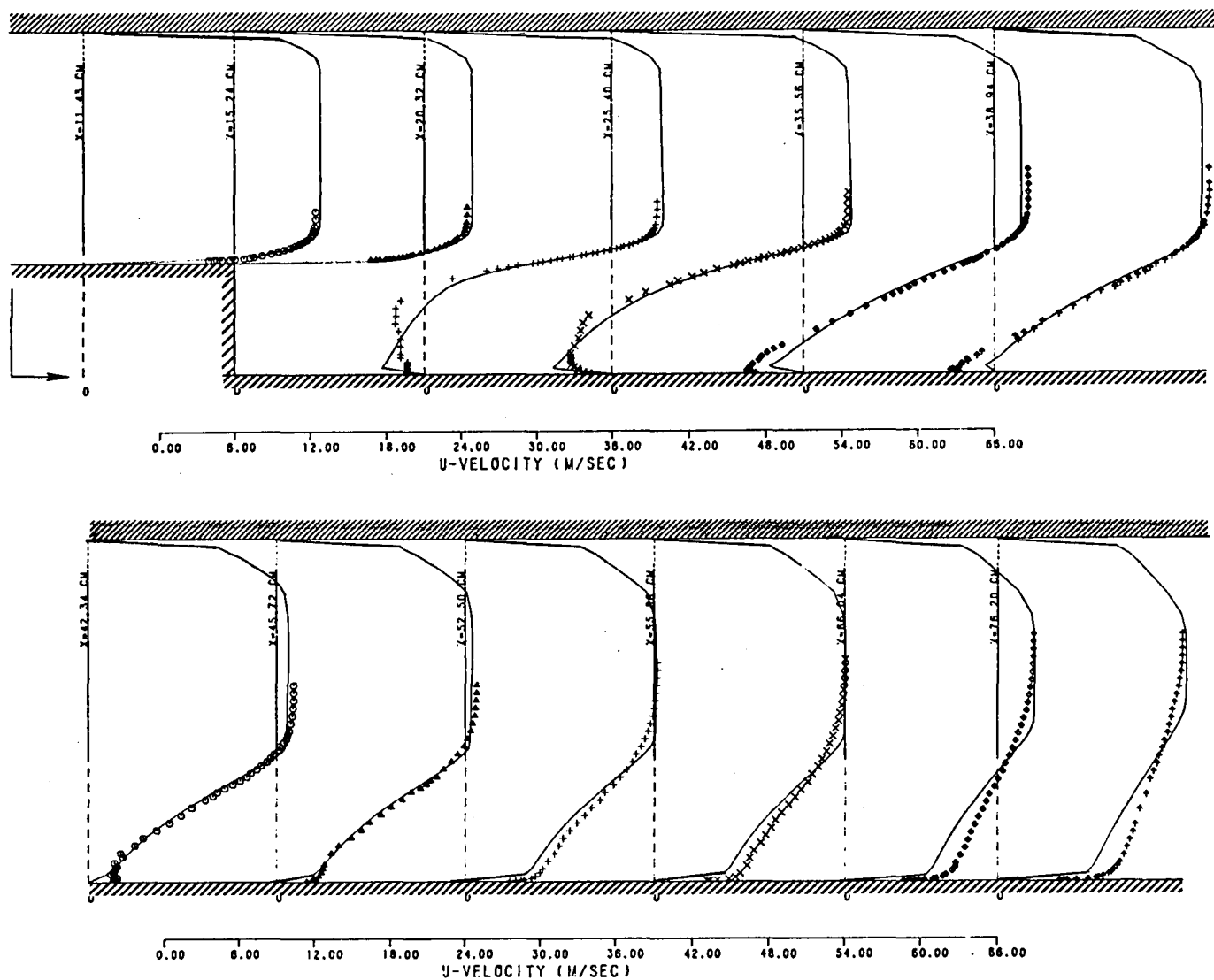


Figure 7.2-5. $k-\epsilon$ Model With Richardson Number Correction Axial Velocity Profiles for the 3.81-cm Step.

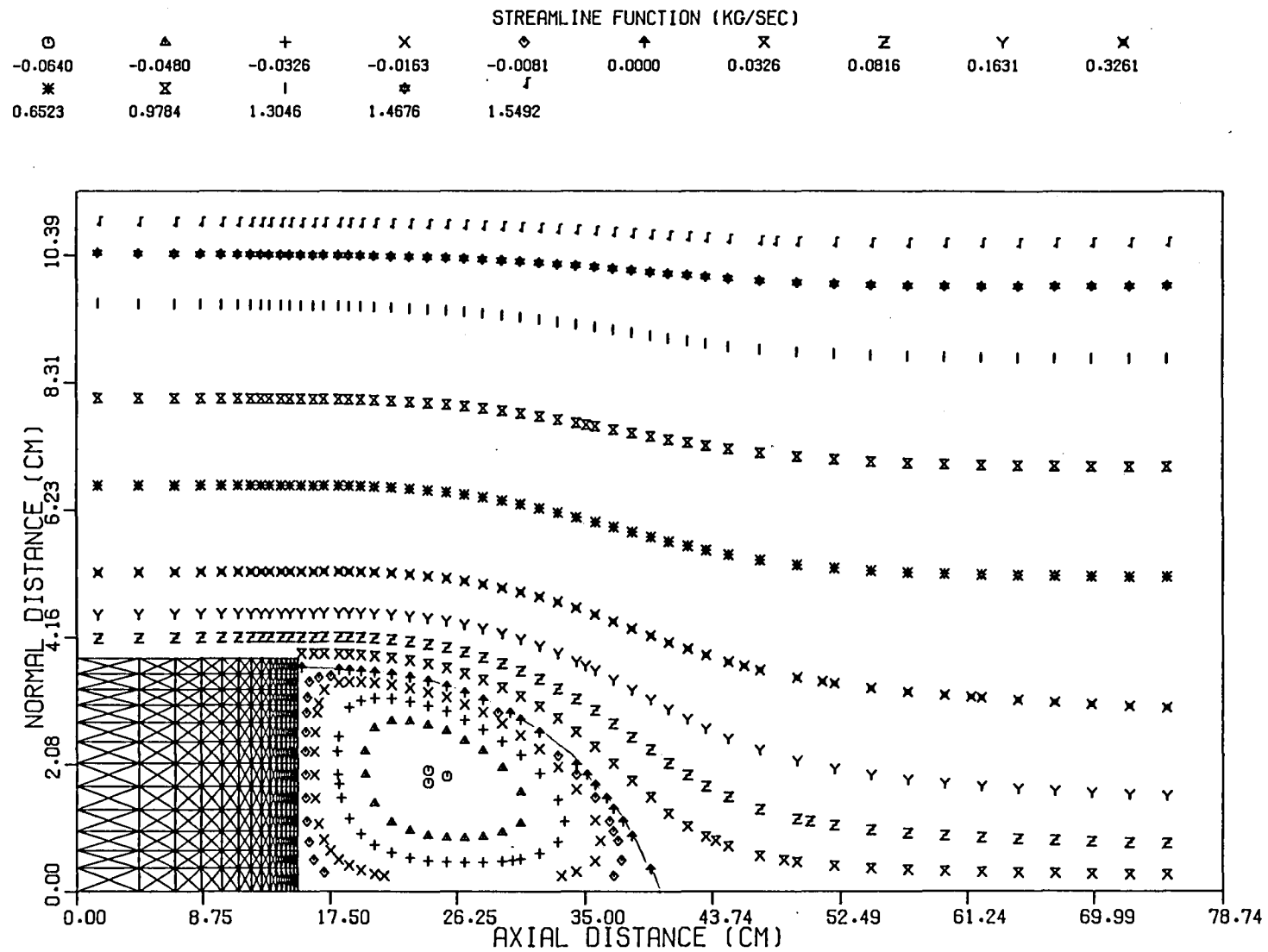
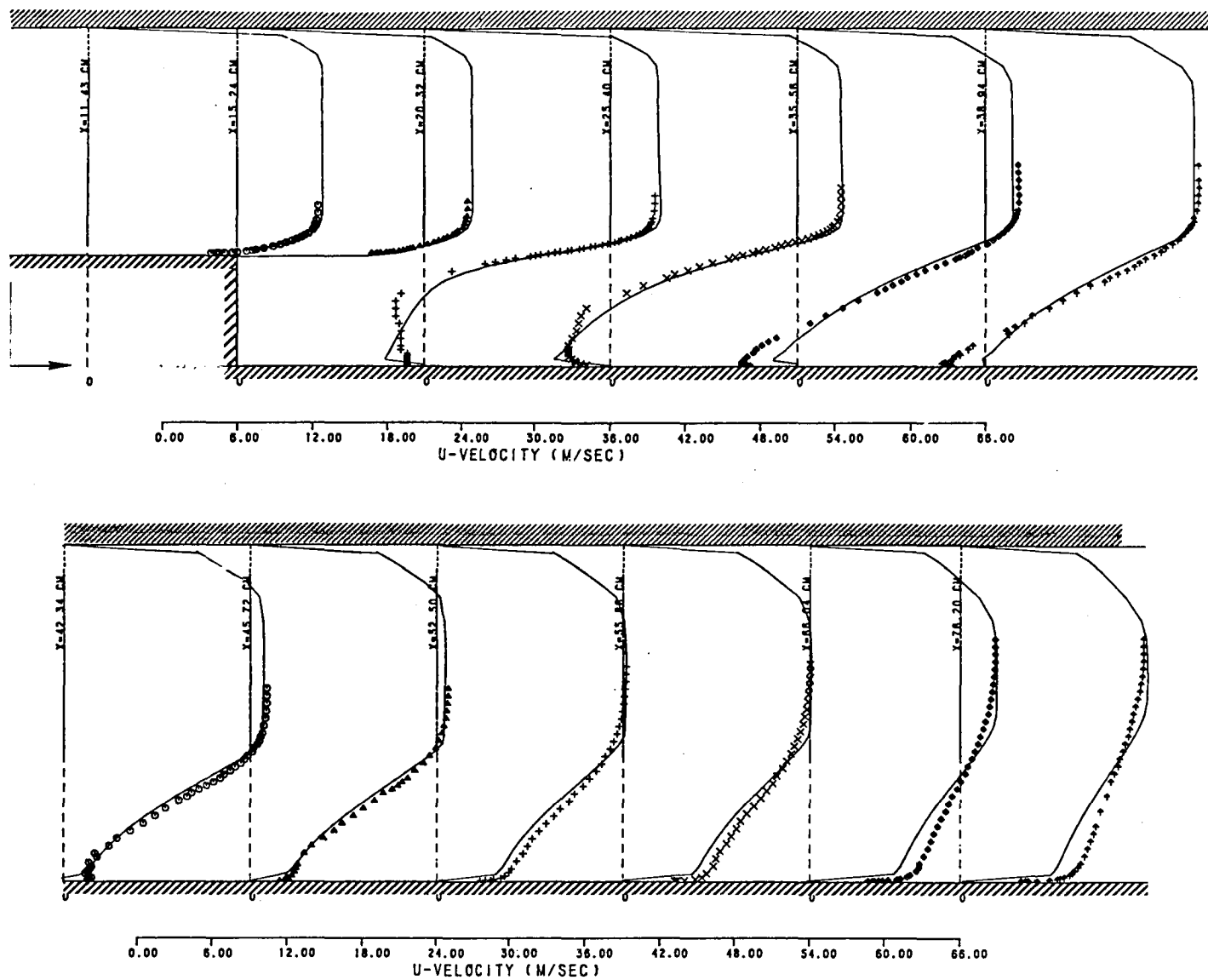


Figure 7.2-6. Predicted Streamline Plot With Richardson Number Correction.



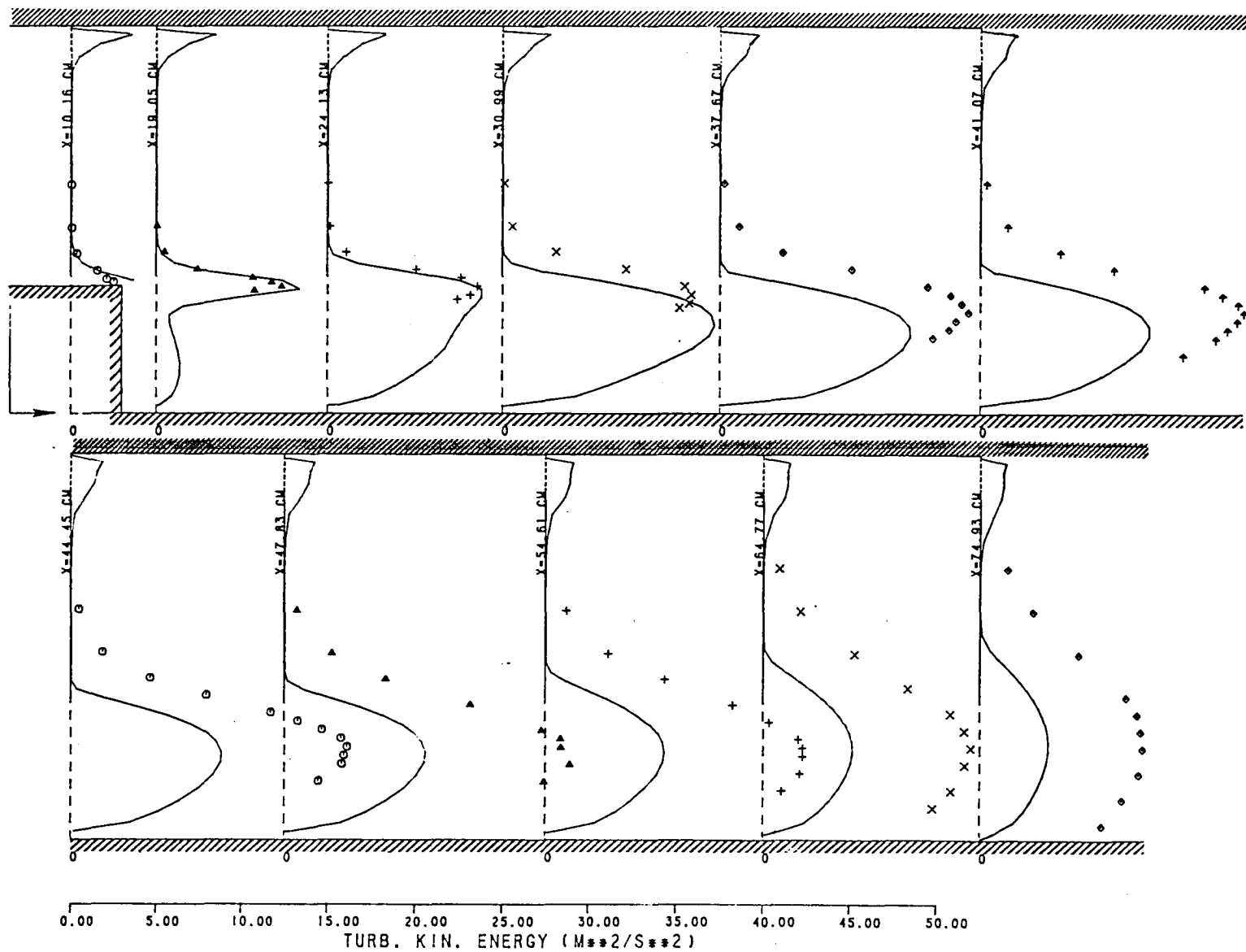


Figure 7.2-8. ASM With Richardson Number Correction -- Turbulence Kinetic Energy Profiles for the 3.81-cm Step.

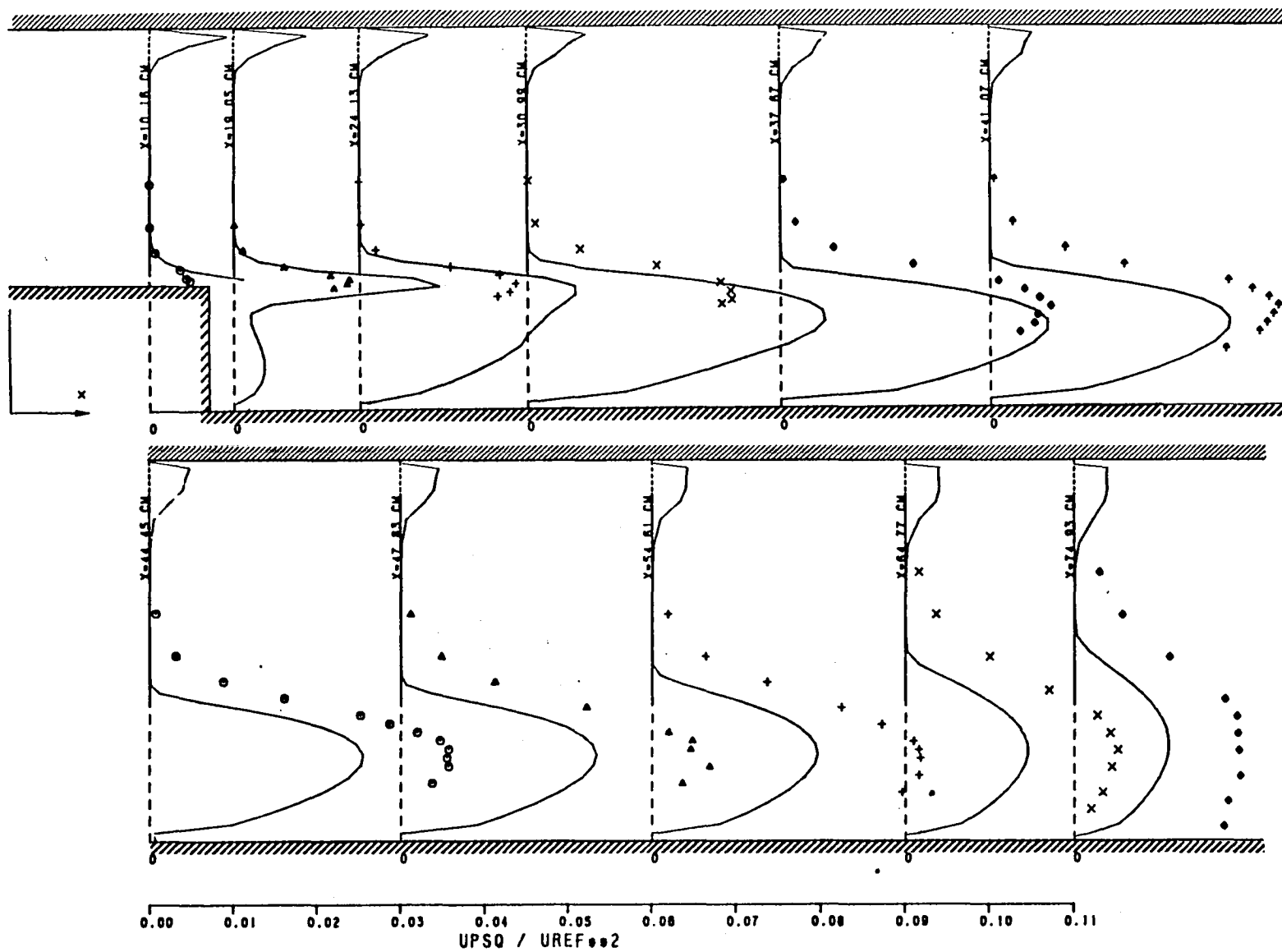


Figure 7.2-9. AMS With Richardson Number Correction -- RMS Axial Velocity Profiles (u^2/U_{Ref}^2) for the 3.81-cm Step.

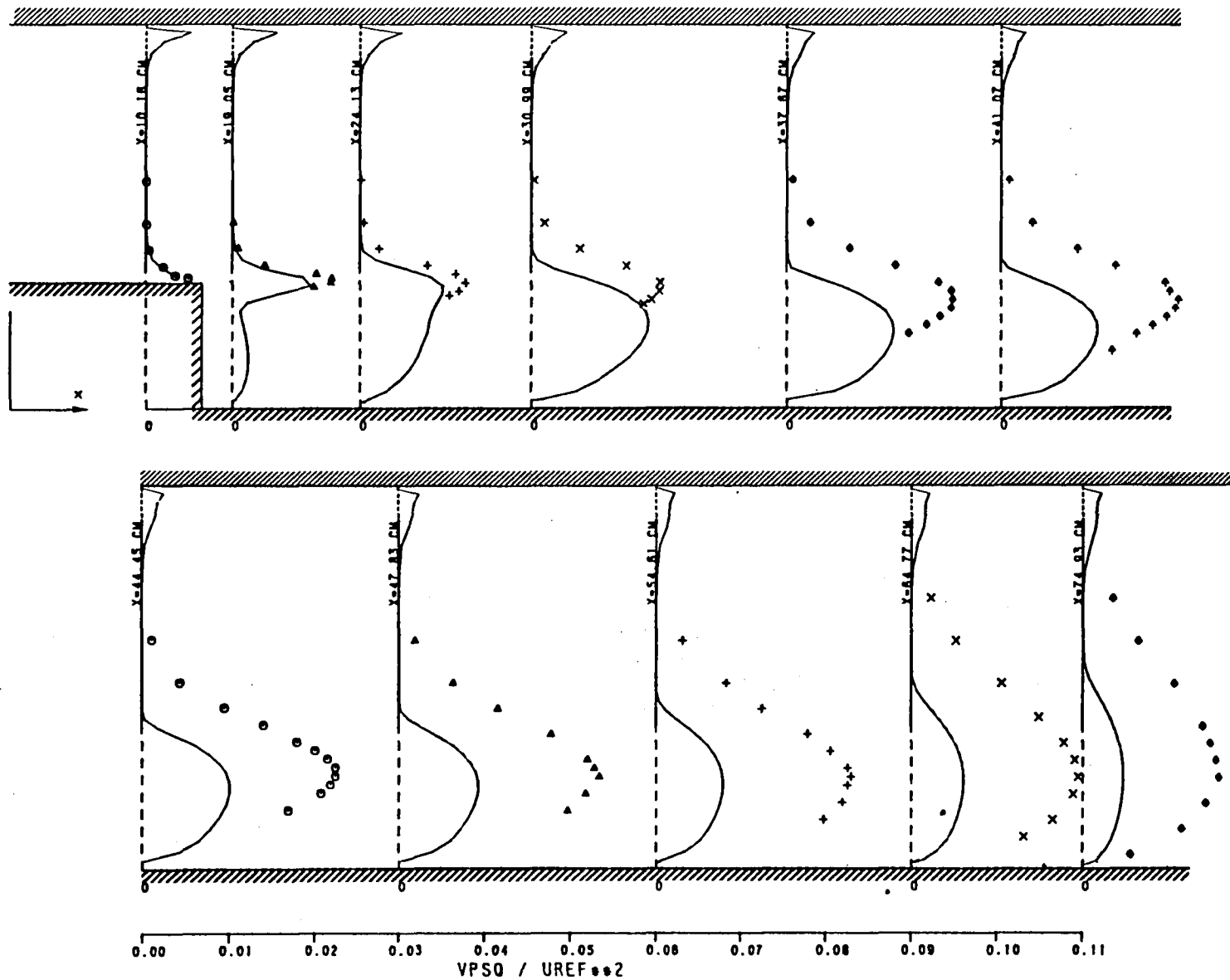


Figure 7.2-10. ASM With Richardson Number Correction -- RMS Radial Velocity (v^2/U_{Ref}^2) for the 3.81-cm Step.

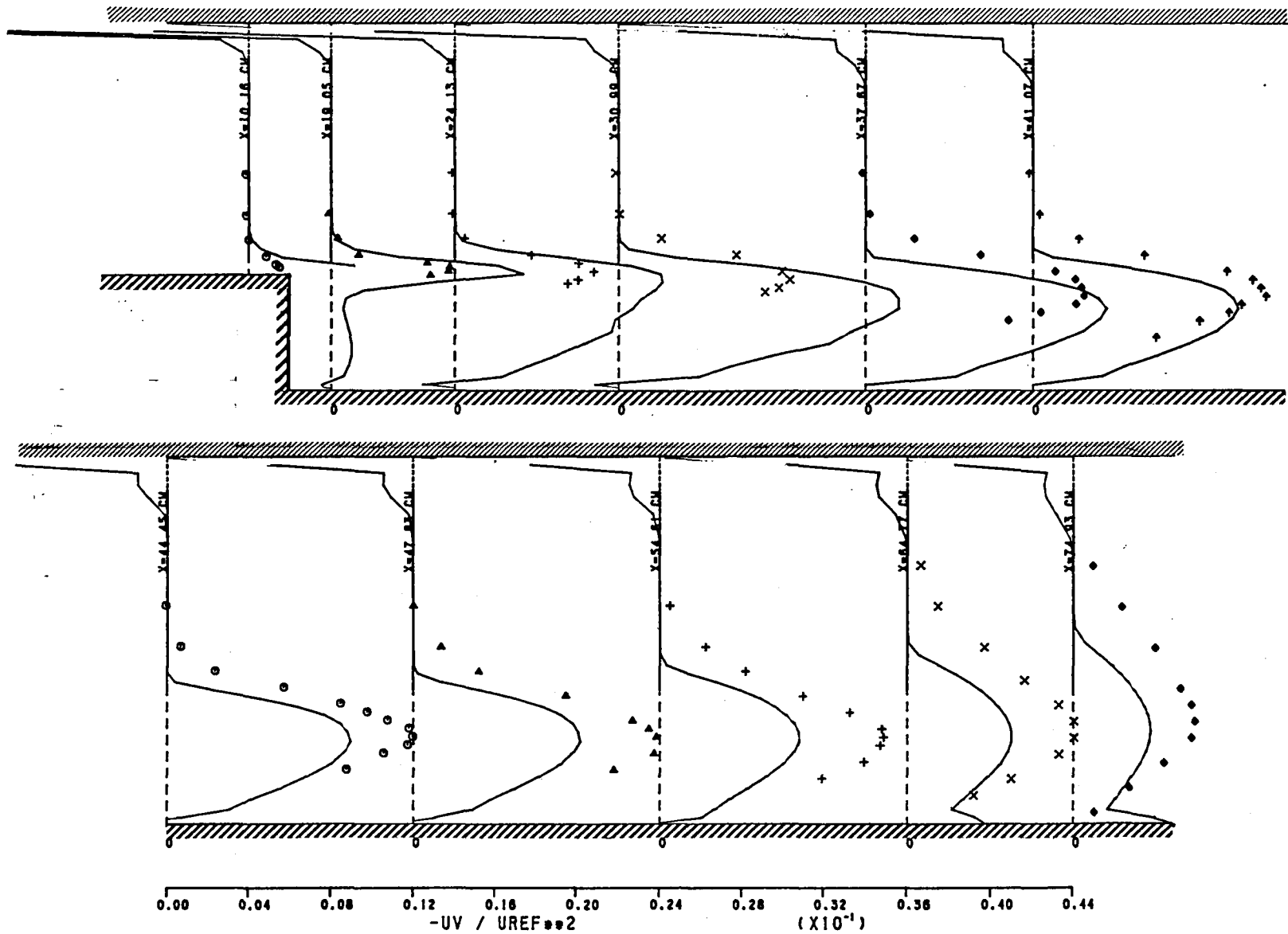


Figure 7.2-11. ASM With Richardson Number Correction -- Shear Stress (\overline{uv}/U_{Ref}^2) Distribution.

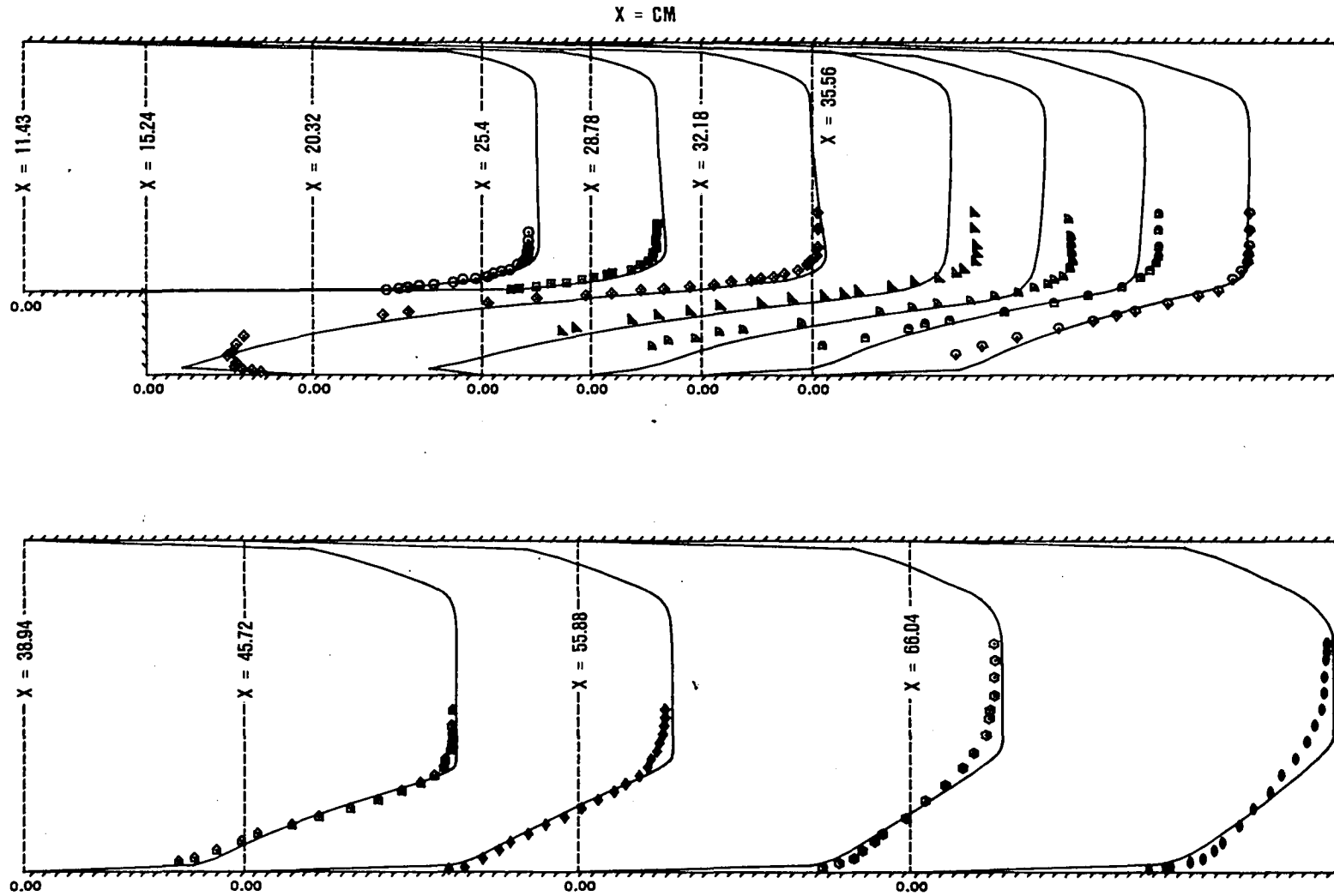


Figure 7.2-12. Comparison Between Standard $k-\epsilon$ Model Predictions and Measured Streamwise Velocity Components for 2.54-cm Step Height.

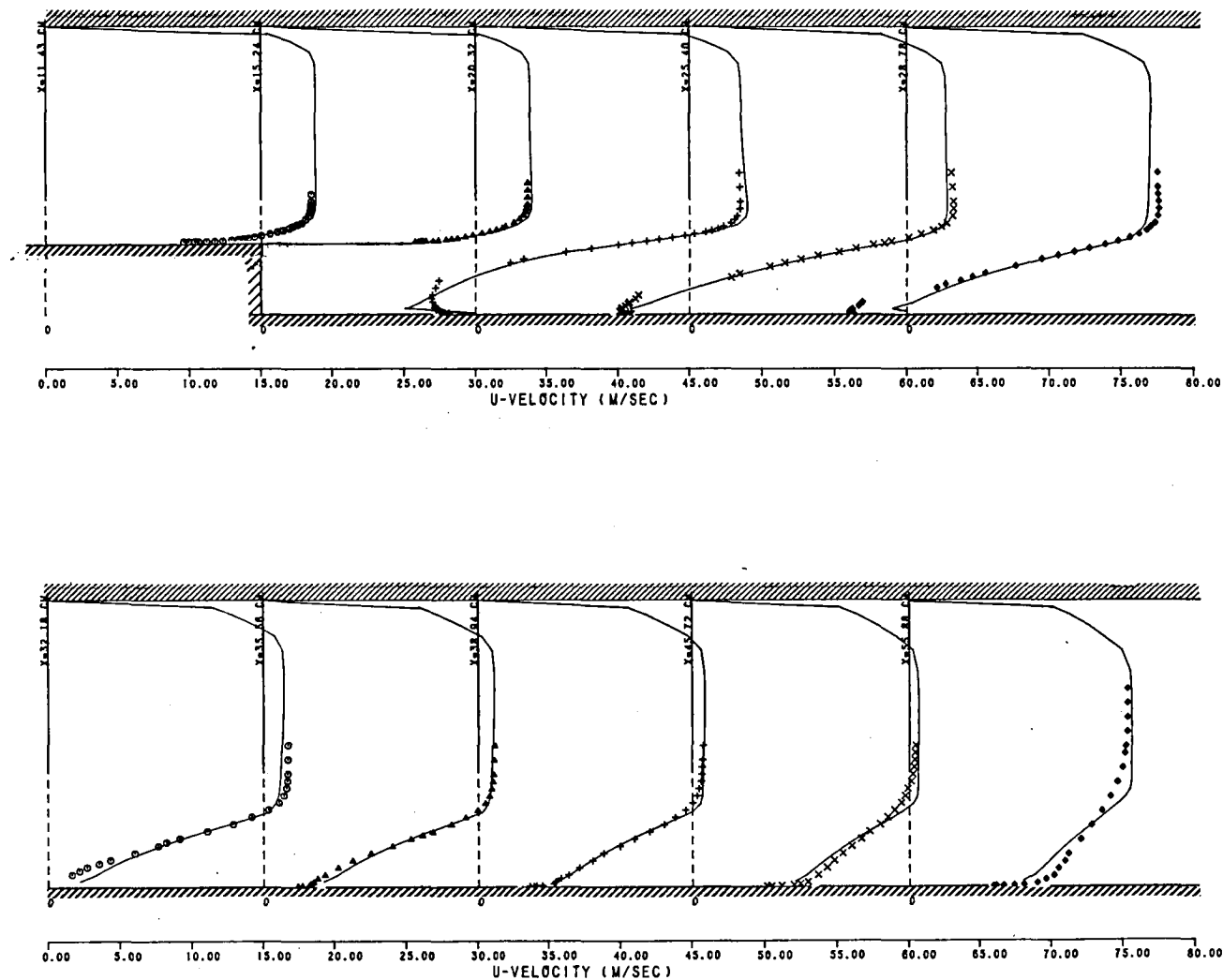


Figure 7.2-13. k - ϵ Model With Richardson Number Correction - Axial Velocity Profile for the 2.54-cm Step.

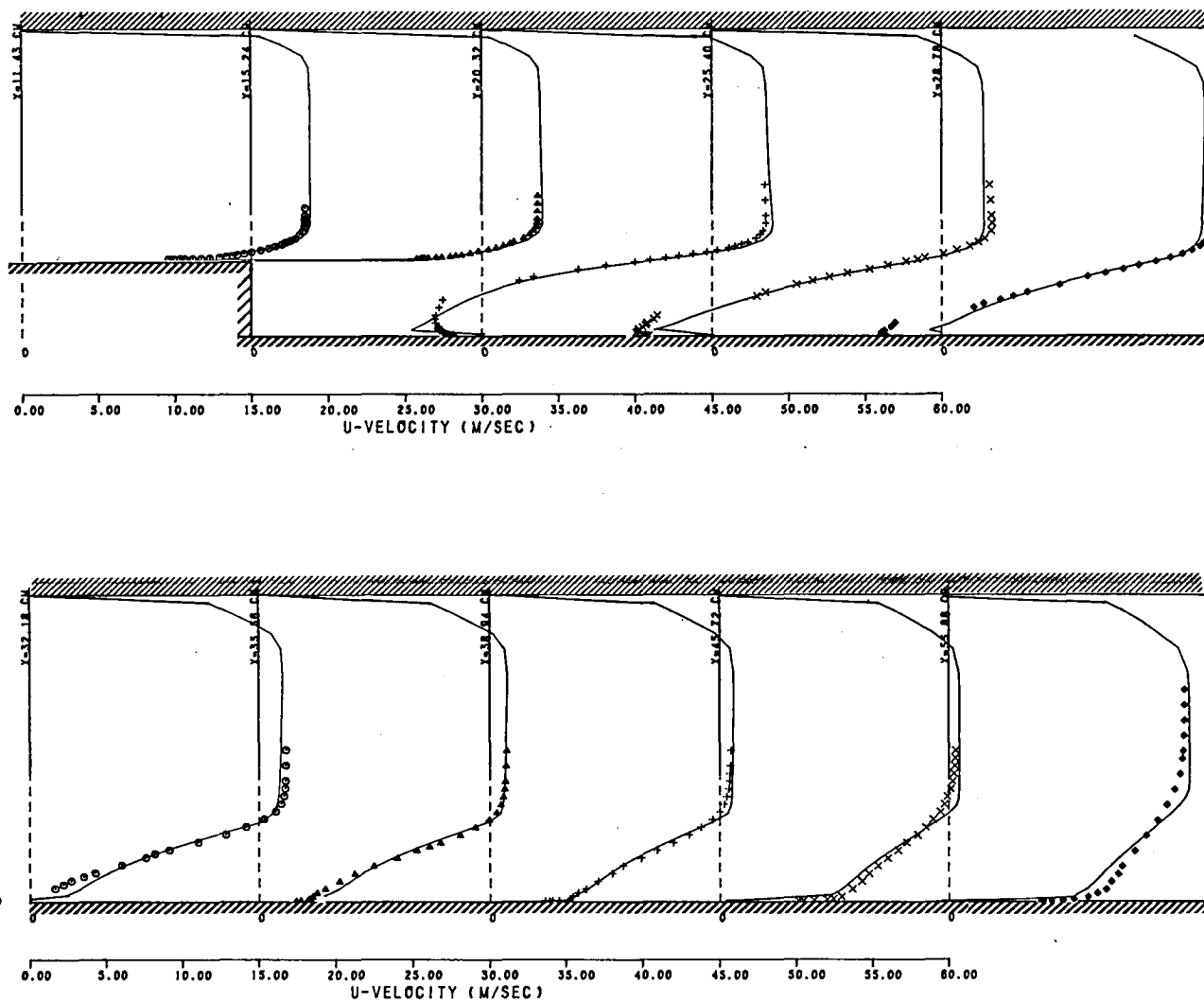


Figure 7.2-14. ASM with Richardson Number Correction - Axial Velocity Profile.

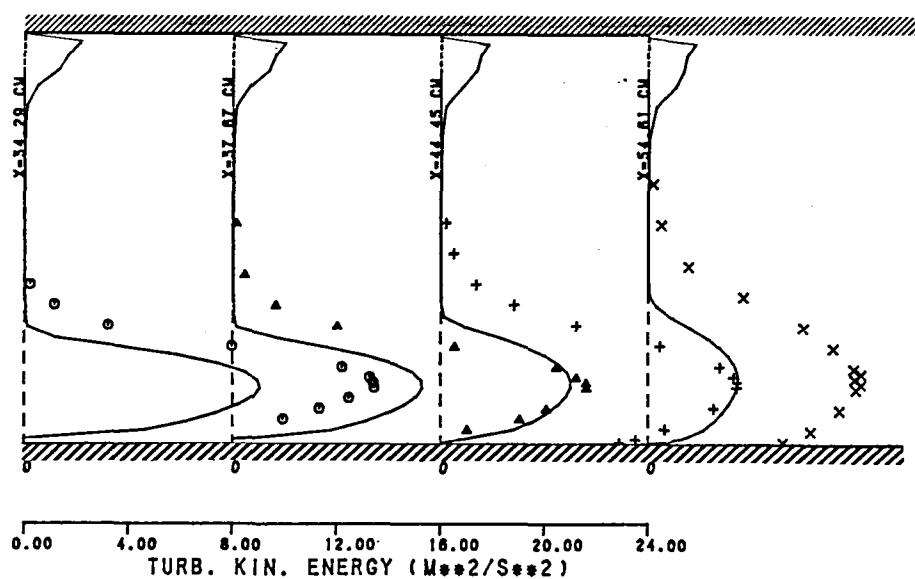
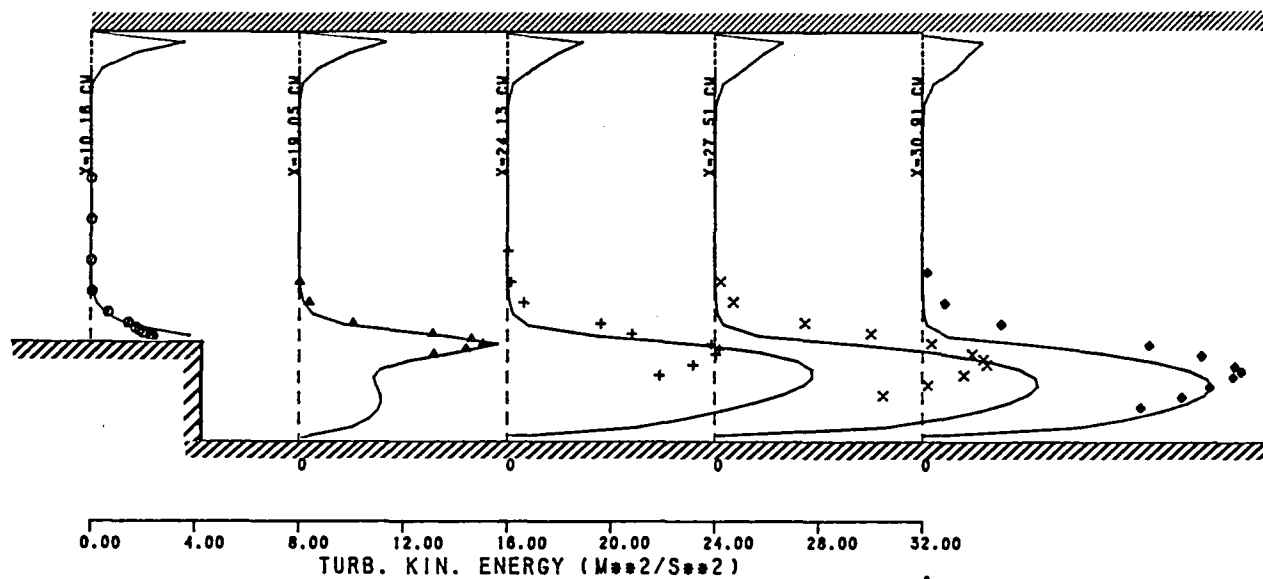


Figure 7.2-15. ASM with Richardson Number Correction - Turbulence Kinetic Energy Profile.

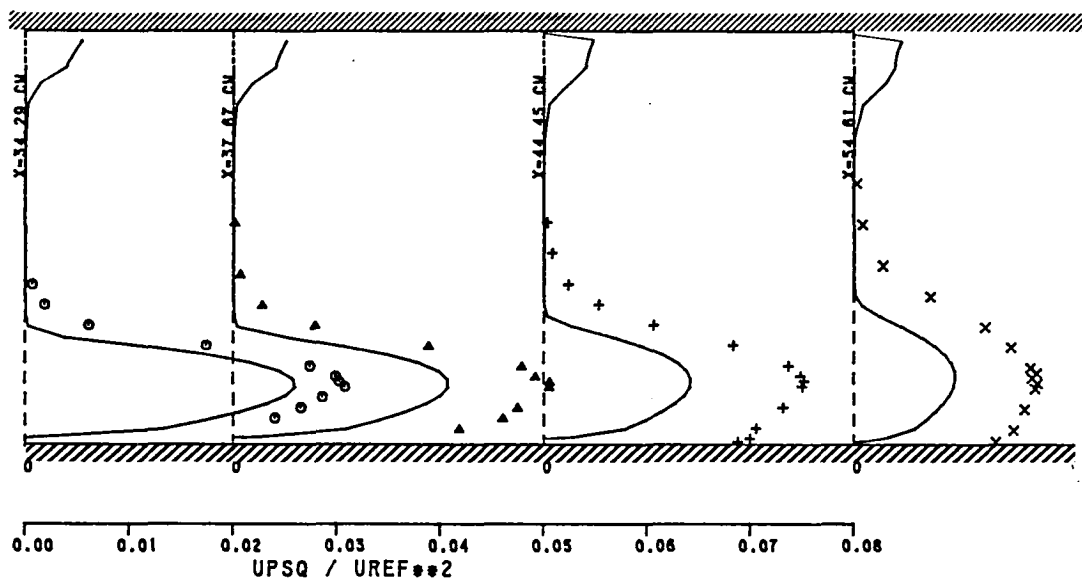
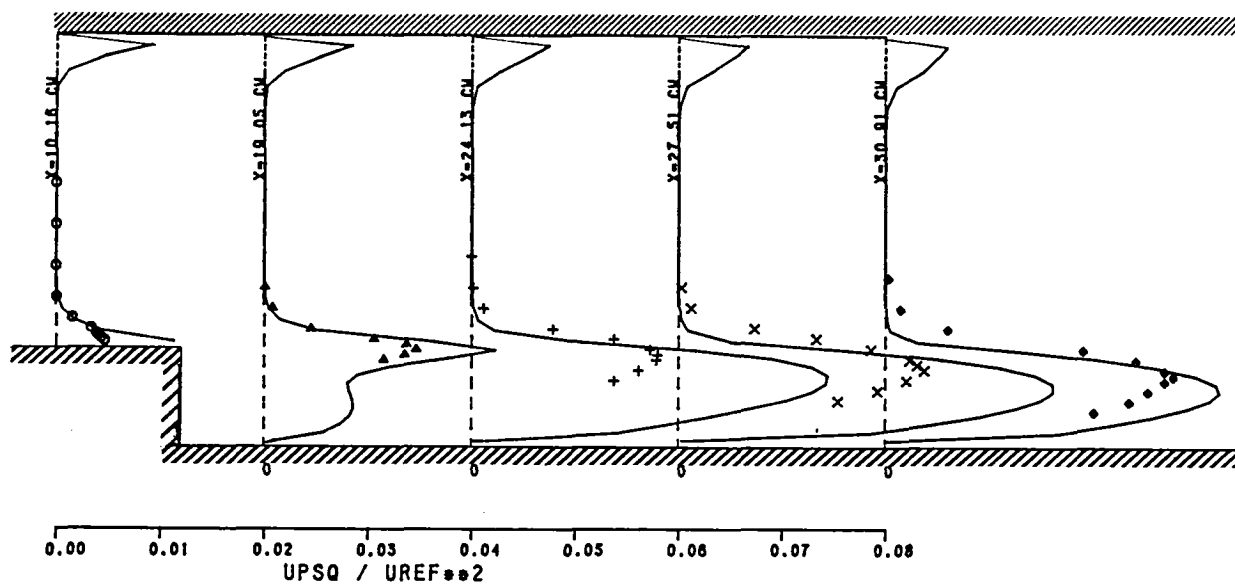


Figure 7.2-16. ASM with Richardson Number Correction - Axial Velocity Fluctuations ($\overline{u^2}/U_{ref}^2$).

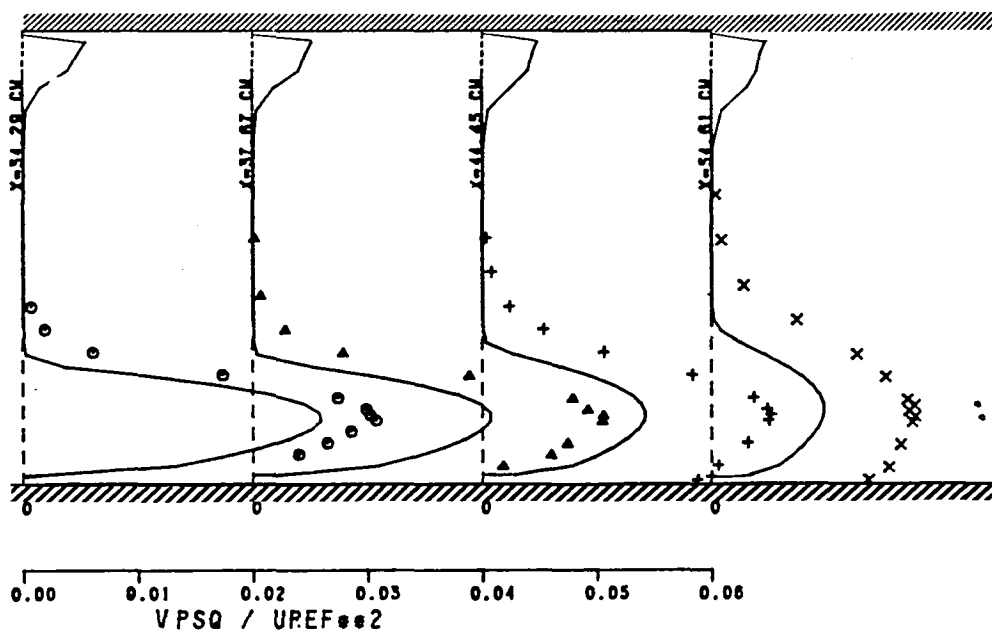
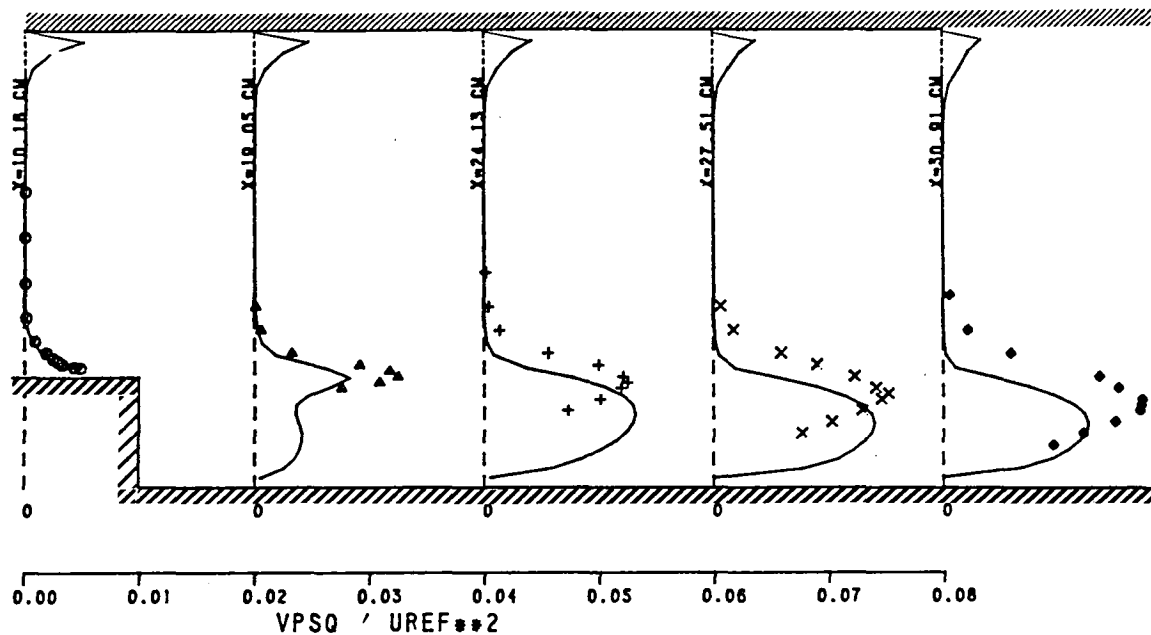


Figure 7.2-17. ASM with Richardson Number Correction - Normal Velocity Fluctuations ($\overline{v^2}/U_{Ref}^2$).

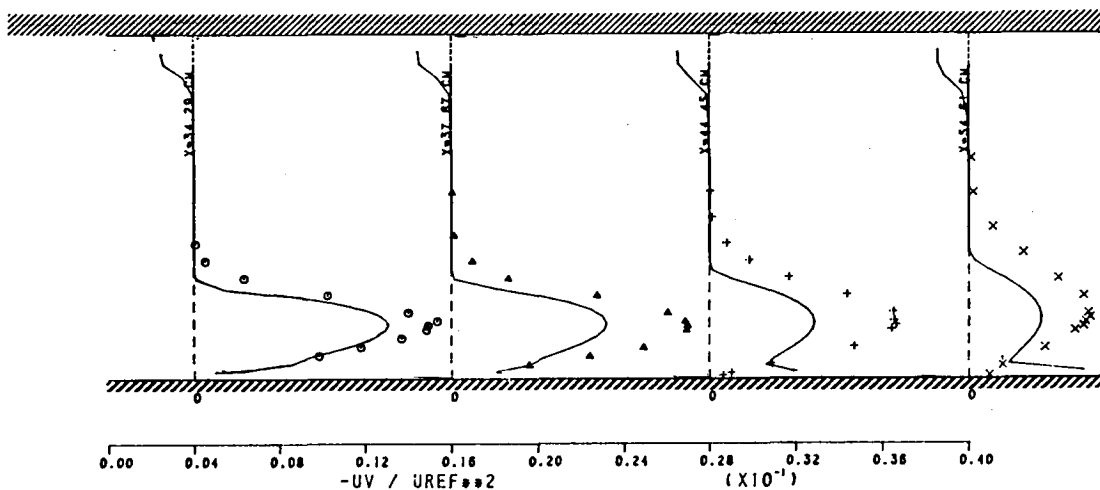
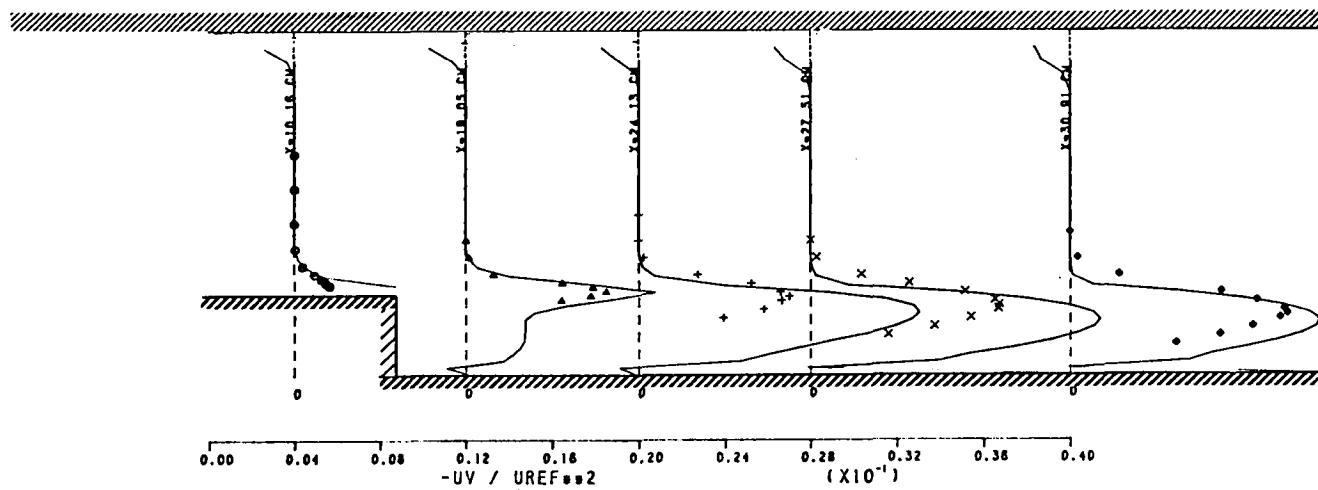


Figure 7.2-18. ASM with Richardson Number Correction - Shear Stress (\overline{uv}/u_{Ref}^2) Profiles for the 2.54-cm Step.

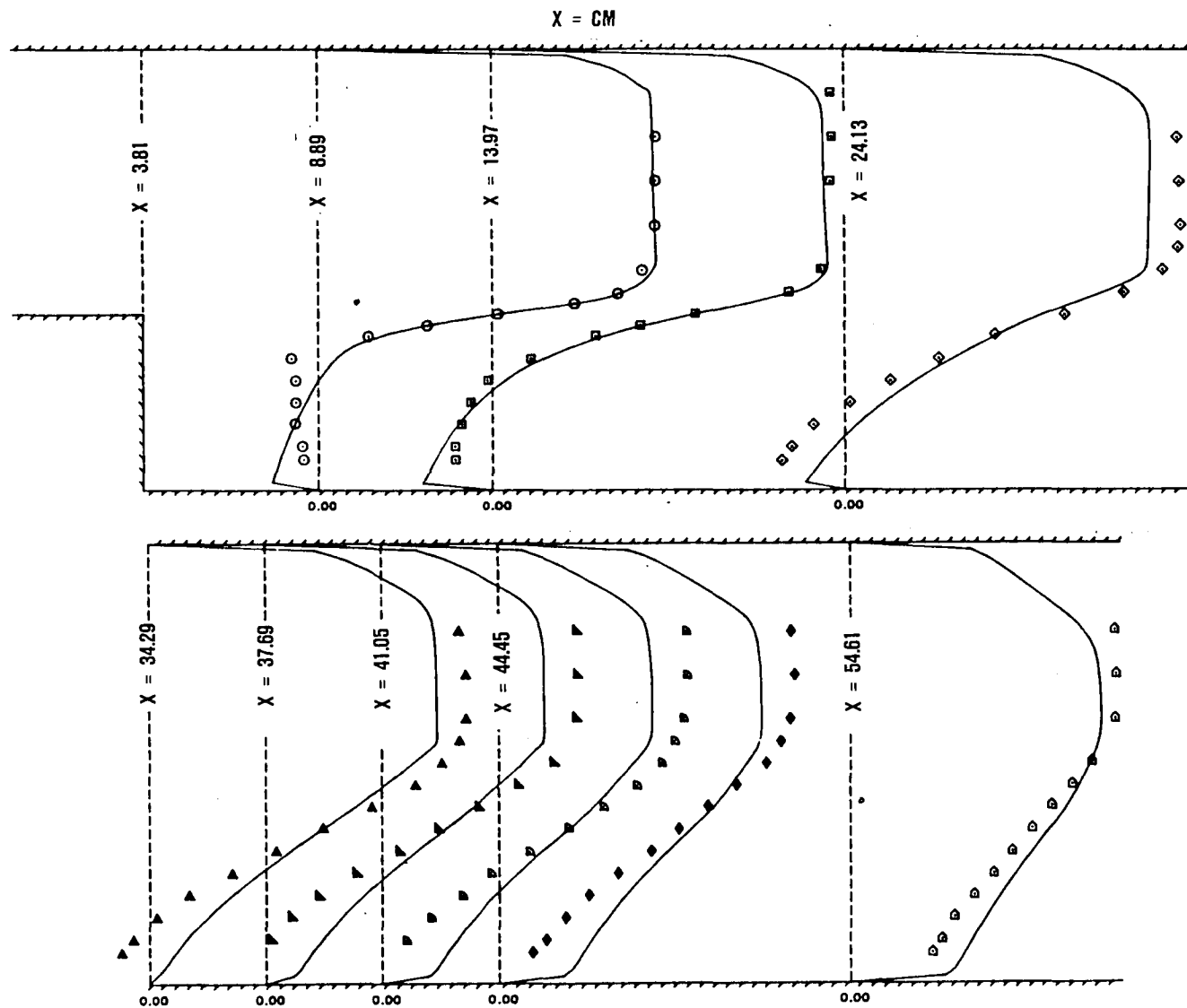


Figure 7.2-19. Comparison Between the Standard $k-\epsilon$ Model Predictions and Measured Streamwise Velocity Components for the 5.08 cm Step.

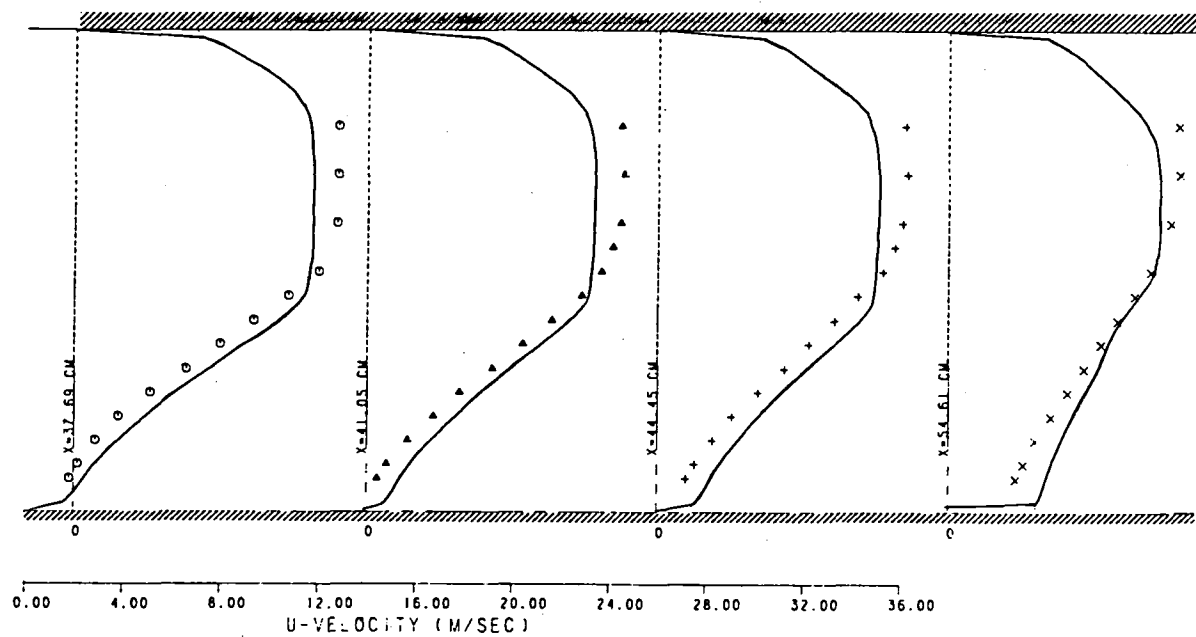
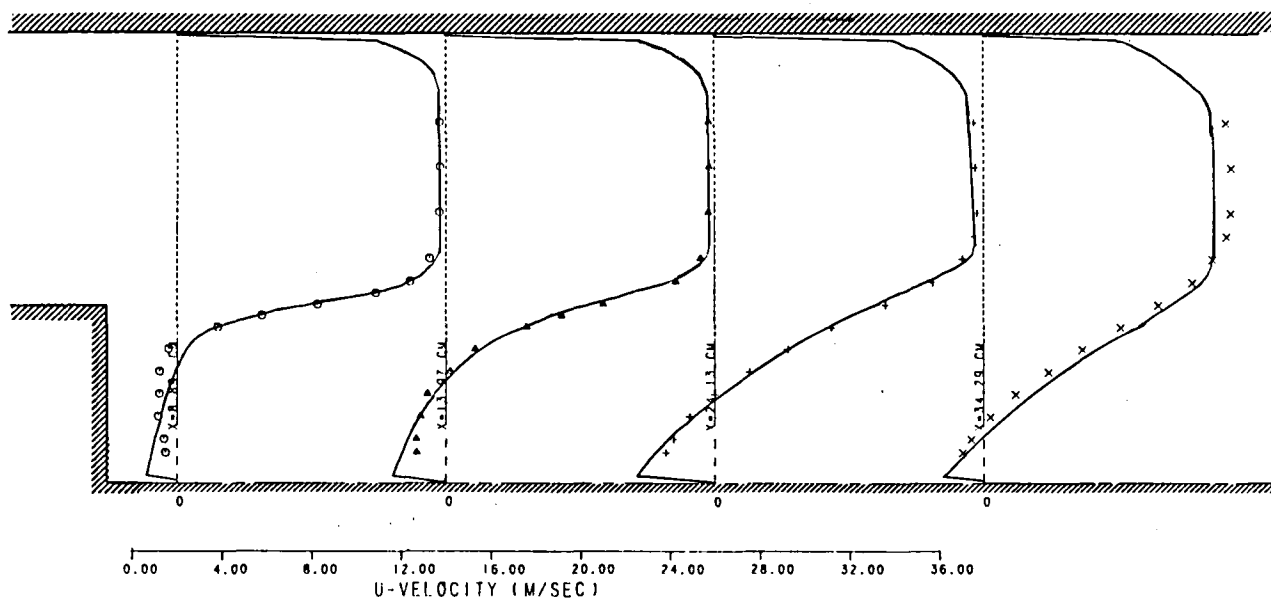


Figure 7.2-20. k - ϵ Model with Richardson Number Correction - Axial Velocity Profile.

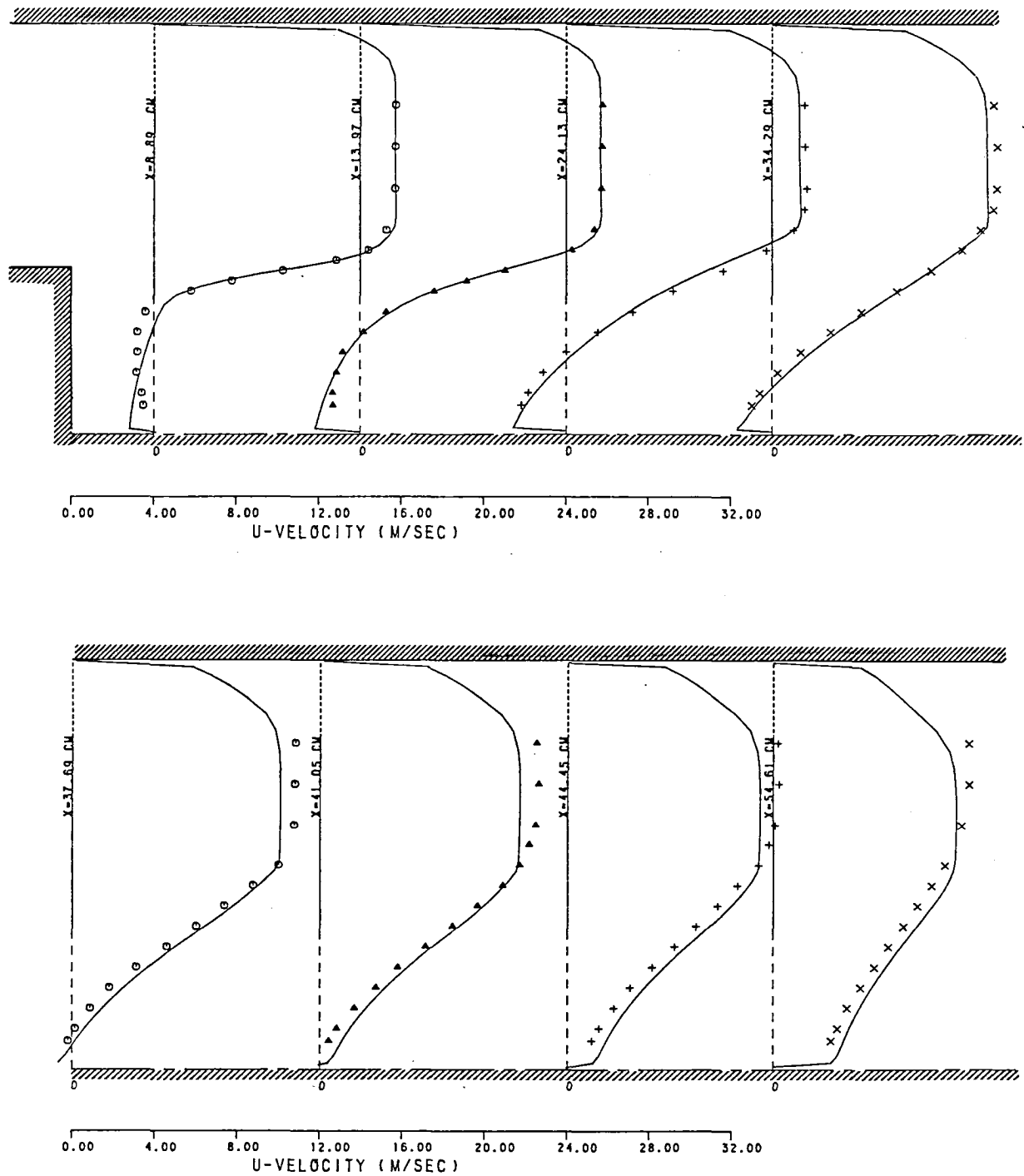


Figure 7.2-21. ASM with Richardson Number Correction - Axial Velocity Profile.

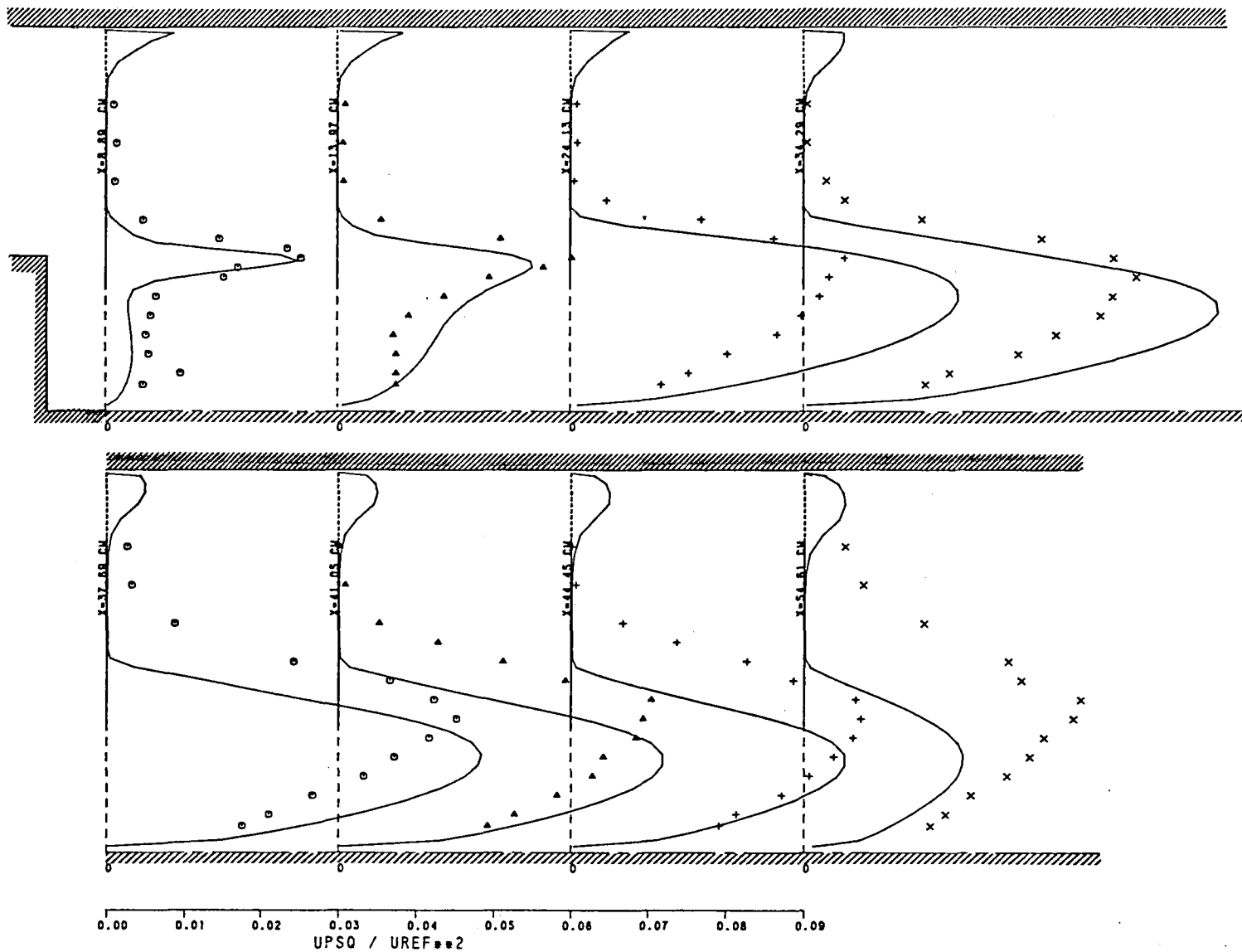


Figure 7.2-22. ASM with Richardson Number Correction - Axial Velocity Fluctuations ($\overline{u^2} / U_{Ref}^2$).

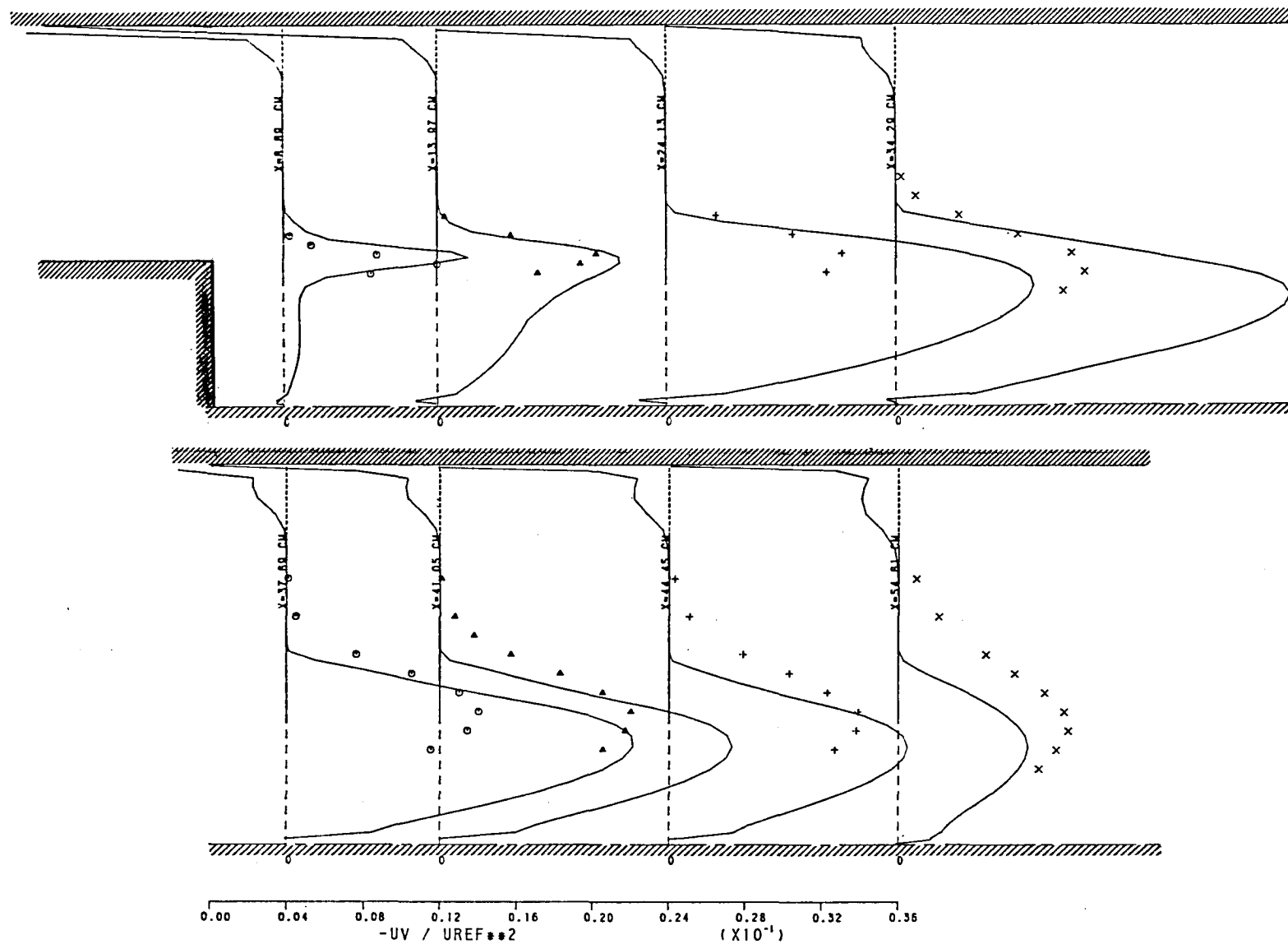


Figure 7.2-23. ASM with Richardson Number Correction - Shear Stress ($\overline{uv} / U_{Ref}^2$) Distribution.

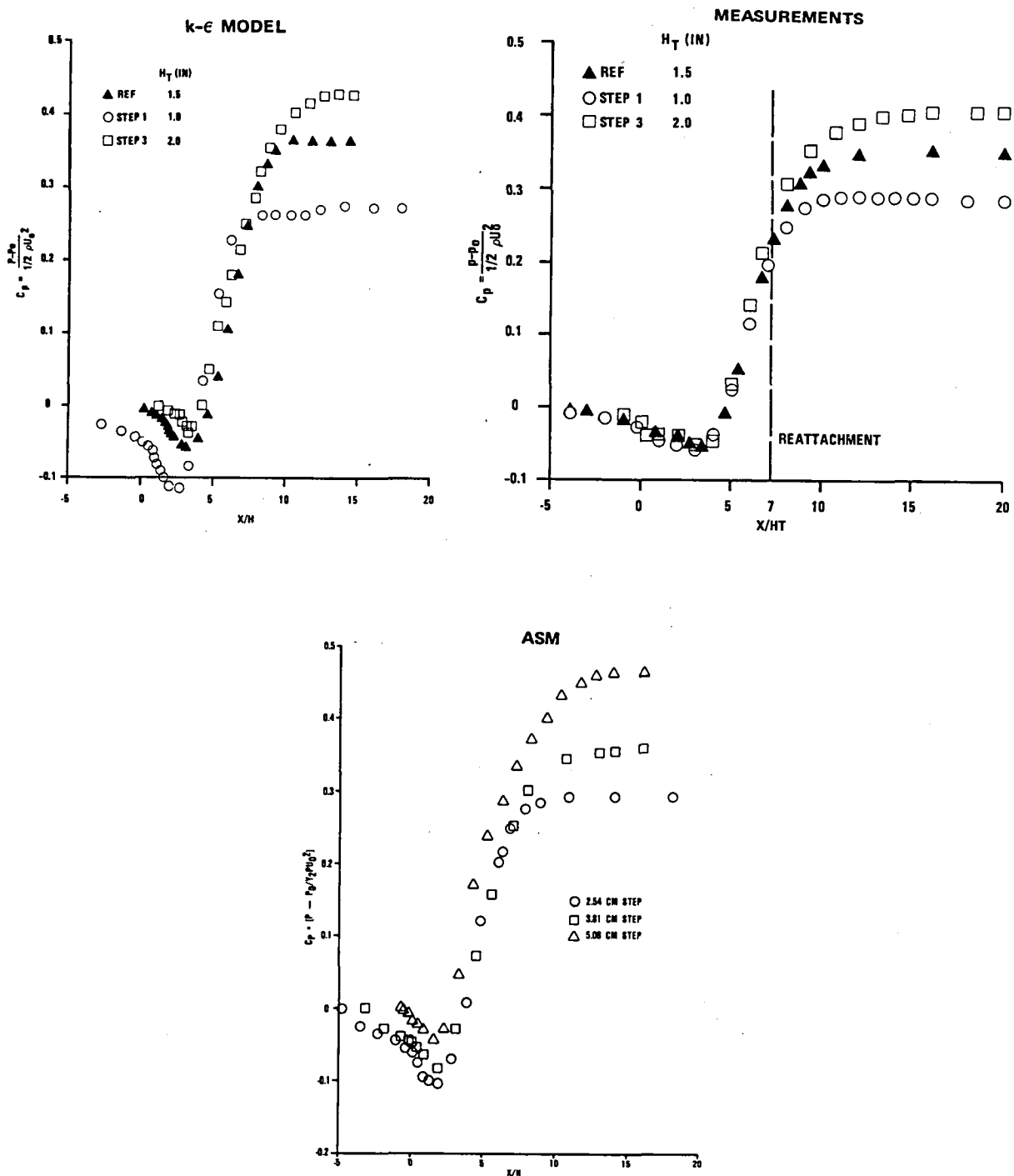


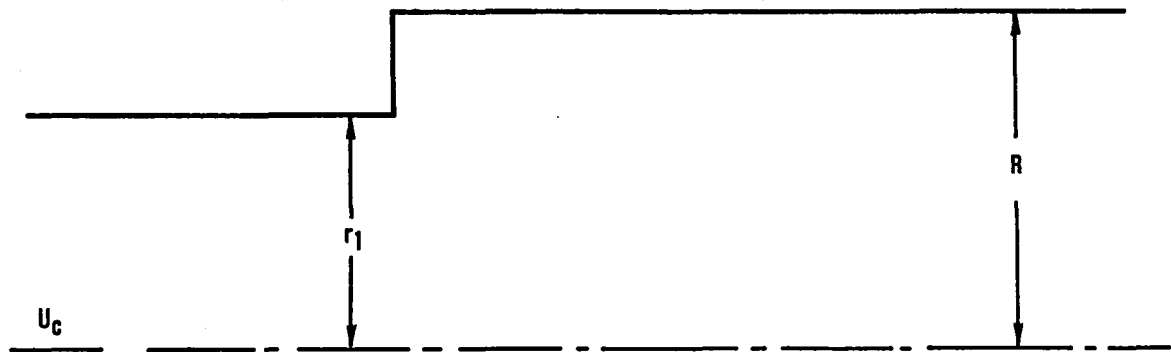
Figure 7.2-24. Comparison Between Predicted and Measured Wall Static Pressure Distribution.

7.3 Flow Through a Sudden Pipe Expansion

A detailed experimental study of the flow behind a sudden expansion in a circular duct of 100 mm diameter (D) was made by Moon and Rudinger⁸⁹ using a laser Doppler velocimeter (LDV), as shown in Figure 7.3-1. The diameter of the inlet tube was 7 mm, thus giving an expansion ratio of approximately 2.0, which is representative of typical dump combustors. The inlet tube was long enough (1260 mm or 18 tube diameters) to give a fully developed velocity profile upstream of the step.

The 2-D elliptic computations were performed with the standard k- ϵ model for the region extending 10.2 mm upstream of the dump and 169.2 mm downstream from the dump (1.69D). A total of 55 x 40 nodal points were used to simulate the geometry. A fully developed pipe flow profile was used for the inlet station. The predicted axial velocity profiles (Figure 7.3-2) are compared with the measured data at five axial stations: $\frac{X}{D} = 0.25, 0.75, 1.0, 1.25$ and 1.5; here X is the axial distance downstream from the step. The overall agreement between predictions and data is acceptable.

Similar to the plane-step results presented in Section 7.2 for the standard k- ϵ model, the axisymmetric step calculations stress the following. The shear layer region is predicted well. The predicted recirculation zone height and the maximum reverse-flow velocities are smaller than data. The reattachment point is predicted reasonably well. Further improvements can be made by using the streamline curvature corrections. Because of the limited range of the data available, no other computations were made for this configuration.



$R_1 = 0.035 \text{ M}$
 $R = 0.05 \text{ M}$
 $U_c = 64.8 \text{ M/S}$

Figure 7.3-1. Sudden Pipe-Expansion Setup of Moon and Rudinger⁸⁹.

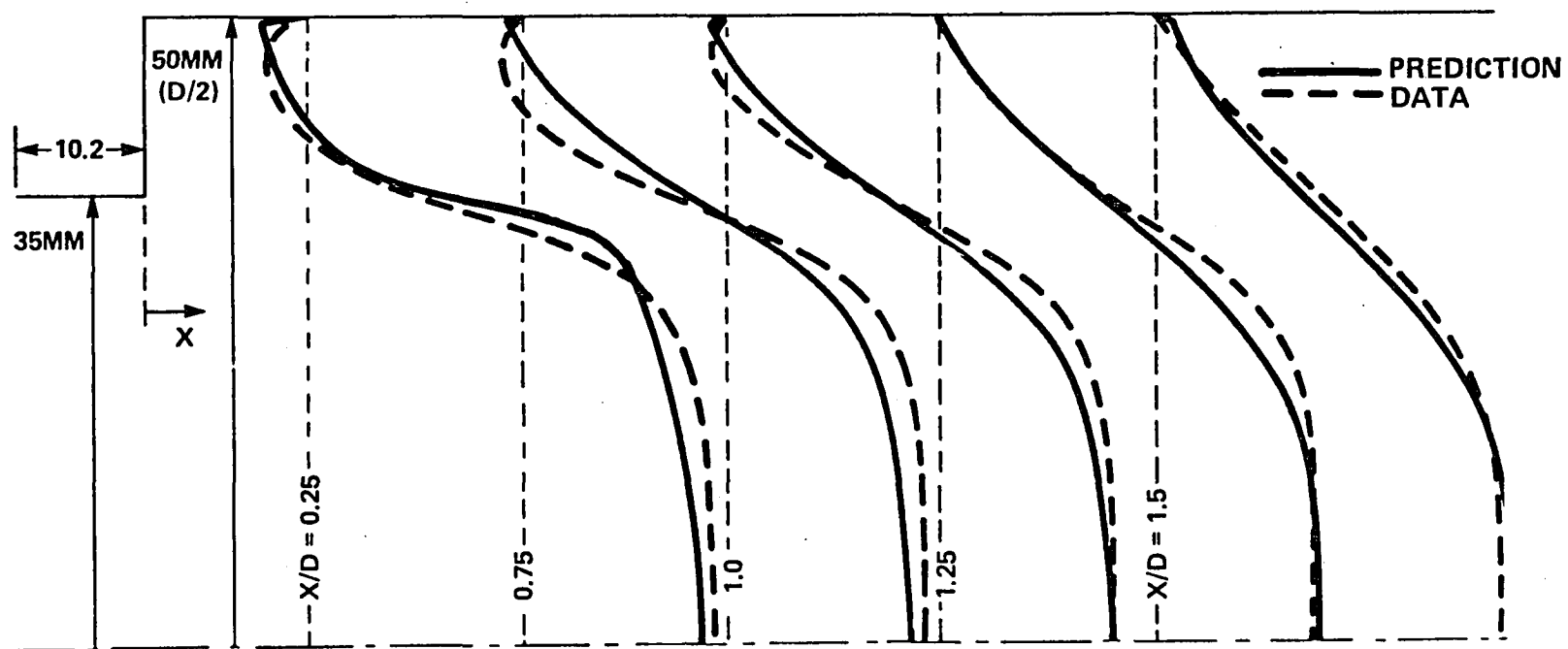


Figure 7.3-2. Comparison Between the Standard $k-\epsilon$ Prediction and Measured Axial Velocity Profiles in a Tube with Sudden Expansion.

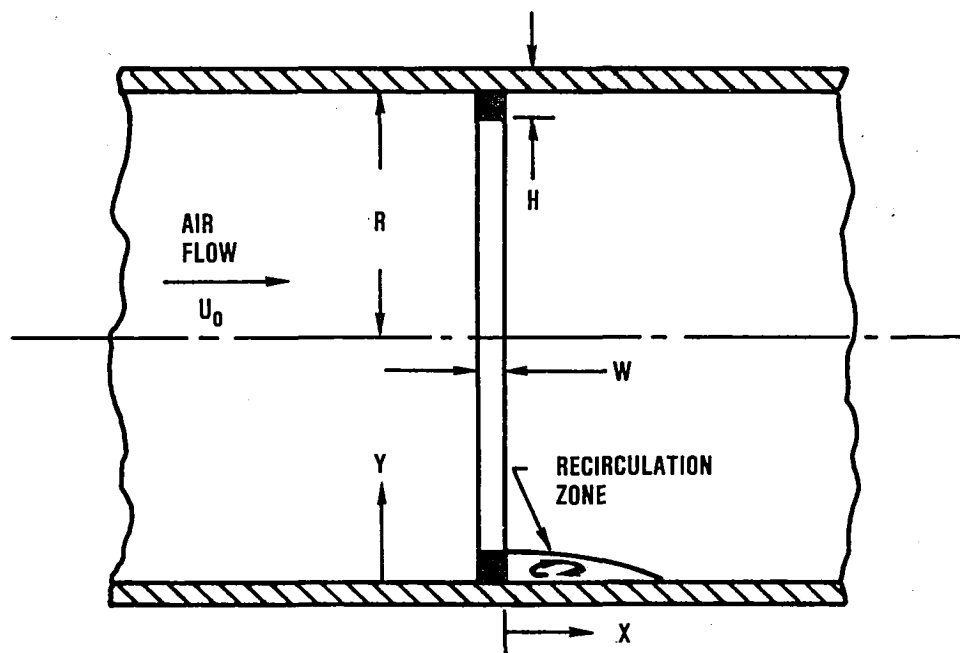
7.4 Flow Over a Circular Ring

An axisymmetric equivalent of a 2-D fence is a ring in a tube. A detailed mapping of the turbulent flow past a ring (rectangular roughness element) was made by Phataraphruk, et al.⁹¹ for several ring heights (0.125 to 0.375 inches) and widths (0.131 to 0.655 inches). A circular pipe of 2.44-inch diameter was used with a ring-type roughness attached to the wall as shown in Figure 7.4-1. The flow approaching the ring was a fully developed pipe flow. The calculations with the standard $k-\epsilon$ model were made for a total of four rings, configurations A, E, H and I in Table 17. Typical comparison between data and predictions is shown in Figure 7.4-2 for H-ring, 0.375-inch high and 0.131-inch wide ring. Axial velocity profiles at most of the axial stations agree reasonably well except for the discrepancy near the tube centerline, which cannot be explained. However, for the station $18.67H$ downstream from the ring, the agreement is excellent. Similarly, acceptable comparison is achieved for the turbulent kinetic energy profile.

In summary, the standard $k-\epsilon$ model predicts reasonably well the meanflow field behind circular rings. The predictions of the turbulence structure are qualitatively good.

TABLE 17. RING CONFIGURATIONS INVESTIGATED BY LOGAN, ET AL.

CONFIGURATION	H HEIGHT (IN.)	W WIDTH (IN.)
A	0.125	0.131
B	0.125	0.262
C	0.188	0.131
D	0.188	0.262
E	0.250	0.131
F	0.250	0.262
G	0.250	0.524
H	0.375	0.131
I	0.375	0.655



$$\begin{aligned}
 R &= 0.031 \text{ M} \\
 H &= 0.0095 \text{ M} \\
 W &= 0.0033 \text{ M} \\
 U_0 &= 30.5 \text{ M/S}
 \end{aligned}$$

Figure 7.4-1. Schematic of Logan's Setup for Studying Flow Over a Ring in a Pipe.

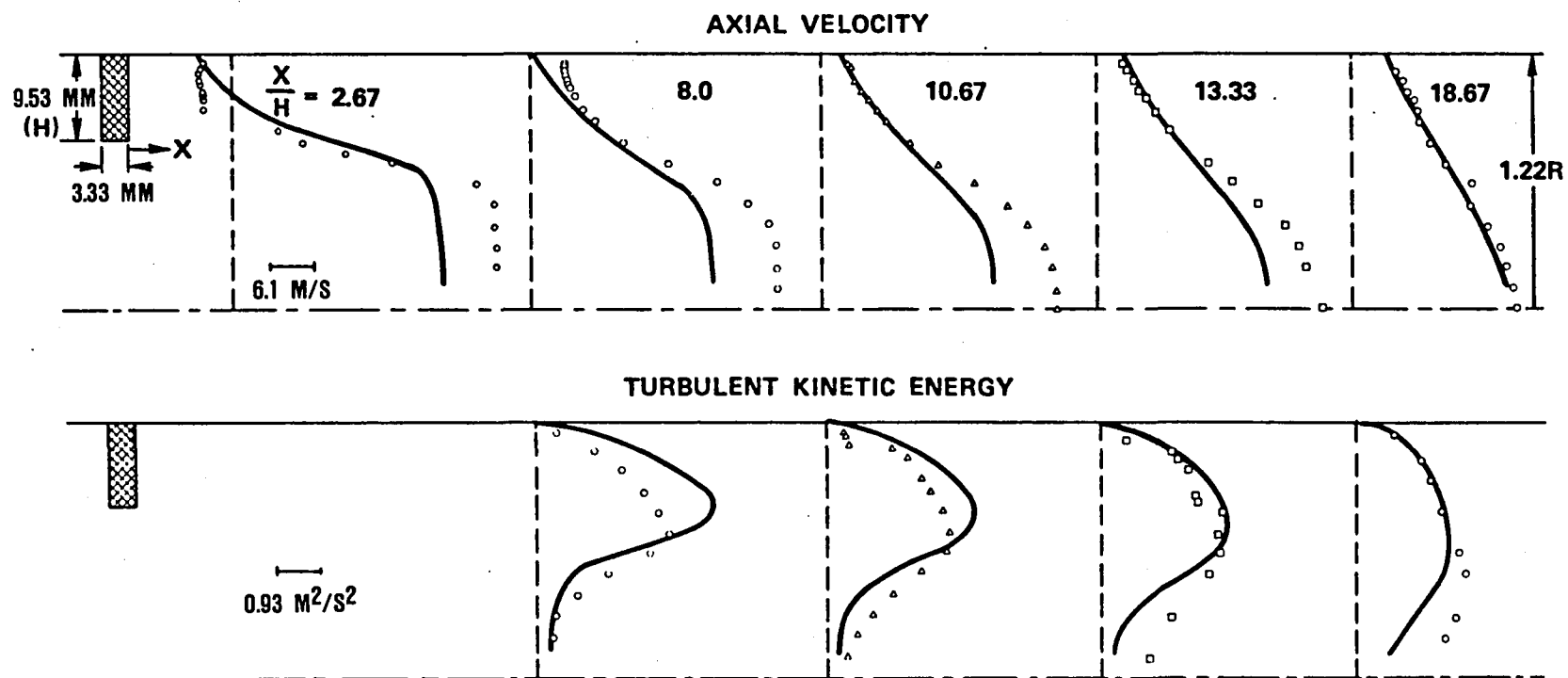


Figure 7.4-2. Comparison Between $k-\epsilon$ Model Predictions and Measured Axial Velocity and Turbulent Kinetic Energy for Logan's H-Ring.

7.5 Flow Around a Wedge-Shaped Flameholder

The flow-field behind a 2-D flame stabilizer is quite complex because of the shape of the flame stabilizer. The aerodynamic characteristics of separated flow behind a wedge-shaped flame stabilizer was studied experimentally by Fujii, et al., as shown in Figure 7.5-1,⁹⁰ with the aid of laser Doppler velocimetry. The flame stabilizer was an equilateral triangle in cross section with each side (B) being 25 mm. The measured streamline plot is shown in Figure 7.5-2 for an average freestream velocity of 10 m/s. The measured parameters were:

Length of the recirculation zone = $2.2B$

Amount of air being recirculated = $0.1 W_a$

Maximum reverse flow velocity = $0.4 U_\infty$

where

W_a = Inlet Airflow Rate

U_∞ = Free-stream Velocity

Flow-field predictions of the Fujii flame stabilizer were obtained by using the 2-D elliptic code with 60×32 grid nodes for upper half of the setup because of the symmetry of the test geometry. The triangular shape of the bluff-body was simulated by a stair-step approximation. The standard $k-\epsilon$ model was used. The predicted streamlines are presented in Figure 7.5-2, expressed as percent W_a . The following predicted parameters agree reasonably well with measurements:

Length of the recirculation zone = $2.3 B$

Amount of air being recirculated = $0.08 W_a$

Maximum reverse-flow velocity = $0.37 U_\infty$

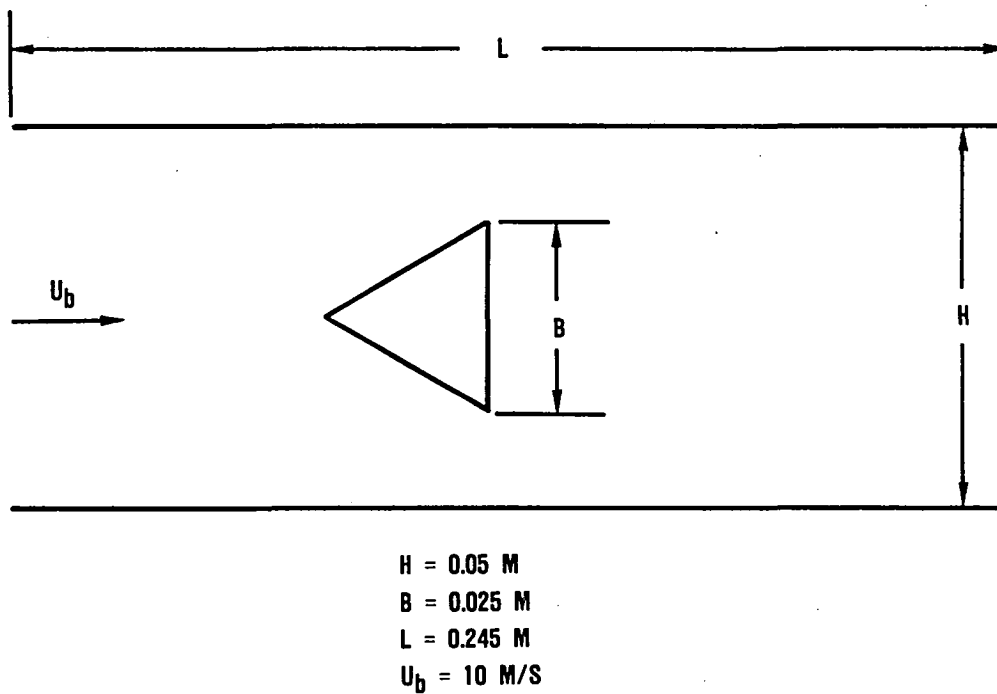


Figure 7.5-1. Wedge-Shaped Flameholder Setup.

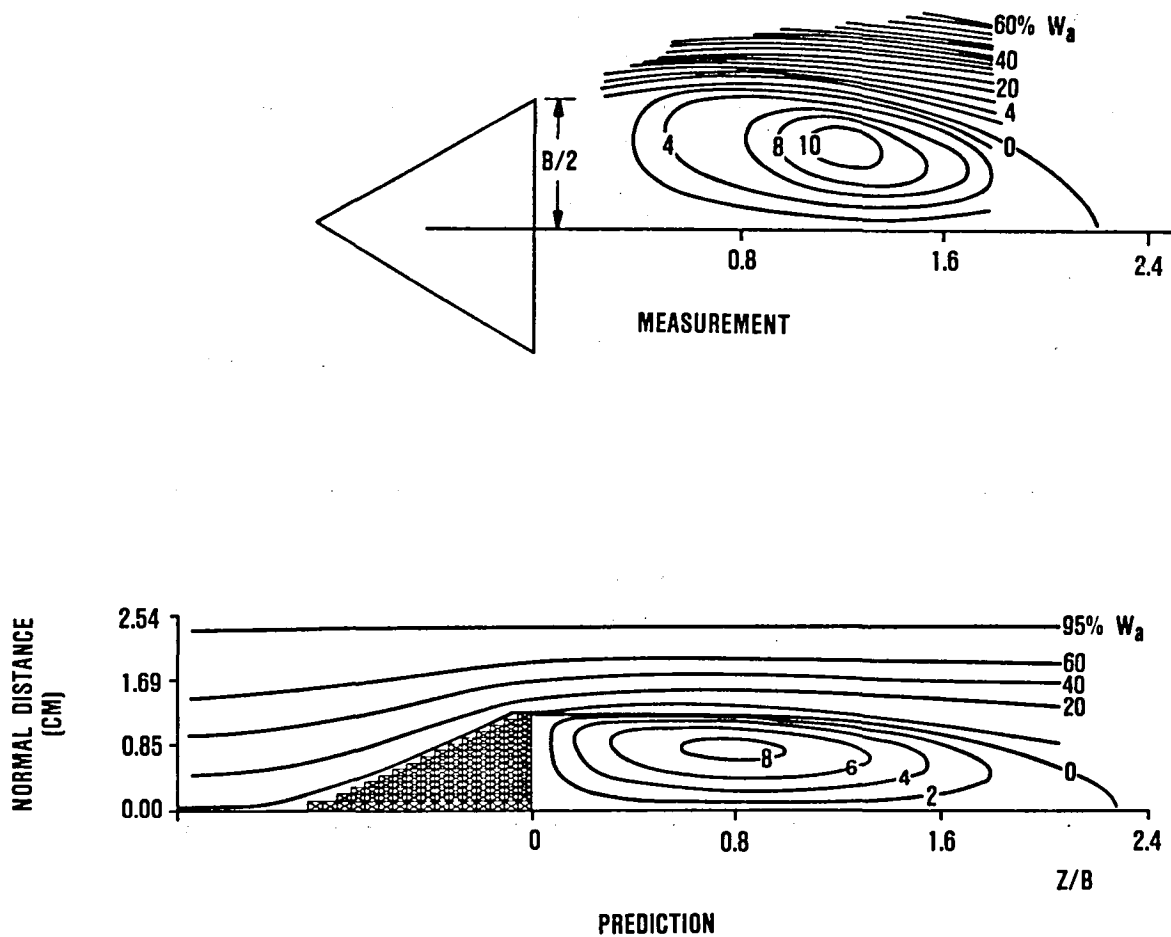


Figure 7.5-2. Comparison Between Measured and Predicted Streamline Plots Around a Wedge-Shaped Flameholder.

7.6 Flow Around a Confined Disk

A detailed nonintrusive laser Doppler measurement in a nonreacting flow behind a confined disk was made by Roquemore et al.⁹² The LDV measurements were made in the Air Force Aeropropulsion Laboratory combustion tunnel with and without fluid injector through the nozzle. The geometry of the experimental setup is shown in Figure 7.6-1. For the nonreacting case, CO₂ gas was injected axially at the disk centerline. The downstream flow field was mapped for different CO₂ flow rates and a constant annulus flow rate.

2-D elliptic computations were made for each of the CO₂ flow rates using the standard k- ϵ model. The predicted axial velocity variation along the centerline is presented along with the corresponding measured data in Figure 7.6-2. Both predictions and measurements show a gradual reduction in the negative velocity region at the centerline as well as downstream movement of this region as the CO₂ injection rate is increased. The predictions agree reasonably well with data in regard to the size of the negative velocity region.

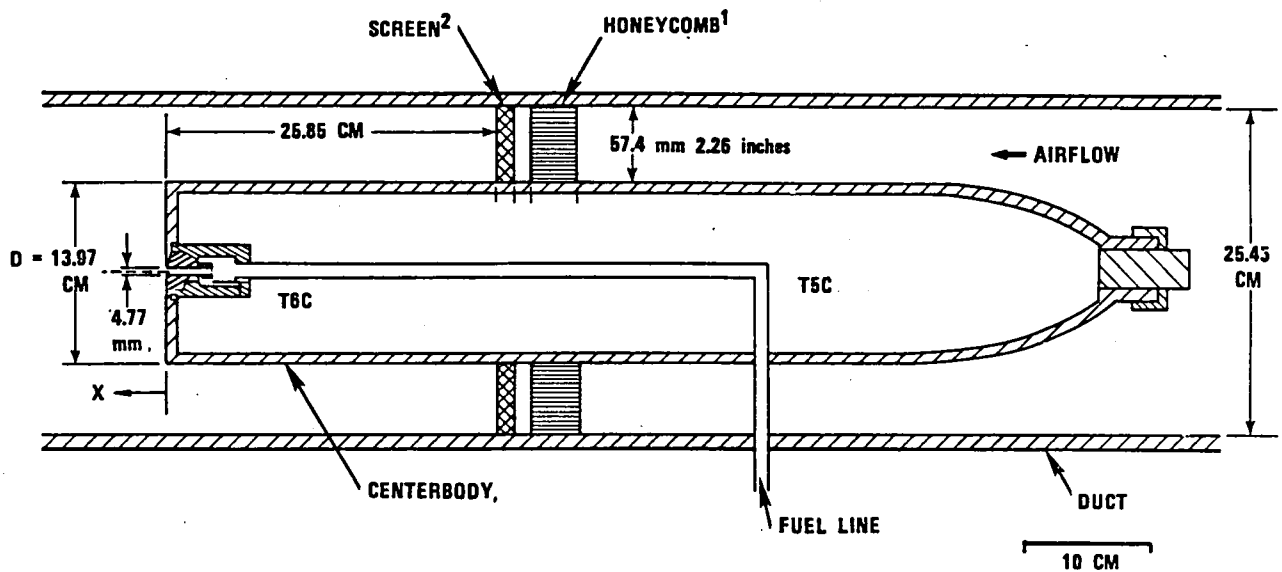


Figure 7.6-1. APL Combustion Tunnel Setup.

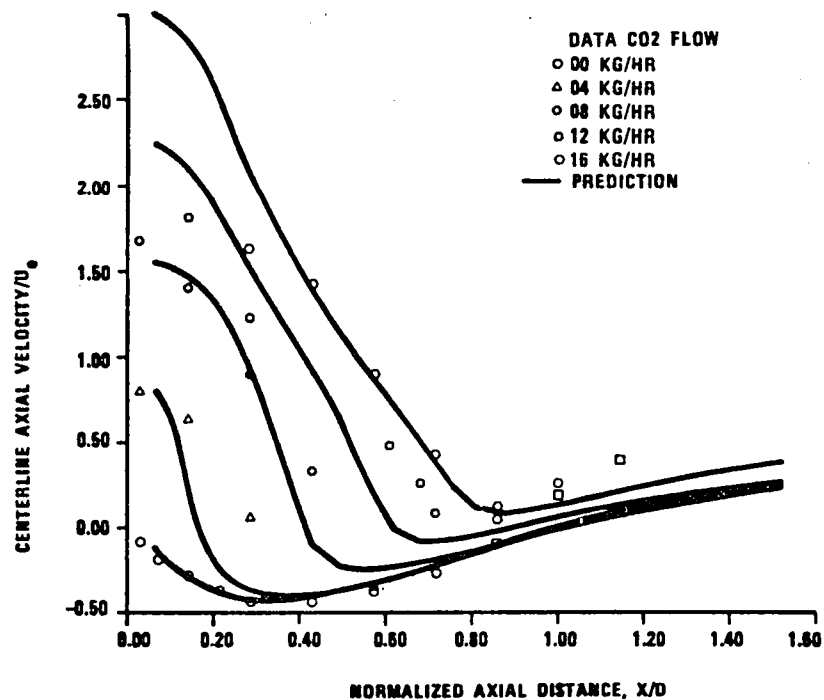


Figure 7.6-2. Comparison Between Measured and Predicted Centerline Velocity Profile Behind a Confined Disk.

7.7 Confined Coaxial Jet Expansion

Another benchmark test case selected for the recirculating flow model validation was the coaxial jet expansion in a pipe. This flow field is used to evaluate the model for the case of flow behind an axisymmetric step. Measurements were made by Johnson and Bennett⁸⁸ in a water test rig for the test configuration shown in Figure 7.7-1.

Measurements of mean velocity and turbulence fluctuations were made using a laser Doppler velocimeter. Furthermore, scalar transport measurements were made using the laser-induced fluorescence method.

Computations for this case were made using a 2-D elliptic code with 2200 nodes. The grid network used in the computations is shown in Figure 7.7-2. Initial profiles are applied at the station where pipe expansion occurs. The initial velocity and turbulence kinetic energy profiles were assumed to correspond to a fully developed pipe flow with the appropriate mass flow rate. Computations were made with:

- o Standard $k-\epsilon$ model
- o $K-\epsilon$ model with streamline curvature correction
- o ASM with streamline curvature correction

The mean velocity profiles predicted by the standard $k-\epsilon$ model and the measured values are illustrated in Figure 7.7-3. The predicted mean velocity profiles are in good agreement with the data. Between $x = 15.2$ cm and $x = 25.4$ cm, some differences between the data and the predictions are seen. However, the overall predictions are in agreement with data in the recirculation zone.

The k - ϵ model predictions for turbulence kinetic energy and the data are shown in Figure 7.7-4. The predicted k values are in agreement with the data near the inlet plane. The k - ϵ model underestimates k values further downstream. This characteristic is very similar to that in the plane step case.

The mean velocity profiles predicted by the k - ϵ model with Richardson number correction are presented in Figure 7.7-5. These profiles are similar to the results without the Richardson number corrections. In this flow field, the average mean velocities are very low (less than 2 m/s) with a Reynolds number of about 50,000. In such flows, the velocity gradients are not very large and hence the Richardson number corrections do not cause significant changes in the mean velocity profiles. The predicted turbulence kinetic energy obtained from the k - ϵ model with the Richardson number corrections are shown in Figure 7.7-6. These profiles are also identical to those obtained without the k - ϵ model (Figure 7.7-4).

The ASM predictions for mean velocity with streamline curvature correction are presented in Figure 7.7-7. These profiles are virtually identical to the k - ϵ model predictions and therefore compare well with the data.

The axial RMS fluctuating velocity components, u' , are shown in Figure 7.7-8. The ASM predictions are represented by solid lines and the data correspond to the symbols. The ASM underpredicts the turbulence intensity in the recirculation zone, and at $x = 30.5$ cm the u' predictions are in good agreement with the data. In the ASM, simplifying assumptions were made by assuming that the Reynolds numbers of the flow were very high. In the present case, the Reynolds numbers are relatively low ($Re_D \approx 50,000$) and the validity of those assumptions is questionable.

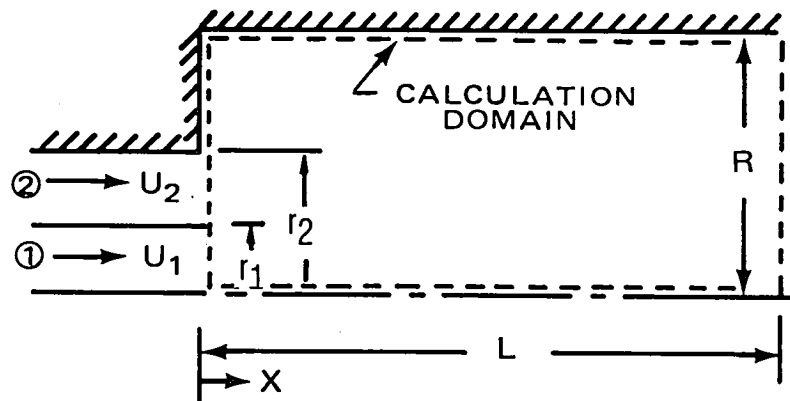
The ASM predictions for the v' velocity components are illustrated in Figure 7.7-9. The predicted v' profile at $x = 1.3$ cm is

in good agreement with the data near the axis of the pipe. In the recirculation zone, however, the ASM underpredicts the radial turbulence intensity. At the downstream stations, the model underestimates the v' values, even in the vicinity of the axis of the tube.

Figure 7.7-10 illustrates the comparison between the data and ASM predictions for the shear stress component, \overline{uv} . At $x = 1.3$ cm, the large negative peak value for \overline{uv} near the axis corresponds to the shear layer between the inner and the outer coaxial streams and the large positive \overline{uv} peak corresponds to the shear layer associated with the pipe expansion. The predicted \overline{uv} profiles are in good agreement with the data, even though the predicted normal stresses u' and v' are smaller than the measurements.

The $k-\epsilon$ model and the ASM correctly predict the mean velocity profiles. But, the predicted turbulence kinetic energy levels are lower than the data. The ASM underpredicts both u' and v' levels in the recirculation zone of axisymmetric expansion. In the plane expansion (Paragraph 7.2), it was observed that the ASM overpredicted u' and underpredicted v' in the recirculation zone. The ASM predictions for \overline{uv} are in very good agreement with the data of Johnson and Bennett.

JOHNSON AND BENNETT
FLOW THROUGH A SUDDEN EXPANSION IN A PIPE



$$r_1 = 0.012M$$

$$r_2 = 0.0295M$$

$$R = 0.061M$$

$$U_1 = 0.52 \text{ M/S}$$

$$U_2 = 1.66 \text{ M/S}$$

$$Re_0 = \frac{2\rho_2 U_2 r_2}{\mu_2} = 47,500$$

Figure 7.7-1. Geometry of Confined Coaxial Jet Expansion Setup.

COMPUTATION GRID FOR JOHNSON & BENNETT TEST CASE

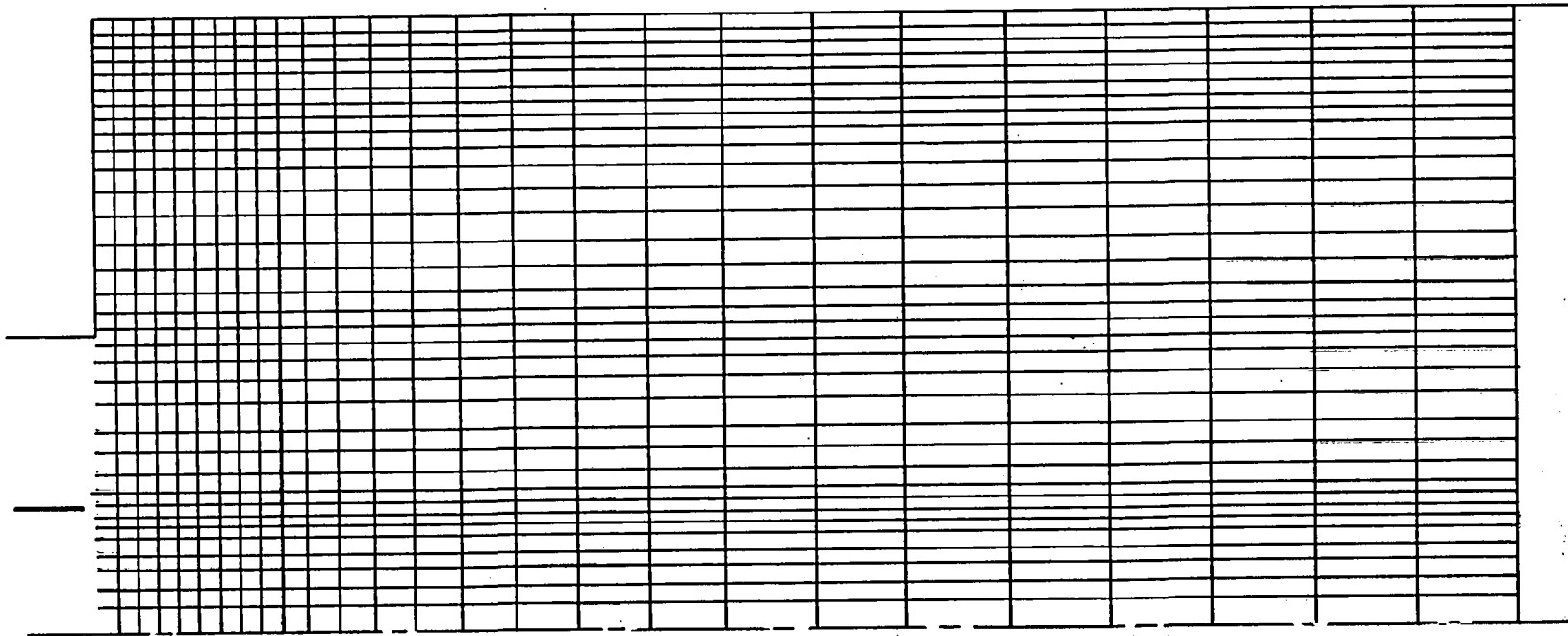


Figure 7.7-2. Finite Difference Grid Network for Confined Coaxial Jet Expansion.

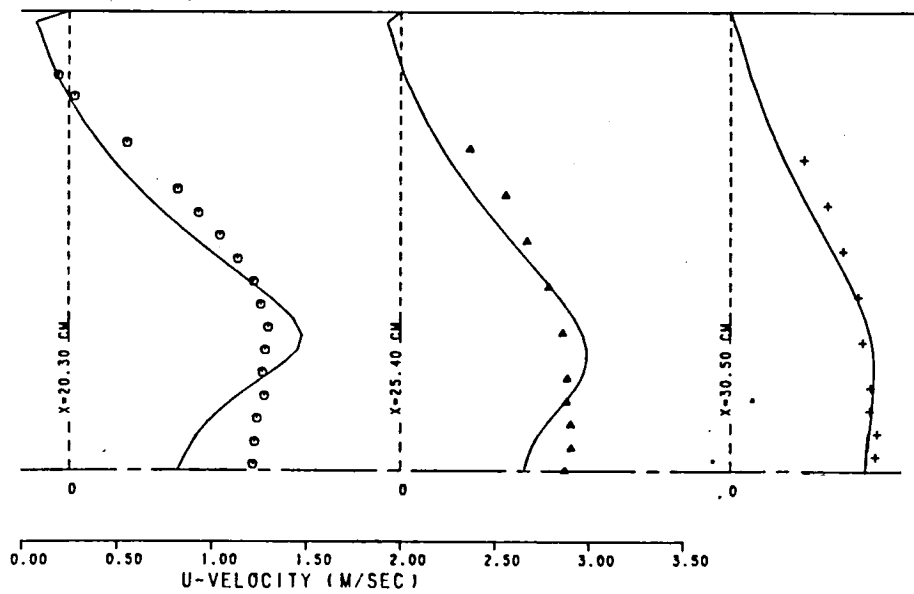
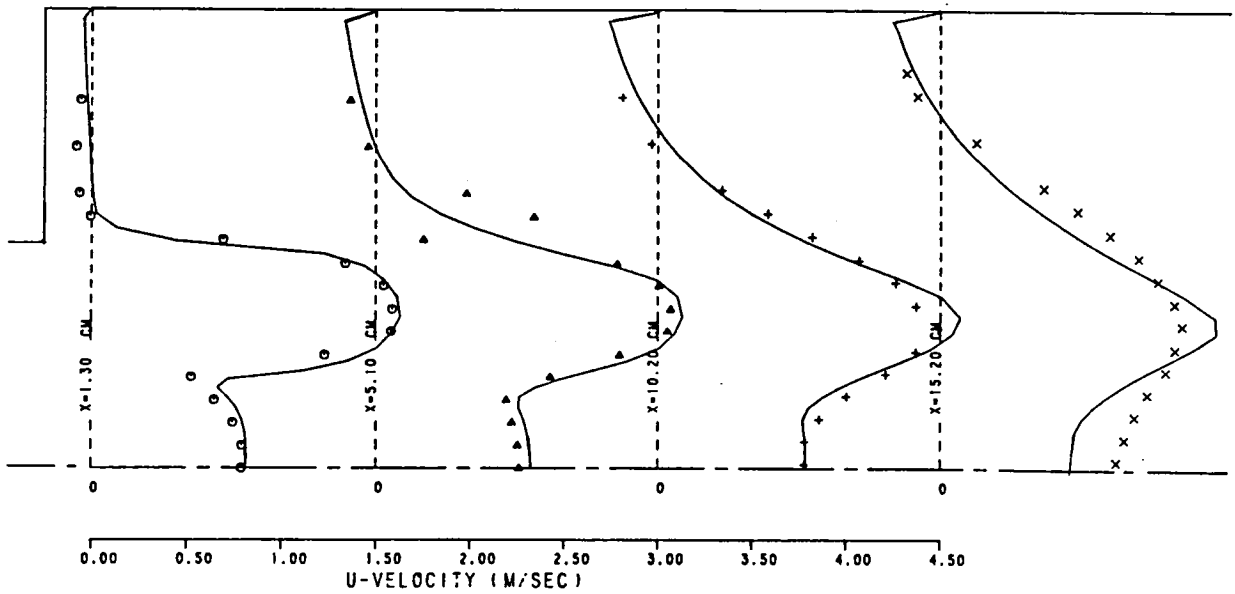


Figure 7.7-3. Standard $k-\epsilon$ Model - Axial Velocity Profiles.

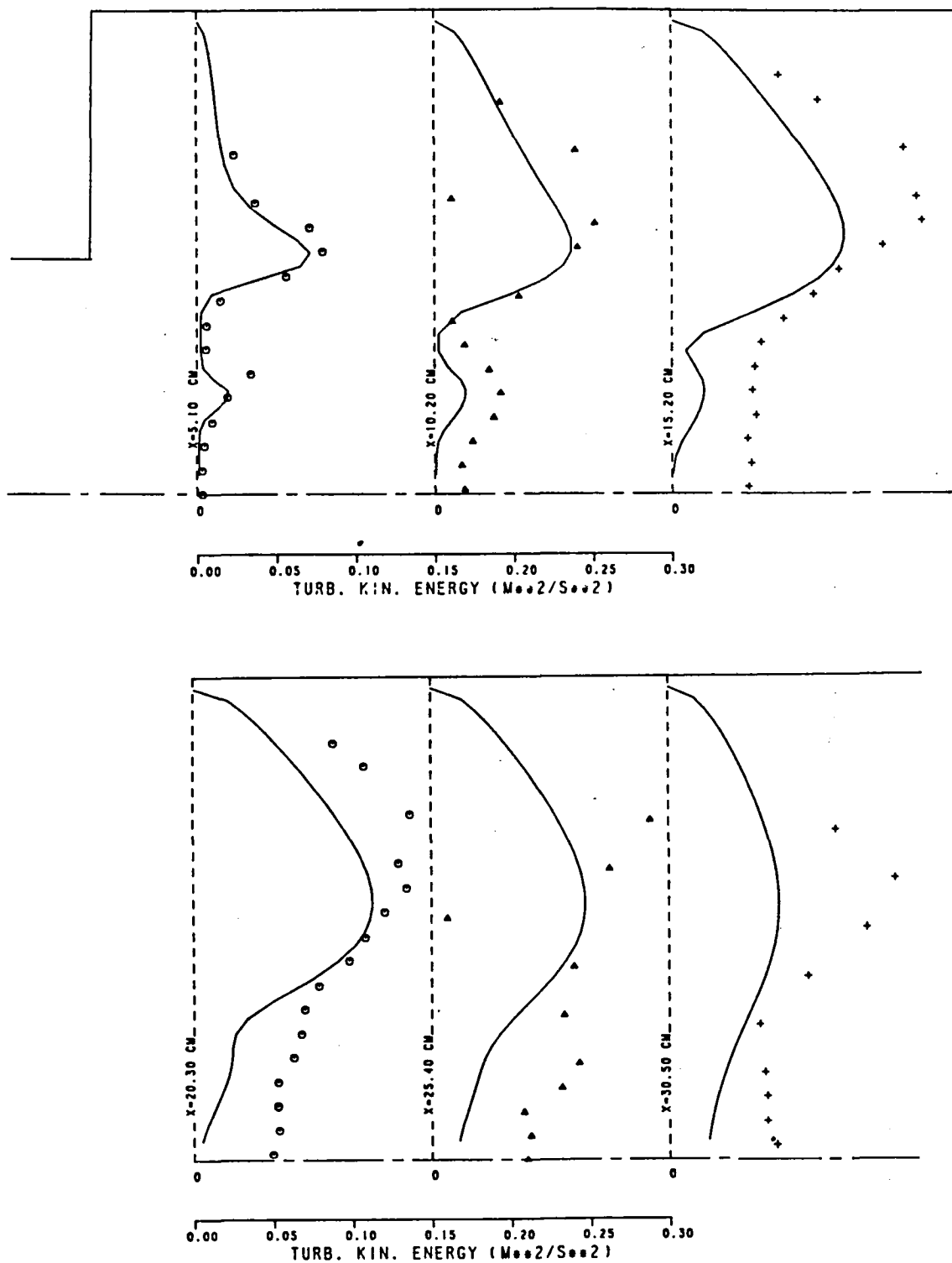


Figure 7.7-4. Standard $k-\epsilon$ Model - Turbulence Kinetic Energy Profiles.

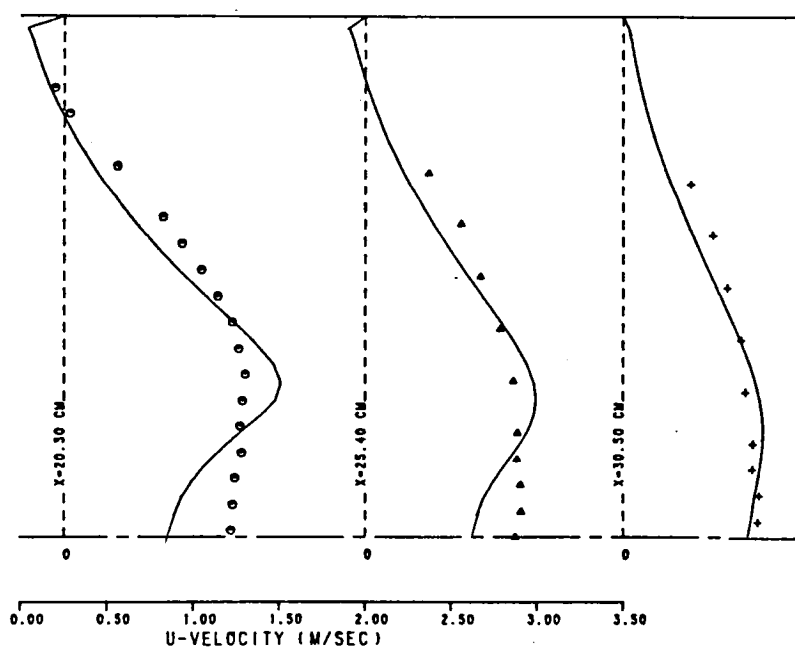
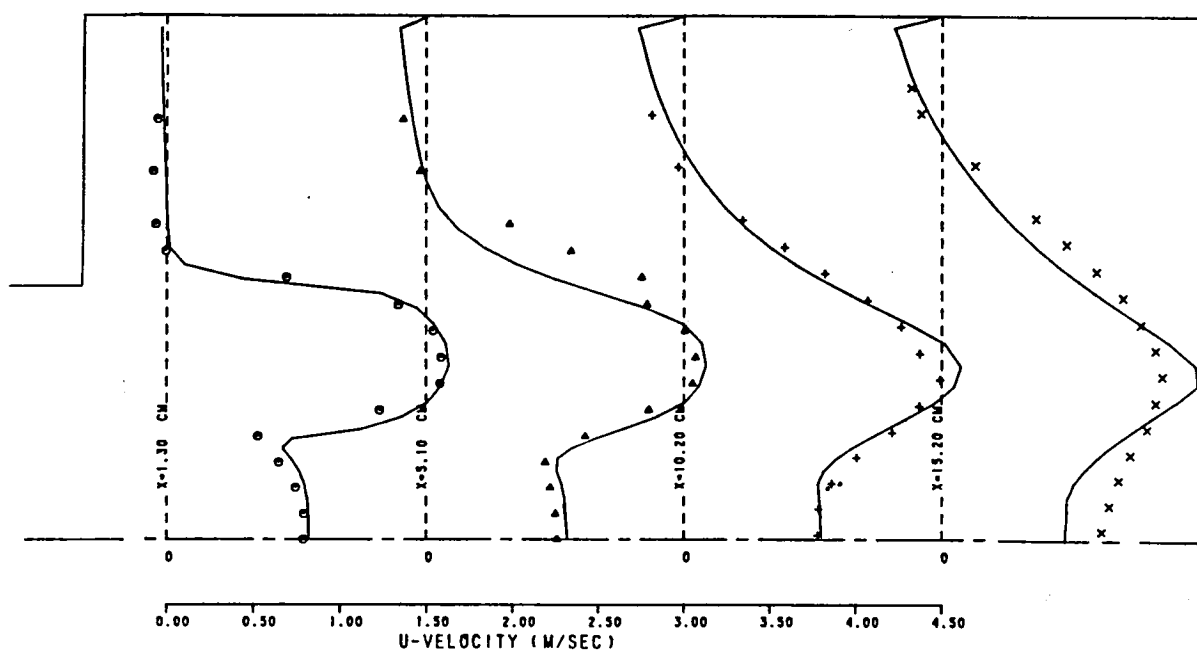


Figure 7.7-5. $k-\epsilon$ Model with Richardson Number Correction - Mean Axial Velocity Profiles.

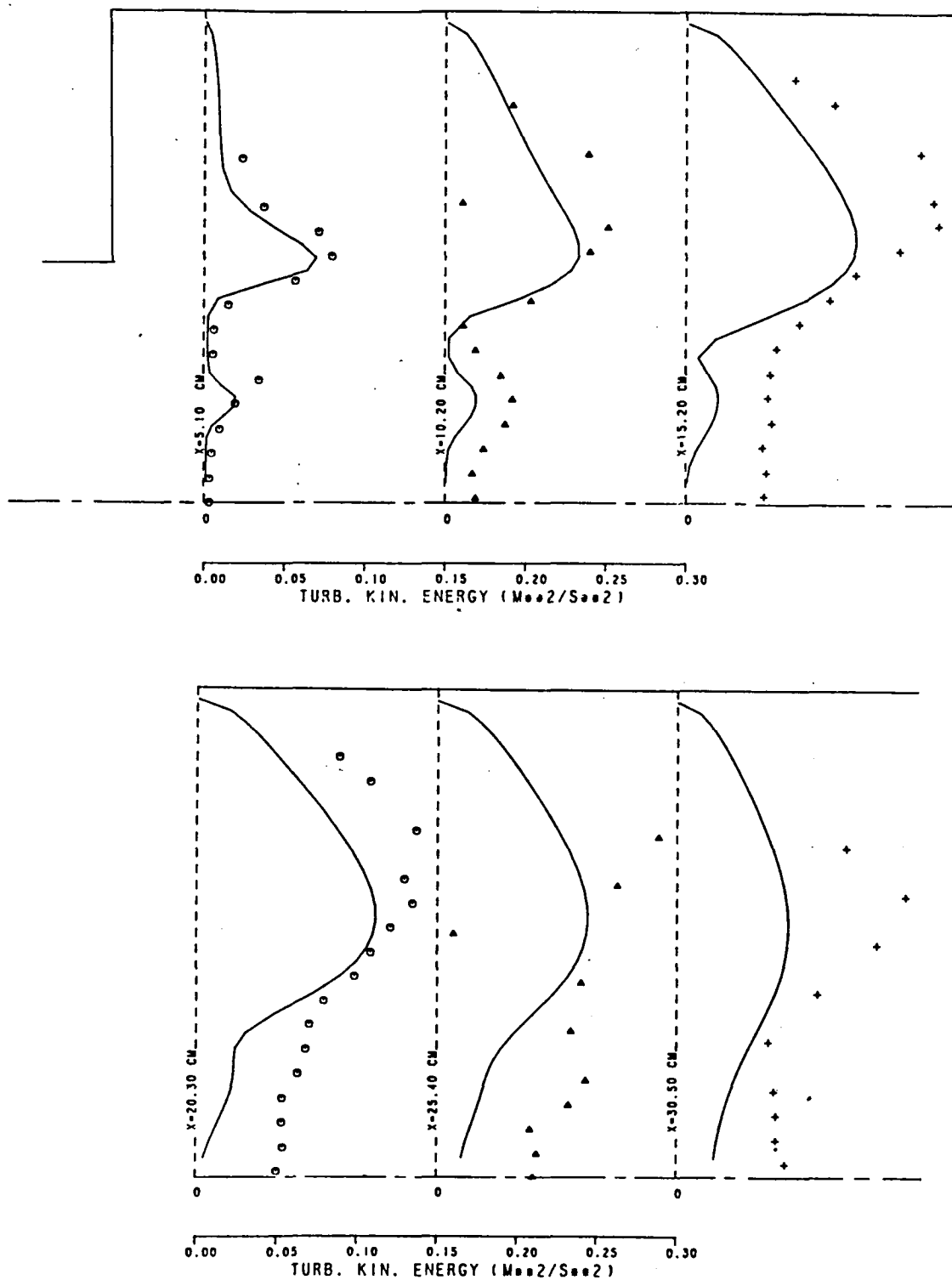


Figure 7.7-6. $k-\epsilon$ Model with Richardson Number Correction - Turbulence Kinetic Energy Profiles.

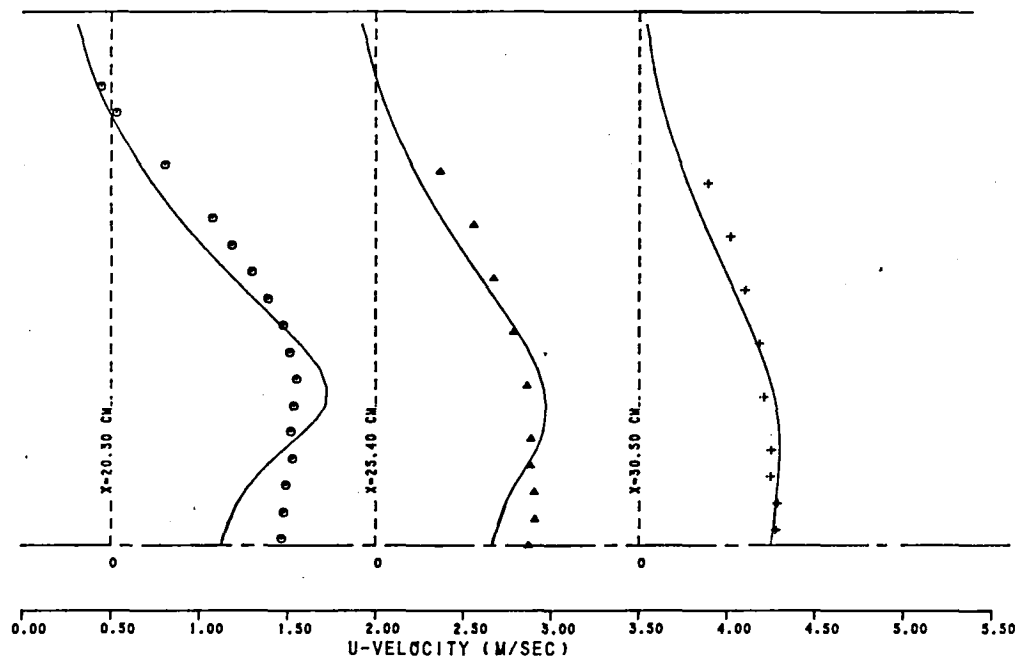
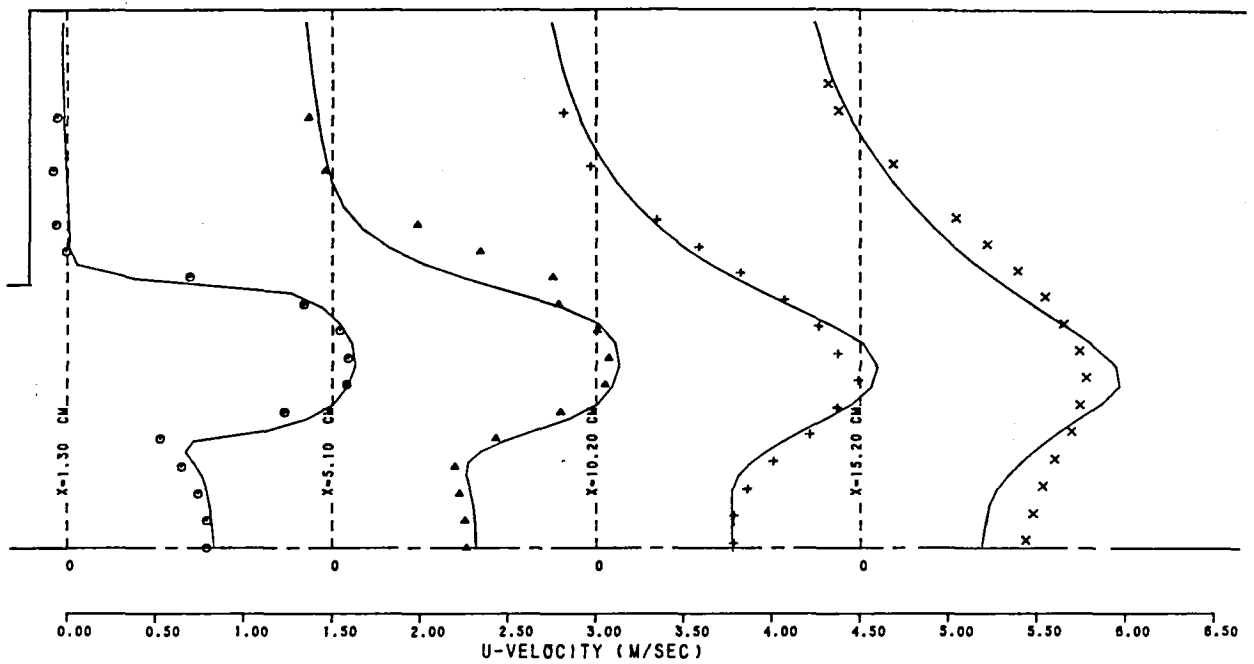


Figure 7.7-7. ASM with Richardson Number Correction - Mean Axial Velocity Profiles.

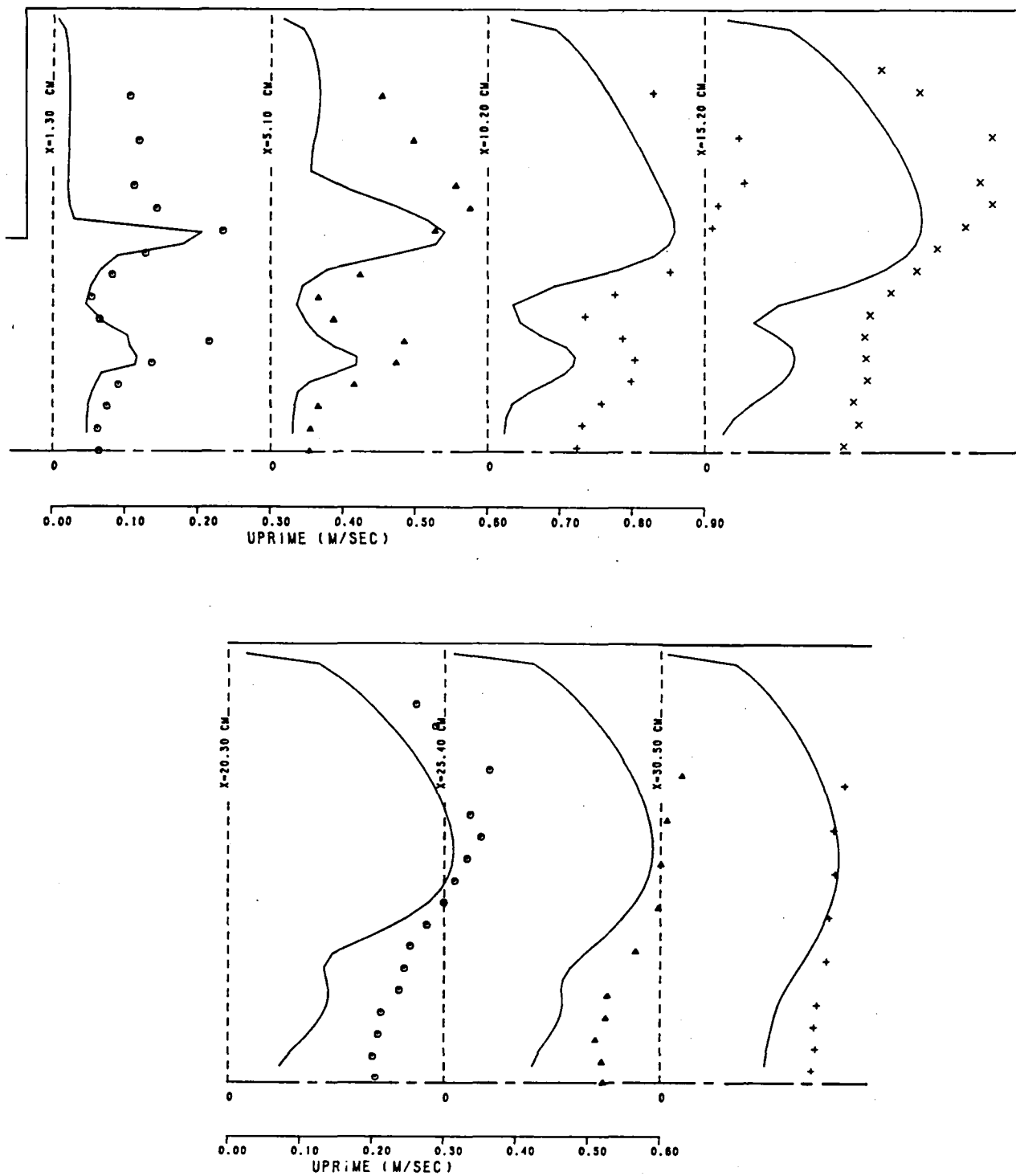


Figure 7.7-8. ASM with Richardson Number Correction - Fluctuating Axial Velocity Profiles.

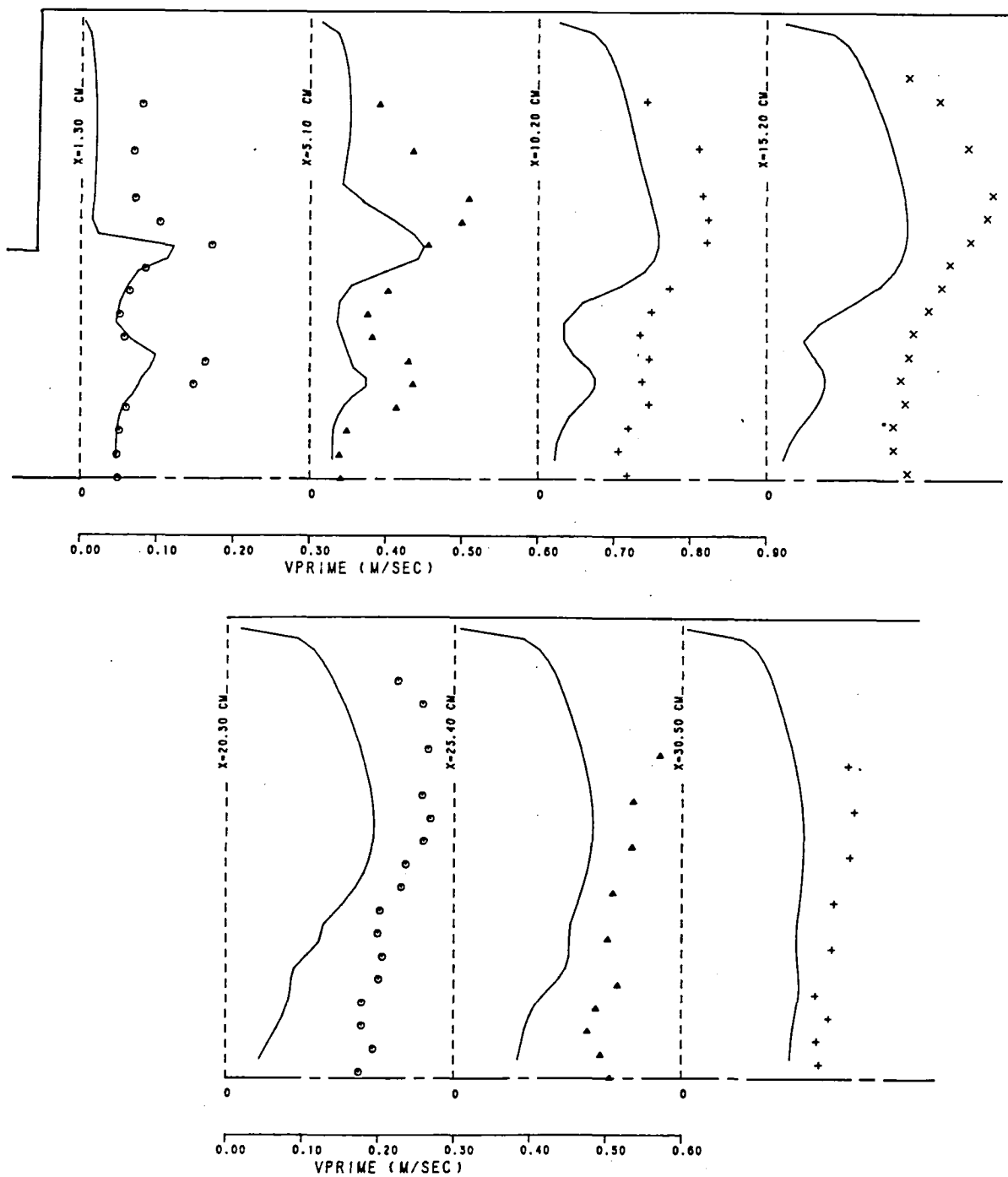


Figure 7.7-9. ASM with Richardson Number Correction - Fluctuating Radial Velocity Profiles.

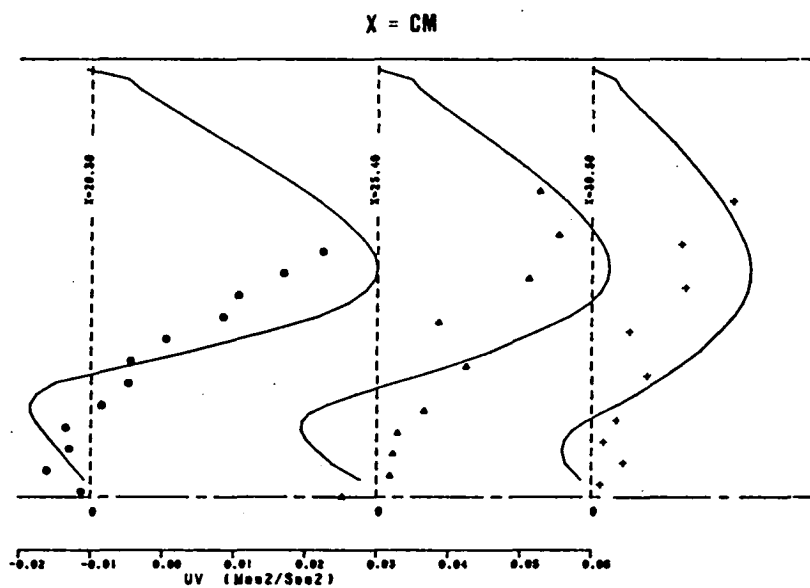
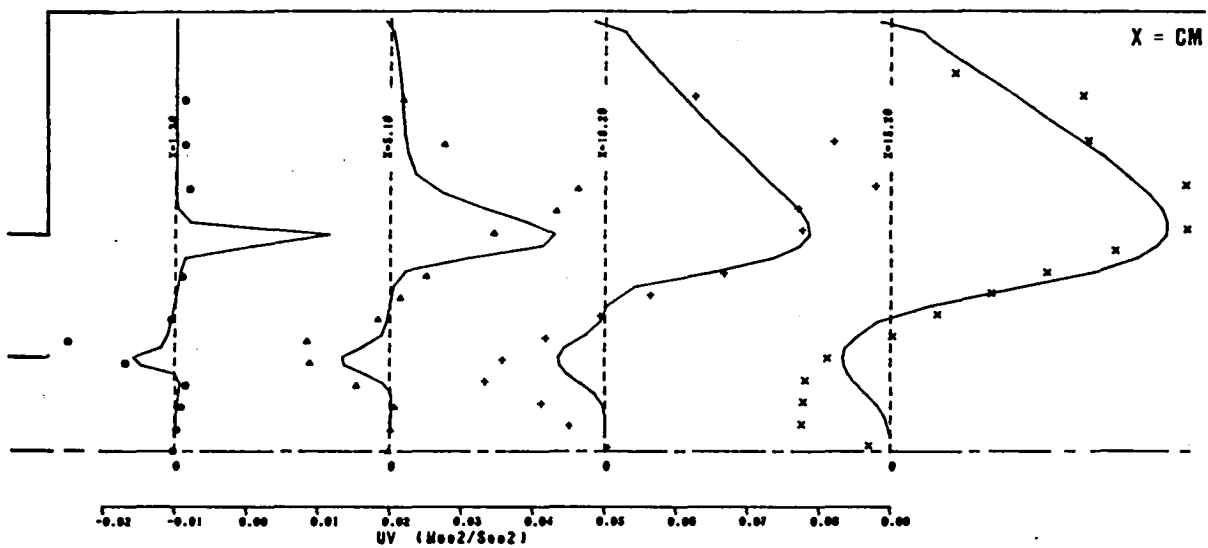


Figure 7.7-10. ASM with Richardson Number Correction - Shear Stress Profiles.

7.8 Nonreacting and Reacting Flow Behind a Step

Detailed measurements of the turbulent structure behind a step with and without combustion was made by Pitz.⁸⁶ For their flow condition, measurements of species (CO , CO_2) and temperature were made by Ganji and Sawyer.¹³² The measurements were made in a test setup shown schematically in Figure 7.8-1. The step height was 25.4 mm.

This test case was selected for evaluating the model in non-reacting and reacting environments. In the nonreacting flow, computations were made with $k-\epsilon$ model as well as the ASM with streamline curvature corrections.

Nonreacting Flow

Computations of the nonreacting flow were made with a 2-D elliptic program consisting of 2200 nodes. Measured profiles at the step plane were used as initial profiles with an average velocity of 22.2 m/s. Along the walls, the boundary conditions are imposed through wall functions; and at the exit plane, zero axial gradient conditions were imposed.

The $k-\epsilon$ model predictions for mean velocity in the high Reynolds number case of Pitz are shown in Figure 7.8-2. The predictions are in close agreement with data outside the recirculation zone. Inside the reverse flow region, the agreement is relatively inferior. The regions in the vicinity of flow reversal are known to produce high levels of turbulence diffusive transport. The $k-\epsilon$ model does not predict as large a turbulence diffusion rate as the measurements indicate.

The ASM predictions for mean velocity are shown in Figure 7.8-3. In these predictions, streamline curvature (Richardson

number) corrections were included. These predictions are in good agreement with the data. The data shows that the recirculation zone extends farther out in the cross-stream (y) direction than the location predicted by ASM.

The ASM predictions of axial turbulence intensity are presented in Figure 7.8-4. The measurements are shown in symbols. The ASM underpredicts the turbulence intensity levels in the recirculation zone. For $x > 5.08$ cm, the ASM underestimates the turbulence levels in the regions outside the recirculation zone. In the case of the flow near the inlet, the turbulence intensities are correctly predicted.

Premixed Propane/Air Combustion Behind a Step

In the reacting flow case, a premixed propane/air mixture with an equivalence ratio of 0.56. was used. The average velocity at the inlet was 13.3 m/s and the inlet temperature was 295°K. Computations for this case were made using a standard $k-\epsilon$ model with both two-step and four-step schemes. In the experimental setup, the rig was cooled by passing cooling air around it. The bulk exit temperature of the cooling air was reported to be 500°K. In the computations, initially, a constant wall temperature was assumed to be 500°K. In the two-step model, the Army Design Criteria reaction rate constants were used.

The mean velocity predictions by the two-step model with $T_w = 500^\circ\text{K}$ are reported in Figure 7.8-5. The mean velocity profiles are in agreement with the data in the core of the flow. In the region behind the step, the predictions agree with measurements in the recirculation zone, but comparison becomes comparatively inferior in the recovery zone, ($X \geq 12$ cm).

The two-step scheme predictions for temperature distributions are presented in Figure 7.8-6. At $x = 1$ cm, the data and predictions are in good agreement. Beyond this station, the predicted temperatures are slightly higher than the measured values. Furthermore, the predicted temperature profiles do not indicate as much convective heat flux in the radial direction as those shown by the data.

The four-step model predictions for mean velocity are illustrated in Figure 7.8-7. Comparison with two-step model prediction (Figure 7.8-5) shows that the four-step scheme predicts a slightly stronger recirculation zone. However, the agreement between the data and the predictions are good, especially in the core of the flow. The four-step model predictions for temperature are shown in Figure 7.8-8. The four-step scheme initially overpredicts the temperatures; and beyond $x = 9$ cm, it underpredicts the temperatures. The four-step scheme is expected to be slower than the two-step scheme because of the higher number of reaction steps. Consequently, the predicted temperature levels are also smaller. Furthermore, rate constants used in the four-step scheme (obtained from Hautman, et al.) are applicable to higher inlet temperatures than the experimental conditions. The four-step scheme also predicts a substantially lower radial heat transfer than the data.

In the case of combustion behind a step, the wall temperature distributions can play very significant roles on the combustion performance. Ganji and Sawyer had reported wall temperature values at a few stations. From these profiles, a wall temperature distribution was deduced. This temperature distribution, as shown in Figure 7.8-9, was used in the next series of computations. This wall temperature distribution is significantly higher than 500°K everywhere except near the inlet.

The two-step scheme predictions using the measured wall temperature distributions are shown in Figures 7.8-10 through 7.8-12. Figure 7.8-10 shows the comparison between the data and the two-step scheme predictions for mean velocity. Comparison between Figures 7.8-5 and 7.8-10 shows the effect of wall temperature distribution on mean velocity. With a hotter wall temperature, (Figure 7.8-10), the two-step model predicts a slightly stronger recirculation zone. Figure 7.8-11 shows that due to the higher wall temperatures, the predicted temperature distributions are also higher. However, the radial heat diffusion is still underpredicted by the model.

The two-step model predictions for CO and CO₂ concentrations are illustrated in Figure 7.8-12. The predicted CO concentrations are significantly smaller than the data in the recirculation zone. In the stream layer coming off the step, the CO concentrations are initially overestimated. The predicted CO₂ profiles are in good agreement with the data at $x = 10$ mm. At the downstream stations, the predicted CO₂ profiles do not spread radially outward as much as shown by the data. This trend is consistent with the temperature profiles shown in Figure 7.8-11.

The four-step model results with the measured wall temperature distributions as input are presented in Figures 7.8-13 through 7.8-15. In Figure 7.8-13, the four-step results for mean velocity and the data are reported. Comparison with Figure 7.8-7 shows that the four-step model predicts a slightly weaker recirculation zone with a hotter wall temperature distribution.

The predicted temperature distributions at $x = 1.0$ and 3.0 cm by the four-step model (Figure 7.8-14) are overpredicted, and for $x = 9$ cm, they are significantly underestimated. These profiles demonstrate the strong influence of wall temperature on the kinetic scheme.

The four-step predictions for CO and CO₂ concentrations are shown in Figure 7.8-15. The CO concentrations are overestimated by the model in the vicinity of the bottom wall. The radial spreading of CO concentrations are substantially underpredicted by the model. The predicted CO₂ profiles are in very good agreement with the data except at x = 15.0 cm, where the level of CO₂ is underestimated. Because of the low levels of CO₂, the predicted temperature values are also lower at 15.0 cm.

Figures 7.8-16 through 7.8-18 illustrate the results obtained with the rate constants in the first two reaction steps (see Table 9) modified as

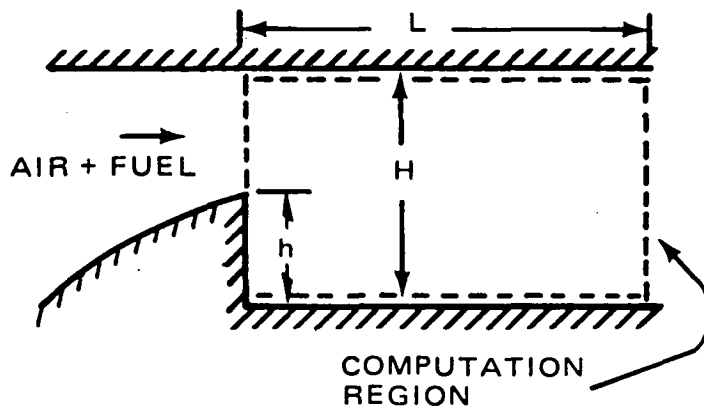
$$\begin{aligned} K_{O_1} &= 2.0893 \times 10^{24} & C_{R_1} &= 6.0 \\ K_{O_2} &= 5.0117 \times 10^{21} & C_{R_2} &= 6.0 \end{aligned}$$

In these computations, a constant wall temperature of 500°K was prescribed in the region behind the step. Significant improvements in the predictions for mean velocity and temperature can be seen in these results. However, the predicted CO levels are higher than those shown in Figure 8.4-15 with Hautman's rate constant. This demonstrates the need for further work on the four-step scheme.

For the nonreacting flow, the k- ϵ model and ASM underpredict turbulence intensities. For the case of premixed propane flame with low inlet temperatures, the two-step scheme predictions are in better agreement with the data than the four-step results. Further modifications in the four-step rate constants are expected to improve the correlation. The wall temperature distribution has a significant influence on the predicted results.

PITZ AND DAILY

FLOW BEHIND A BACKWARD FACING STEP



$h = 0.025 \text{ M}$
 $H = 0.051 \text{ M}$
 $L = 2.20 \text{ M}$
TEST SECTION WIDTH = 0.173 M
 $U_{IN} = 13.3 \text{ M/S}$
EQUIVALENCE RATIO = 0.57
 $T = 300^\circ \text{K}$

Figure 7.8-1. Schematic of the Test Rig for Nonreacting and Reacting Flow Behind a Step.

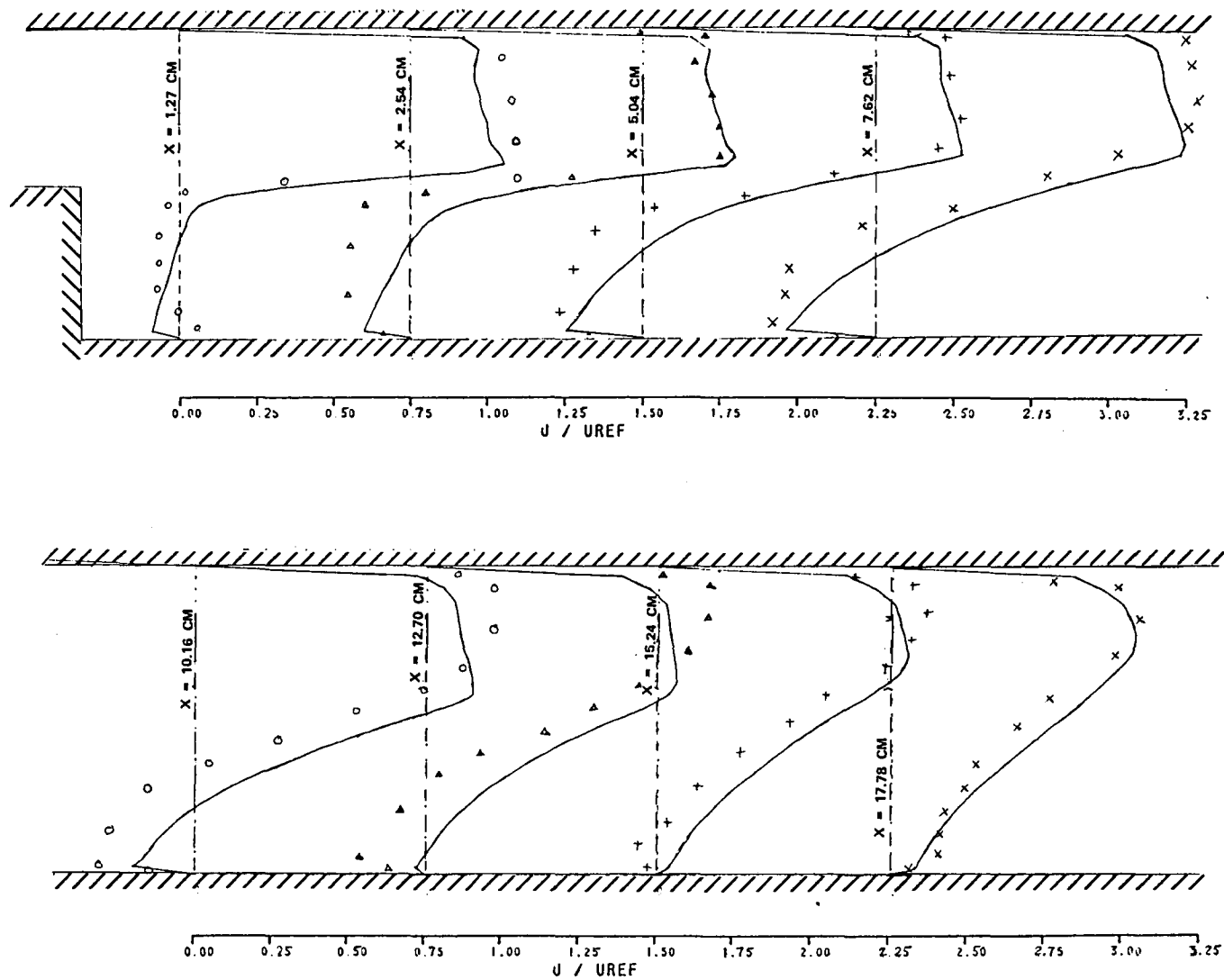


Figure 7.8-2. Comparison Between the $k-\epsilon$ Model Prediction and Measured Streamwise Velocity Components for Nonreacting Flow Behind a Step.

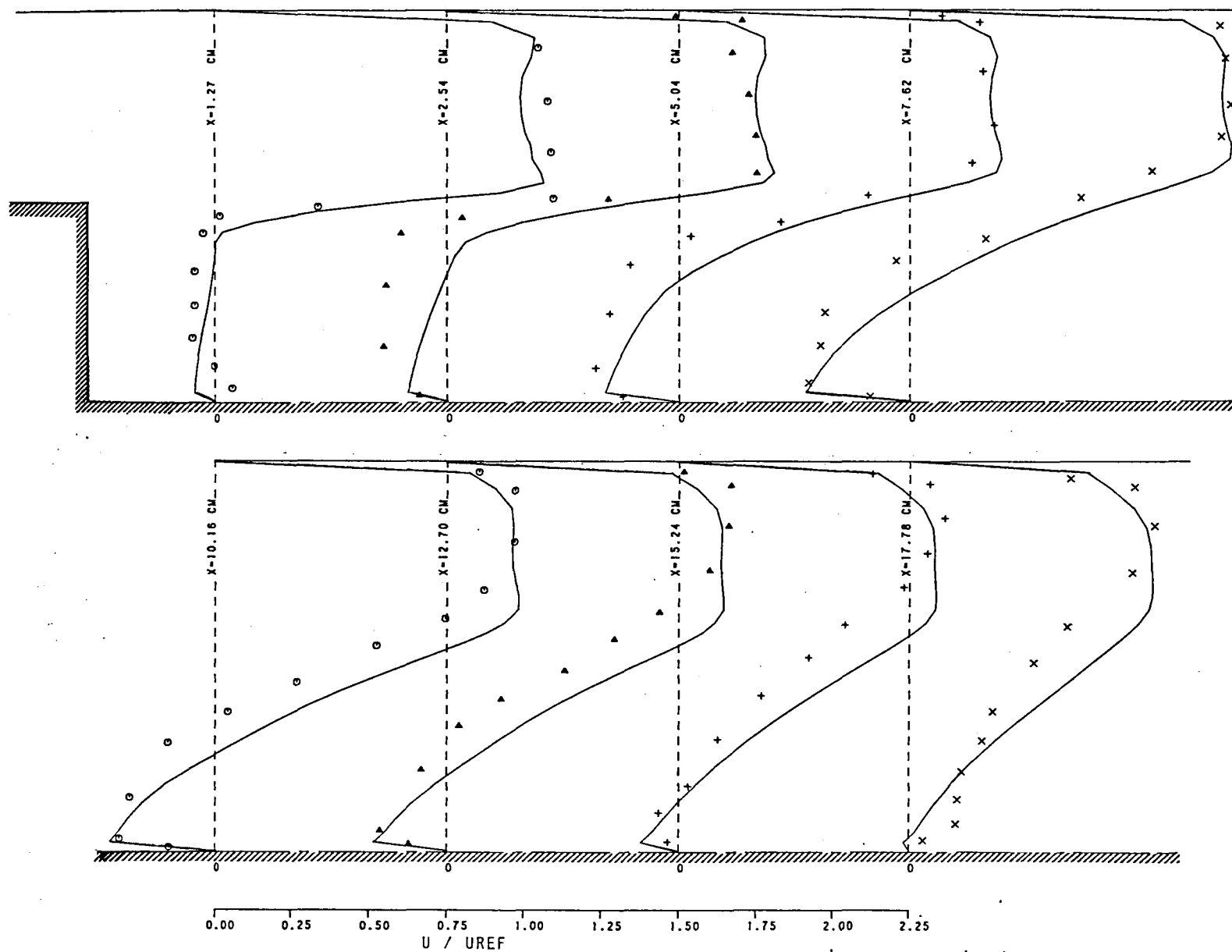


Figure 7.8-3. ASM with Richardson Number Correction - Nonreacting Mean Axial Velocity Profile.

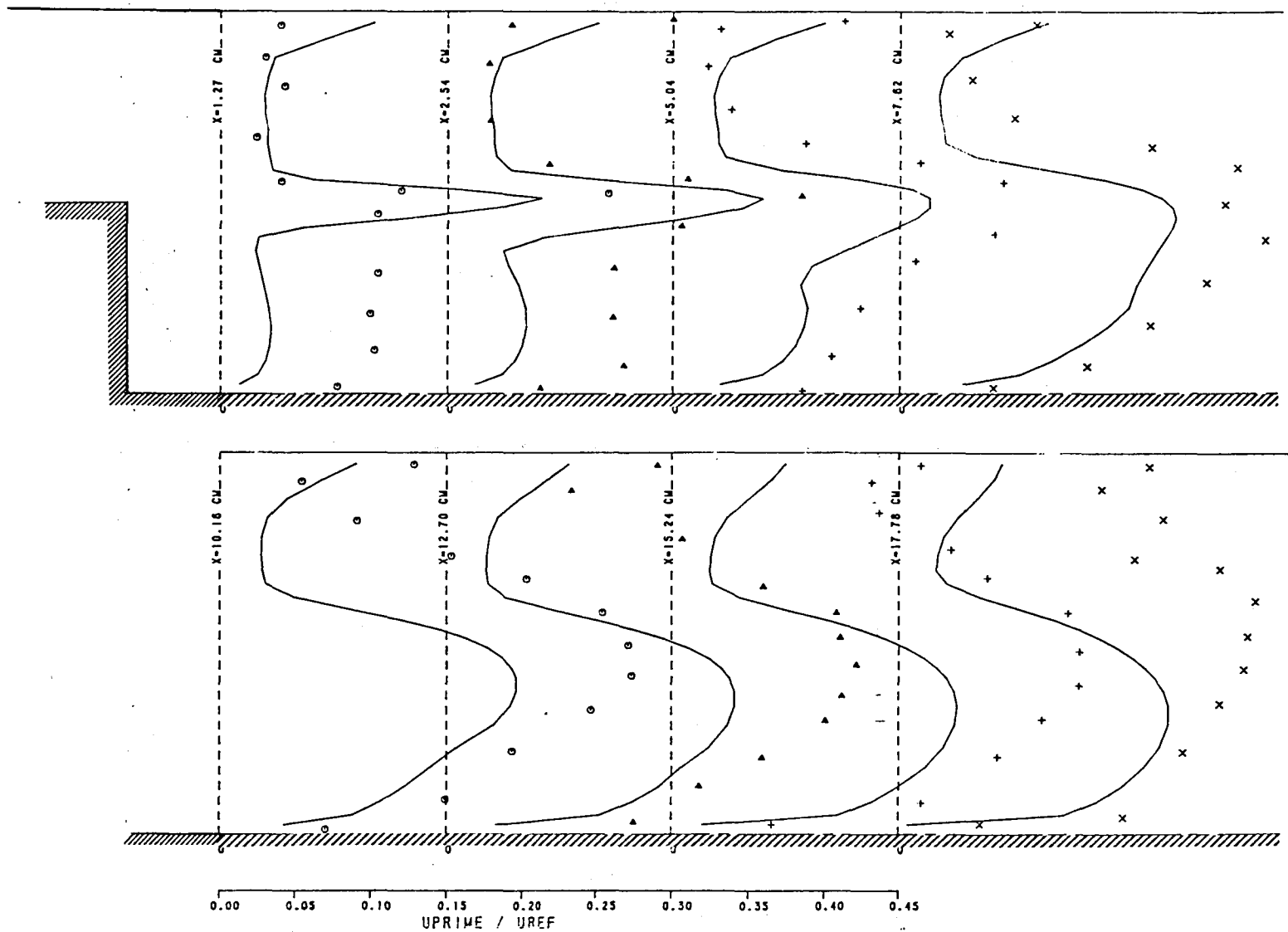


Figure 7.8-4. ASM with Richardson Number Correction - Nonreacting Axial Turbulence Intensity Profiles.

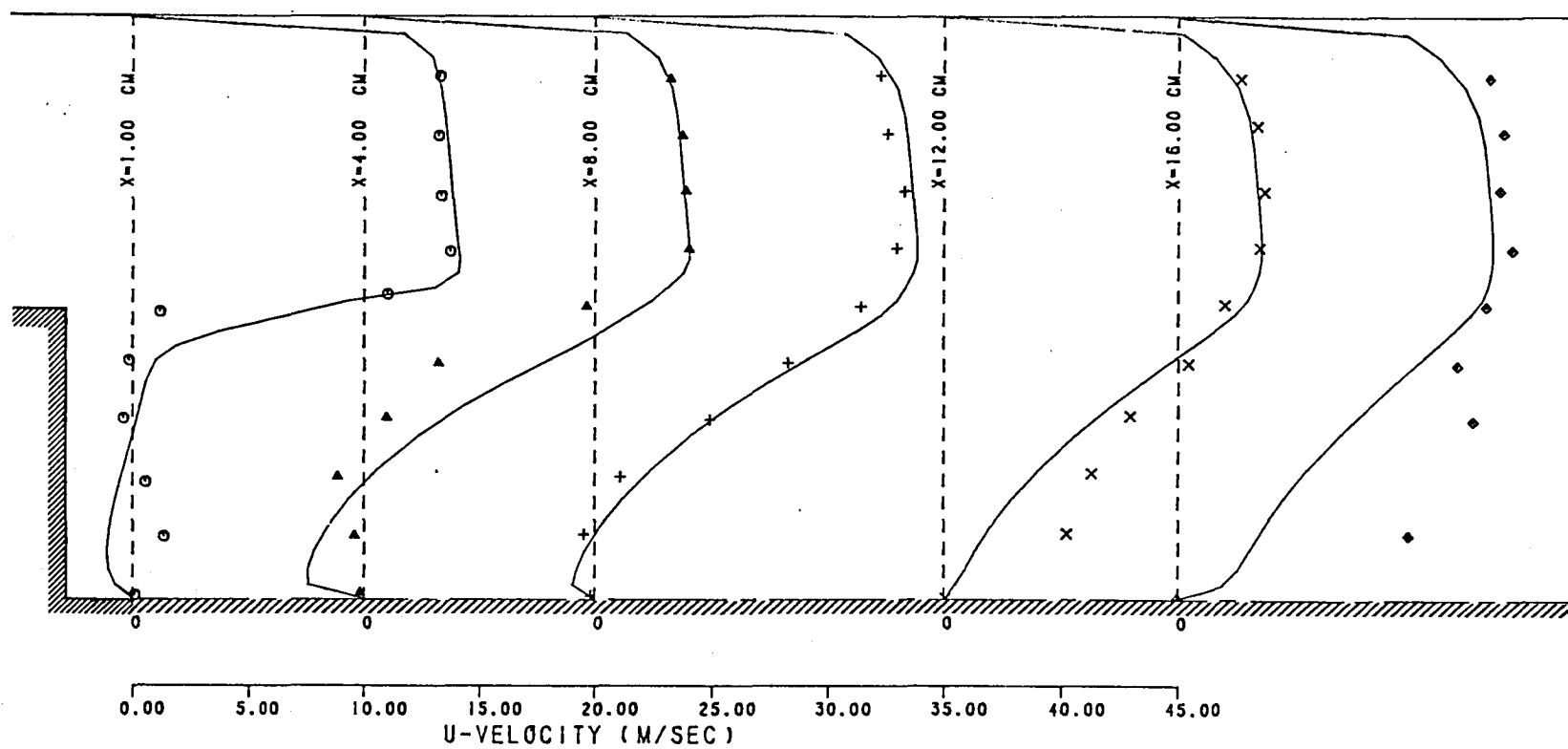


Figure 7.8-5. k - ϵ Model with 2-Step Reaction Scheme - Mean Axial Velocity Profiles.

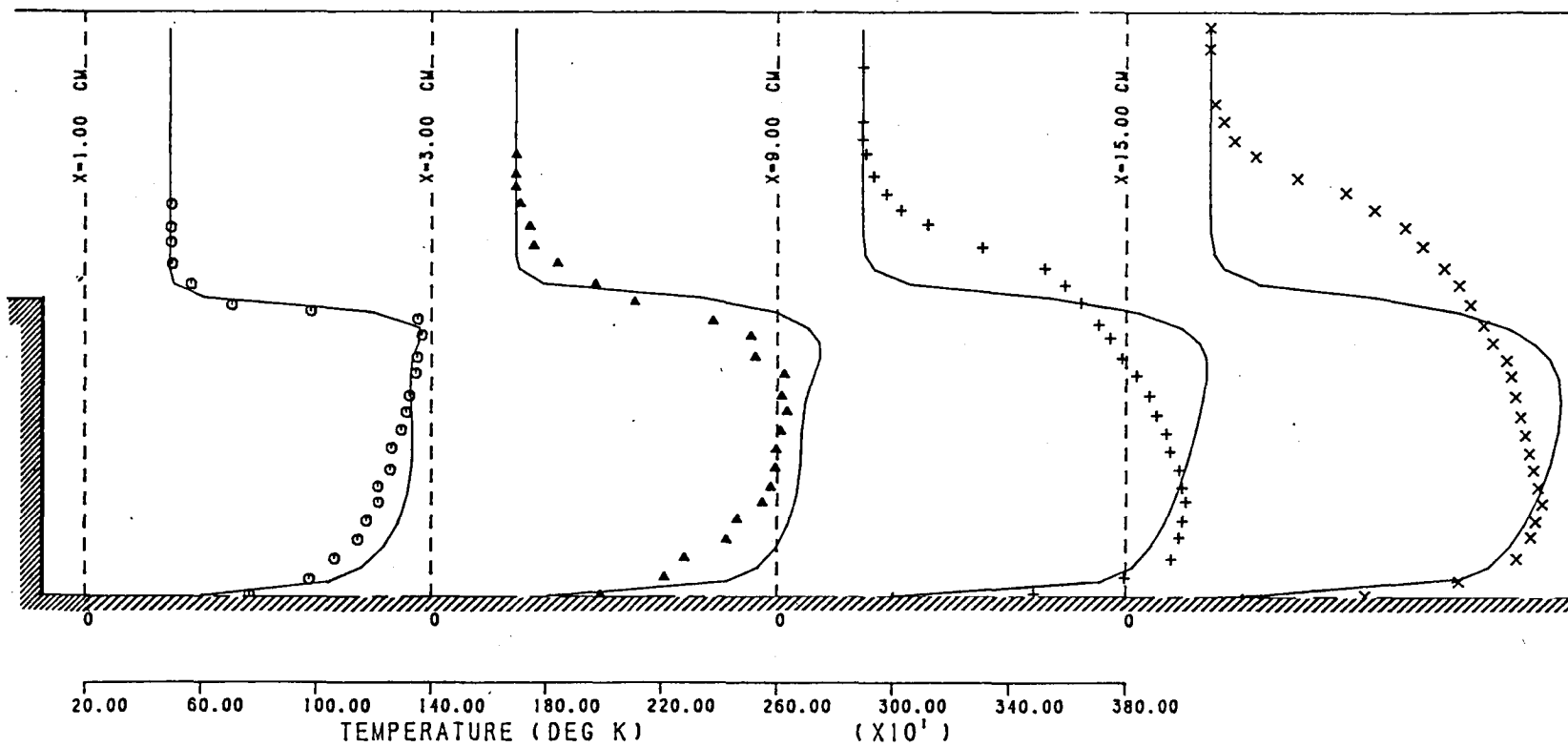


Figure 7.8-6. 2-Step Reaction Scheme - Mean Temperature Profiles.

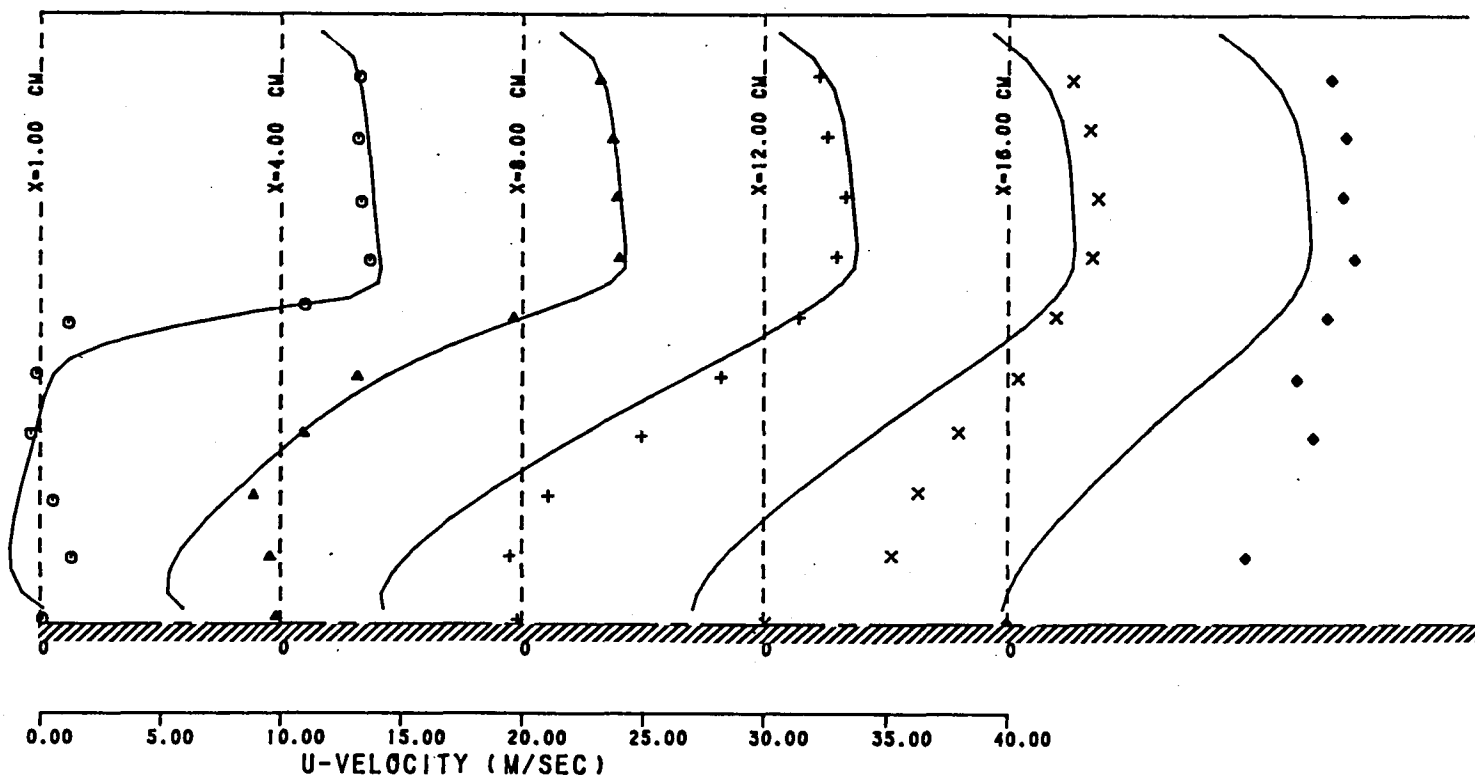


Figure 7.8-7. Four-Step Reaction Scheme-Mean Axial Velocity Profiles.

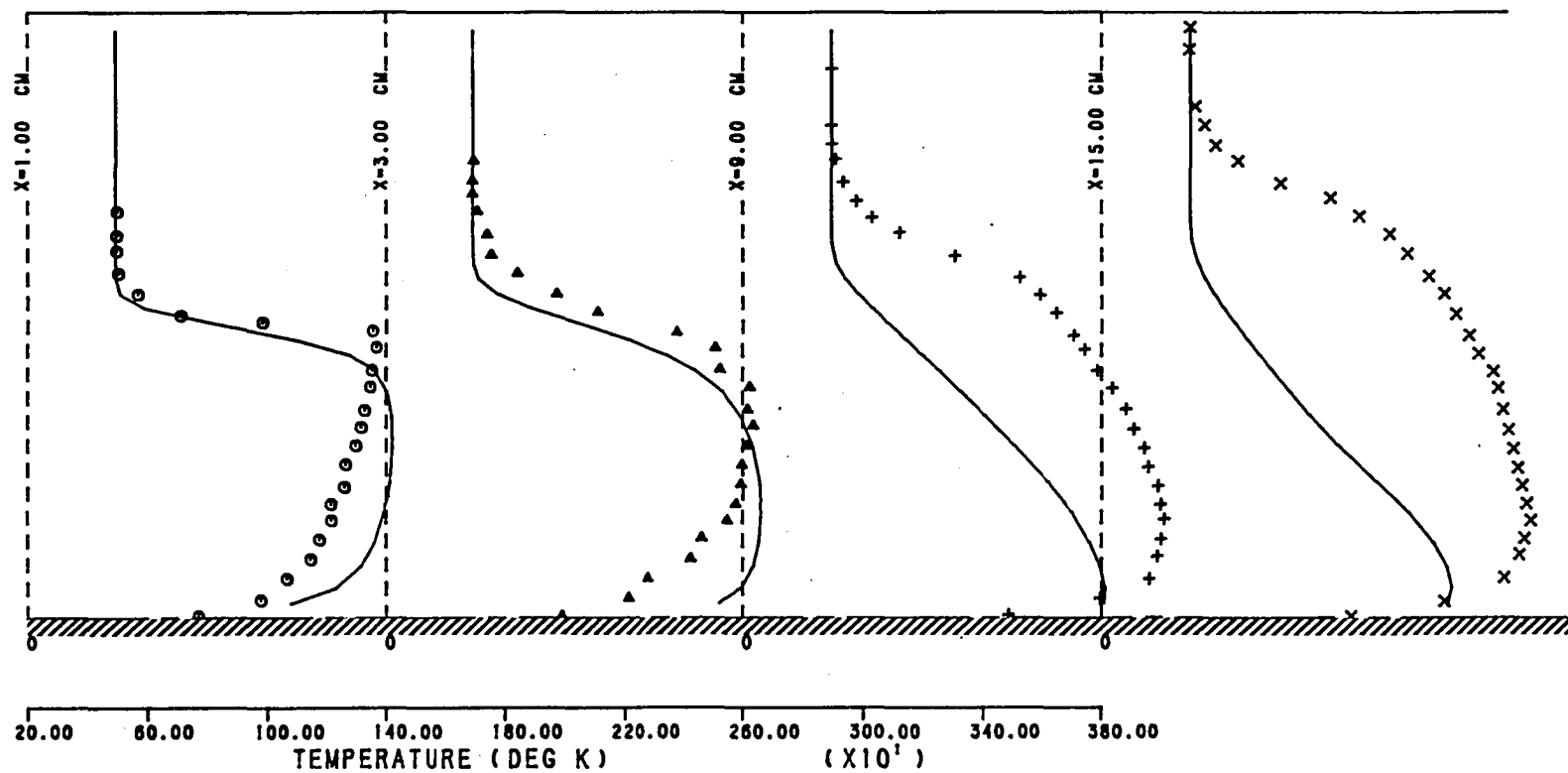


Figure 7.8-8. Four-Step Reaction Scheme - Mean Temperature Profiles, $T_w = 500^\circ\text{K}$.

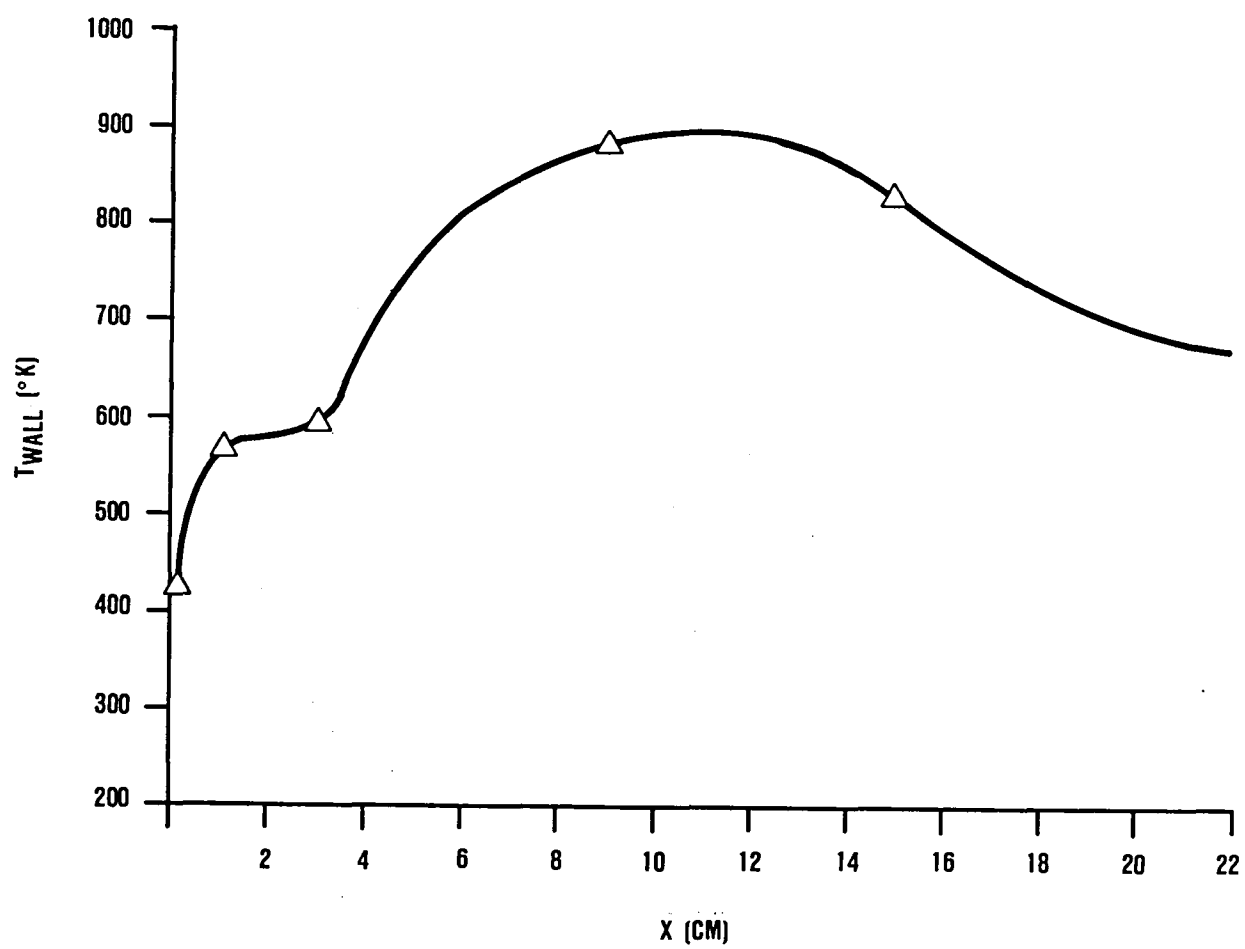


Figure 7.8-9. Measured Wall Temperature Distribution Behind the Step.

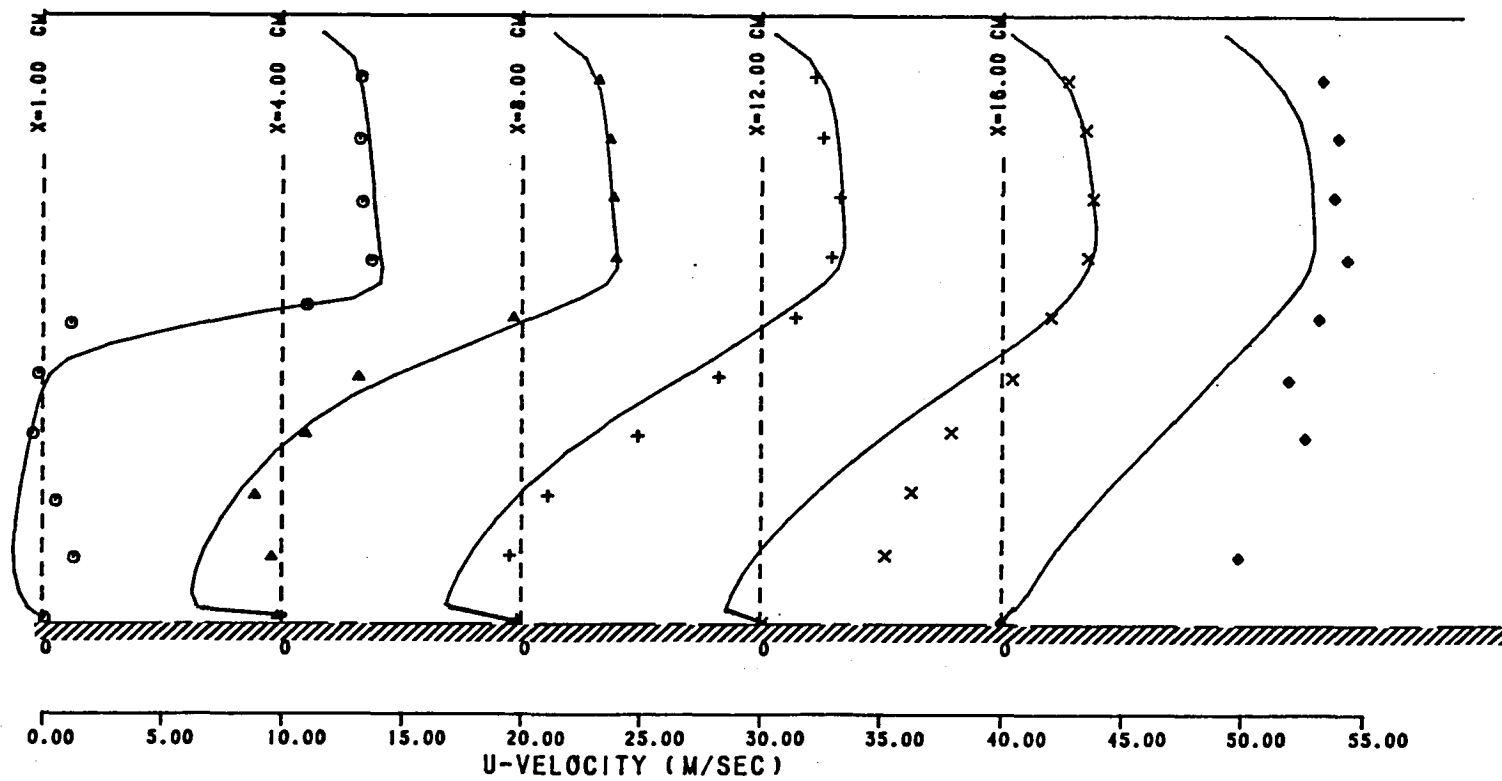


Figure 7.8-10. Two-Step Reaction Scheme with Measured Wall Temperature Distribution - Mean Axial Velocity Profiles.

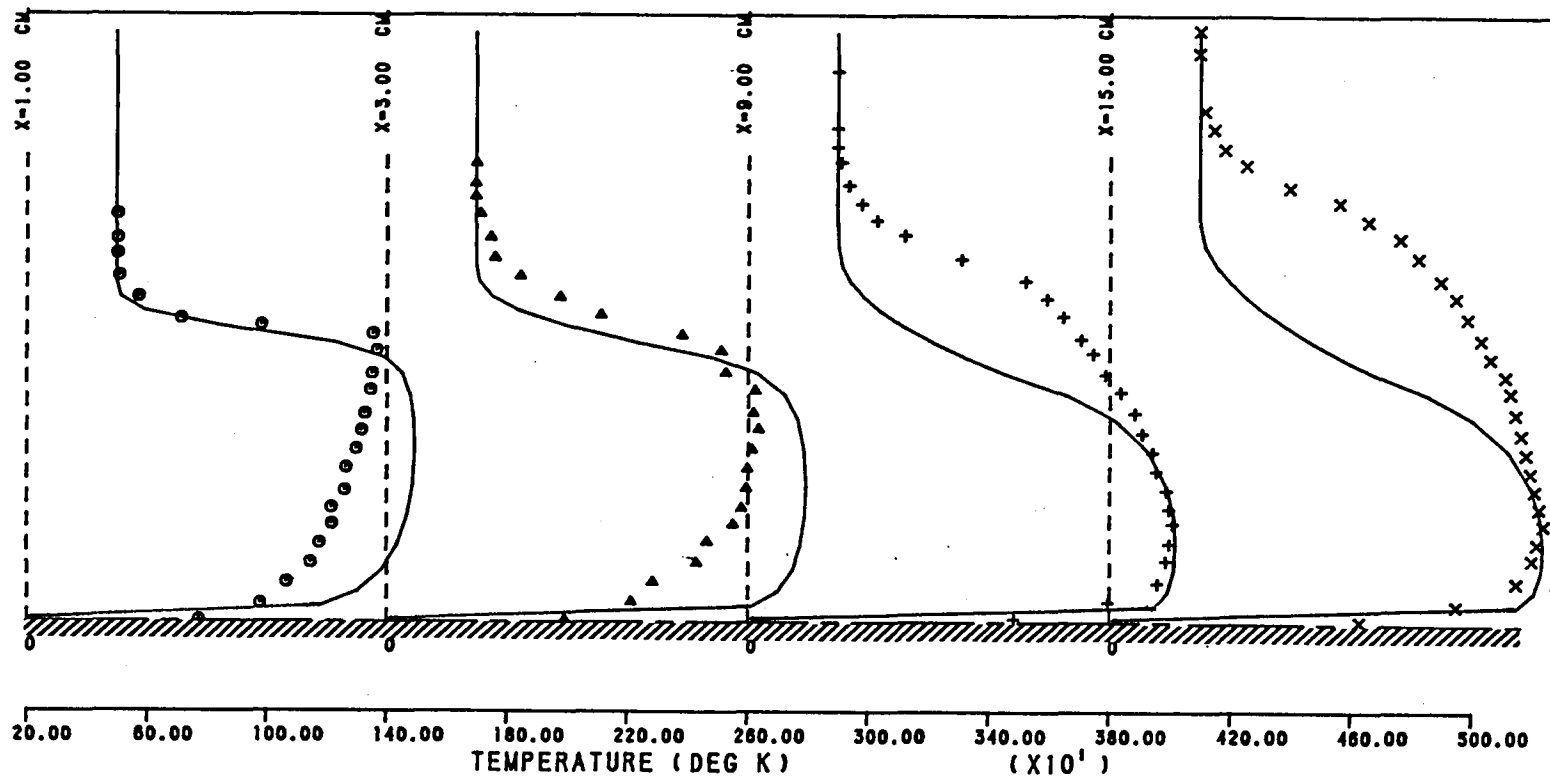


Figure 7.8-11. Two-Step Reaction Scheme With Measured Wall Temperature Distribution - Mean Temperature Profiles.

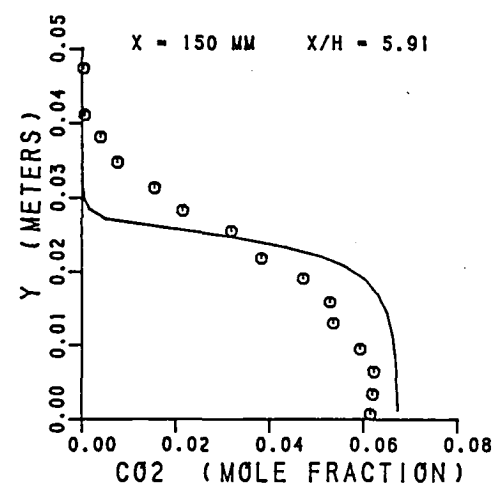
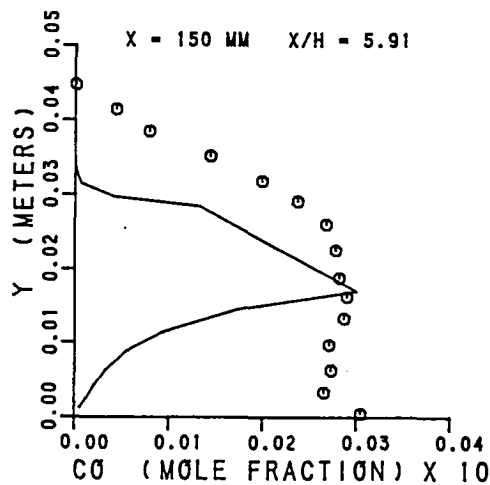
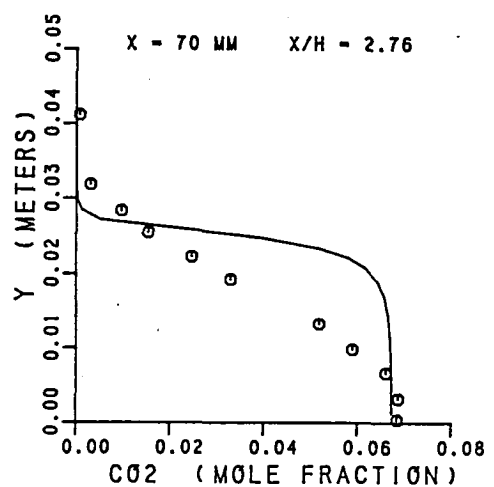
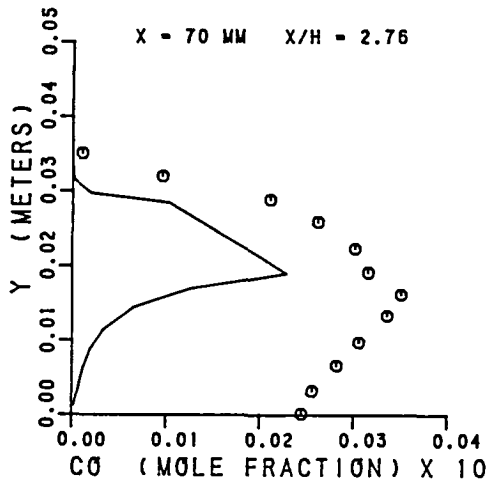
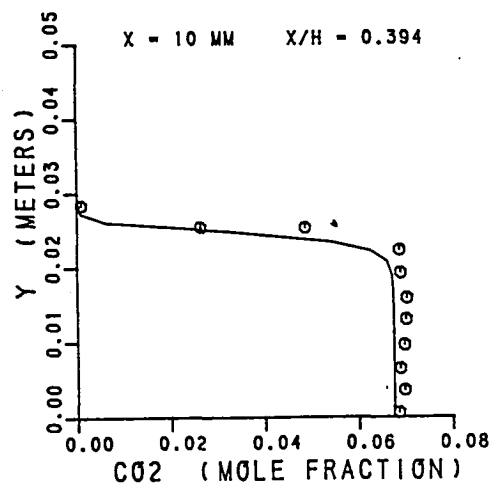
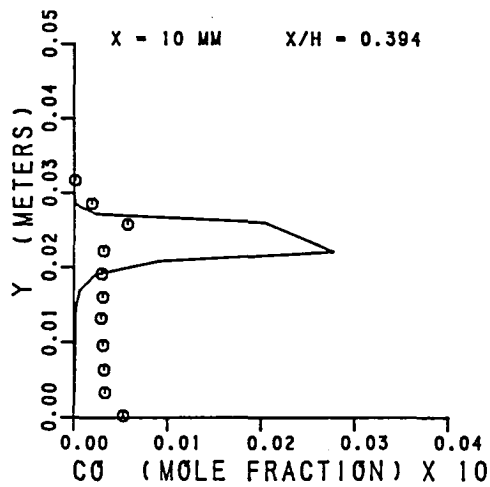


Figure 7.8-12. Two-Step Reaction Scheme With Measured Wall Temperature Distribution - CO and CO₂ Profiles.

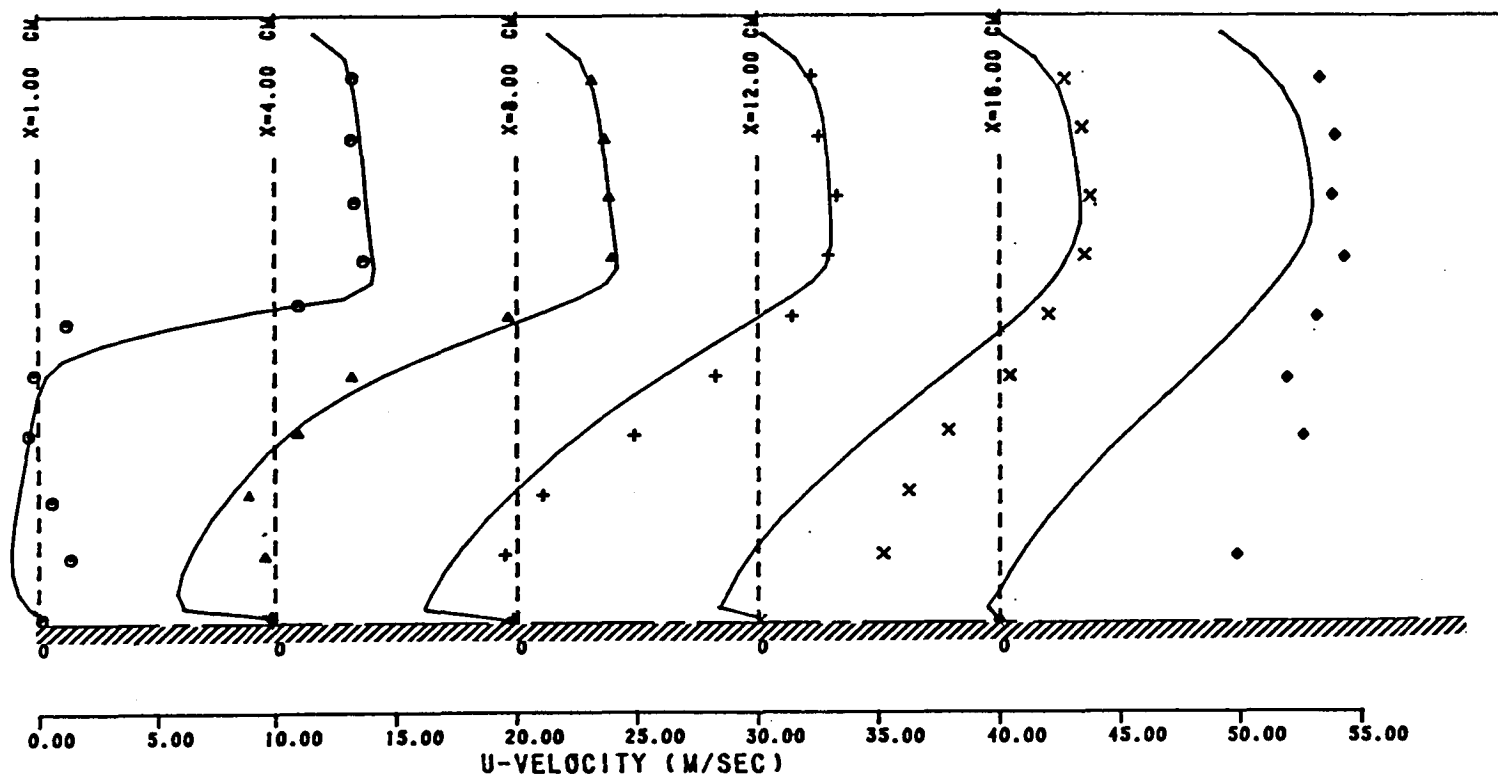


Figure 7.8-13. Four-Step Reaction Scheme With Measured T_w Distribution - Mean Axial Velocity Profiles.

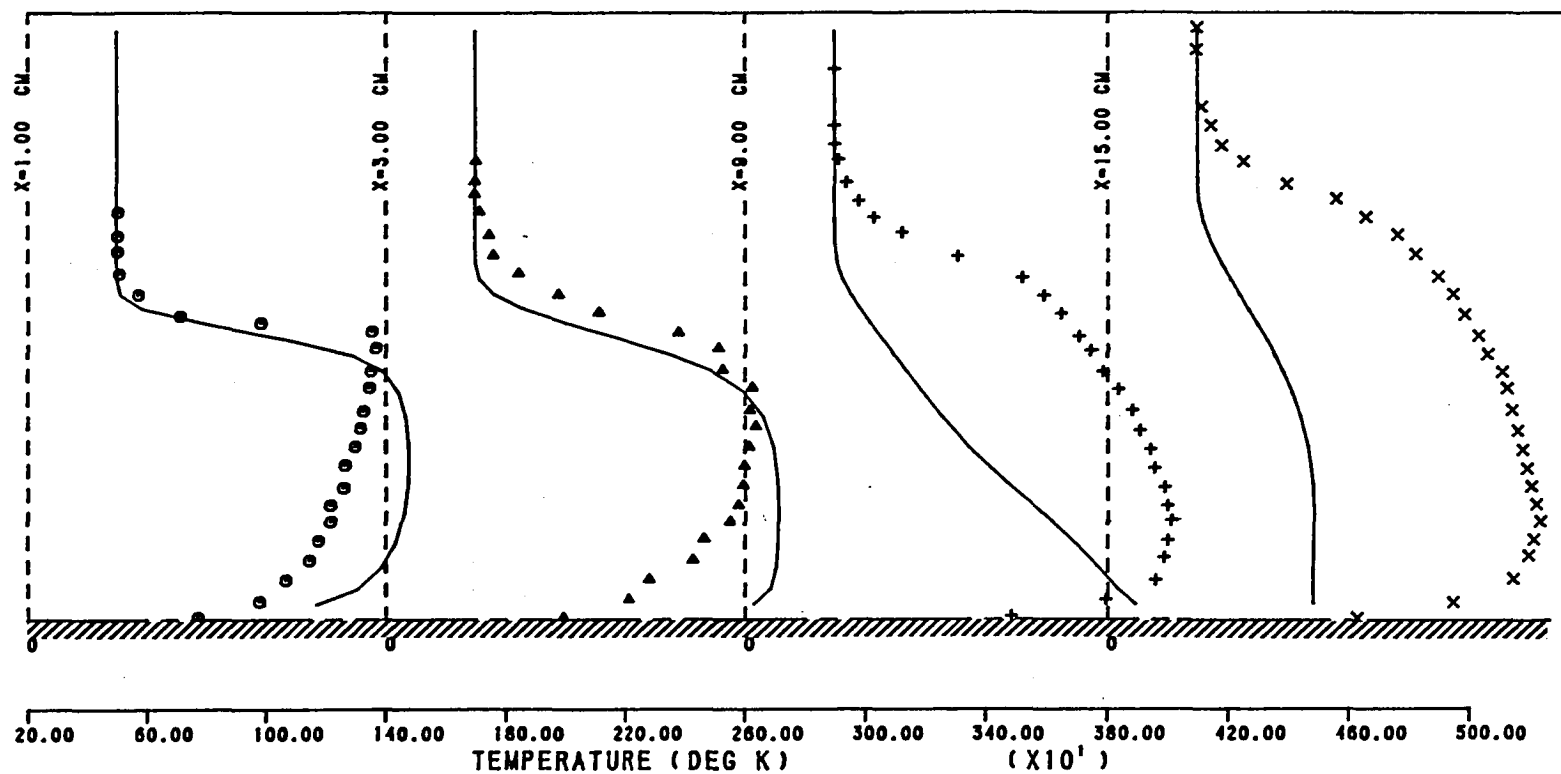


Figure 7.8-14. Four-Step Reaction Scheme With Measured T_w Distribution - Mean Temperature Profiles.

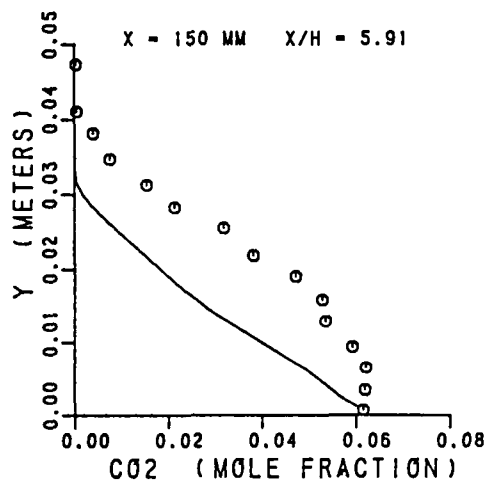
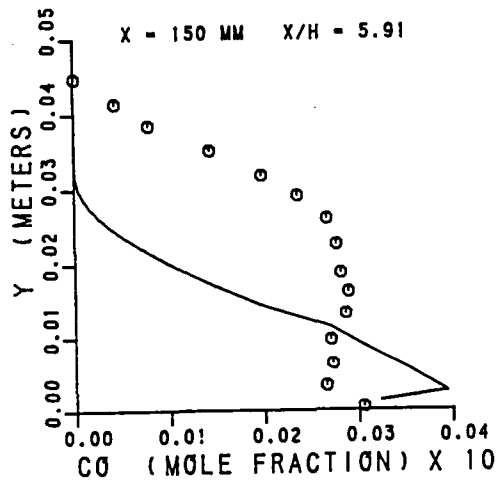
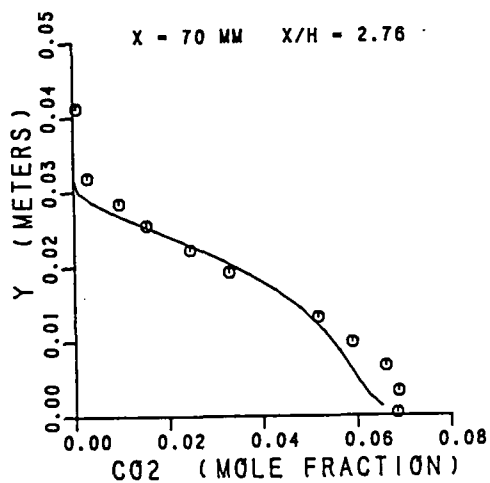
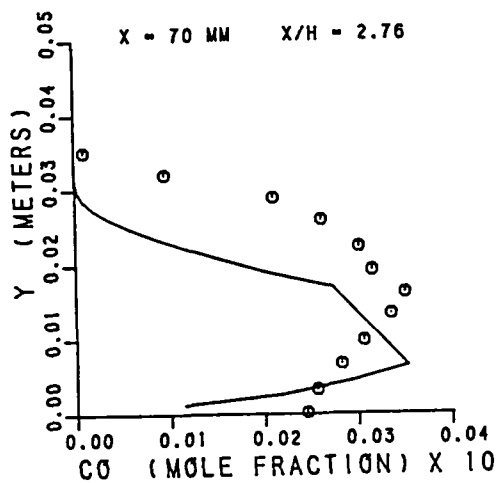
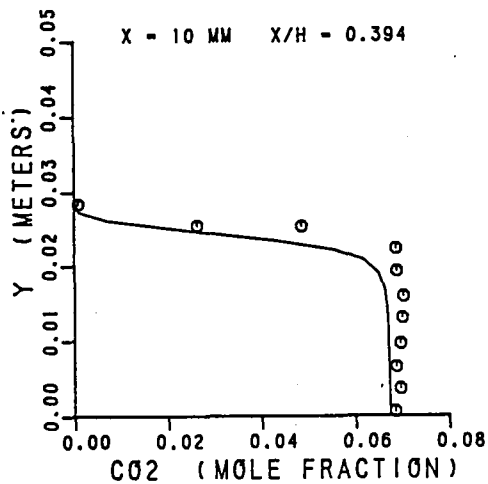
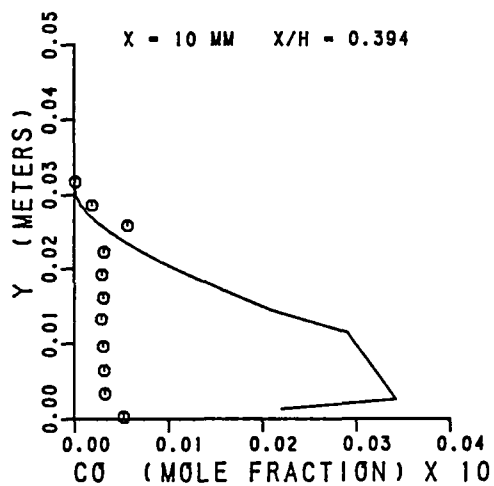


Figure 7.8-15. Four-Step Reaction Scheme With Measured T_w Distribution - CO and CO₂ Profiles.

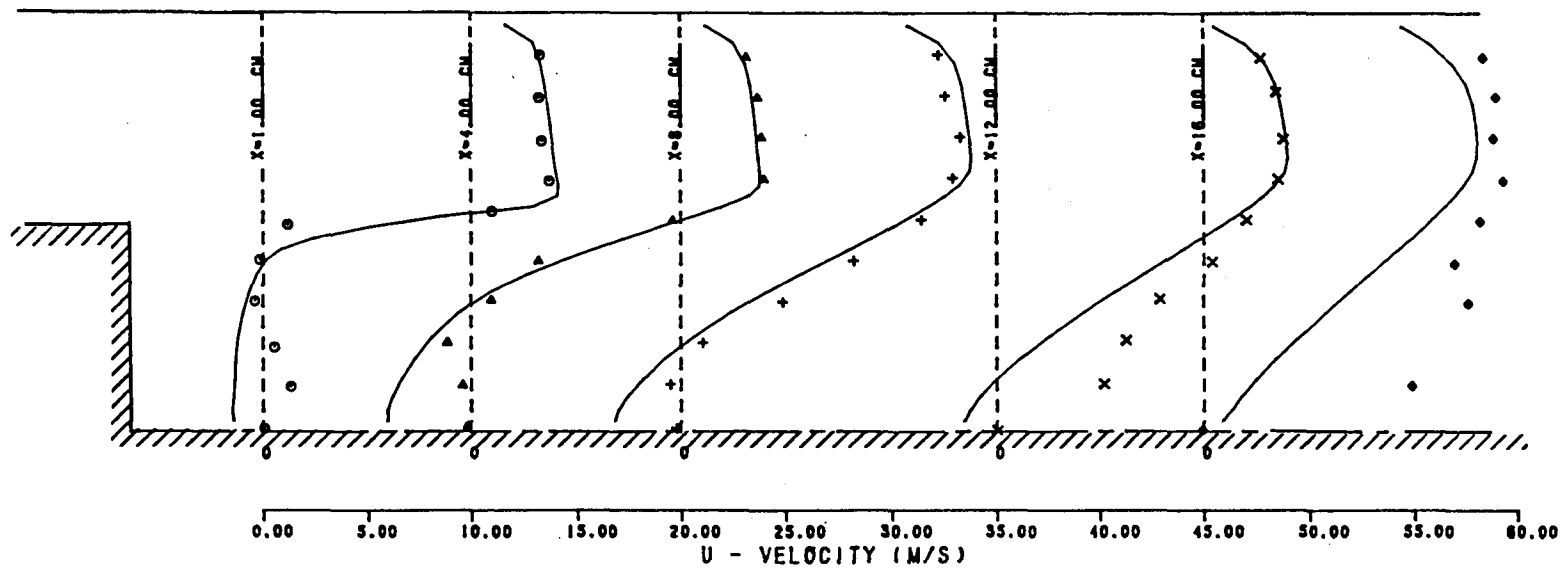


Figure 7.8-16. Four-Step Reaction Scheme With Modified Rate Constants - Mean Axial Velocity Profiles.

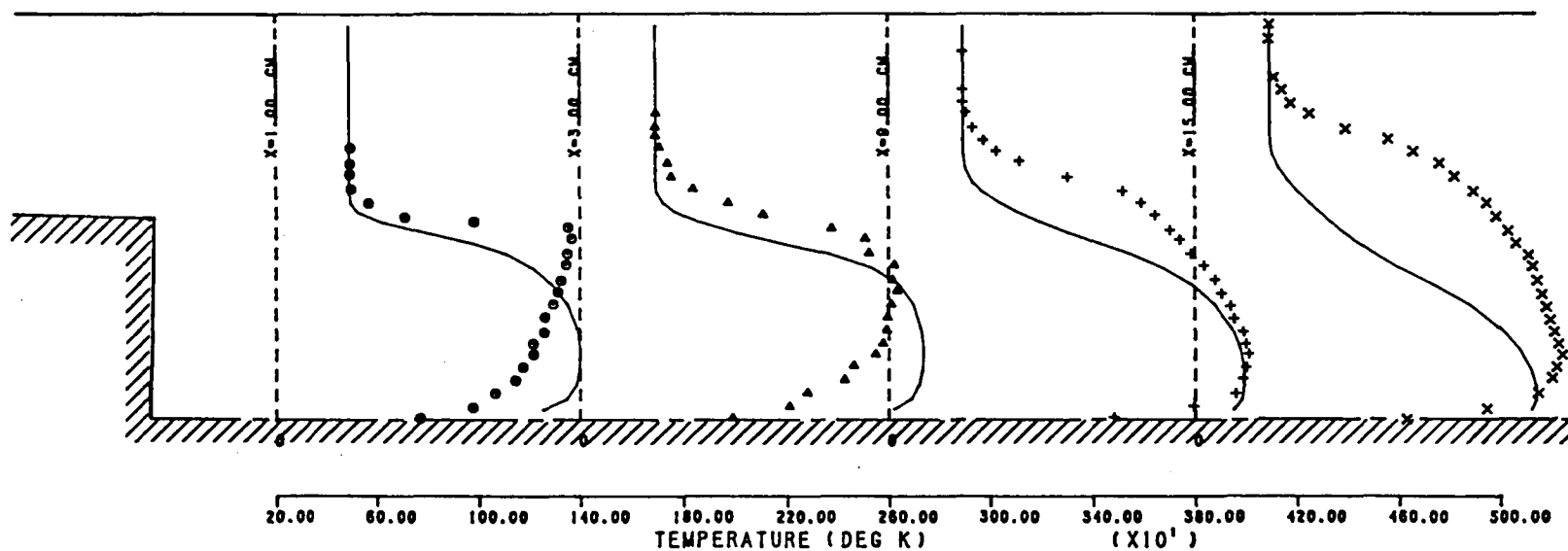


Figure 7.8-17. Four-Step Reaction Scheme With Modified Rate Constants - Mean Temperature Profiles.

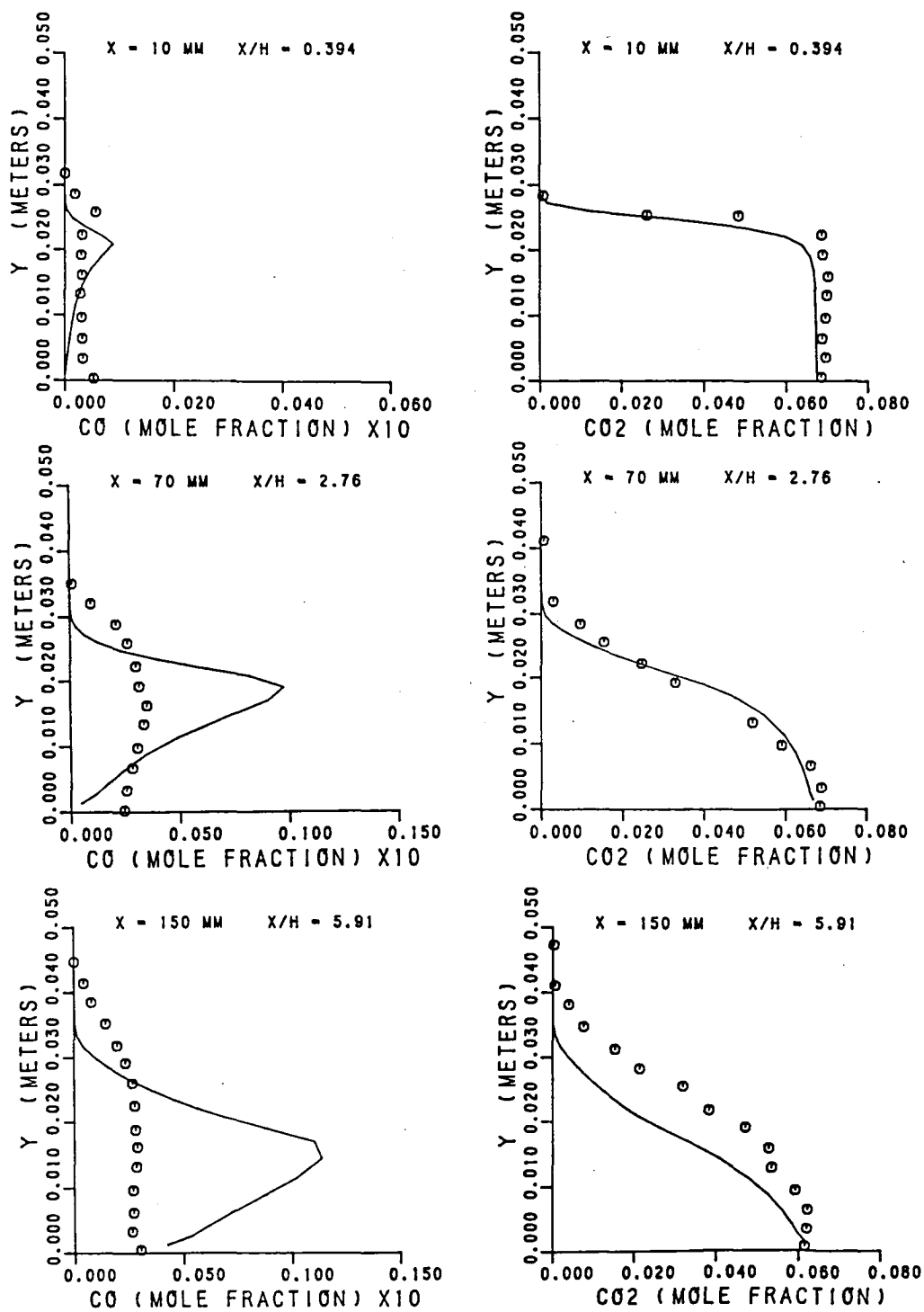


Figure 7.8-18. Four Step Scheme With Modified Rate Constants - CO and CO₂ Profiles.

7.9 Opposed Reacting Jet Flow

Another benchmark test case selected for evaluating the kinetic scheme is the recirculating flow in an axisymmetric opposed reacting jet combustor. Species concentration and temperature measurements were made by Scheffer and Sawyer¹⁴⁶ in a premixed opposed jet combustor shown schematically in Figure 7.9-1.

A premixed propane and air mixture was used for both the mainstream and the opposed jet with an equivalence ratio of 0.625. For the test case selected, the following were the flow parameters:

Mainstream average velocity = 7.74 m/sec

Mainstream Temperature = 300°K

Jet velocity = 95.9 m/sec

Jet temperature = 295°K

Computations of the flow field were made using a 2-D elliptic program with 1400 nodes. Predictions were obtained with both two-step and four-step kinetic schemes. Initial profiles for the mainstream were specified using a plug flow profile with $U = 7.74$ m/s and $T = 300^\circ\text{K}$. The inlet kinetic energy profile was assumed to be uniform with a value of $0.18 \text{ m}^2/\text{s}^2$, and the inlet length scale was assumed to be constant with a value of 0.00058 m. Computations were performed for half of the flow domain by assuming symmetry around the centerline. Adiabatic boundary conditions along the wall were applied. Along the axis of symmetry, zero radial gradients were prescribed for all the variables except v , which was set to zero. At the exit boundary, zero axial gradient conditions were imposed on all of the dependent variables.

The two-step model predictions for temperature are shown in Figure 7.9-2. The two-step scheme with the Design Criteria rate constants overestimates the gas temperatures everywhere. The model overpredicts fuel consumption rate as shown by the unburned fuel mole fraction profiles in Figure 7.9-3. The two-step model predicts a faster reaction than the measurements, and hence the unburned fuel concentrations are underestimated.

Since the two-step model predicts a faster reaction rate for the opposed jet flame, the predicted CO_2 concentrations are also higher, as seen in Figure 7.9-4. The CO concentrations predicted by the two-step scheme are significantly higher than the data, as seen in Figure 7.9-5. Because of the faster reaction scheme, the predicted H_2O mole fractions are higher (Figure 7.9-6) and the predicted oxygen concentrations (Figure 7.9-7) are smaller.

The four-step model predictions (with the original rate constants) for the opposed jet flame are presented in Figures 7.9-8 through 7.9-13. The four-step model results for temperature are illustrated in Figure 7.9-8. The profiles are in better agreement with the data compared to the two-step model results (Figure 7.9-2). The four-step scheme predictions for unburned fuel mole fractions are shown in Figure 7.9-9. These profiles are also underpredicted by the two-step model. However, the four-step predictions of CO_2 concentrations, as seen in Figure 7.9-10, are in good agreement with the data. This suggests that the four-step model with Hautman, et al., rate constants overestimate the reaction rates of fuel oxidation, but the oxidation rates of CO and the intermediates are correctly modeled. This conclusion is substantiated by the CO profiles shown in Figure 7.9-11, which are in good agreement with the data. The predicted H_2O concentrations (Figure 7.9-12) and oxygen mole fractions (Figure 7.9-13) are in good agreement with the data and are consistent with the reaction rates of the other species.

For the case of the opposed jet flame, the two-step kinetic scheme overestimates the reaction rates of fuel and CO oxidation, and hence the predicted temperatures are much higher than the data. The four-step scheme overestimates the fuel reaction rates, but correctly predicts the reaction rates for the other steps. Consequently, the four-step results are in much better agreement with the data than the two-step results.

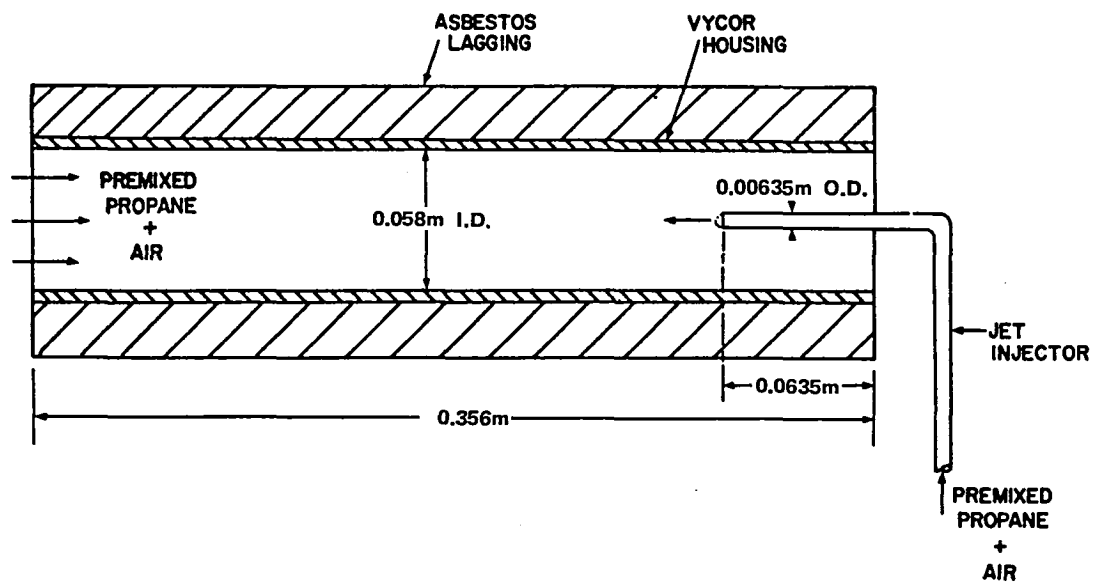


Figure 7.9-1. Geometry of the Opposed Jet Combustion Setup.

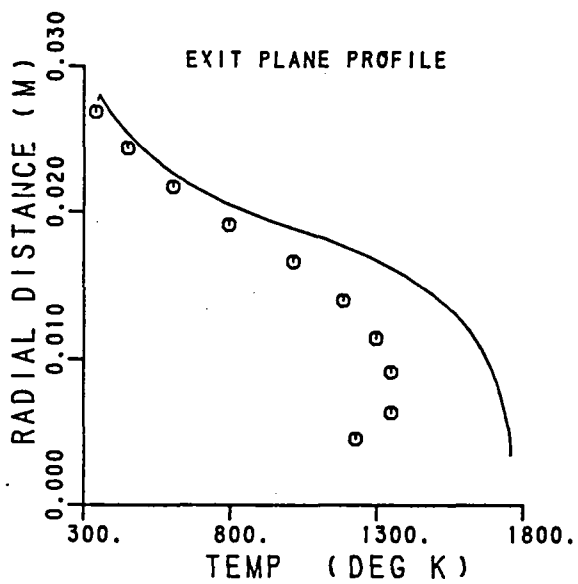
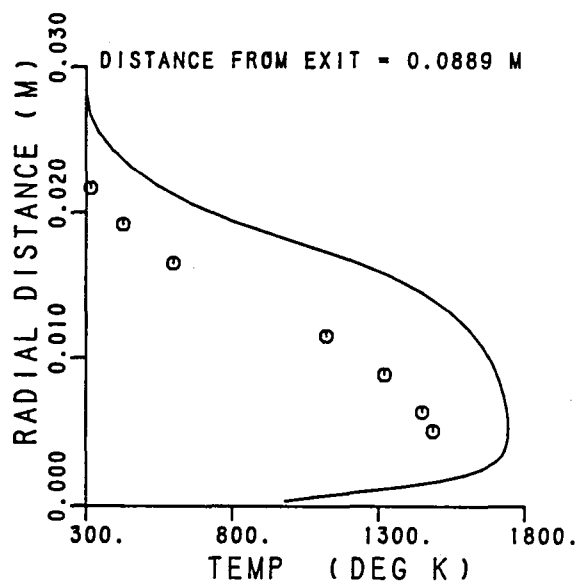
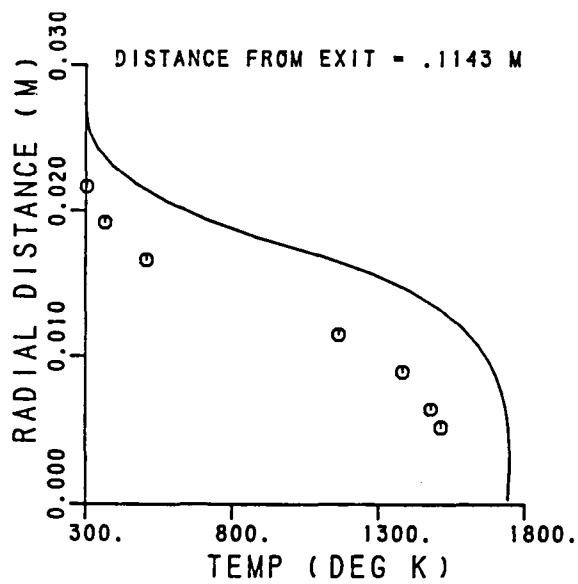


Figure 7.9-2. 2-Step Kinetic Scheme - Mean Temperature Profile.

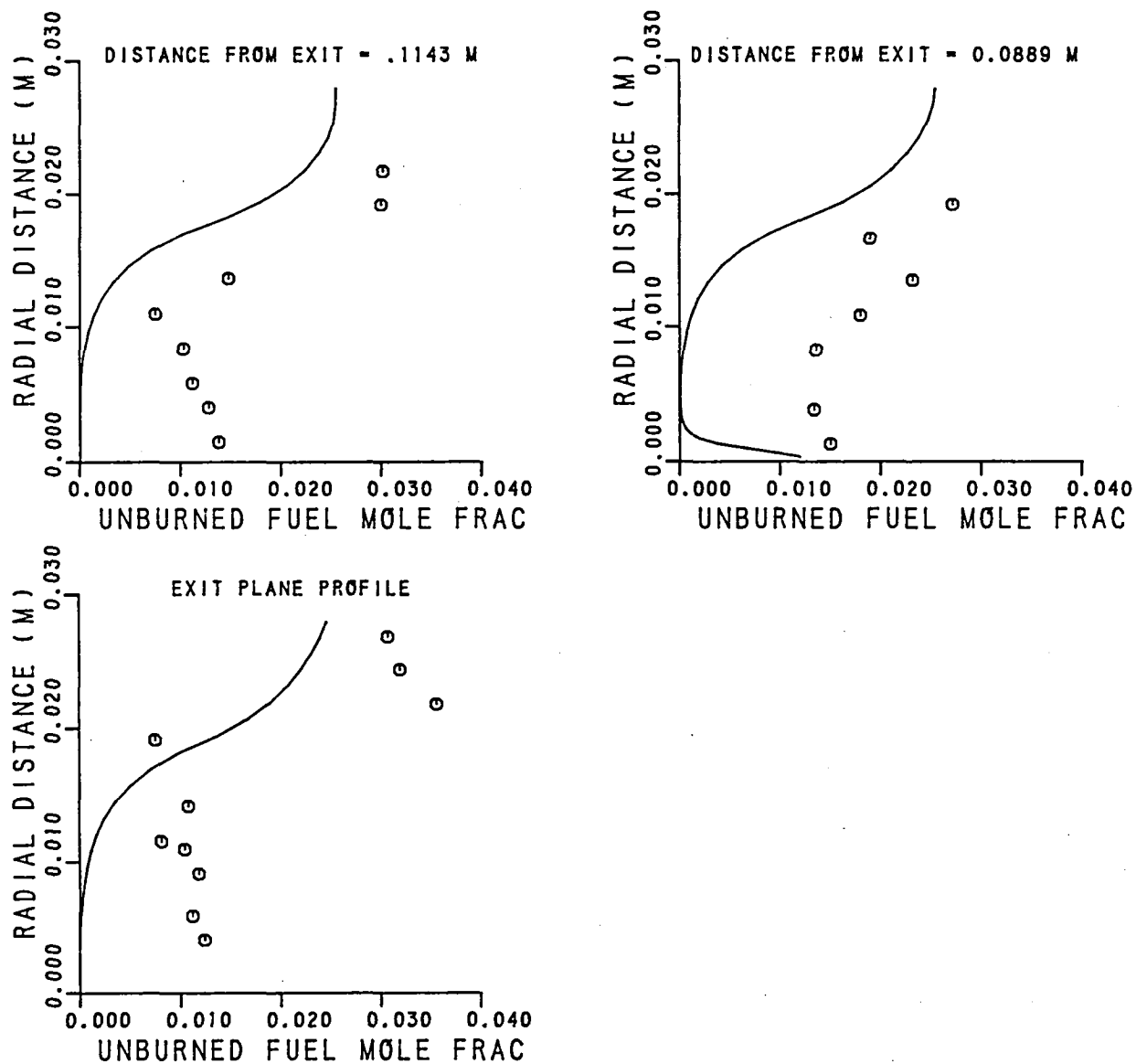


Figure 7.9-3. 2-Step Scheme - Unburned Fuel Profiles.

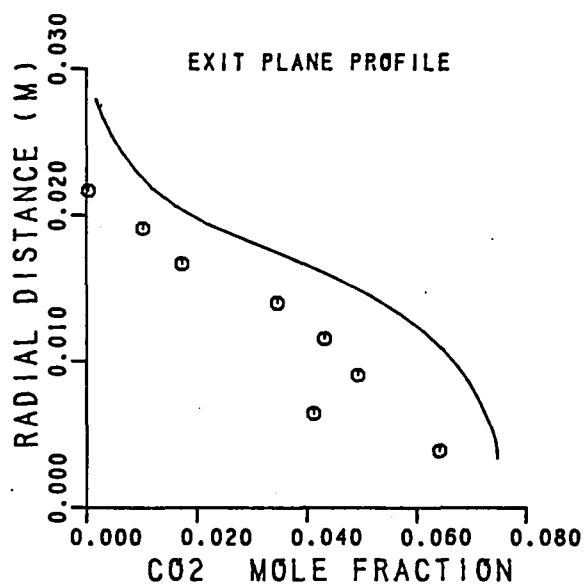
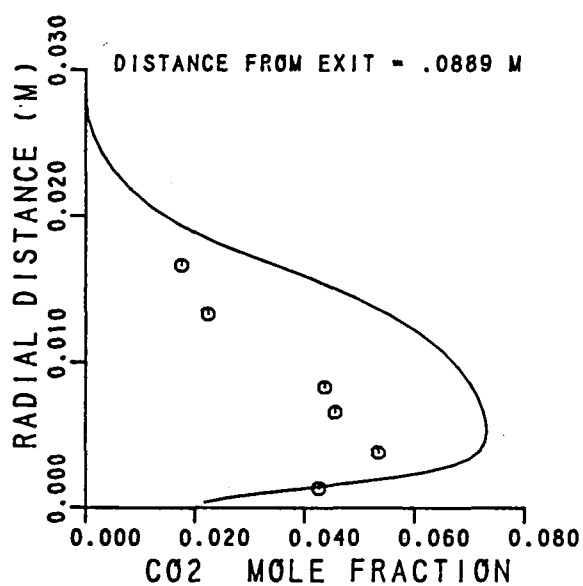
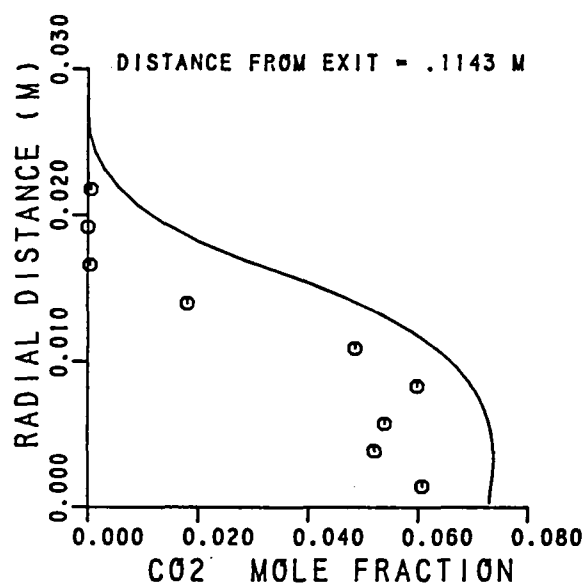


Figure 7.9-4. 2-Step Scheme - CO₂ Profiles.

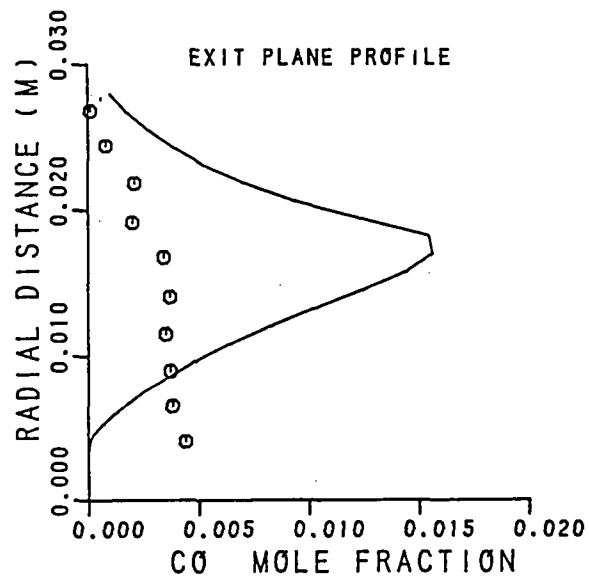
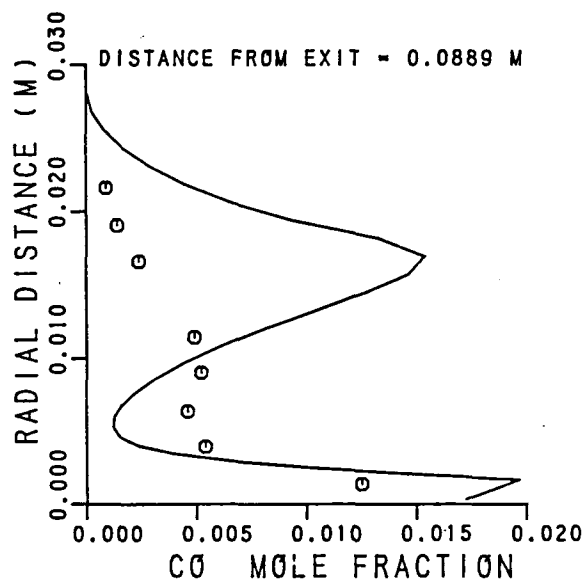
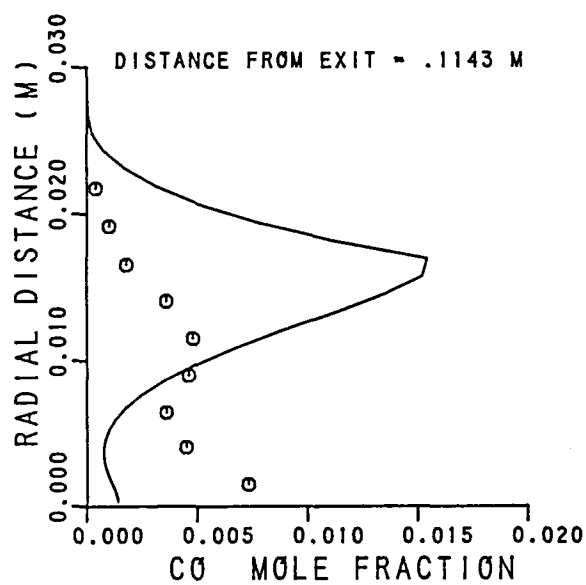


Figure 7.9-5. 2-Step Scheme - CO Profiles.

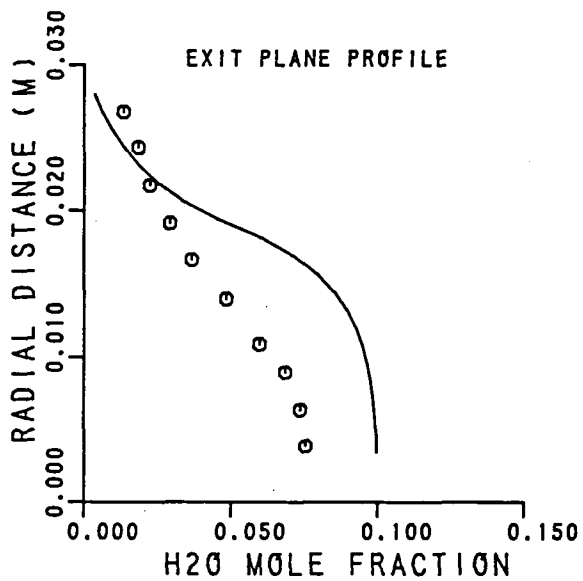
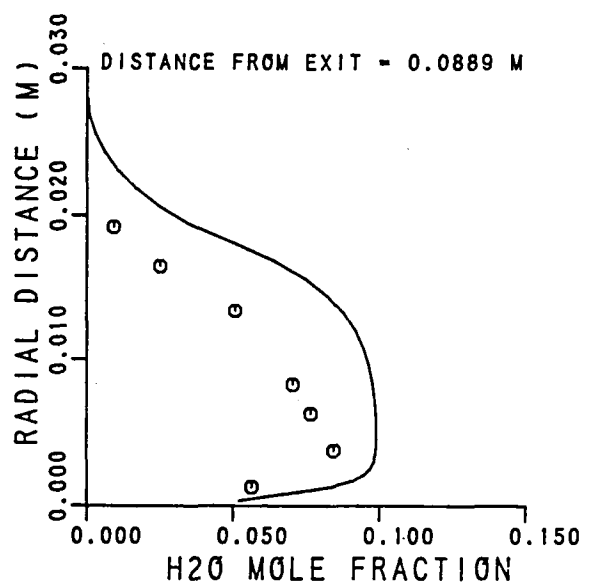
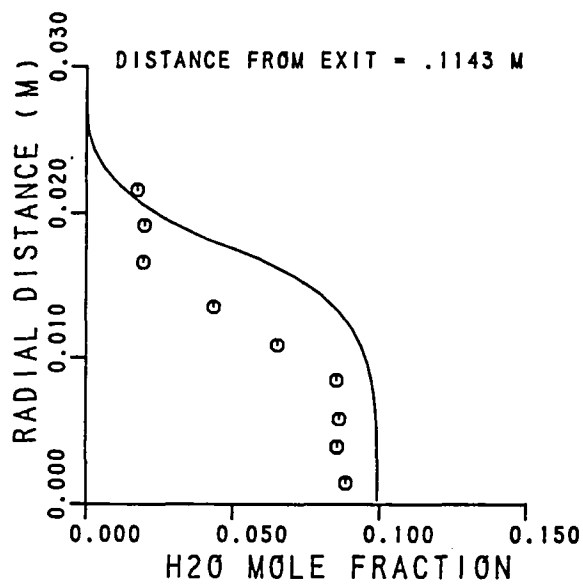


Figure 7.9-6. 2-Step Scheme - H₂O Profiles.

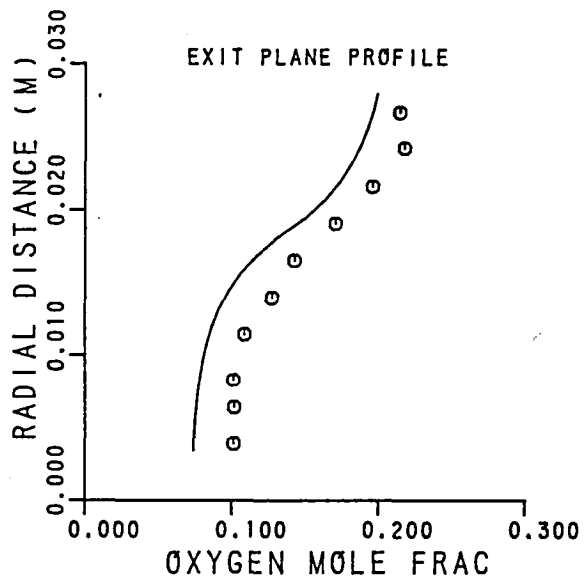
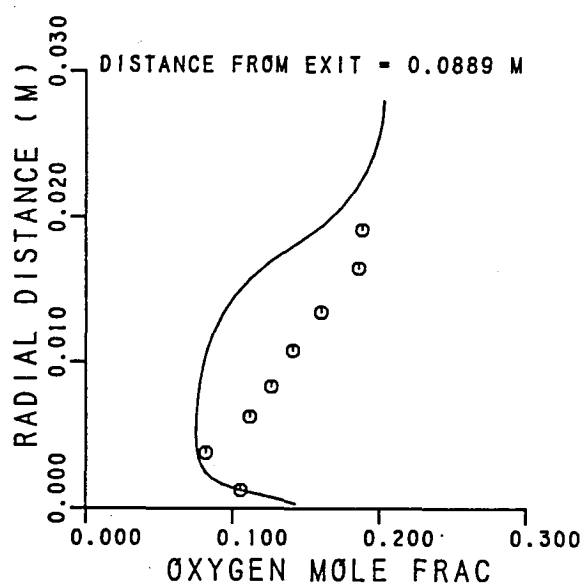
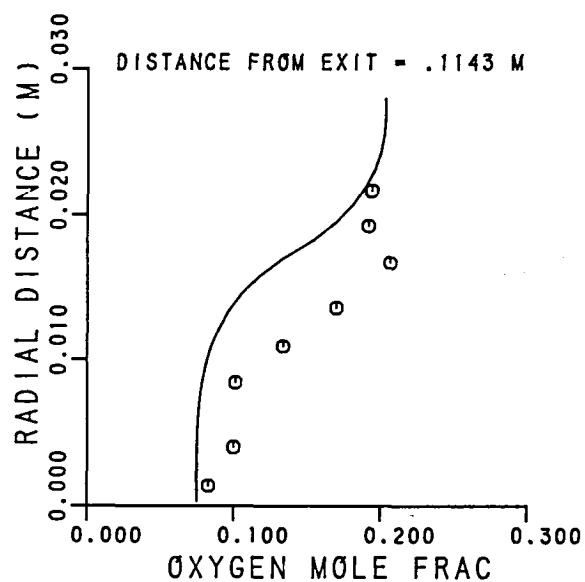


Figure 7.9-7. 2-Step Scheme - O_2 Profiles.

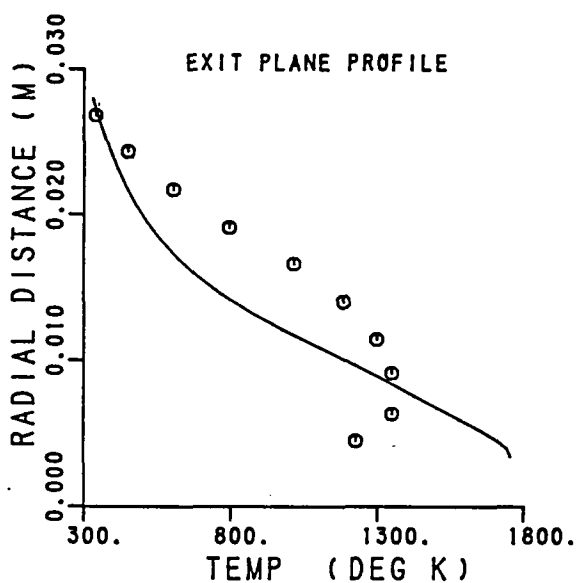
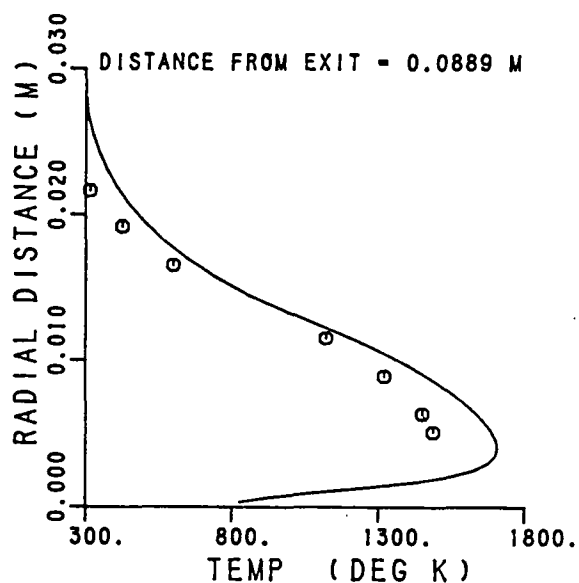
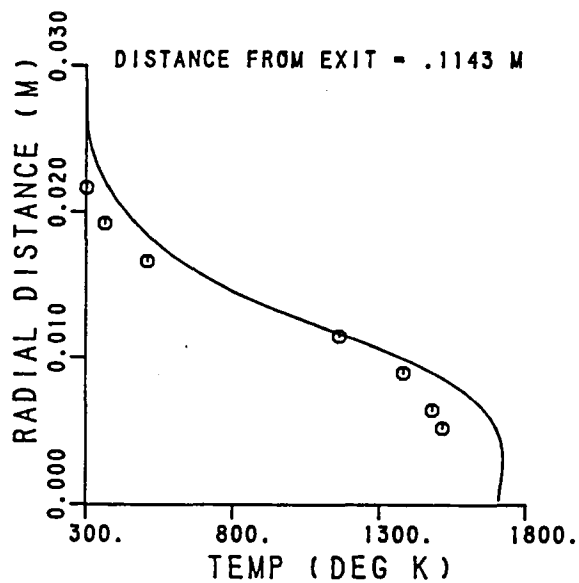


Figure 7.9-8. 4-Step Reaction Scheme with Original Rate Constants - Temperature Profiles.

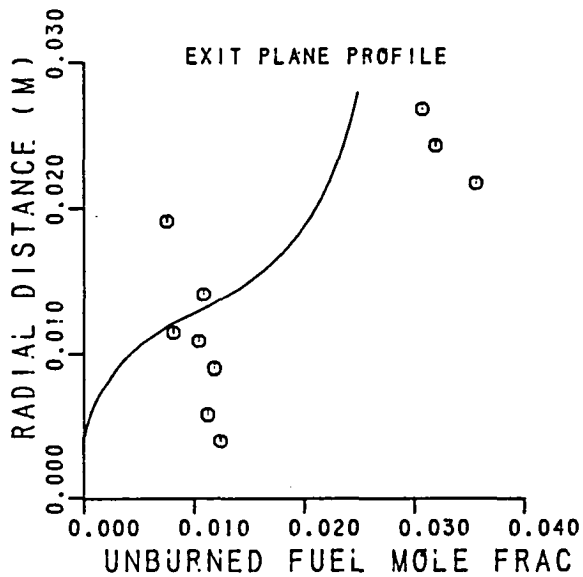
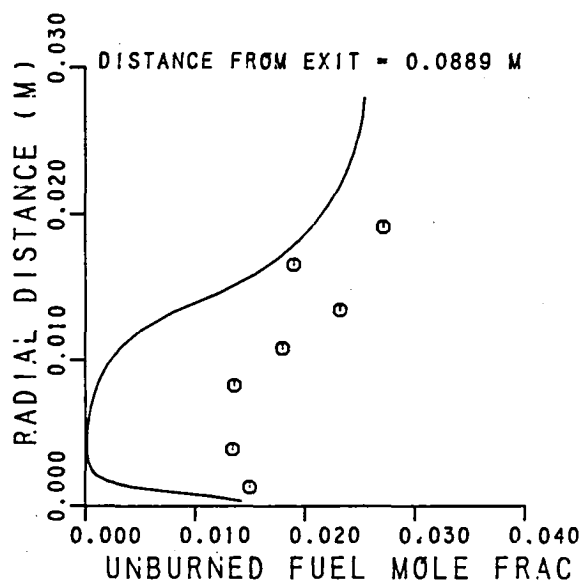
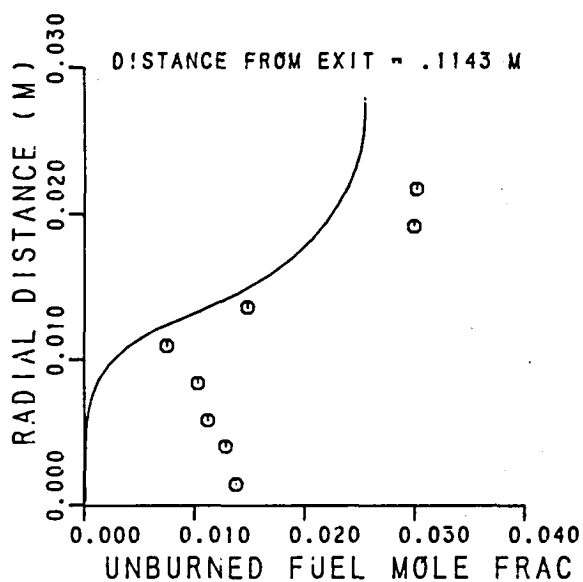


Figure 7.9-9. 4-Step Scheme - Unburned Fuel Profiles.

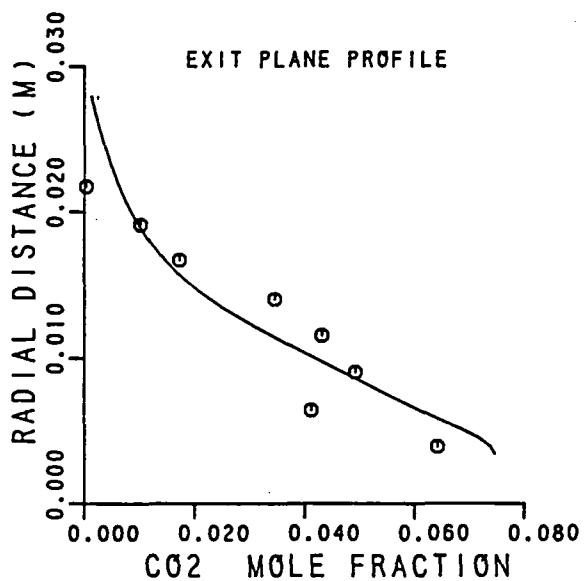
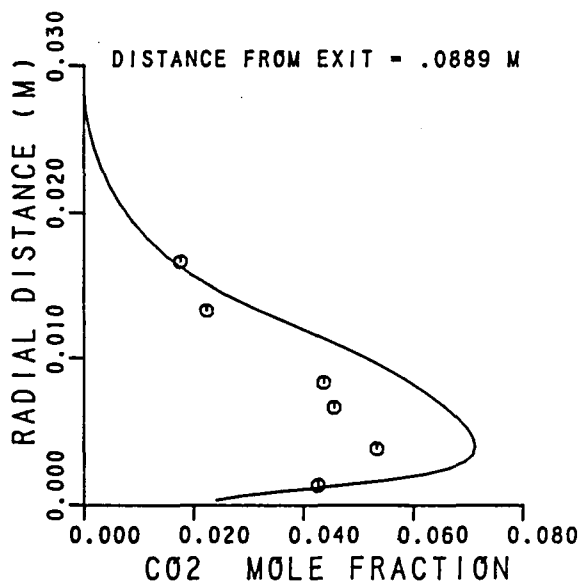
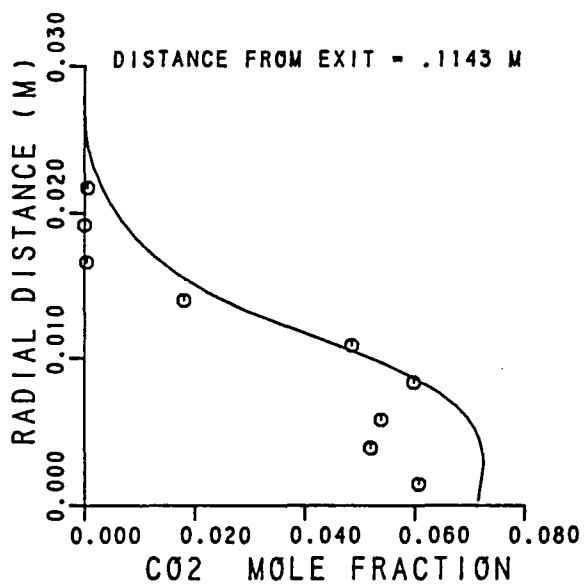


Figure 7.9-10. 4-Step Scheme - CO₂ Profiles.

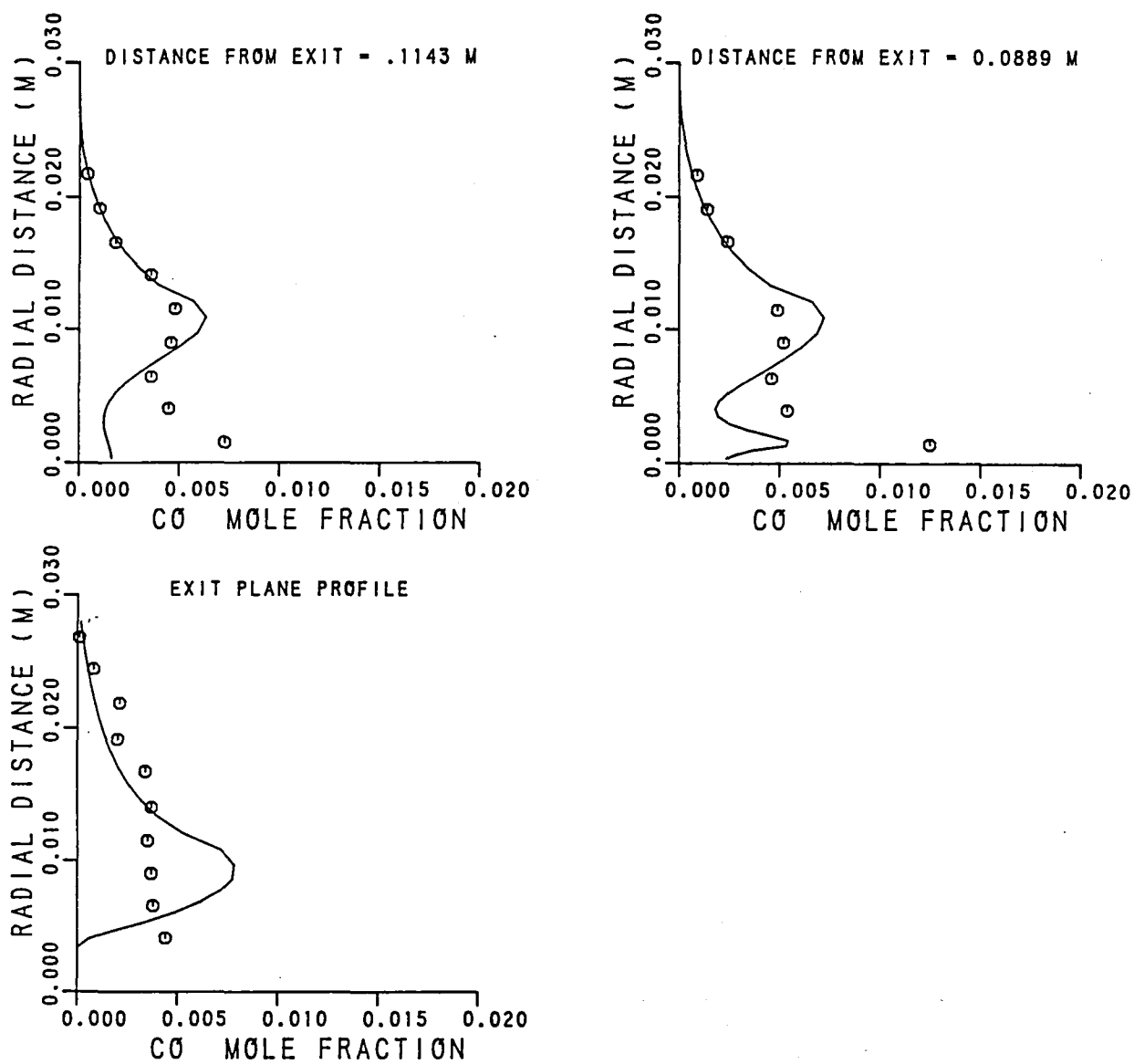


Figure 7.9-11. 4-Step Scheme - CO Profiles.

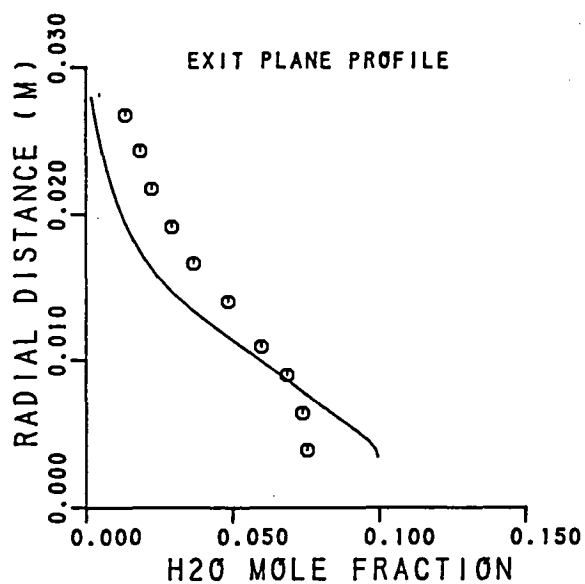
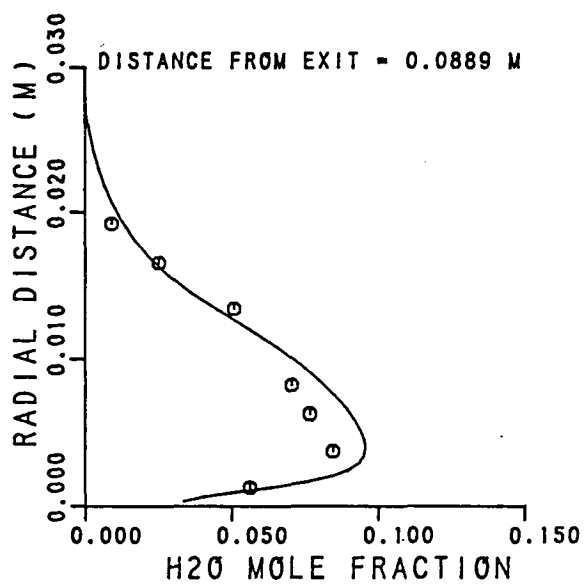
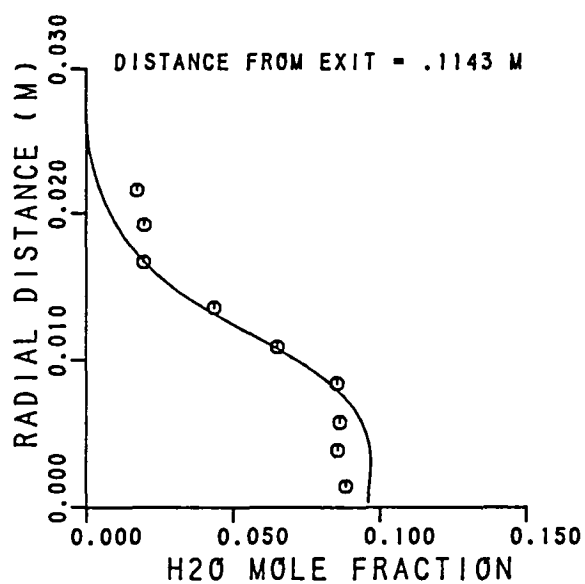


Figure 7.9-12. 4-Step Scheme - H₂O Profiles.

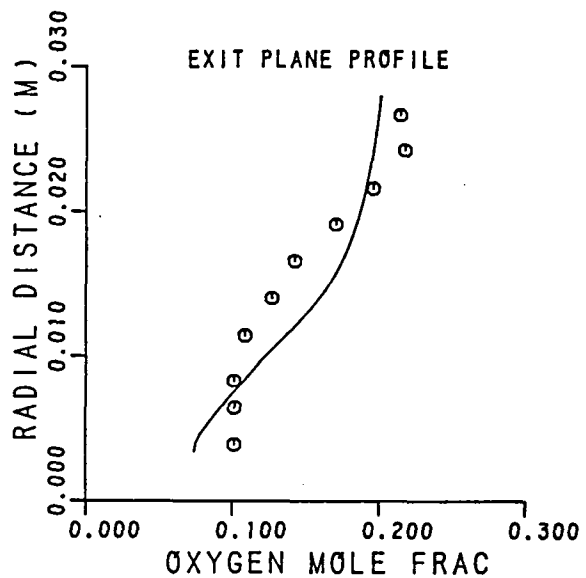
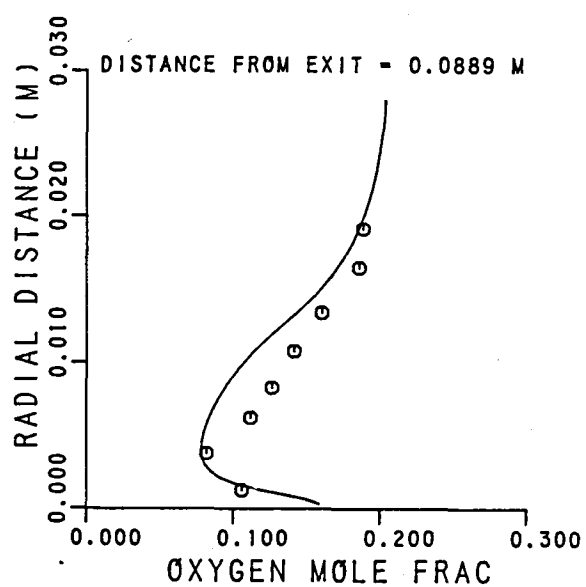
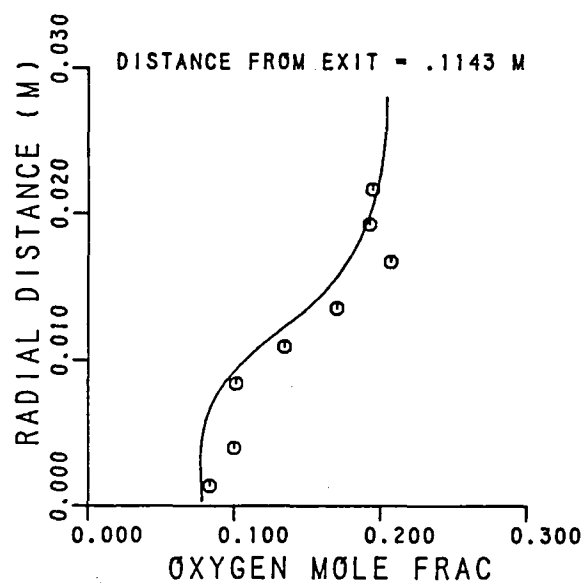


Figure 7.9-13. 4-Step Scheme - O_2 Profiles.

7.10 Axisymmetric Combustor with Coaxial Fuel and Air Jets

The reacting flow test cases considered thus far do not represent the geometries in the practical combustor dome. A more realistic geometry of an axisymmetric combustor with coaxial fuel and air jets was chosen for the next benchmark test case. Measurements of species concentration and temperature were made by Lewis and Smoot¹⁴⁰ in a test geometry shown schematically in Figure 7.10-1.

For the test case selected, methane was used through the fuel tubes, and the average inlet conditions were as follows:

Air Velocity, $U_{\text{air}} = 34.3 \text{ m/sec}$

Air Temperature, $T_{\text{air}} = 589^\circ\text{K}$

Fuel Velocity, $U_{\text{fuel}} = 21.3 \text{ m/sec}$

Fuel Temperature, $T_{\text{fuel}} = 300^\circ\text{K}$

Inlet Pressure, $P = 94 \text{ KPa}$

The computations for this case were made using the 2-D elliptic code with standard $k-\epsilon$ model, and two-step and four-step kinetic schemes. A total of 1400 nodes were used in the computations. Uniform inlet profiles were specified with inlet velocity and temperatures as given above. The inlet kinetic energy for air was given in the measurements as $11.765 \text{ m}^2/\text{s}^2$, and the corresponding value for the fuel jet was measured to be $1.633 \text{ m}^2/\text{s}^2$. The inlet length scales were assumed to be 0.00057 m for air jet and 0.000016 m for fuel jet, respectively. Along the (adiabatic) walls, standard wall function treatment was employed. Along the inner boundary, symmetry conditions were specified and at the exit plane, zero axial gradient conditions were imposed. At the inlet, the fuel mixture fraction was set equal to one in fuel and zero else where.

Two-step scheme with Design Criteria rate constants predictions are shown in Figures 7.10-2 through 7.10-4. Figure 7.10-2 shows the comparison between the data and the predictions for the mean mixture fraction. The data and predictions are in good agreement. The profiles of unburned fuel are shown in Figure 7.10-3. The two-step overestimates the unburned fuel concentrations. The predicted reaction rates are slower than the measured rates. This conclusion is substantiated by the CO concentrations shown in Figure 7.10-4. The predicted CO levels beyond $x = 47.6$ cm are significantly lower than the data. Near the inlet ($x = 9.5$ cm), the predicted temperature profiles is in good agreement with the data. However, at $x = 39.8$ cm, the two-step scheme overestimates the temperature level.

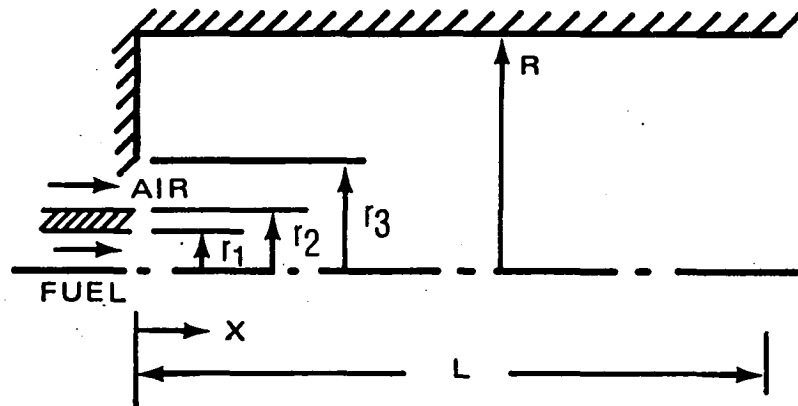
The four-step scheme predictions with the original rate constants are presented in Figures 7.10-5 through 7.10-10. In the four-step scheme, the kinetic rate constants suggested by Hautman, et al., were used. Figure 7.10-5 shows the comparison between data and four-step predictions for the mixture fraction. These profiles are in good agreement with each other. The unburned fuel mole fractions are presented in Figure 7.10-6. The four-step model initially overestimates the unburned fuel concentrations (up to $x = 47.6$ cm), and beyond that station, the predictions are in excellent agreement with the data. This is due to the relatively slow reaction rates (compared to the two-step scheme) associated with the four-step model. Because of the estimated slow reaction scheme, the four-step model predictions for CO_2 concentrations (Figure 7.10-7) are also smaller than the data initially and beyond $x = 47.6$ cm, the predicted CO_2 values are in good agreement with the data. The CO mole fractions predicted by the four-step scheme (Figure 7.10-8) are smaller than the measured values, especially in regions close to the axis of the combustor. The four-step model predictions for temperature (Figure 7.10-8) are in better agreement with the data than the two-step results.

Because of the relatively slow reaction rates in the four-step scheme, the predicted oxygen concentrations are higher than the measured values near the inlet (Figure 7.10-9). However, beyond $x = 47.6$ cm, the predicted O_2 values and the data are in good agreement. Similarly, the predicted H_2O profiles are smaller in magnitude compared to the data up to $x = 47.6$ cm, as seen in Figure 7.10-10. The concentration of hydrogen is overpredicted by the four-step scheme (Figure 7.10-11) everywhere except at $x = 78.5$ cm.

For the case of an axisymmetric combustor with coaxial fuel and air jets, the four-step model predictions are in closer agreement with measurements than the two-step scheme. This is partially due to the higher inlet air temperatures at which the rate constants in the four-step scheme were established.

LEWIS AND SMOOT

AXISYMMETRIC COMBUSTOR WITH COAXIAL FUEL AND AIR JETS



$$r_1 = 0.008 \text{ M}$$

$$r_2 = 0.0111 \text{ M}$$

$$r_3 = 0.0286 \text{ M}$$

$$R = 0.1016 \text{ M}$$

$$L = 1.524 \text{ M}$$

$$U_{\text{AIR}} = 34.3 \text{ M/S}$$

$$U_{\text{FUEL}} = 21.3 \text{ M/S}$$

$$T_{\text{AIR}} = 589^\circ\text{K}$$

$$T_{\text{FUEL}} = 300^\circ\text{K}$$

Figure 7.10-1. Geometry of Axisymmetric Combustor With Coaxial Fuel and Air Jets.

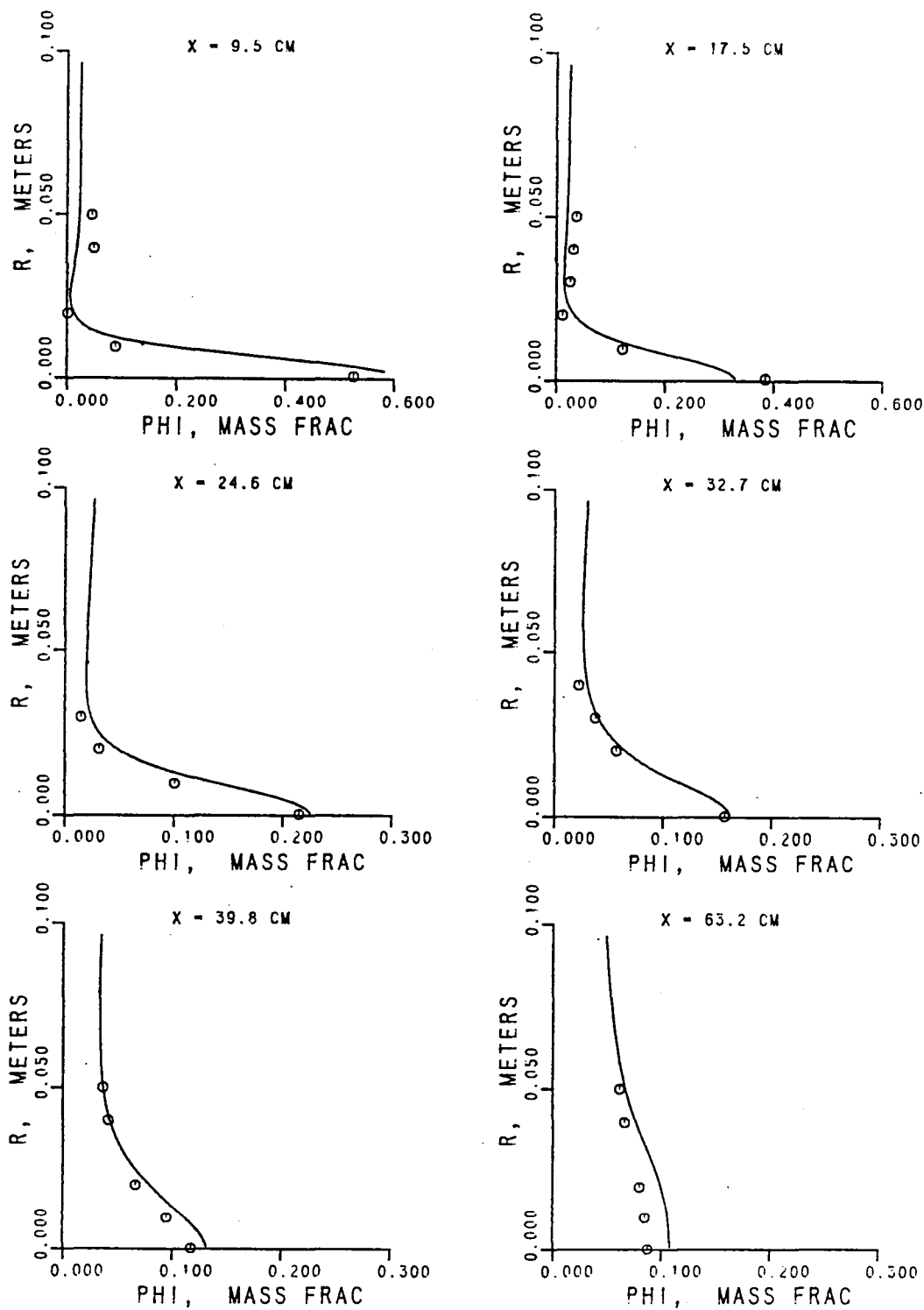


Figure 7.10-2. 2-Step Scheme - Total Fuel Profiles.

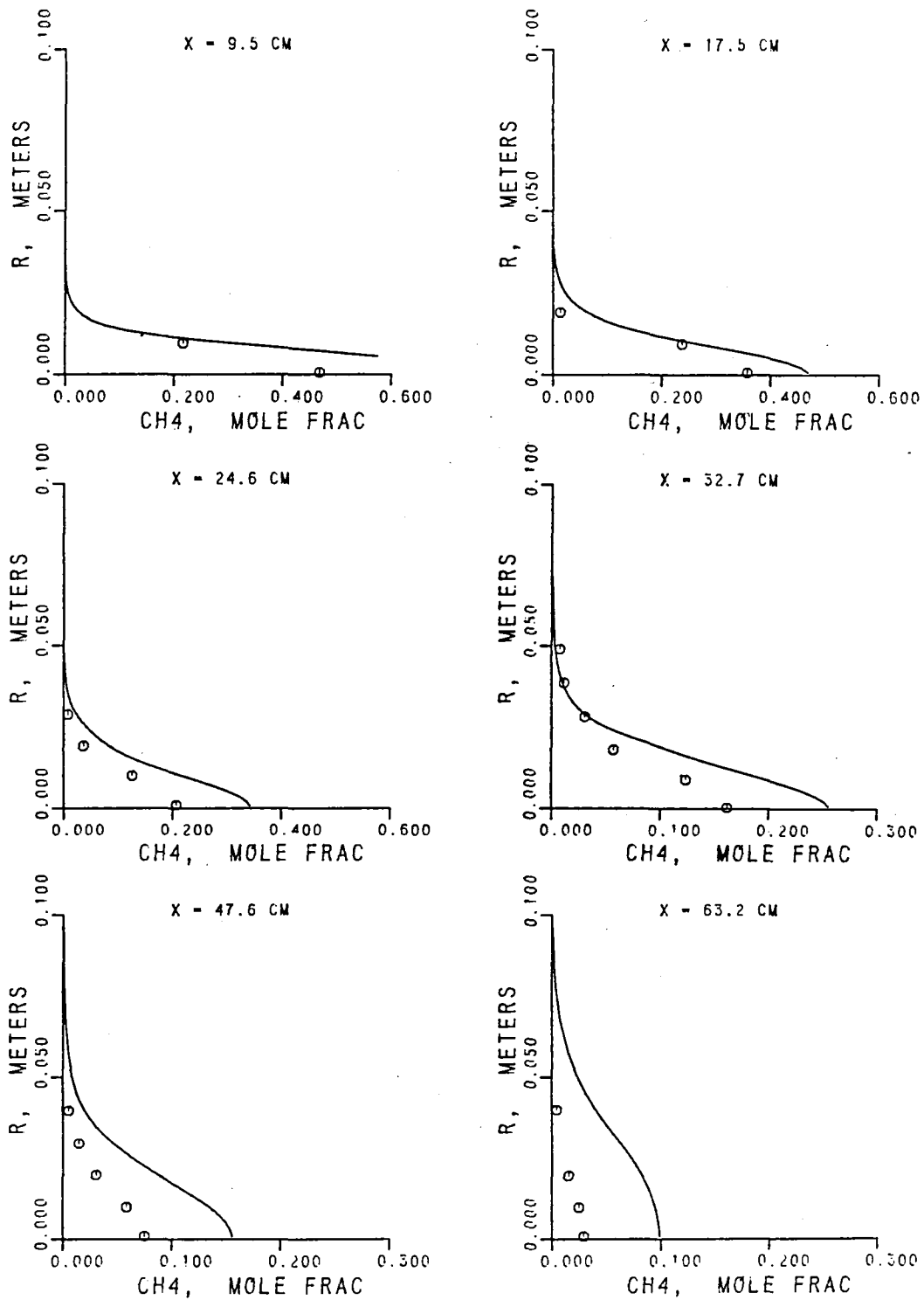


Figure 7.10-3. 2-Step Scheme - Unburned Fuel Profiles.

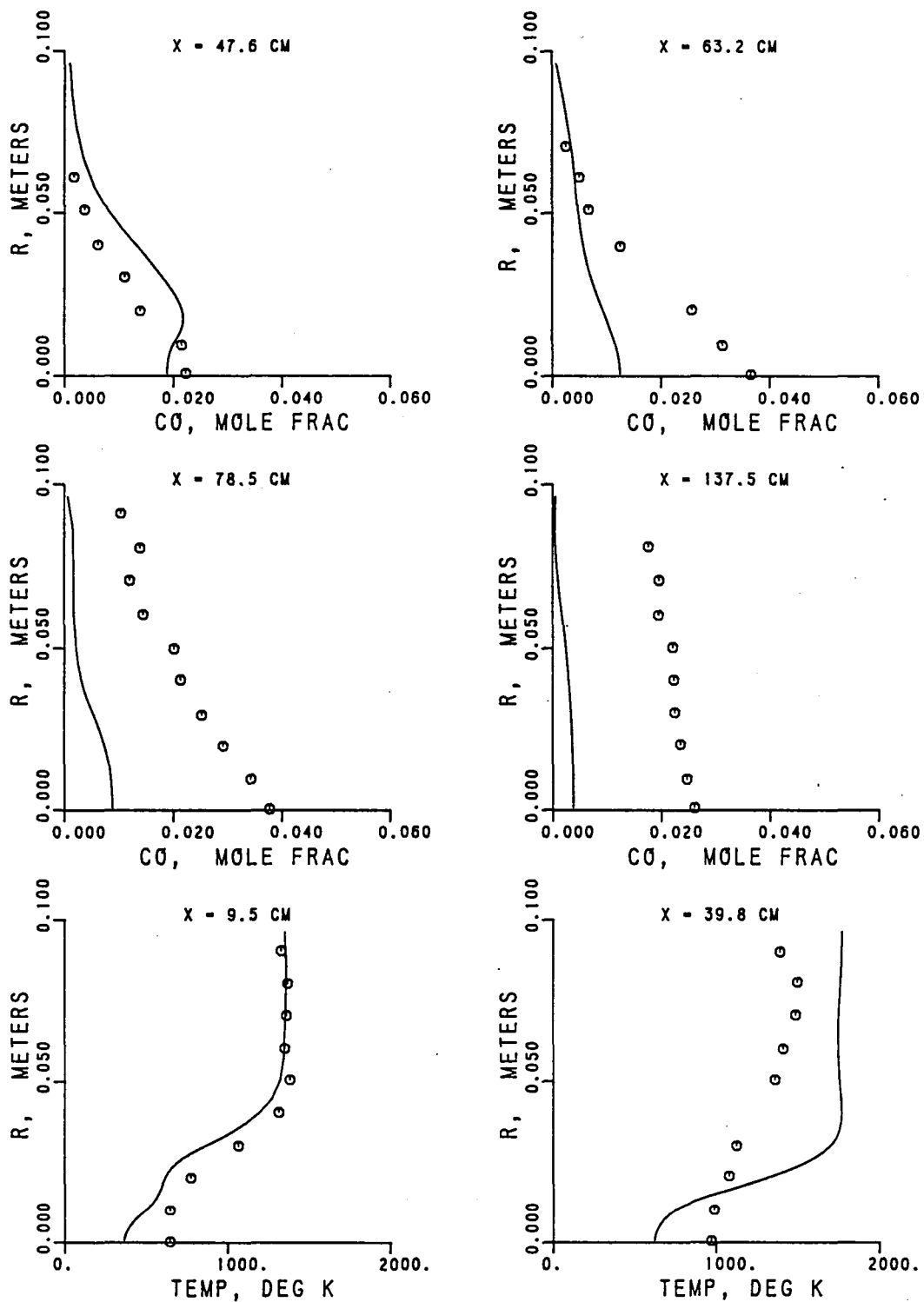


Figure 7.10-4. 2-Step Scheme - CO and Temperature Profiles.

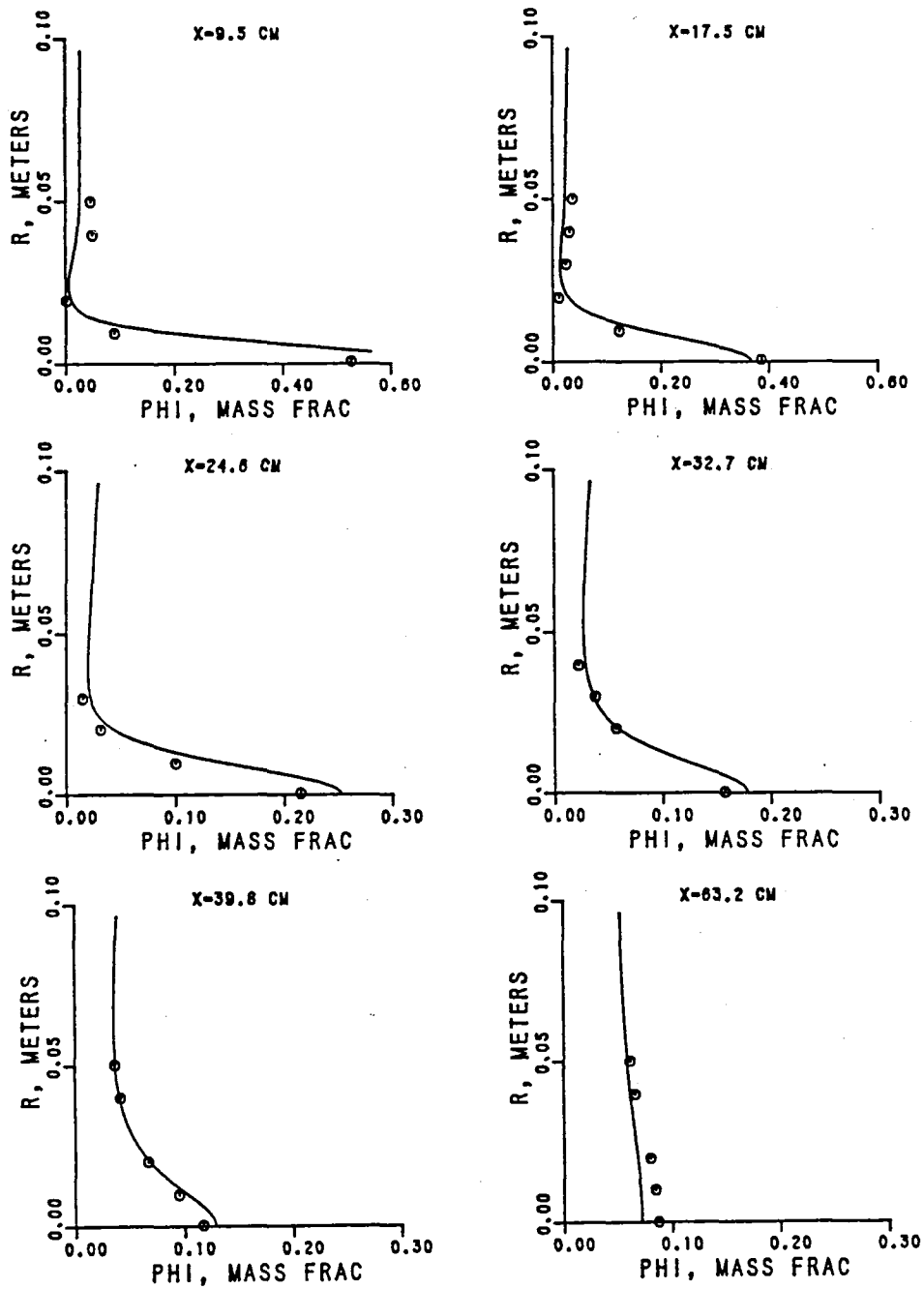


Figure 7.10-5. 4-Step Scheme - Total Fuel Profiles.

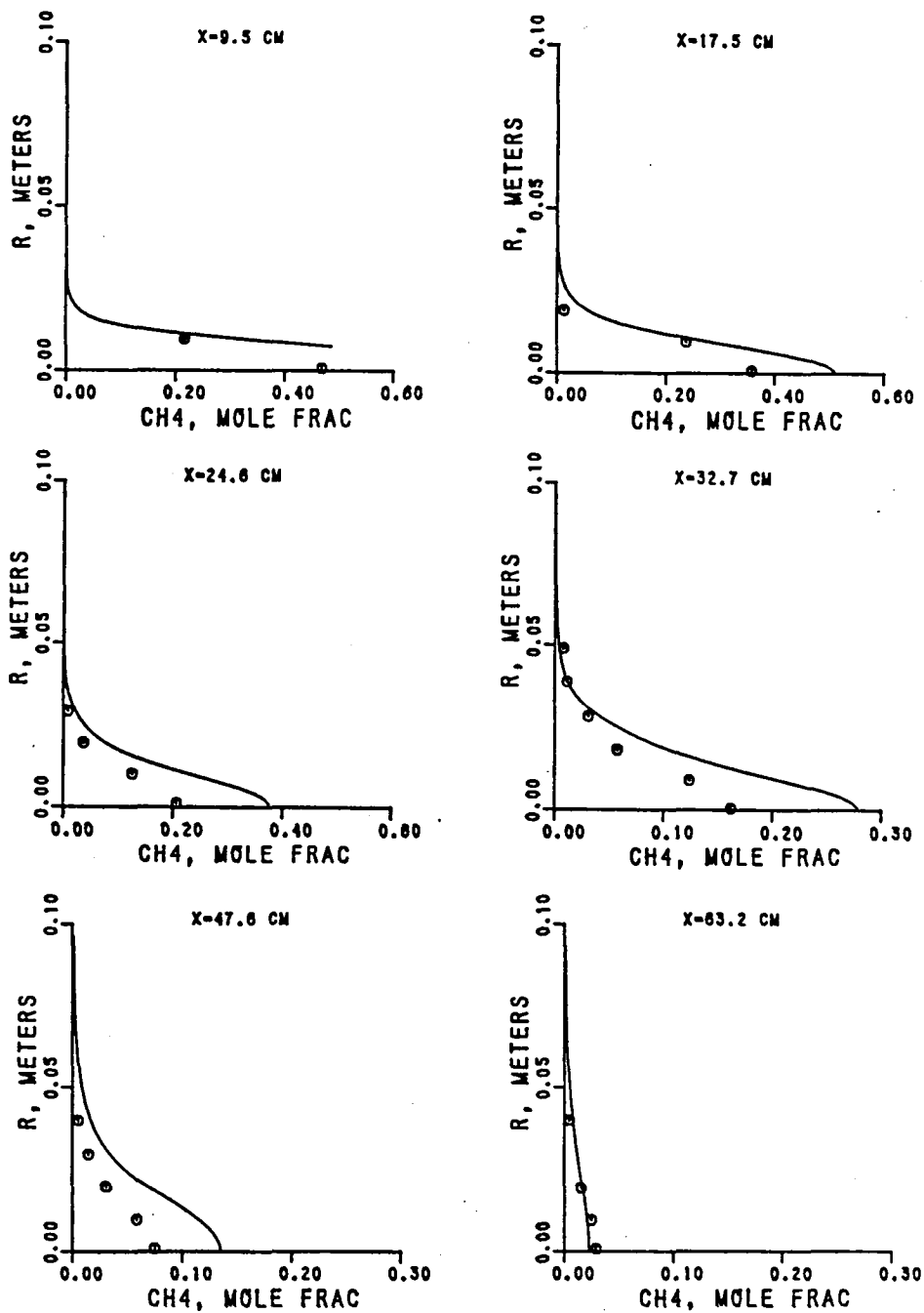


Figure 7.10-6. 4-Step Scheme - Unburned Fuel Profiles.

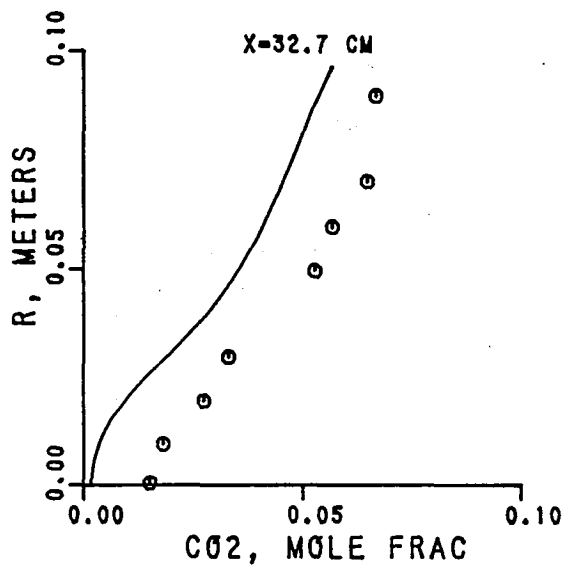
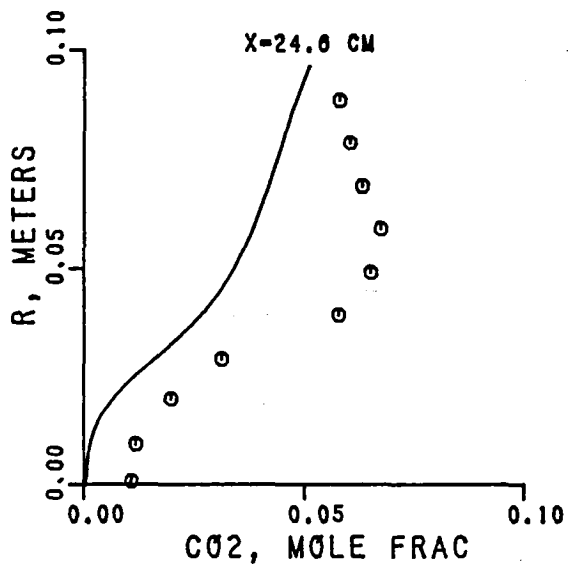
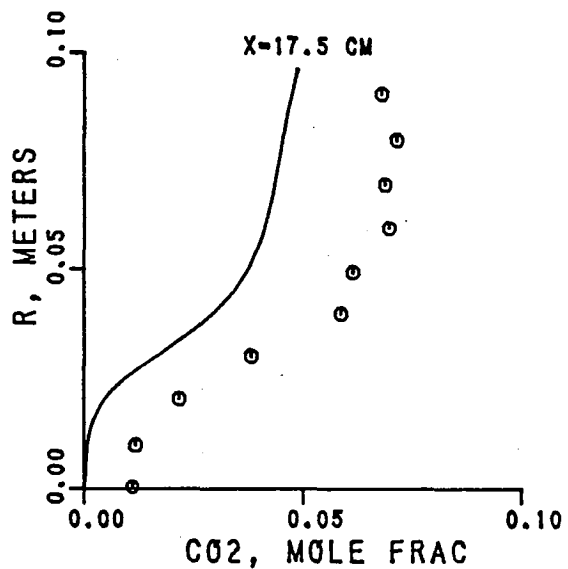
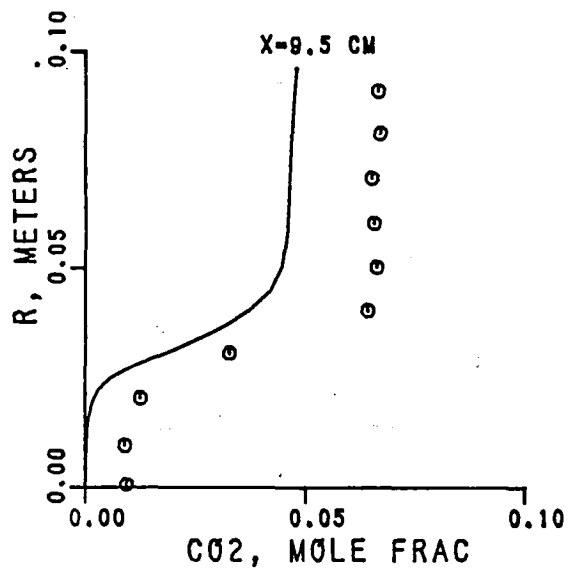


Figure 7.10-7. 4-Step Scheme - CO₂ Profiles.

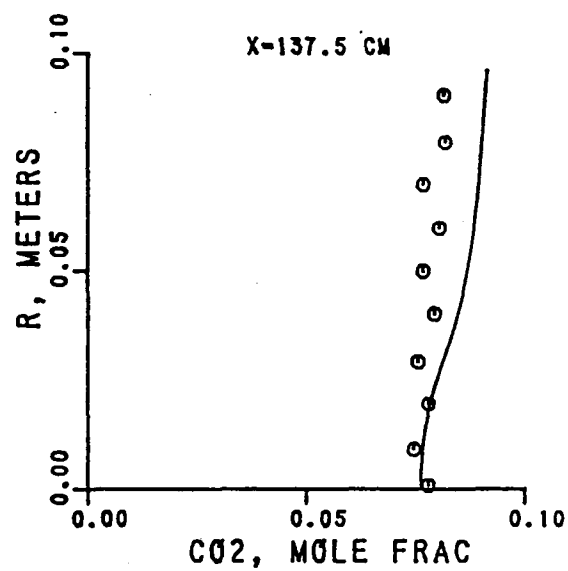
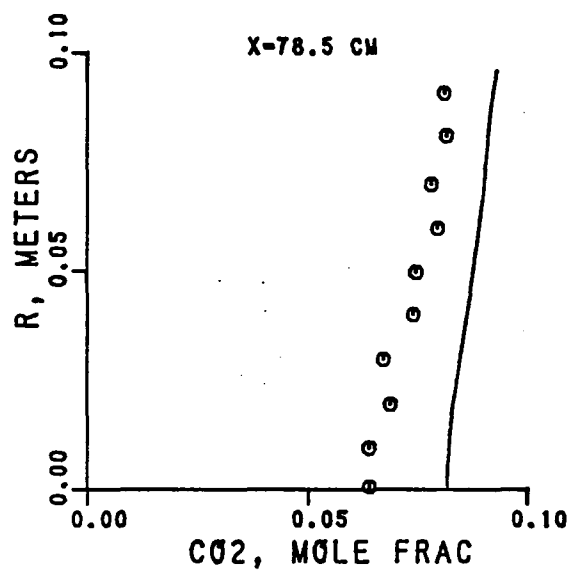
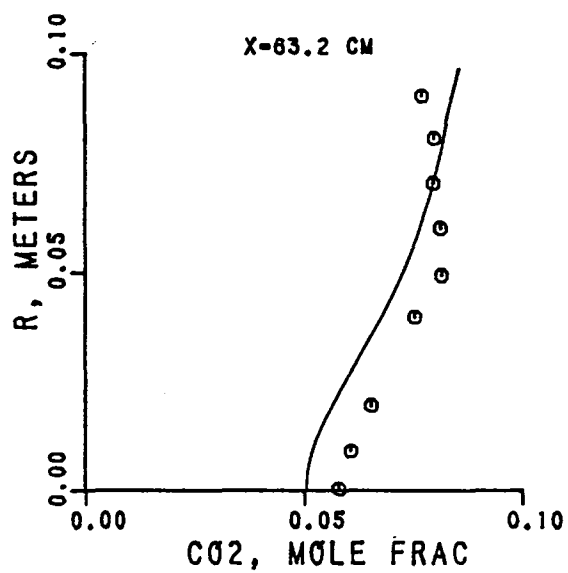
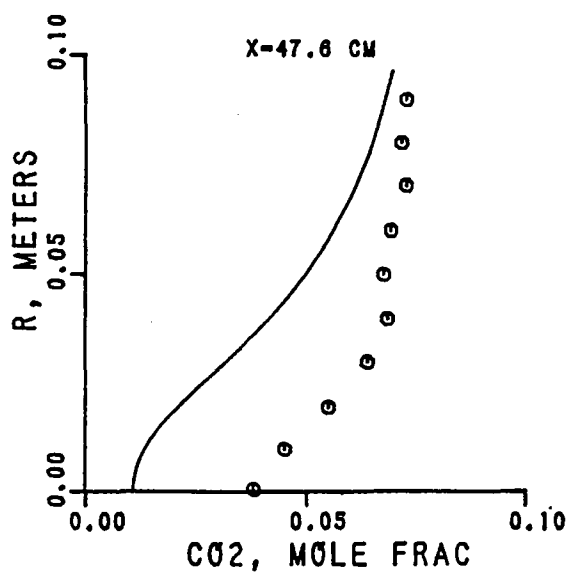


Figure 7.10-7. 4-Step Scheme - CO₂ Profiles. (Contd)

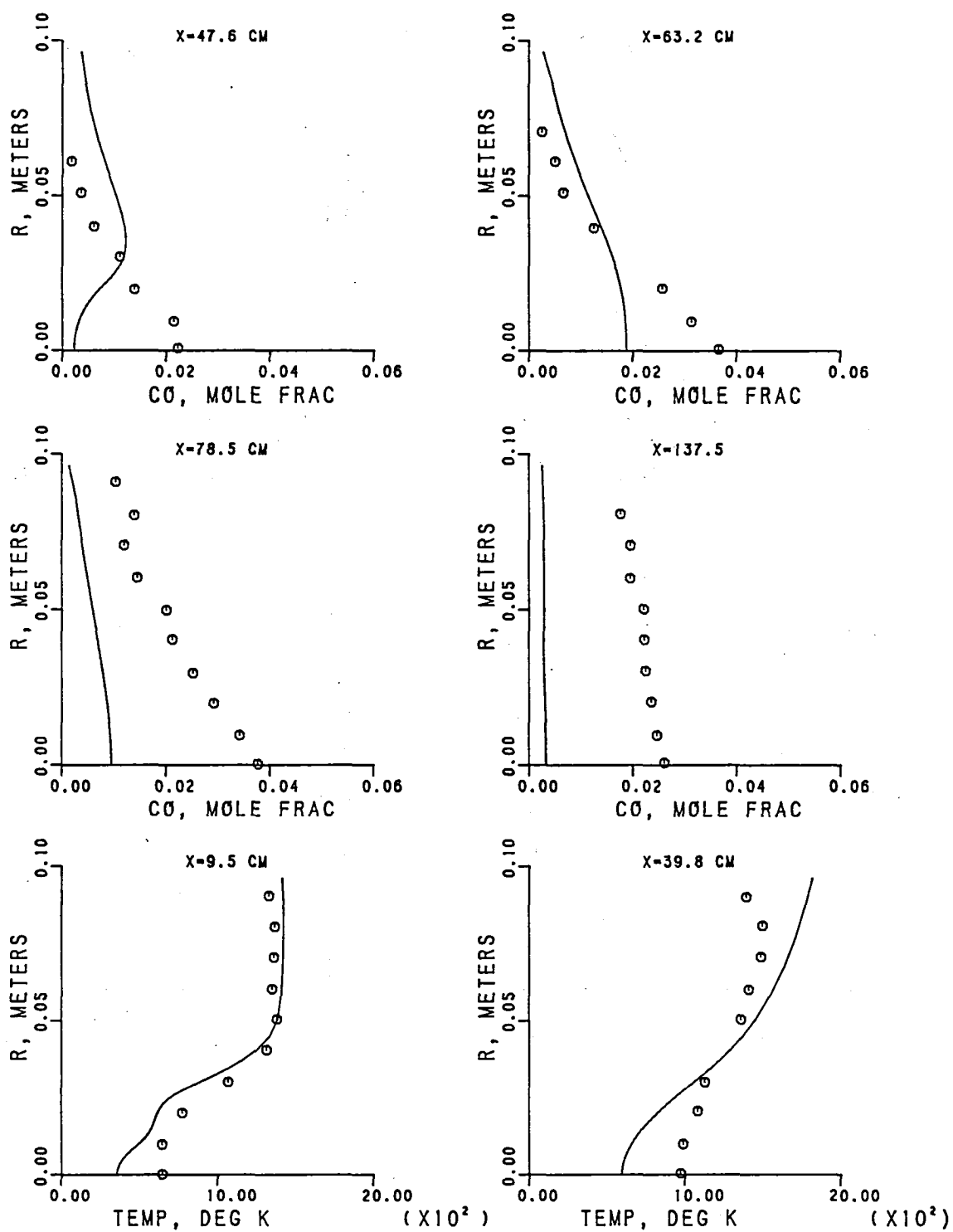


Figure 7.10-8. 4-Step Scheme - CO and Temperature Profiles.

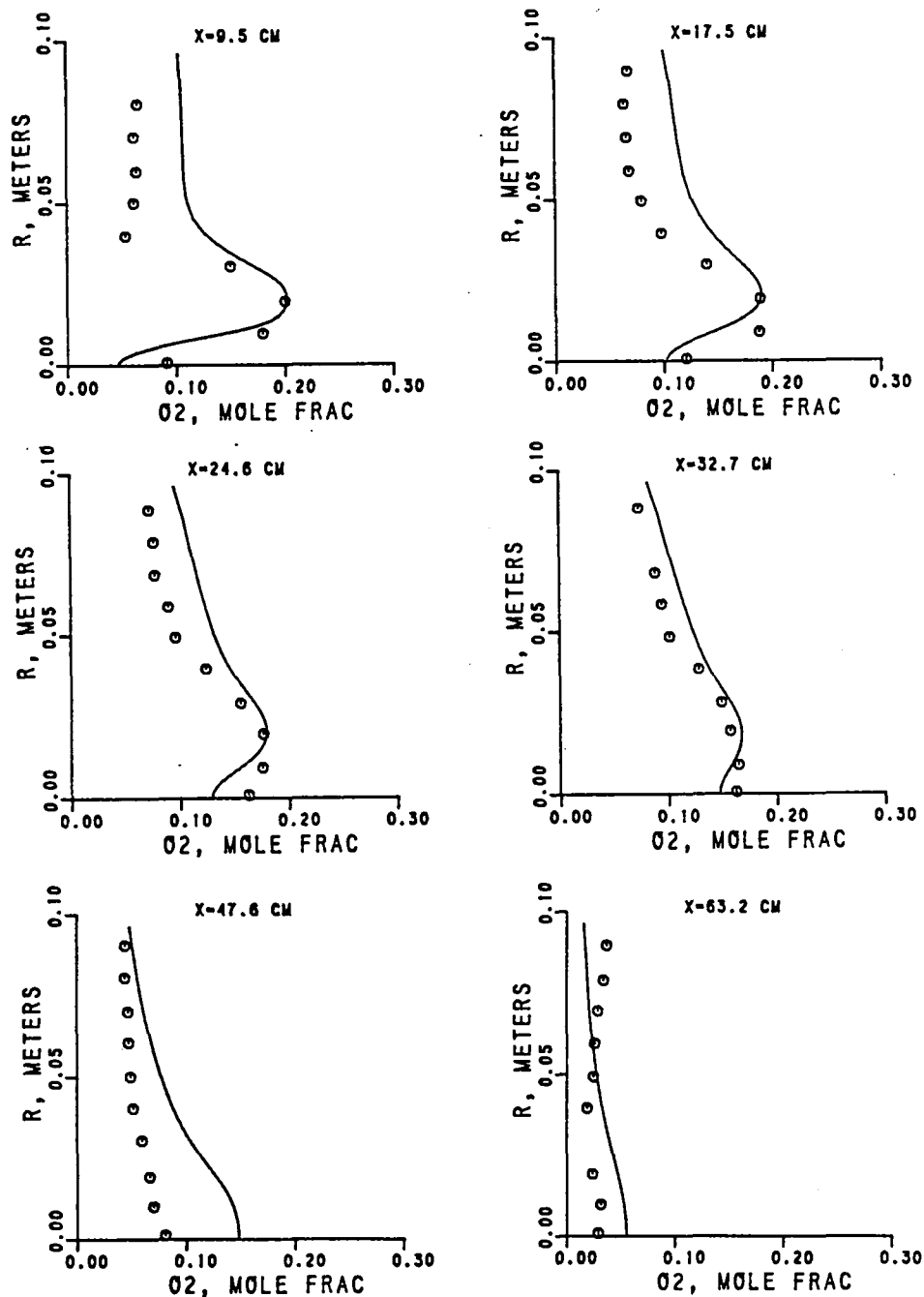


Figure 7.10-9. 4-Step Scheme - O₂ Profiles.

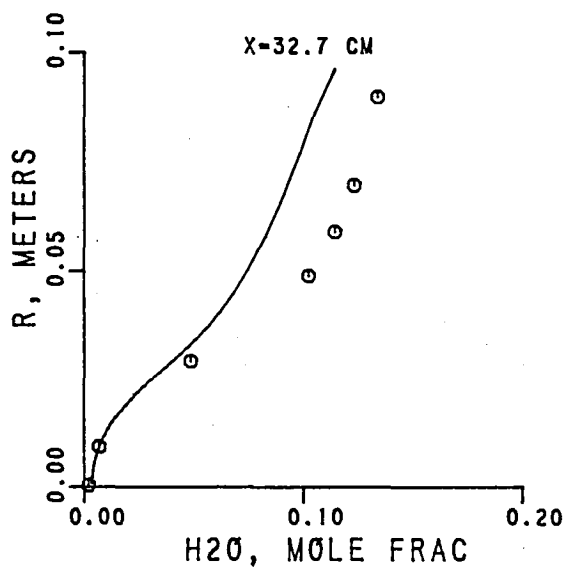
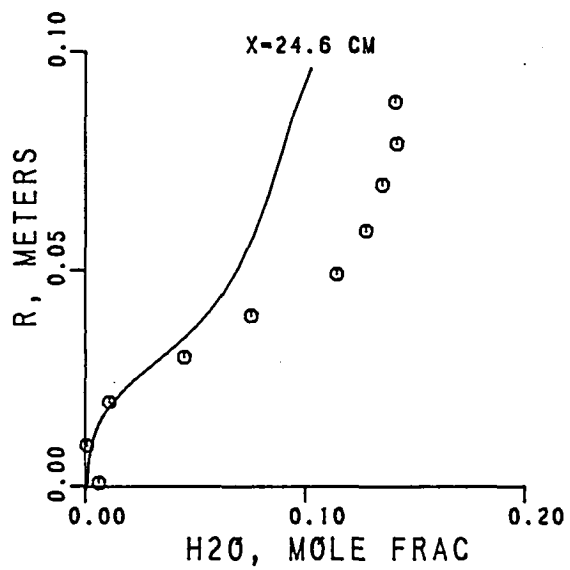
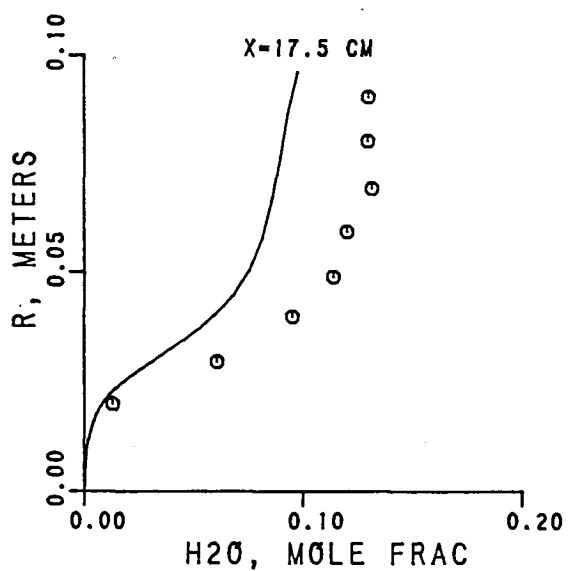
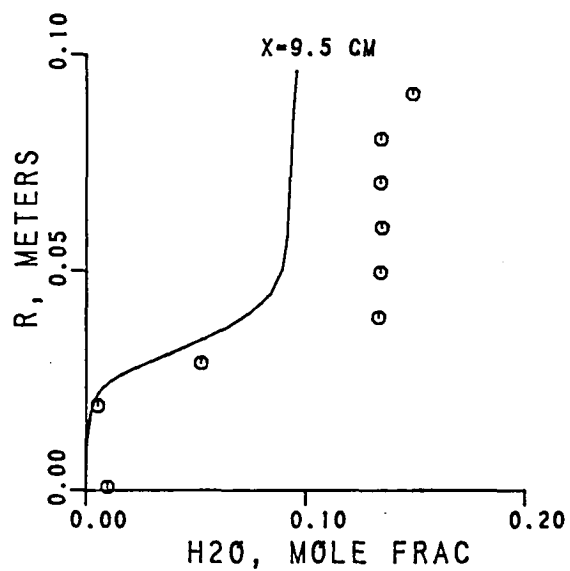


Figure 7.10-10. 4-Step Scheme - H_2O Profiles.

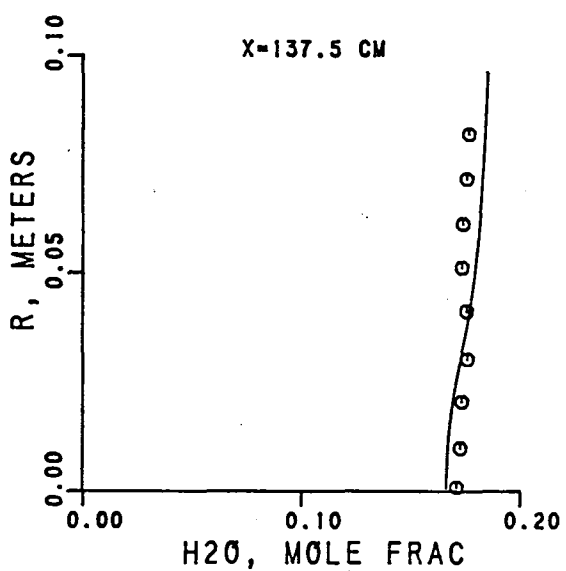
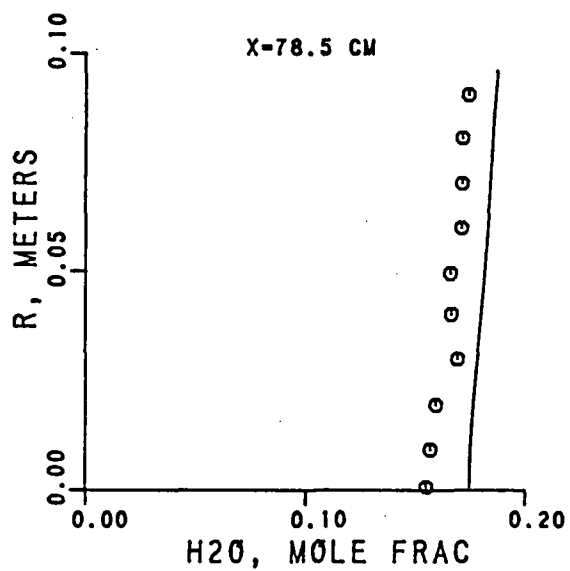
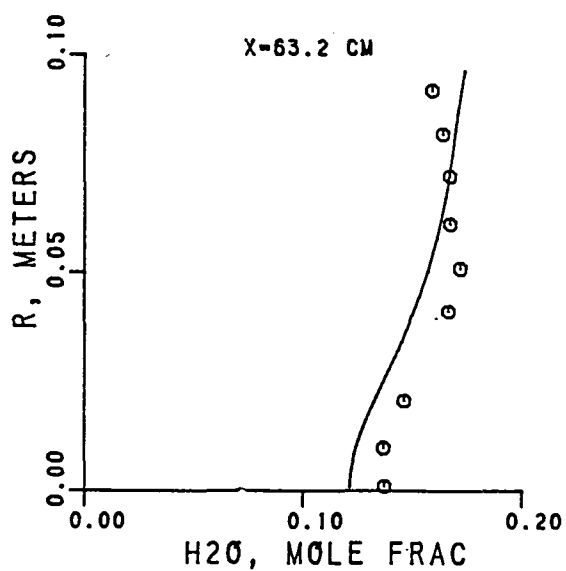
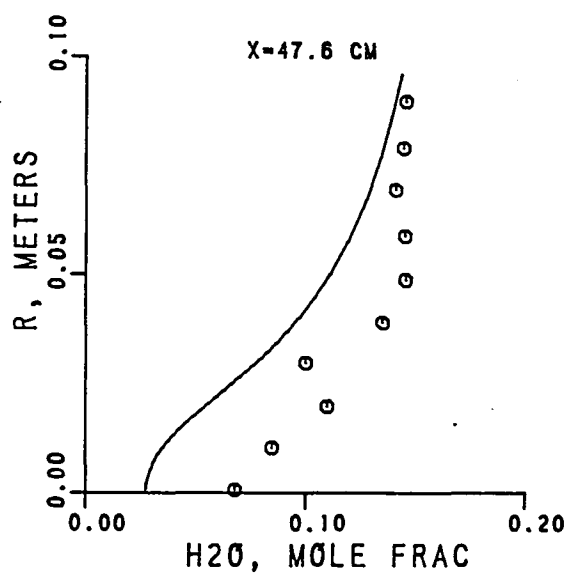


Figure 7.10-10. 4-Step Scheme - H_2O Profiles. (Contd)

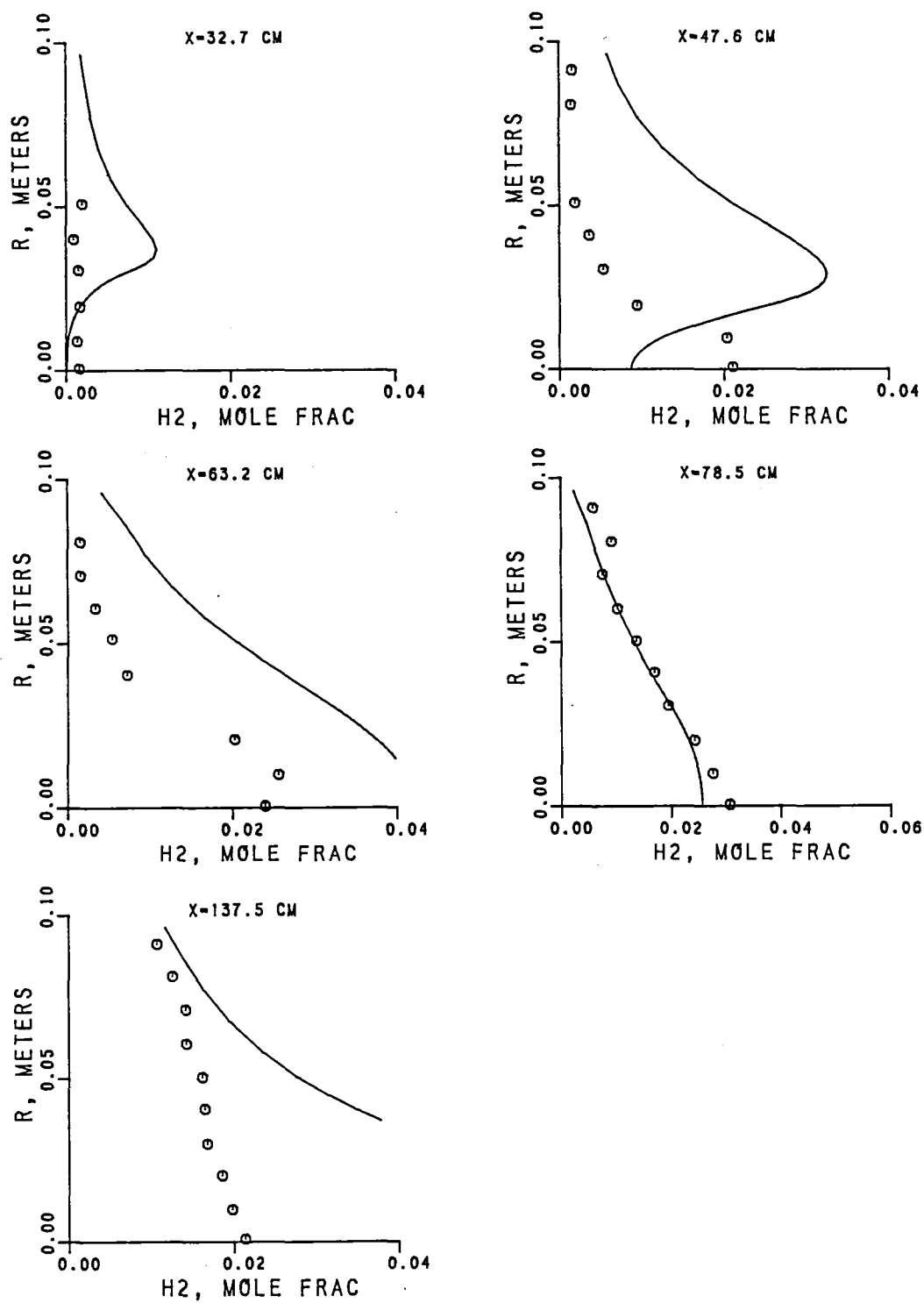


Figure 7.10-11. 4-Step Scheme - Hydrogen Profiles.

SECTION VIII

8.0 Swirling Flows

In Section 7.0 various submodels were evaluated with complex flows without swirl. The introduction of swirl into the flow creates much faster mixing, caused by radial pressure gradients and increase in turbulence generation. These phenomena are more difficult to predict than the effects due to geometrical streamline curvatures, like the curved duct, and sudden expansion. This section will address flow fields with swirl. Both unconfined and confined swirling flows will be studied (see Table 6 for the test cases considered). Due to the limited data available in swirling flows, most of the swirling flow validation will be done on non-reacting flows. Only one test case will be presented for the reacting swirling flows.

8.1 Free Swirling Jet in a Stagnant Medium

The first benchmark test case selected for swirling flows was the case of a round swirling jet injected into a stagnant medium. Measurements of mean velocity components and Reynolds stresses were made by Morse¹⁰¹ in a 2.54-cm-diameter swirling air jet exiting into a stagnant medium, as shown schematically in Figure 8.1-1. The exit velocity of the jet was 32.5 m/s with a swirl number of 0.25. The swirl number is a measure of the overall swirl strength and is defined by

$$SN = \frac{\int_0^R \rho U V_\theta r dr}{R \int_0^R \rho U^2 r dr} \quad (8.1)$$

Measurements of mean axial and swirl velocities and the Reynolds stress profiles were made at $X/D = 0.5$ ($X = 1.27$ cm) downstream of

the nozzle exit. These measurements were used as initial profiles in the computations. Computations of the free swirling flow were made using the 2-D parabolic code with 100 cross-stream nodal points spaced nonuniformly across the jet. Along the inner boundary ($r = 0$), zero radial gradients were specified for all the variables. Along the outer free boundary, entrainment rates were computed from jet theory. The free boundary location is computed from the velocity field. For swirling flows, the turbulence diffusion rates are different in the three orthogonal directions. The standard $k-\epsilon$ model does not adequately account for this characteristic of the flow field. An artificial means to avoid this is to introduce a Prandtl/Schmidt number of V_θ . Computations for the free swirling jet were made with the following models.

- o Standard $k-\epsilon$ model
- o $k-\epsilon_1$ model
- o Effect of Prandtl/Schmidt number for V_θ
- o Richardson number correction for swirl
- o ASM

The standard $k-\epsilon$ model predictions for mean axial velocity along with the data are presented in Figure 8.1-2. The profile shown at $X/D = 0.5$ was the one used at the initial station. The standard $k-\epsilon$ model underestimates the decay of centerline velocity. The jet half width variation, however, is correctly predicted. The standard $k-\epsilon$ model predictions for swirl velocity components are illustrated in Figure 8.1-3. The $k-\epsilon$ model underestimates the decay of the peak swirl velocity. In these calculations, the Prandtl/Schmidt number of V_θ was set equal to 1.0.

The standard $k-\epsilon$ model predictions with Prandtl/Schmidt number of 0.7 for V_θ are shown in Figures 8.1-4 and 8.1-5. The predicted mean axial velocity profiles (Figure 8.1-3) are almost identical to the results with $Pr_{V_\theta} = 1$. However, the predicted swirl velocity profiles with $Pr_{V_\theta} = 0.7$ are closer to the measured values. These profiles still underestimate the decay of swirl velocity.

The mean axial velocity profiles predicted by the standard $k-\epsilon$ model in swirling flow are very similar to those of free jet (Section 6.8). In the case of free nonswirling jet, the $k-\epsilon_1$ model (Equations 60-63) was observed to predict the mean velocity profiles accurately. Computations were made for the free swirling flow using the $k-\epsilon_1$ model, and these results are shown in Figures 8.1-6 and 8.1-7. The $k-\epsilon_1$ model predictions for mean axial velocity profiles are illustrated in Figure 8.1-6. The $k-\epsilon_1$ model predicts the axial velocity decay accurately even in swirling flows. The $k-\epsilon_1$ model predictions for swirl velocity are in better agreement with the data than the standard $k-\epsilon$ model. It is recalled that in the $k-\epsilon_1$ model, the turbulent viscosity is increased according to Equation 62. Note that the $k-\epsilon_1$ model conserves the angular momentum. Consequently, with increased turbulent viscosity, the swirl velocity peaks are reduced and the swirl velocity spreads out farther radially. The $k-\epsilon_1$ model underpredicts the decay of swirl velocity peaks.

The $k-\epsilon_1$ model predictions with Prandtl/Schmidt number for V_θ of 0.7 are shown in Figures 8.1-8 and 8.1-9. Figure 8.1-8 illustrates the mean axial velocity profiles, which are virtually identical to the results with Pr_{V_θ} of 1.0 (see Figure 8.1-6). However, the predicted swirl velocity profiles with $Pr_{V_\theta} = 0.7$, as shown in Figure 8.1-9, are significantly different from those with $Pr_{V_\theta} = 1$. The location of the predicted peak V_θ is farther from the axis as the Prandtl number is reduced. But the predicted results with $Pr_{V_\theta} = 1$ are in better overall agreement with the data than those with $Pr_{V_\theta} = 0.7$, indicating that the Prandtl number should be around 0.9 as has been generally used.

The additional strain in swirling flows can be approximately accounted for by introducing the swirl Richardson number, defined as

$$Ri_{V_\theta} = \frac{\left(\frac{V_\theta}{r}\right) \frac{\partial}{\partial r} (rV_\theta)}{\left(\frac{\partial U}{\partial r}\right)^2 + \left(r \frac{\partial}{\partial r} \left[\frac{V_\theta}{r}\right]\right)^2}$$

The Richardson number can be used to modify the turbulence model constant C_2 in the ϵ equation by the relation

$$C_2 = 1.92 \exp (-0.2 Ri_{V_\theta})$$

This correction can account for the extra turbulence production due to the streamline curvature. However, this correction is applicable only to small values of the Richardson number, and the value of C_2 is constrained to vary between 1.45 and 3.84.

The mean axial velocity profiles predicted by the k- ϵ 1 model with Richardson number correction are presented in Figure 8.1-10. The Richardson number correction predicts a slightly faster decay of centerline axial velocity compared to the k- ϵ 1 model (Figure 8.1-6). The swirl velocity profiles predicted by the k- ϵ 1 model with Richardson number correction are illustrated in Figure 8.1-11. These profiles indicate a slightly faster jet spreading rate compared to the ones without the streamline curvature correction. These results demonstrate that the Richardson number correction does not predict appreciably different velocity profiles compared to the k- ϵ 1 model.

The predicted results obtained from the ASM for the Morse swirling flow are presented in Figures 8.1-12 through 8.1-19. Figure 8.1-12 illustrates the ASM predictions and data for mean axial velocity. The ASM slightly underestimates the centerline velocity decay compared to the data. However, the ASM predictions are in better agreement with the data than the standard k- ϵ model, with no necessary heuristic modification of the turbulence model constants.

The ASM predictions for tangential velocity are shown in Figure 8.1-13. The ASM underpredicts the decay of the swirl velocity but nevertheless is in better agreement with the data than the standard k- ϵ model.

The ASM predictions for the RMS axial velocity fluctuations, u' , predicted by the ASM and the data are presented in Figure 8.1-14. The ASM slightly underpredicts the magnitude of u' near the axis of the jet. However, the location of the peak value is correctly predicted. The ASM predictions for radial RMS velocity fluctuations, v' , are presented in Figure 8.1-15. The ASM underestimates the magnitude of v' compared to the data by as much as 40 percent at $X/D = 2$. However, at $X/D = 10$, the data and predictions are in good agreement. Most of the differences between the data and the predictions are in the region close to the axis, where significant differences in the mean velocity components between data and predictions exist.

The tangential component of RMS turbulence velocity fluctuations, w' , are presented in Figure 8.1-16. The ASM predictions are shown by solid lines, and the data correspond to symbols. In the ASM, the w' components are computed from the relation

$$w' = \sqrt{(2k - \overline{u^2} - \overline{v^2})}$$

The ASM initially underestimates the centerline w' values and at $X/D = 10$, it overestimates the w' values by about 20 percent. A similar trend was also observed in the predicted turbulence kinetic energy profiles. The underestimation of the centerline k values is partly responsible for the low centerline axial velocity decay rate. In Figures 8.1-14 through 8.1-16, the predicted results at $X/D = 0.5$ were deduced from the initial conditions for k .

The predicted Reynolds shear stress component, \overline{uv} , is illustrated in Figure 8.1-17. These profiles exhibit a trend very similar to the normal stress components (Figures 8.1-14 through 8.1-16); namely, the peak \overline{uv} values are initially underpredicted and beyond $X/D = 6$, they are overestimated by the ASM. At $X/D = 4$ and $X/D = 6$, the ASM predicts the location of \overline{uv} peak closer to the axis than the data does. These effects are due to the differences in the mean velocity profiles between the data and the predictions.

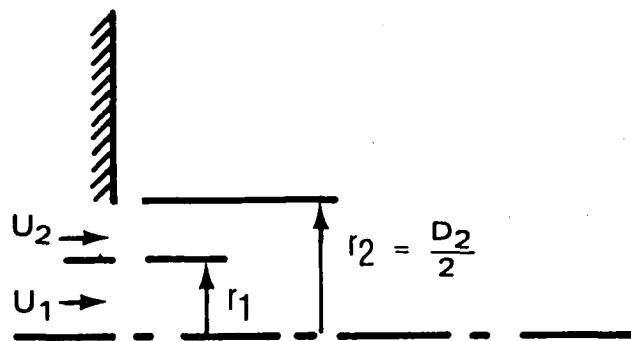
The comparison between the measured and predicted Reynolds stress component, \overline{vw} , is shown in Figure 8.1-18. The ASM predicts a large negative value for \overline{vw} values at the axis, while the data shows a zero value there. But the peak \overline{vw} value and its location are in good agreement with the data. The ASM predictions and measurements for the Reynolds stress component, \overline{uw} are illustrated in Figure 8.1-19. The predicted \overline{uw} profiles are only in qualitative agreement with the data. It is recalled that the Reynolds stress components \overline{vw} and \overline{uw} are functions of swirl velocity gradients. When the agreement between the data and the predictions is poor, the Reynolds stress comparisons are not expected to be good.

The standard $k-\epsilon$ model underpredicted the axial and tangential velocity decay. When a Prandtl number of 0.7 was used for V_θ , the diffusion rate for swirl velocity was increased, and hence a slightly faster swirl velocity profile decay was predicted. The decay of axial and swirl velocity was still lower than the data. The $k-\epsilon_1$ model, which was shown to give good results for circular jets (Section 6.0), predicted the axial velocity profiles accurately, and yet the decay of the swirl velocity profiles was underpredicted. The $k-\epsilon_1$ model results were in much better agreement with the data than the standard $k-\epsilon$ model. When $Pr_{V_\theta} = 0.7$ was used in the $k-\epsilon_1$ model, there were no substantial improvements in the predicted results. The Richardson number correction for this

swirling flow did not appreciably improve the $k-\epsilon$ model predictions. The ASM also underpredicted the decay of mean axial and tangential velocity peak values. However, the ASM predictions were in better agreement with the data than the standard $k-\epsilon$ model. The ASM predicted lower turbulence intensity values at the axis in the regions near the exit plane of the jet, and at $X/D > 6$, the predicted turbulence intensities were slightly higher than the data. The turbulent mean stress, \overline{uw} , follows the same trend as the turbulence intensity profiles. The predicted \overline{vw} values near the axis of the jet were in disagreement with the data, while the peak \overline{vw} values were in good agreement with the measurements. The predictions for \overline{uw} were in qualitative agreement with the measurements. The ASM needs further refinement to improve the quantitative correlations.

MORSE

TWO COAXIAL JETS IN STAGNANT AIR



$r_1 = 0.0127 \text{ M}$
 $r_2 = 0.2413 \text{ M}$
 $U_1 = 32.46 \text{ M/S}$
 $W_1 = 12.25 \text{ M/S}$
 $U_2 = 0.0$

Figure 8.1-1. Test Setup for Swirling Air Injected into Stagnant Air.

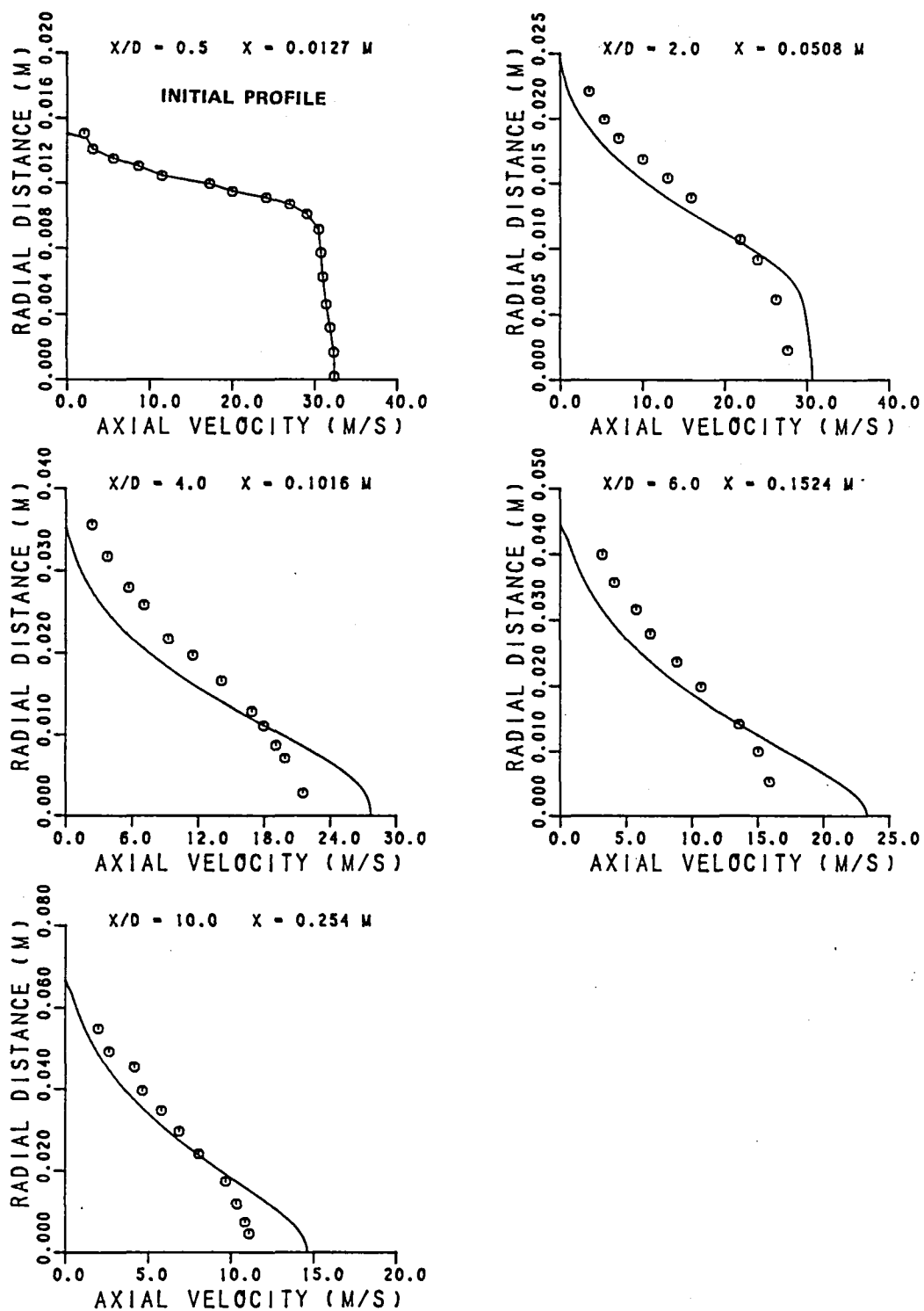


Figure 8.1-2. Standard $k-\epsilon$ Model - Mean Axial Velocity Profiles.

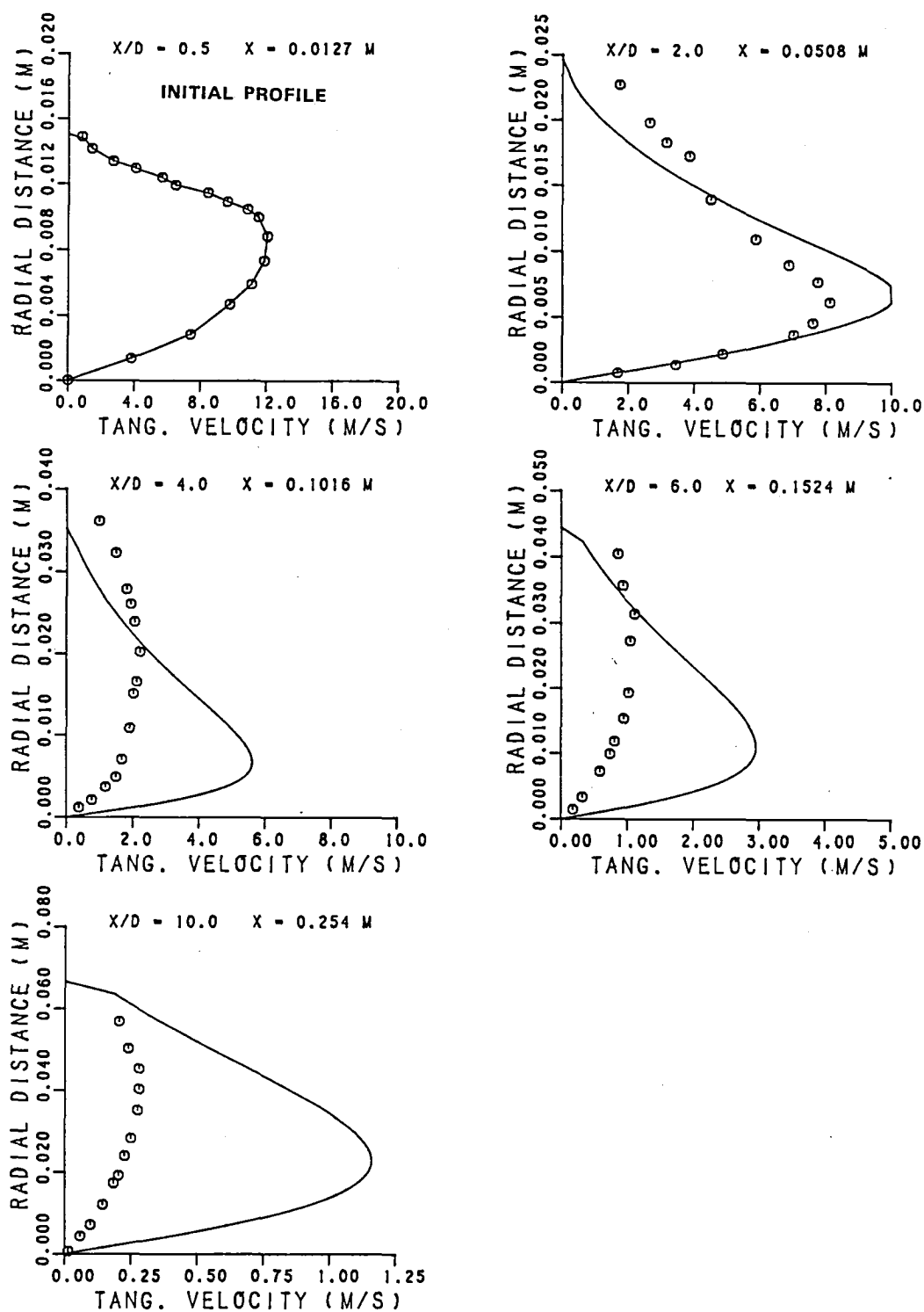


Figure 8.1-3. Standard k- ϵ Model - Mean Tangential Velocity Profile.

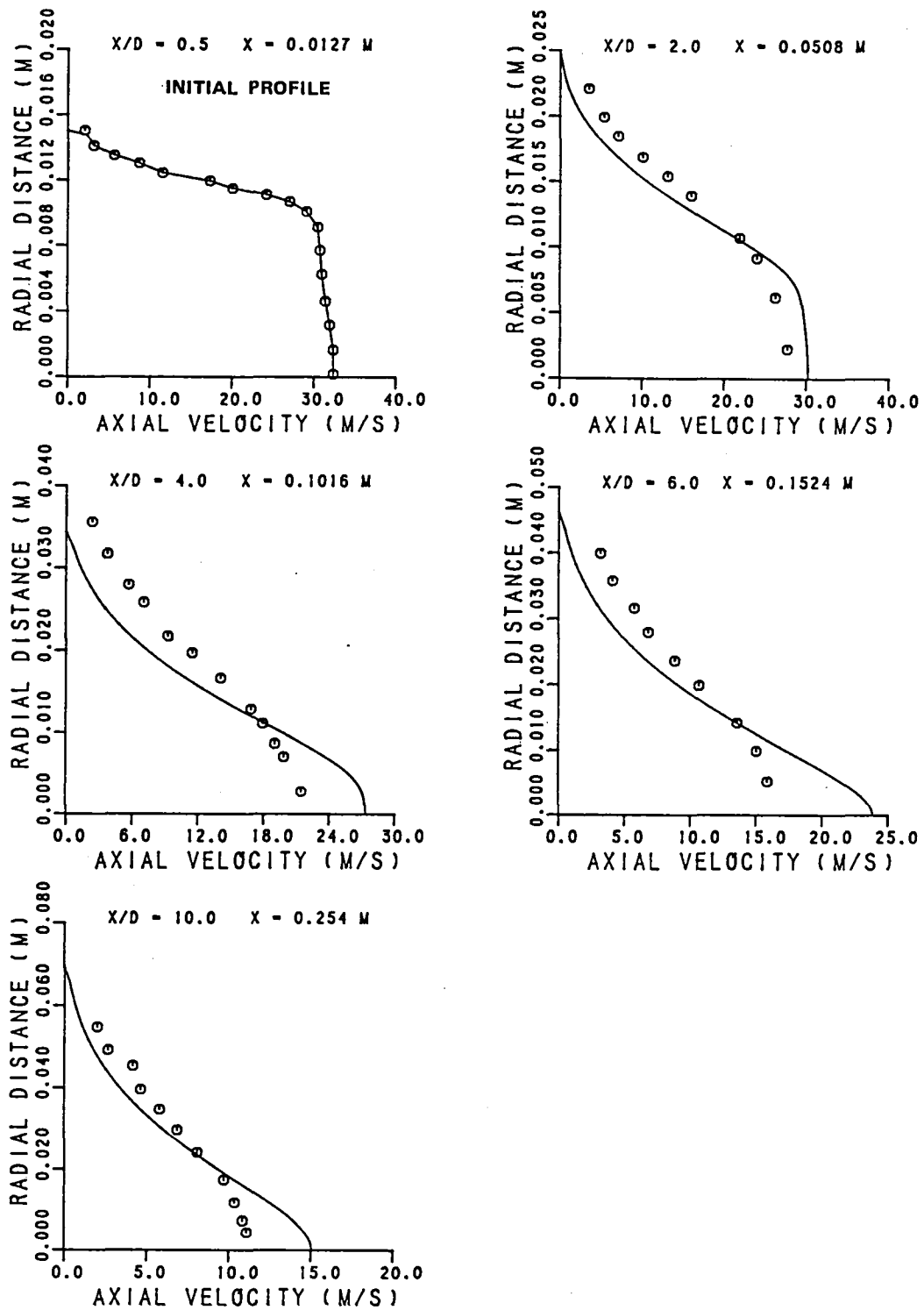


Figure 8.1-4. Standard $k-\epsilon$ Model with 0.7 Prandtl Number - Mean Axial Velocity Profiles.

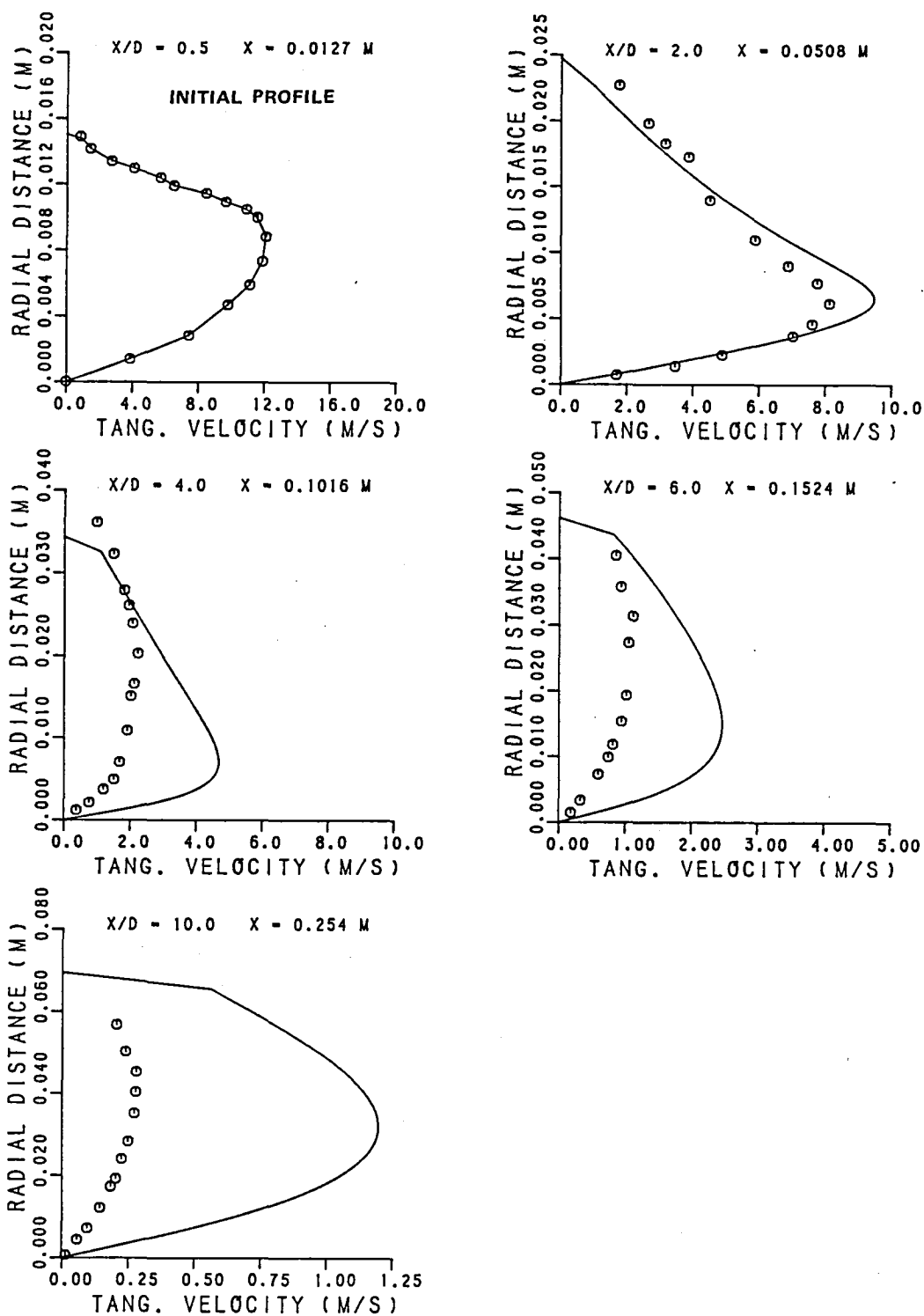


Figure 8.1-5. Standard $k-\epsilon$ Model with 0.7 Prandtl Number - Mean Tangential Velocity Profiles.

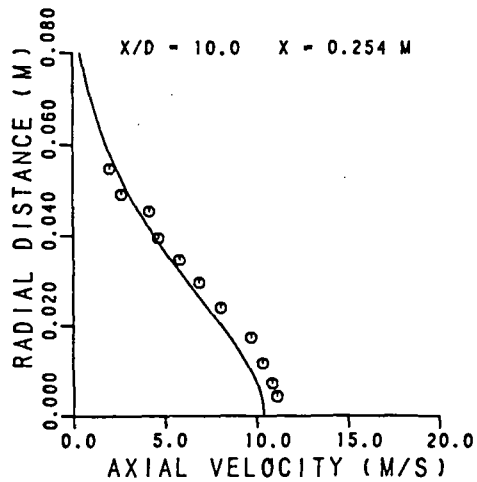
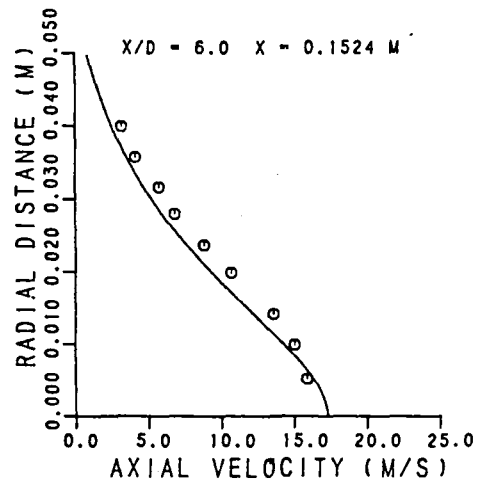
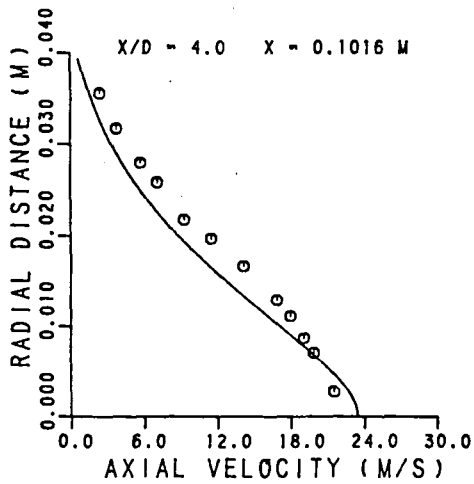
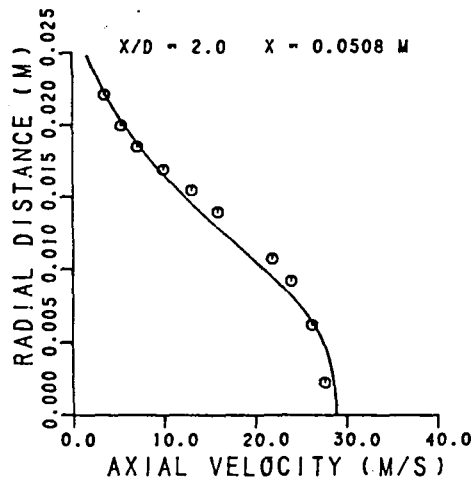
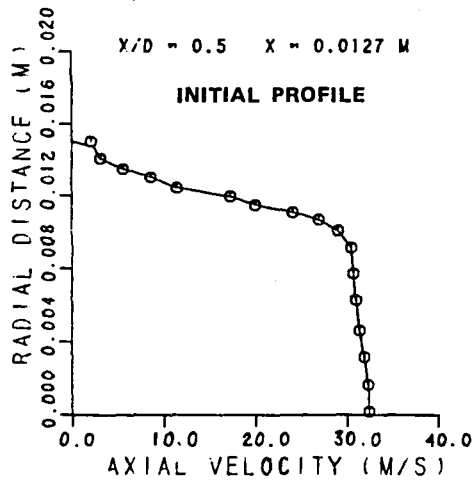


Figure 8.1-6. $k-\epsilon$ 1 Turbulence Model - Mean Axial Velocity Profiles.

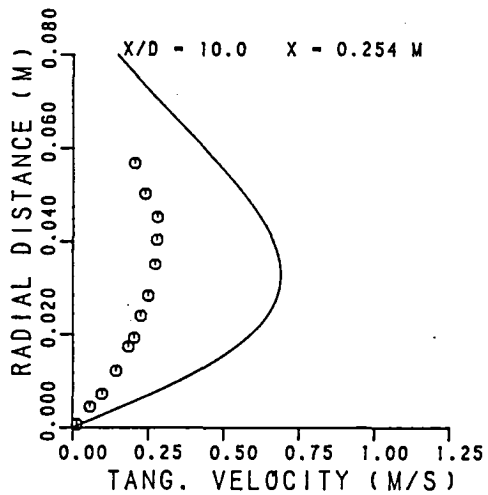
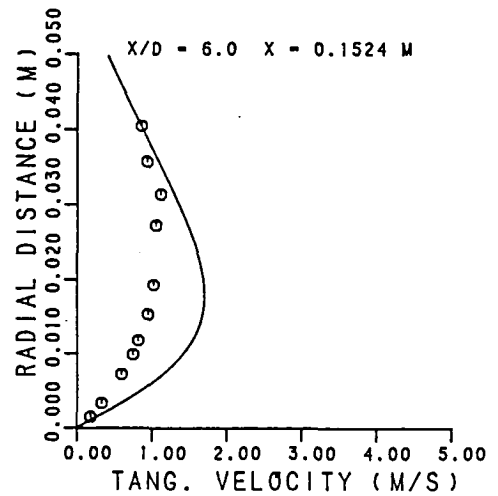
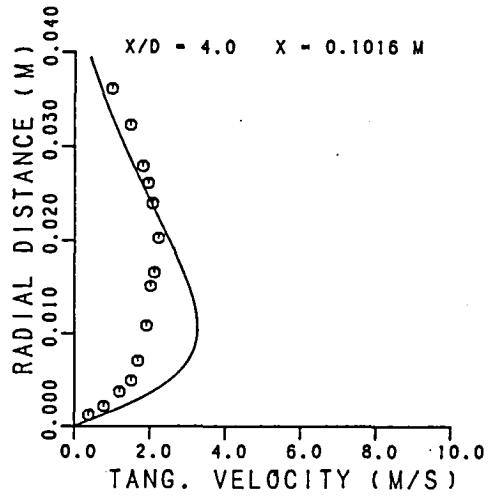
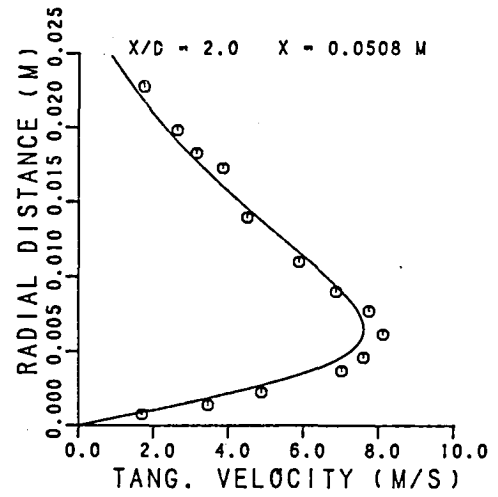
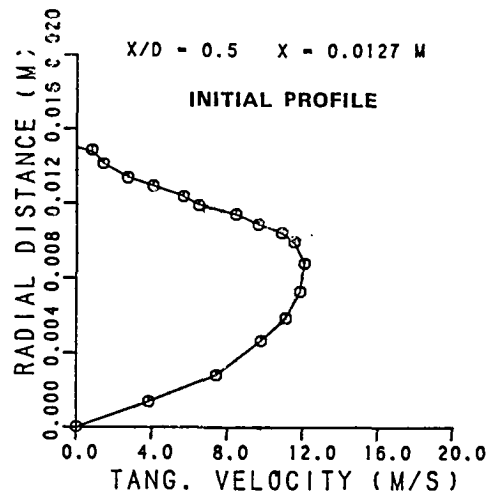


Figure 8.1-7. $k-\epsilon$ 1 Turbulence Model - Mean Tangential Velocity Profiles.

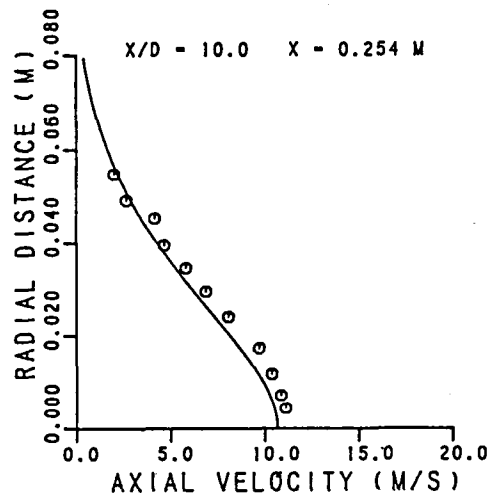
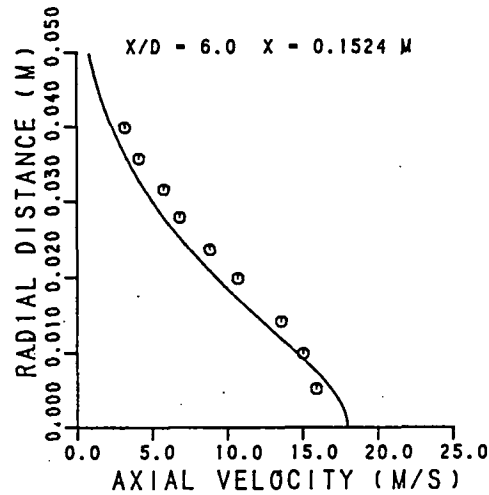
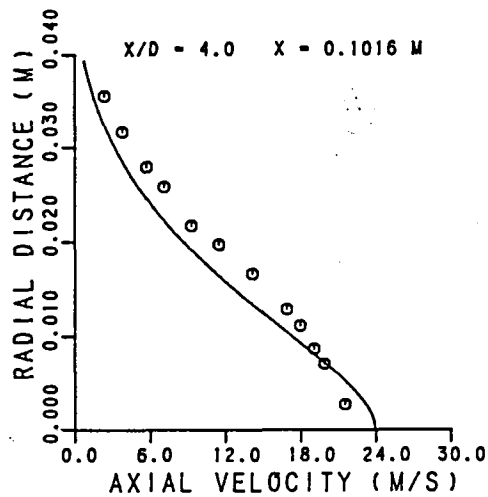
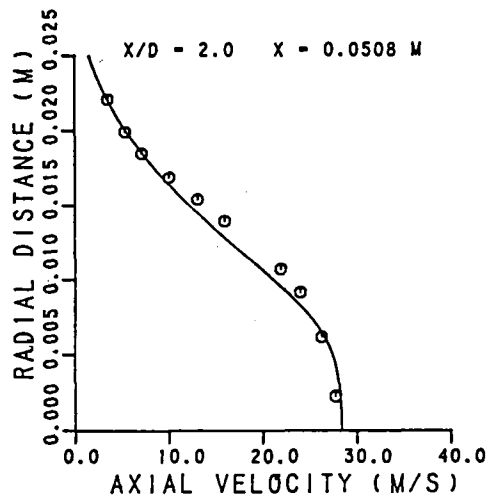
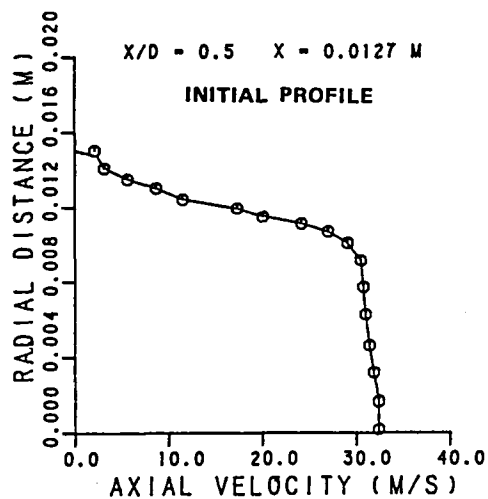


Figure 8.1-8. $k-\epsilon$ 1 Model with 0.7 Prandtl Number - Mean Axial Velocity Profiles.

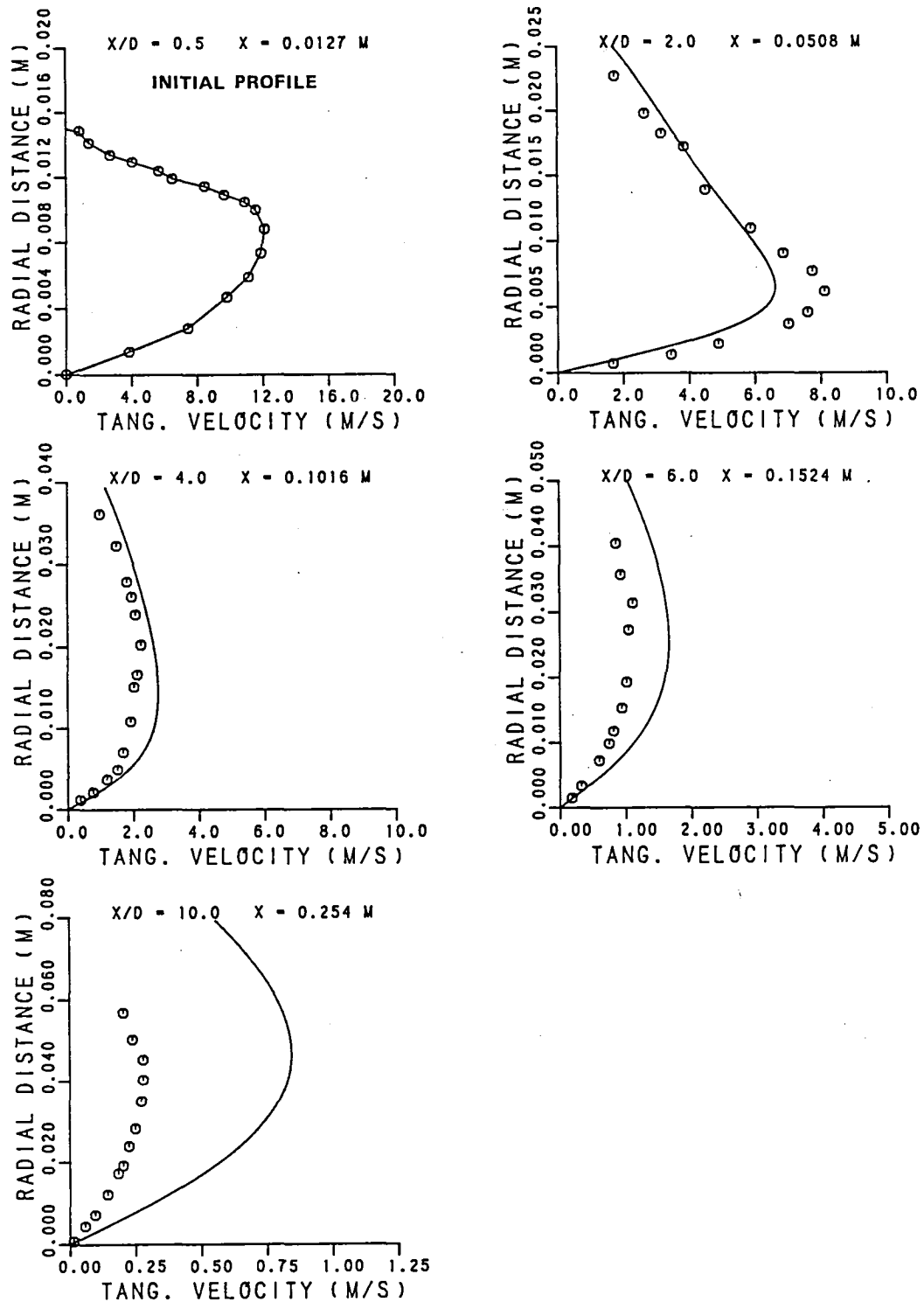


Figure 8.1-9. $k-\epsilon$ 1 Model with 0.7 Prandtl Number - Mean Tangential Velocity Profiles.

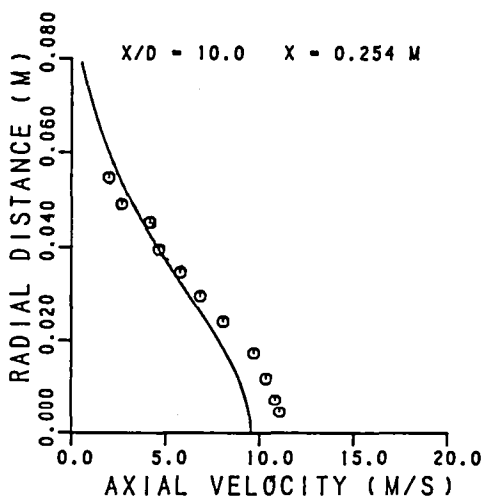
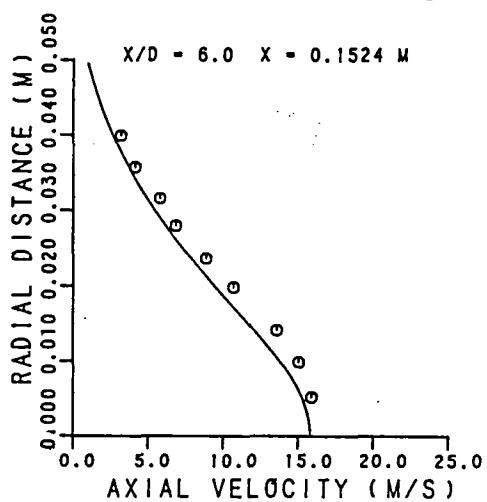
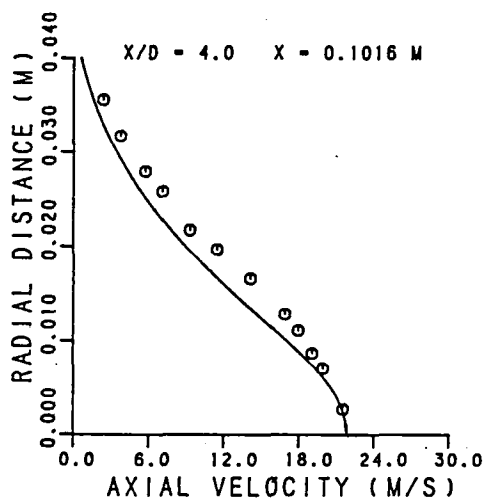
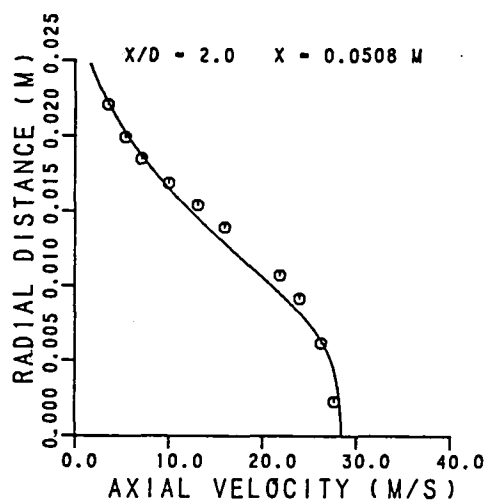
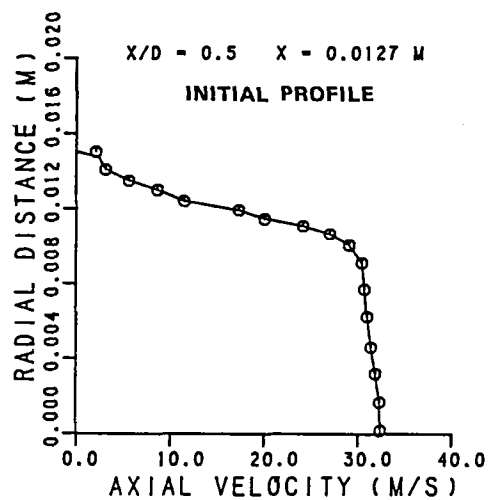


Figure 8.1-10. $k-\epsilon$ 1 Model with Richardson Number Correction - Mean Axial Velocity Profiles.

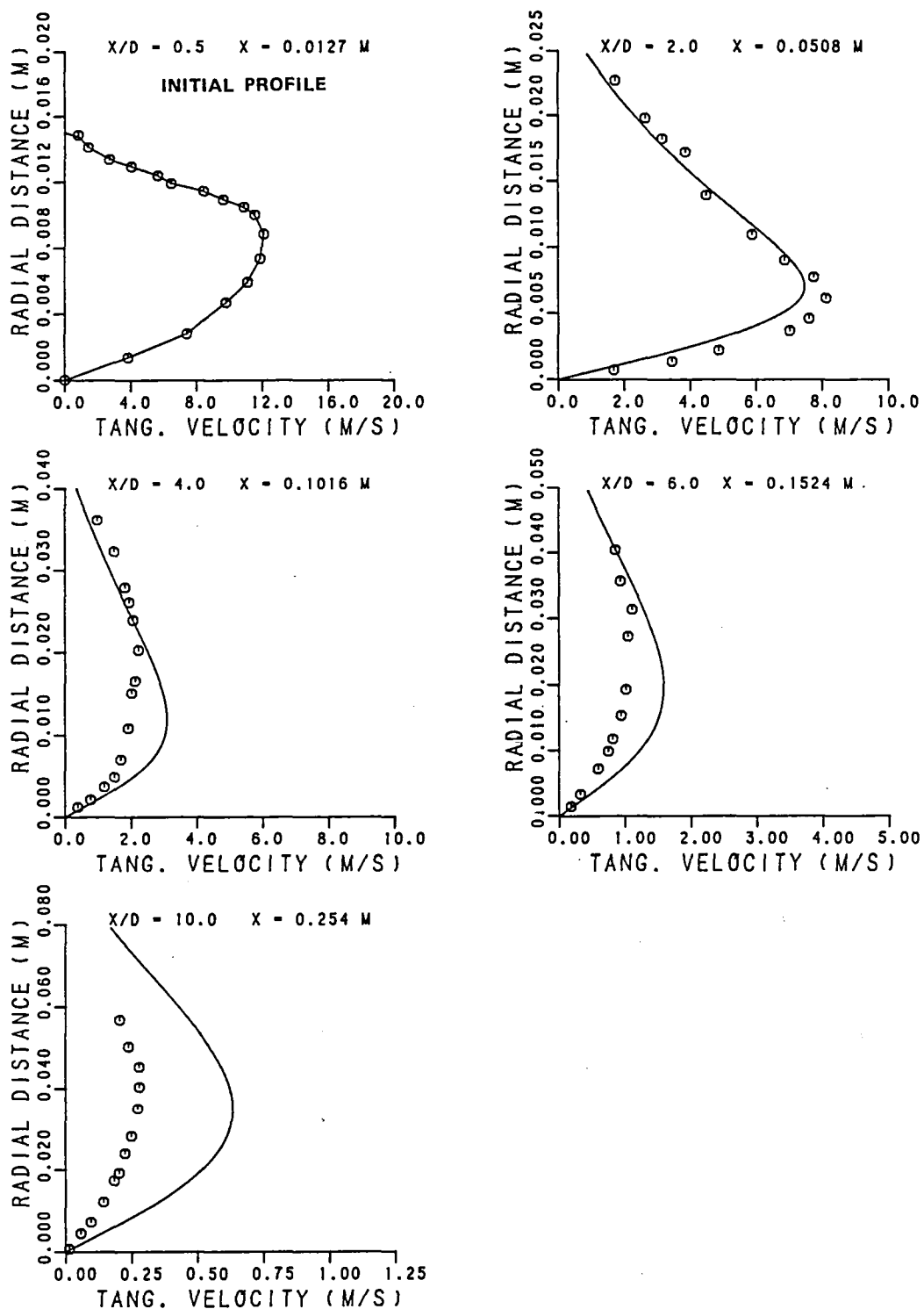


Figure 8.1-11. $k-\epsilon$ 1 Model with Richardson Number Correction - Mean Tangential Velocity Profiles.

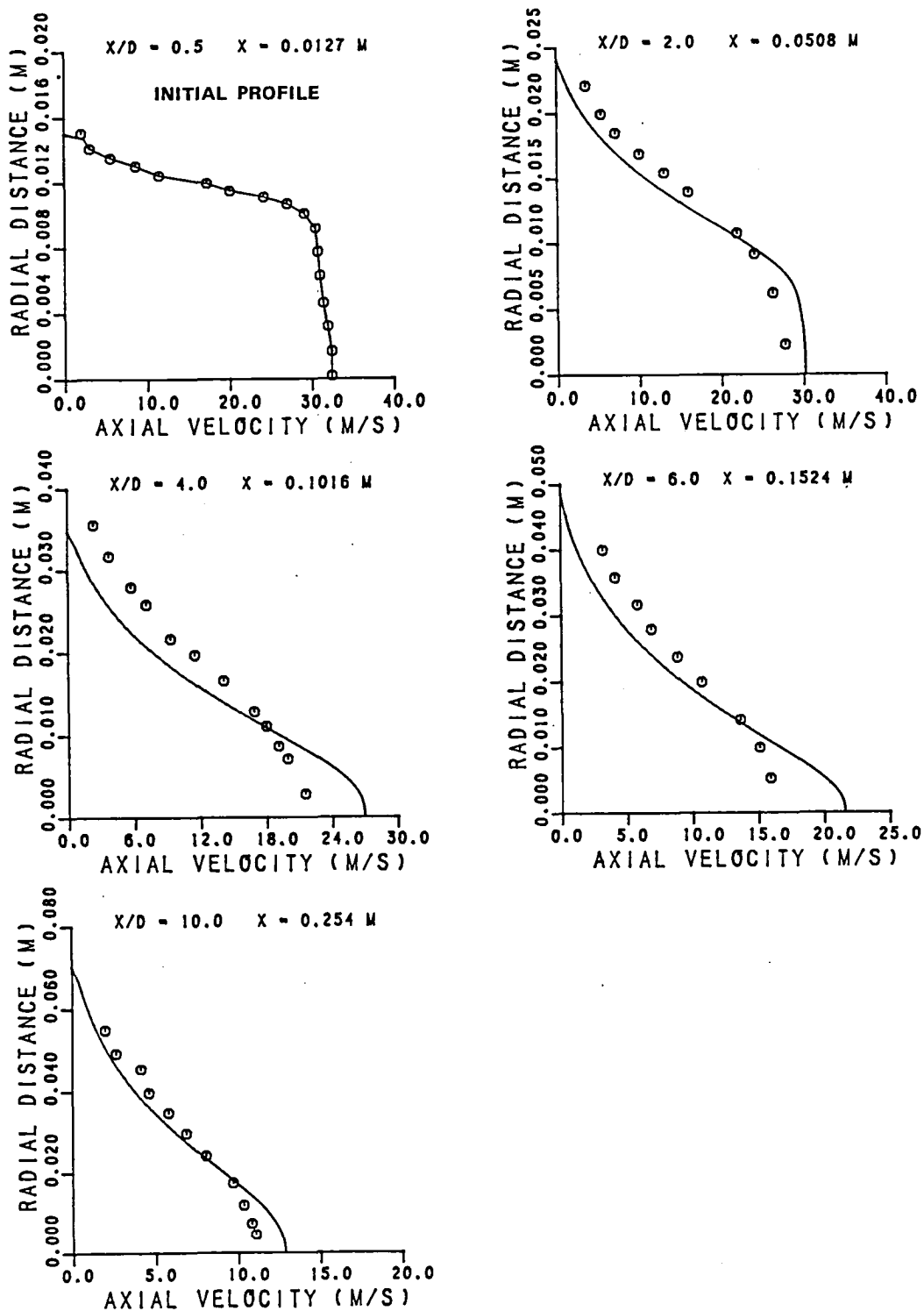


Figure 8.1-12. ASM - Mean Axial Velocity Profiles.

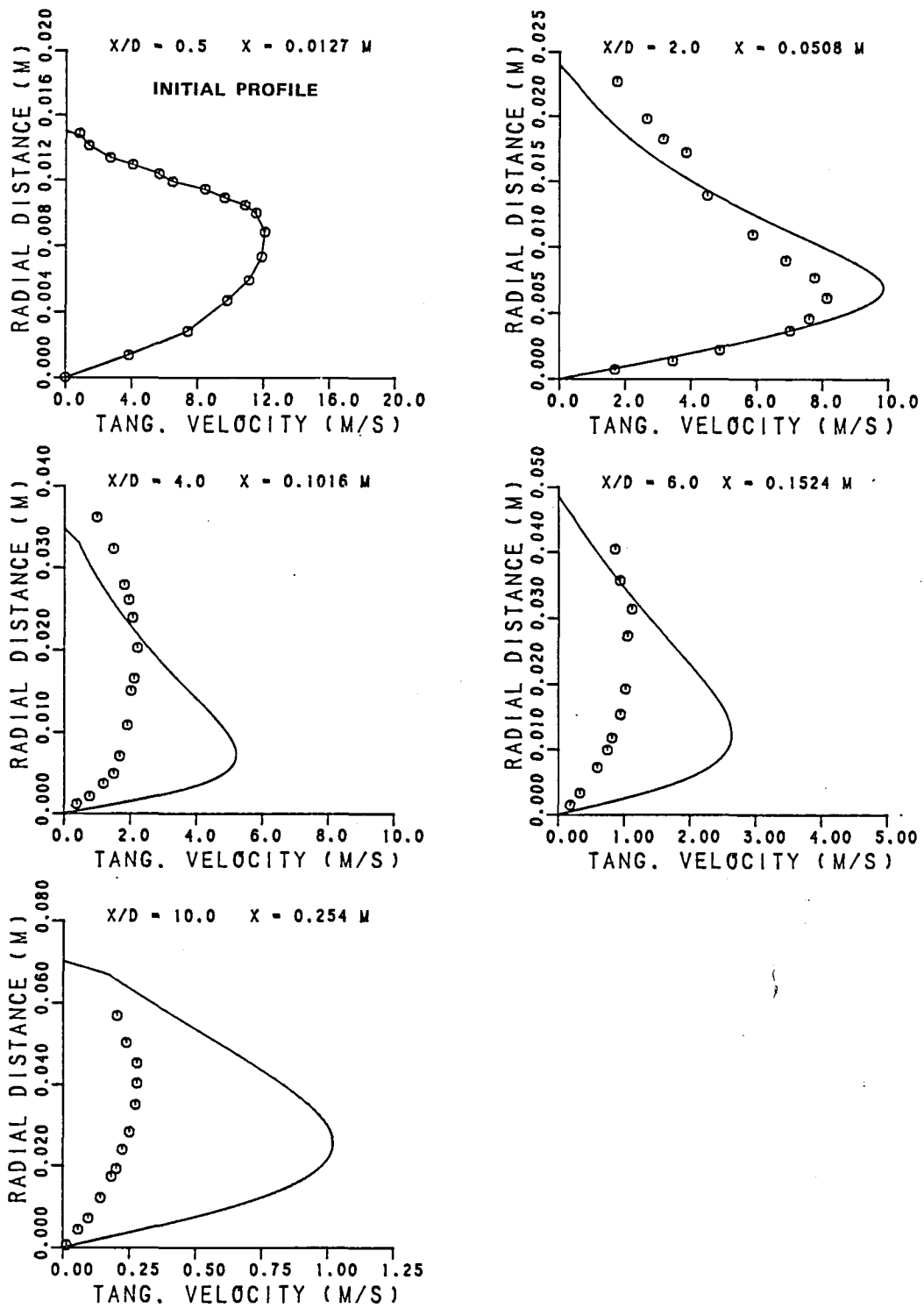


Figure 8.1-13. ASM - Mean Tangential Velocity Profiles.

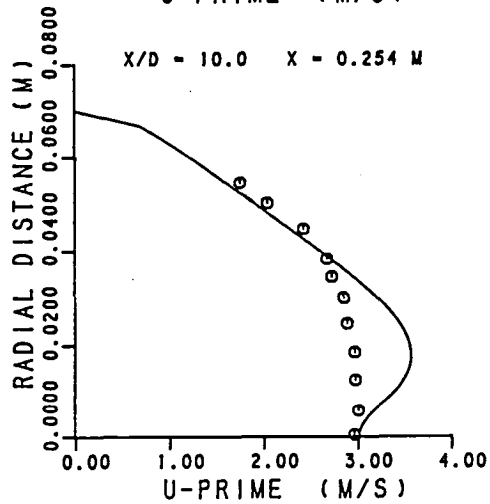
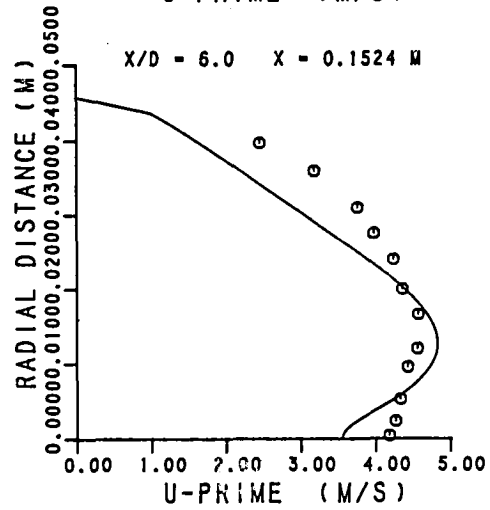
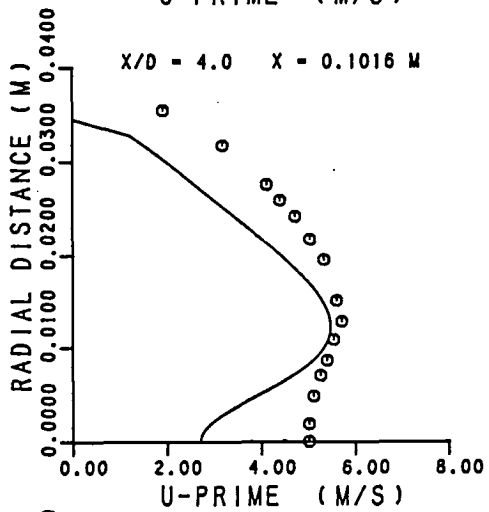
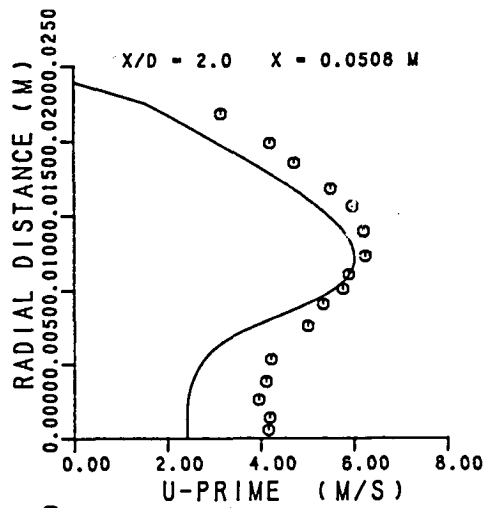
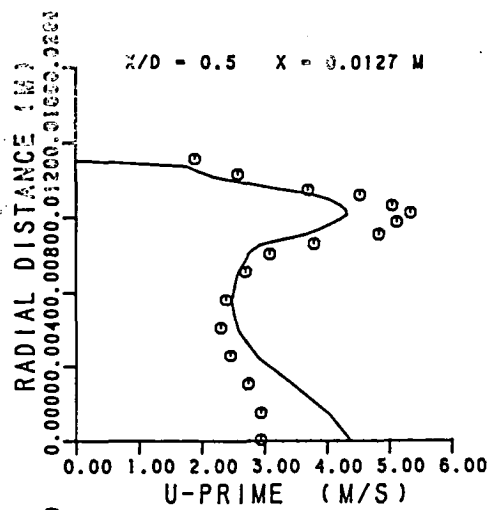


Figure 8.1-14. ASM - u' Profiles.

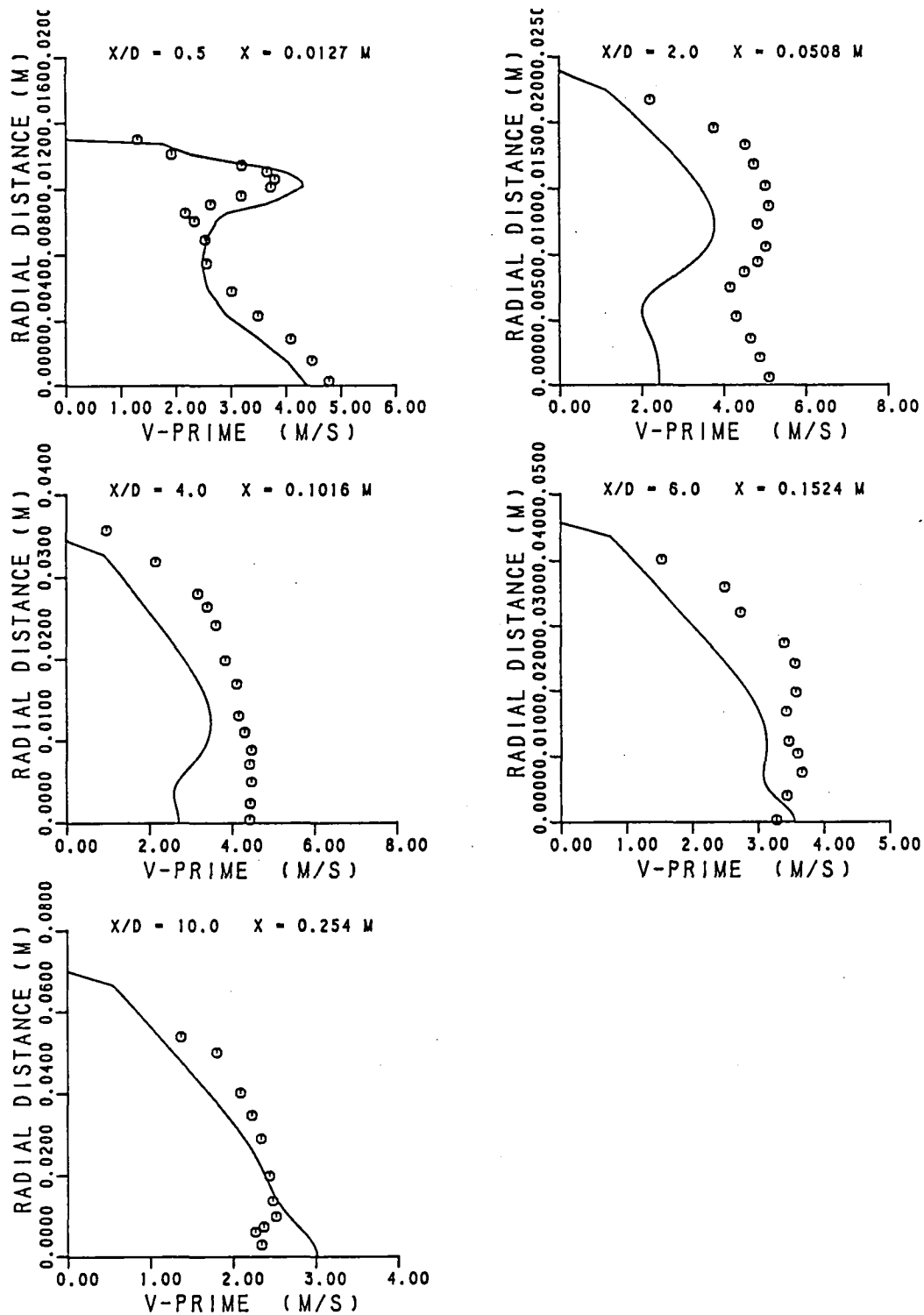


Figure 8.1-15. ASM - v' Profiles.

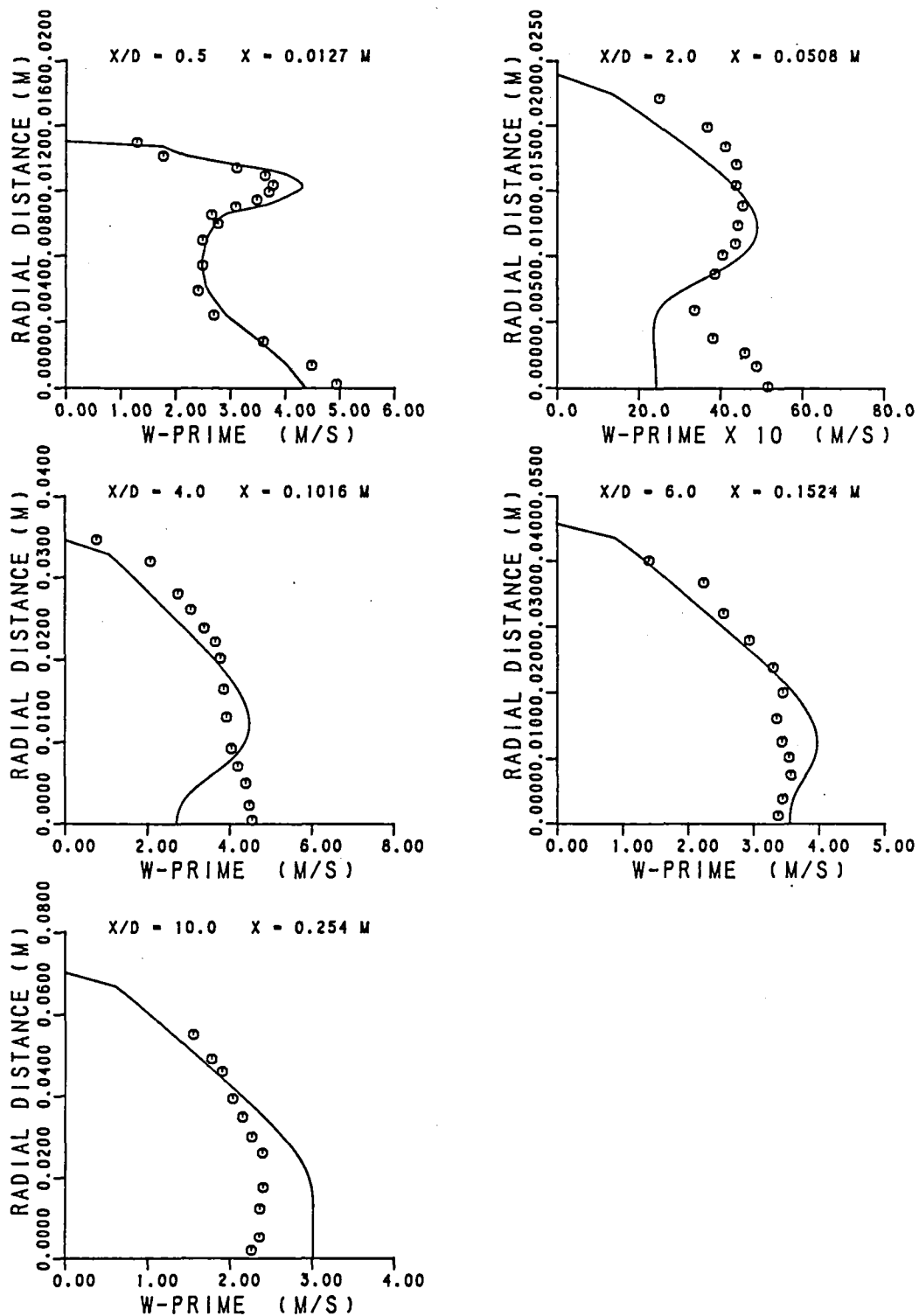


Figure 8.1-16. ASM - w' Profiles.

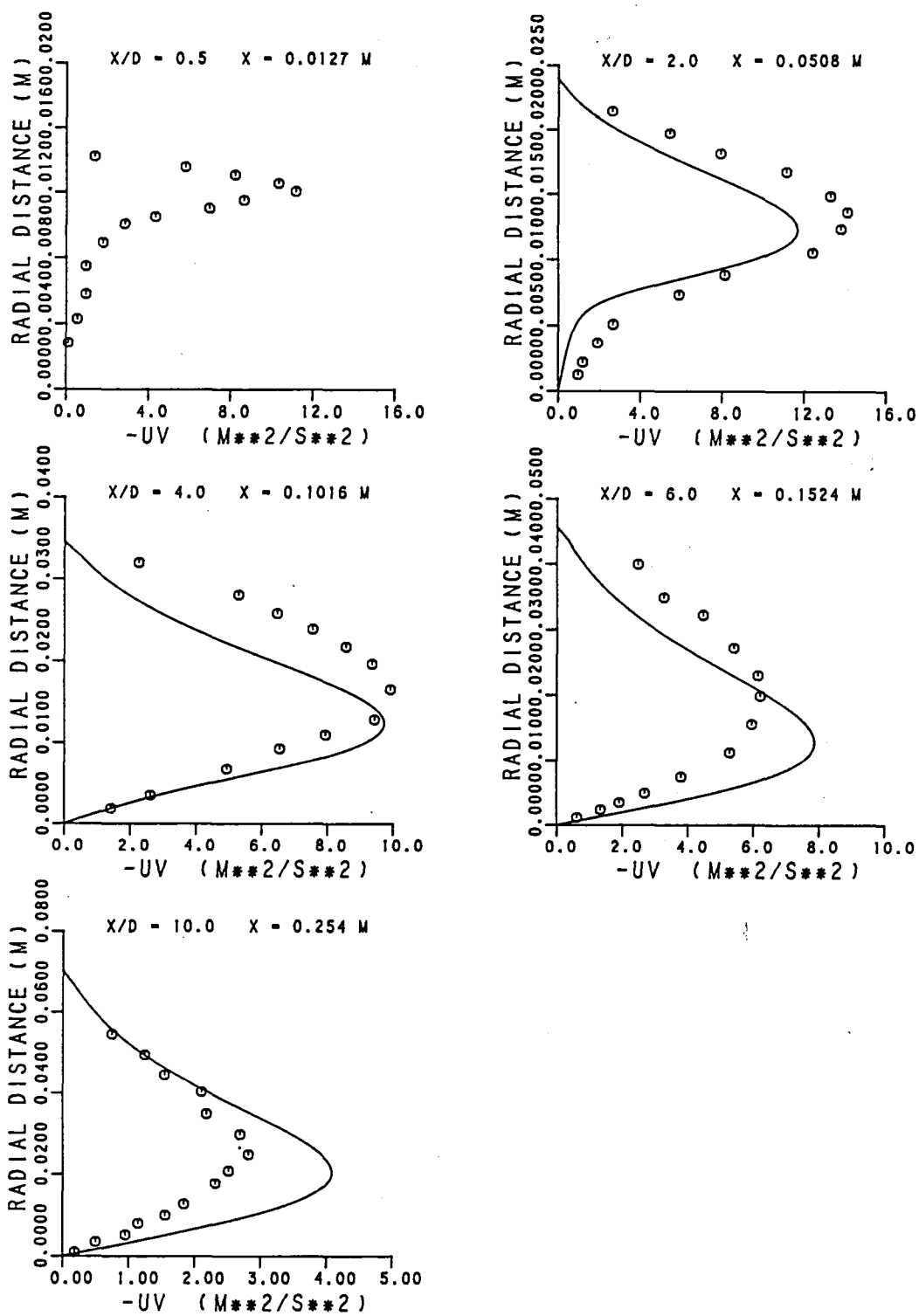


Figure 8.1-17. ASM - Shear Stress (uv) Profiles.

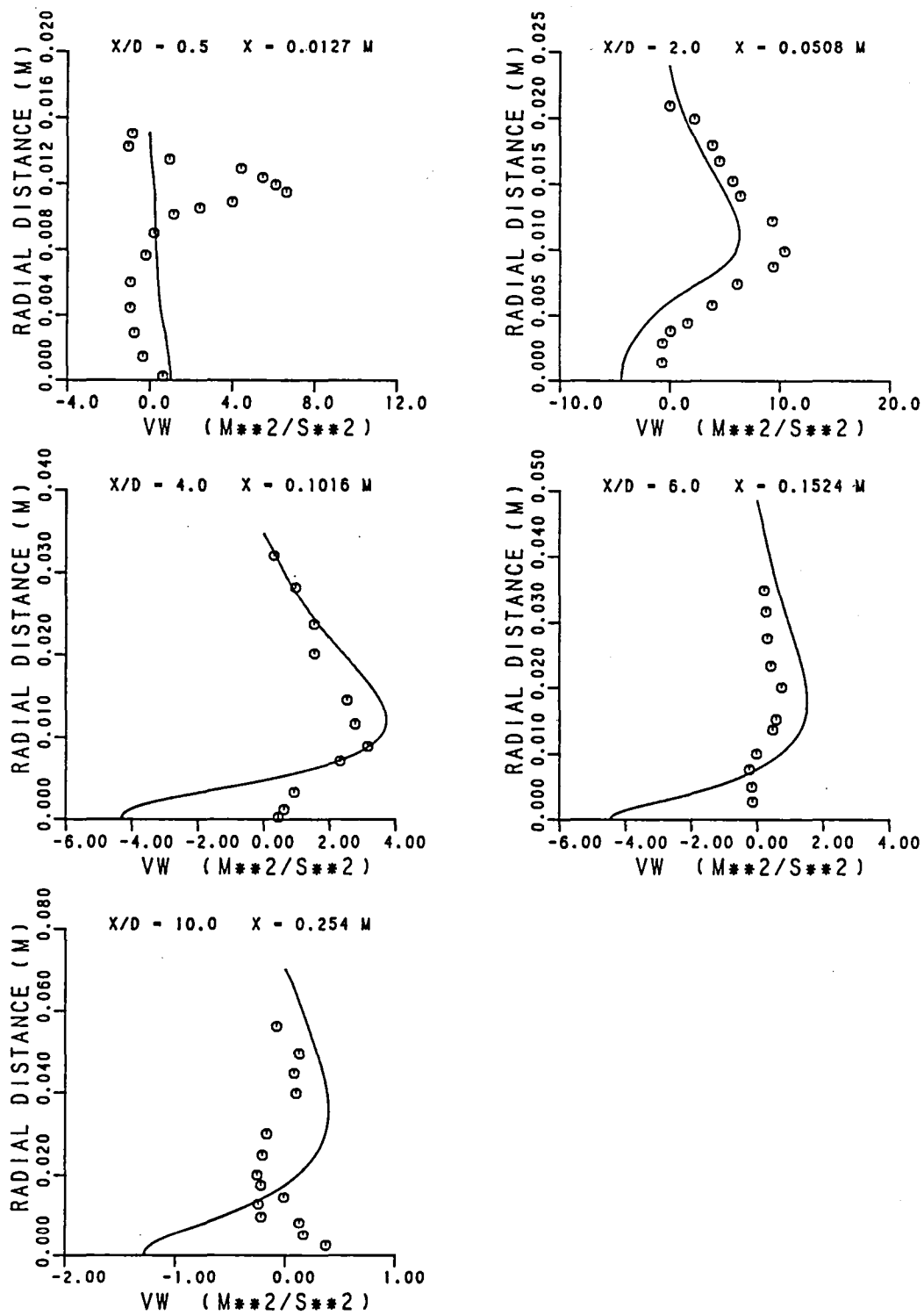


Figure 8.1-18. ASM - (vw) Profiles.

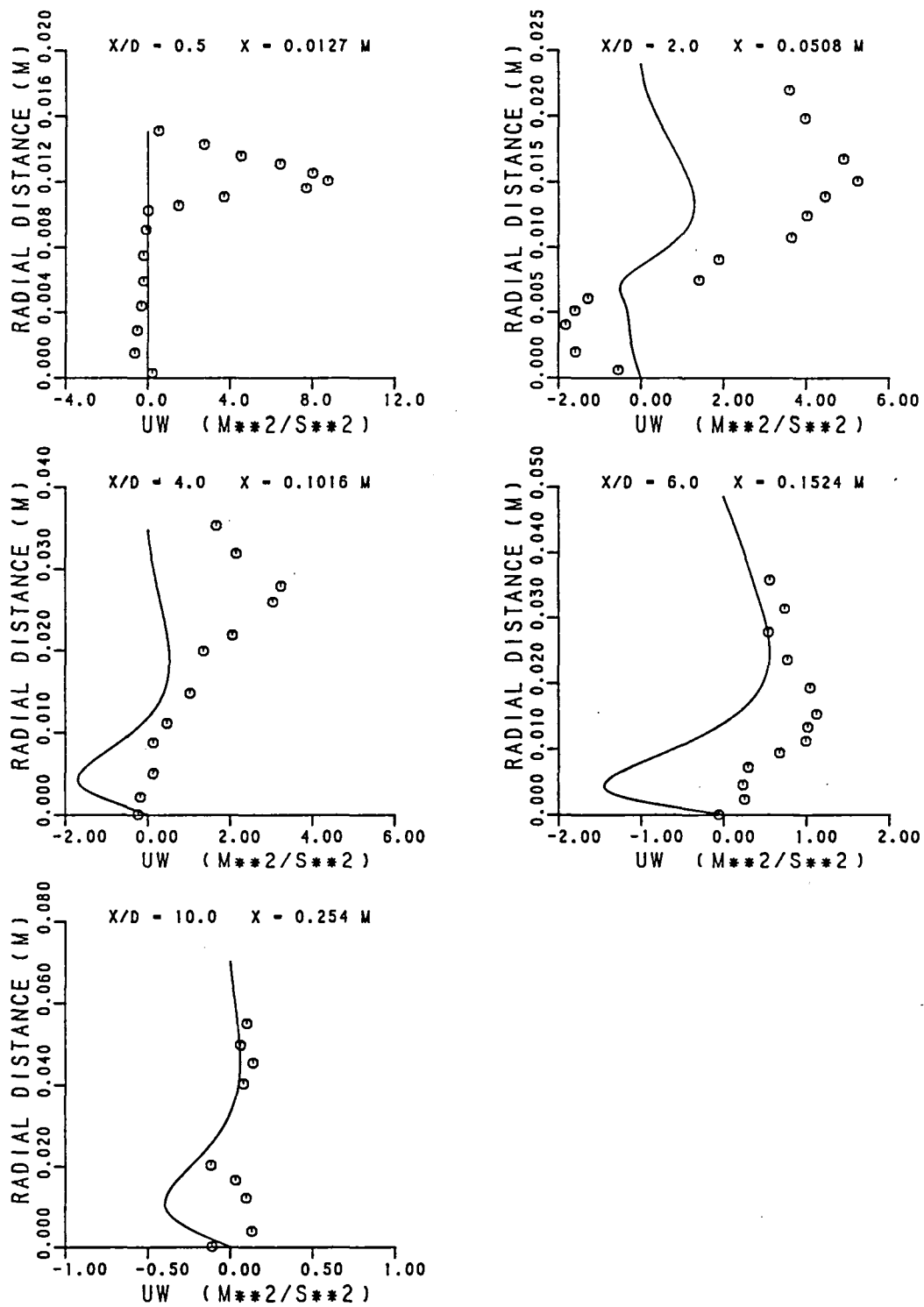


Figure 8.1-19. ASM - (uw) Profiles.

8.2 Nonreacting Swirling Combustor

One of the early investigations at Garrett¹⁰⁴ involved a cold-flow mapping of a can combustor (shown in Figure 8.2-1) along with estimated airflow splits. A co-rotating set of two radial inflow swirlers with 60-degree vanes established a swirling recirculating flow region within the primary zone. The can combustor employed two dome swirlers and four cooling slots as indicated in Figure 8.2-1. A calibrated three-hole wedge probe was used to determine axial and swirl velocity components at different stations from the dome: $\frac{x}{R} = 0.33, 0.55, 0.75, 1.25, 1.47, 1.72, 1.94, 2.17, 2.63$ and 2.86 where R , radius of the can, is 8.27 cm.

Computations for this test case were made using the 2-D elliptic program with 30 x 25 finite-difference nodes. Calculations were made with the standard $k-\epsilon$ model using uniform inlet velocity profiles corresponding to the flow splits shown in Figure 8.2-1. The comparison between predicted and measured mean axial velocity profiles is presented in Figure 8.2-2. The $k-\epsilon$ model accurately predicts the recirculation zone near the axis of the combustor. However, the agreement in the vicinity of the combustor wall is only qualitative. The differences between data and predictions are probably due to discrepancies in the flow split and boundary condition specification, and $k-\epsilon$ model limitations.

The $k-\epsilon$ model predictions for angular momentum, rV_θ , and the measured values are illustrated in Figure 8.2-3. Near the axis of the combustor, the predicted and the measured profiles are in agreement. The region near the combustor wall contains discrepancies between data and predictions.

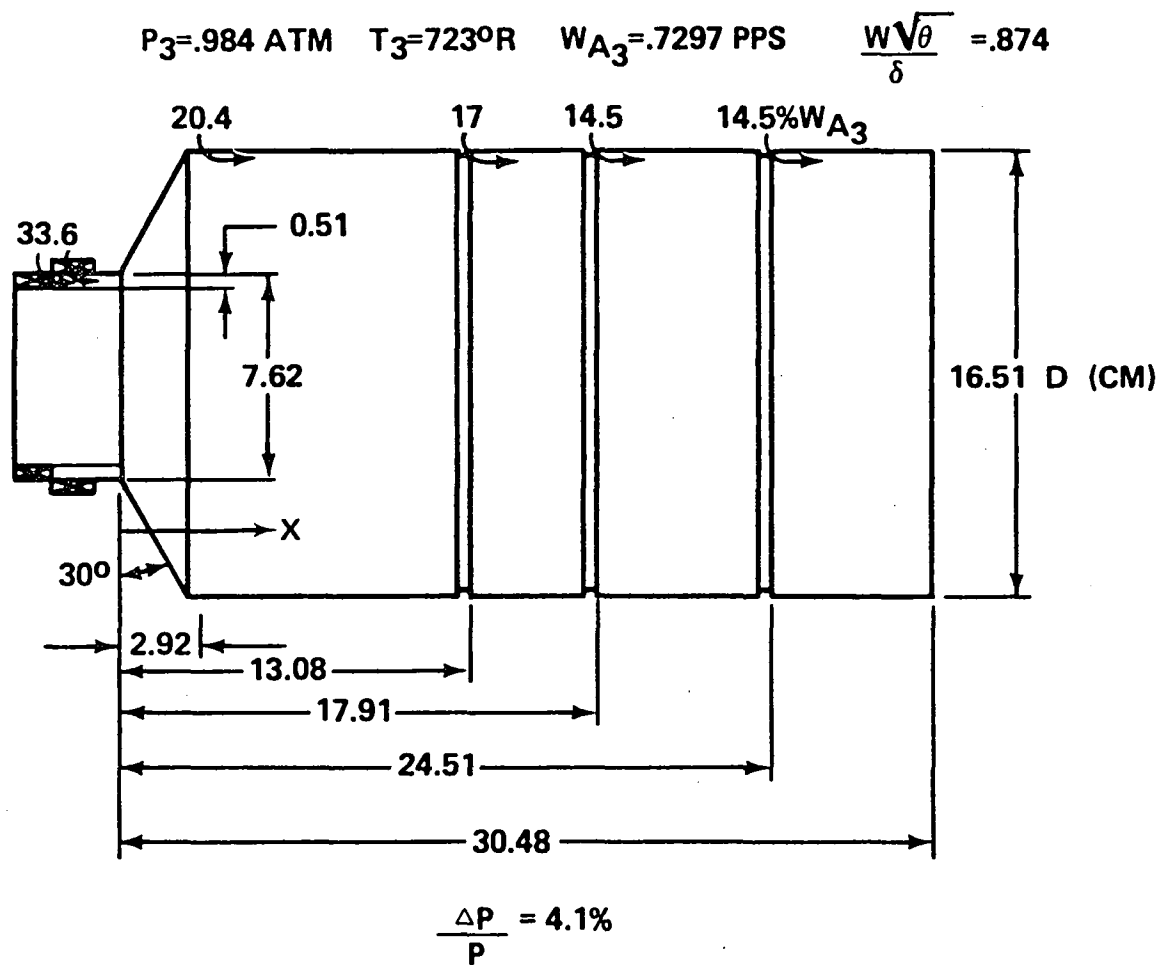


Figure 8.2-1. Nonreacting Swirling Combustor Flow Validation.

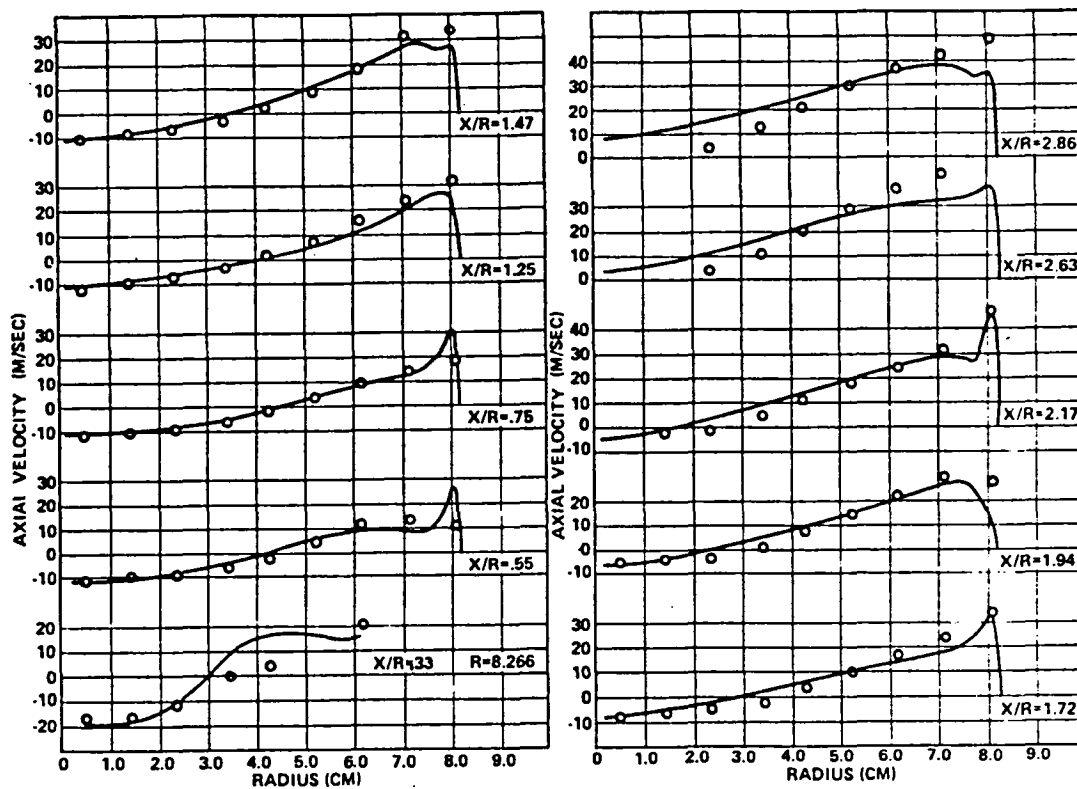


Figure 8.2-2. Comparison Between Measured Axial Velocity and $k-\epsilon$ Turbulence Model.

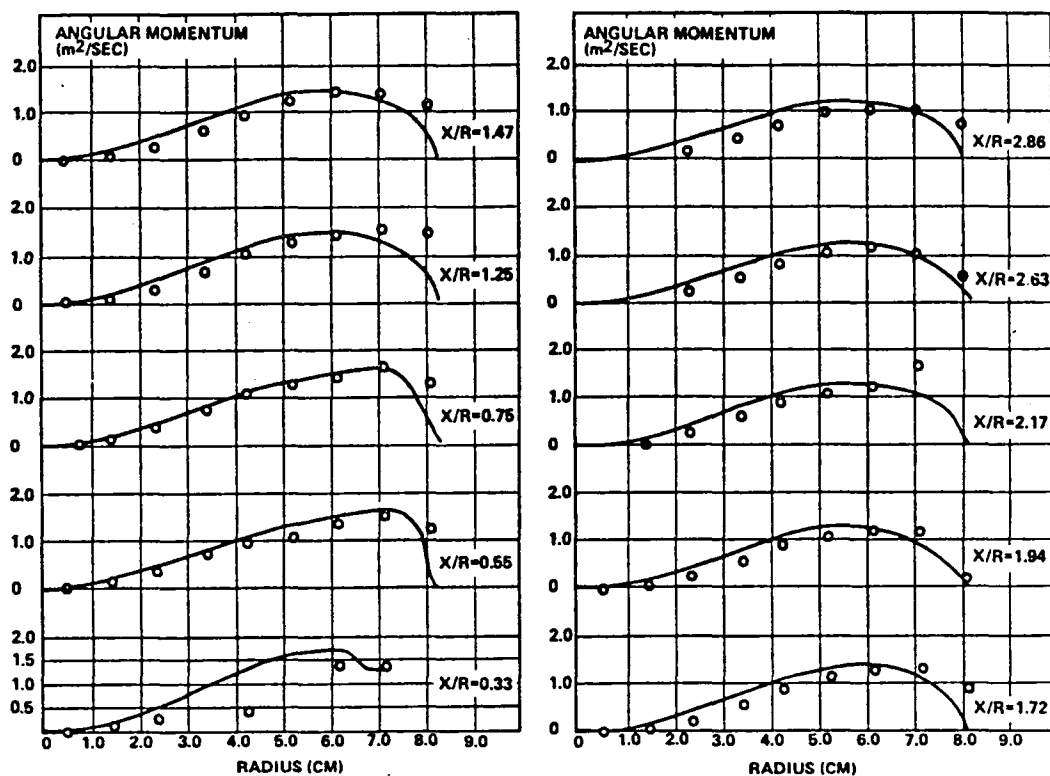


Figure 8.2-3 Comparison Between Measured Angular-Momentum and Predictions of $k-\epsilon$ Turbulence Model.

8.3 Confined Swirler Flow

Another early investigation at Garrett¹⁰³ involved cold flow laser Doppler velocimeter (LDV) measurements in a 12.7 cm diameter can combustor with different inlet swirl angles and swirler configurations in regard to the expansion ratio. Among the inlet swirl angles considered in the measurements were the zero degree (non-swirling) and 60° swirler. Different inlet configurations were used with the 60-degree inlet swirl angle. The geometries of the test cases are illustrated in Figure 8.3-1. For each of these flow tests, the inlet mass flow rates were measured. Computations for these tests used the 2-D elliptic code with standard $k-\epsilon$ model. The computations were started upstream of the swirler station with a uniform velocity corresponding to the mass flow rate. The inlet turbulence kinetic energy was assumed to be constant with a value of $0.003 U_{in}^2$.

Flow Around a Disk

The standard $k-\epsilon$ model predictions for the flow around a disk were obtained by using a grid network consisting of 70 axial and 25 radial nodes. The inlet axial velocity for this case was 19.54 m/sec. Figure 8.3-2 shows a typical comparison between predicted and measured mean axial velocity profiles at five planes located at $X/H = 0.048, 0.92, 1.87, 2.22$ and 5.68 downstream of the disk; here H denotes the radius of the disk. The predicted recirculation zone is shorter than the measured value, and the predicted maximum reverse flow velocity magnitudes are also smaller than the measured values. However, at the far downstream station ($X/H = 5.68$), the agreement between data and $k-\epsilon$ model predictions is very good.

60-Degree Swirler with Expansion Ratio of 1.2

For the configuration having a 60-degree swirler with an expansion ratio of 1.2, the average inlet velocity was 7.26 m/sec.

For this case, the calculations were performed by using 65 x 30 nodes. The computations were started at a station located one pipe radius upstream of the swirler. Figure 8.3-3 shows a comparison between data and the k- ϵ model predictions for mean axial velocity at $X = 1.17, 2.44, 5.0, 7.52, 15.14$ and 20.22 cm downstream of the swirler. Near the swirler exit, the velocity profile in the recirculation zone is correctly predicted by the data. However, in the core of the flow, the data shows much larger radial gradients than the predictions. At the far downstream stations, the agreement between data and predictions is only qualitative. The discrepancies between the data and predictions are probably due to the boundary condition specification in addition to the model deficiencies.

60-Degree Swirler with Expansion Ratio of 2.2

This configuration has two axisymmetric steps, one at the hub of the swirler and the second at the tip of the swirler. The radius of the swirler hub was 2.67 cm and the swirler tip radius was 5.08 cm. The average inlet velocity upstream of the swirler was 5.33 m/sec. Computations for this case were started one pipe radius upstream of the swirler with a uniform inlet velocity of 5.33 m/sec and a turbulence kinetic energy level of $0.0203 \text{ m}^2/\text{sec}^2$. Predictions were obtained from the standard k- ϵ model by using 56 x 35 nodes. Comparison between predictions and the data for mean axial velocity are illustrated in Figure 8.3-3 for different axial stations: $X = 5.0, 7.52, 15.14$ and 20.22 cm downstream of the swirler. The predicted profiles are in qualitative agreement with the data. The predicted velocities in the recirculation zone are smaller than the measurements. Consequently, the predicted maximum positive velocities are also smaller than the data in order to satisfy the conservation of mass. The predicted and measured locations of peak axial velocities are in good agreement.

In conclusion, the standard $k-\epsilon$ model predictions are in good agreement with the measurements, especially outside the recirculation zone of nonswirling flows. In the recirculation region, the production of turbulence is relatively high, and the structure of turbulence is expected to be anisotropic. In such anisotropic regions, the standard $k-\epsilon$ model predictions are not expected to be accurate. In swirling flows, the standard $k-\epsilon$ model results are only in qualitative agreement with the data.

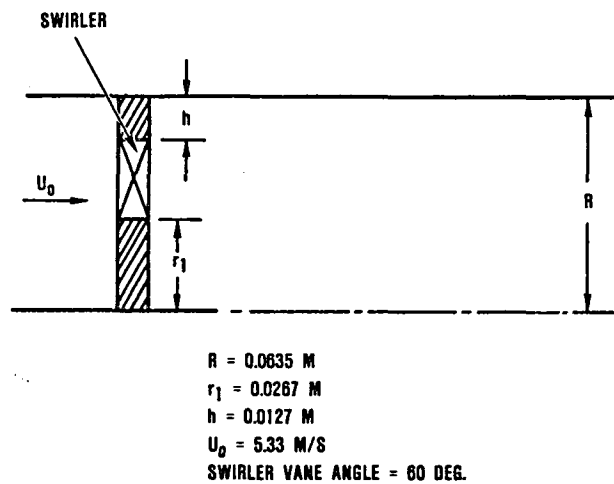
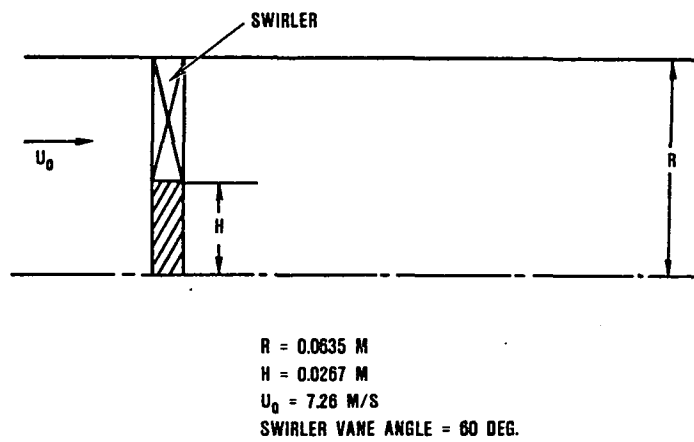
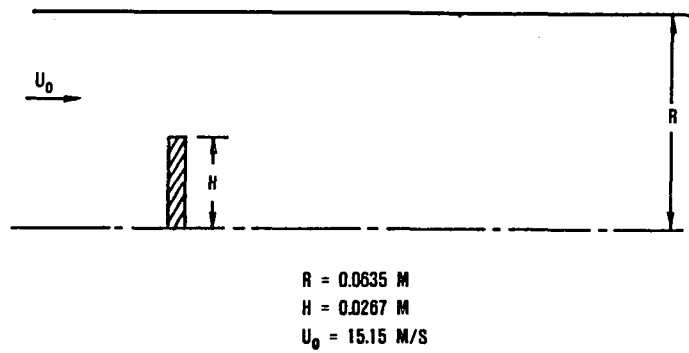


Figure 8.3-1. Configuration of the Swirling Flow Investigation at Garrett.

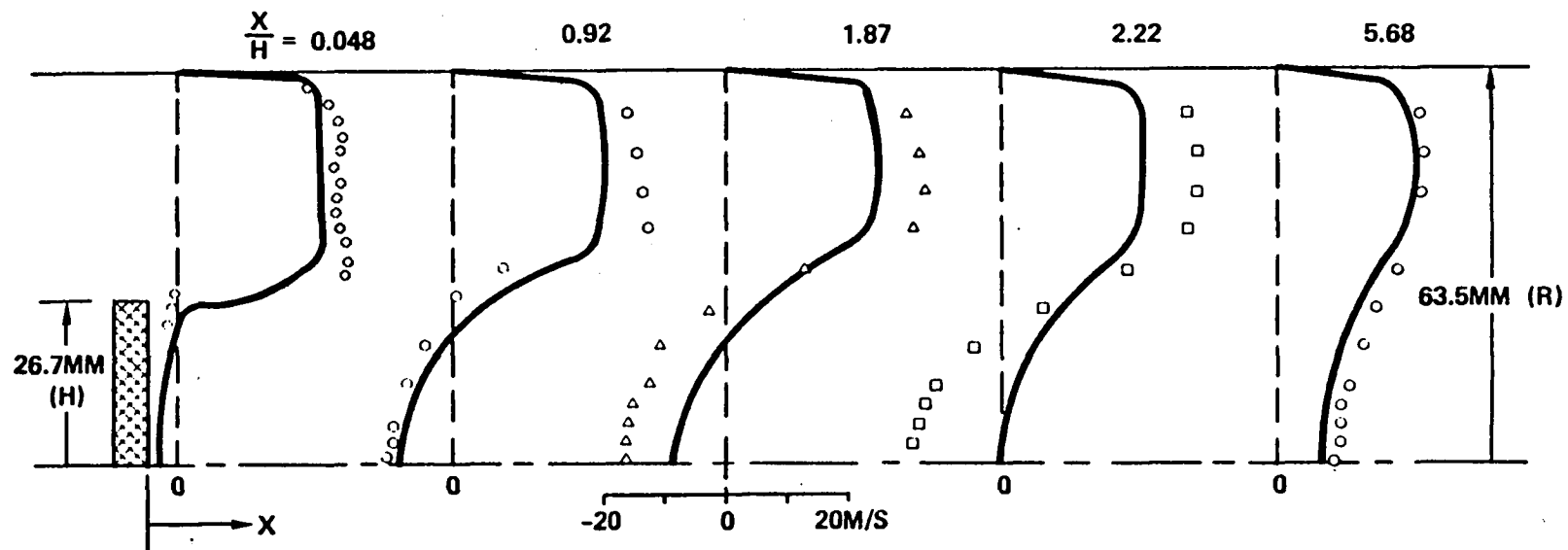
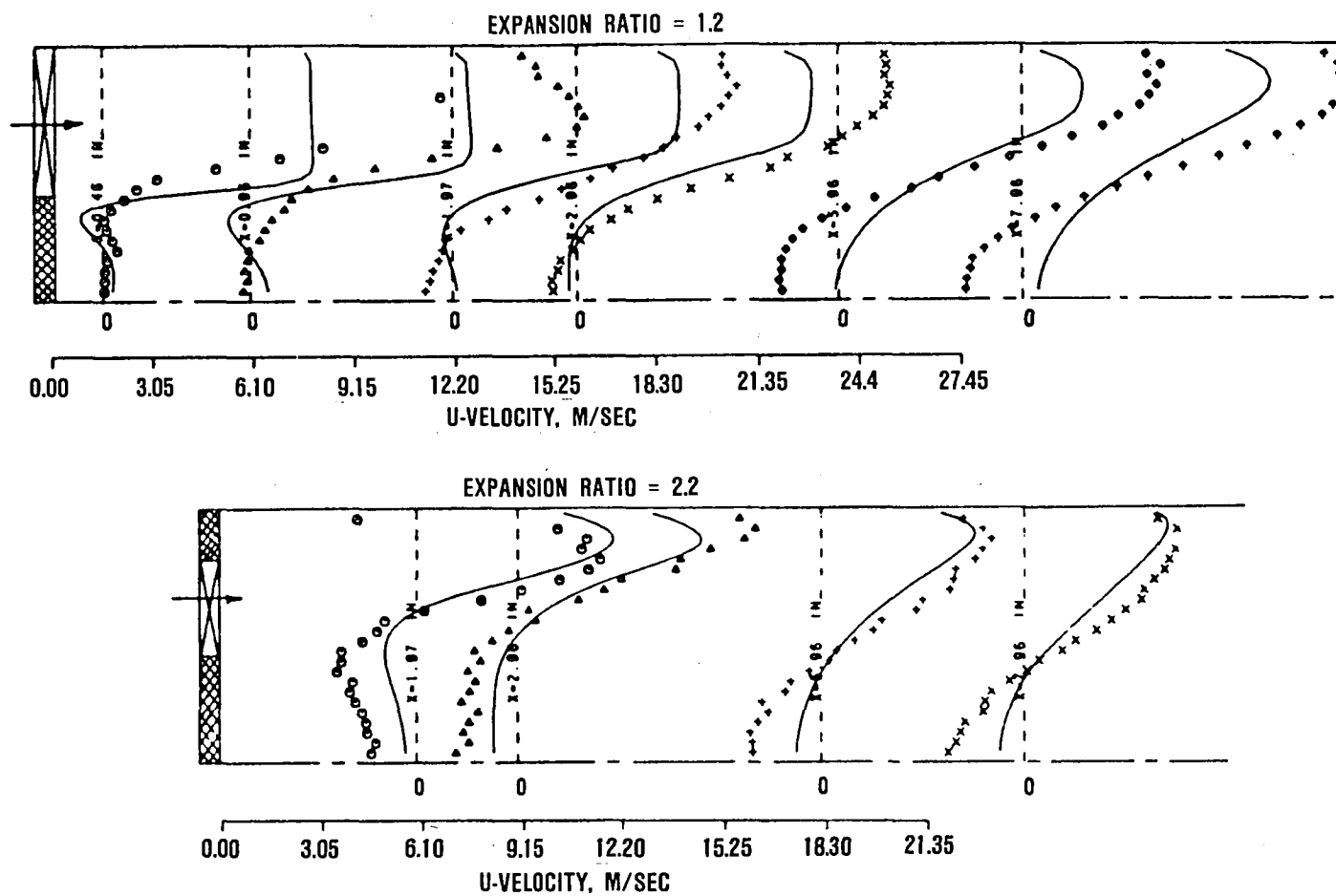


Figure 8.3-2. Comparison Between Predicted and Measured Axial Velocity Profiles Behind a Confined Disk.



8.4 Swirl Combustor with Cooling Air

Experimental Description

The velocity and turbulence measurements of Brum and Samuelsen¹⁴⁴ (Figure 8.4-1) have been compared with calculations of the 2-D elliptic program. The flow field measured was a nonreacting, confined swirling flow in an 8-cm-diameter tube (see Table 11). The tube was 50 cm long with rectangular windows on each side to measure the axial and swirl components of velocity using forward scatter measurement techniques with a two-color laser anemometry system. Two electronic counters and a minicomputer were used to acquire and separate the mean and time fluctuating components of velocity and determine the crosscorrelation $\overline{u'w'}$ levels. The swirl was generated by a 12-vane sheet metal swirler at the inlet cross-section. The hub of the 60° swirler was 19 mm in diameter and the tip was 57 mm in diameter with solid body rotation. In the hub or centerbody, a cone/annular nozzle was installed for injection of CO₂ in the nonreacting measurements. The nozzle had an 8.65-mm outer diameter, a 1-mm gap, and a 20° included half angle. Dilution or cooling air was admitted between the outer diameter of the swirler and duct wall. For these measurements a 50-percent split of swirler to cooling air was maintained.

2-D Elliptic Modeling Considerations

Computations were made with a rectilinear node arrangement of 45 axial nodes, extending from -4.5 mm to 280 mm, and 31 radial nodes, where the swirler exit was located at $X = 0.0$. The radial node spacing duplicated the hardware dimensions with 7 nodes in the center body, 14 nodes in the swirler, and 9 in the outer annulus. Three nodes were provided before the inlet boundary to facilitate the radial pressure gradient development caused by upstream interaction of the flow field. Axial grid spacing started with 1.5-mm spacing at the inlet and expanded geometrically to the exit.

Inlet profiles were taken partially from bulk flow measurements and laser anemometer measurements near the inlet (5 and 1 mm downstream). The outer annulus had a bulk velocity of 15.4 m/sec, zero swirl and a turbulent kinetic energy (k) taken from the measured profile. The swirler mean velocity components and turbulence kinetic energy were taken from the measured profiles. Turbulence length scale was assumed to be 1.6 mm.

A total of three different sets of calculations were performed in this investigation. It has been recognized for some time¹³ that in two-stream mixing within a recirculating flow field, the inlet profiles cannot be independently defined. Instead, they are strongly influenced by interaction between the streams as well as by the flow field they establish. Therefore, in the first set of calculations, inlet profiles were specified for both streams at a station 4.5 mm upstream of the swirler exit. The second and third cases were computed starting with inlet stream profiles at the swirler exit. Measured velocity and turbulence profiles at the swirler exit were used in the second case, whereas solid-body rotation with a constant axial velocity component was assumed in the third set of calculations.

The predicted results of the first case are presented in Figures 8.4-2 through Figure 8.4-7. These results are converged solutions with the total mass source error of about 0.04 percent. In these figures, the predictions are represented by the solid line, and the symbols correspond to the data. Figure 8.4-2 illustrates the comparison between predicted and measured centerline axial velocity. The predicted maximum flow reversal velocity is approximately -5.3 m/s, while the corresponding measured value is about -8.8 m/s. The length of flow reversal region along the centerline is measured to be about 0.105 m, while the prediction results show a value of about 0.051 m. Furthermore, the location of the maximum negative velocity is predicted closer to the swirler exit compared to the data.

The predicted radial profiles of the mean axial velocity component are shown in Figure 8.4-3. The data shown in this figure were obtained with 1.3 percent CO_2 injected along the centerline. The estimated injection velocity of CO_2 based upon the mass flow and nozzle area was quite high (27.9 m/s). Such velocities would tend to eliminate the recirculation zone. Accurate inlet injection velocity measurements are needed to correctly predict the flow field in the recirculation zone. Since that data is not available for this case, the CO_2 flow was not included in the computations. Furthermore, the CO_2 flow rate is a small percentage of the total mass flow rate and is not expected to alter the flow field substantially in the regions far downstream (greater than approximately 10 nozzle diameters) of the injector. The predicted results shown in Figure 8.4-3 do not include the CO_2 injection. This accounts for the difference between predicted and measured velocities near the axis at $X = 5$ mm. However, in the regions corresponding to the swirler and the cooling air region, the predicted axial velocities are in agreement with the data. The predicted maximum flow reversal velocities are smaller than the data. However, beyond the recirculation zone, the data and predictions are in good agreement.

Figure 8.4-4 shows the comparison between predicted and measured swirl velocity profiles. The predicted peak swirl velocity values are about 15 percent higher than the data up to the station where recirculation exists. However, at the far downstream stations, the swirl velocity profiles are accurately predicted.

A comparison between predicted and measured turbulence kinetic energy profiles is shown in Figure 8.4-5. In this figure, the data was obtained by assuming isotropic turbulence structure with the measured u' values. The overall levels of the turbulence kinetic energy are correctly predicted. In swirling flows, the assumption of isotropy is questionable, and the actual turbulence kinetic energy profiles are unknown.

The measured and predicted normalized streamline contour plots are presented in Figure 8.4-6 and 8.4-7, respectively.

Comparison between these two figures shows that the measured maximum recirculation mass is 3 percent, while the predicted value is 0.5 percent. The predicted reattachment length is considerably shorter than the data.

A second set of calculations was made wherein the inlet conditions were applied at the swirler exit ($X = 0$) using the measured values of velocity and turbulence intensities. The grid network used in this case was identical to the one used in the first set of calculations. The predicted results for the second set of calculations are shown in Figures 8.4-8 through 8.4-11. These results are very similar to the first set of calculations, shown in Figures 8.4-2 through 8.4-5.

The third set of calculations was made in which the inlet axial velocity profile was assumed to be uniform and a solid-body-rotation profile was used for the inlet swirl velocity. These inlet profiles were applied at the swirler exit, ($X = 0$). The results of these computations are illustrated in Figures 8.4-12 through 8.4-15. The predicted length of the recirculation zone in this case is about 0.03 m, which is even smaller than predictions in the previous sets of calculations. The predicted mean axial velocity profiles in this case (Figure 8.4-13) are significantly different from the data, especially near the inlet station. However, beyond $X = 10$ cm, the predicted axial velocity profiles are in good agreement with the data.

The predicted swirl velocity profiles (Figure 8.4-14) show larger peak values than the data. However, near the axis of the tube, the predicted profiles are in agreement with the data beyond $X = 4$ cm. The predicted turbulence kinetic energy profiles are

smaller than the data by a factor of 2 up to $X = 10$ cm. Beyond $X = 10$ cm, the turbulence kinetic energy levels are correctly predicted.

The following conclusions can be made for the computations of a swirl combustor with cooling air:

- o The initial axial and swirl velocity profiles have a dominant effect on the predictions downstream.
- o The size of the recirculation zone and the maximum flow reversal velocities are underestimated by the $k-\epsilon$ model, even though the trends are correctly predicted. The profiles in the far field (beyond $X = 10$ cm) are accurately predicted by the model. This is consistent with the conclusions of Paragraph 8.3.
- o When plug flow axial velocity and solid-body-rotation swirler velocity profiles were used at the inlet, the predicted results were in poor agreement with the data. However, the predicted profiles in the far field are in good agreement with the data.

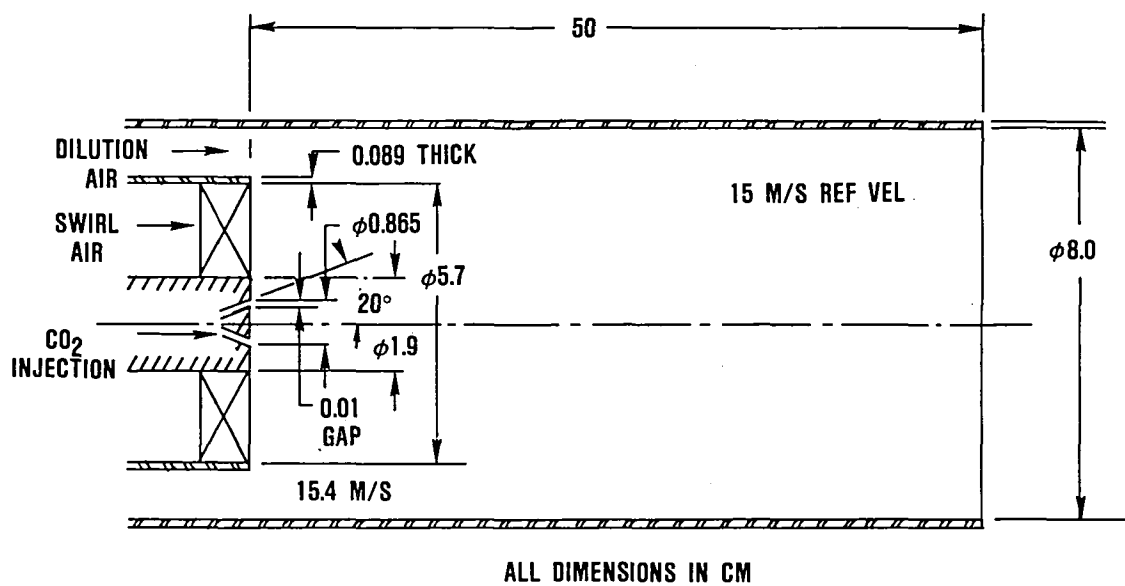


Figure 8.4-1. Brum and Samuelson Setup for Swirl Combustor with Cooling Air.

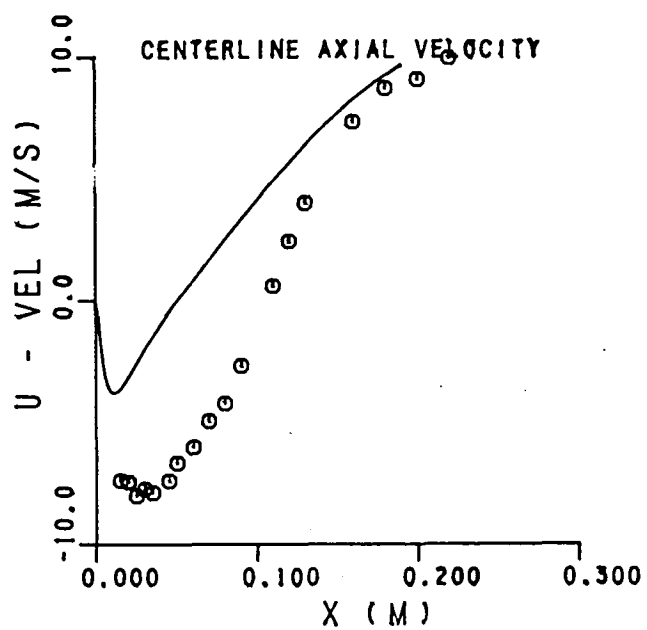


Figure 8.4-2. Comparison Between Measured and Predicted Centerline Axial Velocity.

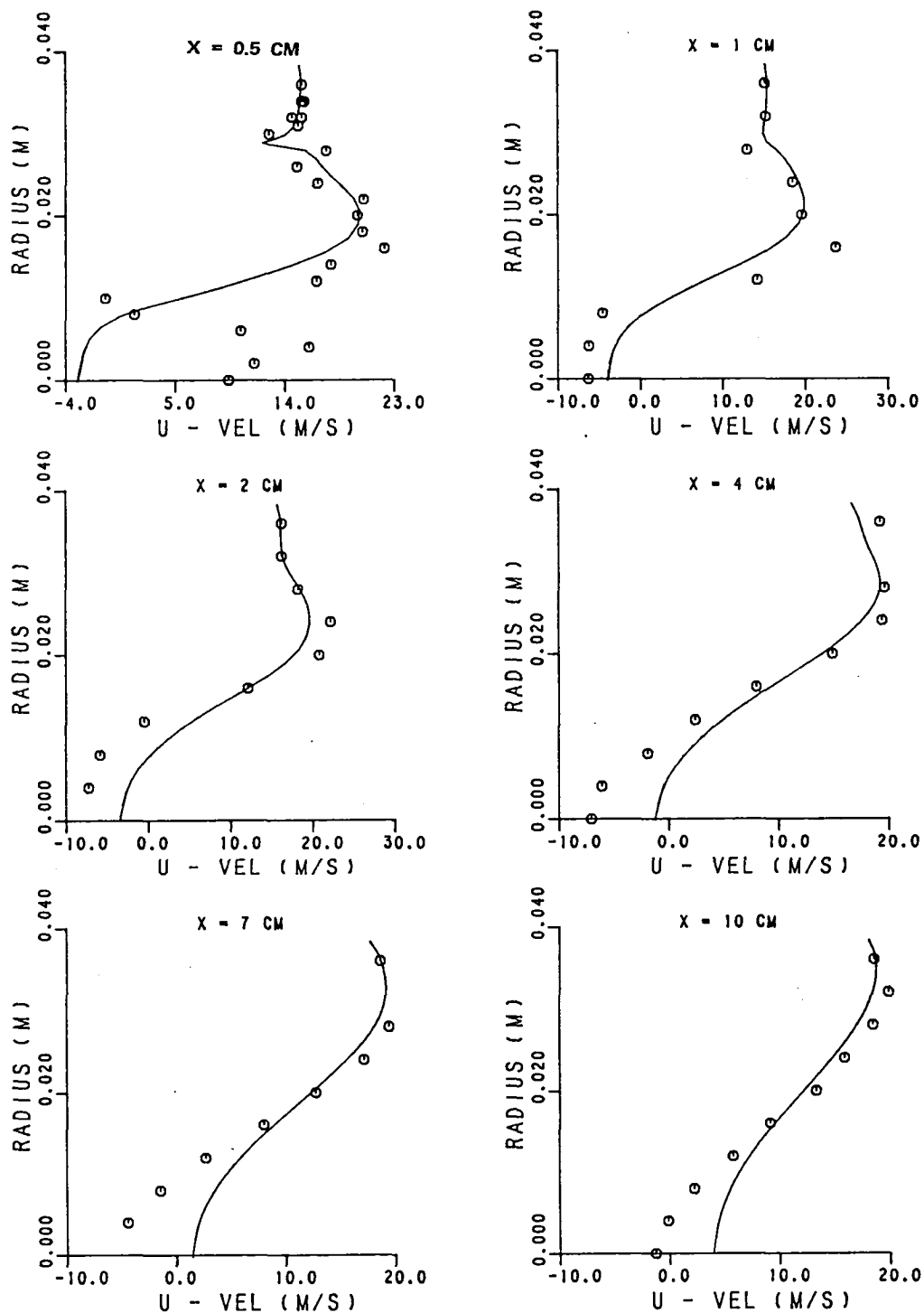


Figure 8.4-3. Comparison Between Measured and Calculated Axial Velocity Profiles.

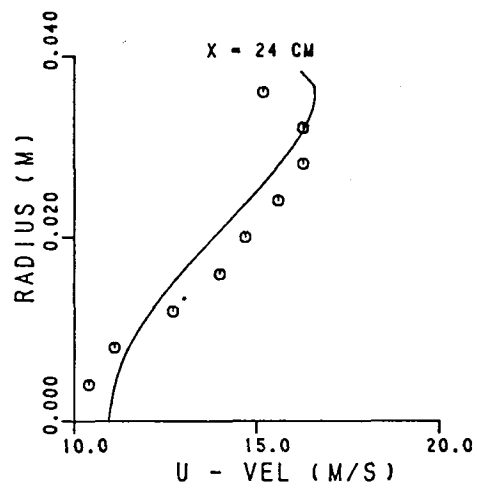
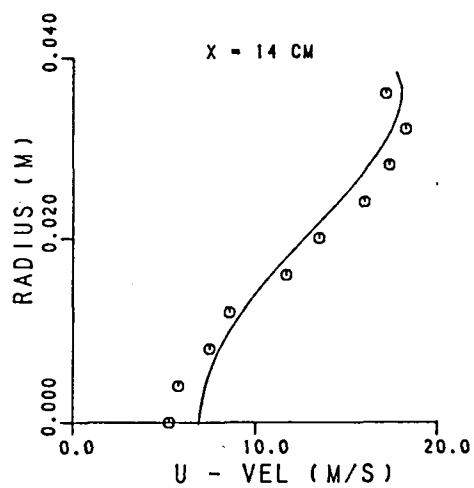


Figure 8.4-3. Comparison Between Measured and Calculated Axial Velocity Profiles (Cont'd).

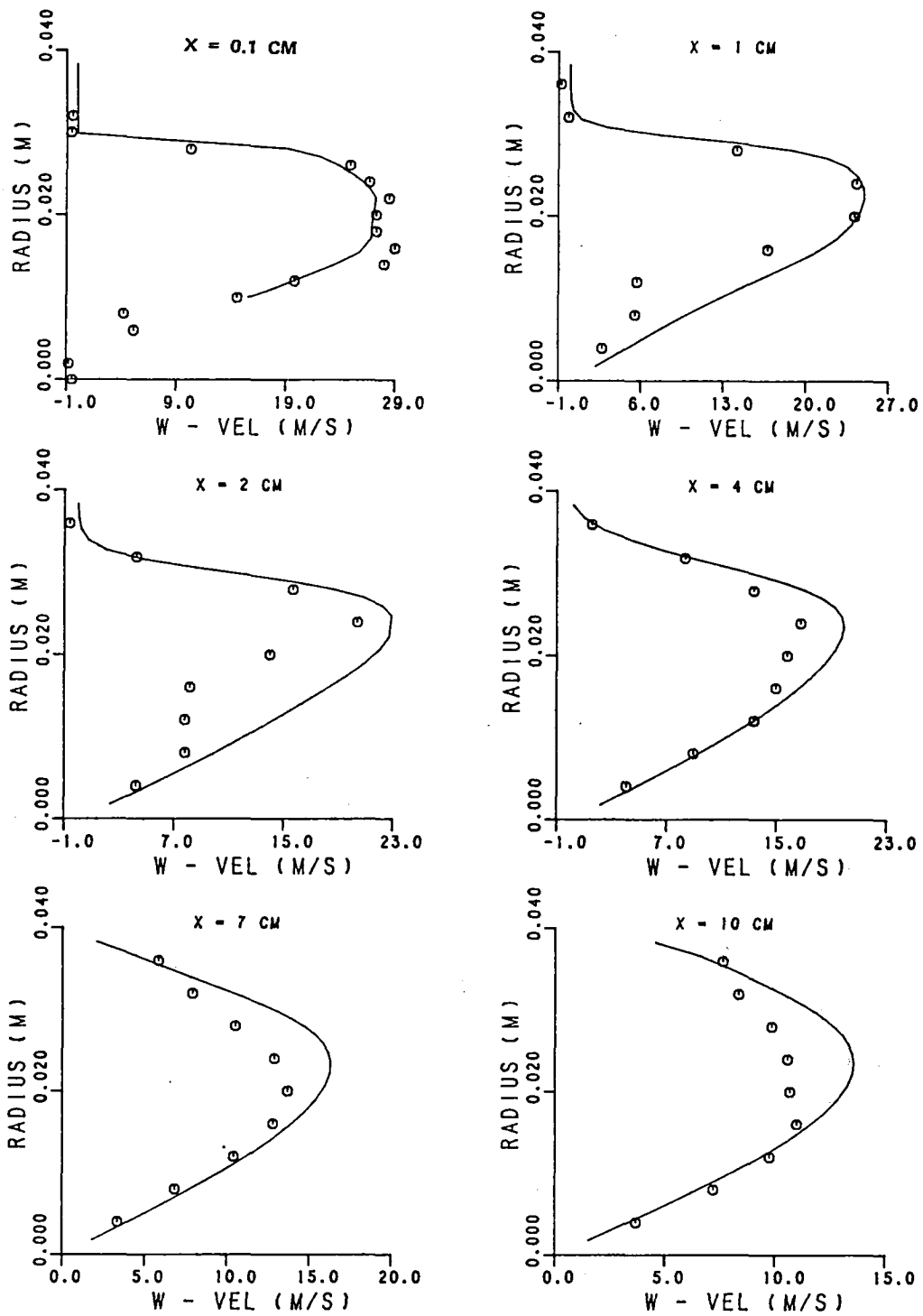


Figure 8.4-4. Comparison Between Measured and Calculated Swirl Velocity Profiles.

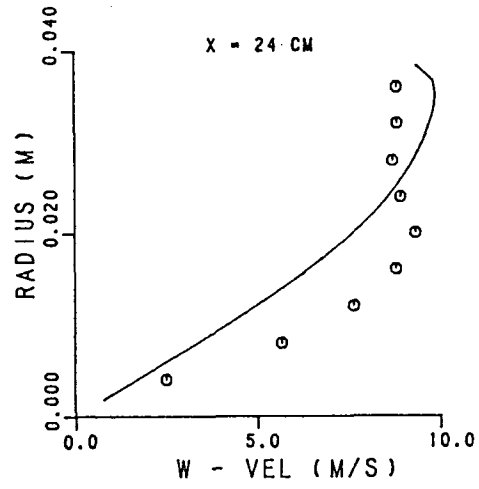
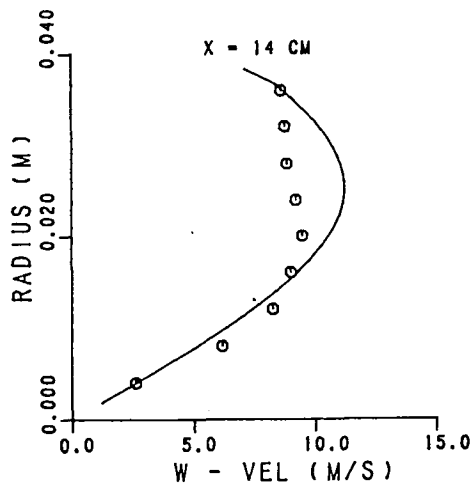


Figure 8.4-4. Comparison Between Measured and Calculated Swirl Velocity Profiles (Cont'd).

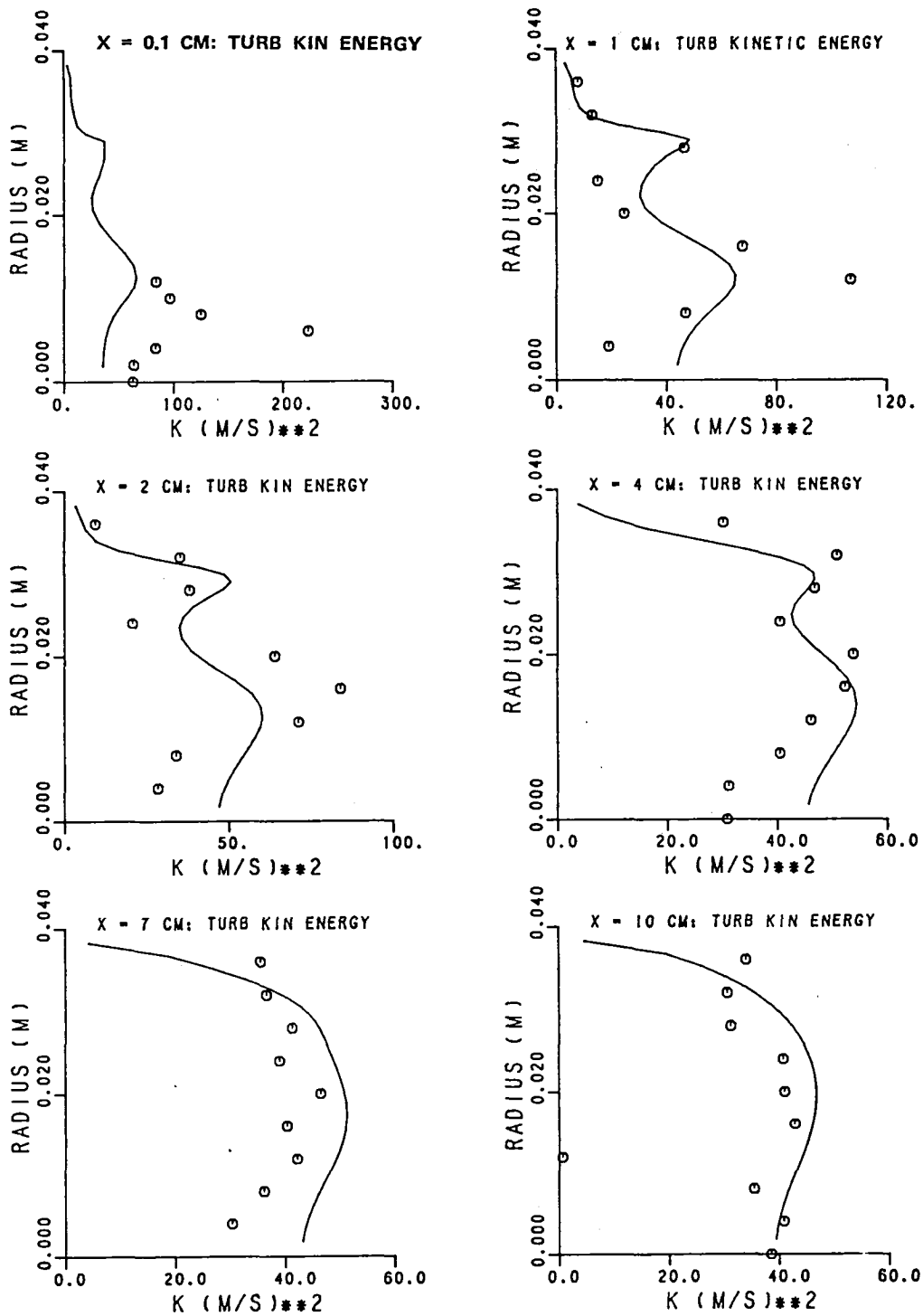


Figure 8.4-5. Turbulence Kinetic Energy Profiles.

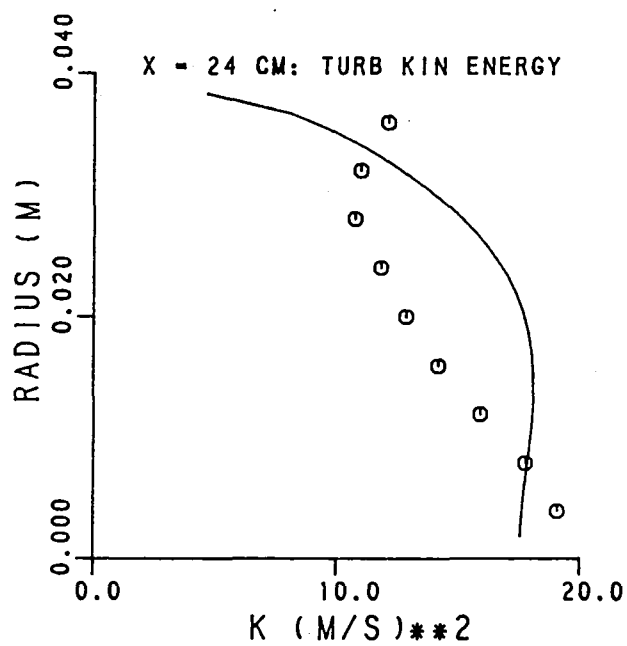
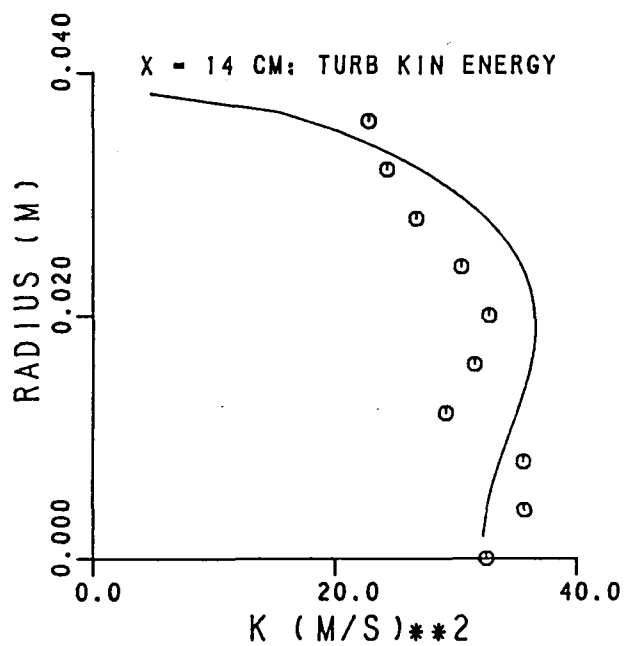


Figure 8.4-5. Turbulence Kinetic Energy Profiles (Cont'd).

CONTOUR VALUE

1	-0.0300
2	-0.0200
3	-0.0100
4	-0.0050
5	0.0000
6	0.0050
7	0.0100
8	0.0500
9	0.1000
10	0.2000
11	0.4000
12	0.6000
13	0.8000
14	0.9000
15	1.0000

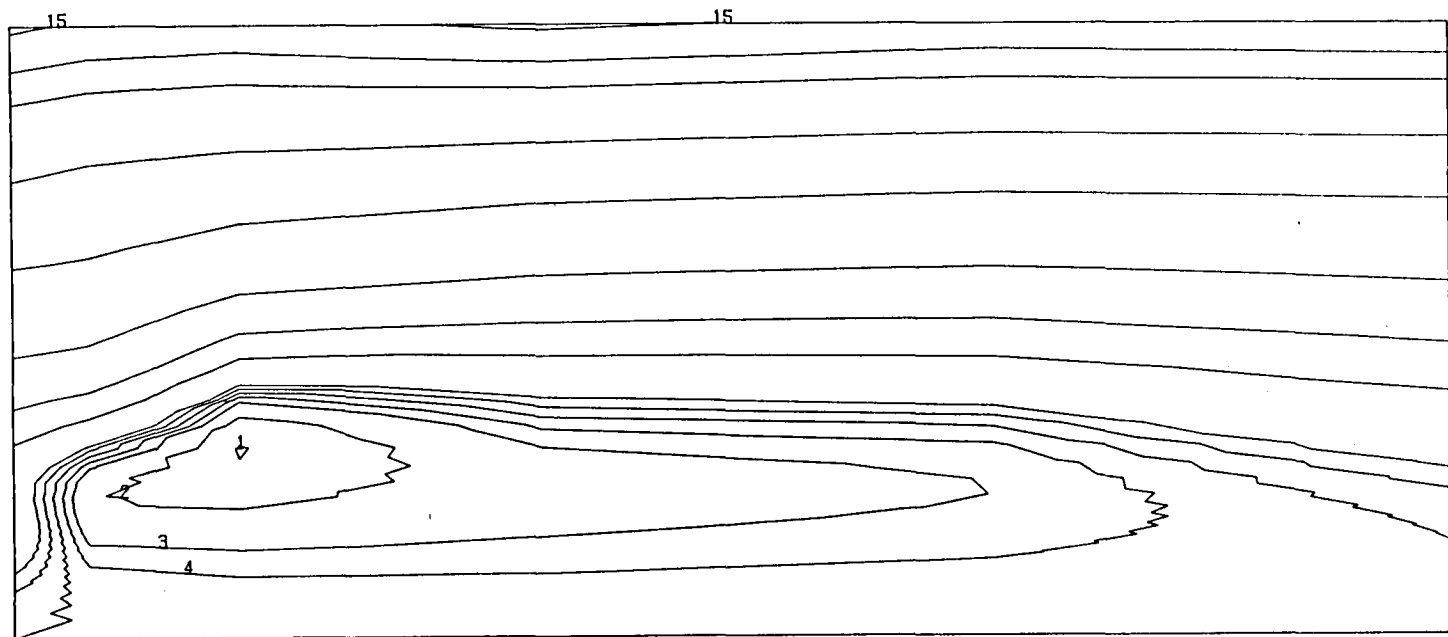


Figure 8.4-6. Measured Streamline Plot.

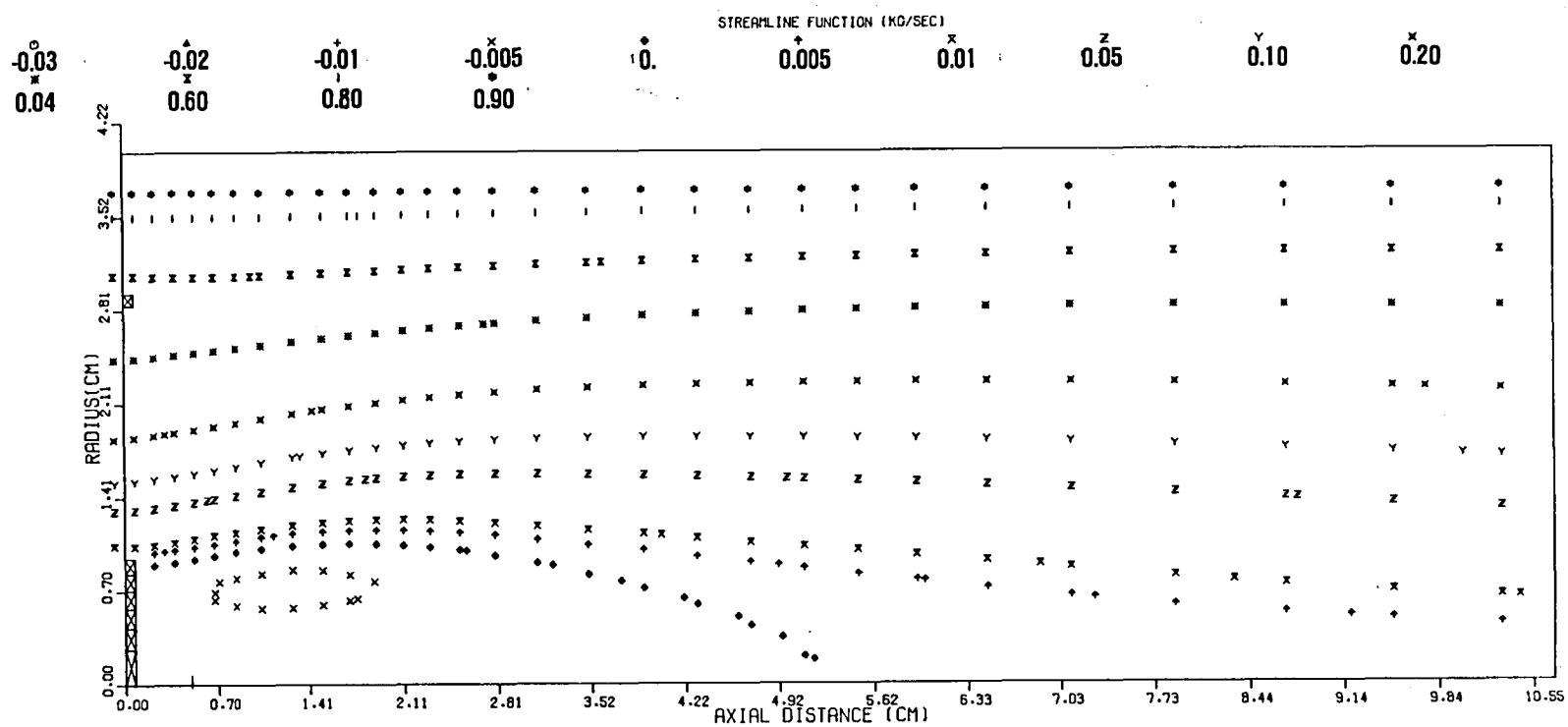


Figure 8.4-7. Calculated Streamline Plot.

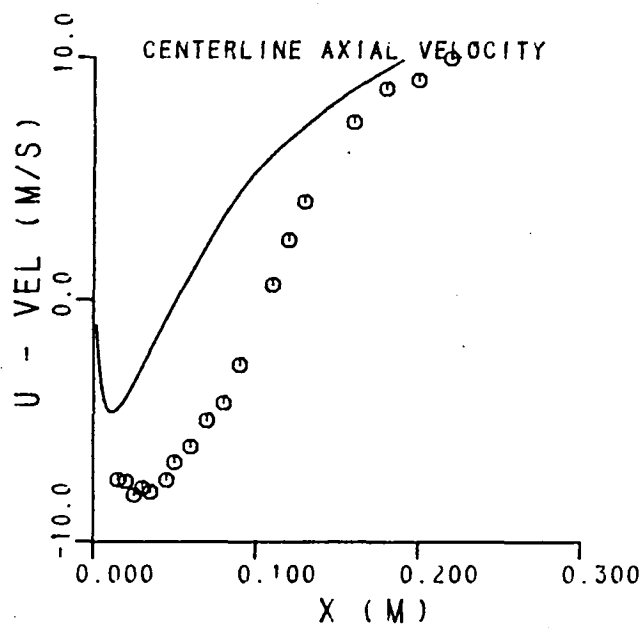


Figure 8.4-8. Second Set of Calculations - Centerline Axial Velocity Development.

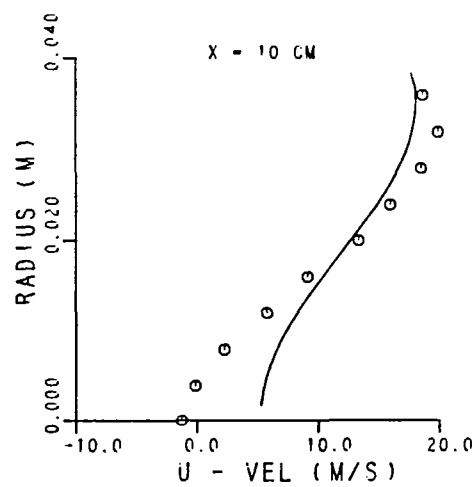
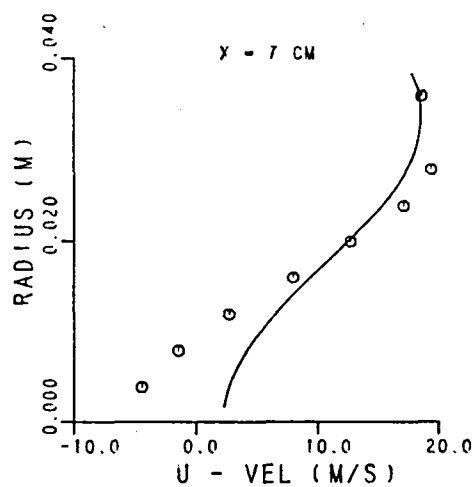
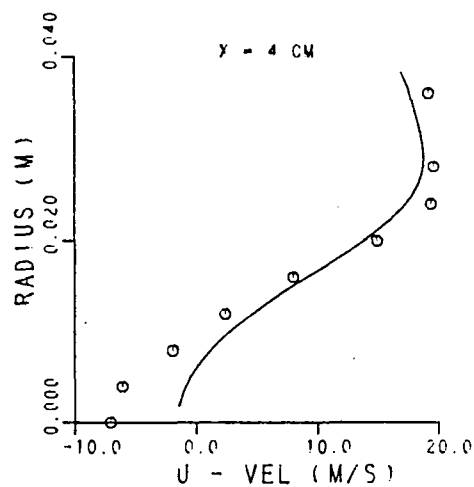
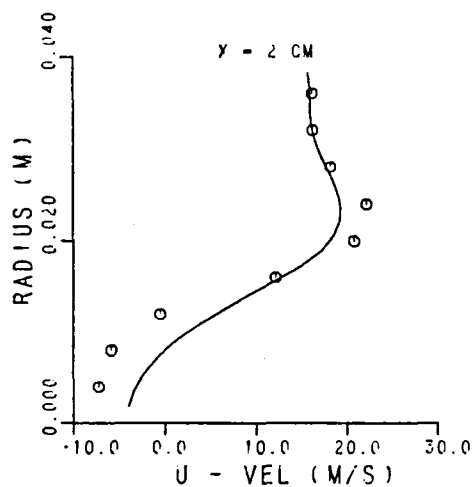
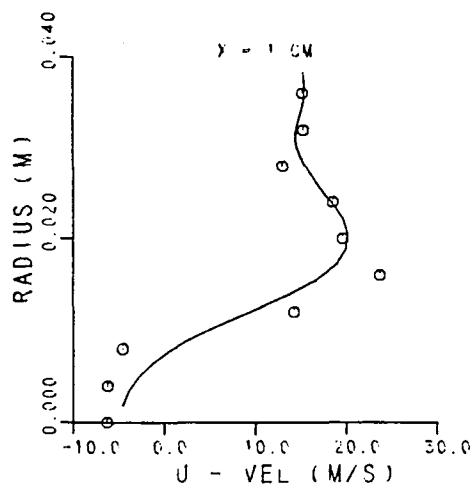
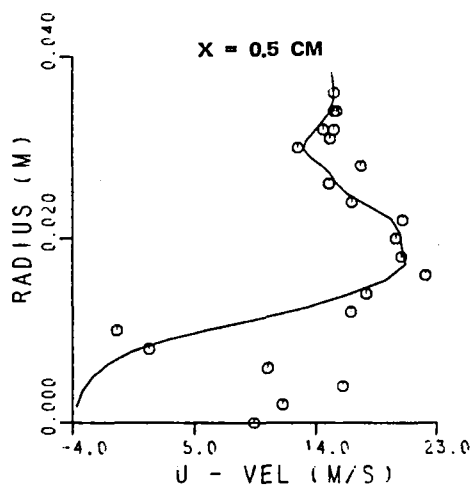


Figure 8.4-9. Second Set of Calculations - Axial Velocity Profiles.

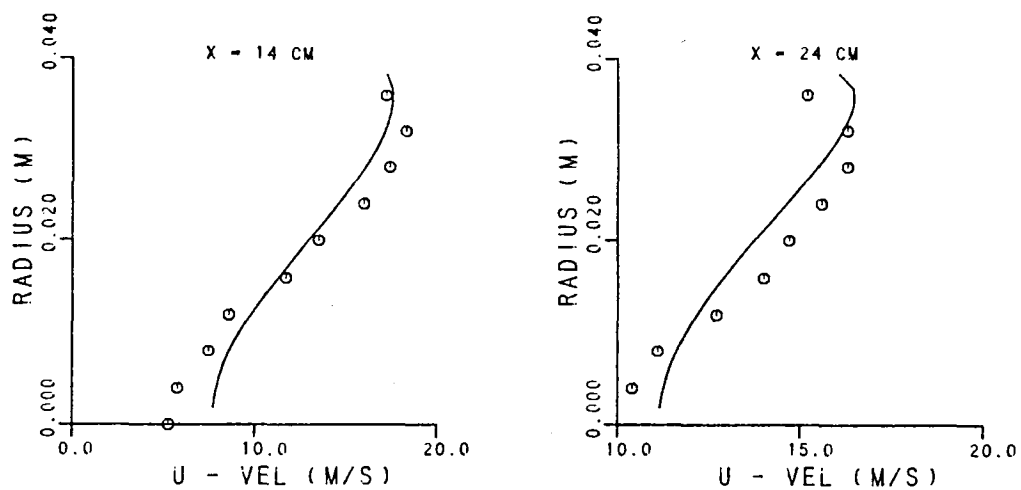


Figure 8.4-9. Second Set of Calculations - Axial Velocity Profiles (Cont'd).

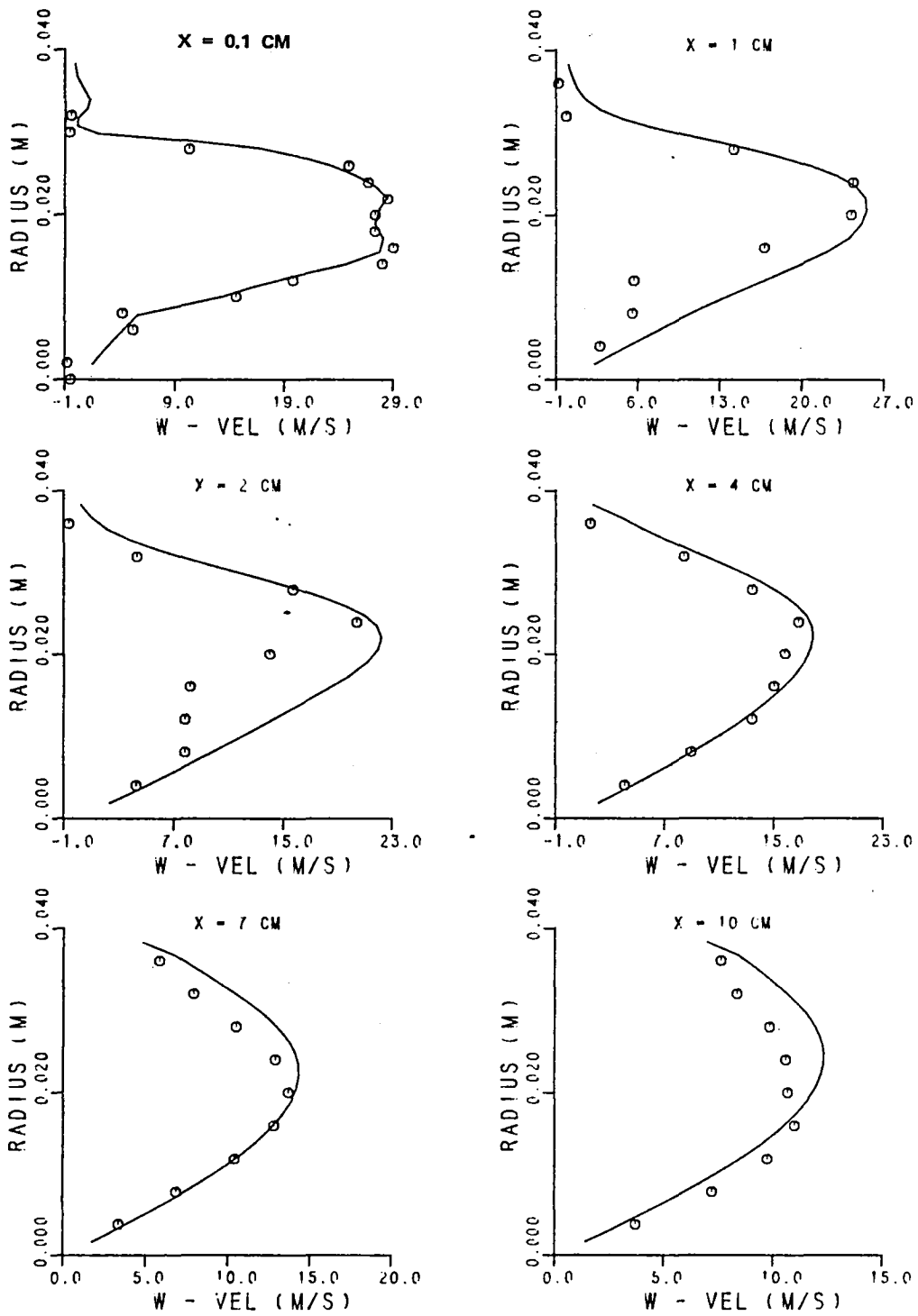


Figure 8.4-10. Second Set of Calculations - Swirl Velocity Profile.

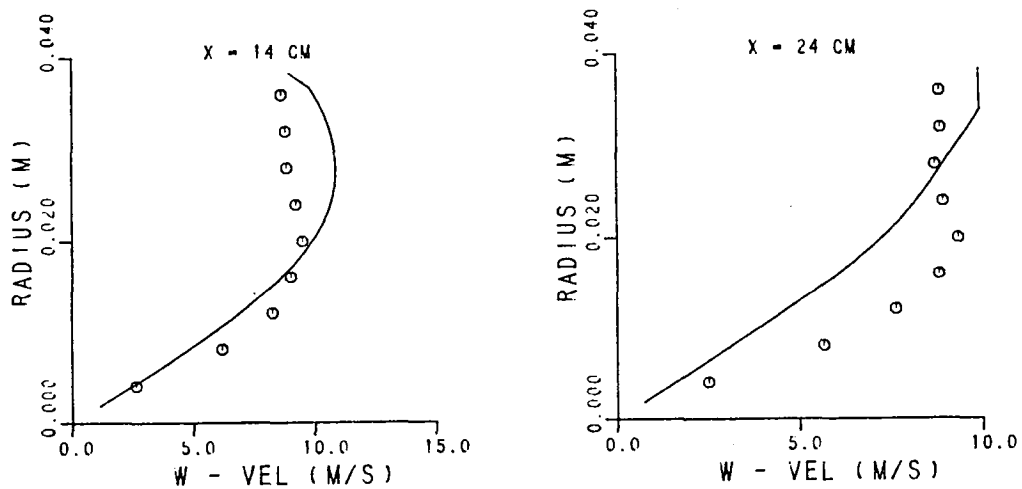


Figure 8.4-10. Second Set of Calculations - Swirl Velocity Profile (Cont'd).

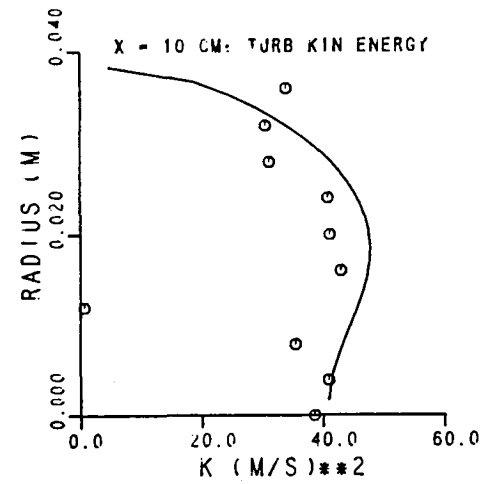
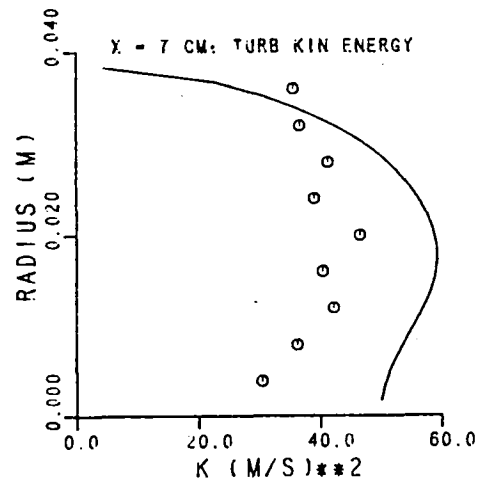
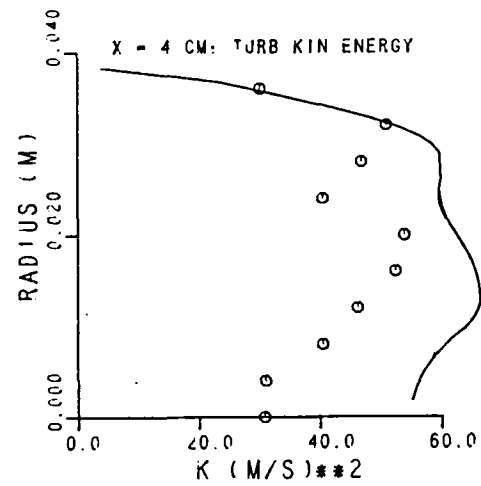
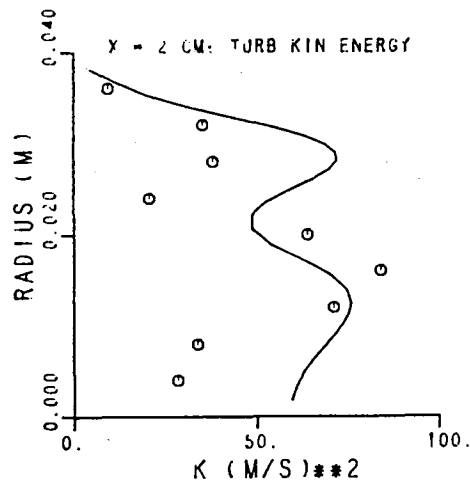
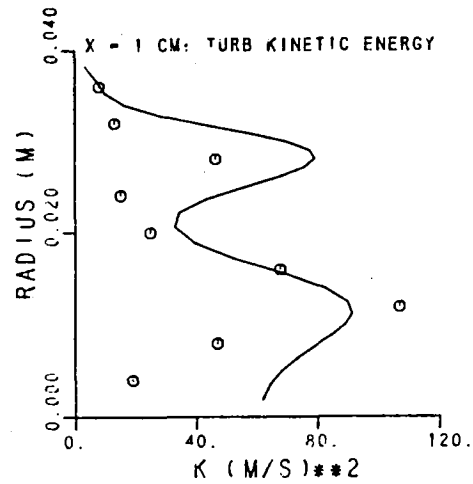
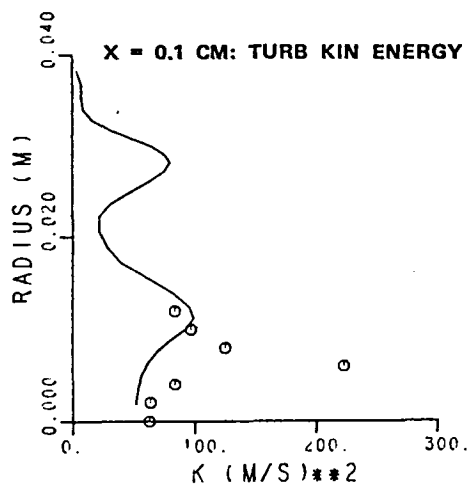


Figure 8.4-11. Second Set of Calculations- Turbulence Kinetic Energy Profiles.

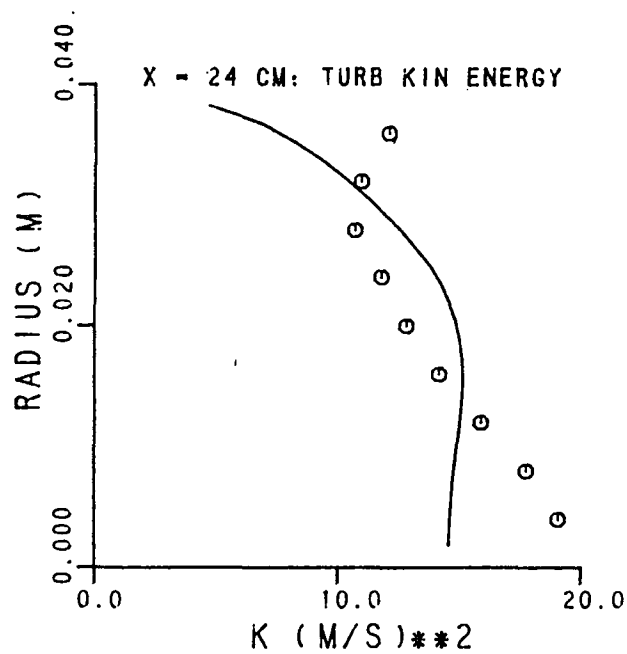
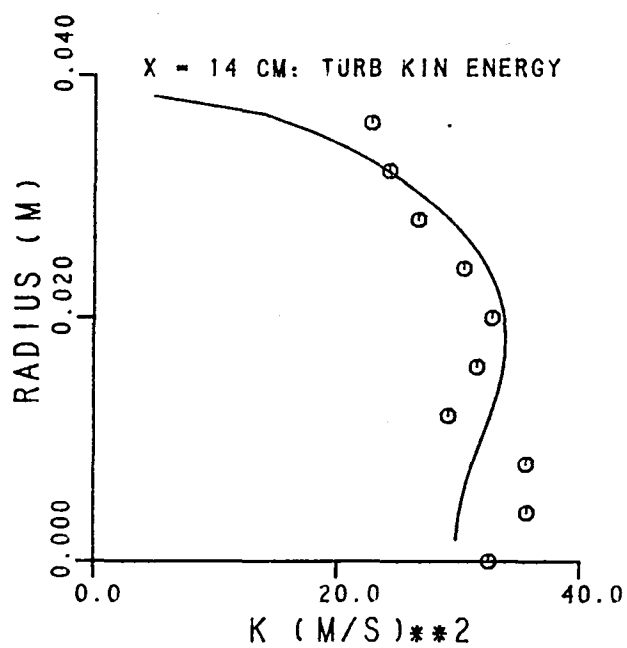


Figure 8.4-11. Second Set of Calculations- Turbulence Kinetic Energy Profiles (Cont'd).

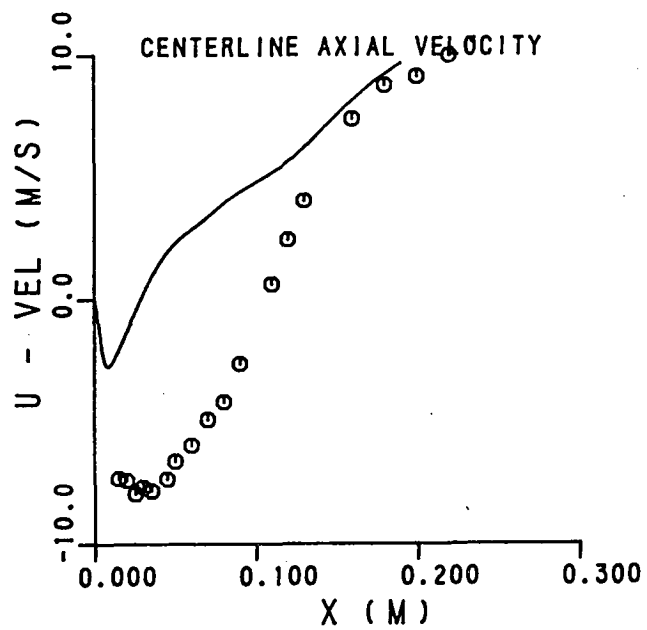


Figure 8.4-12. Third Set of Calculations - Centerline Axial Velocity Development.

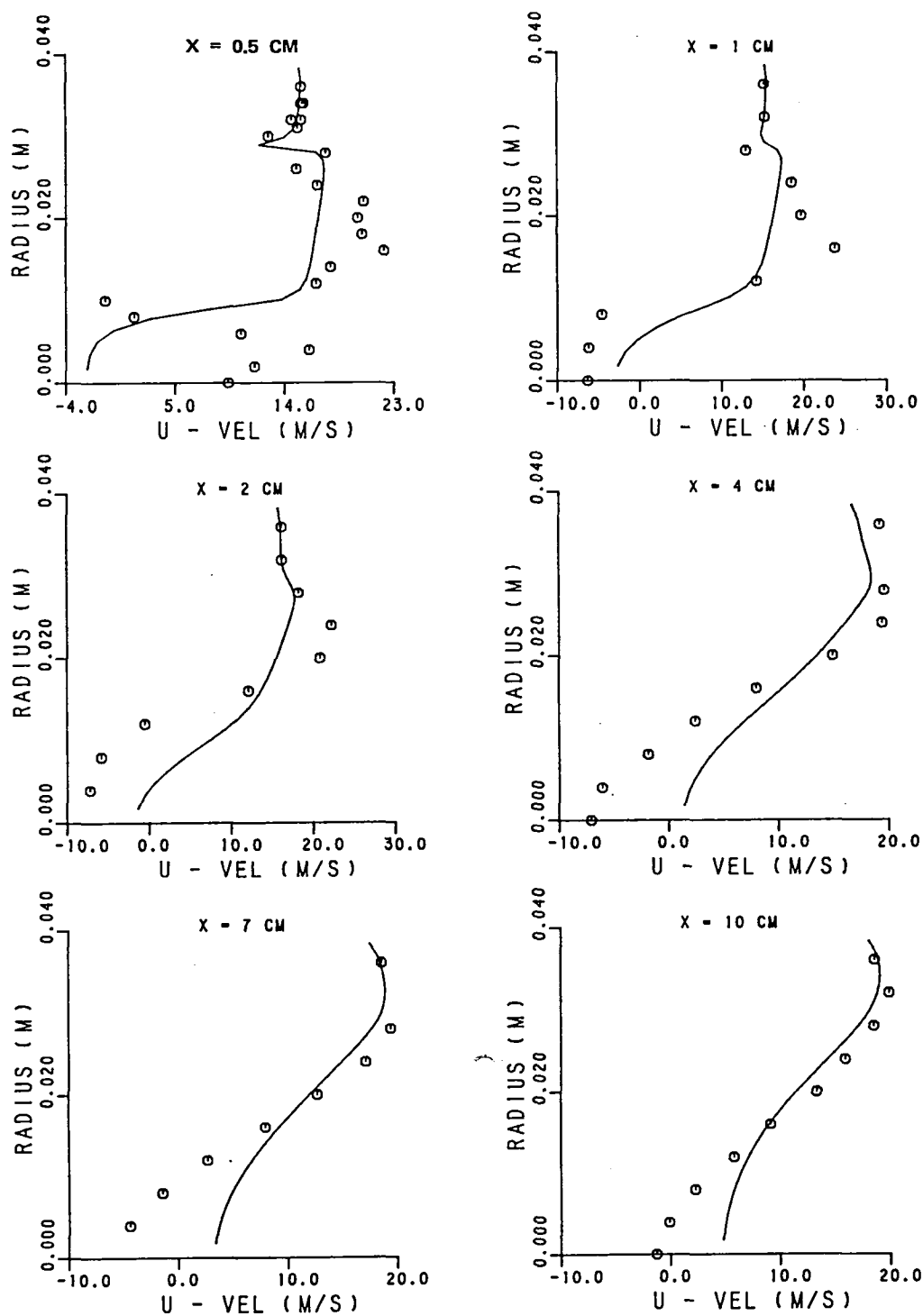


Figure 8.4-13. Third Set of Calculations - Axial Velocity Profiles.

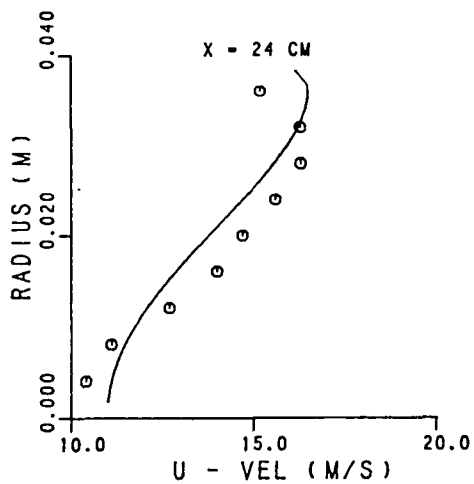
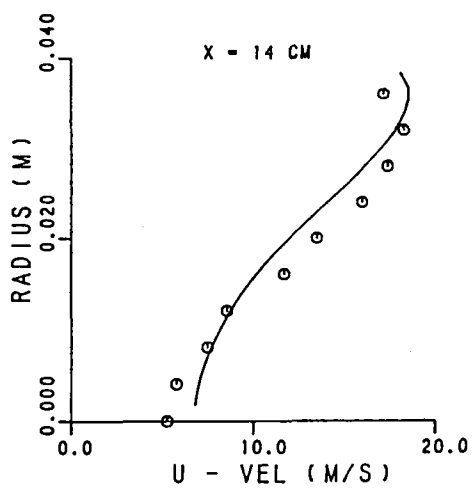


Figure 8.4-13. Third Set of Calculations - Axial Velocity Profiles (Cont'd).

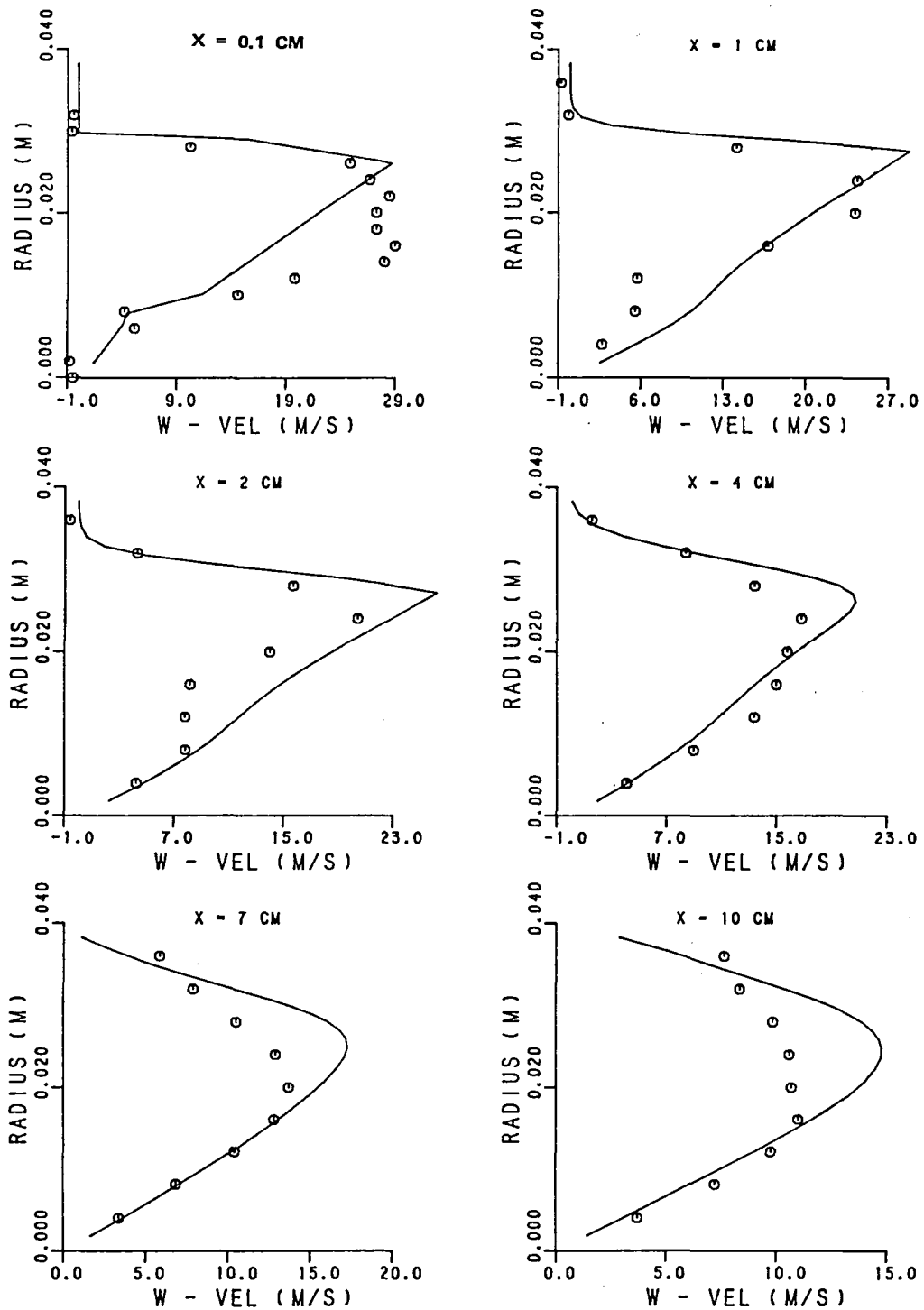


Figure 8.4-14. Third Set of Calculations - Swirl Velocity Profiles.

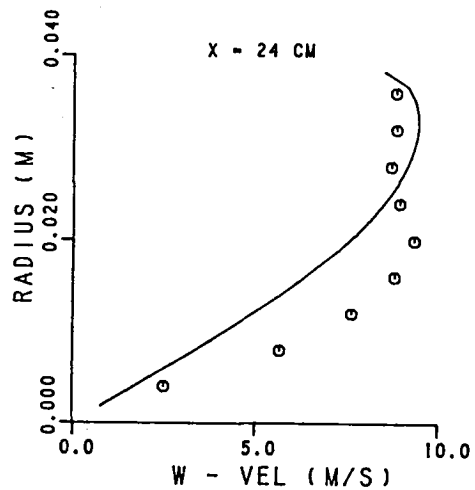
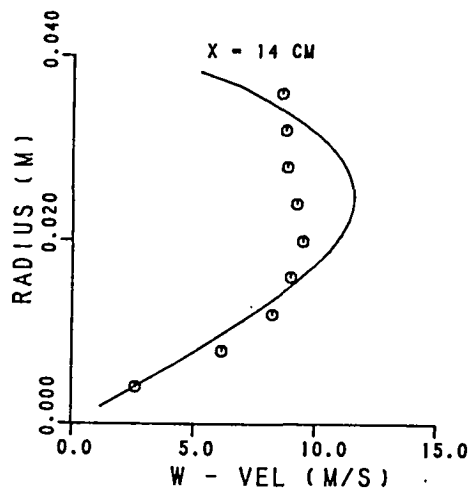


Figure 8.4-14. Third Set of Calculations - Swirl Velocity Profiles (Cont'd).

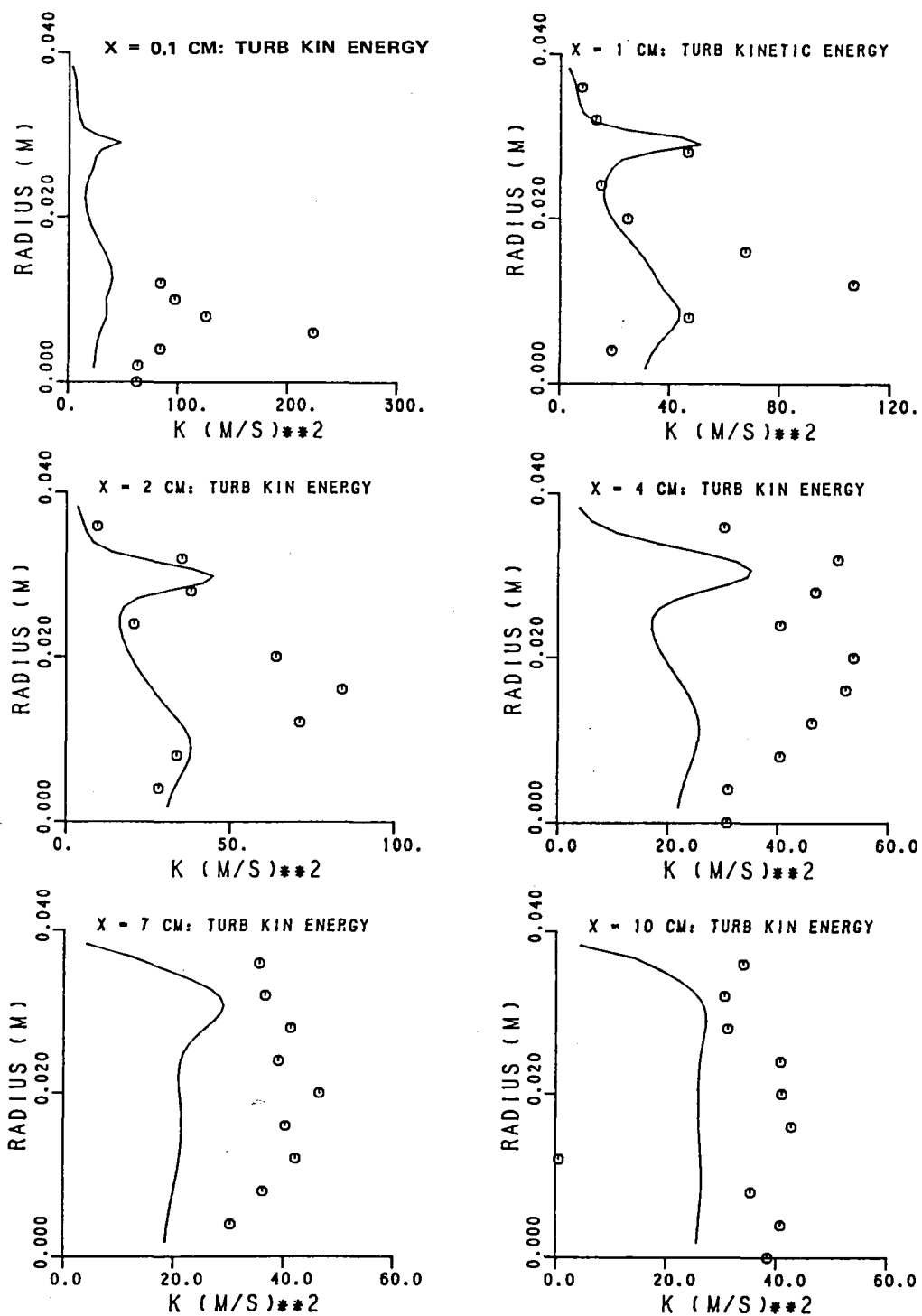


Figure 8.4-15. Third Set of Calculations - Turbulence Kinetic Energy Profiles.

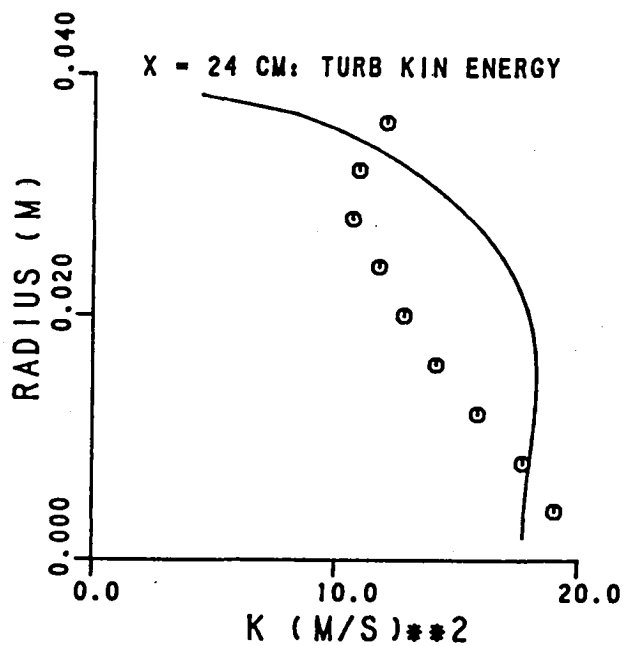
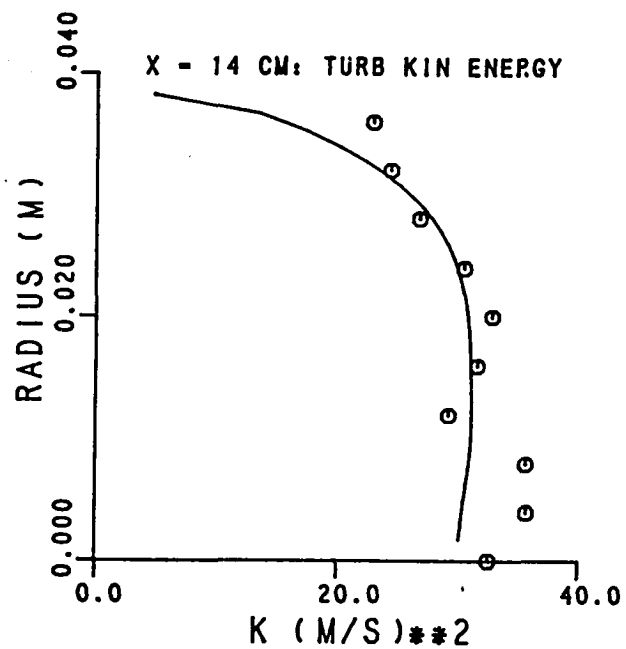


Figure 8.4-15. Third Set of Calculations - Turbulence Kinetic Energy Profiles (Cont'd).

8.5 Swirling Flow in a Pipe Expansion

Another benchmark test case selected was the swirling flow in a pipe expansion. Measurements in this flow field were made by Janjua,¹⁰⁰ et al., using a six-orientation, hot-wire anemometer with and without swirl. A schematic of this test setup is shown in Figure 8.5-1.

This figure illustrates the geometry of the test section for both swirling and nonswirling cases. For the nonswirling case, however, the hub radius of the swirler vane was equal to zero. Computations were started with plug flow at the inlet 4.0 cm upstream of the pipe expansion plane. Along the axis of the pipe, symmetry conditions were specified, and at the near wall nodes, wall boundary conditions were specified through the use of wall functions. At the exit boundary, zero axial gradient conditions were specified. The computational domain extended from 4.0 cm upstream of the sudden expansion to 220 cm downstream of the step in the axial (X) direction and from $R = 0$ to $R = 15$ cm in the radial direction.

Computations were made for nonswirling and swirling flows using the 2-D elliptic code with the following models:

- o Standard $k-\epsilon$ model
- o $k-\epsilon$ model with Richardson number correction
- o Algebraic stress model

Janjua Nonswirling Flow

For the nonswirling flow, the average inlet axial velocity upstream of the expansion was 5.385 m/sec. The inlet turbulence kinetic energy and length scale were assigned uniform values of $1.075 \text{ m}^2/\text{sec}^2$ and 0.003 meters, respectively. The inlet average

velocity is used to nondimensionalize the flow variables of interest in presenting the results.

Figure 8.5-2 presents for the nonswirling flow the standard $k-\epsilon$ model predictions and the data of Janjua, et al., for mean axial velocity profiles. In the region behind the step, the data does not show any recirculation zone even at $X = 19$ cm ($X/D = 0.5$). However, the predicted velocity profiles show the recirculation zone extending up to $X = 64$ cm ($X/D = 2.0$). Because of this, the predicted axial velocity values near the axis of the pipe are larger than the data.

In nonswirling flows, the streamline curvature effects are represented by the Richardson number, Ri_i , defined in Equation 18. The Richardson number is used to modify the turbulence model constant C_2 in the $k-\epsilon$ model to account for the extra turbulence production according to Equation 22. When the Richardson number corrections are included in the $k-\epsilon$ model, the predicted recirculation zone near the wall (Figure 8.5-3) has slightly higher reverse-velocity values than the standard $k-\epsilon$ model results.

The algebraic stress model predictions with Richardson number correction for the nonswirling flow in a pipe expansion are shown in Figures 8.5-4 and 8.5-5. The comparison between Janjua data and ASM predictions for mean axial velocity is shown in Figure 8.5-4. The algebraic stress model also predicts a recirculation zone that extends up to $\frac{X}{D} = 2$. ASM results are similar to the $k-\epsilon$ model results beyond $X = 64$ cm.

The ASM predictions for u' , v' , and $u'v'$ are shown in Figure 8.5-5 along with the data of Janjua, et al. The predicted u' values are slightly higher than data in the recirculation zone. Near the tube centerline, the algebraic stress model underestimates the u' values. Very similar characteristics are also seen in the v' profiles. The predicted \overline{uv} values are larger in magnitude than the

data in the recirculation zone. At the axis of the pipe, the data shows a nonzero \overline{uv} values beyond $\frac{X}{D} = 1$, while the predictions show a value of zero at the axis.

Chaturvedi Nonswirling Flow

In their publication, Janjua, et al., had compared their measurements with the hot-wire data of Chaturvedi.²¹⁷ In that report, significant differences were seen between the data of Chaturvedi and Janjua. To further elucidate flow field through a pipe expansion, Figures 8.5-6 through 8.5-9 show comparison between calculations and Chaturvedi data.

Figure 8.5-6 presents the results with the standard $k-\epsilon$ for mean axial velocity. These results are in good agreement with each other. The $k-\epsilon$ model as well as the Chaturvedi data show flow reversal regions near the wall of the pipe up to $\frac{X}{D} = 2$. The $k-\epsilon$ model predictions are also in agreement with the data near the axis of the tube.

Figure 8.5-7 shows the mean axial velocity comparison between Chaturvedi data and predictions obtained from a $k-\epsilon$ model with streamline curvature (Richardson number) corrections. These profiles are similar to the ones shown in Figure 8.5-6. The magnitude of maximum reverse velocities predicted is slightly greater when the Richardson number corrections are applied.

The comparison between Chaturvedi data and ASM predictions is shown in Figures 8.5-8 and 8.5-9. Figure 8.5-8 shows the results for mean axial velocity and u' . The mean axial velocity profiles are in good agreement with each other, especially in the recirculation zone. At $\frac{X}{D} = 0.5$, the ASM predictions for nondimensionalized RMS axial turbulence velocities (u'/U_{Ref}) are in good agreement with the data in the region behind the pipe expansion step. The u'

values are slightly overpredicted in the region near the axis of the pipe. Beyond $\frac{X}{D} = 1$, the u' values near the axis of the tube are underestimated. However, the predicted u' profiles in the region behind the step are in good agreement with the data. A similar trend is also seen in the results for the RMS radial velocity fluctuations (v'), as shown in Figure 8.5-9.

The ASM predictions and Chaturvedi data for the Reynolds shear stress (\overline{uv}) are shown in Figure 8.5-9. The data and predictions are in good agreement at $\frac{X}{D} = 0.5$. Beyond this station, the ASM overestimates the magnitude of \overline{uv} in the recirculation zone. The Chaturvedi data shows a faster decay rate of the peak \overline{uv} value than the predictions. In the region close to the axis of the tube, the Chaturvedi data and predictions are in good qualitative agreement.

Swirling Flow

Velocity measurements in a swirling flow through a pipe expansion were made by Janjua, et al., in a test setup shown schematically in Figure 8.5-1. The average inlet axial velocity was estimated to be 10.5 m/sec. For the swirl angle of 38 degrees, the average inlet swirl velocity was 8.2 m/sec. Computations for this case also were started 4.0 cm upstream of the sudden expansion, with uniform profiles for axial velocity, turbulence kinetic energy, and length scale of 10.5 m/sec, $3.308 \text{ m}^2/\text{sec}^2$, and 0.003 m, respectively. The 2-D elliptic code with 2200 nodes was used to obtain solutions. Computations were made with the following turbulence models:

- o Standard k- ϵ model
- o k- ϵ model with streamline curvature correction due to swirl
- o Algebraic stress model.

The standard $k-\epsilon$ model predictions are presented in Figure 8.5-10. At $\frac{X}{D} = 0.5$, the predictions show flow reversal regions near the axis as well as in the region behind the axisymmetric step. The data shows a recirculation zone near the axis of the pipe. The measured recirculation zone height is much larger than the predictions. The data as well as the $k-\epsilon$ model predictions show a maximum reverse velocity of about 32 percent of the reference velocity. The location of the maximum reversal velocity is predicted to be at the axis, while the data shows it to lie off-axis. The peak reverse-flow velocity values at $\frac{X}{D} = 0.5$ are under-predicted by the $k-\epsilon$ model. At $\frac{X}{D} = 1$, the agreement between data and predictions is improved. The predicted profile shows the location of the peak u -velocity occurring at a higher radial location than that at $\frac{X}{D} = 0.5$. This is because of the centrifugal acceleration caused by swirl. At $\frac{X}{D} = 1.5$, the agreement between data and predictions is good.

The $k-\epsilon$ model predictions and the measured values for tangential velocity are shown in Figure 8.5-10. The $k-\epsilon$ model predictions as well as the data show a solid-body rotational structure ($W/r = \text{const.}$). At $\frac{X}{D} = 0.5$, the data shows some scatter near the peak location, but the data indicates that location of the peak tends to shift toward the axis of the pipe. In view of the centrifugal acceleration caused by a swirl, it is reasonable to expect the peak W values to occur closer to the wall of the pipe. This behavior is correctly predicted by the $k-\epsilon$ model.

The predictions obtained from the $k-\epsilon$ model with streamline curvature corrections due to swirl are illustrated in Figure 8.5-11. The streamline curvature correction due to swirl is applied in a manner identical to that outlined in Paragraph 8.1. The figure shows the comparison between data and predictions for

mean axial and tangential velocity profiles. The predicted profiles in this figure have similar characteristics to those obtained from standard $k-\epsilon$ model. At $\frac{X}{D} = 0.5$, a slight reduction in the peak positive as well as negative values is predicted with the Richardson number correction compared to the standard $k-\epsilon$ model results. Similarly, a slight reduction in the peak W values can be seen in the swirl velocity profiles when compared to the standard $k-\epsilon$ model results. At the downstream stations, the effects of streamline curvature correction are negligible.

The ASM predictions are illustrated in Figures 8.5-12 through 8.5-17. The ASM results for mean axial velocity have very similar characteristics to the $k-\epsilon$ model results. The agreement between the data and ASM results is good at $\frac{X}{D} = 1.5$. The ASM predictions for swirl velocity are also similar to the $k-\epsilon$ model results.

The ASM predictions and the data for RMS axial turbulence velocity fluctuations are shown in Figure 8.5-13. At $\frac{X}{D} = 0.5$, the predicted u' profile shows two peaks, one corresponding to the shear layer from the hub of the swirler and the other from the tip of the swirler vanes. The data shows only the peak corresponding to the tip. The ASM overestimates the u' value in the recirculation zone behind the hub and underestimates it in the region behind the pipe expansion step. At $\frac{X}{D} = 1$, the agreement between the data and ASM prediction is poor; at $\frac{X}{D} = 1.5$, the agreement is good.

The comparison between data and ASM prediction for the radial turbulence intensity (v') is also shown in Figure 8.5-13. At $\frac{X}{D} = 0.5$, the ASM substantially overpredicts the v' magnitudes. But further downstream the correlation is good. Similar observations can be made for W' as shown in Figure 8.5-14.

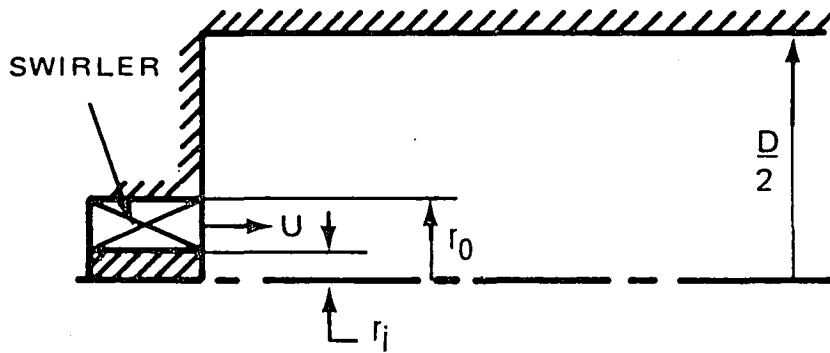
The Reynolds shear stress components (\overline{uv} , \overline{uw} and \overline{vw}) predicted by the ASM are shown in Figures 8.5-15 through 8.5-17. Other than the last station ($\frac{X}{D} = 1.5$), the agreement between the data and the predictions is generally poor.

The results presented in this paragraph can be summarized as follows:

- o The standard $k-\epsilon$ model and the ASM predicts the mean velocity profiles accurately for the nonswirling flow through the pipe expansion. The ASM predictions for the Reynolds stress are in agreement with the data of Chaturvedi.
- o In swirling flows, the standard $k-\epsilon$ model correctly predicts the axial velocity far downstream from the step. In the near wake region behind the sudden expansion, the agreement is qualitative. The predictions for mean swirl velocity are only in qualitative agreement with the data.
- o The streamline curvature correction due to swirl improves the model predictions slightly.
- o The ASM predictions for mean velocity are similar to the standard $k-\epsilon$ model results. The ASM predictions for Reynolds normal stresses are in good agreement with data for the downstream region. In the region near the sudden expansion, the ASM predictions and the Janjua data are in qualitative agreement. The agreement between data and ASM predictions for shear stress is poor.

JANJUA ET AL

SWIRLING FLOW IN A PIPE EXPANSION



$$r_i = 0.04 \text{ M}$$

$$r_o = 0.075 \text{ M}$$

$$D = 0.30 \text{ M}$$

$$Re_D = 50000$$

$$U = 4.45 \text{ M/S}$$

$$W = 3.47 \text{ M/S}$$

AND

$$U = 5.985 \text{ M/S}$$

$$W = 0$$

Figure 8.5-1. Test Setup of Swirling Flow in a Pipe Expansion.

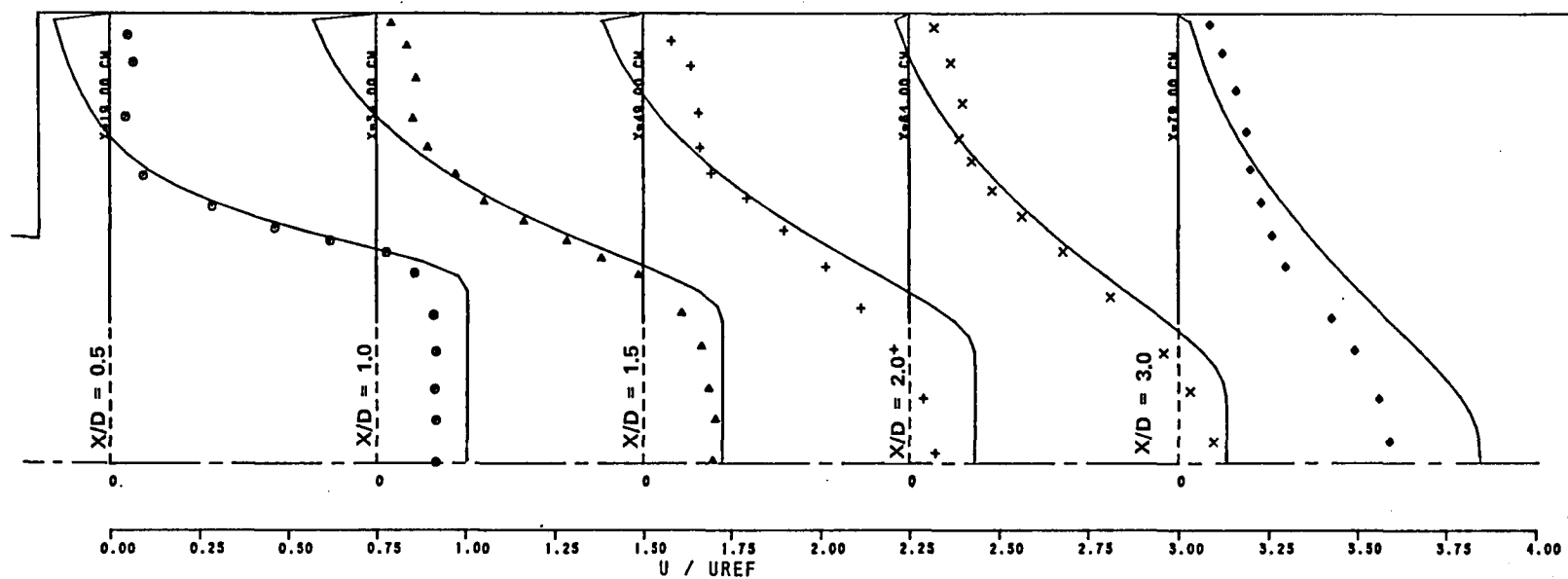


Figure 8.5-2. $k-\epsilon$ Model for Nonswirling Flow - Axial Velocity Profiles.

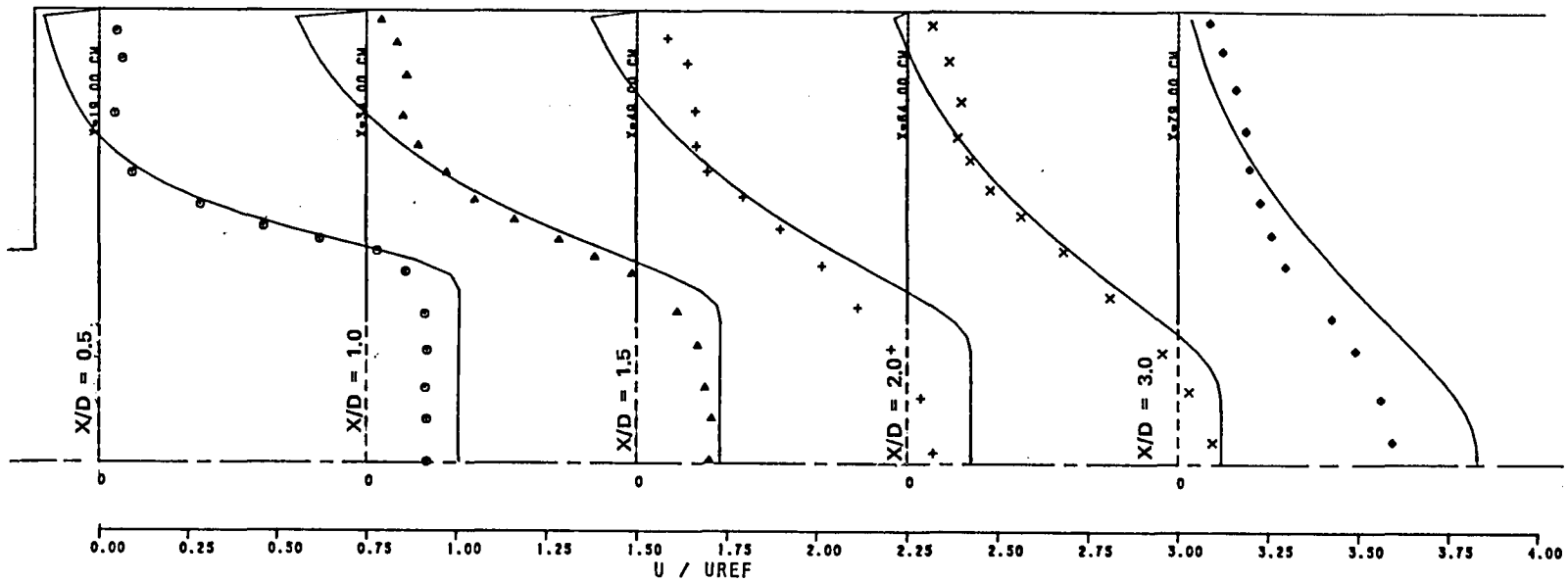


Figure 8.5-3. k - ϵ Model with Richardson Number Correction - Axial Velocity Profiles in Nonswirling Flow Field.

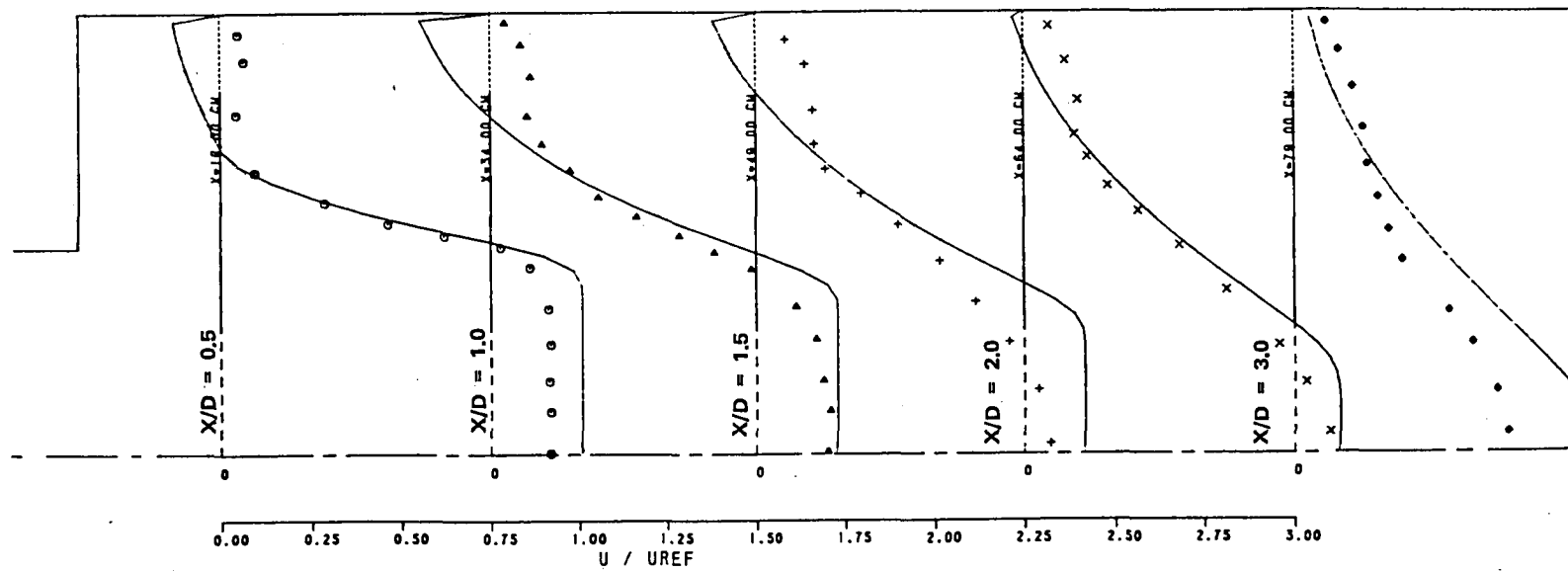


Figure 8.5-4. ASM - Axial Velocity Profiles (Nonswirling).

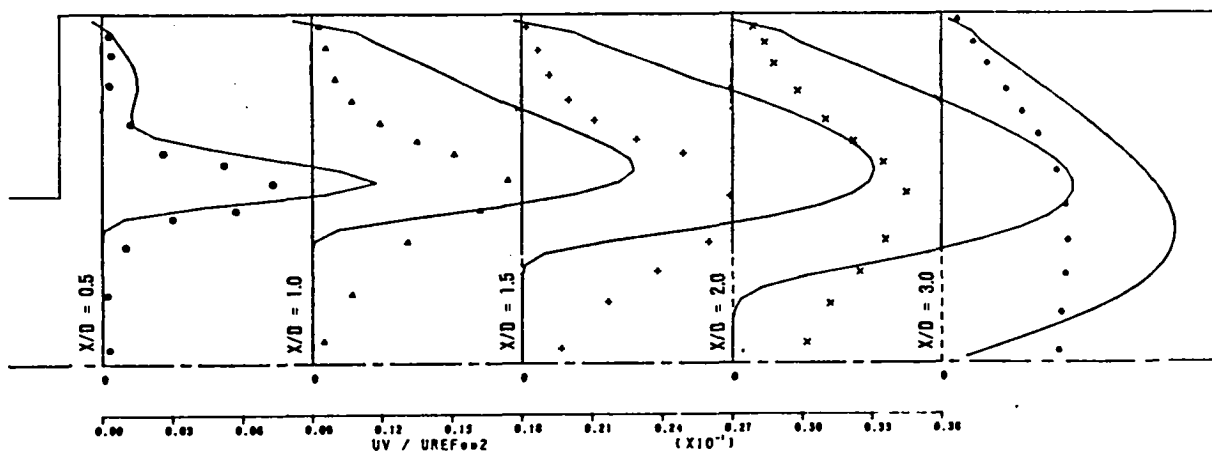
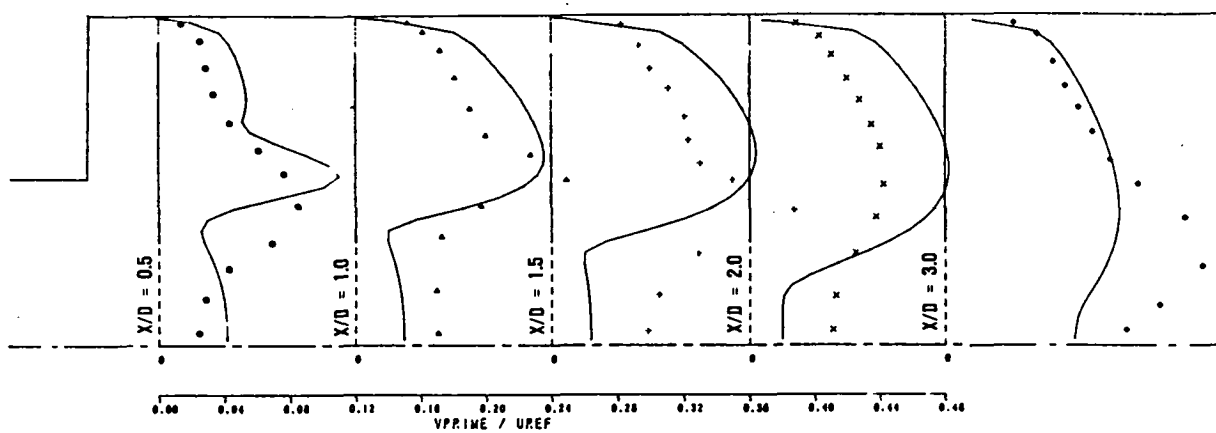
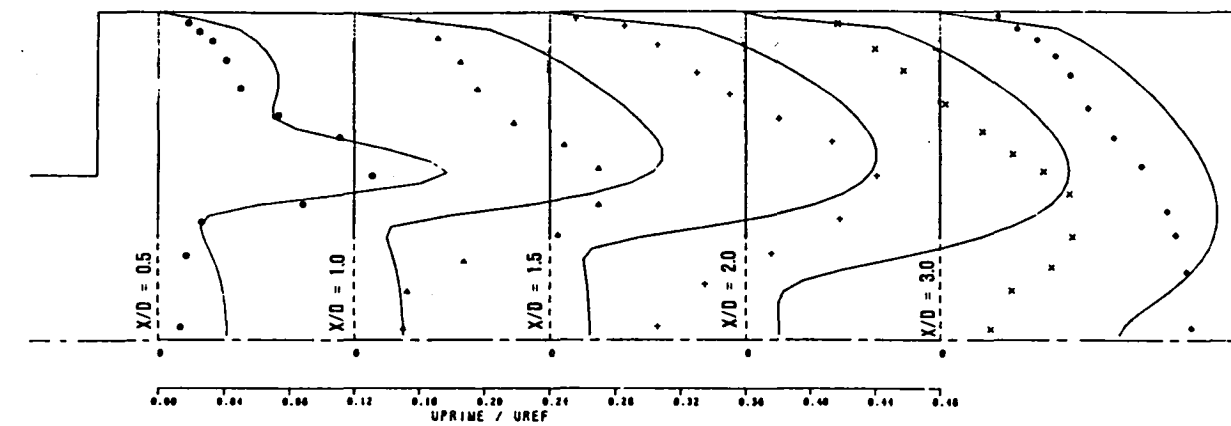


Figure 8.5-5. Nonswirling u' , v' and \overline{uv} Profiles.

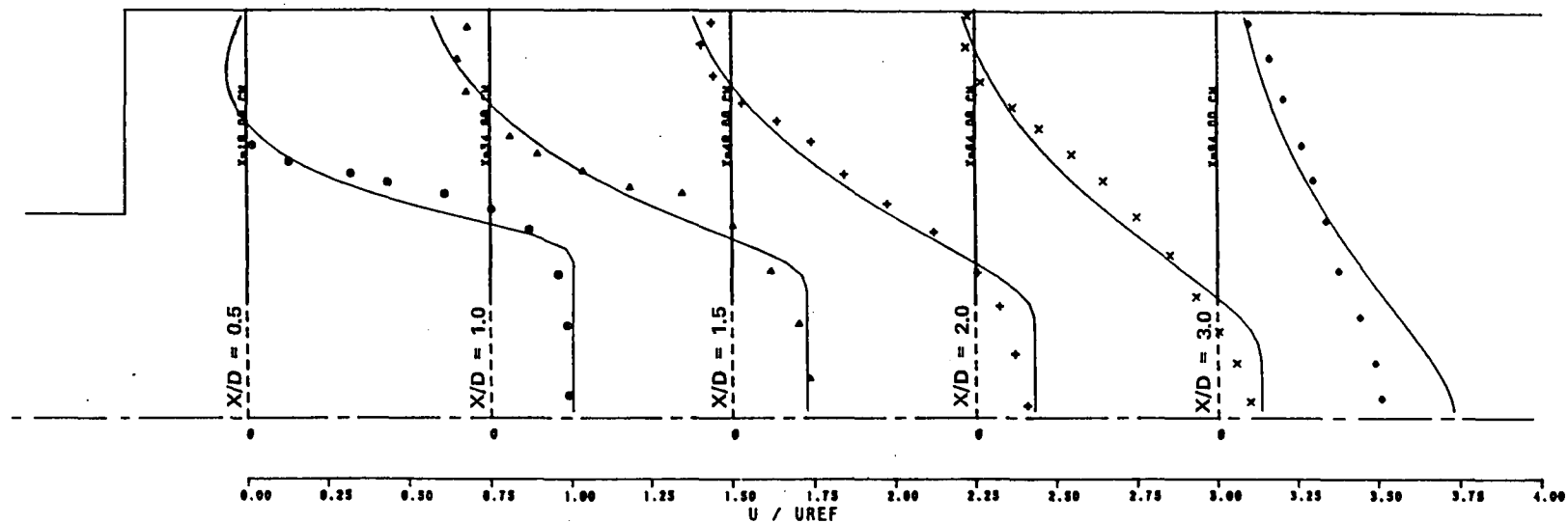


Figure 8.5-6. Comparison Between $k-\epsilon$ Model Prediction and Chaturvedi Data of Mean Axial Velocity.

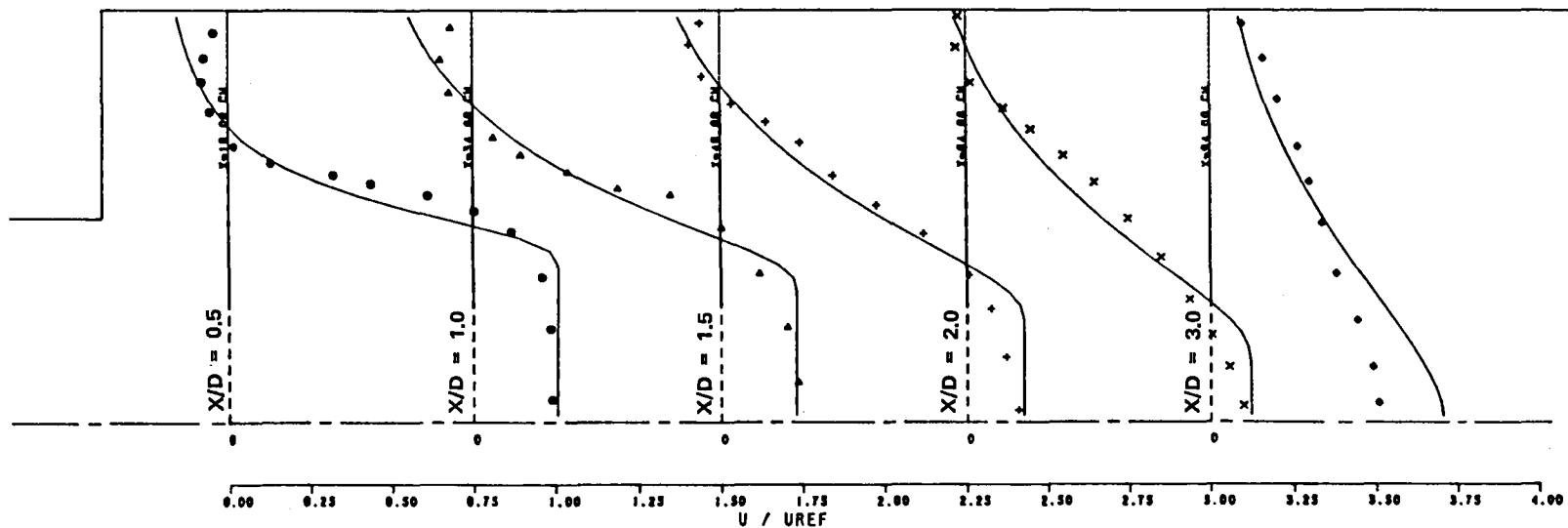


Figure 8.5-7. Chaturvedi Mean Axial Velocity Data and $k-\epsilon$ Model with Richardson Number Correction.

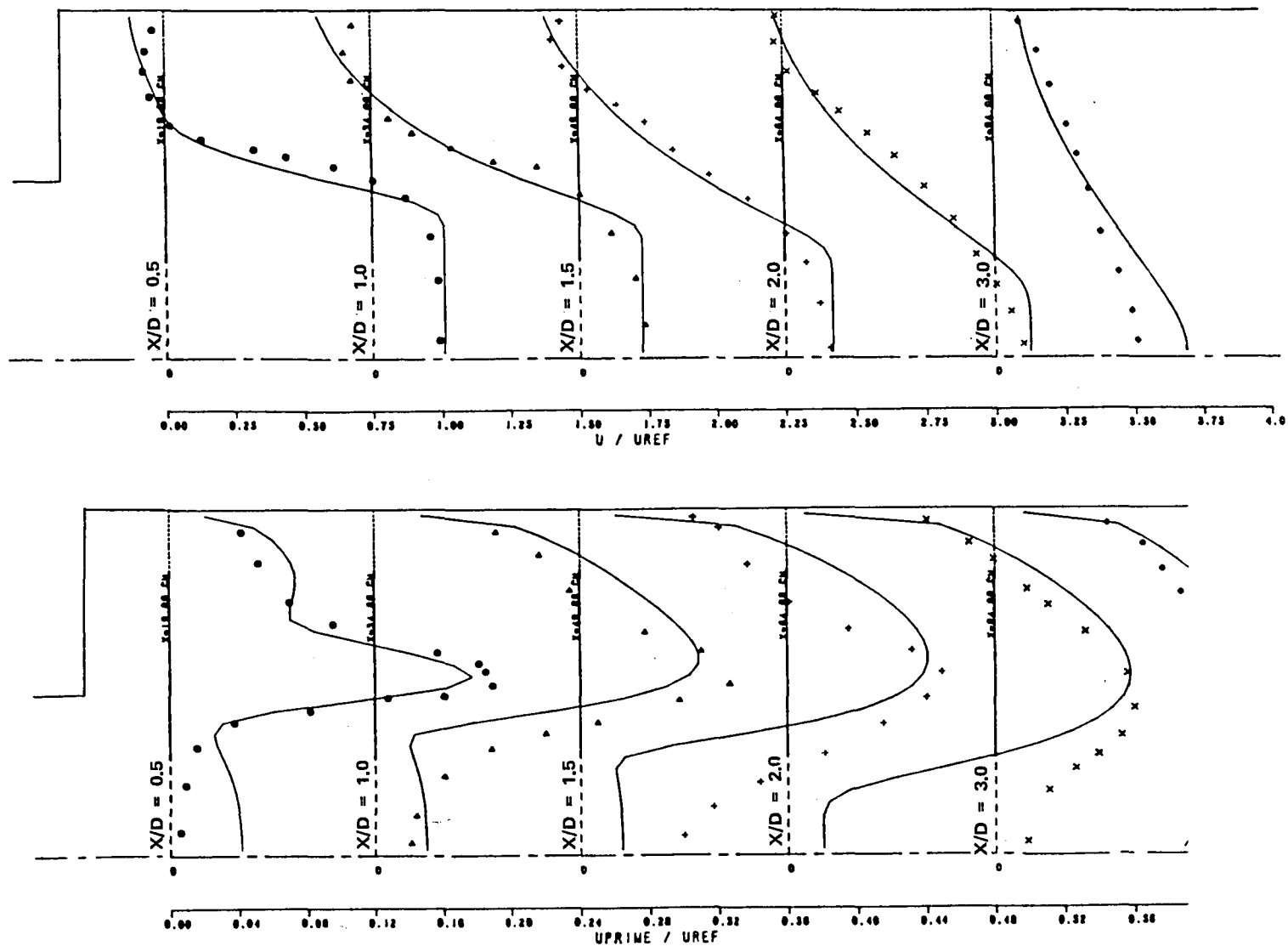


Figure 8.5-8. ASM Prediction and Chaturvedi Data - Mean and Fluctuating Axial Velocity Profiles.

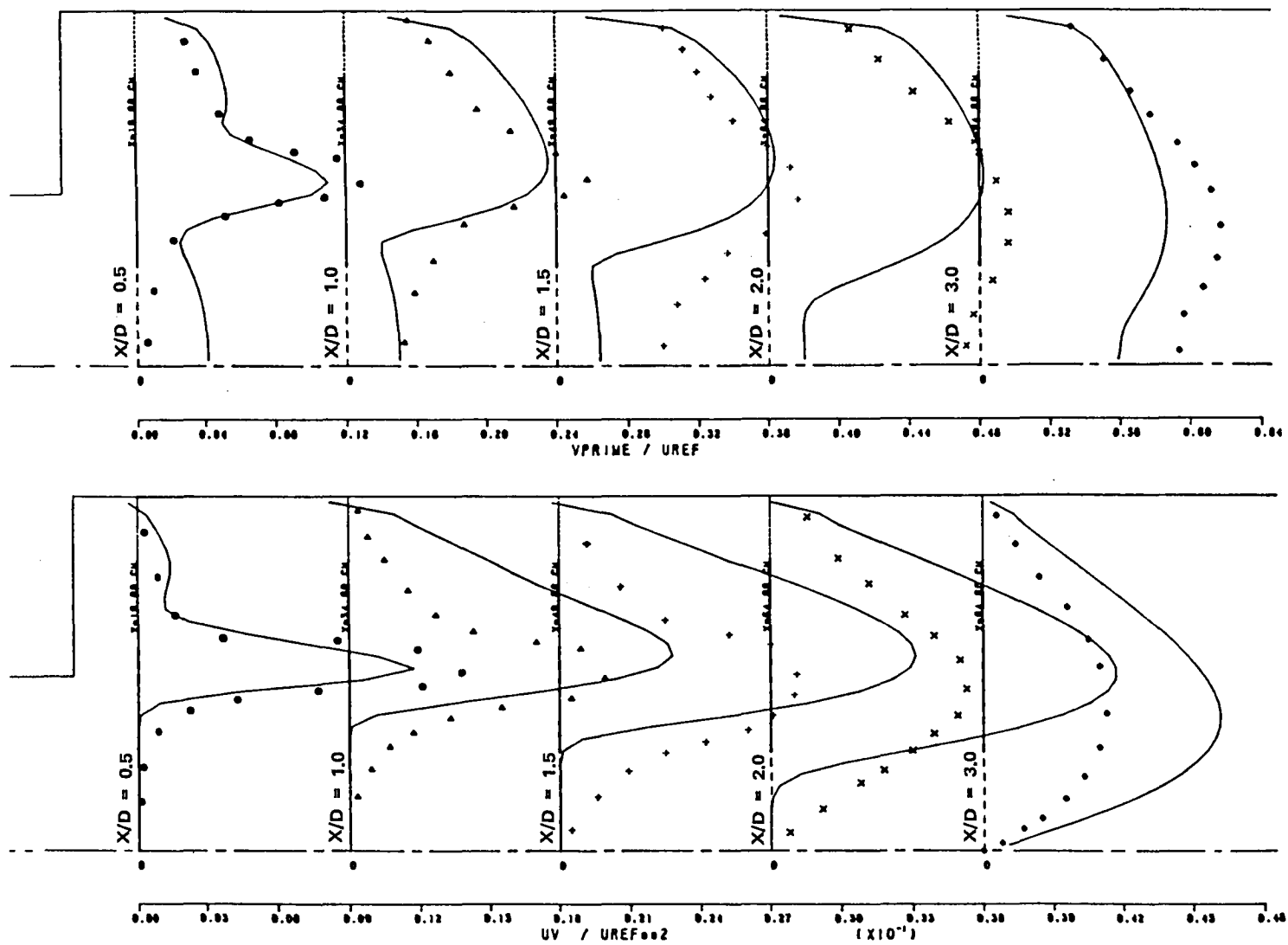


Figure 8.5-9. ASM Predictions and Chaturvedi Data - v' and uv Profiles.

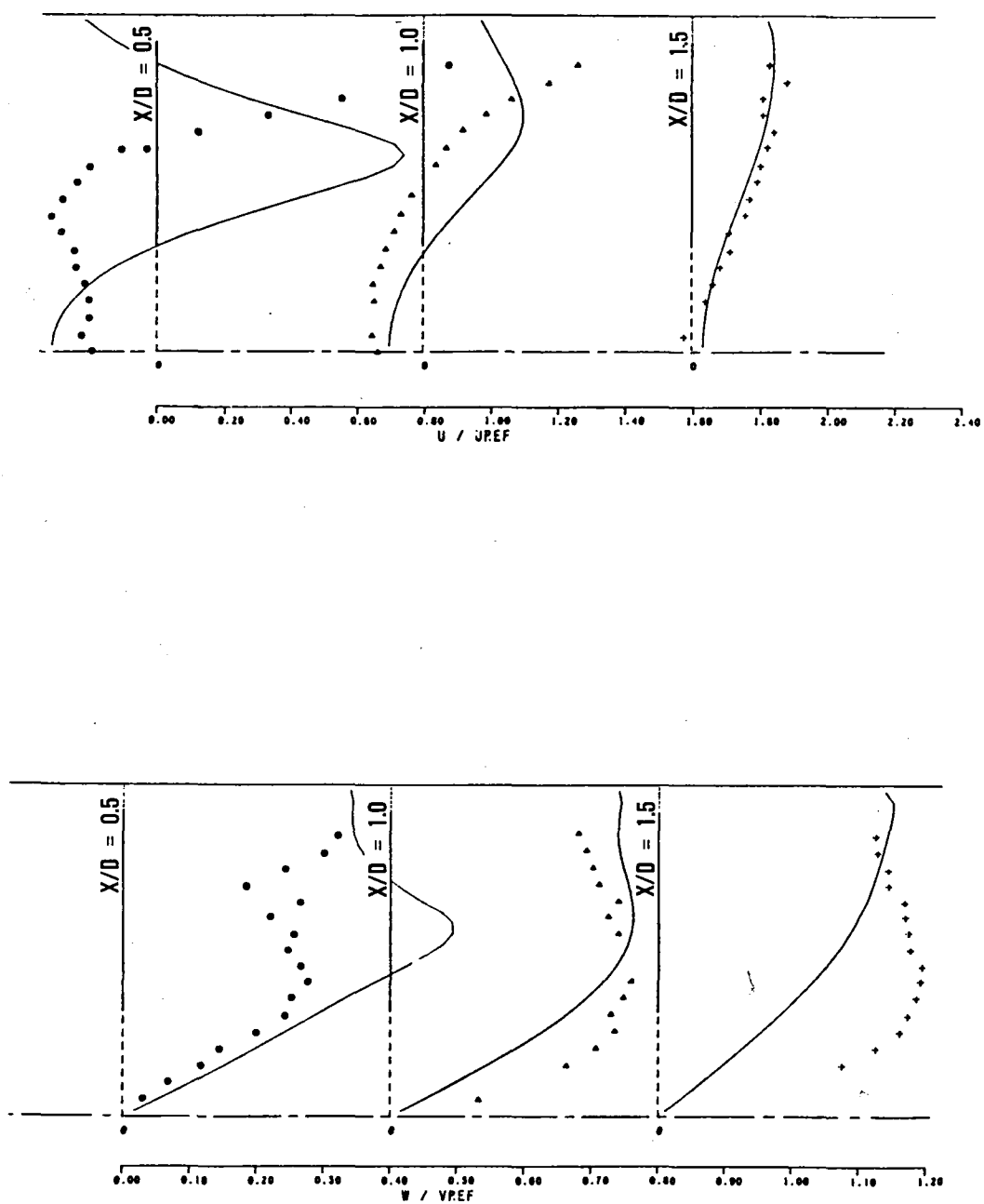


Figure 8.5-10. Standard $k-\epsilon$ Model - Mean Axial and Tangential Velocity Profiles.

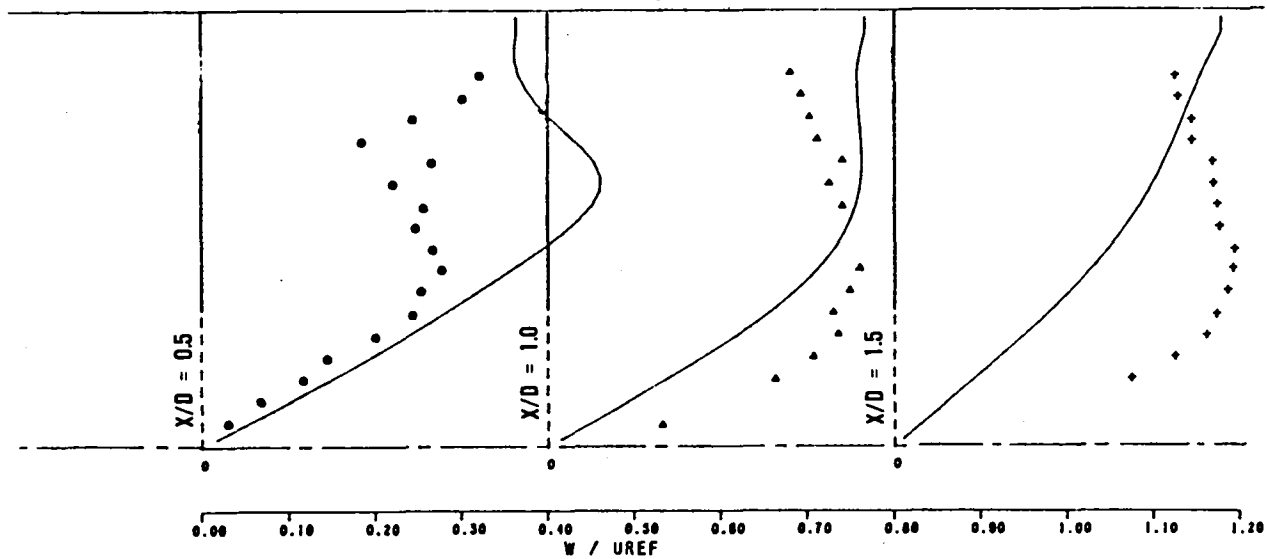
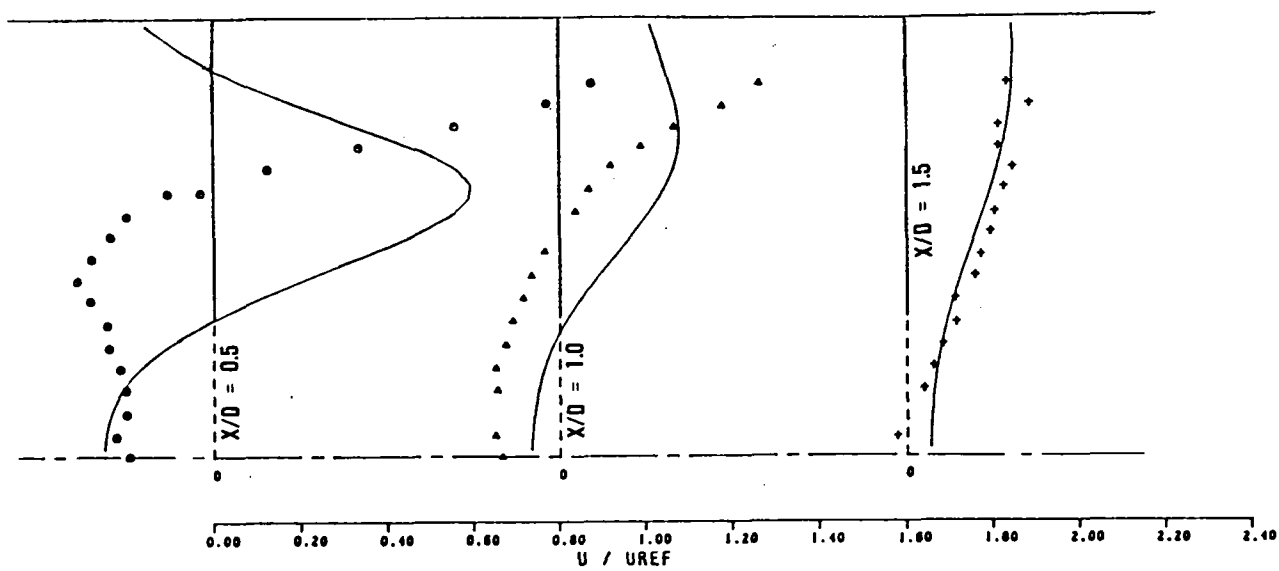


Figure 8.5-11. $k-\epsilon$ Model with Richardson Number Correction - Mean Axial and Tangential Velocity Profiles.

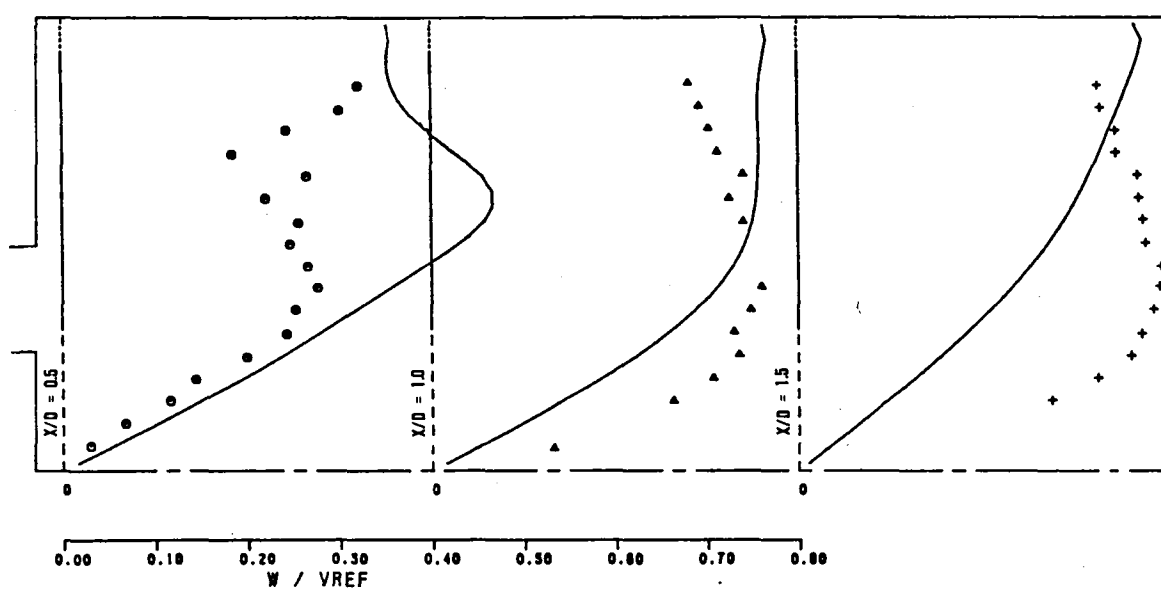
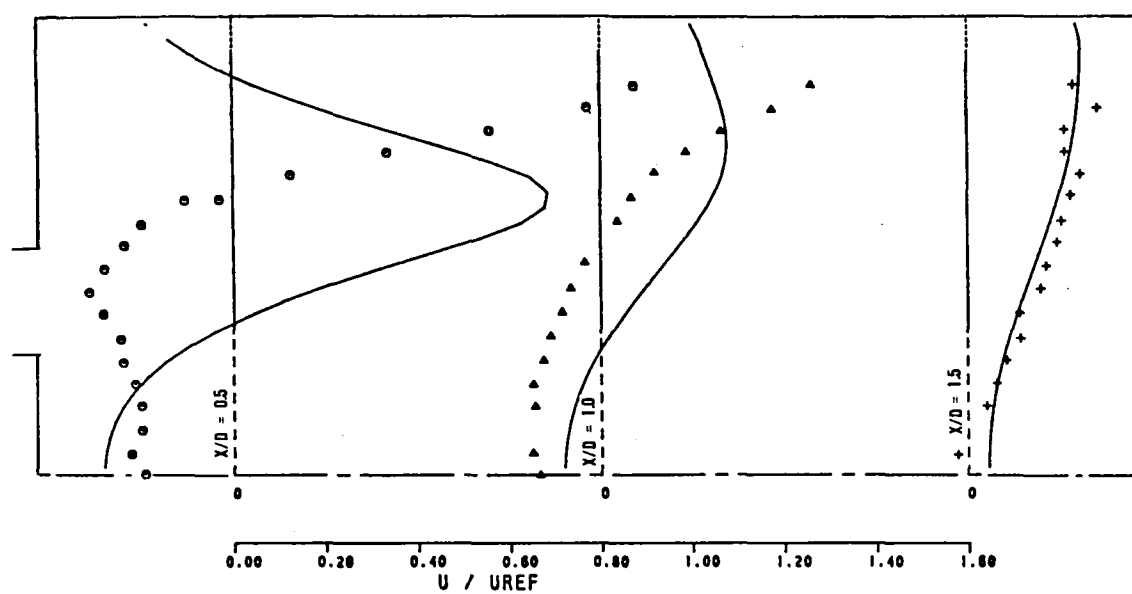


Figure 8.5-12. ASM - Mean Axial and Tangential Velocity Profiles.

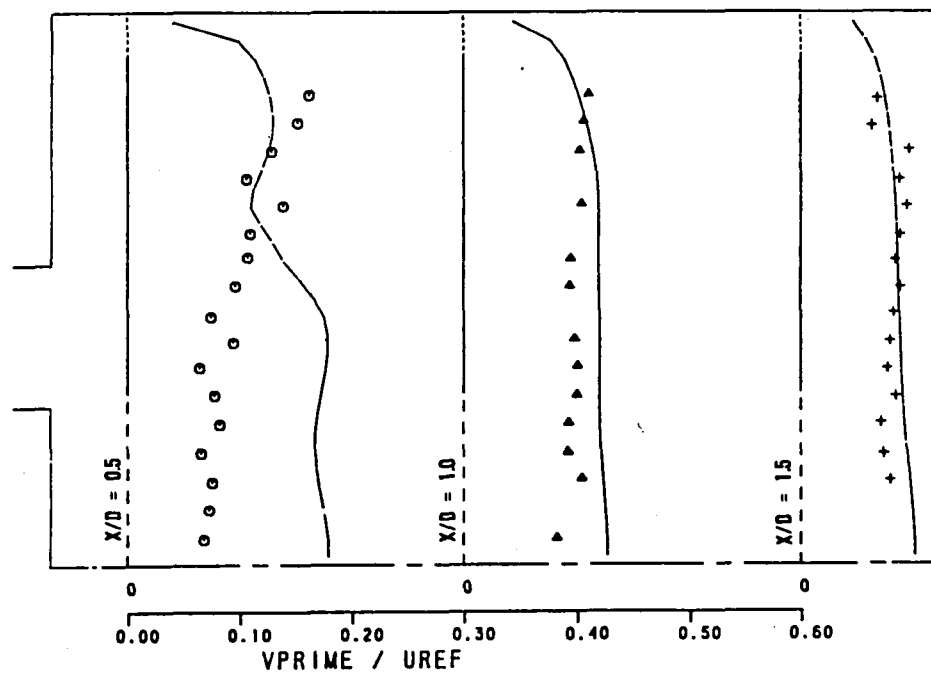
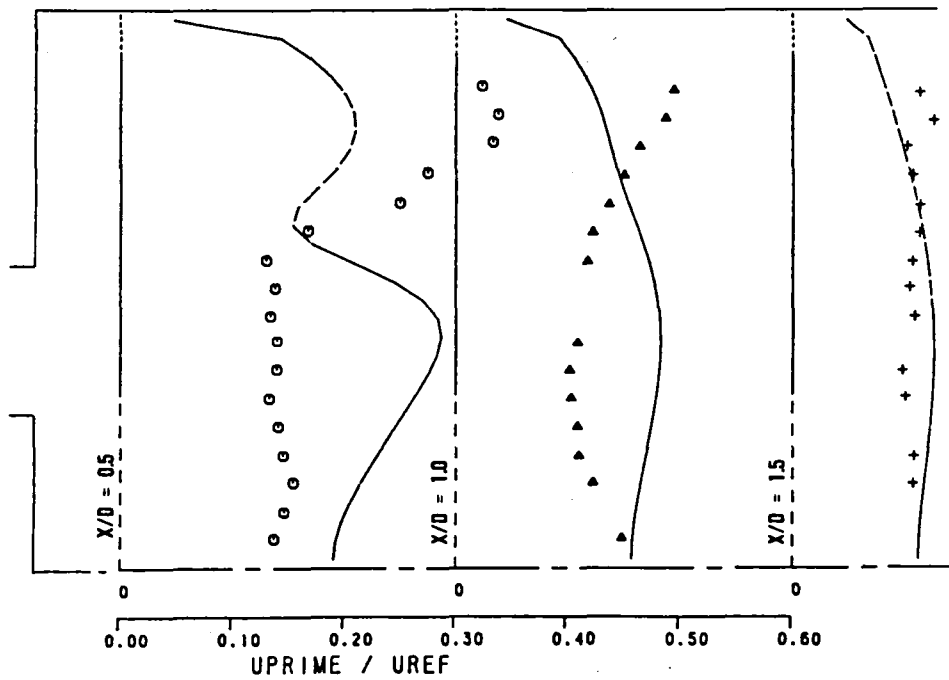


Figure 8.5-13. ASM - u' and v' Profiles.

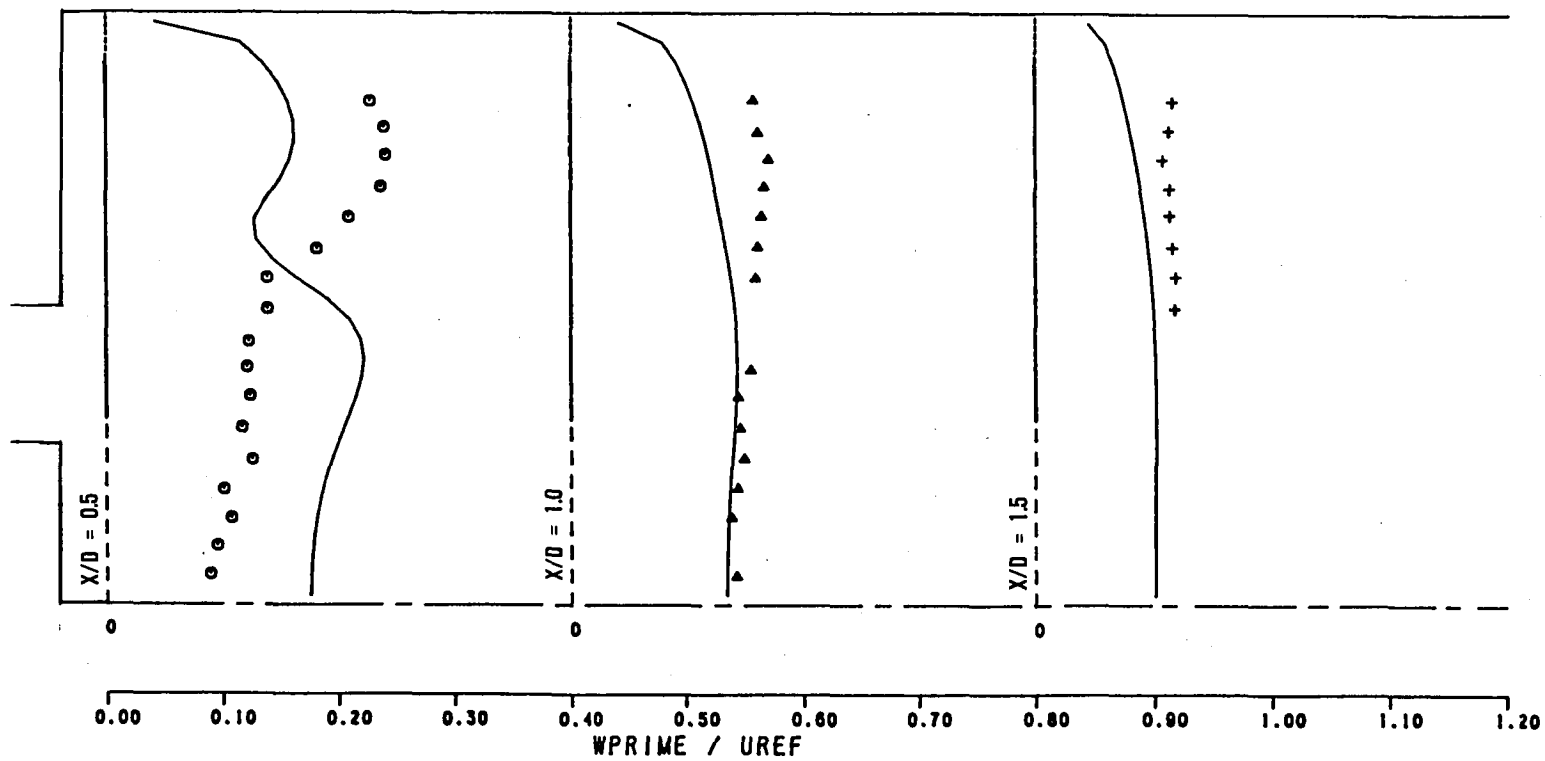


Figure 8.5-14. ASM - W' Profiles.

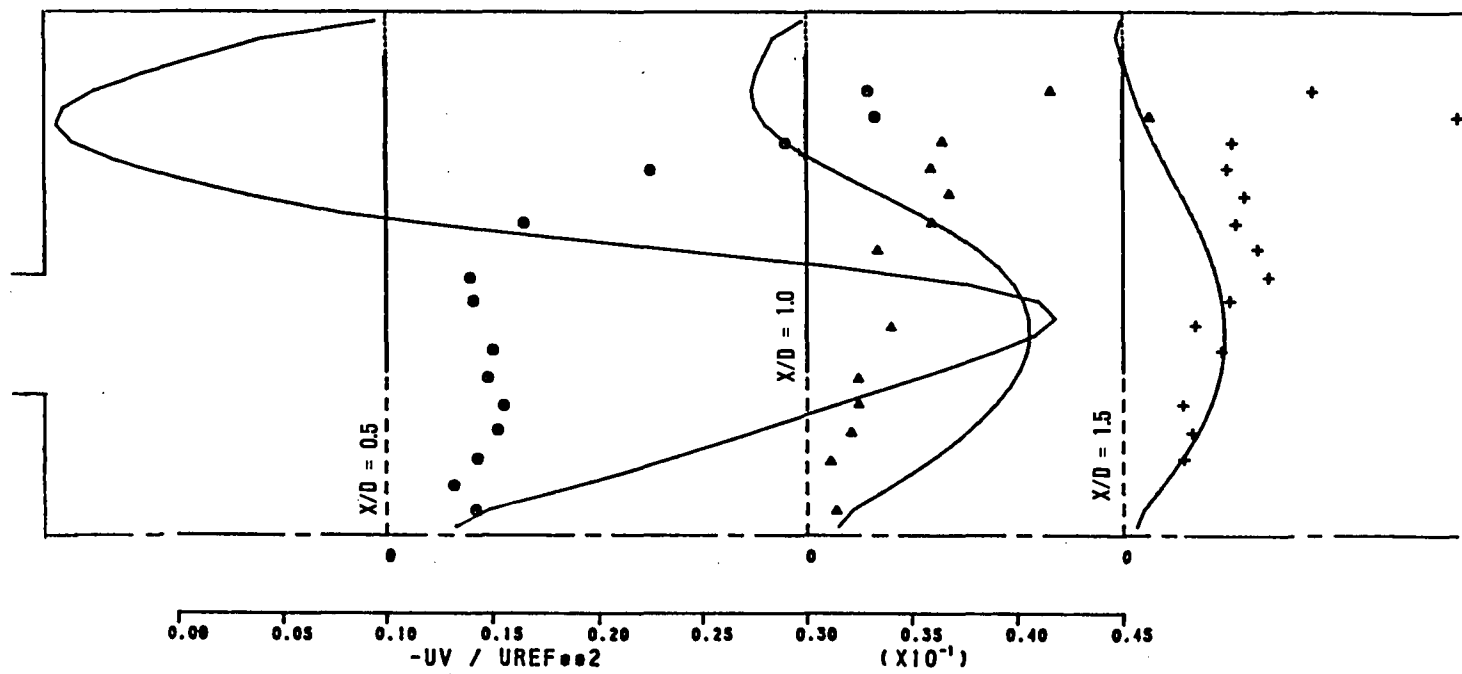


Figure 8.5-15. ASM - Reynolds Stress Shear Component (\overline{uv}) .

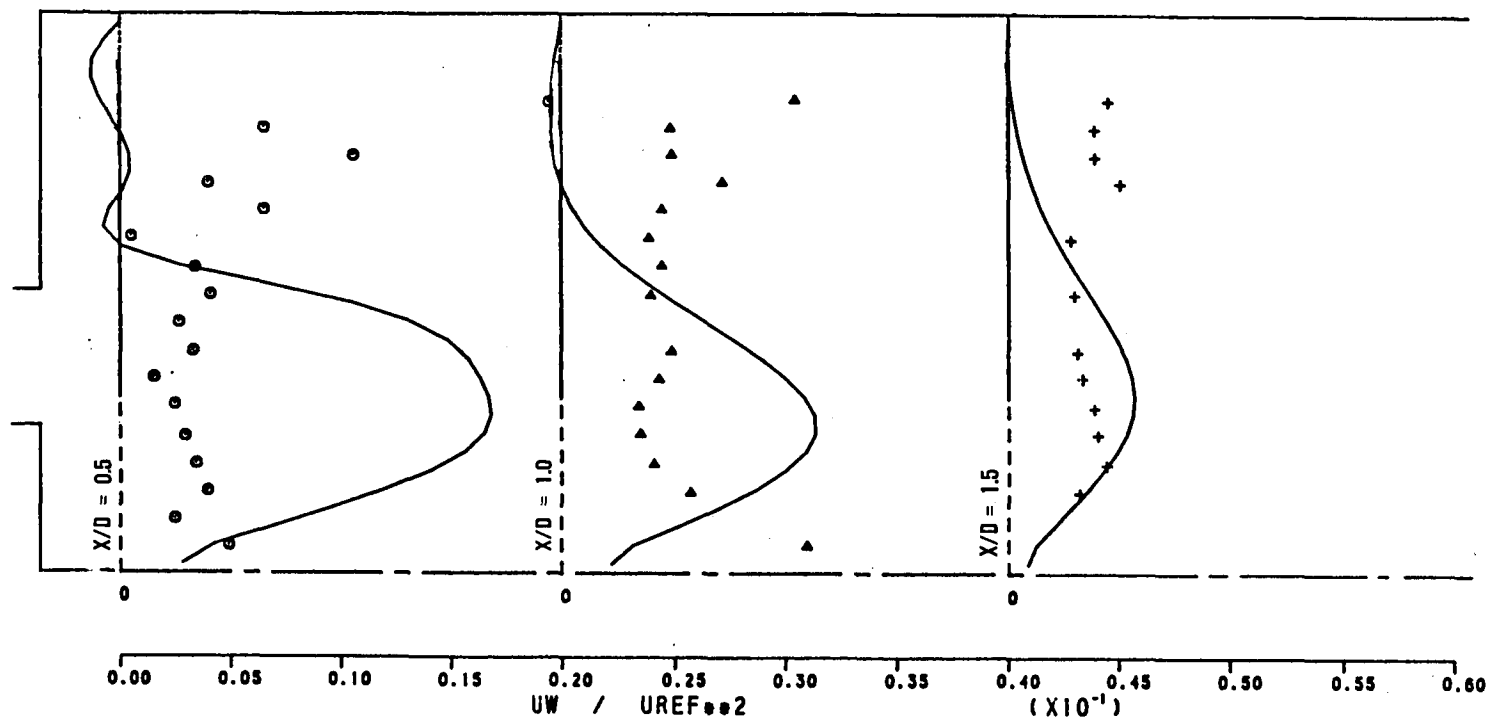


Figure 8.5-16. ASM - Reynolds Shear Stress Component ($\overline{u_w}$).

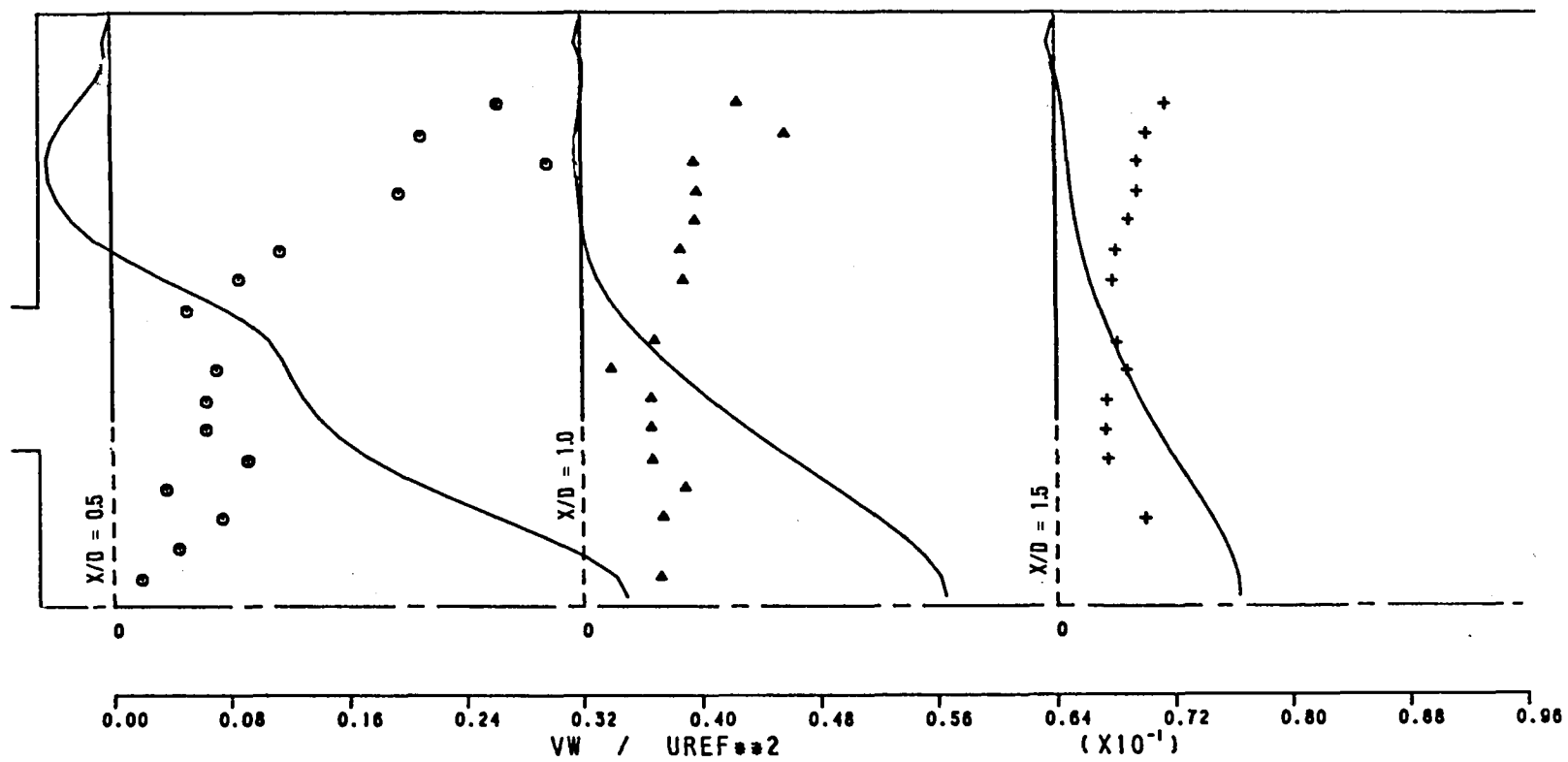


Figure 8.5-17. ASM- Reynolds Stress Shear Component ($\overline{v_w}$).

8.6 Confined Swirl-Driven Flow

Confined swirl-driven flow field characteristics have been recently reported by Altgeld, Jones and Wilhelmi.²¹⁸ They used a 10-cm-diameter quartz tube 30 cm in length, as shown schematically in Figure 8.6-1. A swirler was installed at the tube inlet. The baseline swirler hub and tip diameters were 21 mm and 42 mm, respectively. The swirler vane angle was 45°, with a corresponding swirl number of 0.78.

The mean and fluctuating velocity components were made for a fixed through-flow (3.3 m/sec reference velocity based on the tube flow area).

Two configurations were investigated:

- o Configuration I - The swirler has a 7-mm-diameter orifice at the hub center. This orifice axially injected 20 percent of the swirler mass flow rate.
- o Configuration II - The baseline swirler in the tube with a 4-mm-thick baffle 67 mm in diameter. The baffle was located 285 mm from the inlet.

A nonuniformly spaced node arrangement was used in the computations. It consisted of 53 axial nodes extending from 0 to 30 cm and 26 radial nodes. The radial node spacing duplicated the hardware dimensions with 3 nodes in the core jet, 6 nodes in the swirler, and 20 nodes covering the baffle. The minimum node spacing in each direction was 1 mm, and the axial nodes increased geometrically to the exit, with the maximum node size being 10.3 mm.

Uniform inlet profiles were used in the computations. The swirler and core jet axial velocities were determined from the specified reference velocity of 3.3 m/sec, the air flow splits, the hardware dimensions, and an assumed 4-percent passage blockage. For the swirler, the axial and circumferential velocities were taken as equal. All radial and swirl velocities in the core jet were modeled as zero. Inlet turbulence intensity was assumed to be 5 percent, and mixing length was taken as 3 percent of the inlet passage height.

Figure 8.6-2 presents a comparison between measured and predicted mean axial velocity profiles of Configuration I at different axial stations. At $X = 2, 4, 6$ and 8 cm, both measured and calculated profiles show three distinct regions. Near the tube axis, a high-velocity region is set up by the jet from the hub center. This jet is responsible for destroying the center portion of the swirl-induced recirculation zone. Consequently, only a part of this reverse-flow region exists as shown in Figure 8.6-2. Beyond $X = 10$ cm, both model and data indicate no reverse-flow region. Measurements show faster decay of the center jet than the calculations do.

Configuration I tangential (swirl) velocity profiles are shown in Figure 8.6-3. There is some discrepancy between predictions and data in the initial portion of the tube, but further downstream the agreement is reasonable. The model is predicting a slightly less angular momentum decay rate. Overall, the correlation is satisfactory.

Figure 8.6-4 presents axial velocity profiles for the second configuration (exit baffle). The outer portion of the tube is well predicted by the $k-\epsilon$ model, whereas in the reverse-flow region the model predicts higher flow rate than the data indicates. The tangential velocity profiles are shown in Figure 8.6-5. Initially,

the agreement is quite acceptable. Further downstream, predictions show solid-body rotation near the center portion of the tube. That appears plausible. However, data indicates relatively uniform V_θ in the radial direction.

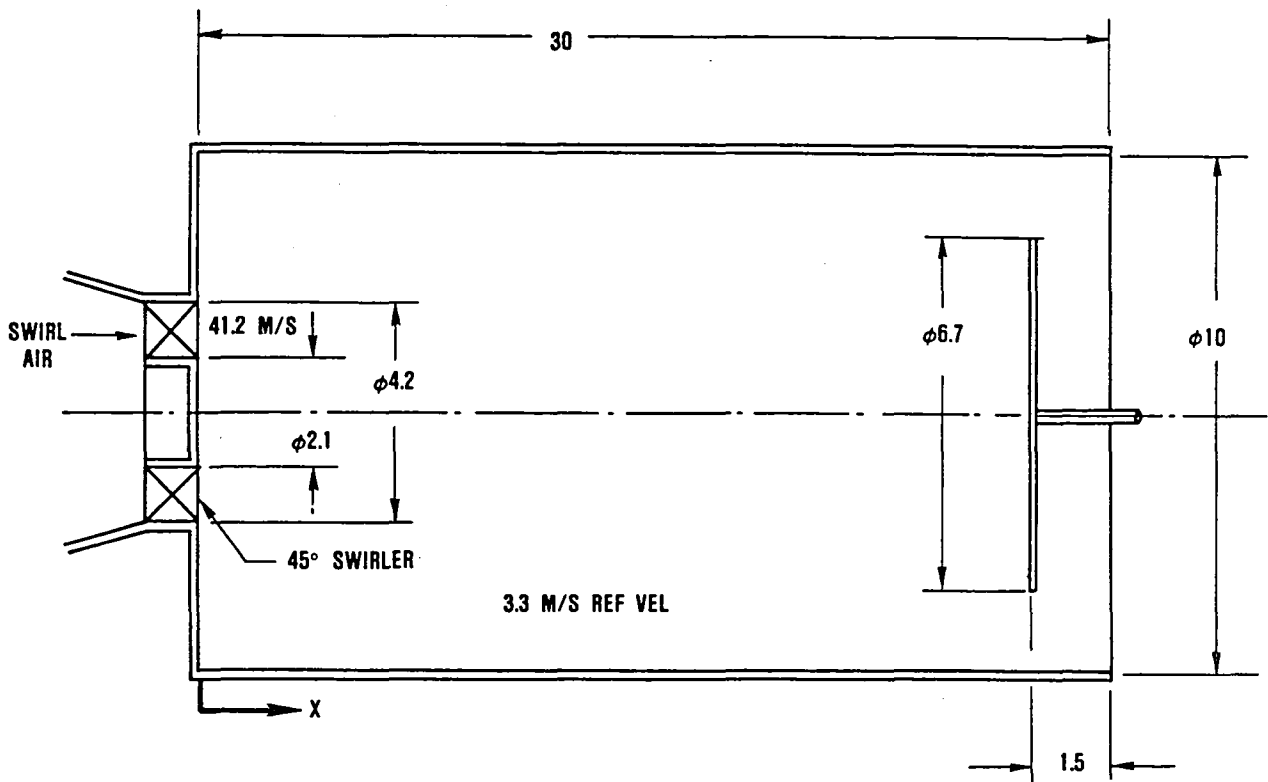
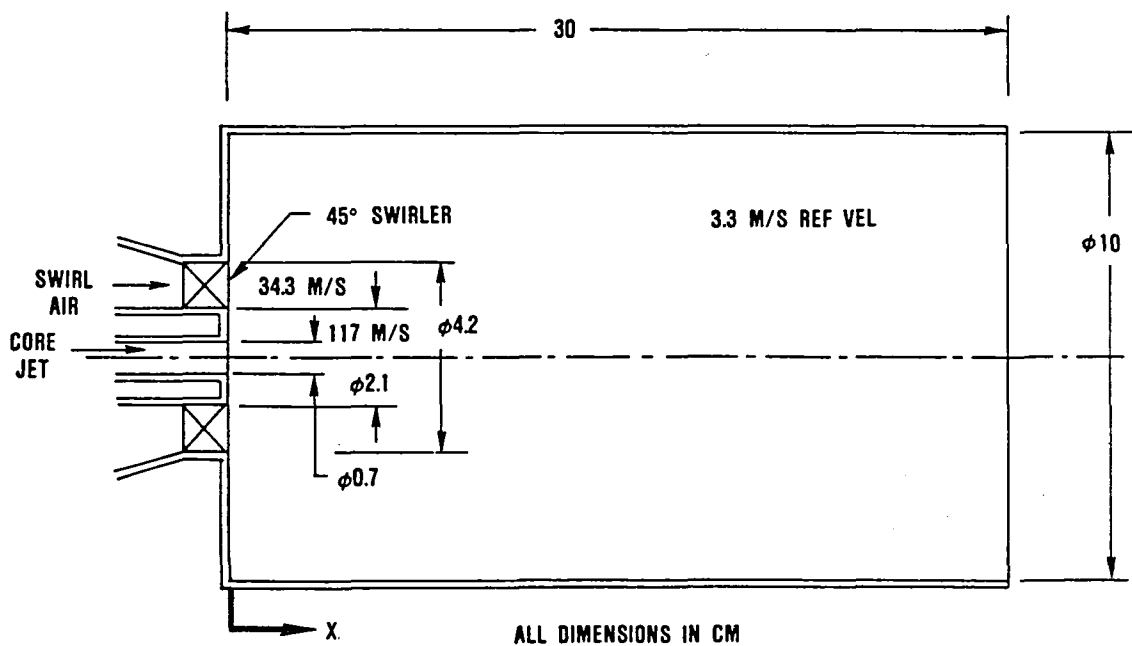


Figure 8.6-1. Confined Swirl-Driven Flow Setup of Altgeld, Jones and Wilhelmi.

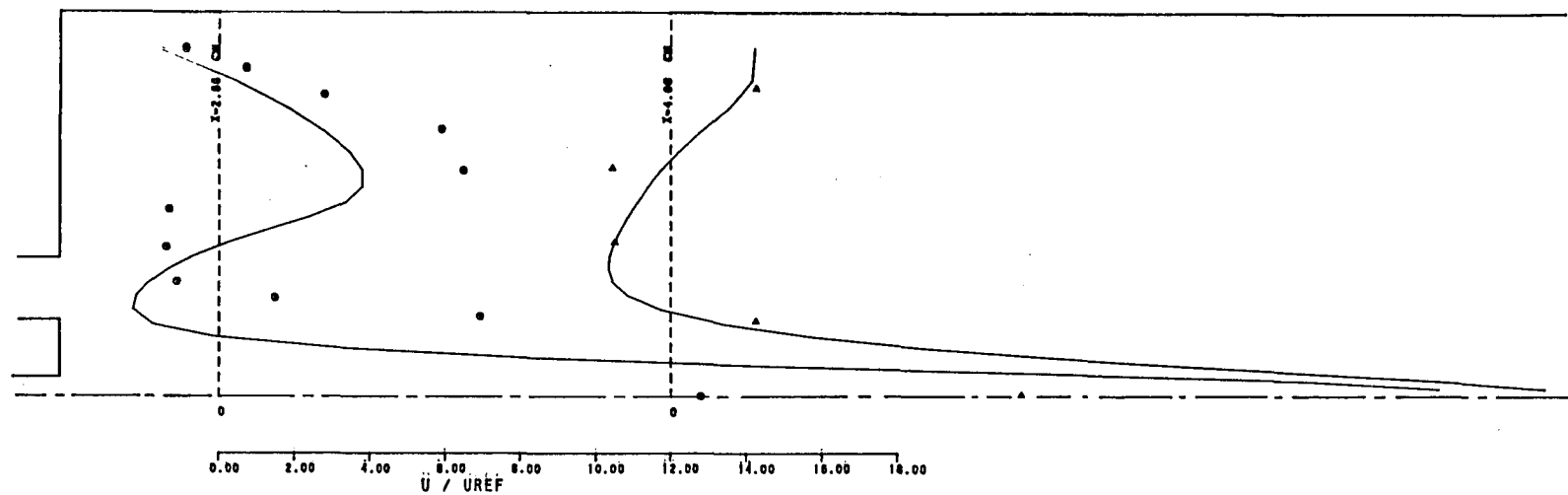


Figure 8.6-2. Comparison Between $k-\epsilon$ Model Prediction and Measured Axial Velocity Profile in Configuration I.

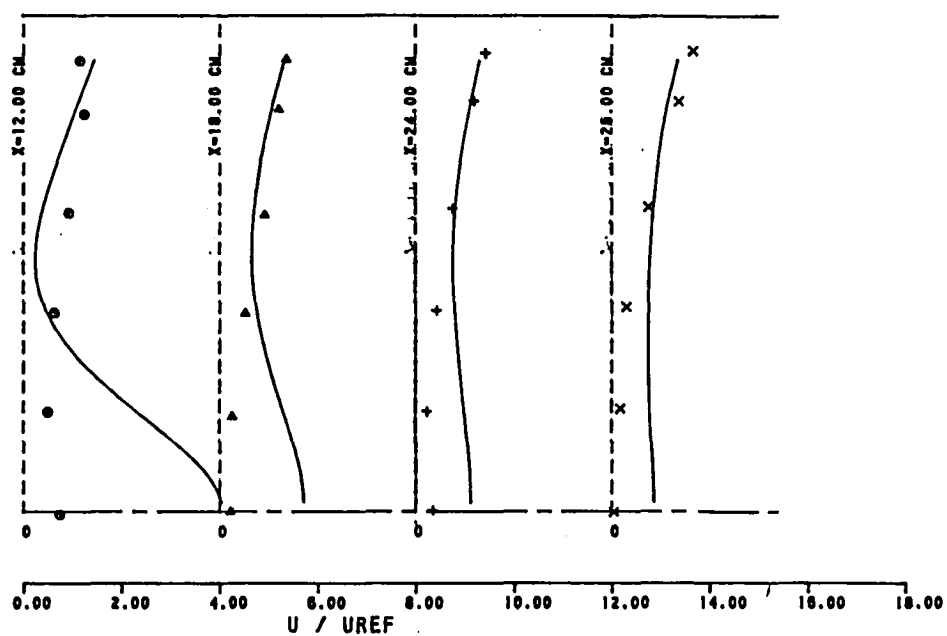
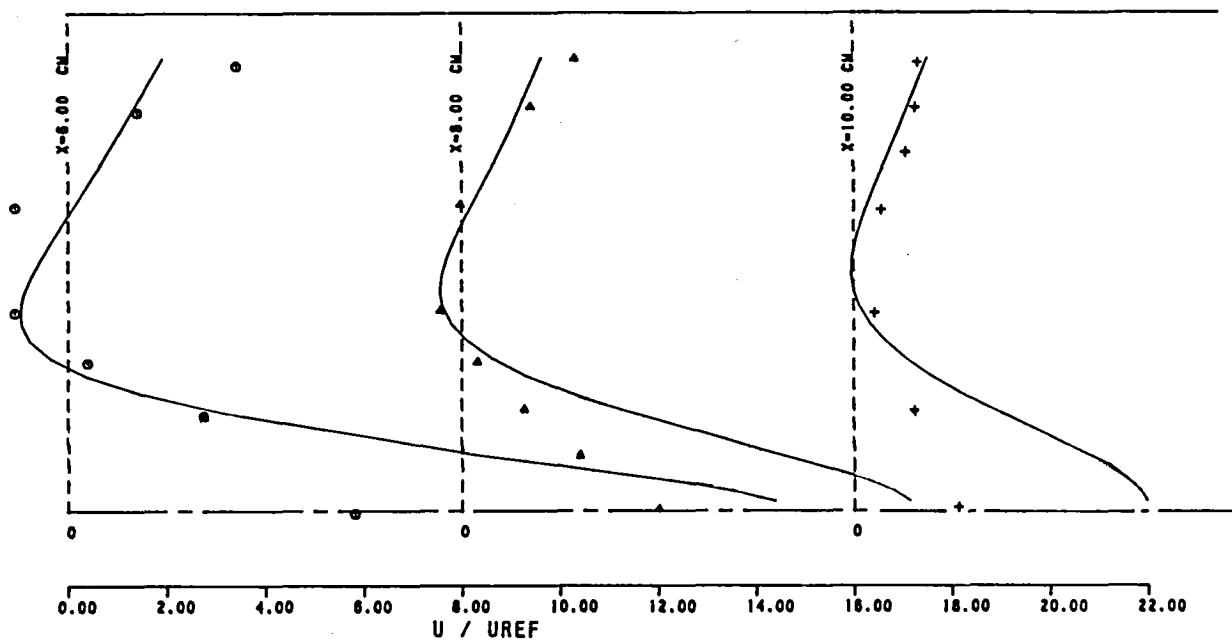


Figure 8.6-2. Comparison Between $k-\epsilon$ Model Prediction and Measured Axial Velocity Profile in Configuration I (Cont'd).

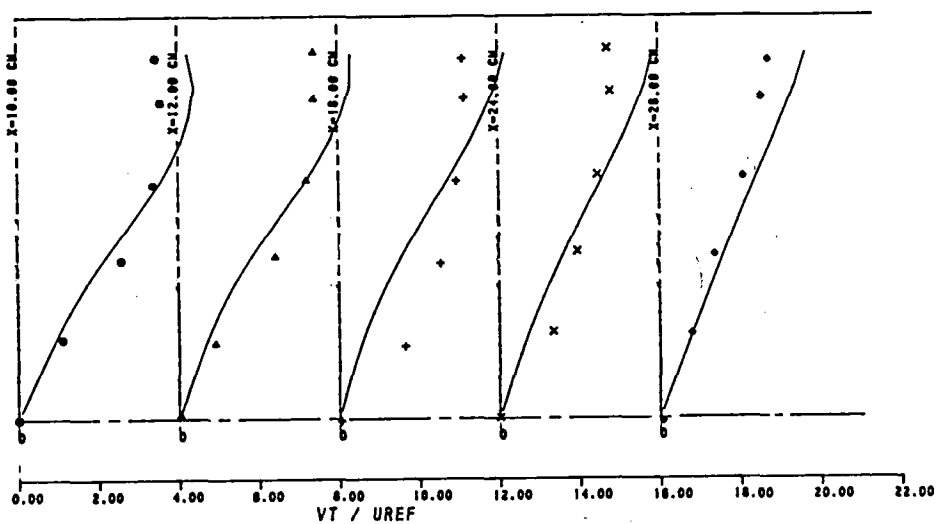
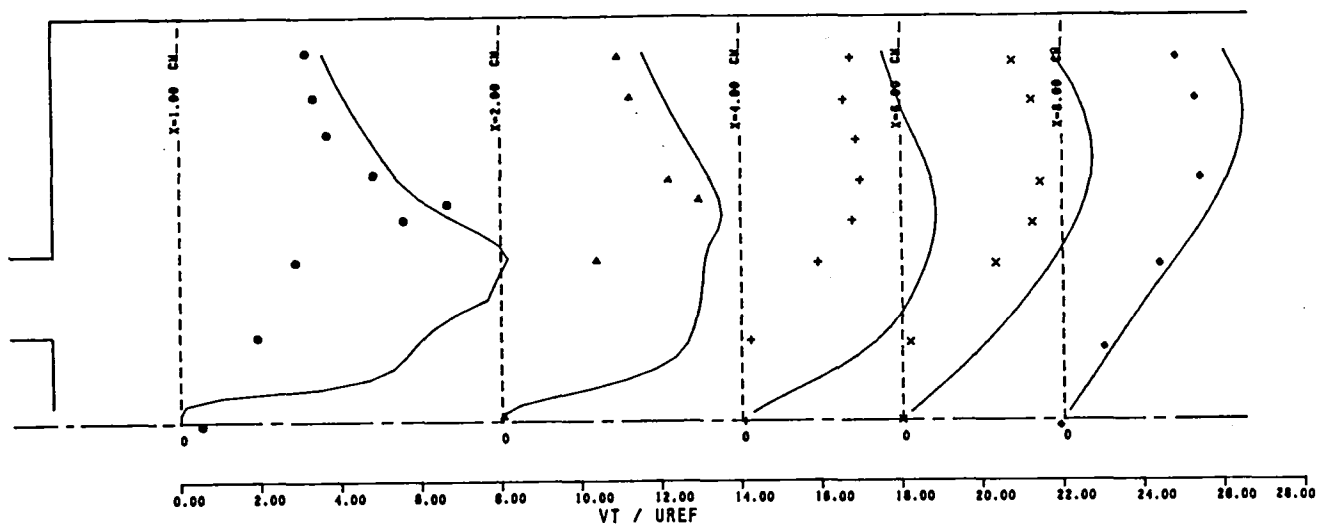


Figure 8.6-3. Configuration I - Tangential Velocity Profiles.

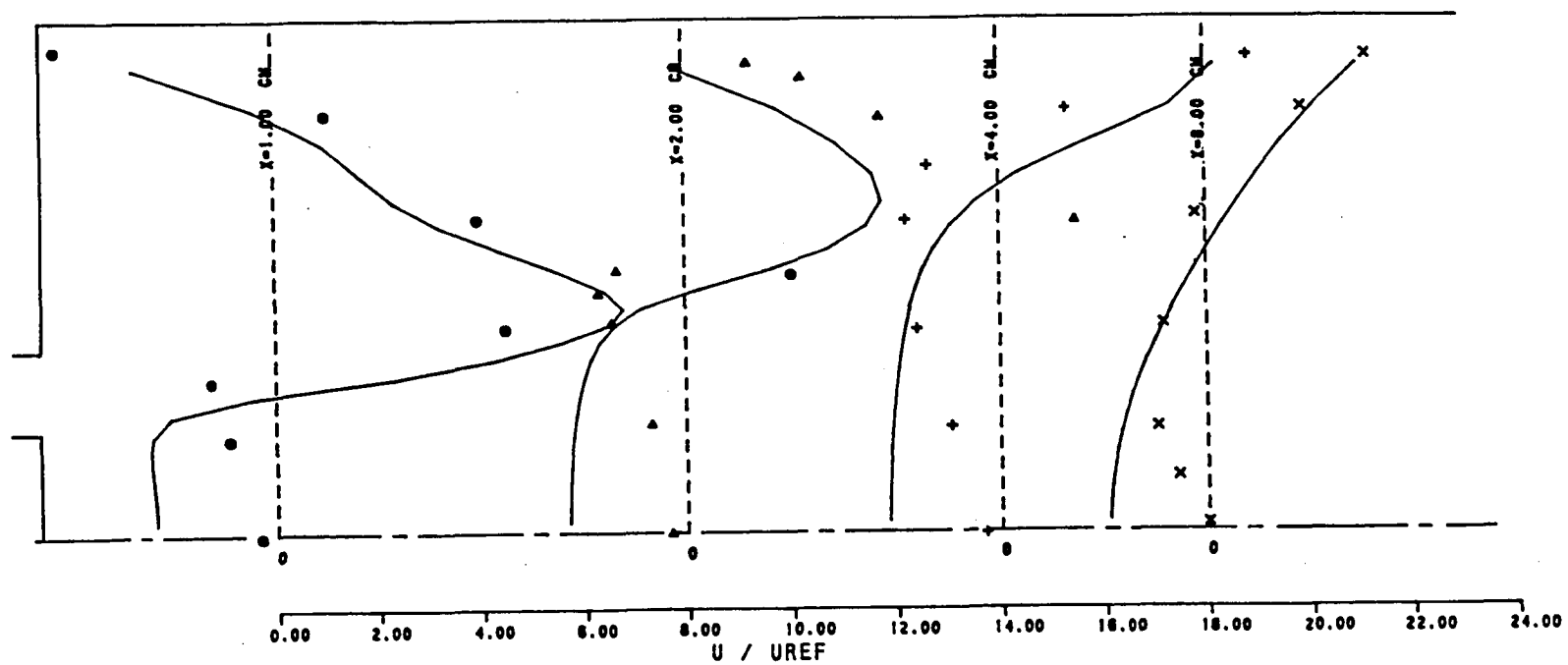


Figure 8.6-4. Configuration II (Exit Baffle) - Axial Velocity Profiles.

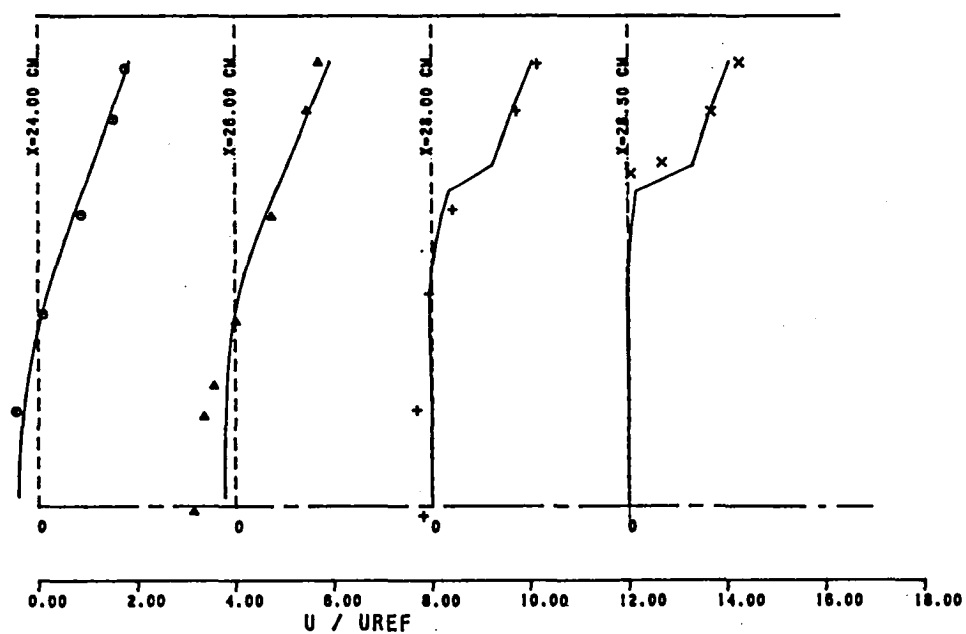
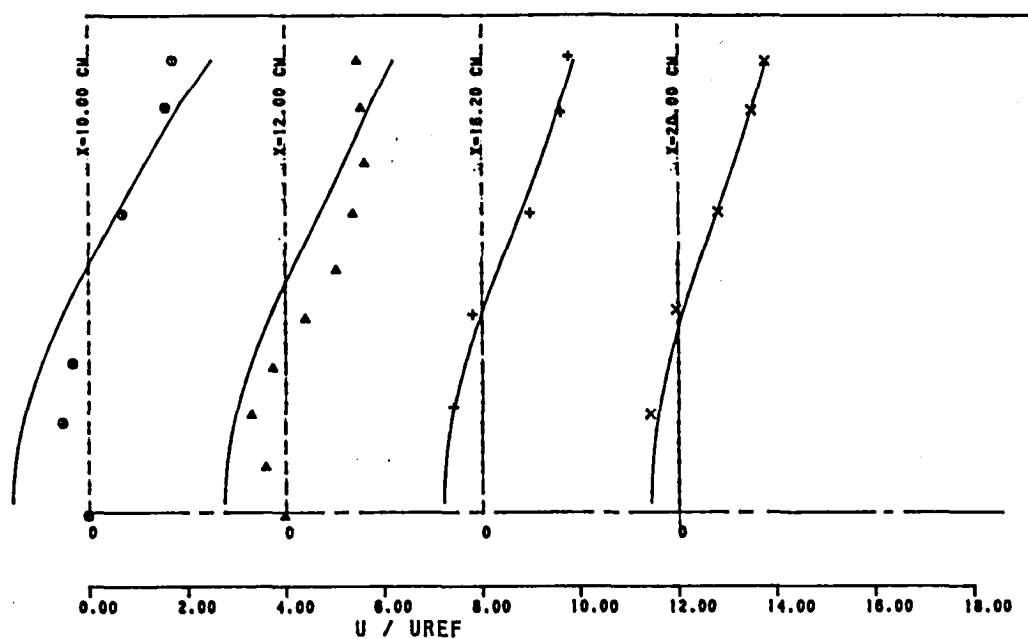


Figure 8.6-4. Configuration II (Exit Baffle) - Axial Velocity Profiles (Cont'd).

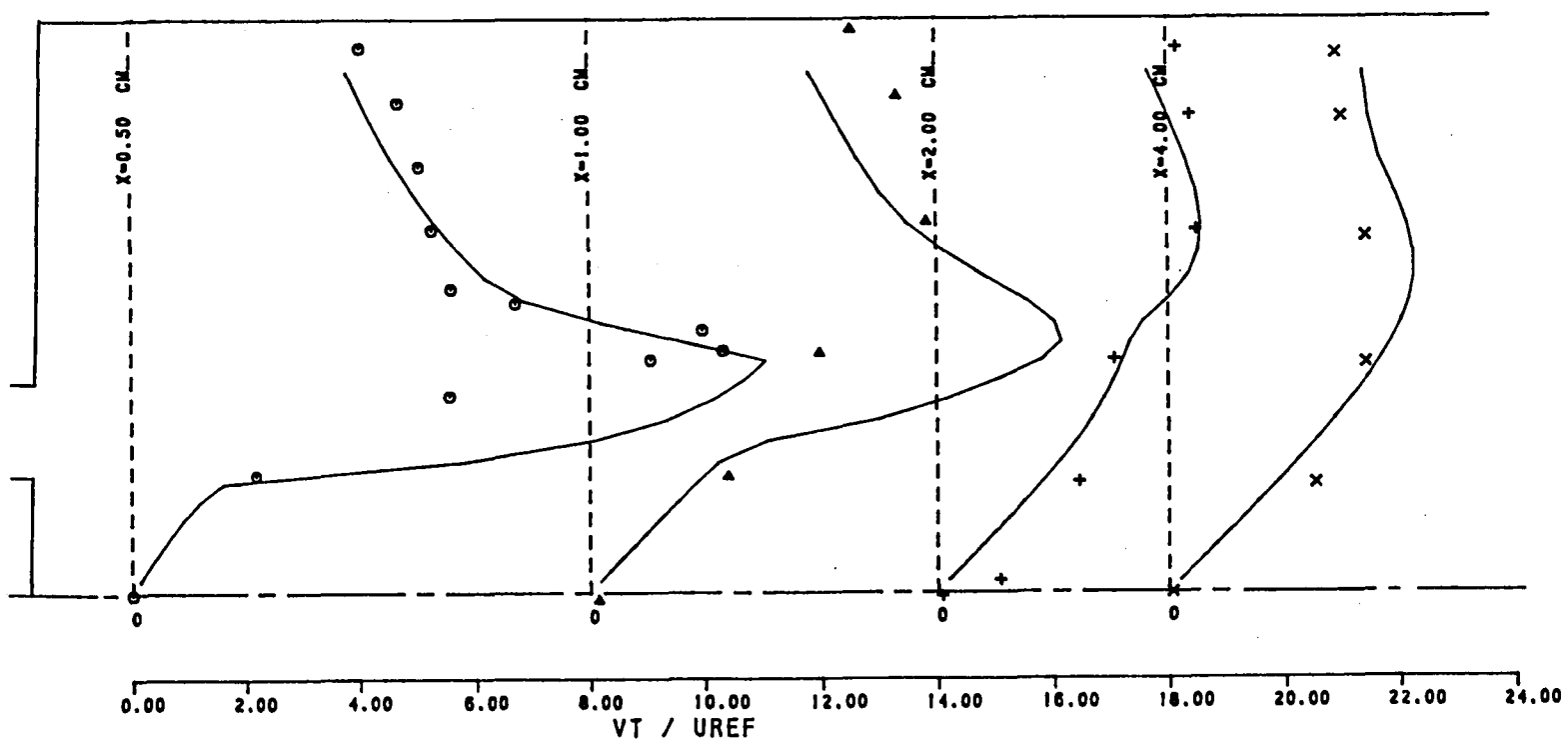


Figure 8.6-5. Configuration II (Exit Baffle) Tangential (Swirl) Velocity Profiles.

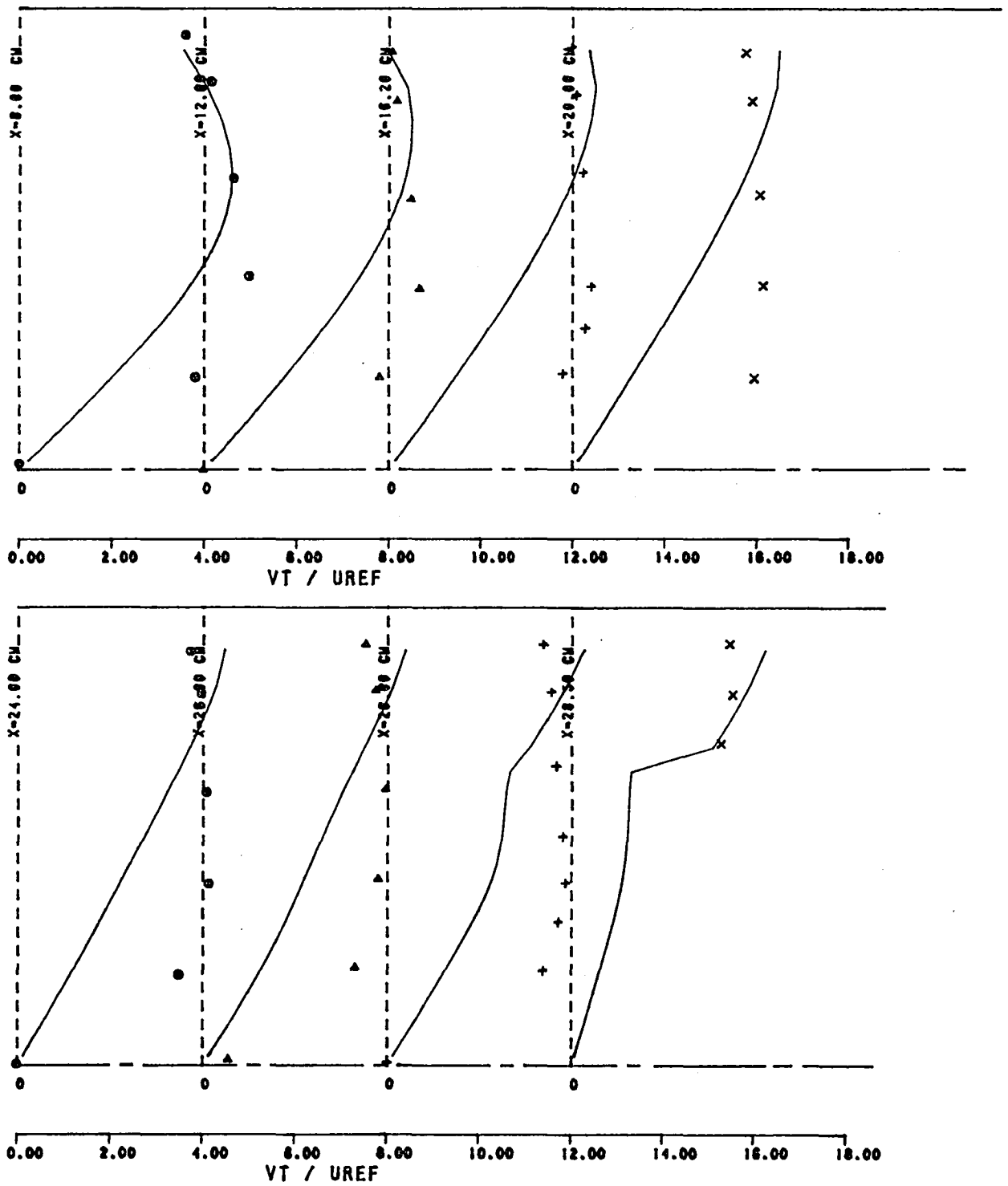


Figure 8.6-5. Configuration II (Exit Baffle) Tangential (Swirl) Velocity Profiles (Cont'd).

8.7 Combusting Spray in Confined Swirling Flow

Internal flow fields of most of the practical combustors have fuel spray interacting with swirling air, the swirl being introduced for flame stabilization. The flow field in such a system is characterized by the turbulence, kinetic and spray combustion models. For the benchmark test case selected in this category, measurements were made by El Banhawy and Whitelaw¹⁷⁹. A schematic of their experimental arrangement is shown in Figure 8.7-1. The test setup comprised a 155-mm-diameter combustion chamber and systems for supplying kerosene fuel, combustion and cooling air. The combustion air entered the chamber through a swirler assembled coaxially with a fuel atomizer, which was a rotating cup atomizer. The fuel spray emerged from the atomizer in the form of droplets with an average diameter of 33 microns. The droplet size was determined from a separate spray test. For the test condition selected, the inlet conditions were:

- o Combustion air flow rate: 0.0556 kg/sec
- o Kerosene flow rate: 0.00132 kg/sec
- o Nozzle airflow rate: 0.00229 kg/sec
- o Inlet air temperature: 300°K
- o Inlet fuel temperature: 300°K
- o Swirler vane angle: 60 degrees

The droplet velocity was measured by a laser Doppler velocimeter, and the reported droplet velocity components were:

$$\begin{aligned}U_p &= 0.9 - 8 \quad \text{m/sec} \\V_p &= 1.0 - 2.34 \quad \text{m/sec} \\W_p &= 11.69 - 25.3 \quad \text{m/sec}\end{aligned}$$

The combustor internal flow field measurements included temperature and species concentration profiles at different axial stations.

Predictions for this case were obtained from the 2-D elliptic program with the standard k - ϵ model. Computations were made with the two-step and the four-step kinetic scheme using the Garrett spray model. Computations were made using 51 x 27 grid nodal points. A partial layout of the grid system used for this test case is shown in Figure 8.7-2. The fuel nozzle body shape was approximated by a stair-step boundary. The inlet velocity components and turbulence kinetic energy were assumed to be constant, with

$$\begin{aligned}U_{in} &= 7.708 \text{ m/sec} \\V_{\theta in} &= 13.351 \text{ m/sec} \\k_{in} &= 0.713 \text{ m}^2/\text{sec}^2\end{aligned}$$

The cooling air through the fuel nozzle body was introduced into the combustor as radial jets, with velocities corresponding to the droplet velocities.

The comparison between data and model predictions is shown in Figures 8.7-3 through 8.7-6. Predictions were made with both two-step and four-step schemes. The top parts of these figures show the measured data, while the bottom parts show predictions with the two-step and four-step models.

Figure 8.7-3 illustrates the results for temperature distribution. The predicted peak-temperature region is bigger than the data. In obtaining four-step results, the rate constants recommended by Hautman, et al., were used. The four-step model also predicts bigger, higher flame-temperature regions than the data. However, these contours are in better agreement with the measurements than the two-step results. The data shows that temperature contours are pushed radially outward closer to the wall compared to the data. This implies that the heat flux in the radial direction

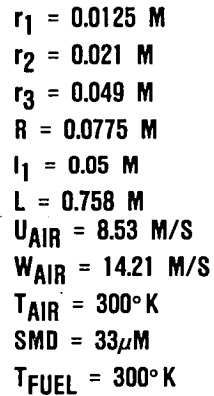
is underpredicted by the $k-\epsilon$ model. This trend is consistent with the characteristics observed in other diffusion flame calculations.

The measured and predicted CO mole fractions are illustrated in Figure 8.7-4. The measured peak CO mole fraction is 11 percent, while the predicted peak CO concentration is 4 percent with the two-step model. However, the location of maximum CO concentrations is correctly predicted by the model. The CO concentrations predicted by the four-step model are much smaller than the data. The maximum CO mole fraction predicted is about 3 percent. The location of the peak CO is in agreement with the data.

The CO₂ mole fractions measured and predicted by the two-step model are illustrated in Figure 8.7-5. The maximum CO₂ concentration in data and predictions are 13 percent. However, the predicted peak CO₂ concentrations occur farther downstream compared to the data. The high CO₂ isopleths are also located in the regions where high isotherms are predicted. The four-step predicted peak CO₂ concentration zone is smaller than that indicated by the data; the predicted peak CO₂ value was 12 percent.

Comparison of measured and predicted oxygen mole fractions is shown in Figure 8.7-6. With the two-step scheme, the predicted regions of low oxygen concentrations occur further downstream compared to the data. The four-step predictions and measured contours are in better qualitative agreement than the two-step model.

**CYLINDRICAL COMBUSTOR WITH ROTATING CUP
ATOMIZER AND AIR INTRODUCED THROUGH A SWIRLER
SURROUNDING THE ATOMIZER**



542

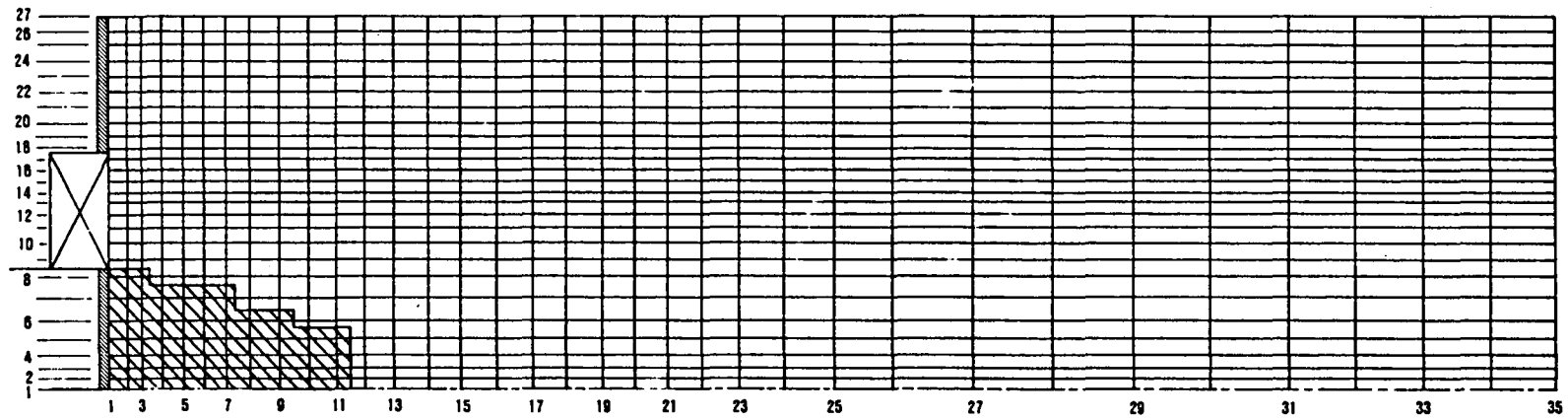


Figure 8.7-2. El Banhawy and Whitelaw Test Case
Partial Grid Network.

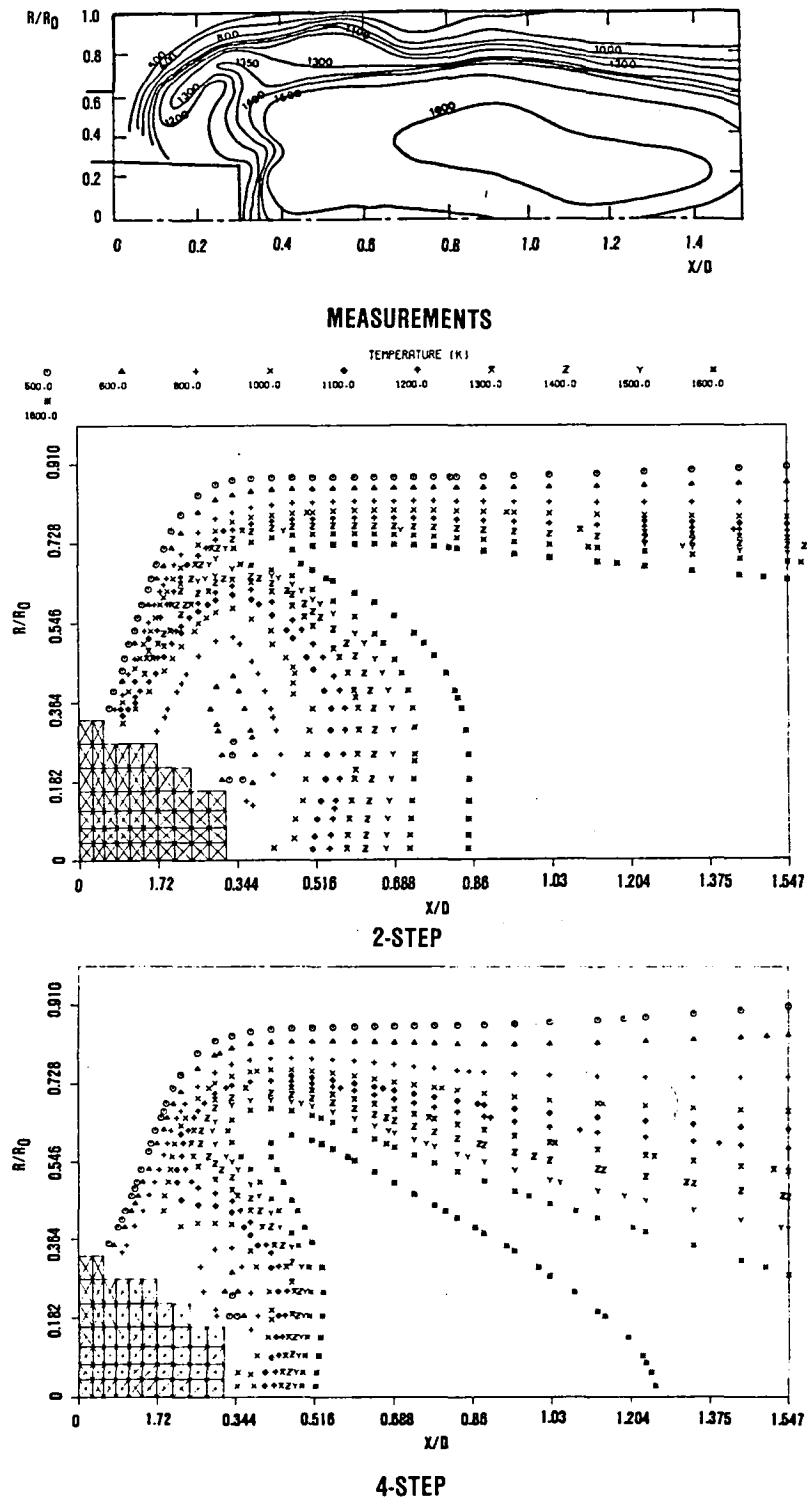


Figure 8.7-3. Temperature Contours.

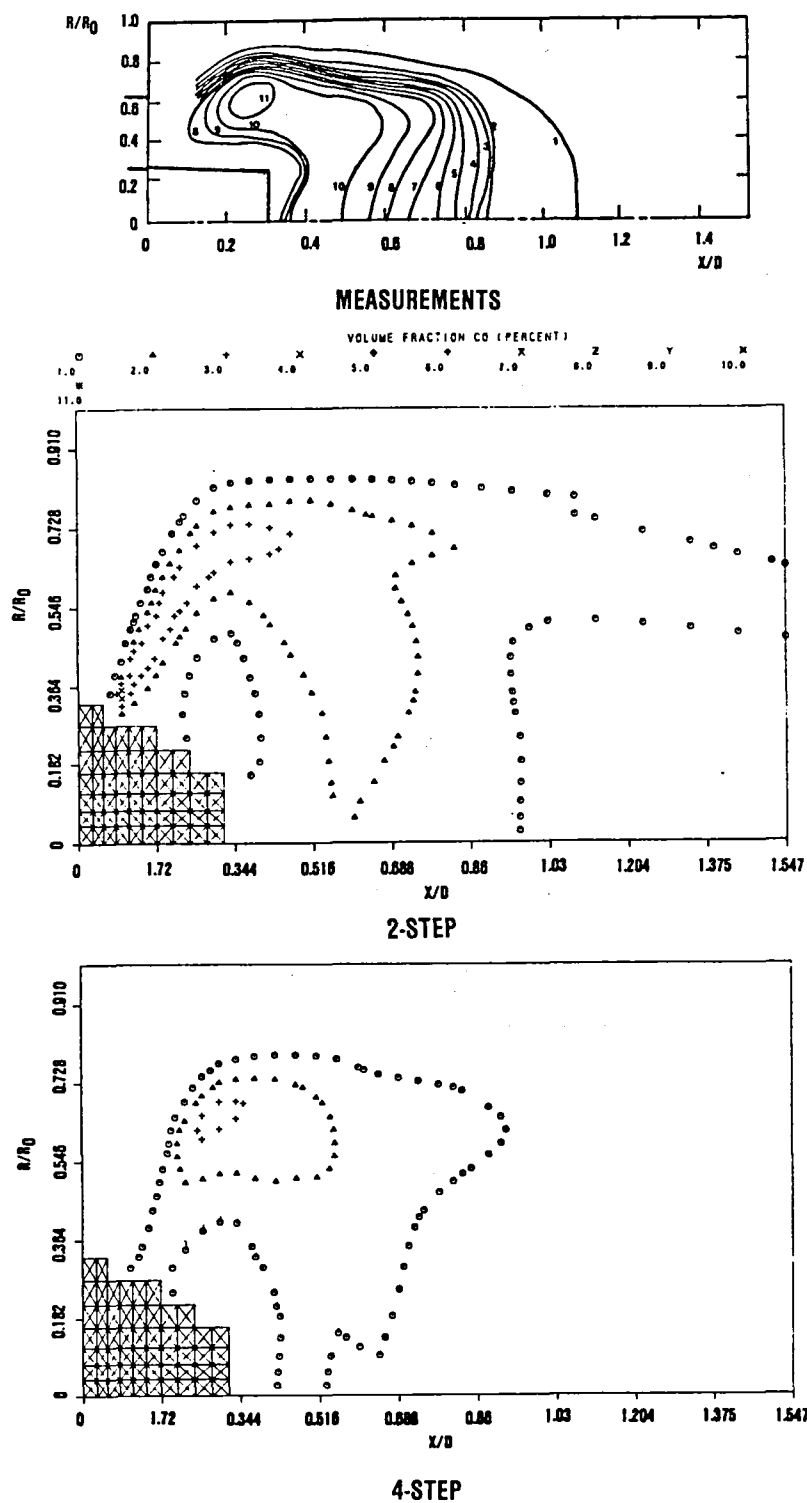


Figure 8.7-4. Contour Maps of CO Volume Concentrations (%).

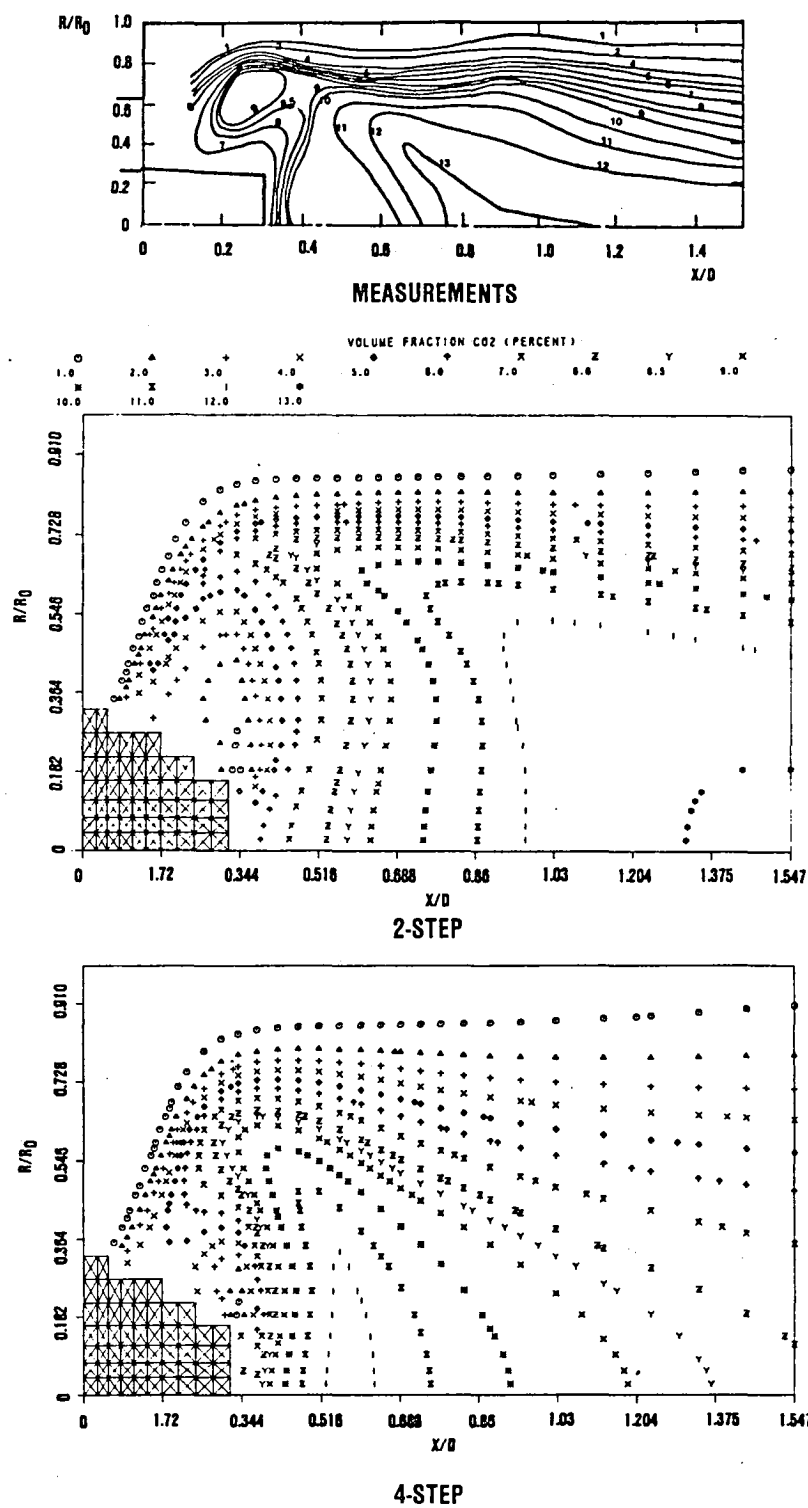


Figure 8.7-5. Contour Maps of CO₂ Volume Concentration (%).

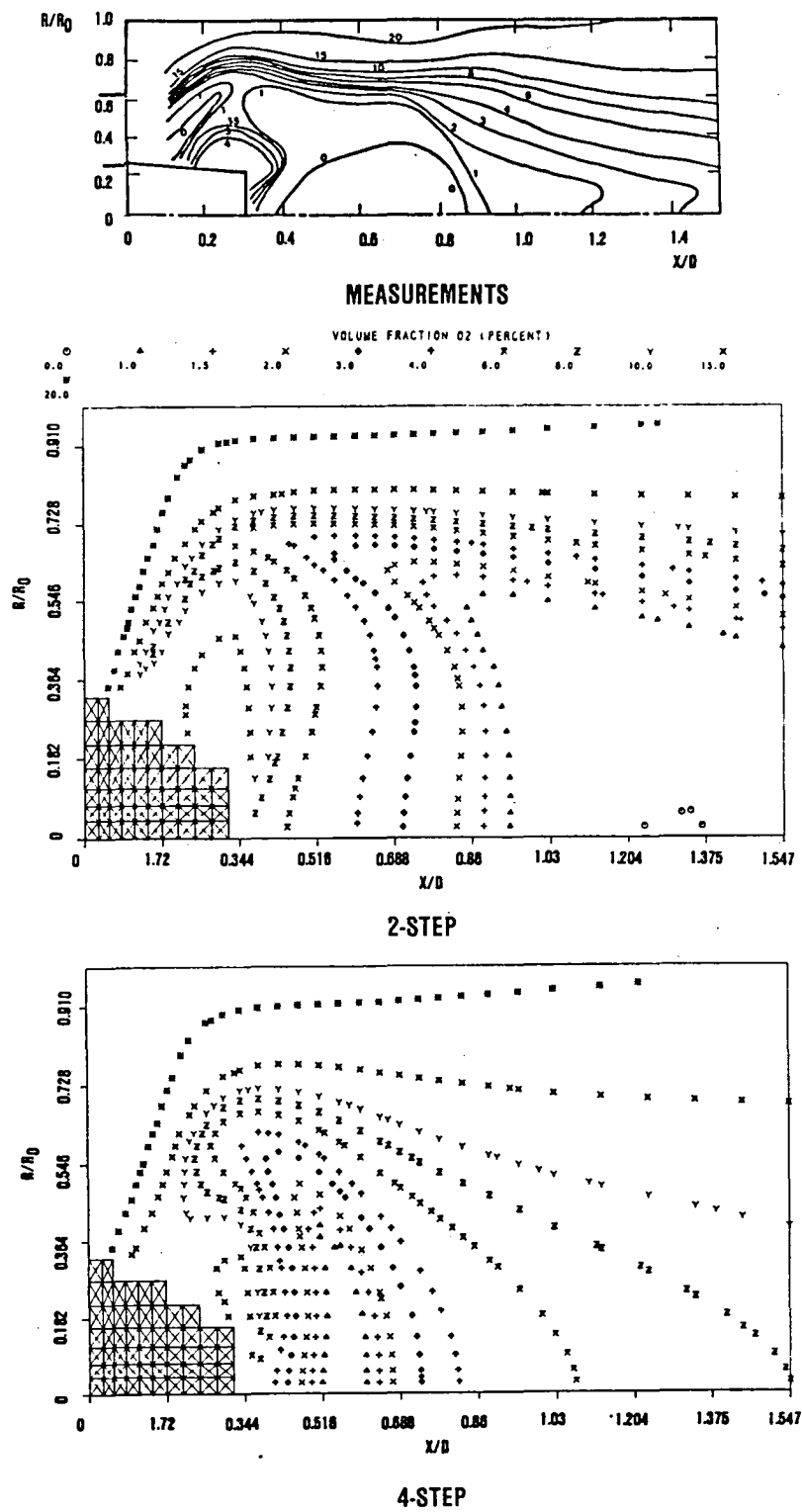


Figure 8.7-6. Contour Maps of O_2 Volume Concentrations (%).

9.0 Dilution Jet Mixing Validation

Modern advanced technology combustor designs require shorter combustors and higher turbine inlet temperatures. In such combustion systems, the role of the dilution zone to achieve the turbine inlet radial profile quality plays an important part. It is very important to characterize the mixing of the dilution jets with the hot combustor gases. The dilution jet mixing flow is a very complex 3-D flow characterized by highly turbulent scalar transport. Detailed analytical flow characterization of such flows can be done only by a 3-D flow computation. As a part of the NASA HOST (Hot Section Technology) Program, temperature field measurements were made at Garrett as in several idealized dilution zone configurations. Some of these test results were used to validate the 3-D analytical model.

One of the major difficulties in the 3-D models lies in obtaining grid-independent solutions. The predictions obtained can depend upon grid density distributions as well as the number of grid points. A detailed discussion on the grid insensitivity is presented in Paragraph 9.1. Paragraph 9.2 contains the discussion on the effects of size and spacing for a single row of jets injected from one side into a ducted cross flow. For this case of single-sided injection, the effects of the jet-to-cross-flow momentum ratio and the cross-stream nonuniform temperature profile are presented in Paragraph 9.3. The effects of injection from two sides into a confined cross flow with in-line as well as staggered jets are described in Paragraph 9.4.

9.1 Effects of Finite-Difference Grid Distribution

The 3-D calculations for the jet mixing test cases were performed for the geometry shown schematically in Figure 9.1-1. All the computations were made for the case of a single row of jets

injected perpendicularly to the ducted cross stream. The cross stream had a constant duct height, H_0 , of 10.16 cm. The diameters of the jets were equal, and the jets were spaced apart at a distance, S . The walls of the mainstream duct were insulated. The distances along the mainstream were measured from the plane formed by the injected air from the row of jets, and the distances across the duct were measured from the duct wall where the jets are located. Computations were performed from mid-plane to mid-plane along the Z direction using cyclic boundary conditions at the first and the last planes. The computational domain extended from the top wall to the bottom wall. In the streamwise direction, the grid network was extended up to $x/H_0 = 2$ although in some test cases the computations did not extend beyond $x/H_0 = 1.5$.

One of the jet mixing test cases selected consisted of 12 jets (1.27 cm diameter) with a jet-to-mainstream momentum ratio, J , of 25.32. The momentum ratio, J , is defined as

$$J = \rho_j V_j^2 / \rho_m U_m^2$$

The ratio of orifice spacing to diameter in this test case was 2.0, and the ratio of duct height to diameter was 8.0. The flow conditions were:

Average mainstream velocity, $U_m = 15.04$ m/s
 Average mainstream temperature, $T_m = 648.7^\circ\text{K}$
 Jet exit velocity, $V_j = 51.87$ m/s
 Jet exit temperature, $T_j = 308.3^\circ\text{K}$
 Mainstream static pressure, $P_m = 97,726$ n/m²
 Mainstream turbulence kinetic energy = 1.27 m²/s²
 Jet turbulence kinetic energy = 8.07 m²/s²

Calculations for this case were made by using 45 x 26 x 17 (19,890) grid nodes in the axial, radial and transverse directions, respectively. The grid network selected for this computation is shown in Figure 9.1-2. In this case, a total of 49 nodes were used inside the jet. The mainstream inlet conditions were assumed to be uniform with U_m , T_m and inlet turbulence intensity as obtained from the measurements.

Predictions were obtained with the standard k- ϵ model, wherein the wall functions were used to specify the adiabatic wall boundary conditions. At the exit axial plane, diffusion in the upstream direction was set equal to zero. For the jet midplanes in the transverse direction, cyclic boundary conditions were applied. The predicted temperature distributions are expressed in nondimensional form by the variable θ , defined as

$$\theta = \frac{T_m - T}{T_m - T_j}$$

Thus, higher θ values correspond to colder regions, and low θ values correspond to hot zones.

The comparison between data and predictions obtained with 49 nodal points simulating the jet is presented in Figure 9.1-3. The predictions shown in this figure are converged results with the total mass source error of about 0.02 percent of the total mass flow rate after 350 iterations. The top part of the figure shows the predicted and measured isopleths of θ at three axial planes, $x/H_0 = 0.5, 0.75$ and 1.0 . For each axial plane, the figure on the left shows the predicted results and the one on the right shows the measurements. The bottom part of the figure shows the comparison between predicted and measured θ profiles along the centerplane of the jet. In this figure the jets are injected from the top.

The predicted jet penetration is slightly less than the data. The predictions show much larger temperature variations in the

transverse direction than the data. The predicted peak θ values are slightly larger than the measured values. The predicted radial profiles are in qualitative agreement. It is also important to recognize that in this case a difference in the value of theta, ($\Delta\theta$), by a magnitude of 0.1 corresponds to a temperature difference of 34°K.

In most gas turbine combustor flow calculations even with 20,000 nodes, it is not possible to have as many as 49 nodal points to simulate each of the radial jets. In practice, two nodes in the axial and two nodes in the transverse direction are used. In order to determine the accuracy of the predictions in such cases, calculations were made with a new grid system in which only four nodes were located inside the jet. The grid network selected for this computation is shown in Figure 9.1-4. The centerline was situated between $I = 5$ and 6 along the axial coordinate and between $K = 4$ and 5 along the transverse coordinate. For this case, a total of $27 \times 26 \times 8$ (5616) nodes were used. This grid system is quite coarse compared to the one shown in Figure 9.1-2. Predictions obtained by using this grid system are shown in Figure 9.1-5. These results had a total mass residual of about 0.02 percent, which is comparable to the results shown for the fine grid network. The coarse grid results are in very good agreement with the data. The coarse grid results also show smaller gradients in the transverse direction compared to the fine grid results. The centerplane radial profiles of θ are in excellent agreement with the data.

A comparison of the centerplane temperature profiles for the fine-grid and the coarse-grid predictions are shown in Figure 9.1-6. In the fine grid, the computations were made up to $x = 14.3$ cm, while the coarse grid predictions were performed up to $x = 16.72$ cm. Near the exit boundary, the θ contours are horizontal, which is a result of the zero axial gradient boundary condition.

However, at the upstream stations, the exit boundary condition does not have any influence on the temperature profiles.

In order to ascertain that this behavior is not a characteristic of a specific momentum ratio range, these computations were also made for a high momentum ratio of 107.8. The grid systems used in these efforts were identical to those shown in Figure 9.1-2 and 9.1-4. The fine grid predictions (45 x 26 x 17 nodes) for nondimensional temperature are illustrated in Figure 9.1-7. At $x/H_0 = 0.5$, the data and the predictions show the jet penetration to be about 70 percent of duct height. As observed in the case of $J = 25.3$, the fine grid predictions underpredict the mixing, and hence the peak θ values are overestimated by the model. The predicted θ distributions show larger gradients in the transverse direction than the data.

The predicted θ distributions with four nodes inside the jet at a momentum ratio of 107.78 are presented in Figure 9.1-8. These results have converged to within approximately 0.02 percent in total mass source error after 350 iterations. The predicted θ contours are in very good agreement with the data. The coarse grid results again show smaller gradients in the transverse direction than the fine grid results (Figure 9.1-7). The radial profiles predicted with the coarse grid are in excellent agreement with the data.

The centerplane temperature contours for the fine grid and coarse grid results for $J = 107.78$ are shown in Figure 9.1-9. These figures also show that the upstream effects of the exit boundary conditions are minimal.

The results shown for the fine-grid and the coarse-grid system clearly demonstrate that the predictions are not grid-independent solutions. However, the computer memory available at Garrett was

limited to a total of 20,000 nodes and hence the number of grids could not be increased further. However, it is possible to rearrange the grid density. Since the fine-grid system seemed to give higher transverse gradients than the coarse-grid network, it was deemed important to increase the number of grids in the transverse direction. Since the exit boundary is much farther than the region of interest, it is possible to shorten the length of computational domain in the axial direction and pack the nodes closely to increase the resolution in the region of interest.

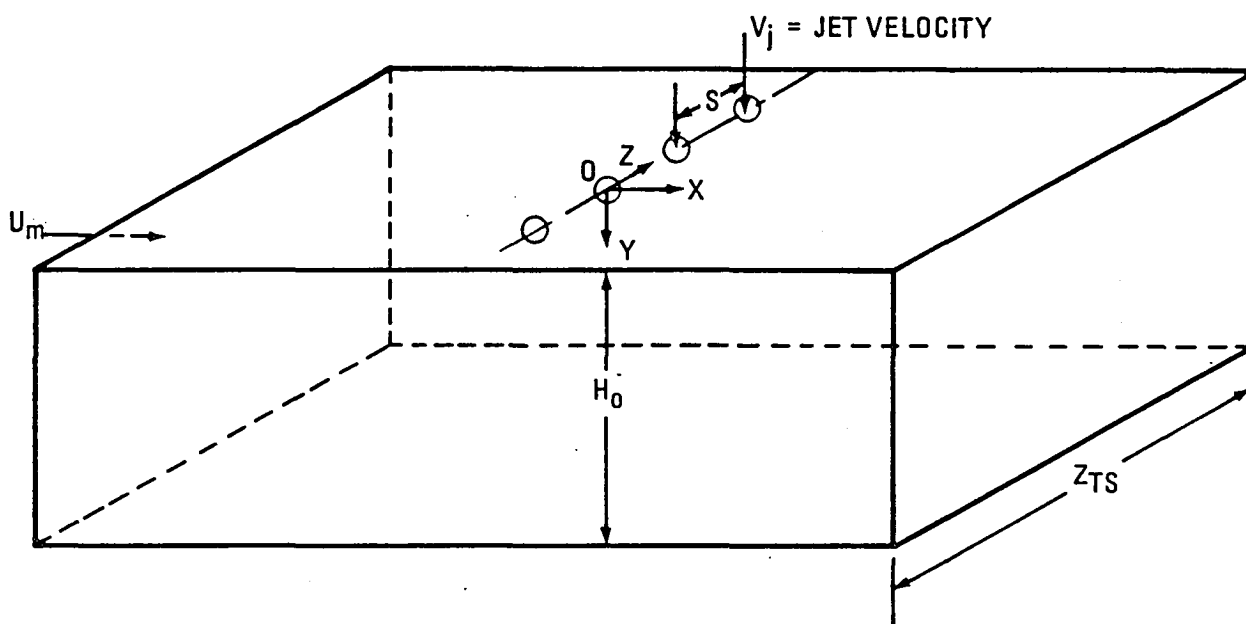
Calculations were made with a fine-grid system and an even finer grid system wherein the grid density was increased by a factor of 1.4. An increase in grid density by a factor of 1.4 is achieved by increasing the number of nodes in the axial and transverse directions by about 18 percent in the region of interest.

Predictions for the two-grid system were obtained for the case of a single row of jets with diameters of 1.8 cm spaced 5.08 cm apart. The jet-to-cross-flow momentum ratio was 25.48. The grid network used in the fine-grid system is illustrated in Figure 9.1-10. For this case, $35 \times 33 \times 17$ nodes were used in the computational domain. The computational domain was extended up to 17.48 cm in the axial direction. A total of 51 nodes were located inside the jet so that sufficient resolution was obtained near the jet exit plane.

The standard $k-\epsilon$ model predictions for this case are shown in Figure 9.1-11. The left side of the contour plot for each axial location corresponds to the prediction, and the figure on the right represents the data. At $x/H_0 = 0.25$, the predicted and measured contours are in good agreement, even though the predicted peak θ values are slightly larger than the data. The radial profiles at this plane are in good agreement except that the predicted jet

penetration is slightly smaller than the data. Very similar characteristics can be seen at $x/H_0 = 0.5$ and 1.0 . The predicted contours still show larger transverse gradients than the data.

The grid system used in the finer network is shown in Figure 9.1-12. For this case, $32 \times 29 \times 21$ grid nodes were used in the computational domain. The computational domain in this case was limited to 13.6 cm in the axial direction. A total of 69 nodes were located inside the jet to increase the resolution near the jet exit location. The predicted results for nondimensional temperature distribution by using the finer grid network are presented in Figure 9.1-13. These contours are similar in character to those shown in Figure 9.1-11. The predicted peak θ values are closer to the measured value at all three axial stations than the results shown in Figure 9.1-11. The differences between these two predictions are not substantial. By increasing the number of nodes inside the jet by about 35 percent, the solutions seem to approach grid-independence criteria. Although this test was performed with the intention of addressing grid-independence criteria, substantially more grid nodes are required to verify the grid independence of the solution scheme.



COORDINATE ORIGIN IS LOCATED AT CENTER OF ORIFICE

- U_m, ρ_m, T_m = MAINSTREAM VELOCITY, DENSITY, AND TEMPERATURE
- V_j, ρ_j, T_j = INITIAL JET VELOCITY, DENSITY, AND TEMPERATURE
- H_0 = TEST-SECTION HEIGHT AT INJECTION PLANE
- H = TEST-SECTION HEIGHT AT ANY X-Y PLANE
- S = ORIFICE SPACING ALONG Z (TRANSVERSE) DIRECTION
- D = ORIFICE DIAMETER
- D_j = $\sqrt{C_D} D$
- Z_{TS} = TEST-SECTION TRANSVERSE DIMENSION = 305mm

Figure 9.1-1. Multiple Jet Mixing Coordinate System and Important Nomenclature.

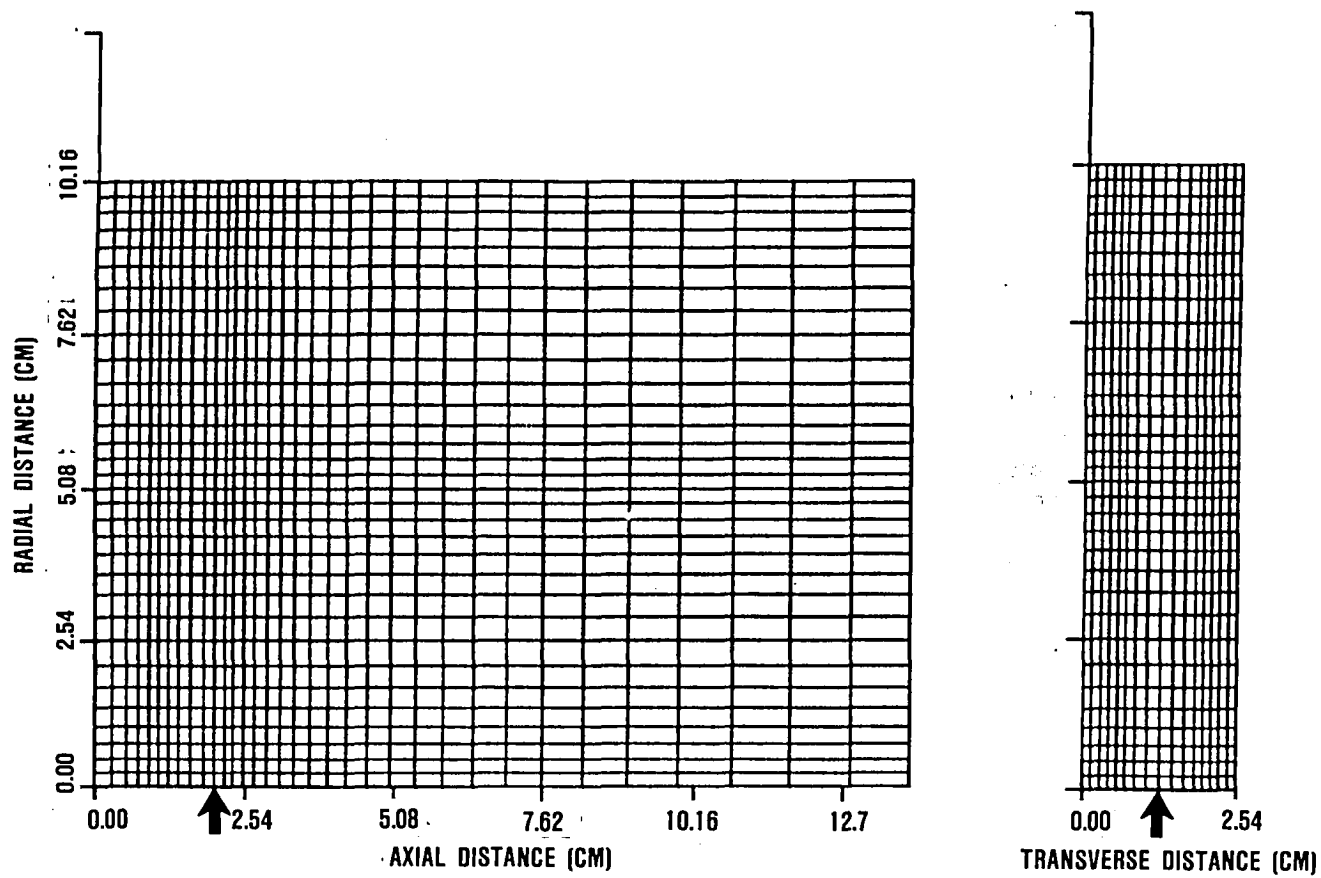
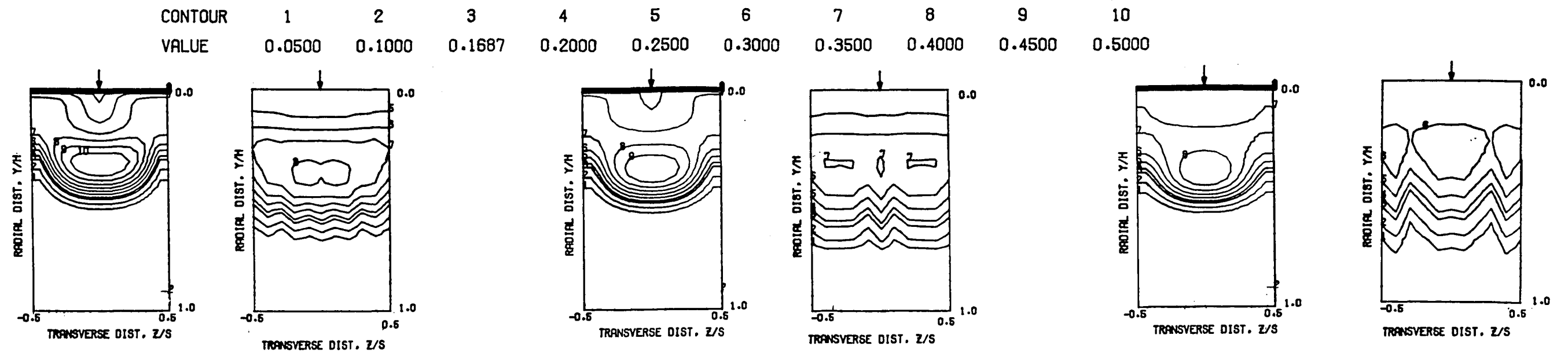
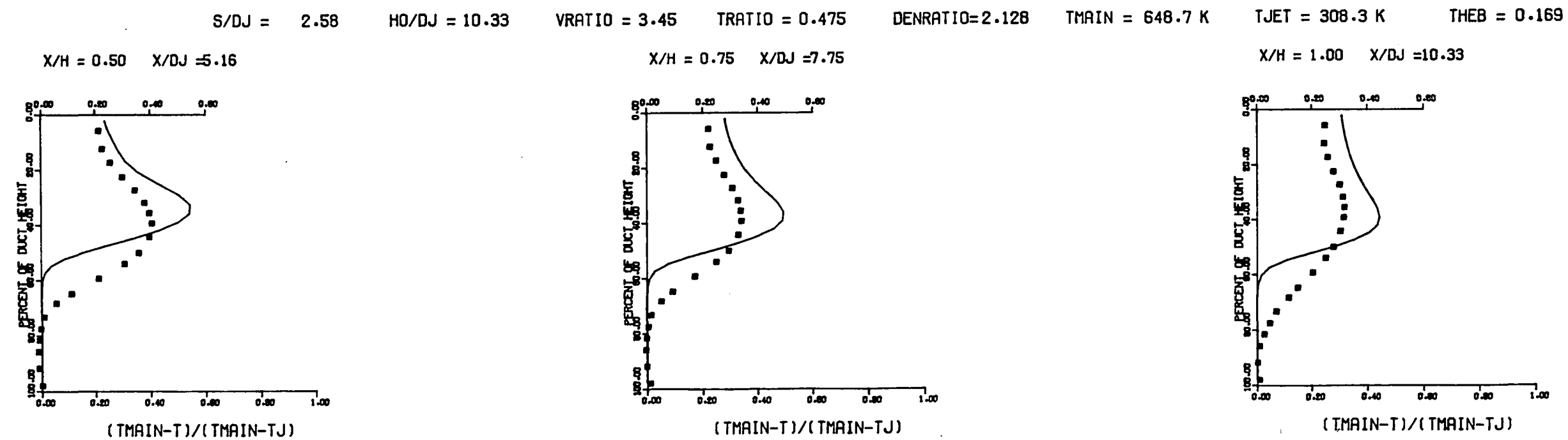


Figure 9.1-2. Finite Difference Grid Network for Fine Grid (45x26x17) Computations, $J = 25.32$, $S/D = 2$, $H/D = 8$.



THETA CONTOURS FOR TEST NO. 1, $H=CONST$, $J=25.32$, $S/D=2.0$, $H/D=8.0$



COMPARISON BETWEEN DATA AND PREDICTIONS FOR TEST NO. 1, STRAIGHT DUCT, $T_M = CONST$,

$J = 25.32$, $S/D = 2.00$, $H/D = 8.00$

Figure 9.1-3.

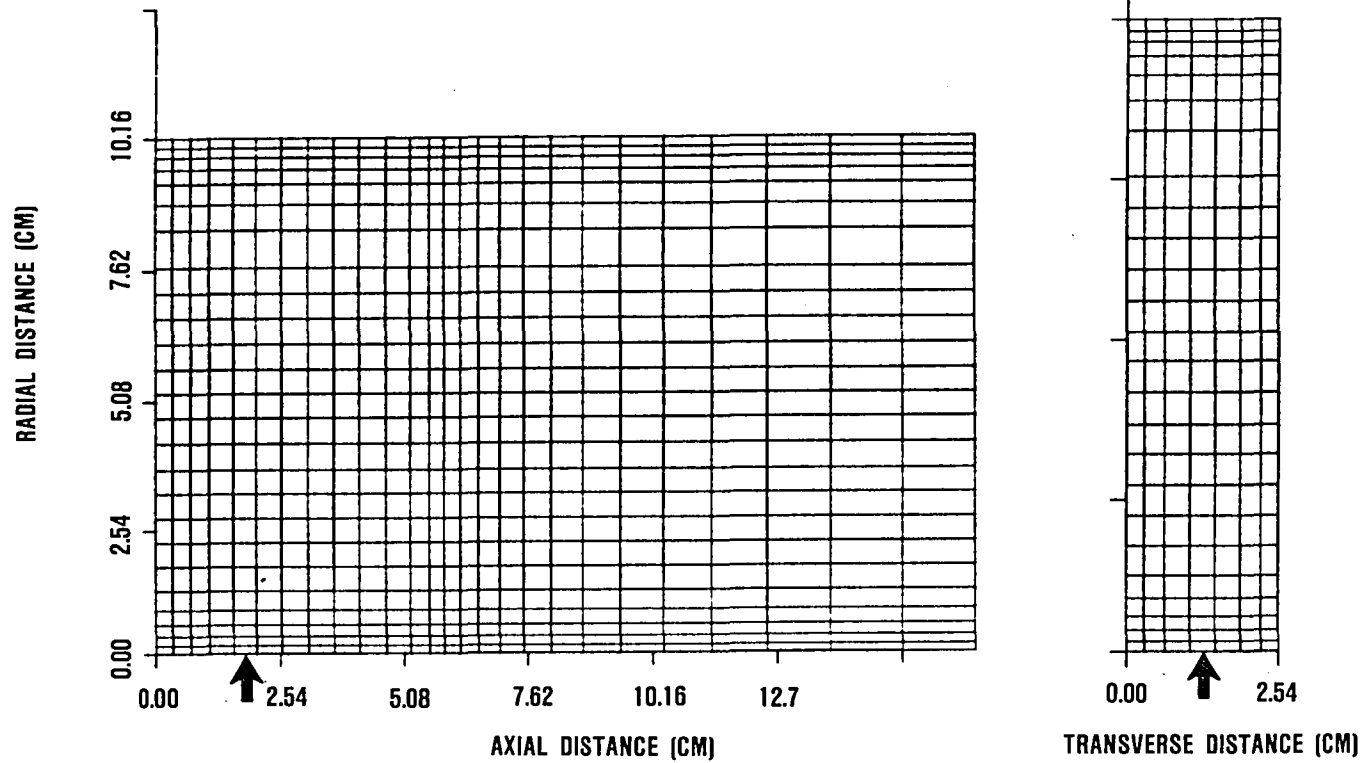
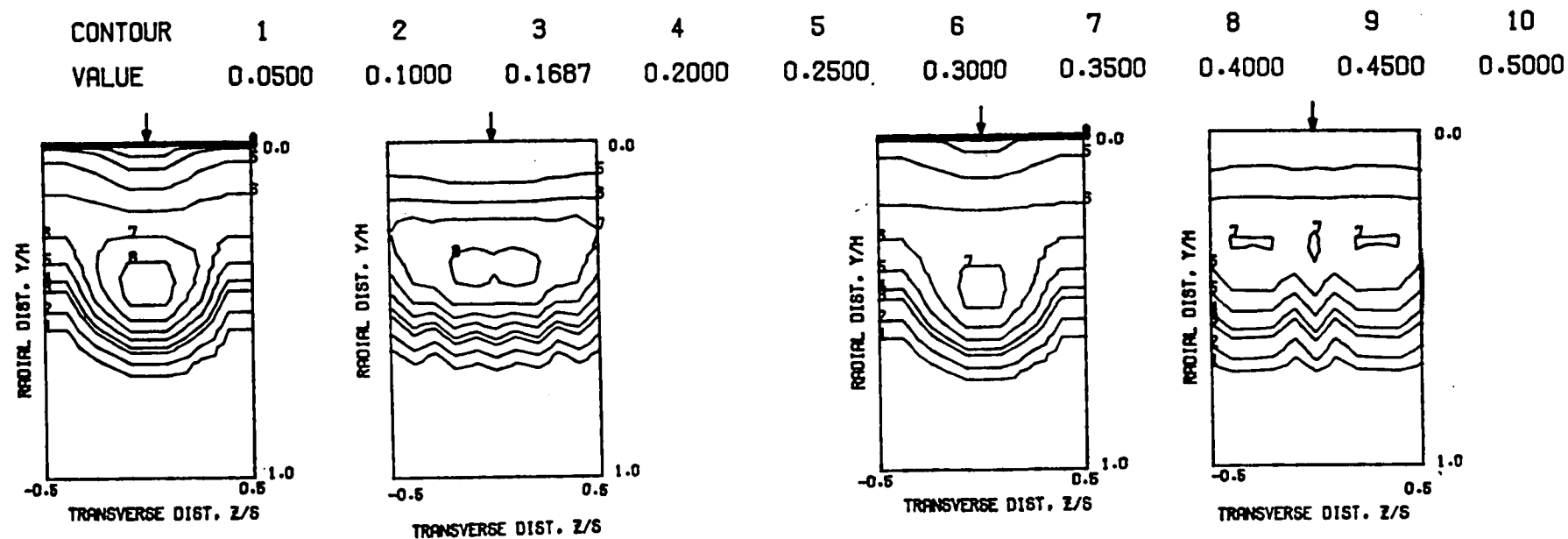
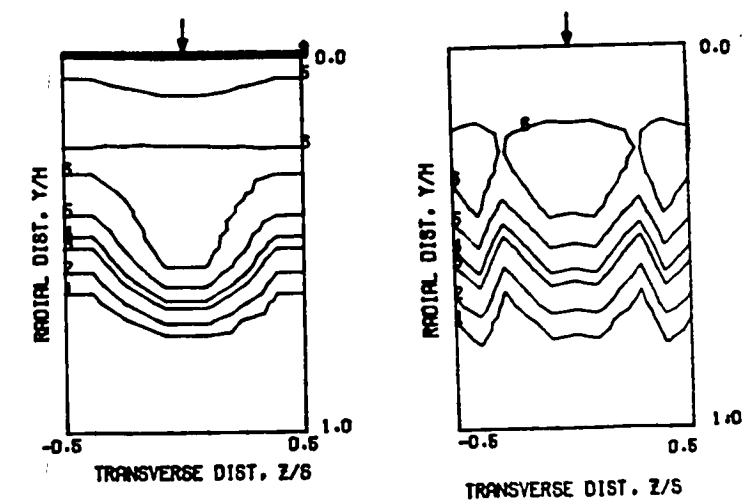


Figure 9.1-4. Finite Difference Grid Network for Coarse Grid (27x26x8) Computations, $J = 25.32$, $S/D = 2$, $H_0/D = 8$.

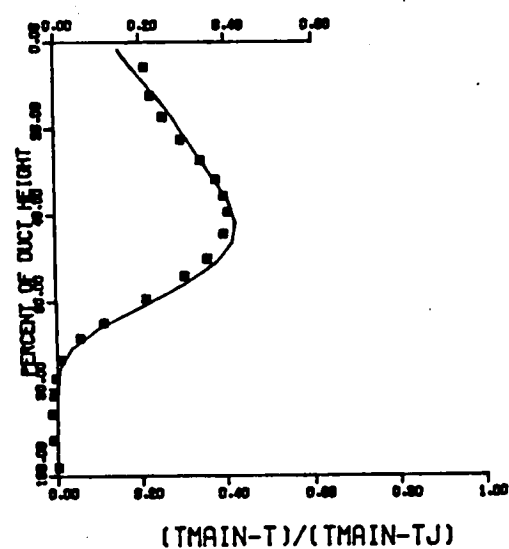


THETA CONTOURS FOR TEST NO. 1, 4-NODES, $J=25.32$, $S/D=2.0$, $H/D=8.0$

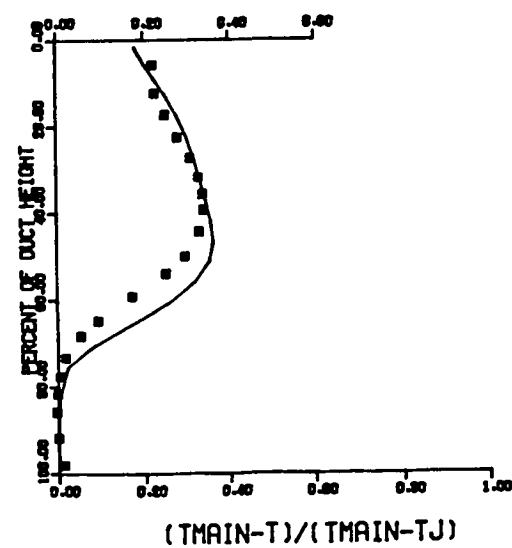


$S/DJ = 2.58$ $H/DJ = 10.33$ $VRATIO = 3.45$ $TRATIO = 0.475$ $DENRATIO=2.128$ $TMAIN = 648.7 \text{ K}$ $TJET = 308.3 \text{ K}$ $THEB = 0.169$

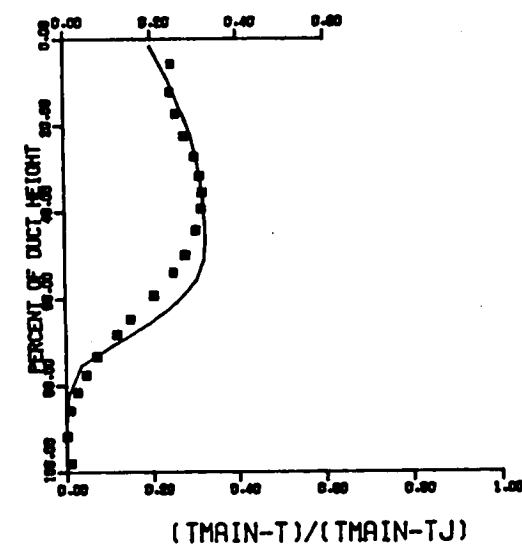
$X/H = 0.50$ $X/DJ = 5.16$



$X/H = 0.75$ $X/DJ = 7.75$



$X/H = 1.00$ $X/DJ = 10.33$



COMPARISON BETWEEN DATA AND PREDICTIONS FOR TEST NO. 1, STRAIGHT DUCT, 4-NODE JET,

$J = 25.32$, $S/D = 2.00$, $H/D = 8.00$

Figure 9.1-5

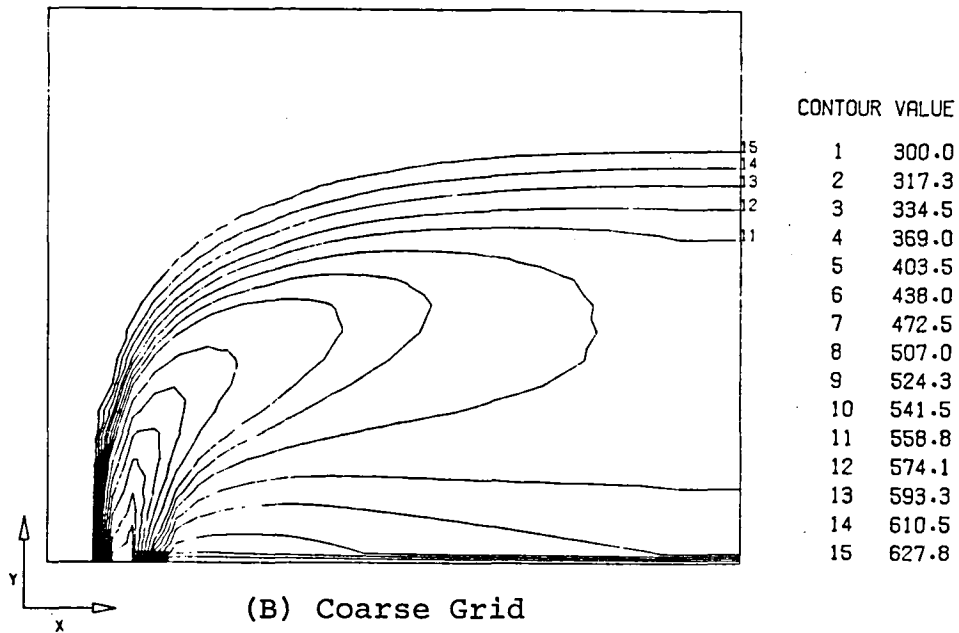
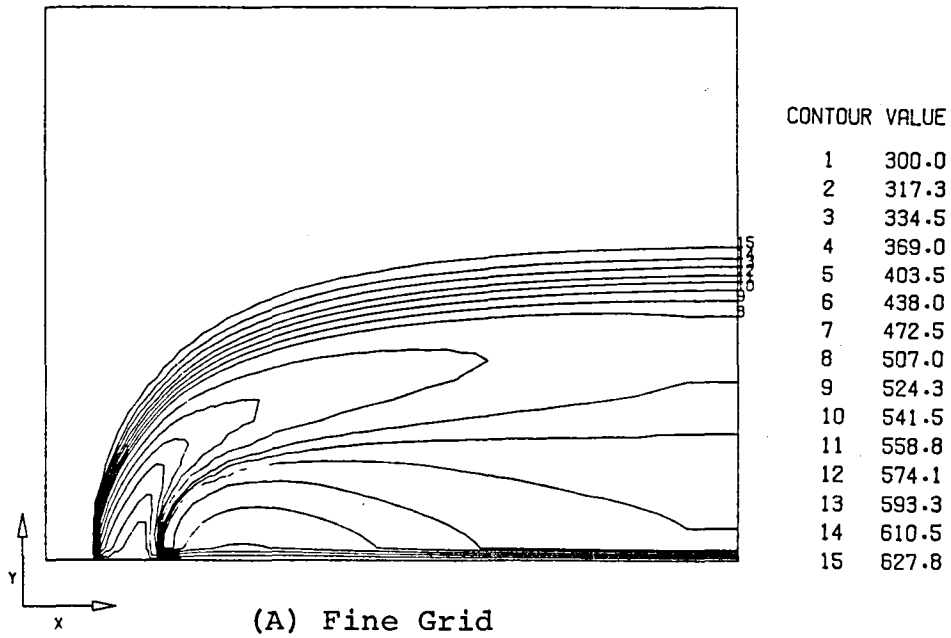
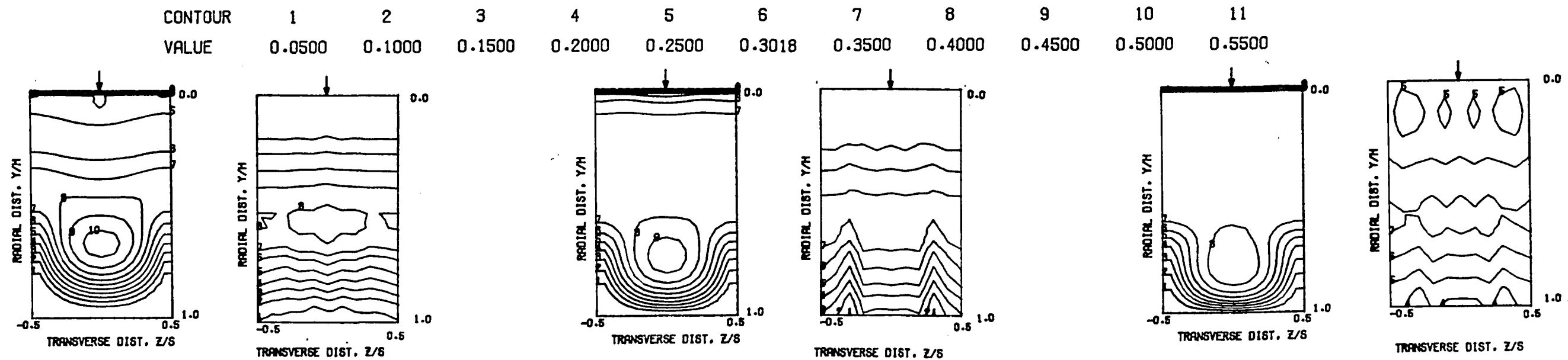


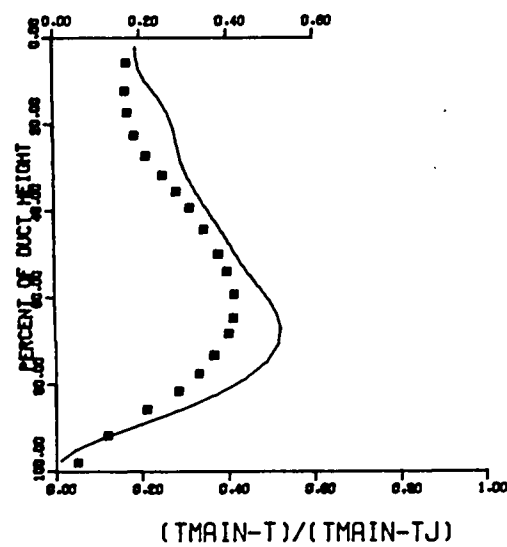
Figure 9.1-6. Predicted Centerplane Temperature Contours with the Fine and Coarse Grid Systems, $J = 25.32$, $S/D = 2$ and $H_0/D = 8$.



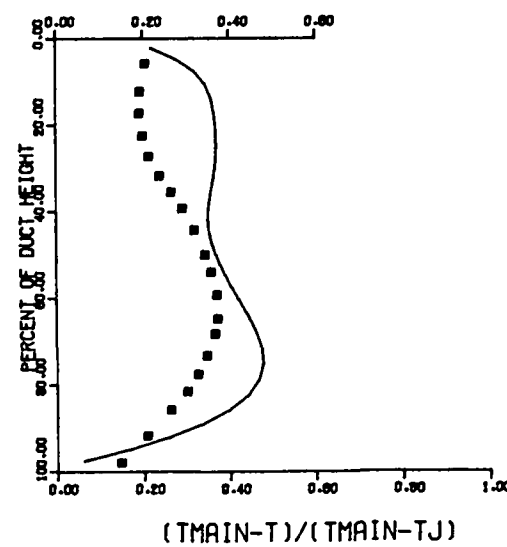
THETA CONTOURS FOR TEST NO. 6, $T_M=CONST$, $J=107.8$, $S/D=2.0$, $H/D=8.0$

$S/DJ = 2.57$ $HO/DJ = 10.29$ $VRATIO = 6.86$ $TRATIO = 0.460$ $DENRATIO=2.287$ $TMAIN = 649.7 \text{ K}$ $TJET = 299.2 \text{ K}$ $THEB = 0.302$

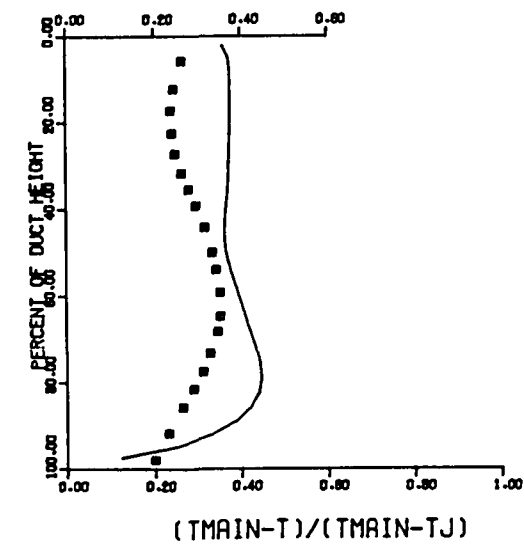
$X/H = 0.50$ $X/DJ = 5.14$



$X/H = 0.75$ $X/DJ = 7.71$

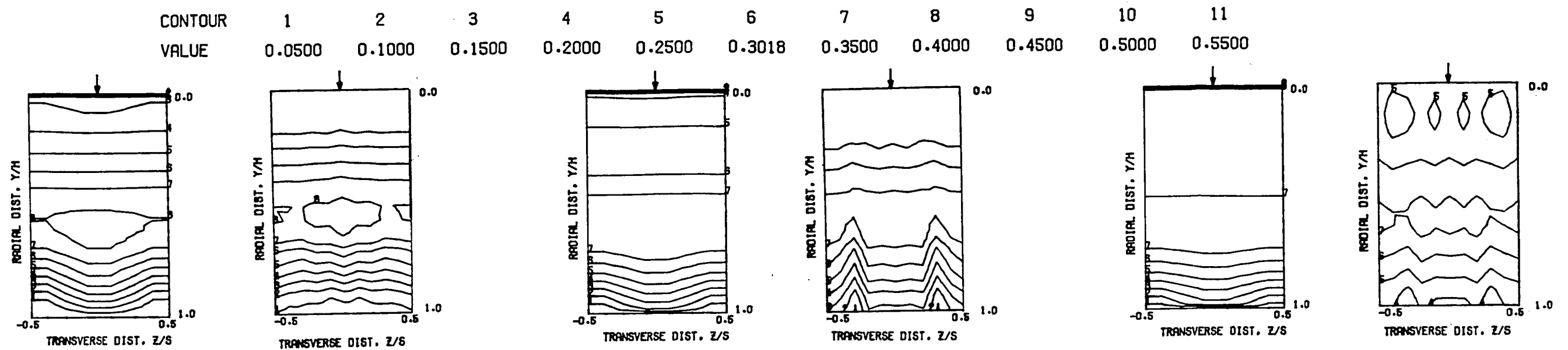


$X/H = 1.00$ $X/DJ = 10.29$

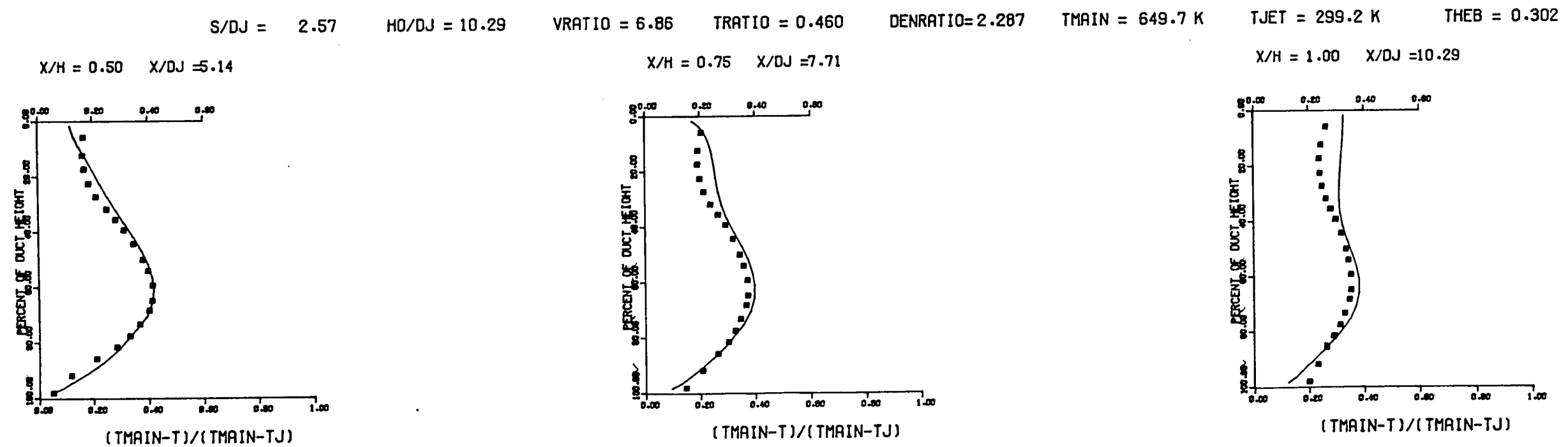


COMPARISON BETWEEN DATA AND PREDICTIONS FOR TEST NO. 6, TEST SECTION I, $TMAIN=CONST$, $J = 107.78$, $S/D = 2.00$, $H/D = 8.00$

Figure 9.1-7



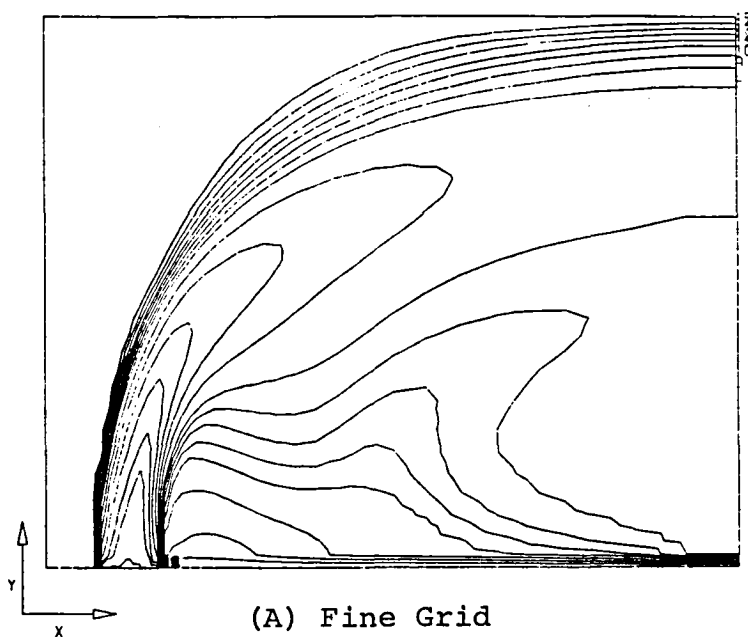
THETA CONTOURS FOR TEST NO. 6, 4-NODES, $J=107.78$, $S/D=2.0$, $H/D=8.0$



COMPARISON BETWEEN DATA AND PREDICTIONS FOR TEST NO. 6, STRAIGHT DUCT, 4-NODE JET,

$J = 107.78$, $S/D = 2.00$, $H/D = 8.00$

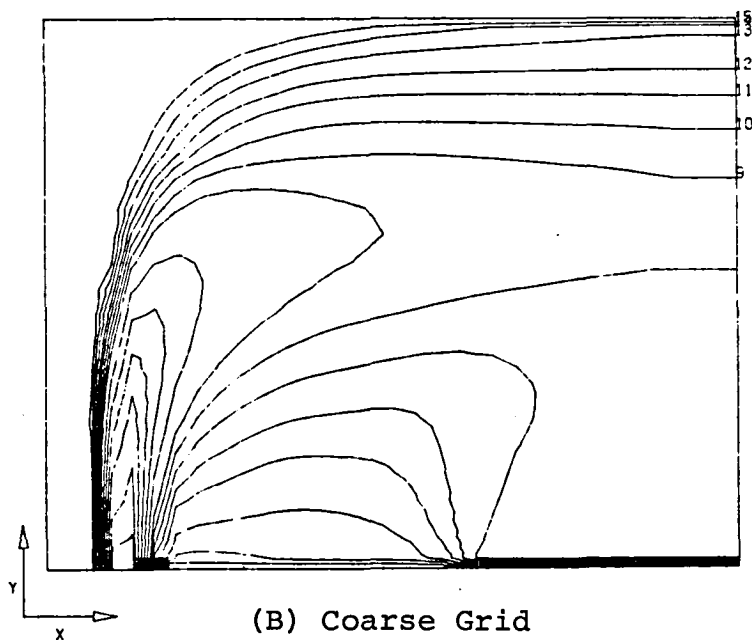
Figure 9.1-8



CONTOUR VALUE

1	300.0
2	317.3
3	334.5
4	369.0
5	403.5
6	438.0
7	472.5
8	507.0
9	524.3
10	541.5
11	558.8
12	574.1
13	593.3
14	610.5
15	627.8

(A) Fine Grid



CONTOUR VALUE

1	300.0
2	317.3
3	334.5
4	369.0
5	403.5
6	438.0
7	472.5
8	507.0
9	524.3
10	541.5
11	558.8
12	574.1
13	593.3
14	610.5
15	627.8

(B) Coarse Grid

Figure 9.1-9. Predicted Centerplane Temperature Contours with the Fine and Coarse Grid Systems, $J = 107.78$, $S/D = 2$ and $H_0/D = 8$.

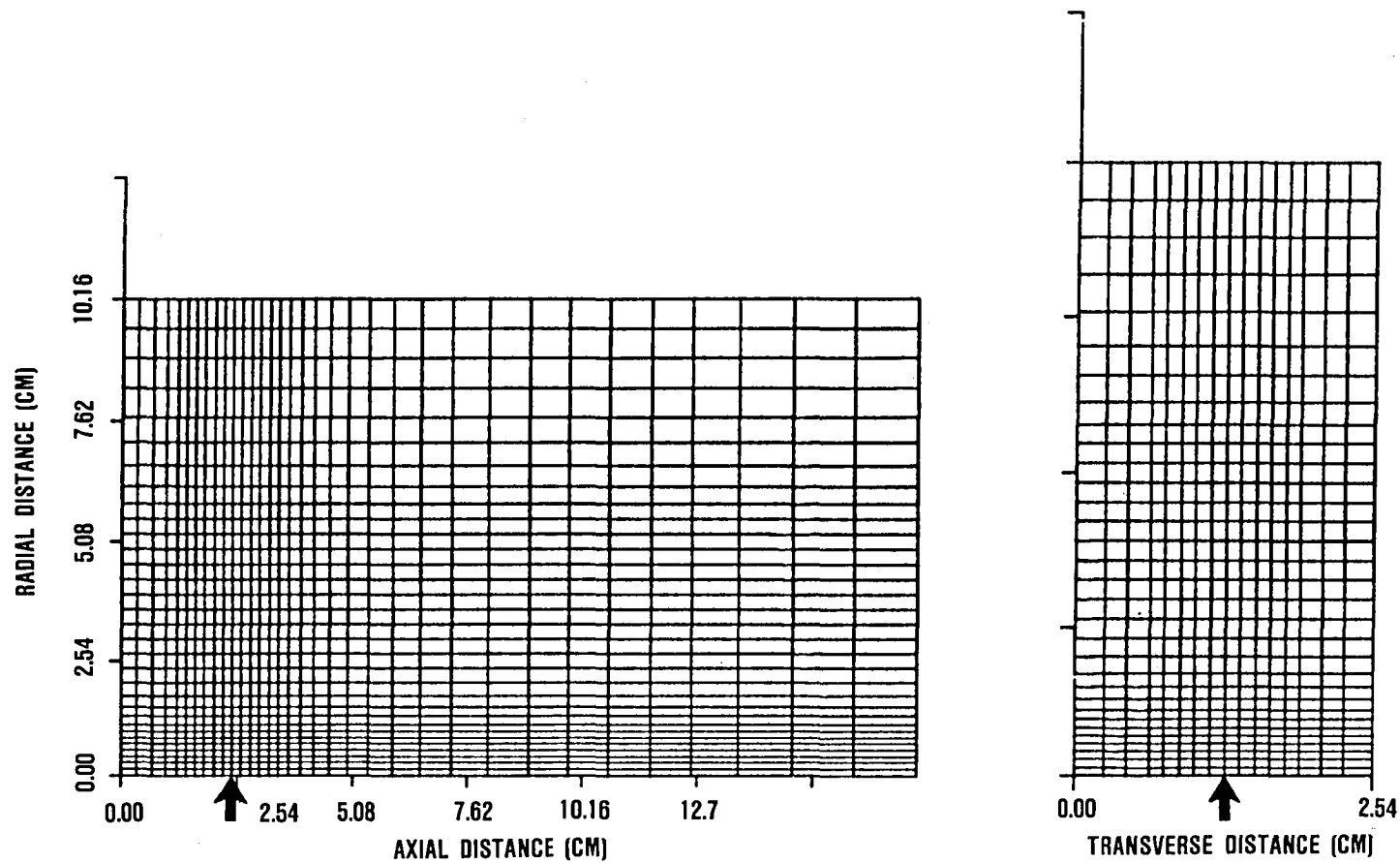
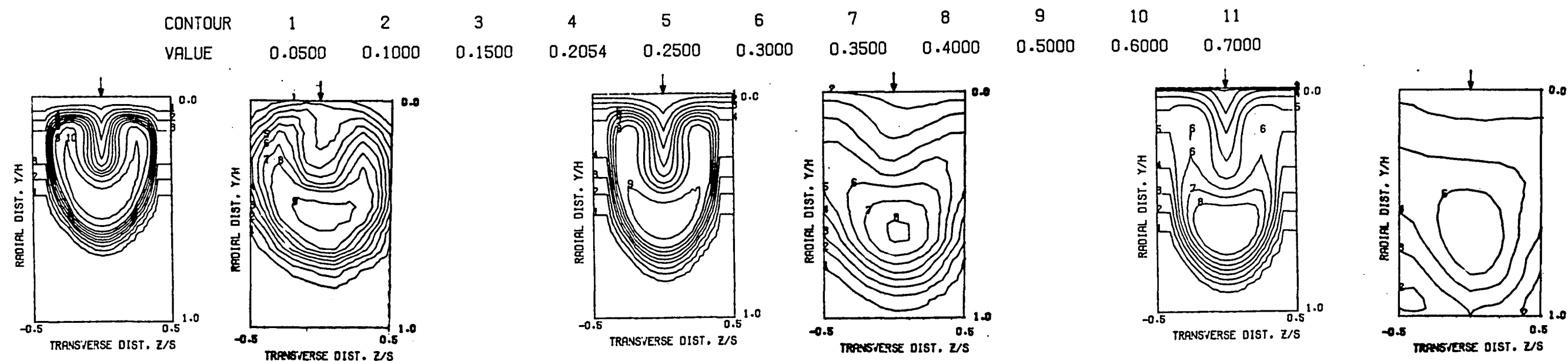
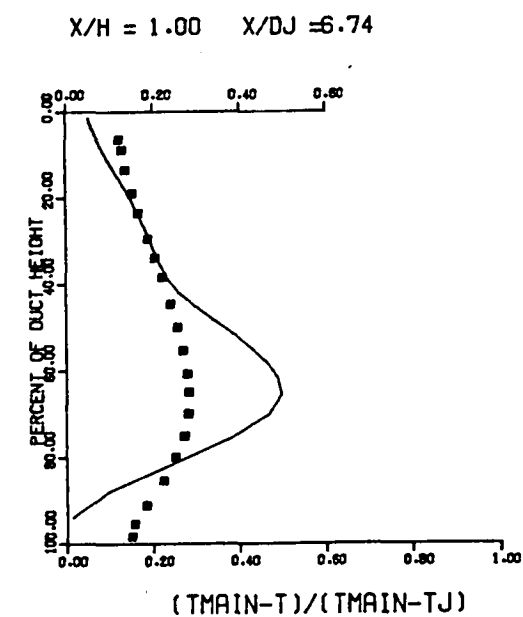
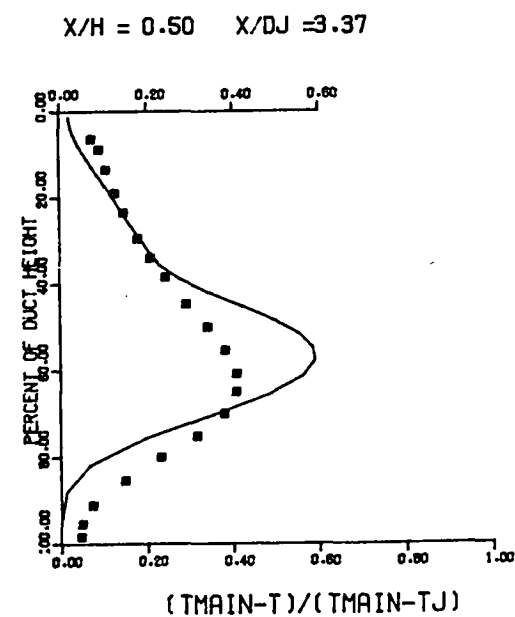
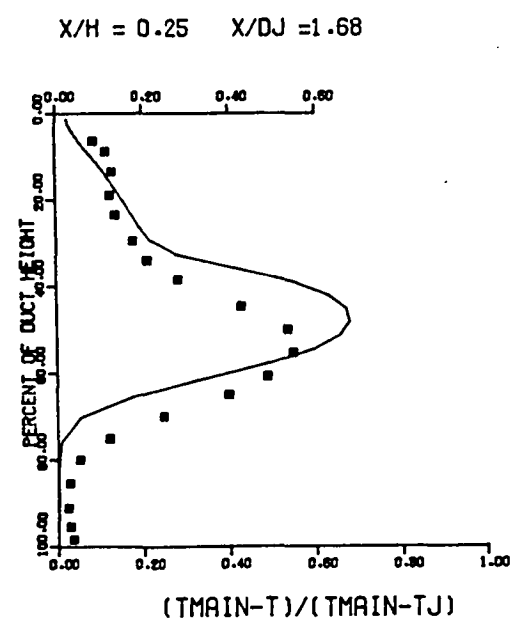


Figure 9.1-10. Finite Difference Grid Network for
Fine Grid (35x33x17) Computations,
 $J = 25.48$, $S/D = 2.83$ and $H_o/D = 5.66$



THETA CONTOURS FOR TEST NO.50, $T_M = \text{CONST}$, $J = 25.48$, $S/D = 2.8$, $H/D = 5.7$

$S/DJ = 3.37$ $H/DJ = 6.74$ $VRATIO = 3.41$ $TRATIO = 0.464$ $DENRATIO = 2.191$ $T_{MAIN} = 644.9 \text{ K}$ $T_{JET} = 299.5 \text{ K}$ $THEB = 0.205$



COMPARISON BETWEEN DATA AND PREDICTIONS FOR TEST NO. 50, TEST SECTION I, $T_M = \text{CONST}$, $J = 25.48$, $S/D = 2.8$, $H/D = 5.66$
Figure 9.1-11

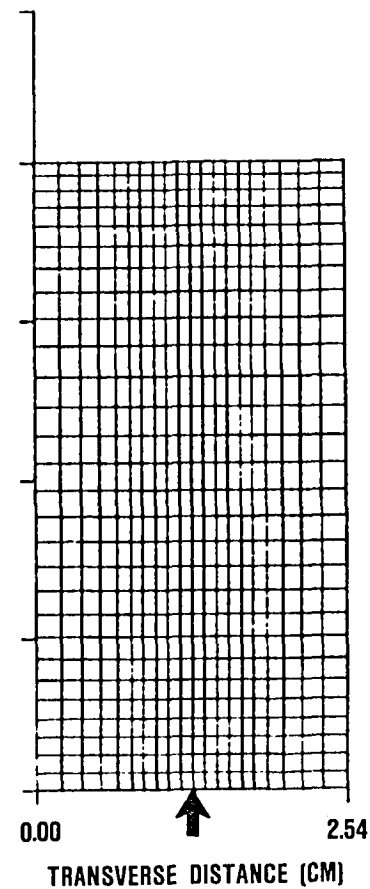
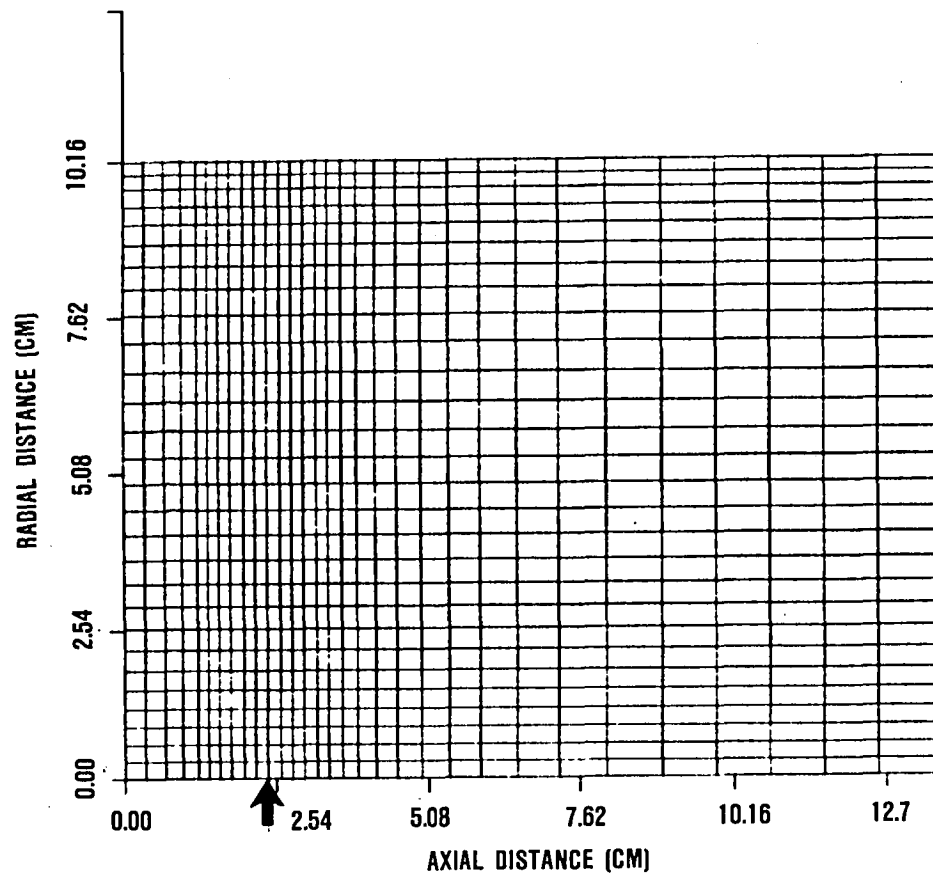
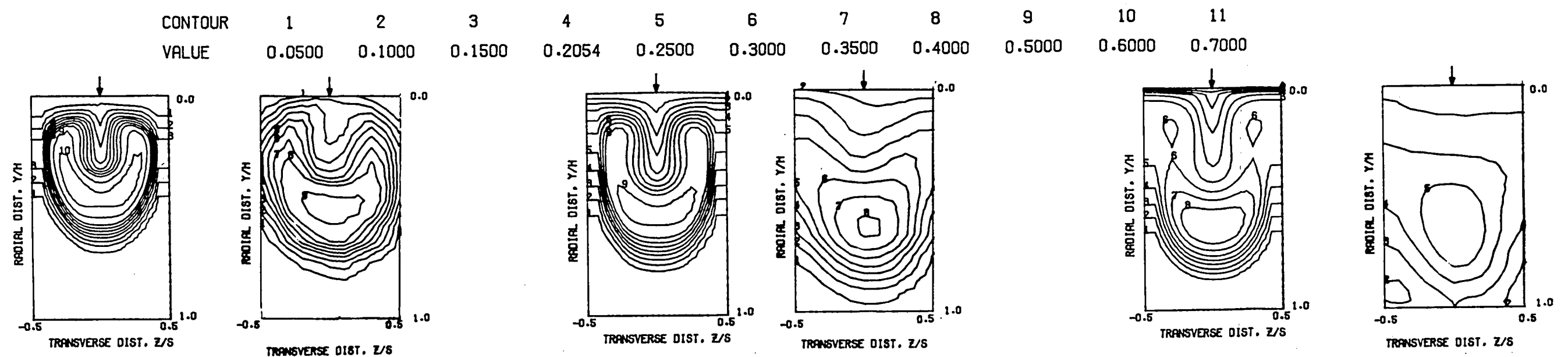


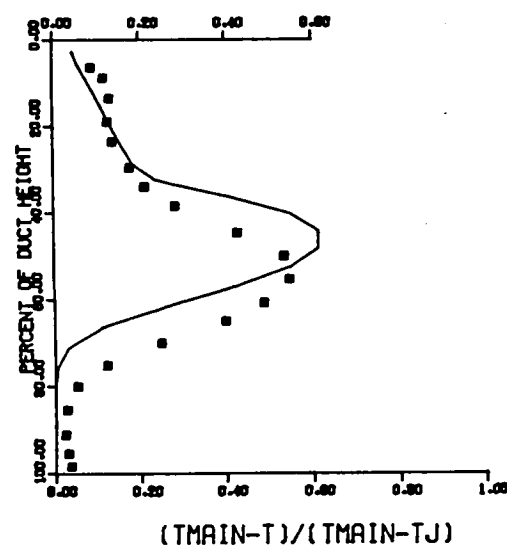
Figure 9.1-12. Finite Difference Grid Network for the Finer Grid (32x29x21) Computations, $J = 25.48$, $S/D = 2.83$ and $H_0/D = 5.66$.



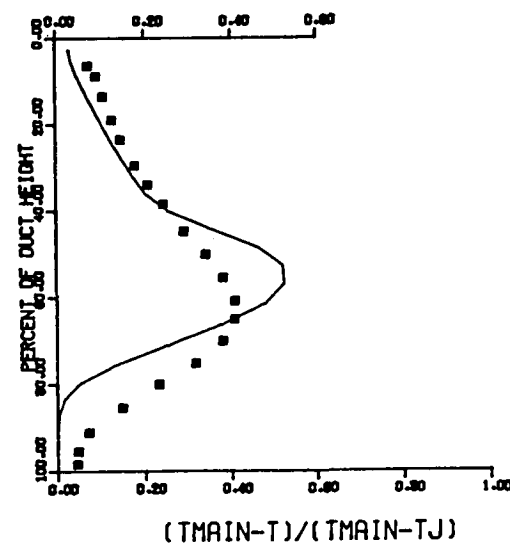
FINER GRID THETA CONTOURS FOR TEST NO 50, $T_M = \text{CONST}$, $J = 25.5$, $S/D = 2.8$, $H/D = 5.7$

$S/DJ = 3.37$ $H/DJ = 6.74$ $VRATIO = 3.41$ $TRATIO = 0.464$ $DENRATIO = 2.191$ $T_{MAIN} = 644.9 \text{ K}$ $T_{JET} = 299.5 \text{ K}$ $T_{HEB} = 0.205$

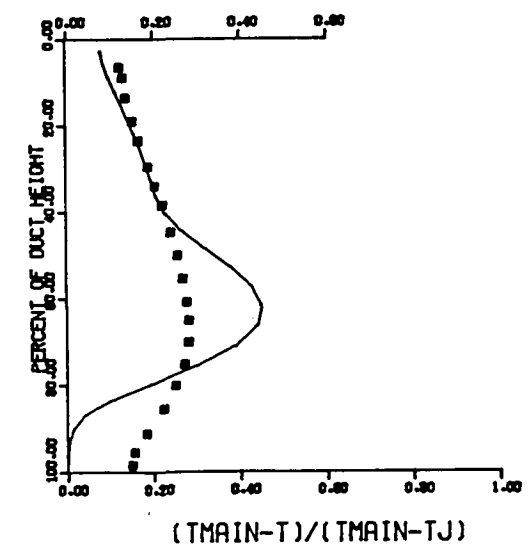
$X/H = 0.25$ $X/DJ = 1.68$



$X/H = 0.50$ $X/DJ = 3.37$



$X/H = 1.00$ $X/DJ = 6.74$



COMPARISON BETWEEN DATA AND PREDICTIONS FOR TEST NO. 50, TEST SECTION I, $T_M = \text{CONST}$, $J = 25.48$, $S/D = 2.83$, $H/D = 5.66$
Figure 9.1-13

9.2 Single-Sided Jet Injection: Effects of Jet Size and Spacing

The 3-D elliptic program was used to analytically predict the effects of orifice size and spacing. A total of four test cases were run covering three different orifice sizes ($D = 1.27, 1.80$ and 2.54 cm), and three spacings ($\frac{S}{D} = 2.0, 2.83$ and 4.0). The analytical results along with the corresponding data are discussed in the following paragraphs

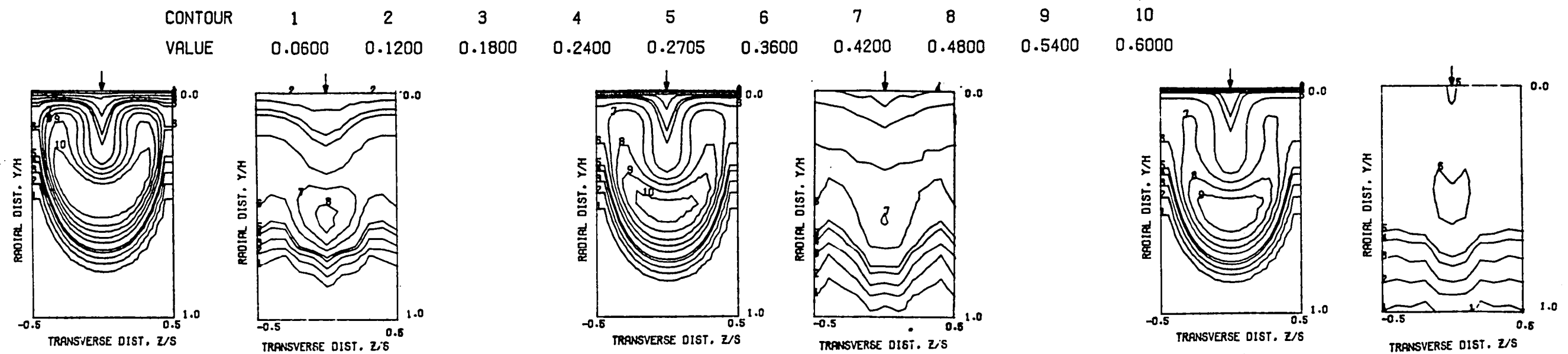
Jet orifice size (and hence H_0/D) and spacing greatly influence jet mixing characteristics as shown experimentally in Reference 219. Figures 9.1-3 and 9.1-13 compare between predicted and measured effects of jet size and spacing on mixing behavior at constant momentum ratio. In the first figure, the jet orifice diameter, D , was 1.27 cm, and the hole spacing, S , was 2.54 cm, with an attendant S/D of 2 and H/D of 8 . For the results presented in Figure 9.1-13 the jet diameter was 1.8 cm and the hole spacing was 5.08 cm, with an S/D of 2.83 and H/D of 5.66 . In order to further assess analytically the effect of hole size, predictions were obtained for a row of 2.54 cm orifices spaced 5.08 cm apart having S/D of 2 and H/D of 4 . For this jet geometry, measurements were available for a momentum ratio of 21.59 . Computation for this case was performed with $45 \times 23 \times 19$ ($19,665$) grid nodes, of which 72 nodes were located inside the jet. Computations were performed until the total mass source error was about 0.09 percent. The converged results for this case are presented in Figure 9.2-1.

The predicted θ contours are in qualitative agreement with the data. The predicted results underestimate the mixing and hence show larger gradients in the transverse direction. The peak centerplane θ values are slightly overpredicted by the model. At $x/H_0 = 0.5$, the actual peak temperature difference between the data and predictions is 41°K , compared to $T_m - T_i = 343^\circ\text{K}$. The jet half-width values, are correctly predicted by the model. Comparison between Figures 9.1-3 and 9.2-1 show that, at a constant momentum

ratio for the same S/D ratios, increasing the diameter increases the jet penetration. However, increasing the jet diameter also increases the transverse gradients. The same trend is also shown by the data.

In order to examine the effects of S/D, computation was made for the case of 2.54 cm diameter jets spaced 10.16 cm apart having an S/D of 4 and H/D of 4 with a jet-to-mainstream momentum ratio of 26.68. For this case, computations were made by using $40 \times 23 \times 21$ (19,320) nodes, of which 63 nodes were located inside the jet. For this case, the mainstream velocity was 14.91 m/s, and the jet velocity was 52.24 m/s. The predicted theta distributions for this case are illustrated in Figure 9.2-2. The predicted results shown are after 350 iterations with a total mass source error of 0.05 percent. The predicted distributions show much greater transverse gradients than the measurements. Along the jet centerplane, the predicted radial profile of θ is in good agreement with the data, with the peak θ value being slightly overpredicted. The jets penetrate to the opposite wall at $x/H_0 = 0.5$. Beyond this station, the data shows a rapid mixing in both radial and transverse directions, whereas the predictions show much slower mixing in the transverse direction.

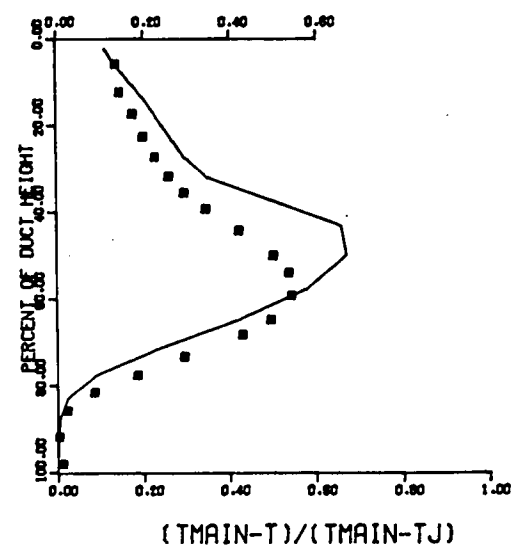
To summarize, the data and predictions are in good agreement in predicting the centerplane profiles. Both of these results show that increasing jet diameter for the same S/D and momentum ratio, increases the jet penetration. Increasing the S/D and keeping the same jet diameter and momentum ratio also increases the jet penetration. However, the predictions show larger gradients in the transverse direction than the measurements. The predicted transverse gradients are larger when S/D is increased.



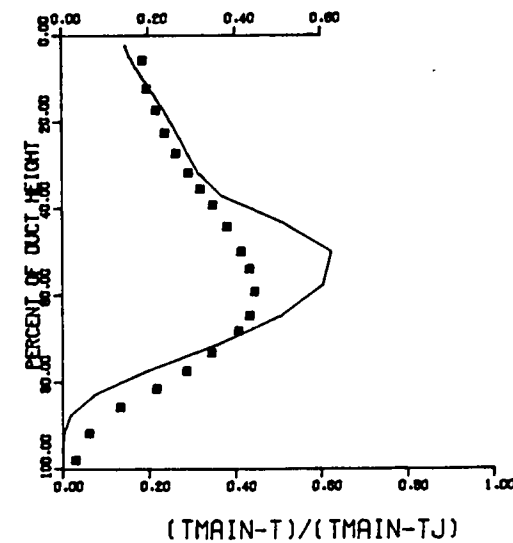
THETA CONTOURS FOR TEST NO. 2, $T_M = \text{CONST}$, $J = 21.59$, $S/D = 2.0$, $H/D = 4.0$

$S/DJ = 2.58$ $H/DJ = 5.16$ $VRATIO = 3.18$ $TRATIO = 0.473$ $DENRATIO = 2.132$ $T_{MAIN} = 651.2 \text{ K}$ $T_{JET} = 308.0 \text{ K}$ $THEB = 0.271$

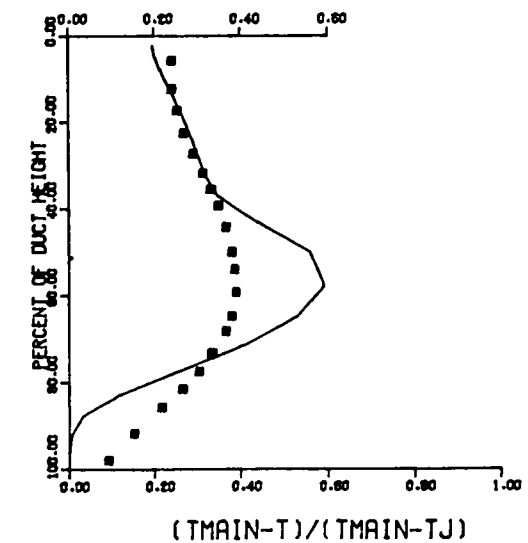
$X/H = 0.50$ $X/DJ = 2.58$



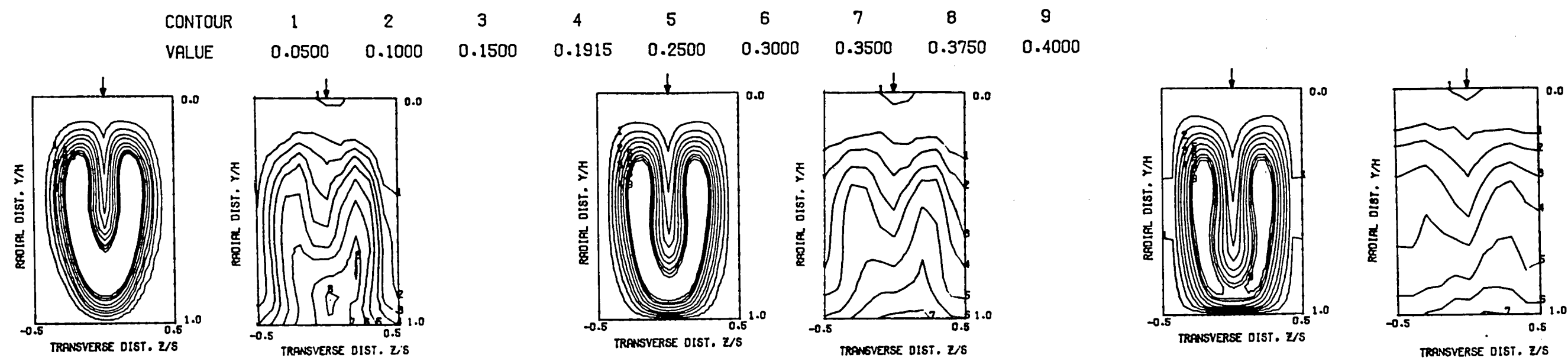
$X/H = 0.75$ $X/DJ = 3.87$



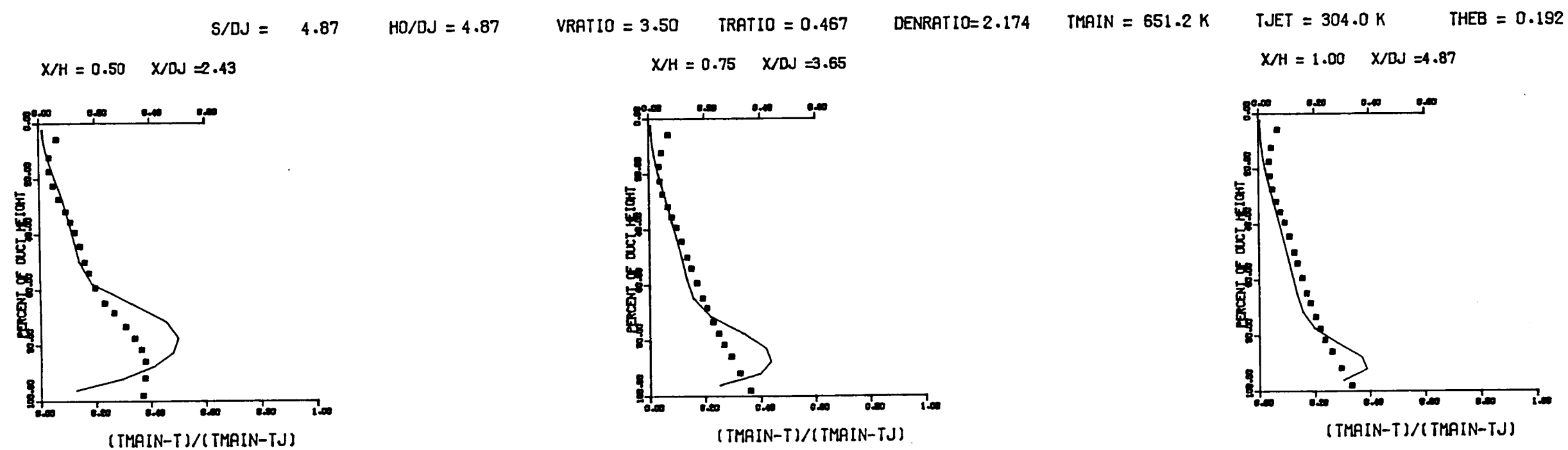
$X/H = 1.00$ $X/DJ = 5.16$



COMPARISON BETWEEN DATA AND PREDICTIONS FOR TEST NO. 02, TEST SECTION I, $T_M = \text{CONST}$, $J = 21.59$, $S/D = 2.00$, $H/D = 4.00$
Figure 9.2-1



THETA CONTOURS FOR TEST NO 4, $T_M = \text{CONST}$, $J = 26.7$, $S/D = 4.0$, $H/D = 4.0$



COMPARISON BETWEEN DATA AND PREDICTIONS FOR TEST NO. 4, TEST SECTION I, ONE SIDED ,

$J = 26.68$, $S/D = 4.00$, $H/D = 4.00$

Figure 9.2-2

9.3 Single-Sided Injection: Effects of Jet Momentum

.Ratio and Cross-Stream Temperature Profile

The results presented in Paragraph 9.2 illustrate the effects of the geometrical parameters of the jet on the predicted mixing characteristics. Another important parameter in the mixing of a row of jets in a confined cross-flow is the jet-to-mainstream momentum ratio (J).

Comparisons between 3-D predictions and data for the following values of J are given in this section

D (cm)	$\frac{S}{D}$	$\frac{H_0}{D}$	J
1.27	2	8	25.32, 107.78
2.54	4	4	6.14, 26.68

In Section 9.1, results were presented in Figures 9.1-3 and 9.1-7 for 1.27 cm orifices spaced 2 Diameters apart with J values of 25.32 and 107.78, respectively. These results showed that by increasing the momentum ratio, the jet penetration was increased from about 40 percent to 70 percent of the duct height. The predictions show higher transverse gradients than the measurements. The gradients in the θ values for J = 25.32 and 107.78 were quite comparable.

Computations were also made for the 2.54 cm jets spaced 4 Diameters apart with low and medium momentum ratios. Figure 9.2-2 illustrates the results for J = 26.68. Both predictions and data indicate jet impingement on the opposite wall of the duct. The comparison between the two is reasonable. To further validate the model, calculations were performed for the same orifice geometry with a low momentum ratio of 6.14. For this case, the mainstream velocity was 15.25 m/s and the jet velocity was 27.93 m/s. Computations for this case were performed with the same grid network as

the one used for $J = 26.68$, having $40 \times 23 \times 21$ (19,320) nodes. Computations were continued until the total mass source error was less than 0.02 percent. The predicted θ distributions along with the data are illustrated in Figure 9.3-1. At $x/H_0 = 0.5$, the predicted θ contours show slightly larger gradients than the measured gradients. The mixing is also underestimated by the model. At the downstream stations, the predicted radial profiles are in qualitative agreement with the data. The peak θ values are overestimated. Comparison between Figures 9.2-2 and 9.3-1 show that the gradients in the θ contours between the two cases are comparable, even though the jet penetrations for these cases are different.

In most combustor flow fields, the primary zone temperature distributions are nonuniform, and the purpose of the dilution jets is to alter the turbine inlet profiles to a desired distribution. For the case of uniform mainstream profiles, it was shown that the centerplane profiles are correctly predicted by the 3-D model. However, the distributions in the transverse directions as indicated by contour plots were only qualitatively well predicted. The predictions were in better agreement with the data for $S/D = 2$ than for the case of $S/D = 4$. In Figure 9.2-1, results were shown for the case of uniform mainstream temperature profile; here the orifice diameter is 2.54 cm, $S/D = 2$ at a momentum ratio of 21.59. For this orifice geometry and a comparable momentum ratio ($J = 22.63$), data is available with a nonuniform mainstream temperature profile. In the test measurements, the hot mainstream air was mixed with cold air from a cooling slot located well upstream of the jet injection plane. The measured temperature profile upstream of the jet injection plane is shown in Figure 9.3-2(a). In this figure, the temperatures are nondimensionalized in the form,

$$\theta = \frac{T_{\max} - T}{T_{\max} - T_j}$$

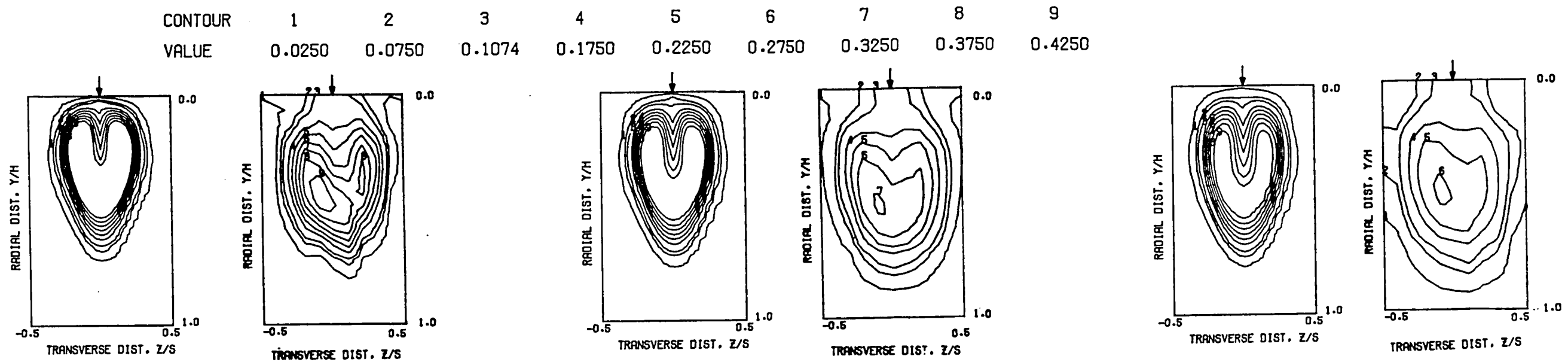
Here T_{\max} is the mainstream maximum temperature which in this case was 748.7°K . By using this expression, the value of θ should be between 0 and 1 even for nonuniform cross-stream θ cases, and has therefore been used to present the results for nonuniform mainstream temperature profiles.

The temperature profile (upstream of the dilution orifices) shown in Figure 9.3-2 indicates that the mainstream is cold near the top wall and hot near the bottom wall of the duct. The corresponding inlet mainstream velocity and turbulent kinetic energy profiles are shown in Figure 9.3-2(b) and 9.3-2(c). The kinetic energy profiles shown were obtained from hot-wire measurements.

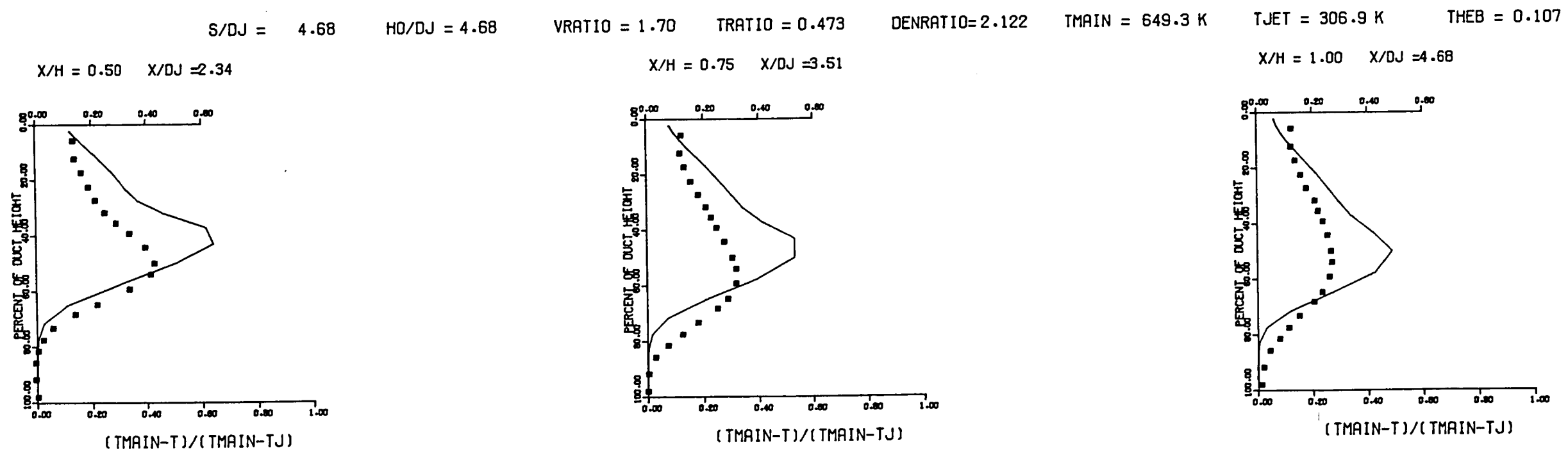
Computations were performed using the same grid network as the one used for the case of uniform mainstream profile, namely, $45 \times 23 \times 19$ (19,665) nodes. The jet velocity and temperature were 59.68 m/s and 293.5°K , respectively. The predicted θ profiles along with the data are shown in Figure 9.3-3. At $x/H_0 = 0.5$, the predicted θ distributions and the data are in good agreement. The predictions slightly underestimate the mixing in the transverse direction, which is responsible for the larger gradients in the θ contours compared to the data. At the downstream stations, the jet spreading is predicted reasonably well. The mixing is still underestimated by the 3-D model. The predicted centerplane θ profiles are in good agreement with the data. Comparison between Figures 9.2-1 and 9.3-3 show that the nonuniform mainstream profile does not significantly alter the mixing behavior of the jets. The mainstream profile has a dominant influence on the temperature profiles throughout the mixing region.

In summarizing the effects of flow parameters, momentum ratio, and mainstream profile, the 3-D model qualitatively correctly predicts those effects on mixing characteristics. The model shows

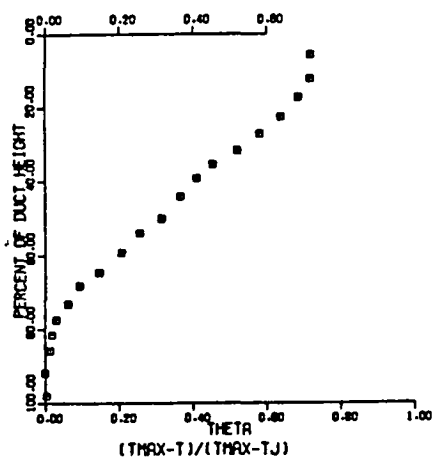
larger gradients for higher S/D , and these gradients are not altered substantially by changing the momentum ratio. Application of a nonuniform mainstream radial profile essentially changes the radial profiles in the mixing region without substantially changing the characteristics of mixing in the transverse direction. For the case of the single-sided jet injection, the 3-D model consistently underestimates the mixing and hence predicts larger gradients, especially in the transverse direction.



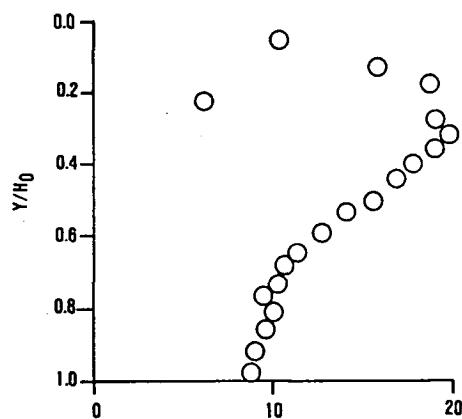
THETA CONTOURS FOR TEST NO.2, $T_M = \text{CONST}$, $J = 6.14$, $S/D = 4.0$, $H/D = 4.0$



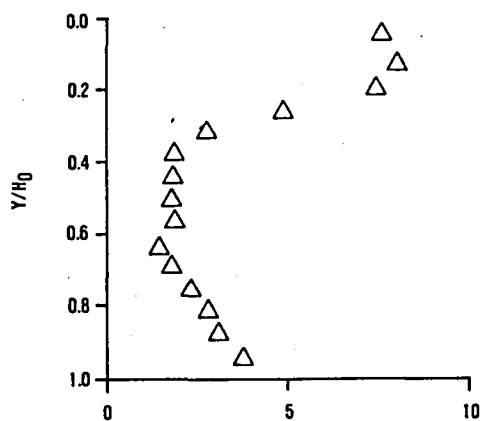
COMPARISON BETWEEN DATA AND PREDICTIONS FOR TEST NO. 2, TEST SECTION I, $T_M = \text{CONST}$, $J = 6.14$, $S/D = 4.00$, $H/D = 4.00$
Figure 9.3-1



(A) TEMPERATURE PROFILE

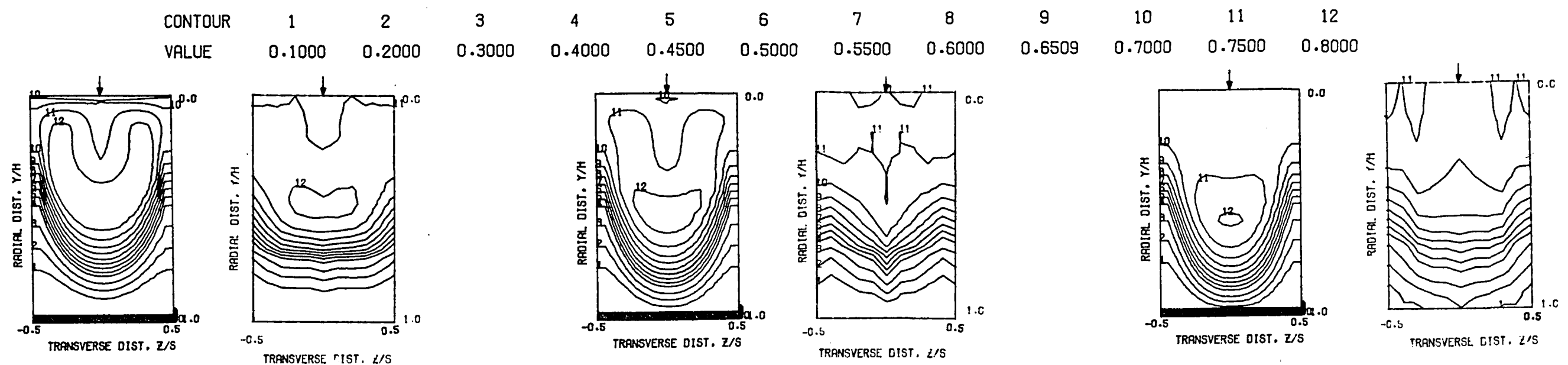


(B) VELOCITY PROFILE

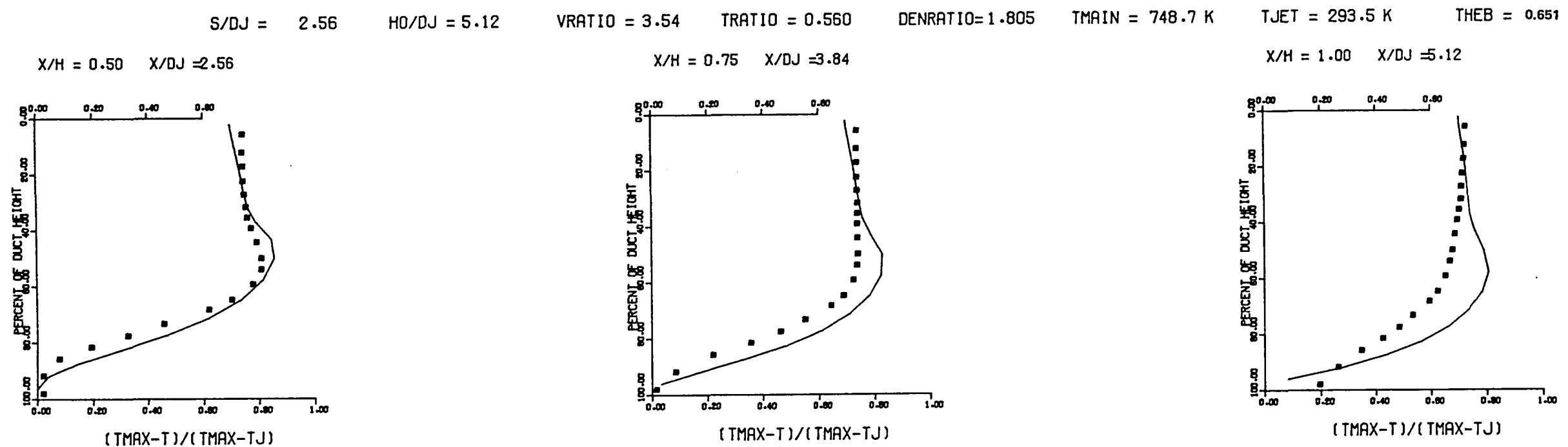


(C) INLET TURBULENCE K.E. (M²/S²)

Figure 9.3-2. Measured Mainstream Inlet Profiles.



THETA CONTOURS FOR TEST NO. 13, TOP COLD, $J=22.63$, $S/D=2.0$, $H/D=4.0$



COMPARISON BETWEEN DATA AND PREDICTIONS FOR TEST NO. 13, TEST SECTION I, TOP COLD TM, $J = 22.63$, $S/D = 2.00$, $H/D = 4.00$
Figure 9.3-3

9.4 Two-Sided Jet Injection

In most annular combustors, the dilution orifices are located on both the inner and the outer walls of the combustor. In order to understand the mixing characteristics of such systems, it is essential to study the flow field in idealized configurations wherein dilution jets are injected from both the top and bottom walls. Detailed temperature measurements were made at Garrett ⁴¹ under NASA Contract No. NAS3-22110 with opposed jets in several jet configurations. Some of this test data was used in this program for evaluating the 3-D analytical model.

The test setup for the case of opposed injection is shown schematically in Figure 9.4-1. In this case, two rows of jets injected air into the ducted cross flow at the same axial station, one row from the top and another from the bottom. The jets could be either in line or staggered. For model validation two test cases were selected, one with an in-line configuration of jets and the other with a staggered arrangement. The jet orifice diameter and S/D were 1.27 cm and 2, respectively.

For the in-line arrangement of the jets, the jet-to-mainstream momentum ratio, temperature, and velocity of the top jets were 24.95, 306.8°K and 53.26 m/s, respectively. The corresponding values for the bottom jet were 24.76, 305.2°K, and 52.92 m/s, respectively. The velocity profiles were uniform with a value of 646.6°K and 15.58 m/s. The mainstream turbulence intensity was 7.5 percent, and the jet turbulence intensities were about 5.5 percent.

Computations were made with 45 x 26 x 17 (19,890) grid nodes that extended from 2.3 cm upstream of the jet injection plane to 23.1 cm downstream of the jet injection plane in the axial direction. In the radial (cross-stream) direction, the computations were performed from the top to the bottom wall. The transverse

direction computational domain extended from mid-plane to mid-plane between two jets. Calculations were performed for 350 iterations with the total mass source error less than 0.02 percent. The predicted θ distributions* and the data for this case are presented in Figure 9.4-2.

At $x/H_0 = 0.25$, the predicted θ contours are in very good agreement with the data. The measured θ contours show the jet penetrations slightly shifted away from the jet centerplane in the transverse direction. It is believed that this was because of very slight misalignment of the jet injections. The predicted radial profiles at this location are in excellent agreement with the data. At $x/H_0 = 0.5$, the data shows a faster mixing than the predicted results. This effect is also seen in the radial profiles. At $x/H_0 = 1$, the data shows that the jets are completely well mixed with the mainstream, and the temperature distributions are nearly uniform in the transverse direction corresponding to the equilibrium value ($\theta_{EB} = 0.3179$). However, the predicted results show significant gradients in the radial and transverse directions.

For the staggered arrangement of jets, the test case consisted of 3 jets of 2.54 cm diameter on each side with the jet spacing-to-diameter ratio, S/D , of 4. The jet-to-mainstream momentum ratios for the top and the bottom jets were 26.4 and 26.1, respectively. The mainstream temperature was uniform with a value of 644.7°K, and the average mainstream velocity was 16.85 m/s. The temperatures of the top and the bottom jets were 307.4°K and 303.6°K, respectively. The jet velocities for the top and bottom jets were 59.43 m/s and 58.59 m/s, respectively.

$$*\theta = \frac{T_m - T}{T_m - T_j}$$

Computations for this case were performed with $22 \times 27 \times 33$ (19,602) finite-difference grid nodes. The computational domain extended from 1.4 cm upstream to 14.8 cm downstream of the jet injection plane in the axial direction. In the radial (cross-stream) direction, the computational domain extended from the top to the bottom wall, and in the transverse direction. The computations were made from mid-plane to mid-plane of the top row of jets. With respect to the bottom row of jets, the computational domain in the transverse direction extended from centerplane to centerplane of the two adjacent jets. Along the boundaries in the transverse direction, cyclic boundary conditions were employed. This is valid even though these end planes correspond to the jet centerlines. Calculations were performed until the total mass source error converged to about 0.1 percent.

The predicted θ distributions and the measurements are illustrated in Figure 9.4-3. At $x/H_0 = 0.25$, the predicted θ distributions and the data are in good qualitative agreement. The predictions show larger gradients in the transverse direction than the data. The radial profiles of the predicted results are in qualitative agreement with the data. The peak θ values are overestimated by the 3-D model. At $x/H_0 = 0.5$, both the data and the predictions show gradual mixing in both radial and transverse directions. The predicted mixing rate is slower than the measured mixing rate. At $x/H_0 = 1$, the data shows that the jets are completely well mixed and reach the equilibrium θ value of 0.3271. But the predicted results show larger variation along the transverse direction. The predicted radial centerplane profile, however, is in good agreement with the data.

To summarize, the predicted results for opposed injection are in qualitative agreement with the data. In the near field ($x/H_0 = 0.25$), the predictions are in good agreement with the measurements for the in-line configuration. However, in the mixing region down-

stream, the 3-D model underestimates the mixing in both radial and transverse directions. For the case of staggered injection, the model correctly predicts the mixing in the radial direction, but significantly underestimates the mixing in the transverse direction. In this regard, it has the same characteristics as the single-sided jets.

The conclusions reached in this program are based upon calculations with approximately 20,000 nodes. Even though these results are not strictly grid-independent, effort was made to demonstrate that these computations approach grid independence by increasing the grid density. Further work with a finer grid network is needed to address grid independence of the solution.

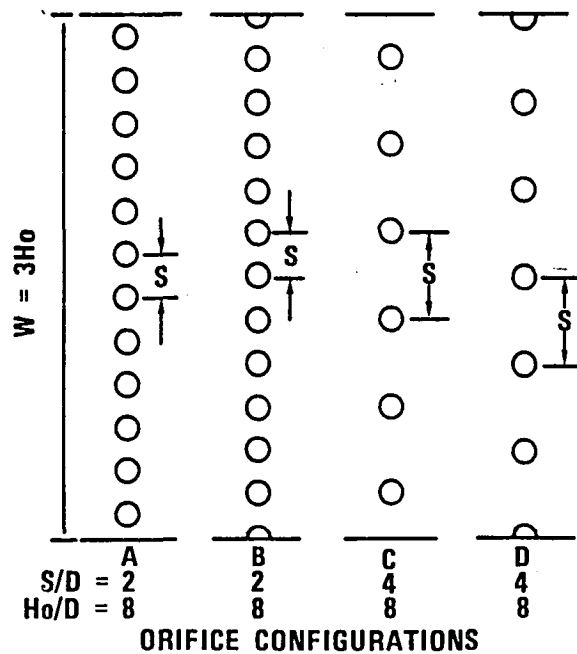
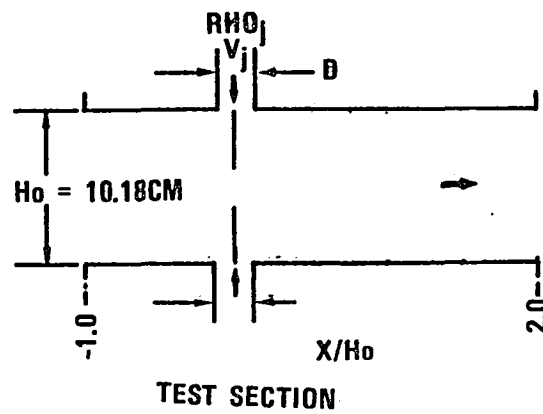
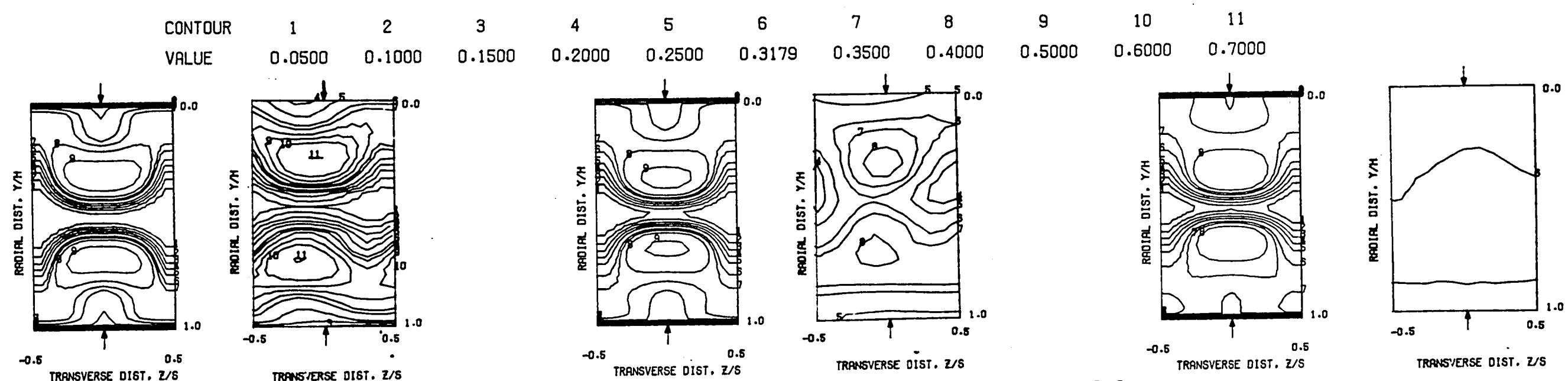


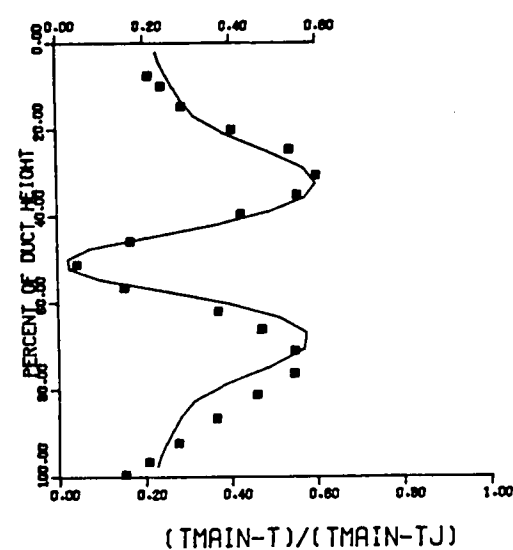
Figure 9.4-1. Schematic of the Test Setup and Typical Orifice Configurations for Two-Sided Jet Injection.



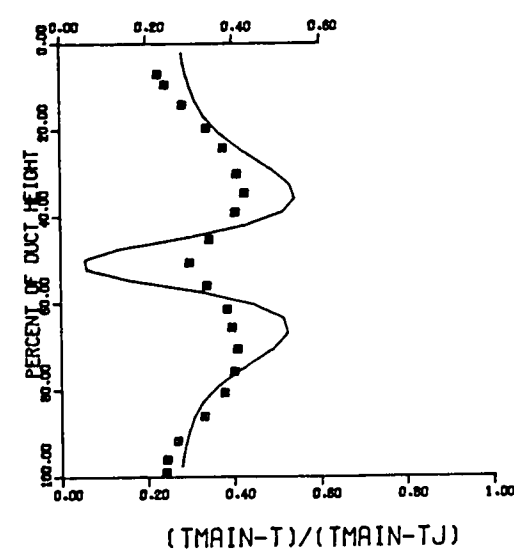
THETA CONTOURS FOR TEST NO. 2, IN-LINE, $J=24.95$, $S/D=2.0$, $H/D=8.0$

$S/DJ = 2.48$ $H/DJ = 9.92$ $VRATIO = 3.42$ $TRATIO = 0.474$ $DENRATIO = 2.135$ $TMAIN = 646.6 \text{ K}$ $TJET = 306.8 \text{ K}$ $THEB = 0.318$

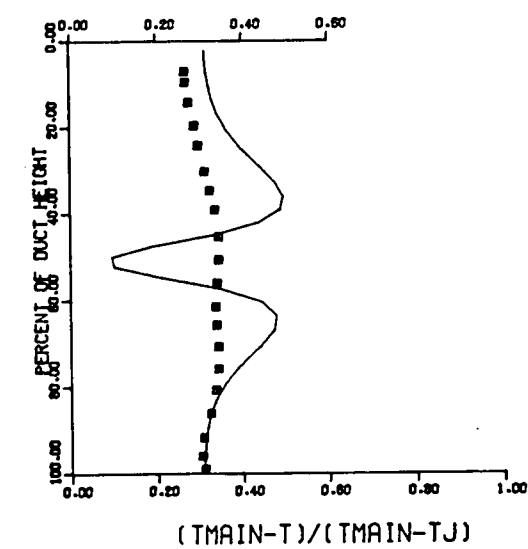
$X/H = 0.25$ $X/DJ = 2.48$



$X/H = 0.50$ $X/DJ = 4.96$

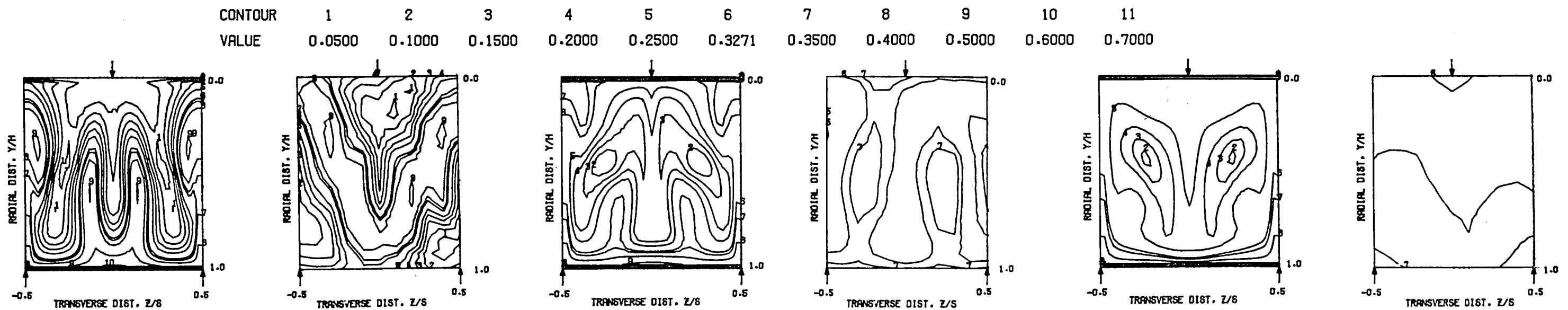


$X/H = 1.00$ $X/DJ = 9.92$



COMPARISON BETWEEN DATA AND PREDICTIONS FOR TEST NO. 2, TEST SECTION I, OPPOSED (INL), $J = 24.95$, $S/D = 2.00$, $H/D = 8.00$

Figure 9.4-2

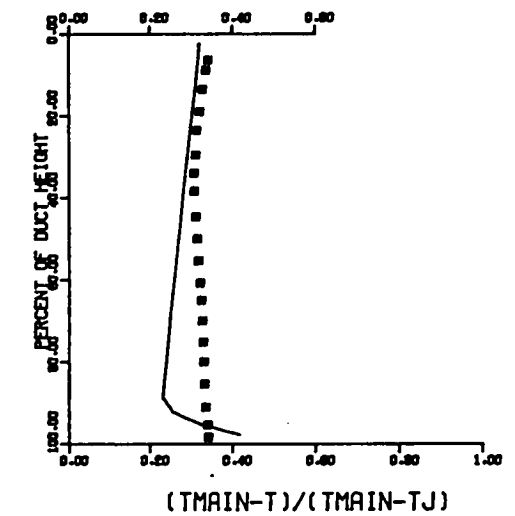
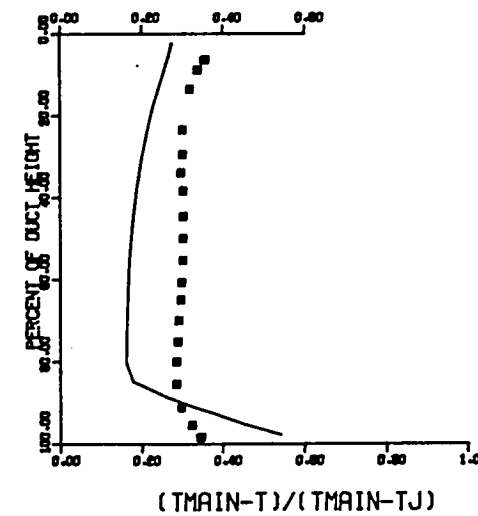
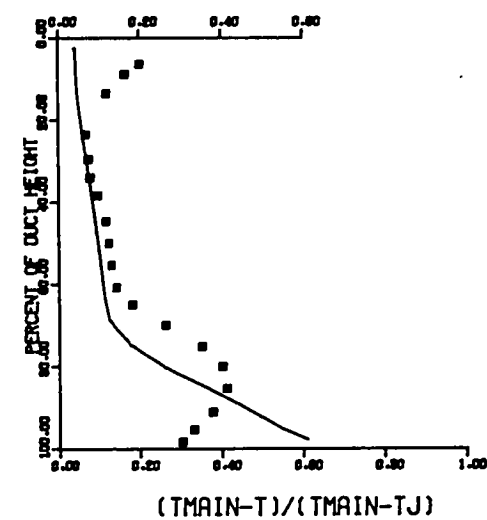


$S/DJ = 4.97$ $H/DJ = 4.97$ $VRATIO = 3.53$ $TRATIO = 0.477$ $DENRATIO=2.125$ $TMAIN = 644.7 \text{ K}$ $TJET = 307.4 \text{ K}$ $THEB = 0.327$

$X/H = 0.25$ $X/DJ = 1.24$

$X/H = 0.50$ $X/DJ = 2.49$

$X/H = 1.00$ $X/DJ = 4.97$



COMPARISON BETWEEN DATA AND PREDICTIONS FOR TEST NO. 28, TEST SECTION I, OPPOSED (STG), $J = 26.42$, $S/D = 4.00$, $H/D = 4.00$

Figure 9.4-3

10.0 CONCLUSIONS AND RECOMMENDATIONS

Important specific conclusions for each of the sections in Chapters 6 through 9 were provided at the end of each section. General conclusions of this study and recommendations for future investigations are presented here in Sections 10.1 and 10.2, respectively.

10.1 Conclusions

General conclusions for an extensive investigation, such as the present one, can be made in a number of ways. Here the conclusions are made for each of the major submodels and what their capabilities are in predicting various types of flows: simple, complex nonswirling, swirling, and dilution jet mixing. Observations are also made concerning numerical accuracy and grid-independence of the solution. Throughout this chapter, statements are frequently made regarding a model giving good results, reasonable results, trends, or unsatisfactory results. This implies the following: A model is termed good when it can correlate data within ± 25 percent. A reasonable correlation implies within a factor of 2.0. When a model is called qualitatively good or is described as predicting trends, no claim is made in regard to quantitative accuracy of this model. Predictions of such a model when used in a design system should be cautiously interpreted for guiding an engineering design.

k- ϵ Turbulence Model

This includes the standard k- ϵ model of turbulence and its various modifications including corrections for the low Reynolds number, additional strain due to streamline curvature and swirl (Richardson number correction), and other ad hoc assumptions for changing empirical constants C_D , C_2 , and Prandtl/Schmidt numbers.

The following general conclusions are made regarding the $k-\epsilon$ model capabilities:

- o Gives good correlation for simple flows
- o Requires low Reynolds number correction for predicting wall shear layers
- o Requires different model modifications for accurately predicting curved (convex and concave) boundary layers
- o Gives good correlation for the far-field regimes of complex swirling or nonswirling flows involving regions of recirculation
- o Gives reasonable results for nonswirling recirculating flows. The correlation is not as good in the vicinity of reattachment points
- o Gives reasonable correlation for confined disk flow with jet at the center
- o Gives good correlation for nonrecirculating swirling flows
- o Outer regions of strong swirling flows can be predicted well. A reasonable correlation is achieved for the shear layer between the outer region and the recirculation zone. Trends are properly predicted for the recirculating flow regions
- o Gives reasonable correlation for most of the flow region established by a confined swirler with expansions on both hub and shroud sides

- o Predicts trends for confined swirler with no outer expansion.

Algebraic Stress Model and Its Modifications

This model predicts mean flow field properties as well as the $k-\epsilon$ model does. Therefore, the comments in the previous paragraph apply to the ASM as far as the mean velocity field is concerned. The following conclusions are made in regard to the Reynolds stresses, both normal and shear stress components:

- o All Reynolds stress components are predicted reasonably well for simple flows.
- o A low Reynolds number correction is required for predicting wall shear layers.
- o Different modifications are required for predicting convex and concave wall shear flows.
- o Normal stress trends are correctly predicted in nonswirling recirculating flows. The shear stresses are reasonably well predicted in such flows.
- o For flows with swirl, the normal stress components are predicted with reasonable accuracy. The shear stress predictions, especially the ones involving the tangential component, are unsatisfactory.
- o Further model refinements are needed to improve the accuracy of the ASM predictions.

Scalar Transport Model

The $k-\epsilon$ model with specified Prandtl number predicts scalar fluxes reasonably well for the flows where gradient diffusion approximation is valid. The proposed algebraic scalar transport model has shown advantages over the $k-\epsilon$ modeling approach. Further work is needed to establish its validity for recirculating swirling flows.

Turbulence/Chemistry Interaction Models

Both two-step and four-step reaction schemes show promise for application in gas turbine combustors. They need to be further validated with simple flames (plug flow reactor, diffusion and premixed laminar, and turbulent jet flames) to establish rate constants so that major species including unburned fuel, CO and H_2 can be accurately predicted.

The modified eddy breakup model predicts trends and should be pursued because this can be easily extended to multistep kinetic schemes, unlike other more vigorous approaches.

Bilger's two-reaction zone model gives good results for jet flames but needs to be further evaluated for gas turbine combustion application. Its deficiency in regard to PDF specifications needs to be addressed.

Dilution Jet Mixing

For dilution jet mixing calculations, it is extremely important to determine the grid independence of the predicted results. Although good agreement between predictions and measurements may be obtained in some cases with 7000 nodes, those results are not grid-independent. However, by increasing grid density and the number of

nodes, it was shown that the predictions tend to approach a grid-independent solution. The predicted results with 20,000 nodes were in good agreement with the measurements.

The Garrett 3-D model correctly predicts the jet centerplane profiles. However, in the transverse direction, the predicted results underestimate the mixing. The effects of jet geometrical parameters (S/D , H/D , etc.) as well as the momentum ratio (J) are well predicted by the model. The effects of nonuniform cross-stream profiles are well correlated by the 3-D model.

For the case of two-sided jet injection, with an in-line configuration of jets, the model accurately predicts the temperature distribution in regions close to the jet injection plane. The mixing in regions farther downstream is underestimated by the model. For the case of staggered configuration of the jets, the predicted results are in good agreement throughout the region of interest in the flow field.

10.2 Recommendations

Due to numerical diffusions involved in analyzing recirculating flows, it has been difficult to assess model accuracy in predicting such flows. It is therefore considered vital to develop a numerical scheme with a higher order of accuracy to minimize numerical errors.

During the course of the present investigation, it was recognized in many instances that there was a lack of a benchmark quality data base relevant to gas turbine combustion. Such a data base is badly needed for making further model assessment.

It appears that significant improvement in turbulence modeling may be achieved after a major investment of money and time. Therefore, turbulence/chemistry interaction models need to be developed and calibrated without using turbulence modeling techniques that are more complicated than the algebraic stress models, which include various modifications for low Reynolds number, additional strain due to streamline curvature, and swirl.

Although current aerothermal models give reasonable predictions, an intensive model development and validation effort should be continued, especially for the following submodels:

- o Algebraic stress model
- o Algebraic scalar transport model
- o Two-step and four-step kinetic schemes
- o PDF approach for a two-step scheme
- o Double reaction zone model.

REFERENCES

1. Reynolds, R.S., T.E. Kuhn and H.C. Mongia: "An Advanced Combustor Analytical Design Procedure and its Application to the Design and Development Testing of a Premix/Prevaporized Combustion System," Spring Meeting of the Central States Section of the Combustion Institute, 1977.
2. Johansen, K.M., B.H. Johnston, H.C. Mongia and J.W. Sanborn: "Combustion Process Testing for Reduced Wall-Temperature Gradients." Proceedings 1977 DARPA/NAVSEA Ceramic Gas Turbine Demonstration Engine Program Review, 1977.
3. Mongia, H.C. and K.F. Smith: "An Empirical/Analytical Design Methodology for Gas Turbine Combustor," AIAA Paper 78-998.
4. Mongia, H.C., R.S. Reynolds, E. Coleman and T.W. Bruce: "Combustor Design Criteria Validation, Volume II, Development Testing of Two Full-Scale Annular Gas Turbine Combustors," USARTL-TR-78-55B, 1979.
5. Austin, G.F. and H.C. Mongia: "Improved Combustor-Dome Operating Characteristics Program, Phase I Design Report," U.S. Navy Contract No. N00140-79-C-3384, 1980.
6. Dins, C.R., R.J. Evershed, H.C. Mongia and J. Wimmer: "Advanced Material Segmented Combustor, Phase II Interim Report," AFAPL-TR-80-2065, 1980.
7. Mongia, H.C., E.B. Coleman and T.W. Bruce: "Design and Testing of Two Variable-Geometry Combustors for High-Altitude Propulsion Engines," AIAA Paper 81-1389.
8. Kuhn, T., H.C. Mongia, T. Bruce and E. Buchanan: "Small Gas Turbine Augmentor Design Methodolgy," AIAA Paper 82-1179.
9. Mongia, H.C. and D.J. Brandes: "Design Documentation Report, Counter-Flow Film-Cooled Combustor Program," NASA CR-167922, 1982.
10. Sanborn, J.W., H.C. Mongia and J.R. Kidwell: "Design of a Low-Emission Combustor for an Automotive Gas Turbine," AIAA Paper 83-0338.
11. Hunter, S.C., K.M. Johansen, H.C. Mongia and M.P. Wood: "Advanced, Small, High-Temperature-Rise Combustor Program, Volume I, Analytical Model Derivation and Combustor-Element Rig Tests (Phases I and II)," AD778766, 1974.

REFERENCES (CONTD.)

12. Bruce, T.W., H.C. Mongia and R.S. Reynolds: "Combustor Design Criteria Validation Volume I, Element Tests and Model Validation," USARTL-TR-78-55A, 1979.
13. Srinivasan, R. and H.C. Mongia: "Numerical Computations of Swirling Recirculating Flow, Final Report," NASA CR-165196, 1980.
14. Srivatsa, S.K.: "Computations of Soot and NO_x Emissions from Gas Turbine Combustors," NASA-CR-167930, 1982^x.
15. Patankar, S.V.: "Numerical Prediction of Three-Dimensional Flows," in Studies in Convection: Theory, Measurement and Applications, Volume I, Edited by B.E. Launder, New York: Academic Press, 1975.
16. Patankar, S.V. and D.B. Spalding: Heat and Mass Transfer in Boundary Layers, London: Intertext Books, 1970.
17. Chien, K.Y.: "Predictions of Channel and Boundary Layer Flows with a Low Reynolds Number Two-Equation Model of Turbulence," AIAA-80-0134, 1980.
18. Launder, B.E., G.J. Reece, and W. Rodi: "Progress in the Development of a Reynolds Stress Turbulence Closure," Journal of Fluid Mechanics 68:3, p. 537, 1975.
19. Hautman, D.J., F.L. Dryer, K.P. Schug, and I. Glassman: "A Multiple-step Overall Kinetic Mechanism for the Oxidation of Hydrocarbons," Combustion Science and Technology 25, pp. 219-235, 1981.
20. Donaldson, C.duP.: "On the Modeling of the Scalar-Correlations Necessary to Construct a Second-Order Closure Description of Turbulent Flow," in Turbulent Mixing in Non-reactive and Reactive Flows, Edited by S.N.B. Murthy, New York: Plenum Press, 1974.
21. Borghi, R.: Advances in Geophysics 18B, p. 349, 1974.
22. Lockwood, F.C.: "The Modeling of Turbulent Premixed and Diffusion Combustion in the Computation of Engineering Flows," Combustion and Flame, 29, pp. 111-122, 1977.
23. Spalding, D.B.: "Mixing and Chemical Reaction in Steady Confined Turbulent Flames," in Thirteenth Symposium (International) on Combustion, Pittsburgh, PA: The Combustion Institute, 1973.

REFERENCES (CONTD.)

24. Spalding, D.B.: "The Influences of Laminar Transport and Chemical Kinetics on the Time-Mean Reaction Rate in a Turbulent Flame," in Seventeenth Symposium (International) on Combustion, Pittsburgh, PA: The Combustion Institute, 1979.
25. Pope, S.B.: "Monte Carlo Calculations of Premixed Flames," in Eighteenth Symposium (International) on Combustion, Pittsburgh, PA: The Combustion Institute, 1981.
26. Bilger, R.W.: "Perturbation Analysis of Turbulent Nonpremixed Combustion," Combustion Science and Technology 22, pp. 251-261, 1980.
27. Bilger, R.W. and S.H. Starner: "A Double Reaction Zone Model and Perturbation Analysis for Finite Rate Kinetics in Hydrocarbon Fueled Combustors," AIAA-83-0599, January 1983.
28. Jensen, D.E. and G.A. Jones: Combustion and Flame, 32, pp. 1-34, 1978.
29. Duterque, J., R. Borghi and H. Tichtinsky: Combustion Science and Technology 26, pp. 1-15, 1981.
30. Williams, F.A.: "Combustion of Droplets of Liquids Fuels: A Review," Combustion and Flame 21, pp. 1-31, 1973.
31. Faeth, G.M.: "Spray Combustion Models - A Review," AIAA Paper 79-0293, 1979.
32. Faeth, G.M.: "Evaporation and Combustion of Sprays" to be published in Progress in Energy and Combustion Science.
33. Dimmons, U.C.: "The Correlation of Drop Size Distributions in Fuel Nozzle Sprays," ASME 76-WA/GT-9, 1977.
34. Swithenbank, J., A. Turan, P.G. Felton, and D.B. Spalding: "Fundamental Modeling of Mixing, Evaporation, and Kinetics in Gas Turbine Combustors," Report HIC 320, University of Sheffield, Sheffield, England SI 3JD, September 1979.
35. Gosman, A.D. and E. Ioannides: "Aspects of computer simulation of liquid-fuelled combustors," Paper AIAA-81-0323, 1981.
36. Priem, R.J. and M.F. Heidmann: "Propellant Vaporization as a Design Criteria for Rocket-Engine Combustion Chambers," NASA technical Report R-67, 1960.

REFERENCES (CONTD.)

37. Briffa, F.E.: "Transient Drag in Sprays," in Eighteenth Symposium (International) on Combustion, Pittsburgh, PA: The Combustion Institute, 1981.
38. Rose, J.W. and J.R. Cooper, (Ed): Technical Data on Fuel, Seventh Edition, New York: John Wiley & Sons, 1977.
39. Radcliffe, S.W. and J.P. Appleton, Combustion Science and Technology 3, p. 255, 1971.
40. Blazowski, W.S., R.B. Edelman, and E. Wong: "Fundamental Characterization of Alternate Fuel Effects in Continuous Combustion Systems," Technical Progress Report, EXXON CR.2EBA.80, Linden, NJ, 1980.
41. Tesner, P.A. et al.: "Kinetics of Dispersed Carbon Formation,:" Combustion and Flame 17, p. 253, 1971.
42. Khan, I.M. and G. Greeves: Heat Transfer from Flames, International Seminar, Trogir, Yugoslavia, 1973.
43. Nagle, J. and R.F. Strickland-Constable: "Oxidation of Carbon between 1000-2000°C," in Proceedings of the Fifth Conference on Carbon, Volume I, New York: Pergamon Press, 1962.
44. Park, C. and J.P. Appleton: "Shock-Tube Measurements of Soot Oxidation Rates," Combustion and Flame 20, pp. 369-379, 1973.
45. Magnussen, B.F. and B.H. Hjertager: "On Mathematical Modeling of Turbulent Combustion with Special Emphasis on Soot Formation and Combustion: in Sixteenth Symposium (International) on Combustion, Pittsburgh, PA: The Combustion Institute, 1977.
46. Magnussen, B.F., B.H. Hjertager, J.G. Olsen, and D. Bhaduri: "Effects of Turbulent Structure and Local Concentration on Soot Formation and Combustion in C₂H₂ Diffusion Flames," in Seventeenth Symposium (International) on Combustion, Pittsburgh, PA: The Combustion Institute, 1978.
47. Hamaker, H.C.: "Radiation and Heat Conduction in Light-Scattering Material," Philips Research Report, Volume 2, pp. 55-67, 1947.
48. Spalding, D.B.: Report RF/TN/A/8, London: Imperial College, 1971.
49. Siddall, R.G.: "Flux methods for the analysis of radiant heat transfer," presented at Fourth Symposium on Flames and Industry, British Flame Research Committee and the Institute of Fuel, Imperial College, London, September 1972.

REFERENCES (CONTD.)

50. Whitacre, G.R., and R.A. McCann: "Comparison of Methods for the Prediction of Radiant Heat Flux Distribution and Temperature," ASME paper 75-HT-9, 1975.
51. Lockwood, F.C. and N.G. Shah: "A New Radiation Solution Method for Incorporation in General Combustion Prediction Procedures," presented at Eighteenth Symposium on Combustion London: Imperial College of Science and Technology, 1980.
52. Modak, A.T.: "Radiation from Products of Combustion," Fire Research 1, pp. 339-361, 1978/79.
53. Edwards, D.K. and A. Balakrishnan: "Thermal Radiation by Combustion Gases," International Journal of Heat and Mass Transfer 16, pp. 25-40, 1973.
54. DeRis, J.: "Fire Radiation - A Review," in Seventeenth Symposium (International) on Combustion, Pittsburgh, PA: The Combustion Institute, 1979.
55. Leckner, B.: "Spectral and Total Emissivity of Water Vapor and Carbon Dioxide," Combustion and Flame 19, pp. 33-48, 1972.
56. Felske, J.D. and C.L. Tien: "Calculation of the Emissivity of Luminous Flames," Combustion Science and Technology 7, pp. 25-31, 1973.
57. Sarofim, A.F.: "Flame Emissivities: Alternate Fuels," in Alternative Hydrocarbon Fuels: Combustion and Chemical Kinetics, Edited by C.T. Bowman and J. Birkeland, New York: AIAA, 1978.
58. Patankar, S.V. and D.B. Spalding: Heat and Mass Transfer in Boundary Layers, London: Intertext Books, 1970.
59. Champagne, F.H. Y.H. Pao, and I.J. Wygnanski: "On the Two Dimensional Mixing Region" Journal of Fluid Mechanics, Volume 74, pp. 290-251, 1976.
60. Saiy, M. and S.J. Peerless: "Measurement of Turbulence Quantities in a Two-Stream Mixing Layer," Journal of Fluid Mechanics, Volume 89, pp. 709-722, 1978.
61. Biringen, S.: "An Experimental Study of a Turbulent Axisymmetric Jet Issuing into a Coflowing Airstream," von Karman Institute for Fluid Dynamics Technical Note 110, April 1975.
62. Habib, M.A. and J.H. Whitelaw: "Velocity Characteristics of a Confined Coaxial Jet," ASME Paper 79-WA/FE-9, ASME Winter Annual Meeting, December 2-7, 1979.

REFERENCES (CONTD.)

63. Smith, D.J. and T. Hughes: "Some Measurements in a Turbulent Circular Jet in the Presence of a Co-flowing Free Stream," Aeronautical Quarterly, Volume 28, pp. 185-196 August 1977.
64. Champagne, F.H. and I.J. Wygnanski: "Coaxial Turbulent Jets," Report DL-82-0958, Boeing Scientific Research Laboratories, February 1970.
65. Emery, A.F. and F.B. Gessner: "The Numerical Prediction of the Turbulent Flow and Heat Transfer in the Entrance Region of a Parallel Plate Duct," ASME Paper 76-HT-39, ASME-AICHE Heat Transfer Conference, August 9-11, 1976.
66. Wieghardt, K. and W. Tillman, U & M 6617, 1944, translated as "On the Turbulent Friction Layer for Rising Pressure," NACA TM1314, 1951.
67. Watts, K.C., and E. Brundrett: "Turbulence and Momentum Properties of Zero Pressure Gradient Boundary Layers with Suction on a Flat Plate," Turbulent Boundary Layers, H.E. Weber Editor, ASME, 1979.
68. Barbin, A.R. and J.B. Jones: "Turbulent Flow in the Inlet Region of a Smooth Pipe," ASME Journal of Basic Engineering 85, pp. 29-33, March 1963.
69. Laws, E.M., E.H. Lim and J.L. Livesey: "Turbulent Pipe Flows in Development and Decay," Second Symposium on Turbulent shear Flows, London, June 1979.
70. Everitt, K.W. and A.G. Robins: "The Development and Structure of Turbulent Plane Jets," Journal of Fluid Mechanics, Volume 88, pp. 563-583, 1978.
71. Prabhu, A. and B.N.S. Rao: "Effect of Concave Streamline Curvature on Turbulent Boundary Layers," AIAA-81-1193, presented at the 14th Fluid and Plasma Dynamics Conference, June 1981.
72. Hunt, I.A. and P.N. Joubert: "Effects of Small Streamline Curvature on Turbulent Duct Flow," Journal of Fluid Mechanics, Volume 91, part 4, pp. 633-659, 1979.
73. Schultz, J.R.: "An Investigation of Ducted, Two-Stream Variable Density, Turbulent Jet Mixing with Recirculation," AEDC-TR-76-152, January 1977.

REFERENCES (CONTD.)

74. Shivaprasad, B.G. and B.R. Ramapriyan: "Turbulence Measurements in Boundary Layers Along Mildly Curved Surfaces," Journal of Fluids Engineering, Trans. ASME, Volume 100, pp. 37-46, 1978.
75. Jeans, A.H., and J.P. Johnston: "Effect of Streamwise Concave Curvature on Turbulent Boundary Layer Structure," Report MD-40, ThermoSciences Division, Dept. Mechanical Engineering, Stanford University, June 1982.
76. Gillis, J.C., and J.P. Johnston: "Turbulent Boundary Layer on a Convex Curved Surfaces," Report HMT. No. 31, Dept. of Mech. Eng., Stanford University, 1980.
77. Smyth, R.: "Turbulent Flow Over a Disk Normal to a Wall," Journal of Fluids Engineering, Trans. ASME, Volume 101, pp. 461-465, December, 1979.
78. Durao, D.F.G., and J.H. Whitelaw: "Velocity Characteristics of the Flow in the Near Wake of a Disc," Journal of Fluid Mechanics, Volume 85, part 2, pp. 369-385, 1978.
79. Moss, W.D., and S. Baker: "Recirculating Flows Associated with Two-Dimensional Steps," Aeronautical Quarterly, Volume XXXI, pp. 151-172, August 1980.
80. Bremmer, R., H.D. Thompson and W.H. Stevenson: "An Experimental and Numerical Comparison of Turbulent Flow Over a Step," AFAPL Technical Report AFWAL-TR-80-2108, July 1980.
81. Schofield, W.H., and T.S. Keeble: "Measurements of Mean Velocity and Mass Exchange in a Separated Recirculating Flow," Fluid Mechanics of Combustion, 1974.
82. Kim, J., S.J. Kline and J.P. Johnston: "Investigation of Separation and Reattachment of a Turbulent Shear Layer: Flow Over a Backward-Facing Step," Report MD-37, ThermoSciences Division, Dept. of Mech. Engr., Stanford University, 1978.
83. Eaton, J.K. and J.P. Johnston: "Turbulent Flow Reattachment: An Experimental Study of the Flow and Structure Behind a Backward-Facing Step," Report MD-39, ThermoSciences Division, Dept. of Mech. Engr., Stanford University, 1980.
84. Owen, F.K.: "Measurements and Observations of Turbulent Recirculating Jet Flows," AIAA Journal, Volume 14, No. 11, p. 1556, 1976.

REFERENCES (CONTD.)

85. Chigier, N.A. and J.M. Beer: "The Flow Region Near the Nozzle in Double Concentric Jets," Journal of Basic Engineering, Trans. of ASME pp. 797-804, December 1964.
86. Pitz, R.W.: "An Experimental Study of Combustion: The Turbulent Structure of a Reacting Shear Layer Formed at a Rearward-Facing Step," NASA CR-165427, 1981.
87. " " Gürüz, K. and C. Ilicali: "An Investigation of the Isothermal Confined Double Concentric Jet System," Combustion Science and Technology, Volume 25, pp. 193-208, 1981.
88. Johnson, B.V. and J.C. Bennett: "Mass and Momentum Turbulent Transport Experiments with Confined Coaxial Jets," NASA-CR-165574, November 1981.
89. Moon, L.F. and G. Rudinger: "Velocity Distribution in an Abruptly Expanding Circular Duct," Journal of Fluids Engineering, Trans. ASME, pp. 226-230, 1977.
90. Fujii, S., M. Gomi and K. Eguchi: "Cold Flow Tests of a Bluff-Body Flame Stabilizer," Journal of Fluids Engineering, Trans. ASME, Volume 100, pp. 323-332, 1978.
91. Phataraphruk, P., and E. Logan: "Turbulent Pipe Flow Past a Rectangular Roughness Element," Turbulent Boundary Layers, Forced, Incompressible, non-reacting, presented at the Joint ASME-CSME Applied Mechanics, Fluids Engineering and Bioengineering Conference, Niagara Falls, Niagara, pp. 187-196 June 1979.
92. Lightman, A.J., R.D. Richmond, L. Krishnamurthy, P.D. Magill, W.M. Roquemore, R.P. Bradley, J.S. Stutand and C.M. Reeves: "Velocity Measurement in a Bluff-Body Diffusion Flame," AIAA paper 80-1544, AIAA 15th Thermophysics Conference, July 1980.
93. Pratte, B.D. and J.F. Keffer: "A Counter Rotating Pair of Turbulent Jets," Journal of Basic Engineering. Trans. ASME, ASME paper 72-WA/FE-17, 1972.
94. Ribiero, M.M. and J.W. Whitelaw: "Coaxial Jets With and Without Swirl," Journal of Fluid Mech., Volume 96, part 4, pp. 769-795, 1980.
95. Syred, N., J.M. Beer, and N.A. Chigier: "Turbulence Measurements in Swirling Recirculating Flows," Symposium on Internal Flow, University of Salford, Paper 13, B27.

REFERENCES (CONTD.)

96. Escudier, M.P., J. Bornstein, and N. Zehnder: "Observations and LDA Measurements of Confined Turbulent Vortex Flow," *Journal of Fluid Mechanics*, Volume 98, part 1, pp. 49-63, 1980.
97. Scott, C.J. and D.R. Rask: "Turbulent Viscosities for Swirling Flow in a Stationary Annulus," *Journal of Fluids Engineering*, Trans. ASME, pp. 557-566, 1973.
98. Rhode, D.L. and D.G. Lilley: "Mean Flow Fields in Axi-Symmetric Combustor Geometries with Swirl," AIAA paper 82-0177, 1982.
99. Vu, B.T., and F.C. Gouldin: "Flow Measurements in a Model Swirl Combustor," AIAA paper No. 80.0076, presented at the 18th Aerospace Sciences Meeting, Pasadena, Calif., January 1980.
100. Janjua, S.I., D.K. McLaughlin, T.W. Jackson and D.G. Lilley: "Turbulence Measurements in a Confined Jet Using a Six-Oriented Hot-Wire Probe Technique," AIAA paper AIAA-82-1262, 1982.
101. Morse, A.P.: "Axisymmetric Free Shear Flows With and Without Swirl," Ph.D Thesis, University of London, 1980.
102. Mathur, M.L. and N.R.L. MacCullum: "Swirling Air Jets Issuing From Vane Swirlers: Part 2: Enclosed Jets," *Journal of the Institute of Fuel*, pp. 238-245, June 1967.
103. Unpublished work, Garrett Turbine Engine Company, 1981.
104. Unpublished work, Garrett Turbine Engine Company, 1981.
105. Keffer, J.F., G.J. Olson and J.G. Kawall: "Intermittency in a Thermal Mixing Layer," *Journal of Fluid Mechanics*, Volume 79, p. 595, 1977.
106. Hishida, M. and Y. Nagano: "Simultaneous Measurements of Velocity and Temperature in Non-isothermal Flows," *Journal of Heat Transfer*, Trans. ASME, Volume 100, pp. 340-345, May 1978.
107. Johnson, D.S.: "Velocity and Temperature Fluctuation Measurements in a Turbulent Boundary Layer Downstream of a Stepwise Discontinuity in Wall Temperature," *Journal of Applied Mechanics*, pp. 325-336, September 1959.

REFERENCES (CONTD.)

108. Chevray, R. and N.K. Tutu: "Kinematic and Thermal Structures of a Round Heated Jet," Proceedings of the 1st Symposium on Turbulent Shear Flows, Volume 1, p. 15.1, 1977.
109. Fabris, G.: "Turbulent Temperature and Thermal Flux Characteristics in the Wake of a Cylinder," Proceedings of the 1st Symposium on Turbulent Shear Flows, Volume 1, p. 15.11, 1977.
110. Charnay, G., J.P. Schon, E. Alcaraz, and J. Mathieu: "Thermal Characteristics of a Turbulent Boundary Layer with Inversions of Wall Heat Flux," Proceedings of the 1st Symposium on Turbulent Shear Flows, Volume 1, p. 15.47, 1977.
111. Flair, K.L.: "A Theoretical Study of a Laminar Diffusion Flame," NASA CR-158110, 1978.
112. Heys, N.W., F.G. Roper and P.J. Kayes: "A Mathematical Model of Laminar Axisymmetrical Natural Gas Flames," Computers and Fluids, 9, pp. 85-103, 1981.
113. Most, J.M., N. Harivel, P. Joulain, and B. Sztal: "Study of a Turbulent Diffusion Flame in a Channel Flow," Third Symposium on Turbulent Shear Flows, UC, Davis, 1981.
114. Takagi, T. and S. Kotoh: "Computation and its Comparison With Experiments of Time-Mean and Fluctuating Properties in Round Jets With and Without Flame," Third Symposium on Turbulent Shear Flows, University of California, Davis, CA, 1981.
115. Eickhoff, H. and K. Grethe, "Investigations on a Reaction Model for Turbulent Diffusion Flames," Third Symposium on Turbulent Shear Flows, University of California, Davis, CA, 1981.
116. Smith, G.D., T.V. Giel, and C.G. Catalano: "Experimental Investigation of Reactive Turbulent Recirculating Jet Mixing in a Dump Combustor Flowfield," AIAA 81-1122, 1981.
117. Kimoto, K., I. Shiraishi, and R. Matsumoto: "Structure of Turbulent Jet Flames Stabilized in Annular Air Jet," Comb. Sci. Tech., 25, pp. 31-41, 1981.
118. Takagi, T., H.D. Shin, and A. Ishio, "A Study on the Structure of Turbulent Diffusion Flame: Properties of Fluctuations of Velocity, Temperature, and Ion Concentration," Comb. and Flame, 41, pp. 261-271, 1981.
119. Ueda, T., M. Mizomoto, S. Ikai, and T. Kobayashi: "Velocity and Temperature Fluctuations in a Flat Plate Boundary Layer Diffusion Flame," Comb. Sci. Tech., 27, pp. 133-142, 1982.

REFERENCES (CONTD.)

120. Bittker, D.A. and G. Wolfbrandt: "Effect of Fuel Nitrogen and Hydrogen Content on Emissions in Hydrocarbon Combustion," NASA TM-81612, 1981.
121. Lockwood, F.C. and A.S. Naguib: "The Prediction of the Fluctuations in the Properties of Free, Round-Jet, Turbulent, Diffusion Flames," Comb. and Flame, 24, pp. 109-124, 1975.
122. Meunier, S., M. Champion, and J.C. Bellet: "Premixed Combustion in a Turbulent Boundary Layer with Injection," Third Symposium on Turbulent Shear Flows, University of California, Davis, CA, 1981.
123. Somer, H.T. and W. Adams: "Stable Species Concentration of a Turbulent Premixed Methane-air Flame," The Fluids Engineering Conference, Boulder, Colorado, p. 227, 1981.
124. Chang, C. and T.O. Tiernan: "Mass Spectrometric Measurements of the Concentrations of Gaseous Species in Reactive Flow Systems," AFWAL-TR-81-2139, 1981.
125. Cook, S.J. and R.F. Simmons, "A Flame Structure Study of Lean Propane-Oxygen Flames Diluted with Argon," Comb. and Flame, 46, pp. 177-190, 1982.
126. Bechtel, J.H., R.J. Blint, C.J. Dasch, and D.A. Weinberger, "Atmospheric Pressure Premixed Hydrocarbon-Air Flames: Theory and Experiment," Comb. and Flame, 42, pp. 197-213, 1981.
127. Hahn, W.A., J.O.L. Wendt, and T.J. Tyson: "Analysis of the Flat Laminar Opposed Jet Diffusion Flame With Finite Rate Detailed Chemical Kinetics," Comb. Sci. Tech., 27, pp. 1-17, 1981.
128. Kawamura, T., K. Asato, and T. Mazaki, "Structure Analysis of the Stabilizing Region of Plane, Laminar Fuel-jet Flames," Comb. Sci. Tech. 22, pp. 211-216, 1980.
129. Mitchell, R.E., A.F. Sarofim, and L.A. Clomburg: "Experimental and Numerical Investigation of Confined Laminar Diffusion Flames" Comb. and Flame, 37, pp. 227-244, 1980.
130. Moreau, P. and J. Labbe: "Laser Velocimetry in a High Velocity Combustion Flow," Reunion de Travail Internationale sur la Velocimetrie Laser, Third, 1978.

REFERENCES (CONTD.)

131. Pitz, R.W. and J.W. Daily: "Experimental Study of Combustion in a Turbulent Free Shear Layer Formed at a Rearward Facing Step," AIAA 81-0106, 1981.
132. Ganji, A.R. and R.F. Sawyer: "An Experimental Study of the Flow Field and Pollutant Formation in a Two Dimensional, Premixed, Turbulent Flame," AIAA Paper No. 79-0017, 1979.
133. Hassan, M.M.A., F.C. Lockweed, and H.A. Moneib: "Fluctuating Temperature and Mean Concentration Measurements in a Vertical Turbulent Free Jet Diffusion Flame," Imperial College, London, Report FS/80/21, 1980.
134. Takeno, T. and Y. Kotani: "A Study on the Structure of Turbulent Jet Diffusion Flames," Comb. Sci. Tech. 10, pp. 45-57, 1975.
135. Paauw, Th.T.A.: "Some Measurements and Numerical Calculations on Turbulent Diffusion Flames," in AGARD Conference Proceedings No. 164 on "Analytical and Numerical Methods for Investigation of Flow Fields With Chemical Reactions, Especially Related to Combustion," April 1974.
136. You, H.Z. and G.M. Faeth: "Buoyant Axisymmetric Turbulent Diffusion Flames in Still Air," Comb and Flame, 44, pp. 261-275, 1982.
137. Howe, N.M., C.W. Shipman, and A. Vranos, "Turbulent Mass Transfer and Rates of Combustion in Confined Turbulent Flames," 9th Symp. (International) on Combustion, pp. 36-47, 1963.
138. Cushing, B.S., J.E. Faucher, S. Gandbhir, and C.W. Shipman: "Turbulent Mass Transfer and Rates of Combustion in Confined, Turbulent Flames, II," 11th Symp. (International) on Combustion, pp. 817-824, 1967.
139. Hellat, J., W. Lenz, and R. Gunther: "Measurements of Fluctuating Temperature in Unclosed Swirling Flames," Univ. of Karlsruhe, 1977.
140. Lewis, M.H. and L.D. Smoot: "Turbulent Gaseous Combustion Part I: Local Species Concentration Measurements," Comb. and Flame, 42, pp. 277-285, 1981.
141. Smith, P.J. and L.D. Smoot: "Turbulent Gaseous Combustion Part II: Theory and Evaluation for Local Properties," Comb. and Flame, 42, pp. 277-285, 1981.

REFERENCES (CONTD.)

142. Lightman, A.J., R.D. Richmond, L. Krishnamurthy, P.D. Magill, W.M. Roquemore, R.P. Bradley, J.S. Stutrud, and C.M. Reeves: "Velocity Measurements in a Bluff Body Diffusion Flame," AIAA Paper 80-1544, 1980.
143. Peck, R.E. and G.S. Samuelsen: "Analytical and Experimental Study of Turbulent Methane-Fired Backmixed Combustion," AIAA Journal, Volume 15, No. 5, p. 730, 1977.
144. Brum, R.D. and G.S. Samuelsen: "Assessment of a Dilute Swirl Combustor as a Bench Scale, Complex Flow Test Bed for Modeling, Diagnostics, and Fuels Effects Studies," AIAA-82-1263, 1982.
145. El-Mahallawy, F.M., F.C. Lockwood, and D.B. Spalding: "An Experimental and Theoretical Study of the Turbulent Mixing in a Cylindrical, Gas-fired Furnace," Combustion Institute, European Symposium, 1973.
146. Schefer, R.W. and R.F. Sawyer: "Pollutant Formation in Fuel Lean Recirculating Flows," NASA CR-2785, 1976.
147. Chigier, N.A. and K. Dvorak: "Laser Anemometer Measurements in Flames With Swirl," 15th Symposium (International) on Combustion, 1975.
148. Thomson, D., N.A. Chigier, and A. Ungut: "Flame Characteristics of a NASA Contra Swirler Module," Central States Section/The Combustion Institute Technical Meeting, NASA Lewis, 1977.
149. Thompson, D., N.A. Chigier, and J.M.P. Ventura: "The Effect of Preheat on the Structure of a Swirl Stabilized Flame," AIAA 78-28, 1978.
150. Owen, F.K.: "Laser Velocimeter Measurements of a Confined Turbulent Diffusion Flame Burner," AIAA 76-33, 1976.
151. Claypole, T.C. and N. Syred: "The Effect of Combustion on the Aerodynamics of Swirling Jets," The Fluids Engineering Conference, Boulder, Colorado, p. 137, 1981.
152. Toral, H.: "Velocity, Temperature and Concentration Measurements in One and One Half Sectors of a Gas-turbine Combustor with Natural Gas Fuel," Imperial College, London, Report FS/80/18, 1980.
153. Toral, H. and J.H. Whitelaw: "Velocity and Scalar Characteristics of the Isothermal and Combusting Flows in a Combustor Sector Rig," Comb. and Flame, 45, pp. 251-272, 1982.

REFERENCES (CONTD.)

154. Noyce, J.R., C.G.W. Sheppard, and F.D. Yamba: "Measurements of Mixing and Species Concentrations Within a Gas Turbine Type Combustor," Comb. Sci. Tech., 25, pp. 209-217, 1981.
155. Jones, W.P., W.C. Clifford, C.H. Priddin, and R. de Chair: "A Comparison Between Predicted and Measured Species Concentrations and Velocities in a Research Combustor," 16th Symposium (International) on Combustion, 1977.
156. Markham, D.L.: "The Dispersion of Drop Sizes in Gas Turbine Fuel Nozzle Sprays," the ASME Fluids Engineering Conference, Boulder, Colorado, 1981.
157. Foster, H.H. and R.D. Ingebo: "Evaporation of JP-5 Fuel Sprays in Air Streams," NACA RM E55K02, 1956.
158. Mizutani, Y., H. Kodama, and K. Miyasaka: "Doppler-Mie Combination Technique for Determination of Size-Velocity Correlation of Spray Droplets," Comb. and Flame, 44, pp. 85-95, 1982.
159. Tishkoff, J.M., D.C. Hammond, and A.R. Chraplyvy: "Diagnostic Measurements of Fuel Spray Dispersion," ASME Paper 80-WA/HT-35, 1980.
160. Gollahalli, S.R. and J.D. Lin: "A Comparative Study of the Structure of Burning Sprays of Number 2 and SRC-II Fuel Oils," Comb. and Flame, 44, pp. 125-135, 1982.
161. Mao, C.P., Y. Wakamatsu, and G.M. Faeth: "A Simplified Model of High Pressure Spray Combustion," 18th Symposium (International) on Combustion, p. 337, 1981.
162. Faeth, G.M.: "Evaporation and Combustion of Sprays," To be Published in Progress in Energy and Combustion Science.
163. Owen, F.K. and W.D. Bachalo: "Laser Measurements of Droplet Velocity and Size in Spray Flames," AIAA 79-0022, 1979.
164. Chigier, N.A.: "Instrumentation Techniques for Studying Heterogeneous Combustion," Central States Section/The Combustion Institute Technical Meeting, NASA-Lewis, 1977.
165. Chigier, N.A., C.G. McCreath, and R.W. Makepeace: "Dynamics of Droplets in Burning and Isothermal Kerosene Sprays," Comb. and Flame, 23, pp. 11-16, 1974.

REFERENCES (CONTD.)

166. Hayashi, S., S. Kumagai, and T. Sakai: "Propagation Velocity and Structure of Flames in Droplet-Vapor-Air Mixtures," Comb. Sci. Tech., 15, pp. 169-177, 1976.
167. Polymeropoulos, C.E. and S. Das: "The Effect of Droplet Size on the Burning Velocity of Kerosene-Air Sprays," Comb. and Flame, 25, pp. 247-257, 1975.
168. Mizutani, Y. and A. Nakajima: "Combustion of Fuel-Vapor-Drop-Air Systems: Part I - Open Burner Flames," Comb and Flame, 21, pp. 343-350, 1973.
169. Coghe, A., U. Ghezzi, and S. Pasini, "Optical Temperature Measurements in a Continuous Flow Combustion Chamber," 2nd Int. Symp. on Air Breathing Engines, Sheffield, 1974.
170. Hirano, T. and M. Kinoshita: "Gas Velocity and Temperature Profiles of a Diffusion Flame Stabilized in the Stream Over Liquid Fuel," 15th Symp. (International) on Combustion, 1975.
171. Yule, A.J., C.A. Seng, P.G. Felton, A. Ungut, and N.A. Chigier: "A Study of Vaporizing Fuel Sprays by Laser Techniques," Comb. and Flame, 44, pp. 71-84, 1982.
172. Shearer, A.J. and G.M. Faeth: "Evaluation of a Locally Homogeneous Model of Spray Evaporation," NASA CR-3198, 1979.
173. Mao, C.P., G.A. Szekely and G.M. Faeth: "Evaluation of a Locally Homogeneous Flow Model of Spray Combustion," NASA CR-3202, 1980; and Journal of Energy, Volume 4, No. 2, pp. 78-87, 1980.
174. Onuma, Y. and M. Ogasawara: "Studies on the Structure of a Spray Combustion Flame," 15th Symposium (International) on Combustion, p. 453, 1975.
175. Spadaccini, L.J., F.K. Owen, J.B. Kennedy, J.B. McVey, and C.T. Bowman: "Pollutant Formation and Energy Release in Liquid-Fuel Turbulent Diffusion Flames," AIAA Paper No. 77-53.
176. Wierzbza, I.: "An Examination of the Mechanism of Flame Stabilization by the Interaction of a Rich Two-Phase Combustible Mixture Jet with a Counter Air Stream," ASME Paper No. 82-GT-60, 1982.
177. Proctor, C.L. and A.M. Mellor: "Numerical and Experimental Examination of a Prevaporized/Premixed Combustor," AIAA-82-1074, 1982.

REFERENCES (CONTD.)

178. Ferguson, C.R. and A.M. Mellor: "Probing a Premixed/Prevaporized Type of Combustor," Purdue University Report, June 22, 1979.
179. El-Banhawy, Y. and J.H. Whitelaw: "Assessment of an Approach to the Calculation of the Flow Properties of Spray-Flames," AGARD Conference Proceedings No. 275, 1979.
180. El-Banhawy, Y. and J.H. Whitelaw: "Experimental Study of the Interaction Between a Fuel Spray and Surrounding Combustion Air," Comb. and Flame, 42, pp. 253-275, 1981.
181. Attya, A.M. and J.H. Whitelaw: "Velocity, Temperature and Species Concentrations in Unconfined Kerosene Spray Flames," ASME Paper No. 81-WA/HT-47, 1981.
182. Tuttle, J.H., R.A. Shisler, and A.M. Mellor: "Investigation of Liquid Fueled Turbulent Diffusion Flames," Comb. Sci. Tech., 14, p. 229, 1976.
183. Styles, A.C. and N.A. Chigier: "Combustion of Air-Blast Atomized Spray Flames," 16th Symp. (International) on Combustion, pp. 619-630, 1977.
184. Kawaguchi, O., G.T. Sato, Y. Yoshida, J. Suzuki, and T. Seko: "Exploratory Development on the Concept of Low Pollutant Emission Combustor," 14th Int. Congress on Combustion Engines, Helsinki, 1981.
185. Haynes, B.S. and H.G. Wagner: "Soot Formation," Prog. Energy Comb. Sci. 7, pp. 229-273, 1981.
186. Calcote, H.F.: "Mechanisms of Soot Nucleation in Flames - A Critical Review," Comb. and Flame, 42, pp. 215-242, 1981.
187. Beretta, F., A. Cavaliere, and A. D'Allesio: "Laser Excited Fluorescence Measurements in Spray Oil Flames for the Detection of Polycyclic Aromatic Hydrocarbons and Soot," Comb. Sci. Tech. 27, pp. 113-122, 1982.
188. Hurley, C.D.: "Carbon Formation by the Pyrolysis of Gas Turbine Fuels in Pre flame Regions of Gas Turbine Combustors," ASME Paper No. 82-GT-84, 1982.
189. Driscoll, J.F., D.M. Mann, and W.K. McGregor, "Submicron Particle Size Measurements in an Acetylene-Oxygen Flame," Comb. Sci. Tech., 20, pp. 41-47, 1979.

REFERENCES (CONTD.)

190. Koussa, S.S.: "A Model for Computation of Net Local Soot Generation," ASME Paper No. 82-GT-30, 1982.
191. Himes, R.M., R.L. Hack, and G.L. Samuelson: "Chemical and Physical Properties of Soot as a Function of Fuel Molecular Structure in a Swirl-Stabilized Combustor," ASME Paper No. 82-GT-109, 1982.
192. Eckbreth, A.C. and R.J. Hall: "CARS Thermometry in a Sooting Flame," Comb. and Flame, 36, pp. 87-98, 1979.
193. Kowalik, R.M., L.A. Ruth, R.B. Edelman, R.C. Farmer, E. Wong, and T.S. Wang: "Fundamental Characterization of Alternate Fuel Effects in Continuous Combustion Systems," DOE/ET/11313-11, 1982.
194. Gould, R.K., D.B. Olson, and H.F. Calcote: "Correlation of Soot Formation in Turbojet Engines and in Laboratory Flames," ESL-TR-81-09, 1981.
195. Prado, G., J. Jagoda, K. Neoh, and J. Lahaye: "A Study of Soot Formation in Premixed Propane/Oxygen Flames by In-Situ Optical Techniques and Sampling Probes," 18th Symposium (International) on Combustion, pp. 1127-1136, 1981.
196. Bockhorn, H., F. Fetting, U. Meyer, R. Reck, and G. Wannemacher: "Measurement of the Soot Concentration and Soot Particle Sizes in Propane Oxygen Flames," 18th Symposium (International) on Comb., pp. 1137-1147, 1981.
197. Flower, W.L.: "Optical Measurements of Soot Particles in Premixed Flames," Sandia Labs Report, 1982.
198. Roper, F.G. and C. Smith: "Soot Escape From Laminar Air-Starved Hydrocarbon Flames," Comb. and Flame, 36, pp. 125-138, 1979.
199. Dalzell, W.H., G.C. Williams and H.C. Hottel, "A Light-Scattering Method for Soot Concentration Measurements," Comb. and Flame, 14, pp. 161-170, 1970.
200. Kent, J.H., H. Jander and H.G. Wagner: "Soot Formation in a Laminar Diffusion Flame," 18th Symposium (International) on Combustion, pp. 1117-1126, 1981.
201. Magnussen, B.F., B.H. Hjertager, J.G. Olsen, and D. Bhaduri, "Effects of Turbulent Structure and Local Concentrations on Soot Formation and Combustion in C_2H_2 Diffusion Flames," 17th Symposium (International) on Combustion, pp. 1383-1393, 1979.

REFERENCES (CONTD.)

202. Becker, H.A. and D. Liang: "Total Emission of Soot and Thermal Radiation by Free Turbulent Diffusion Flames," Comb. and Flame, 44, pp. 305-318, 1982.
203. Becker, H.A. and S. Yamazaki: "Soot Concentration Field of Turbulent Propane/Air Diffusion Flames," 16th Symposium (International) on Combustion, pp. 681-691, 1977.
204. Prado, G.P., M.L. Lee, R.A. Hites, D.P. Hoult, and J.B. Howard: "Soot and Hydrocarbon Formation in a Turbulent Diffusion Flame," 16th Symposium (International) on Combustion, pp. 649-661, 1977.
205. Hoult, D.P.: "Laboratory Measurements in a Turbulent Swirling Flow," NASA CR-159723, 1979.
206. Janota, M.S., R.J. Crookes, S.J. Daie, M.A.A. Nazha, and M. Sodha: "Soot and Gaseous Pollutant Formation in a Burning Fuel Spray in Relation to Pressure and Air/Fuel Ratio," J. Inst. of Fuel, pp. 10-13, March 1977.
207. Bruce, T.W., H.C. Mongia, and R.S. Reynolds: "Combustor Design Criteria Validation," USARTL-TR-78-55 (B, C), February 1979 [Garrett Report 75-211682(38)].
208. El Telbany, M.M.M., and A.J. Reynolds: "The Structure of Turbulent Plane Couette Flow," Journal of Fluids Engineering, Transactions of the ASME, Volume 104, p. 367, September 1982.
209. Laufer, J.: "The Structure of Turbulence in Fully Developed Pipe Flow," NACA Report 1174, 1954.
210. Wignanski, I., and M. Fiedler: "Some Measurements in a Self Preserving Jet," Journal of Fluid Mechanics, Volume 38, Part 3, pp. 577-612, 1969.
211. Launder, B.E.: "Turbulence Models and Their Experimental Verification," Report No. HTS/73/17, Imperial College of Science and Technology, Department of Mechanical Engineering, London, April 1973.
212. Kays, W.M. and M.E. Crawford: "Convective Heat and Mass Transfer," Second Edition, Chapter 12, McGraw-Hill, 1980.
213. Fristrom, R.M. and A.A. Westenberg: Flame Structure, McGraw-Hill, 1965.
214. Schlichting, H.: Boundary Layer Theory, 6th Edition, McGraw-Hill, 1968.

REFERENCES (CONTD.)

- 215. Townsend, A.A.: The Structure of Turbulent Shear Flow, Cambridge University Press, 1976.
- 216. Wakelyn, N.T. and A.G. McLain, "Polynomial Coefficients of Thermochemical Data for the C-H-O-N System," NASA-TMX-72657, January 1975.
- 217. Chaturvedi, M.C.: Flow Characteristics of Axi-Symmetric Expansions," Proceedings, Journal of Hydraulic Division, ASCE, Volume 89, No. HY3, pp. 61-92, 1963.
- 218. Altgeld, H., W.P. Jones and J. Wilhelm: "Velocity Measurement in a Confined Swirl Driven Recirculating Flow," Experiments in Fluids, 1, pp. 73-78, 1983.
- 219. Srinivasan, R., A. Berenfeld and H.C. Mongia, "Dilution Jet Mixing Program Phase I Report," NASA CR-168031, November 1982.

